Linear Friction Welding of Ti-5.3Al-7.7V-0.5Si to Ti-6Al-4V: Processing, Characterisation and Mechanical Behaviour

by

Yu-Chung Chuang

A thesis submitted to the University of Birmingham for the degree of

Doctor of Philosophy

School of Metallurgy and Materials

College of Engineering and Physical Sciences

University of Birmingham

September 2023

Abstract

In the development of jet engines, where the reduction of component weight is paramount for improvement in efficiency, the choice of materials and manufacturing processes is critical. Titanium alloys, known for their high specific strength and excellent fatigue resistance, are well-suited materials for engine components in lower-temperature stages. Bladed discs (Blisks), offering a substantial weight reduction over the traditional mechanical assemblies, have become a standard component in jet engines, mainly as fan blisks. Linear friction welding (LFW) emerges as an ideal method for manufacturing blisks by joining blades and discs that are machined separately. LFW is capable of joining dissimilar materials, providing the opportunity to exploit different materials for discs and blades, given their exposure to different thermo-mechanical conditions in service. This research focuses on LFW of dissimilar titanium alloys: Ti-6Al-4V (Ti-64) and Ti-5.3Al-7.7V-0.5Si (Ti-575), with a particular emphasis on optimisation of processing, characterisation of microstructure and crystallographic texture, as well as assessment of mechanical performance. This work aims to enhance the understanding of LFW'd dissimilar joints for aerospace applications, specifically for blisks in the fan and compressor stages of next-generation jet engines.

The microstructure of the parent materials (PMs) and the welded joints was characterised by electron microscopy. Ti-575 parent was found to have superior hardness due to its fine secondary and tertiary α laths, compared to Ti-64 parent. In as-welded condition, a reduction of hardness was found in the heat-affected zone (HAZ) of Ti-575, where fine α laths were dissolved due to the heat experienced during LFW. Nevertheless, after applying appropriate post-weld heat treatment (PWHT), the hardness of HAZ can be recovered via the formation of fine α precipitates. The central weld zone (CWZ) and thermo-mechanically affected zone (TMAZ) both possess greater hardness compared to the PMs, thanks to the formation of fine acicular α' laths.

The crystallographic texture of the weld was measured by electron backscatter diffraction and analysed through β reconstruction and texture simulation. The CWZ exhibits an oscillation-dependent transverse α texture, inherited from the $\{11\bar{2}\}\langle 111\rangle_\beta$ simple shear texture during LFW, along with variant selection. In the Ti-575 TMAZ at the bifurcation point, within a 300×300 μm^2 region, this study discovered a unique geometry-dependent basal α texture, derived from $\{110\}\langle 001\rangle_\beta$ texture. The dependency of the texture on geometry can be attributed to the restriction of material extrusion along the bifurcation line.

The high cycle fatigue and fatigue crack growth testing were carried out to evaluate the fatigue resistance of the welded joints. Compared to the PMs, the weld exhibits superior high cycle fatigue strength and a similar fatigue crack growth resistance. PWHT has a significant impact on the fatigue crack growth threshold, as test pieces PWHT'd at 600℃ for 1 hour with furnace cooling have reduced threshold values of approximately 4.5 MPa$\sqrt{m}$, whereas test pieces PWHT'd at 500℃ achieved a threshold value of 8.3 MPa$\sqrt{m}$. The high threshold value is attributed to the strong compressive residual stress on the surface due to insufficient stress relief after PWHT at a lower temperature.

Welding of dissimilar materials presents a challenge: un-even contribution to total upset from the two materials, which is represented by relative upset. High relative upset is detrimental to the structural integrity of the welded joint. This study discovered that the extrusion of Ti-575 was delayed due to its higher flow stress at high temperatures and high heating rates. Increasing friction pressure is an effective way to reduce the conditioning time. It is predicted that the conditioning time can be eliminated by applying approximately 180 MPa of pressure. The discovery of the underlying principles of relative upset could be universally applicable for LFW involving dissimilar titanium alloys. This work provides scientific understanding of LFW of dissimilar titanium alloys and guidance for optimising the process.

Acknowledgements

First of all, I would like to express my sincere gratitude to my academic supervisors, Prof. Paul Bowen and Dr Hangyue Li, for their advice and academic guidance throughout my study at the University of Birmingham. My gratitude extends to the financial support from Rolls-Royce and EPSRC.

From Rolls-Royce, I would like to thank Dr Simon Bray for his industrial supervision and guidance on linear friction welding, Dr Chris Pretty for his support in project operation, and Mr Nigel Martin for his advice and guidance on titanium alloys. I would also like to express my appreciation to Dr David Chapman and Dr Simranjeet Singh from the University of Oxford for conducting the flow stress testing and sharing the data and test pieces.

I must also acknowledge the help I received from a huge number of people at the University of Birmingham. I would like to acknowledge Dr Hiroto Kitaguchi for his tremendous support with FIB/TEM work, Dr Jiayun Jiang for his guidance on fatigue crack growth threshold testing, Dr Tim Doel for his support with hot compression testing, Dr Elizabeth Nuttall for guidance on high cycle fatigue testing, Dr Chris Cooper for his support with tensile testing, Dr Milorad Novovic for his assistance with fracture toughness testing, Mr David Price for technical assistance, and Miss Humayra Ibrahim for her support in the HAP study. I further extend my thanks to my colleagues, Anthony, Cameron, Henry, Huize, Nicole, Nik, Tim, Yuean, and Yunpeng, for cultivating a cheerful work environment.

Finally, I must express my gratitude to my family for their support throughout this journey. In particular, I want to extend heartfelt thanks to my wife, Yu-Jing, for her enduring love, unwavering support, constant encouragement, and dedicated efforts in taking care of our baby, Leo, allowing me to focus on my research and studies.

Table of Contents

List of Tables

List of Figures

Chapter 1

Introduction

1.1 Background

In jet engine development, the choice of materials and the manufacturing processes are essential to improve the engine efficiency. High operating temperature and good fatigue resistance together with low weight of components are the key factors of concern. As illustrated in Figure 1.1, titanium alloys are widely used in jet engine components, specifically in fan and low-pressure compressor stages due to their high strength-to-density ratio, excellent fatigue resistance and strength at temperatures below 600℃, along with good weldability. Figure 1.2 illustrates a Rolls-Royce Trent 900 engine with common load regimes for titanium structural components.

As reducing the weight of jet engines is crucial, integrally bladed discs (Blisks) offer a significant weight reduction by 30% [1], compared to the traditional mechanically assembled blades and discs due to the removal of the mechanical clamp design at the aerofoil root [2], as shown in Figure 1.3. Blisks can be manufactured purely by machining raw material down to the final dimensions. However, this process produces a huge amount of waste material, as

a result, the buy-to-fly ratio of machined components is normally more than 10:1 [3]. Linear friction welding (LFW) is found to be a well-suited method to join the blades and disc, this process helps reduce the buy-to-fly ratio significantly, while still preserving good mechanical properties in the joint. In addition, LFW has many advantages over traditional arc welding techniques, such as solid-state joining nature, which prevents dramatic change in microstructure and mechanical properties, and keeps a narrower heat-affected zone (HAZ). Besides, the self-cleaning mechanism in LFW allows asperities and inclusions to be naturally extruded during the process, leading to a defect-free joint [4]. LFW is also capable of joining dissimilar materials, which allows engine designers to have the freedom to choose different materials for the disc and blades. Since the stress and temperature conditions in service for discs and blades are different [5], dissimilar welds provide the possibility to optimise the choice of materials for requirements specifically for discs and for blades, which is not possible for manufacturing blisks by machining.

In terms of the choice of materials, Ti-6Al-4V (Ti-64) is an $\alpha + \beta$ titanium alloy that has been widely used in the aerospace industry due to its excellent material properties and relatively low cost [6], even though the service temperature of Ti-64 is limited to 300℃ due to its insufficient oxidation resistance and high affinity to nitrogen at higher temperatures [7]. The limitation on service temperature restricts the application of Ti-64, making it only suitable for low-temperature components such as fan blisks in jet engines. Over the years, efforts have been made by titanium manufacturers around the world to develop advanced titanium alloys with better high-temperature capabilities [8]. A variety of $\alpha + \beta$ titanium alloys have been developed with increased maximum service temperature and improved mechanical properties, including IMI-550, Ti-6242, Ti-6246, IMI-834, and Ti-1100. Currently, the maximum service temperature of titanium alloys has been pushed to 600℃, thanks to the development of Ti-1100 [9].

Ti-6246 has been intensively studied by Rolls-Royce for its improved fatigue strength and higher maximum service temperature [10–12]. However, several disadvantages have been found in Ti-6246. For instance, the weldability of Ti-6246 is very poor. When joining Ti-6246 to Ti-64 by LFW, Ti-6246 is significantly harder to weld, uneven amount of material was extruded between Ti-6246 and Ti-64, resulting in high relative upset. Poor weldability of Ti-6246 not only leads to more Ti-64 being wasted during LFW but also hinders the self-cleaning mechanism, causing a higher possibility of inclusions retained in the welds. Furthermore, the price of Ti-6246 is also more expensive than Ti-64. Because of the drawbacks of Ti-6246, engine manufacturers are actively searching for alternative titanium alloys.

Ti-5.3Al-7.7V-0.5Si (Ti-575), commercially known as TIMETAL® 575, is a newly developed $\alpha + \beta$ titanium alloy with improved fatigue and tensile properties whilst maintaining similar ductility and density to Ti-64. The alloying elements in Ti-575 are intentionally chosen to be similar to Ti-64, thus allowing the usage of scrap Ti-64 as raw material to manufacture Ti-575. Due to its novelty, research on Ti-575 [13–17] is limited compared to the number of existing studies on Ti-64. Furthermore, to the best of the author's knowledge, there is yet no study on LFW'd Ti-575 at the time of writing. Therefore, the characterisation and assessment of Ti-575 after LFW are of interest for its potential application in the aerospace industry. As dissimilar welds are more beneficial for their ability to satisfy requirements specifically for blades and discs, welding Ti-575 to Ti-64 is of great interest for the application of fan and compressor blisks in future generation jet engines.

1.2 Objectives

To use the new type of dissimilar LFW of Ti-64 and Ti-575 for blisks applications in jet engines, thorough characterisation and assessment of the weld is necessary. The current study aims to provide an in-depth understanding of LFW'd Ti-64:Ti-575 joints in several

aspects, including microstructure characterisation, texture analysis, mechanical testing, and processing optimisation.

For microstructure characterisation, the objectives include investigating the microstructure within each weld zone, establishing microstructure evolution in as-welded and post-weld heat-treated (PWHT'd) conditions, and identifying the crystal structure and chemical composition of each phase that exists within the microstructure. A comprehensive understanding of the microstructure in the weld helps establish the process-microstructure-properties relationship of the LFW'd joint.

In terms of texture analysis, it is known that anisotropy in mechanical properties of titanium alloys is highly associated with the existence of strong texture. Such texture arises particularly from processes involving linear motion, such as unidirectional rolling and LFW. The study on the texture aims to identify the texture in each weld zone, to appreciate the texture development mechanism, and to rationalise the anisotropy in mechanical properties. Furthermore, it is known that titanium alloys suffer from cold dwell fatigue, which has caused a total of nine engine failures to date [18]. Reports on cold dwell fatigue indicate that the cracks were initiated from macrozones, also called micro-textured regions, which are clusters of adjacent primary α grains with similar crystallographic orientation inherited from α colonies during alloy processing due to insufficient deformation to break down the grains [19, 20]. Therefore, texture analysis is crucial to detect the existence of macrozones in the weld to assess its susceptibility to cold dwell fatigue.

Mechanical testing of the weld is necessary to assess the structural integrity of the weld. In service, the loading condition of blisks involves a combination of low cycle fatigue and high cycle fatigue, as illustrated in Figure 1.4. Low cycle fatigue results from every flight journey, whereas high cycle fatigue results from rotational vibration [21]. Since the number of cycles from the high-frequency vibration is unpredictably large, if the stress induced by the vibration could cause crack growth, the crack will grow unpredictably and eventually lead to a catastrophic failure. Therefore, among all kinds of mechanical properties fatigue crack

growth threshold (ΔK_{th}) is of the most interest, as it is essential to ensure that the stress intensity factor range ΔK induced by the vibration and a crack smaller than the resolution of non-destructive examination never exceeds the ΔK_{th} of the weld. If the criteria of ΔK_{th} is satisfied, the damage tolerance approach based on the fatigue crack growth curve can be used to estimate the fatigue life of the weld in the presence of a crack. In addition, the fatigue life estimated by a stress-based S-N curve is also of interest to learn the number of cycles (i.e. number of flight journeys) the weld can withstand under the in-service loading condition in the absence of a crack. Fracture toughness is also worth investigating for us to learn the maximum allowable crack length under service loading conditions before catastrophic failure occurs. Moreover, as several distinct zones can be observed in the weld, each weld zone has a unique thermal history, hence different microstructure and properties. It is necessary to investigate the mechanical properties of the entire weld to inspect if there is any weakness in the weld. Furthermore, in general, a PWHT is carried out after LFW to relieve the residual stress. The temperature and duration of the PWHT have a huge effect on the mechanical properties of the weld. Higher temperature and longer duration usually result in better stress relief, however, some mechanical properties may be compromised. Therefore, it is crucial to investigate the optimal PWHT condition.

In LFW process, when welding the same materials, a solid, defect-free joint can be achieved as long as suitable welding parameters (e.g. friction pressure, frequency, and amplitude) are used. However, when welding dissimilar materials, the amount of material extruded from each material may not be the same, due to different weldability between the two materials. This uneven extrusion behaviour leads to the waste of material, inhibits the self-cleaning mechanism, and increases the risk of retained inclusions, which is detrimental to the structural integrity. Therefore, the study of processing aims to understand the nature of the uneven extrusion behaviour, to investigate the key material properties that account for this behaviour, and to provide a guide to improve LFW of dissimilar materials.

1.3 Outline of the Thesis

The current thesis consists of detailed studies of microstructure characterisation, texture development, mechanical properties, and processing of LFW'd Ti-64:Ti-575 joints. Beginning with a general introduction in Chapter 1, the literature review is provided in Chapter 2, including metallurgy of titanium alloys, texture, LFW, and fracture mechanics. The methodology and experimental procedures used in this thesis are described in Chapter 3. The results of the current study are presented in the following four chapters. Chapter 4 includes the microstructure characterisation of the weld in both as-welded and PWHT'd conditions. Chapter 5 presents the crystallographic texture analysis results of the weld. Chapter 6 includes the results of mechanical testing of the weld, such as high cycle fatigue, fatigue crack growth and fracture toughness testing. Chapter 7 presents the study on the processing of dissimilar LFW. The nature of the processing issue in dissimilar LFW can be explained, and suggestions for processing optimisation are proposed. Finally, a summary of this thesis and proposed future work are provided in Chapter 8.

A part of results in this thesis has been published in a conference paper at the 15th World Conference on Titanium. This paper is attached in Appendix A. Appendix B to D includes detailed information used in this thesis, including orientation matrices, programming scripts, and fractography. Additionally, preliminary investigation on hard alpha particles in self-similar LFW'd Ti-64 was carried out. The methodology and results can be found in Appendix E.

Chapter 2

Literature Review

This chapter aims to provide in-depth background for the current study of titanium alloys after linear friction welding (LFW). The first part of this chapter will introduce the metallurgy of titanium alloys in terms of alloy classification, phases and phase transformations, as well as processing routes and associated microstructures. Particularly, this part of the chapter focuses on $\alpha + \beta$ titanium alloys as they are the most used type of titanium alloys in the aerospace industry. A detailed review of Ti-6Al-4V (Ti-64) and Ti-5.3Al-7.7V-0.5Si (Ti-575) is also provided. The second part focuses on the review of texture. The basic knowledge of texture is introduced, such as the representation of orientation and texture. Several texture characterisation techniques and typical textures found in titanium alloys are also introduced. The third part of this chapter concentrates on LFW. Details about the phases, process variables, and temperature distribution in LFW'd joints are introduced. Topics related to the product of LFW are also mentioned, such as metallurgy and residual stress of the welds. A review of dissimilar LFW and the application of LFW on blisk repair are also provided. Finally, a review of fracture and fatigue mechanics is presented. The

theory of linear elastic fracture mechanics is introduced, along with some mechanisms of fatigue crack growth in each regime.

2.1 Metallurgy of Titanium Alloys

2.1.1 Pure Titanium

Titanium, like most other pure metals, is a crystalline material in the solid state. There are many stable crystal structures in titanium, each crystal exists within a particular temperature range. The transformation between different crystal structures is defined as allotropic transformation, and the corresponding transformation temperature is defined as transus temperature [22].

At low temperatures, pure titanium exhibits a hexagonal close-packed (HCP) structure, known as α phase or α-Ti. At high temperatures, titanium undergoes an allotropic transformation into a body-centred cubic (BCC) structure, known as β phase or β-Ti. The transus temperature, or so-called β transus, is at 882℃ for pure titanium. For titanium alloys, the exact β transus is affected by the type and the amount of the alloying elements [23].

2.1.2 Titanium Alloys

Titanium is capable of forming solid solutions with substitutional alloying elements as long as their size factor is within $\pm 20\%$ [24]. Titanium and its alloys can also dissolve interstitial alloying elements, such as carbon and oxygen, within a wide range of temperatures [25].

The alloying elements in titanium can be categorised into three types: α stabilisers, β stabilisers, and neutral elements, depending on their ability to affect β transus [22]. This behaviour is related to the number of valence electrons of the alloying element. Elements with less than four valence electrons tend to stabilise the α phase and raise the β transus. These elements are commonly referred to as α stabiliser. On the other hand, alloying

elements with more than four valence electrons are known as β stabiliser. They tend to stabilise the β phase and reduce the β transus. For the elements with exactly four valence electrons, they have limited effect on β transus, hence they are referred to as neutral elements [25].

Figure 2.1 shows typical phase diagrams for each type of alloying elements. Among all α stabilisers, aluminium is the most important and frequently used substitutional element. Boron, gallium, and germanium also belong to α stabilisers, however, they are not used as alloying elements due to their lower solubility compared to aluminium [12]. Interstitial elements, such as carbon, oxygen, and nitrogen, also stabilise α phase. Nevertheless, they are generally not used as the main α stabilising elements. The β stabilisers can be divided into two groups: β isomorphous and β eutectic. These β stabilisers form different phase diagrams, as shown in Figure 2.1. For β isomorphous elements, molybdenum and vanadium are of most importance due to their superior solubility in titanium. β eutectic elements, even with a minimal addition, tend to form intermetallic compounds. Iron, silicon, manganese, and chromium are commonly used β eutectic elements. In terms of neutral elements, elements that share the same group number as titanium on the periodic table, such as zirconium and hafnium, fall within this category. Tin is another neutral element which is commonly used in titanium alloys. These neutral elements are not neutral in terms of strength, as they tend to strengthen the α phase [22].

2.1.3 Classification of Titanium Alloys

With α and β stabilisers, as well as neutral alloying elements, titanium has a variety of alloys. Putting thermo-mechanical processing aside, the alloying elements themselves can have a huge impact on the material properties of the titanium alloys. Titanium alloys are generally categorised into three types: α alloys, $\alpha + \beta$ alloys, and β alloys. There are many

different criteria to classify titanium alloys. Classifying titanium alloys by their composition, although convenient, can be misleading. Generally, titanium alloy classification involves alloy composition, response to heat treatment, and material properties. A widely accepted criterion is illustrated in Figure 2.2.

2.1.3.1 α Alloys

The α alloys include commercially pure titanium (cp-Ti) and alloys with only α stabilisers and/or neutral elements. Occasionally, little β stabilisers can be included in α alloys. Nevertheless, α alloys should exhibit single α phase at room temperature. The α alloys usually have lower density compared to other titanium alloys as the dominant α stabiliser, aluminium, has only half the specific weight of titanium, let alone other heavy elements alloyed in β alloys. The diffusion rate in α alloys is at least two orders of magnitude lower than that in β alloys, this gives rise to its excellent resistance to creep, corrosion, and oxidation [22]. Furthermore, α alloys usually have relatively low strength with good ductility and weldability [23]. In terms of formability, α alloys have prominent work hardening behaviour, which restricts their deformation temperature to above β transus or near β transus [22].

2.1.3.2 $\alpha + \beta$ Alloys

The $\alpha + \beta$ alloys have a good balance of α and β stabilisers. They exhibit a mixture of α and β phase in equilibrium at room temperature. When there is enough β stabiliser present in the alloy, rapid cooling from the β phase can potentially develop a martensitic microstructure. The $\alpha + \beta$ alloys possess a good balance of properties between the α and β alloys. Specifically, they have good fatigue and fracture properties as well as strength and ductility. Consequently, $\alpha + \beta$ alloys has the widest industrial applications compared to other types of titanium alloys. Among all titanium alloys, Ti-64 is by far the most popular

$\alpha + \beta$ alloy. Apart from Ti-64, the other alloy studied in this thesis, Ti-575, is also classified as an $\alpha + \beta$ alloy. Therefore, the rest of this thesis will mainly focus on $\alpha + \beta$ alloys.

2.1.3.3 β Alloys

If the amount of β stabiliser increases to a point where fast cooling from the β phase does not exhibit martensitic transformation, the alloys can be classified as β alloys. The β alloys can be further subdivided into metastable β alloys and stable β alloys, depending on whether dual phase microstructure appears. However, the stable β alloys have not found their commercial applications yet, thus the term 'β alloys' is commonly referred to as metastable β alloys [23]. Compared with α alloys, the β alloys usually have excellent yield strength and high hardness value, while they also maintain good ductility. In terms of formability, β alloys have better cold formability compared with α alloys, since β alloys have a higher volume fraction of the β phase, and that the β phase with BCC structure is softer than the α phase with HCP structure. Certain metastable β alloys can even undergo a cold working process at room temperature [22].

2.1.4 Equilibrium Phases in $\alpha + \beta$ Titanium Alloys

In titanium alloys, equilibrium phases exist when the microstructure achieves steady-state conditions. This kind of phases appear on titanium phase diagrams, and they can be obtained by heat treatments with a slow heating or cooling rate. There are numerous equilibrium phases in titanium alloys, depending on the type and the amount of the alloying elements. The current thesis focuses on $\alpha + \beta$ titanium alloys with a Ti-Al-V system (using aluminium and vanadium as alloying elements), three common equilibrium phases in $\alpha + \beta$ alloys are introduced, namely α, β, and α_2 phase.

2.1.4.1 α Phase

The α phase in titanium alloys (α-Ti) has an HCP crystal structure, as shown in Figure 2.3 (a). The space group of this structure is $P6_3/mmc$, there are two atoms within a unit cell located at (0,0,0) and $(1/3, 2/3, 1/2)$, respectively [26]. The hexagonal unit cell in titanium differs from the ideal HCP structure, where the lattice parameters of α-Ti in pure titanium are $a = 2.95$ Å and $c = 4.68$ Å. The lattice parameters lead to $c/a = 1.587$, which is smaller than the c/a ratio in the ideal HCP structure (1.633) [10], also is significantly smaller than other elements with HCP crystal structure, such as magnesium, zinc, and cadmium [27]. It is worth noting that the reduced c/a ratio plus the different deformation modes have significant impact on the texture development in α-Ti [28].

There are primarily three close-packed planes in α-Ti, namely the basal (0002) plane, prismatic $\{10\bar{1}0\}$ planes, and pyramid $\{10\bar{1}1\}$ planes, as illustrated in Figure 2.4. The close-packed directions in α-Ti are $\langle 11\bar{2}0\rangle$, which is equivalent to the lattice $\langle a\rangle$ directions. The close-packed planes and directions together form the primary slip systems in α-Ti, namely $\langle \vec{a}\rangle$ slips, along either of the close-packed planes [23]. Note that the $\langle \vec{a}\rangle$ slip along the pyramid plane is not considered as an independent slip system, since the deformation produced by a pyramid $\langle \vec{a}\rangle$ slip is exactly the same as the combination of a basal $\langle \vec{a}\rangle$ slip and a prismatic $\langle \vec{a}\rangle$ slip [22].

Secondary slip systems in α-Ti, although being more difficult to activate, have also been observed by transmission electron microscope in numerous titanium alloys [29, 30]. This type of slip systems may be considered as $\{10\bar{1}1\}\langle 11\bar{2}3\rangle$, however, although $\{10\bar{1}1\}\langle 11\bar{2}3\rangle$ can be observed in other materials with a HCP structure, such as magnesium [31], it has not been observed in titanium alloys. Instead, slip along the second order pyramid planes $\{11\bar{2}2\}$ in

$\langle 11\bar{2}3 \rangle$ directions can be activated when the unit cell is subjected to a tensile load parallel to the c-axis, as $\{11\bar{2}2\}$ has a higher Schmid factor compared to $\{10\bar{1}1\}$ in this scenario [23]. Therefore, the second order pyramid slip is usually referred to as pyramid slip or $\langle \vec{c} + \vec{a} \rangle$ slip. The $\{11\bar{2}2\}\langle 11\bar{2}3 \rangle$ slip systems have also been observed in other hexagonal metals such as zinc and cadmium [32].

The activation of the slip systems in α-Ti has a dependency on the temperature. As illustrated in Figure 2.5, the critical resolved shear stress (CRSS) of prismatic $\langle \vec{a} \rangle$ slip is the lowest at low temperatures, indicating that prismatic slip should occur the most at room temperature. Whereas at high temperatures, the difference in CRSS between the basal $\langle \vec{a} \rangle$ slip and prismatic $\langle \vec{a} \rangle$ slip becomes smaller. Across the entire temperature range, pyramid $\langle \vec{c} + \vec{a} \rangle$ slip is always more difficult to activate in comparison to basal and prismatic $\langle \vec{a} \rangle$ slip, this implies that few grains would experience pyramid slip within a polycrystalline α-Ti [23].

With HCP crystal structure, α-Ti naturally inherits the intrinsic anisotropy arising from the c/a ratio. This has significant consequences on its mechanical properties. Figure 2.6 shows the variation of Young's Modulus (E) with respect to the angle between the c-axis and the direction of the tensile load for an α-Ti single crystal. Elasticity modulus varies from 100 to 145 GPa – almost 50% increase when loading parallel to the c-axis, compared to loading perpendicularly. This depicts the maximum degree of effect of texture on the elasticity of titanium alloys, as the degree of anisotropy depends on the intensity of texture in polycrystalline titanium alloys [23].

2.1.4.2 β Phase

The β phase in titanium alloys (β-Ti) has a BCC crystal structure, as shown in Figure 2.3 (b). The space group of this structure is Im3m, there are two atoms within a unit

cell located at (0,0,0) and $(1/2, 1/2, 1/2)$, respectively [26]. The lattice parameter of β-Ti measured in pure titanium at 900℃ is $a = 3.31$ Å [33]. At temperatures above β transus, this BCC structure is more stable than the HCP structure, since BCC is not a close-packed crystal structure and has more space to accommodate thermal vibration at elevated temperatures [24].

The slip systems in BCC structure are generally observed in closed-packed directions, namely $\langle 111 \rangle$. In terms of slip planes, {110}, {112}, and {123} have all been identified as slip planes in BCC structure, since there is no truly closed-packed plane in BCC structure, hence, the slip lines observed in BCC often appear wavy and irregular [32]. With the slip planes and directions mentioned above, there are 48 slip systems in β-Ti in total. As the number of slip systems in β-Ti is far more than that in α-Ti, generally β-Ti has lower resistance to plastic deformation.

2.1.4.3 α_2 Phase

The α_2 phase in titanium alloys has an ordered HCP structure. For Ti-Al system, the chemical formula of α_2 phase is Ti_3Al. The space group of this structure is $P6_3/mmc$, with a DO19 structure. α_2 phase only forms during ageing at elevated temperatures when titanium alloys contain more than 6 wt.% of aluminium [10]. As the alloys studied in the current research (Ti-64 and Ti-575) both do not contain more than 6 wt.% of aluminium, it is not expected to observe the presence of α_2 phase within these alloys.

2.1.5 Phase Transformations in Titanium Alloys

Titanium alloys undergo an allotropic phase transformation when β transus is reached. The allotropic phase transformation can be further divided into two types: diffusional and martensitic transformation. Both types of transformation follow the Burgers Orientation relationship.

2.1.5.1 Burgers Orientation Relationship

The crystallographic relationship between α and β phase is given by the Burgers orientation relationship [34], which can be expressed as

$$\{110\}_\beta \ // \ \{0001\}_\alpha \tag{2.1}$$

$$\langle 1\bar{1}1\rangle_\beta \ // \ \langle 11\bar{2}0\rangle_\alpha \tag{2.2}$$

The Burgers orientation relationship was initially confirmed for zirconium, and then later for titanium [35]. Following the Burgers orientation relationship, the $\{110\}$ planes in the β phase transform into the $\{0001\}$ planes in the α phase. Since the planar distance between the $\{0001\}_\alpha$ planes is slightly larger than the distance between $\{110\}_\beta$ planes, phase transformation between α and β phase causes atomic distortion, as illustrated in Figure 2.7. This results in a reduction of c/a ratio in α-Ti HCP structure, therefore its c/a ratio (1.587) falls below the value of an ideal HCP structure (1.633) [22].

According to the Burgers orientation relationship, there are a total of 12 α variants that can nucleate from the $\beta \rightarrow \alpha$ phase transformation, as there are six distinct $\{110\}$ planes in BCC crystal together with two $\langle 1\bar{1}1\rangle$ directions. From a single β crystal, each combination of the $\{110\}$ planes and $\langle 1\bar{1}1\rangle$ directions can form an α crystal with a distinct crystallographic orientation. The Burgers orientation relationship is of central importance in the microstructure evolution and texture development in titanium alloys [10].

2.1.5.2 Diffusional Transformation

The diffusional transformation occurs when the temperature moves across the β transus at a relatively slow rate during thermal processing, which provides sufficient time for alloying element to diffuse across the phase boundary. The phase in the microstructure transforms when its chemistry reaches the composition of the other phase.

When cooling from β phase, in addition to obeying the Burgers orientation relationship, the diffusional phase transformation also involves nucleation and growth of α phase. The nucleation of α phase can be categorised by the location, for example, grain boundary α, which nucleates at the boundary of β grains. The nucleation of α phase can also be categorised by the time of formation during different steps of heat treatment, such as primary and secondary α [36]. Although both nucleate within β grains, the primary α usually refers to the α grains formed during the first cooling segment while the secondary α refers to those that formed during the second cooling segment within a series of thermal processing. Since the primary α grains formed earlier, they normally have a longer time to grow than the secondary α grains, therefore, in general, the primary α grains appear coarser while the secondary α grains appear finer. If a more elaborate heat treatment procedure is used, even finer tertiary α phase may form.

Figure 2.8 schematically illustrates the diffusional phase transformation process in titanium alloys. In the beginning, the entire microstructure consists of 100% β phase above β transus. When the temperature starts to fall below β transus by slow cooling, the nucleation of α phase preferentially occurs at β grain boundaries [37]. When the temperature reduces further, α phase can nucleate at the grain boundary α and grow into the β grains. Since within a single β grain, the nucleation and growth of the α phase follows the Burgers orientation relationship with that β grain, there are only 12 possible α variants that can form within that β grain. As the α phase can only grow according to the previously mentioned 12 orientation relationships, they tend to form parallel lamellar plates (so-called α colony) [22, 23]. The α plates continue to grow along the orientation relationship until either reaching the β grain boundary or being blocked by other α plates. Thermal processing

with multiple cooling segments allows secondary α phase nucleate from the primary α plates and in turn, grow into the retained β phase. Meanwhile, the primary α plates can grow laterally and become coarser.

The cooling rate primarily determines the rate of α nucleation and growth, therefore it plays an important role in determining the number of α colonies and the size of individual α plate. The Burgers orientation relationship results in multiple repetitively oriented α lamellae, thus the $\alpha + \beta$ titanium alloys usually exhibit a characteristic microstructure, which is commonly referred to as basket-weave or Widmanstätten structure [22].

2.1.5.3 Martensitic Transformation

The martensitic transformation takes place when the thermal processing occurs rapidly across the β transus, restricting the time for diffusion to occur. Hence, it is commonly known as a diffusionless transformation. The critical cooling rate for martensitic transformation to occur depends on the alloying elements, for $\alpha + \beta$ alloys, a cooling rate faster than 1000℃/min is required [23]. Supercooling is essential to activate martensitic transformation [10], in other words, the driving force of martensitic transformation is the drop in free energy of the system [38]. Since the diffusion of alloying elements is limited, the chemical composition of the phases remains unchanged following the transformation. However, the martensitic transformation involves a cooperative movement of atoms. Such movement can happen extremely fast, which allows martensite to grow regardless of thermal activation [39]. Consequently, the phases that form after the martensitic transformation possess distinct crystal structures compared to the prior phase [24]. This distinction in crystal structure serves as the primary criterion for determining the occurrence of a martensitic transformation.

The martensite start temperature (M_s) is approximately 50℃ below the equilibrium β transus in pure titanium [24]. The M_s is a function of the cooling rate, generally, a faster cooling rate yields higher M_s [40]. In most of the titanium alloys, the difference between M_s and martensite finish temperature (M_f) is less than 25℃ [24], therefore, usually the observation of martensitic transformation is fully completed (little to no retained β phase observed with martensite phase) [41].

The phases that result from martensitic transformation are all metastable phases, and as their chemical composition inherits from the prior β phase, their composition does not conform with the equilibrium composition. The martensitic phases can be considered as supersaturated phases, if annealing heat treatment is provided after quenching, they can then transform into equilibrium phases. The metastable phases formed from martensitic transformation are introduced in Section 2.1.6.

2.1.6 Metastable Phases in $\alpha + \beta$ Titanium Alloys

In titanium alloys, metastable phases may appear when the microstructure does not reach steady state conditions. This kind of phases does not appear on phase diagrams, and they can be obtained by heat treatments with a relatively fast heating or cooling rate. Generally, most of the metastable phases arise with martensitic transformation during fast cooling/quenching, where diffusion of alloying elements is limited. There are numerous types of martensite that can form in titanium alloys, they generally are categorised by their crystal structures, such as hexagonal, orthorhombic, face-centred cubic, and face-centred orthorhombic [42]. However, face-centred cubic and face-centred orthorhombic have been considered artefacts or thin foil versions of bulk orthorhombic martensite [43]. The hexagonal and orthorhombic martensite are commonly observed in titanium alloys, they are often referred to as α' with HCP structure and α'' with orthorhombic structure. The athermal omega phase (ω) is a common martensite in β titanium alloys, it may also appear in the $\alpha + \beta$

alloys after quenching when there is sufficient β stabiliser. Figure 2.9 schematically illustrates the quenched products with respect to the atomic fraction of β stabiliser in titanium alloys. Generally, α' phase forms when there is less β stabiliser in the alloy. With the increase of β stabiliser, α'' phase starts to form, followed by the ω phase, until there is enough β stabiliser for 100% β phase to retain after quenching. In this section, details on metastable α', α'', and ω phases in $\alpha + \beta$ titanium alloys are introduced.

2.1.6.1 α' Phase

The α' phase in titanium alloys produced by martensitic transformation has an HCP crystal structure. Similar to the α phase, the α' phase shares the same Burgers orientation relationship with the prior β phase [27], as described in Equation (2.1) and (2.2). The similarity in crystal structure between α and α' phases increases the difficulty in the identification between the two phases, however, it is feasible to distinguish them by their difference in chemical composition. As α' phase forms from diffusionless transformation, its chemistry inherits that of prior β phase. Whereas α phase forms from diffusional transformation, α stabilising elements tend to diffuse into the α phase, while β stabilising elements tend to diffuse away from the α phase. Hence, α phase generally has more α stabiliser than α' phase in titanium alloys, this characteristic can be used as the primary criterion to identify these two phases.

The lattice correspondence between α and β phase is illustrated in Figure 2.10. As α' phase shares the same crystal structure as the α phase, the lattice correspondence also applies to α' phase. As mentioned earlier in Figure 2.7, the phase transformation between BCC and HCP structure is associated with atomic distortion (or some refer to lattice strain). Such transformation is also accompanied by the shearing process, or so-called atomic shuffle [44],

as illustrated in Figure 2.11, where the atoms in layer B collaboratively shift to the atomic stacking positions in the HCP unit cell, as elaborated in several previous literature [34, 43–45].

As martensitic transformation occurs rapidly, the time for the growth of α' phase is extremely limited. Nevertheless, the α' phase still follows the Burgers orientation relationship, hence they tend to grow along specific crystallographic orientations. Therefore, the morphology of α' are usually lath or acicular martensite [42]. The acicular α' laths are extremely fine, their thickness can sometimes be less than 100 nm, depending on the cooling rate.

In ferrous materials, there is a well-known hardening effect associated with martensitic transformation owing to the structural distortion resulting from interstitial carbon [39]. However, even though the fine martensitic α' laths do increase the hardness of titanium alloys, the strengthening mechanism in titanium alloys is different from that in steels. As the martensite in titanium consists of supersaturated substitutional elements, it does not benefit from the interstitial hardening effect which occurs in steels, instead, it is generally considered that martensitic α' increases hardness due to its fine size [46]. If subjected to tempering treatment, it has been reported that the α' laths decompose to α phase with β precipitates forming at the boundaries of α plates [47].

As martensitic transformation still follows the Burgers orientation relationship, a total of 12 variants are possible to grow within a single prior β grain. However, it has been reported that these 12 variants do not always have the same probability of nucleation. In other words, variant selection may occur during martensitic transformation [24, 48].

2.1.6.2 α'' Phase

The martensitic α'' phase in titanium alloys has an orthorhombic crystal structure with shifted face-centred atoms, similar to the orthorhombic structure observed in α-uranium [49–51], which consists of a base-centred orthorhombic unit cell with shifted face-centred atoms, as shown in Figure 2.12. The lattice parameters of α'' phase are $a = 3.01$ Å, $b = 4.97$ Å, and $c = 4.68$ Å [10]. The space group of this structure is Cmcm, there are 4 atoms within a unit cell located at (0,0,0), $(1/2, 1/2, 0)$, $(0, y + 1/2, 1/2)$, and $(1/2, y, 1/2)$, where y is the atomic shearing displacement, or so-called atomic shuffle. The atomic shuffle y is a function of β stabilising content, the value of y ranges from 0 to 1/6. It was measured that y is approximately 0.1 for Ti-V alloys with 25-30 at.% vanadium [44]. The concept of atomic shuffle can be applied to BCC and HCP as well, as illustrated in Figure 2.11, where BCC structure equivalently has $y = 0$, and HCP structure equivalently has $y = 1/6$. As the atomic shuffle of orthorhombic structure always falls between that of BCC and HCP structures, it can be considered that essentially α'' is a transitional phase between β phase and α' phase during martensitic transformation. In other words, $\beta \rightarrow \alpha''$ transformation is crystallographically an incomplete $\beta \rightarrow \alpha'$ transformation, as elaborated in several previous literature [44, 50, 52].

The formation of α'' phase primarily depends on the amount of β stabiliser in the alloy, as illustrated in Figure 2.9, a sufficient amount of β stabiliser is required for the martensitic product changes from α' to α'' [38, 53, 54]. Some studies suggested that β stabilisers like Niobium and Molybdenum tend to retain the eight co-ordinations in BCC structure, hence hindering the formation of hexagonal α' phase [38, 51]. The α'' phase was also found in Ti-Al-V alloys, where aluminium seems to stabilise α'' phase. In addition to rapid cooling, stress-induced martensitic α'' phase has also been reported in several studies [55–57].

The orientation relationship between orthorhombic α'' phase and β phase is given by [58, 59]

$$\{110\}_{\beta} \;//\; \{001\}_{\alpha''} \tag{2.3}$$

$$\langle 1\bar{1}1\rangle_{\beta} \;//\; \langle 110\rangle_{\alpha''} \tag{2.4}$$

Considering the symmetry of BCC and orthorhombic structure, there are a total of 12 possible α'' variants that can form from the same prior β grain, coincidently it is the same number as the hexagonal α' variants.

However, unlike α' phase which is harder than the α phase, the α'' phase is reported soft and ductile at room temperature in numerous studies [10, 38, 60–63]. It is still unclear why martensitic α'' possesses unusual low hardness, a study suggested that the smaller residual stress resulting from BCC to orthorhombic phase transformation in comparison with transformation from BCC to HCP may contribute to less work hardening effect [38]. Nonetheless, the significant difference in hardness between α' and α'' phase serves as a decent criterion to distinguish the two martensitic phases.

2.1.6.3 ω Phase

The ω phase exhibits a hexagonal structure characterised by $a_{\omega} = \sqrt{2}a_{\beta}$ and $c_{\omega} = (\sqrt{3}/2)a_{\beta}$. The basal plane of the ω phase aligns parallel to the $\{111\}_{\beta}$ planes, resulting in the presence of four ω variants within a single β grain [64]. The ω phase has garnered significant interest due to its ability to considerably reinforce the β phase and, in turn, lead to embrittlement of the alloy. This phenomenon has been observed in various metastable β titanium alloys [65] as well as $\alpha + \beta$ titanium alloys [66–68]. As illustrated in Figure 2.9, enough β stabiliser in the alloy is required for the quench product to change from orthorhombic α'' to ω phase.

2.1.7 Microstructures in $\alpha + \beta$ Titanium Alloys

The microstructure in titanium alloys is predominantly determined by the thermo-mechanical processing route. The changes in microstructure can have a significant influence on the mechanical properties of the alloys. Therefore, establishing a process-microstructure-properties relationship is always of interest in research on titanium. Generally, there are three types of microstructures in $\alpha + \beta$ titanium alloys, namely fully lamellar microstructure, fully equiaxed microstructure, and bi-modal microstructures containing equiaxed primary α grains and lamellar $\alpha + \beta$ region. The morphology of these microstructures and associated processing routes will be introduced in the following sections.

2.1.7.1 Lamellar Microstructures

Fully lamellar microstructures typically consist of α lamellae embedded within β matrix. The processing routes to generate fully lamellar microstructure are schematically illustrated in Figure 2.13. In general, every processing route can be divided into four stages: homogenisation, deformation, recrystallisation, and annealing. The most important step to obtain a fully lamellar microstructure is cooling from above β transus [22]. This can happen either at the deformation stage or at the recrystallisation stage, therefore, there are two processing routes that can generate fully lamellar microstructure: β annealed and β processed.

The β annealed processing involves recrystallisation heat treatment above the β transus, this allows equiaxed β grains to recrystallise after deformation. The recrystallisation of β grains forces α plates to grow along the β grain boundaries and within the β grains. And since the growth of α plates follows the Burgers orientation relationship with the prior β grains, they tend to grow in parallel to each other, resulting in the formation of α colonies, as illustrated in Figure 2.14 (a). In β annealed processing, the deformation stage, either done

by forging or rolling, can take place in the β phase field (above β transus) or in the $\alpha + \beta$ phase field. In practical industrial procedures, the deformation stage usually involves two steps, the alloys are firstly deformed in the β phase field for better formability, followed by another deformation in the $\alpha + \beta$ phase field to break down large β grains [23].

The β processed processing, on the other hand, completely removes the recrystallisation heat treatment. Instead, the deformation stage must take place in the β phase field, to allow cooling directly from above β transus. The benefit of β processed condition is that the shape of β grains are limited in one axis by uniaxial rolling, this in turn restricts the dimensions of α colonies and removes the continuous α layers along the β grain boundaries, as shown in Figure 2.14 (b).

Among all the process parameters (temperature, cooling rate, deformation degree, etc.), the most important parameter is the cooling rate from above β transus, as it has the most significant influence on the width of α lamellae and the size of α layer at grain boundaries [69]. The cooling rate also affects the size of α colonies [23], which has a crucial impact on the mechanical properties of the alloy as it determines the effective slip length [70].

2.1.7.2 Bi-Modal Microstructures

The bi-modal microstructure typically consists of primary α grains and transformed β phase with secondary α laths, an example of bi-modal microstructure is shown in Figure 2.15. The processing route for the bi-modal microstructure is similar to the β annealed processing, except the deformation and recrystallisation temperature have to be lower than the β transus, as schematically illustrated in Figure 2.16. This prevents the microstructure from fully transforming into the β phase and leads to a certain amount of retained primary α.

During the cooling process, secondary α forms in the β phase, forming the transformed β phase.

For the bi-modal processing route, the cooling rate of the homogenisation heat treatment affects the size of primary α grains, whereas the cooling rate of recrystallisation treatment influences the width of secondary α laths. The recrystallisation temperature is another crucial processing parameter since it affects the volume fraction of primary α grains, which has influences on fracture and fatigue properties [71]. Texture may arise from the deformation stage for bi-modal microstructures. The temperature of deformation is crucial as different kinds of texture appear at specific temperature ranges. The mode and degree of deformation are also crucial since they determine the intensity of the texture, which is related to the anisotropy in mechanical properties [23].

2.1.7.3 Equiaxed Microstructures

The fully equiaxed microstructure typically consists of primary α grains and intergranular β phase, an example of fully equiaxed microstructure is shown in Figure 2.17. The fully equiaxed microstructure can be obtained by three different processing routes, as schematically illustrated in Figure 2.18. In the first method, the alloys can undergo the same processing route for bi-modal microstructures, except having a much slower cooling rate in the recrystallisation stage, as shown in Figure 2.18 (a). This method allows sufficient time for primary α grains to grow, consequently, primary α would eventually grow up until dominating the whole microstructure with a little amount of remaining intergranular β phase. Another way to achieve equiaxed microstructure is to recrystallise at lower temperatures, as shown in Figure 2.18 (b). Lower recrystallisation temperature increases the volume fraction of primary α phase. With sufficiently low recrystallisation temperature, the volume fraction of primary α phase can be high enough until little β phase is retained. Finally, a common processing route called mill-annealed condition can also give rise to the

equiaxed microstructure. In this process, the recrystallisation treatment is omitted. Therefore, the details of the deformation procedure largely determine the final microstructure. However, since the deformation procedure is difficult to control and the details may even vary between batches, the mill-annealed microstructure is usually considered not well-defined [23].

2.1.7.4 Microstructure-Property Relationships

The microstructures in $\alpha + \beta$ titanium alloys have a significant impact on their properties. Table 2.2 summarises the influence of microstructural features on selected material properties of titanium alloys between lamellar and equiaxed microstructures. Fine-scale microstructures offer a good balance of strength and ductility. Additionally, they hinder crack initiation and are essential for achieving superplastic deformation. In contrast, coarse microstructures provide greater resistance to creep and fatigue crack propagation. Equiaxed microstructures typically exhibit high ductility and fatigue strength, making them favourable for superplastic deformation. On the other hand, lamellar structures possess high fracture toughness and demonstrate exceptional resistance to creep and fatigue crack growth.

It is commonly observed that microstructures with inherent high resistance to fatigue crack initiation often exhibit faster crack propagation, while microstructures with lower resistance to crack initiation tend to have slower crack propagation. These two properties, crack initiation resistance, and crack propagation speed, are typically challenging to optimize simultaneously, similar to the trade-off between strength and ductility. Achieving a balance between these opposing properties requires careful consideration and trade-offs in the design and selection of microstructural features. Bi-modal microstructures, which combine the benefits of both lamellar and equiaxed structures, showcase a well-balanced property profile, making them highly desirable [22].

2.1.8 Ti-5.3Al-7.7V-0.5Si

Ti-64 and Ti-575 are the two $\alpha + \beta$ titanium alloys studied in this research. Ti-64 [72–81] is one of the very first designed titanium alloys, it was developed in the 1950s. Ti-64 has become by far the most popular titanium alloy. Ti-64 alone takes up more than 50% of industrial usage of the whole titanium market [22]. The success of Ti-64 can be attributed to the good balance of its properties. Due to the popularity of Ti-64, the industry has been built around this alloy, therefore it become the most intensively studied, developed, and tested alloy. This further consolidates the dominance of Ti-64.

On the other hand, Ti-575 [13–17, 82, 83] is a newly developed $\alpha + \beta$ titanium alloy for the application in aerospace components. This alloy was first introduced in 2014 [17], but there are still very limited studies on Ti-575. Most of the available literature was published by the alloy designer, TIMET Ltd. Compared to Ti-64, Ti-575 exhibits higher tensile strength and better low cycle fatigue performance, while maintaining acceptable ductility. In addition, under the cold dwell fatigue loading condition, Ti-575 exhibited little debit in fatigue life, suggesting that it is not suspectable to cold dwell fatigue [17]. Allen *et al.* [14] compared the β recrystallisation behaviour between Ti-64 and Ti-575. The results show that the imposed strain has little effect on the recrystallised grain structure in Ti-64, whereas in Ti-575 the grain size was significantly reduced by the imposed strain. With increased applied strain and higher strain rate, further refinement in grain size was observed. M. Thomas *et al.* [15] reported that macrozones are not presented in Ti-575 even after a non-optimised forging route. This explains the reason why Ti-575 does not suffer from the cold dwell fatigue phenomenon. Apart from higher monotonic and cyclic strength, Ti-575 also exhibited 15% increase in fatigue strength compared to Ti-64. The superior strength of Ti-575 can be attributed to the existence of extremely fine tertiary α laths formed during age hardening [13]. Enrique *et al.* [82] characterised the chemical composition and crystallographic orientations of the nano-scale tertiary α laths using advanced transmission electron

microscopy techniques, such as precession electron diffraction and electron energy loss spectroscopy. Bodie, Thomas, and Ayub [16] investigated the effect of the cooling rate on the microstructure and the fatigue performance of Ti-575. The results show that a higher cooling rate leads to a lower volume fraction of primary α grains, which reduces the high cycle fatigue life for air-cooled test pieces. On the contrary, for oil-quenched test pieces, a lower volume fraction of primary α grains appears to increase the fatigue life, which is attributed to the change in the morphology.

As previously discussed, there are many types of α and β stabilising elements available for titanium alloys. However, the variety of alloying elements causes difficulties in the classification and comparison of the alloys. To universally estimate the effect of each alloying element, aluminium equivalent and molybdenum equivalent [84–87] are useful to describe the α and β stability. The amount of each alloying element in titanium alloys can be estimated as equivalent aluminium and molybdenum content, hence giving a quick estimation of the equivalent amount of α and β stabiliser. Their expressions are given by

$$[\mathrm{Al}]_{\mathrm{eq.}} = [\mathrm{Al}] + 0.17[\mathrm{Zr}] + 0.33[\mathrm{Sn}] + 10[\mathrm{O}] \tag{2.5}$$

$$[\mathrm{Mo}]_{\mathrm{eq.}} = [\mathrm{Mo}] + 0.67[\mathrm{V}] + 0.40[\mathrm{W}] + 0.28[\mathrm{Nb}] + 0.20[\mathrm{Ta}] + 2.5[\mathrm{Fe}] + 1.25[\mathrm{Cr}] + 1.25[\mathrm{Ni}] + 1.7[\mathrm{Mn}] + 1.7[\mathrm{Co}]$$

It follows that Ti-64 has equivalently 6.0 wt.% aluminium and 2.7 wt.% molybdenum, whereas Ti-575 has equivalently 5.3 wt.% aluminium and 5.1 wt.% molybdenum. It turns out that Ti-575 has a significantly higher amount of β stabiliser compared to Ti-64, this is expected to cause higher β stability, lower β transus, and more difficult $\beta \rightarrow \alpha$ phase transformation in Ti-575. Compared with Ti-64, Ti-575 behaves more similar to metastable β alloys, even though it is still classified as an $\alpha + \beta$ alloy.

2.2 Crystallographic Texture

2.2.1 Introduction

In material science, the term 'isotropy' refers to a material property that demonstrates uniformity and maintains a consistent value regardless of the direction in which it is measured. Many material properties are considered or assumed to be isotropic as they are usually represented by a scalar value, for example Young's Modulus (E). However, isotropy is rarely observed in single crystal materials. For example, Figure 2.19 shows the Young's Modulus of single-crystalline iron measured in different crystallographic direction. Clearly, the elastic property is dependent on the direction of measurement, and it can be as low as 130 GPa along [100] direction while as high as 280 GPa along [111] direction, both significantly differ from the bulk modulus of 210 GPa. In many cases, it has been found that the influence of crystallographic orientation on material properties can be 20-50% of the property values [88].

Isotropic properties, on the other hand, appears in many polycrystalline materials, which are characterised by a microstructure consisting of numerous crystals, or so-called grains, each with its unique crystallographic orientation. When the grain orientations inside a polycrystalline material are randomly and uniformly distributed, the anisotropy, as opposed to isotropy, of single crystals cancel out with each other, consequently the measured properties become isotropic. However, the grain orientations in polycrystalline metals fabricated by most kinds of thermomechanical processing are rarely randomly distributed, they tend to appear in certain preferred orientations, either due to mechanical deformation along certain directions or crystallisation during heat treatments. The preferred crystallographic orientations in polycrystalline materials, defined as 'texture', can therefore results in anisotropic material properties and have significant impact on the properties along the direction of processing [89]. Examples of material properties that are influenced by texture are mentioned but not limited to strength, ductility, toughness, and fatigue resistance.

The existence of texture in materials is generally not desired, as it creates weakness in certain directions. Compared to anisotropic materials, isotropic materials are easier to deform, and their behaviour is easier to predict. Nevertheless, crystallographic textures can also serve as an extra opportunity to design the properties of materials. One can deliberately control the texture in the component to strengthen the mechanical properties along the loading direction, such as directionally solidified nickel-base superalloys for turbine blades in jet engines. Material engineers have learned to live with anisotropic properties and benefit from texture [22].

2.2.2 Representations of Orientation

The crystallographic orientation is defined as the rotation which transforms specimen coordinate system into the crystal coordinate system [90]. As illustrated in Figure 2.20, the specimen coordinate XYZ is conventionally chosen as the rolling direction (RD), transverse direction (TD), and normal direction (ND) for rolled specimens. The crystal coordinate is referred to as the [100], [010], and [001] crystallographic directions within a grain (single crystal) of interest within the specimen. The orientation (g), specimen coordinates (C_S), and crystal coordinates (C_C) has the following relationship

$$C_C = g \cdot C_S \tag{2.6}$$

The Equation (2.6) can be treated as applying a three-dimensional rotation to the specimen coordinates, yielding the position of crystal coordinates.

The orientation g can be expressed in multiple ways, which are introduced in the following sections. For simplicity, the following discussion on orientation is based on cubic crystal structure. For different crystal structures, the descriptors need to be modified accordingly, details can be found in [89].

The crystallographic orientation can be described in numerous of ways. All descriptors are employed into texture analysis process and each of them provides a unique aspect of orientation. It is beneficial to appreciate all descriptors of orientation to interpret the results

of texture analysis. In this section, several descriptors of orientation are introduced, namely rotation matrix, Miller indices, Euler angles, and angle/axis of rotation. However, the reader should be aware that there are more descriptors, such as quaternion and Rodrigues vector. Although quaternion is not introduced in this thesis, it is commonly used in implementation of computation programs to for orientation calculation, the reader is encouraged to further study it when needed. Details about quaternion can be found in [91].

2.2.2.1 Rotation Matrix

Any general rotation in three dimensions can be considered as the combination of the elemental rotations. Conventionally, a general rotation in three dimensions is represented as elemental rotation about the x-, y- and z-axes in turn with respective angles ϕ, θ, and φ. The general rotation matrix can be obtained by

$$\mathbf{R} = \mathbf{R}_z(\varphi)\ \mathbf{R}_y(\theta)\ \mathbf{R}_x(\phi) \tag{2.7}$$

where

$$\begin{aligned}
\mathbf{R}_x(\phi) &= \begin{bmatrix} 1 & 0 & 0 \\ 0 & \cos\phi & -\sin\phi \\ 0 & \sin\phi & \cos\phi \end{bmatrix} \\
\mathbf{R}_y(\theta) &= \begin{bmatrix} \cos\theta & 0 & \sin\theta \\ 0 & 1 & 0 \\ -\sin\theta & 0 & \cos\theta \end{bmatrix} \\
\mathbf{R}_z(\varphi) &= \begin{bmatrix} \cos\varphi & -\sin\varphi & 0 \\ \sin\varphi & \cos\varphi & 0 \\ 0 & 0 & 1 \end{bmatrix}
\end{aligned} \tag{2.8}$$

Rotation matrices have many useful properties, such as, the inverse of rotation is equivalent to a clockwise rotation, which coincides with the transpose of original rotation. Such that

$$\mathbf{R}(\theta)^{-1} = \mathbf{R}(-\theta) = \mathbf{R}(\theta)^T \tag{2.9}$$

The rotation matrix in Equation (2.7) is an 'active' rotation, where rotation is applied on a body within a fixed coordinate system. Conversely, the crystallographic orientation g defined in Equation (2.6) is a 'passive' rotation, where rotation is applied on the coordinate system

(rotation of reference frame). A passive rotation ($\mathbf{R}_p$) is simply the inverse of active rotation ($\mathbf{R}$), namely

$$\mathbf{R}_p = \mathbf{R}^{-1} \tag{2.10}$$

Therefore, the orientation g can be expressed as

$$g = \mathbf{R}_x(\phi)\ \mathbf{R}_y(\theta)\ \mathbf{R}_z(\varphi) \tag{2.11}$$

Alternatively, the orientation g can also be expressed using the cosines of the angles (see Figure 2.20) between the crystal coordinate system and the specimen coordinate system, as

$$g = \begin{bmatrix} \cos\alpha_1 & \cos\beta_1 & \cos\gamma_1 \\ \cos\alpha_2 & \cos\beta_2 & \cos\gamma_2 \\ \cos\alpha_3 & \cos\beta_3 & \cos\gamma_3 \end{bmatrix} \tag{2.12}$$

since they are coherent to the definition of orientation – the position of the specimen coordinate system with respect to the crystal coordinate system.

Rotation matrix is not commonly used to describe orientation in the field of texture analysis, since rotation about specimen axes usually does not provide useful physical meaning. Nevertheless, it serves as a good steppingstone to understand the nature of three-dimensional orientation.

2.2.2.2 Miller Indices

The Miller indices of an orientation g is expressed as

$$g = (hkl)[uvw] \tag{2.13}$$

where (hkl) is the crystallographic plane that is parallel to the normal direction, and $[uvw]$ is the crystallographic direction that is parallel to the rolling direction. Miller indices can be converted into matrix form, details can be found in Appendix B.1.

For example, as illustrated in Figure 2.21, since the (110) plane in the crystal is parallel to the normal direction and the [001] direction in the crystal is parallel to the rolling direction, the orientation of the crystal can be expressed as (110)[001]. If the family of (hkl) and $[uvw]$ are all crystallographically equivalent, the orientation can be expressed as $\{hkl\}\langle uvw\rangle$ to respect the symmetry of the crystal structure.

Miller indices notation is popular among metallurgists thanks to its simplicity; hence they are used as the main descriptor when referring to crystallographic orientation throughout this thesis.

2.2.2.3 Euler Angles

Both the rotation matrix and the Miller indices overcomplicate the representation of orientation, since only a minimum of three variables are required to specify an orientation. Euler angles is the most well-established descriptor to express orientation in the simplest form [89].

The Euler angles can be presented in many different conventions. In the field of texture analysis, the most popular one is the Bunge system [90], which defines the Euler angles in an intrinsic z_1-x'-z_2'' rotation. The intrinsic z_1-x'-z_2'' rotation involves firstly rotate about z-axis by an angle φ_1, followed by a rotation about the x'-axis (with respect to the rotated crystal coordinate system) by an angle Φ, finally rotate about z''-axis (also with respect to the rotated coordinates after the previous two rotations) by an angle φ_2, as illustrated in Figure 2.22. The orientation g can be expressed using a tuple of three Euler angles as

$$g = \{\varphi_1, \Phi, \varphi_2\} \tag{2.14}$$

Euler angles can be converted into matrix form, details can be found in Appendix B.2.

Although the range of the Euler angles can be generally defined as $(0°, 360]$, due to the symmetry of the crystal structure and specimen geometry, the range of the Euler angles can

be reduced. For example, the range of Euler angles in HCP structure can be reduced to $0° \leq \varphi_1 \leq 90°$, $0° \leq \Phi \leq 90°$, and $0° \leq \varphi_2 \leq 60°$ to avoid the redundant rotation.

Euler angles are commonly used in advanced texture analysis by means of orientation distribution function, which is the simplest expression of complete orientation distribution in three dimensions without any loses of information. Other methods, take pole figures for example, inevitably discards a portion of information due to projection onto a two-dimensional plane. The orientation distribution function is introduced in Section 2.2.3.4 with more details.

2.2.2.4 Angle/Axis of Rotation

Any general rotation, as previously described, composes of three elemental rotations. However, Euler's rotation theorem [92] states that the same rotation can be achieved by a single rotation about a specific axis by a certain angle. This type of descriptor is therefore known as angle/axis of rotation, as illustrated in Figure 2.23. The orientation g can be expressed using a pair of angle θ and axis $\vec{\mathbf{v}}$ in the form of

$$g = \{\theta, \vec{\mathbf{v}}\} \tag{2.15}$$

Angle/axis of rotation can be converted into matrix form, details can be found in Appendix B.3.

The angle/axis of rotation is commonly used to describe 'misorientation', which is defined as the difference in orientation between two crystals within the same polycrystalline specimen. Similar to the definition of orientation, the misorientation can be described as the position of a crystal coordinate system with respect to another crystal coordinate system, as if taking one of the crystals as the main reference frame. Hence, the Equation (2.6) can be rewritten for misorientation Δg as

$$C_{C_2} = \Delta g \; C_{C_1} \tag{2.16}$$

Notice that the misorientation Δg can be expressed by the orientation g of the two crystals with respect to the specimen coordinate system. Specifically, one can first rotate crystal C_1 to align with the specimen coordinates by applying g_1^{-1}, then rotate the crystal to align with the second crystal C_2 by applying g_2. Mathematically, it can be written as

$$\Delta g_{12} = g_2 \; g_1^{-1} \tag{2.17}$$

Expressing misorientation by angle/axis of rotation is beneficial, as it usually provides meaningful physical representation of the adjacent crystals, and can often relate to slip or twinning system in crystallography. Therefore, the angle/axis of rotation is commonly used as a descriptor for misorientation at grain boundaries, phase boundaries, and twin boundaries.

2.2.3 Representations of Texture

To visualise texture, the preferred crystallographic orientations, in polycrystalline materials, it is necessary to visualise the orientation distribution of all crystals within the region of interest. In order to represent the orientation distribution concisely, many ways of visualisation techniques have been invented. There is no specific technique that is superior to others or universal for any purposes, each technique has its own advantages that is useful for certain scenarios, however it comes along with some disadvantages and limitations. Therefore, it is necessary to understand a few representations of texture for the purpose of visualise the texture analysis in the most appropriate way.

2.2.3.1 Pole Figure

Pole figures are two-dimensional representations of the orientation distribution with respect to the specimen coordinate system to obtain semi-quantitative information about the texture of the specimen. Figure 2.24 demonstrates the construction of a pole figure. For a predetermined family of crystallographic planes, e.g. {100}, the normal of each plane is projected onto an imaginary sphere encompassing the specimen. The projection on the sphere

is then projected onto the projection plane (located at the equator of the sphere) by connecting the point on the sphere to the south pole. The procedure of projecting crystallographic planes is carried out for all crystals within the region of interest in a polycrystalline specimen, thus the {100} planes of all crystals are all projected onto the projection plane, each of the {100} planes is represented by a single point. The projection plane together with the stereographic projection of all {100} planes is a {100} pole figure of the specimen. Since in practice millions of planes can all projected into a single pole figure, making it difficult to read, pole figures are commonly presented as a contour plot, for instance as shown in Figure 2.25. The preferred orientations on a contour pole figure are represented by the concentrated poles with high intensity, which is quantified as multiple of random distribution (MUD).

Pole figures are usually aligned with the specimen coordinate system in terms of rolling, transverse, and normal directions, hence they are useful for illustrating the orientation of specific crystallographic planes with respect to the specimen. Due to the clarity of presenting the orientation with respect to the specimen coordinate system, the pole figure is popular in the field of texture analysis, and it is often the first choice of texture representation for an overview of the dominant texture components. However, as pole figures are two-dimensional stereographic projection of three-dimensional orientation, this results in loss of information. For instance, a (0001) pole figure only specifies the orientation of the c-axis in HCP crystals, however, the crystals still have a degree of freedom to rotate about the c-axis. Therefore, often two or more pole figures of characteristic crystallographic planes are presented together for better illustration of the texture information. For example, $\{110\}_\beta$ and $\{111\}_\beta$ pole figures are commonly presented together to illustrate titanium β phase texture. Whereas $\{0001\}_\alpha$ and $\{11\bar{2}0\}_\alpha$ are frequently shown together to represent titanium α phase texture. Nonetheless, even though multiple pole figures can provide more information, ambiguities still arises when different texture components overlap with each other on pole figures. If such

complexity of the preferred orientations is appeared, advanced texture analysis is required, and other means of texture representation may be used.

2.2.3.2 Inverse Pole Figure

Inverse pole figures, similar to pole figures, are also stereographic projection of crystallographic planes. However, inverse pole figures project plane with respect to the local crystal coordinate system, not to the specimen coordinate system as is the case in pole figures, as illustrated in Figure 2.26. Due to the symmetry of crystal structures, take cubic as example, all crystallographic planes can be projected into the stereographic triangle between the projection of [100], [010], and [001] planes, as illustrated in Figure 2.27. Since the other region on inverse pole figures apart from the stereographic triangle only contains duplicated information, inverse pole figures are often presented only showing the stereographic triangle of three orthogonal crystallographic directions. Due to the reduced portion of inverse pole figures, each orientation is only represented by a single point on an inverse pole figure, whereas in the case of pole figures, each orientation can result in multiple points on the figures. Each inverse pole figure is associated with a predetermined specimen direction (e.g. rolling, transverse, or normal direction). For each crystal within the specimen, the crystallographic direction parallel to the predetermined specimen direction is projected onto the inverse pole figure. This procedure is carried out for all crystals within the region of interest. Like pole figures, inverse pole figures are also commonly presented as contour plots.

Inverse pole figures are beneficial to show the tendency of alignment between crystallographic and specimen directions. However, similar to pole figures, inverse pole figures also do not preserve full information of orientation. In fact, the information presented in inverse pole figures are even more limited as they only preserve orientation information in one dimension. Although presenting multiple inverse pole figures can provide a little more information about the orientation distribution, this only shows preferred crystallographic directions along other specimen directions, the information inverse pole figures can provide is still very limited.

Usually, inverse pole figures are used as a colour key for orientation maps, which will be introduced in the following section.

2.2.3.3 Orientation Map

Orientation maps serve as an extension of inverse pole figures by reserving the spatial information, as shown in Figure 2.28. The same as inverse pole figures, a predetermined specimen direction is associated with every orientation map, in the case in the figure normal direction is chosen. For each crystal (or grain) within the polycrystalline specimen, the crystallographic plane parallel to the normal direction is determined and coloured according to the inverse pole figure colour key.

Orientation maps are useful as they reserve the spatial information and can clearly present the spatial variation of orientation within the region of interest. However, they suffer from the same disadvantage as inverse pole figures have, the orientation information is only preserved in one dimension. This leads to a consequence that single orientation map can be misleading, as the same colours in an orientation map does not necessary indicates the same orientations. Since the colour in orientation maps only indicates the crystallographic direction parallel to the observation direction, the crystals sharing the same colour all have the degree of freedom to rotate about that direction. Therefore, multiple orientation maps are needed to be presented together to avoid the ambiguity of orientation representation. Nevertheless, orientation maps serve as a very useful tool to detect regions of commonly oriented crystals in close proximity, which is formally defined as 'macrozones' or 'micro-textured regions', they are considered to have detrimental effect on dwell fatigue life of titanium components [93, 94].

2.2.3.4 Orientation Distribution Functions

Pole figures and orientation maps are useful for texture representation, however, their common disadvantage is loss of information. Orientation distribution functions (ODF) provides complete information of orientation distribution without any loss, thereby they are

powerful for advanced texture analysis. The ODF $f(g)$ is defined as a probability density function of orientations g, as

$$f(g) = \frac{1}{V}\frac{dV(g)}{dg} \tag{2.18}$$

where V is the total volume of interest and dV is the volume of all crystallites with similar orientation g within the angular orientation range dg. For a given set of measured texture data, the ODF $f(g)$ can be solved by either harmonic method, which involves series expansion in a Fourier space, or WIMV method, which divide the orientation space into a finite grid and minimise its local curvature. Details about the mathematical derivation of these two methods can be found in [95] and [89].

The ODF is commonly expressed in the form of Euler angles $\{\varphi_1, \Phi, \varphi_2\}$, within Euler space. This allows ODF to be visually represented in a three-dimensional space, as illustrated in Figure 2.29 (a). Although ODFs can be presented in three dimensions, generally this type of visualisation is not suitable for publication on a printed page. Therefore, often ODFs are presented in a series of sections along φ_2, with steps of 5-10° depending on the location of the characteristic texture components, as shown in Figure 2.29 (b).

The disadvantage of ODF is the difficulty to associate with the actual orientation with respect to the specimen coordinate system, therefore it is only used in advanced texture analysis when a transition between texture components (e.g. fibre) appears. In HCP crystals, the ODF sections along φ_2 is considered to be suffered from the distortion in the Cartesian coordinate system of Euler angles. There is an alternative method of presenting ODF sections for HCP crystal structures, called sigma sections. In principle, the sigma sections are simply a series of (0001) pole figures, with $(11\bar{2}0)$ directions visualised on the pole figures, indicated by the arrows in the pole figures, as shown in Figure 2.30. The series of pole figures is sectioned along the degree of c-axis rotation from 0-60°, consequently, the $(11\bar{2}0)$ direction

rotates about the origin in each pole figure. This method essentially decomposed the traditional (0001) pole figures, and provides an intuitive visualisation of all texture components within HCP crystal without losing any information.

2.2.4 Texture Measurement by Electron Backscatter Diffraction

The work of texture analysis was originated back in late 1940's with the introduction of texture goniometer. Schulz [96] established modern quantitative texture analysis technique by means of x-ray diffraction, since then, many diffraction methods have been developed for texture measurement, including neutron diffraction [97], synchrotron x-ray diffraction [98], electron backscatter diffraction (EBSD) [99]. Currently, EBSD has become the standard technique for both macrotexture and microtexture analysis [100], thanks to this high spatial resolution (~20 nm) and fast data acquisition. In addition, the EBSD system is modulus and can be easily attached to a scanning electron microscope (SEM), which is a widely available instrument in a metallurgy laboratory.

Figure 2.31 illustrates the configuration of electron beam, sample, and EBSD detector within a SEM. The sample is tilted usually in 70° to allow more electrons diffracted toward the detector. When the accelerated electron beam strikes onto a crystalline material, electrons from the atoms near sample surface are scattered in all directions, known as backscatter electrons. These backscatter electrons traveling along each crystallographic plane is diffracted following the Bragg's law [101]

$$n\lambda = 2d\sin\theta \tag{2.19}$$

where λ is the wavelength of electrons, d is the spacing of the crystallographic plane, θ is the angle of incidence, and n is any integer. The electrons satisfying the Bragg's law gain constructive interference, whereas those does not satisfy the Bragg's law have destructive interference. Consequently, a pair of constructively interfered diffraction cones (Kossel cones) is generated along each crystallographic plane, as illustrated in Figure 2.32. Each pair of diffraction cones is then projected onto the detector (phosphor screen), producing Kikuchi

lines. Since the electrons are scattered in all directions, Kikuchi lines are generated along every crystallographic plane, resulting in a Kikuchi pattern (or electron backscatter pattern, EBSP) on the phosphor screen.

The Kikuchi pattern is very useful for crystallographic analysis, since the pattern is essentially a gnomonic projection of all crystallographic planes onto the screen, the information about the crystal is embedded into the Kikuchi pattern, as illustrated in Figure 2.33. By analysing Kikuchi patterns, the type of crystal structure and the orientation of the crystal can be determined. The analysis of Kikuchi patterns is carried out through Hough transform [102], an image processing technique for line detection. The identified Kikuchi lines are compared with analysed structures to find the best fit. The whole process can be done automatically by the commercial software within a millisecond, allowing automated texture measurement over large region of interest.

2.2.5 Typical Textures

To interpret the texture measurement results, it is beneficial to have the idea of some typical textures in mind. Similar type of textures may imply similar type of texture development mechanism during thermo-mechanical processing. In this section, several types of commonly appearing textures are introduced, their corresponding pole figures are also provided.

2.2.5.1 Ideal Cubic Textures

In processed cubic materials (e.g. steels), there are several commonly appearing textures. These textures are named either by the discoverer or by the material frequently exhibiting the texture. The four types of well-known ideal textures, namely Goss $\{110\}\langle 001\rangle$, cube $\{001\}\langle 100\rangle$, copper $\{112\}\langle 11\bar{1}\rangle$, and brass $\{110\}\langle 1\bar{1}2\rangle$ texture. The copper and brass textures are normally found in rolled face-centred cubic (FCC) materials. The cube texture appears predominantly in recrystallised FCC materials. These ideal textures all have dominant orientation with respect to the specimen normal and rolling directions, as shown in Figure 2.34, Figure 2.35, and Figure 2.36. The ideal positions of these texture components

on (110) and (111) pole figures are shown in Figure 2.37. The pole figures of these ideal textures are useful for identifying the texture components measured in experiments.

2.2.5.2 Fibre Textures

In the pole figures of ideal cubic textures, the texture components are concentrated around ideal orientations, this type of texture components are known as peak-type components. On the other hand, materials formed by axially symmetric deformation, such as wire drawing, compression, and extrusion, often exhibit texture with rotational symmetry, so-called fibre textures. In fibre textures, a crystallographic direction $[uvw]$ is preferentially aligned with the axis of deformation, or so-called fibre axis. Apart from the preferential alignment with the fibre axis, there is no other restriction on grain orientation, therefore, the crystals have a degree of freedom to rotate about the fibre axis. Consequently, the fibre texture appears like continuous bands of orientations on pole figures, as illustrated in Figure 2.38.

2.2.5.3 Simple Shear Textures

Textures resulting from a simple shear deformation in cubic materials was initially studied in torsion testing for steels [103], the simple shear textures were later found in many studies on friction stir welding [104–106], and also found to have certain similarities with equal channel angular extrusion [107]. The (110) and (111) pole figures of simple shear textures in BCC materials are shown in Figure 2.39. Four types of texture components are commonly appearing in simple shear conditions, namely D $\{112\}\langle 11\bar{1}\rangle$, E $\{110\}\langle 1\bar{1}1\rangle$, J $\{110\}\langle 1\bar{1}2\rangle$, and F $\{110\}\langle 001\rangle$. The (0001) and $(11\bar{2}0)$ pole figures of simple shear textures in HCP materials are shown in Figure 2.40. Four types of texture components are commonly appearing in simple shear conditions, namely P_1 $\{1\bar{1}00\}\langle 11\bar{2}0\rangle$, B-, C_1-, C_2-, and Y-fibre textures. The Miller Indices representation of fibre textures are not concise, instead, they are defined only by the orientation of $\{0001\}$ planes. For example, C_1- and C_2-fibre textures are defined as $\{0001\}$ planes being $\pm 30°$ from the shear direction towards shear plane

normal. The simple shear textures play an important role in various type of friction welding processes, since the local stress condition at the weld interface is very much similar to the simple shear condition.

2.2.5.4 Textures in $\alpha + \beta$ Titanium Alloys

The $\alpha + \beta$ titanium alloys, with microstructures containing hexagonal α phase and BCC β phase, can develop strong texture during thermo-mechanical processing. The type of the texture and its intensity is determined by the temperature and stress conditions during processing. Subsequent heat treatments such as annealing and tempering at lower temperatures have little to no effect on the texture.

Generally speaking, the textures generated in $\alpha + \beta$ titanium alloys can be classified into four types, depending on the deformation temperature. As shown in Figure 2.41, for titanium alloys sheets after uniaxial rolling at low temperatures, strong texture components along transverse and normal directions are developed, this is commonly referred to as basal/transverse type of texture. This kind of texture is also regarded as α-deformation texture, as its behaviour can be attributed to the deformation of α phase (i.e. basal and prismatic $\langle \vec{a} \rangle$ slip systems), since high volume fraction of α phase is presented at low temperatures. When rolling at temperatures above β transus, β-deformation texture arises. The material achieves 100% β phase and $\beta \rightarrow \alpha$ phase transformation occurs during cooling, resulting in transformation type of textures. Following Burger's orientation relationship, a total of 12 α variants can form from β phase, hence producing many texture components on the pole figure. When rolling at temperatures just below the β transus, high volume fraction of β phase is presented in the material, and $\beta \rightarrow \alpha$ transformation also occurs. However, variant selection occurs during phase transformation, only one of the α variant is preferentially formed, resulting in a strong transverse texture. Previous studies proposed that the variant selection is induced by the superimposed strains resulting from the

deformation process [108, 109]. At temperatures between 900-930℃, texture softening was observed, no particularly strong texture component can be found. As the temperature in this range is in between α-deformation temperature and β-deformation temperature, the intensity of the α-deformation texture reduces as the volume fraction of α phase decreases with the increased temperature. Similarly, the intensity of the β-deformation texture also decreases as there is not enough β phase to exhibit strong β-deformation texture [81]. This processing window is preferred in the industry to obtain texture-free components.

The symmetry of textures is determined by the mode of deformation. In cross rolled titanium sheets, the intensity of the transverse texture component is significantly reduced, as rolling direction is rotated by 90° after each rolling step, the transverse component is suppressed when rolled along the rolling direction. In forged titanium alloys, axial symmetry appears as the material deforms in radial directions, thus fibre texture along the forging direction is developed.

2.2.6 Variant Selection

When texture development involves $\beta \rightarrow \alpha$ phase transformation, a total of 12 possible α variants can form from a single β grain. If all variants share equal possibility to form, in other words, no orientation is preferred, the material will not exhibit strong texture. However, often specific orientation is preferentially selected, resulting in a strong texture component. This process is known as variant selection, and it has been reported in numerous study on titanium alloys [104, 105, 110–120].

The mechanism of variant selection has been studied extensively. Several factors have been proposed to be account for this phenomenon, including dislocation pile-up, internal stress, and transformation-induced strain. Gey *et al.* [118, 119] proposed that deformation in the β phase field is linked with the activation of $\{110\}\langle 1\bar{1}1\rangle$ and $\{112\}\langle 11\bar{1}\rangle$ slip systems. The

most activated slip system produces high density of dislocations pile-up, which are ideal nucleation sites for the α phase. Zeng and Bieler [115] argued that rapid cooling from β phase develops anisotropic thermal contraction of the prior β grains due to anisotropic thermal expansion coefficient of α phase. The anisotropic thermal contraction causes the development of internal stresses, which can affect the transformation texture by means of favouring the formation of specific α variants [121]. Humbert *et al.* suggested that variant selection should base on the accommodation of strain induced from $\beta \rightarrow \alpha$ transformation. The minimisation of elastic strain energy during transformation should be the driving force of variant selection. Particularly, the strain at β grain boundaries and α/β phase boundaries plays an important role [120].

It is worth mentioning that there is still an ongoing debate on the mechanism of variant selection, although various mechanisms have been proposed by different researchers, there is still yet a universal agreement between each mechanism.

2.3 Linear Friction Welding

LFW is one of the friction welding techniques, which join materials solely through generating friction between workpieces in relative motion. LFW process involves the application of high-frequency linear oscillation on one workpiece relative to another along with a large compressive pressure [12, 122–125], as illustrated in Figure 2.42 (a). The friction at the interface generates heat, which increases the temperature and softens the material in proximity to the weld interface. The softened/plasticised material flows along the oscillation direction, and is then expelled from the interface, forming flash, as shown in Figure 2.42 (b). As the material is extruded away from the weld, the two workpieces exhibit axial shortening along the direction of compressive pressure, or so-called 'upset'.

During the whole process, even though the material becomes plasticised, the temperature is never high enough to melt the material. Therefore, LFW is considered as a solid-state joining

process, which is a beneficial feature as it prevents dramatic change in microstructure and mechanical properties and keeps a narrower heat-affected zone (HAZ). Furthermore, thanks to the extrusion of material during LFW, the contaminants on the surface of the workpieces are naturally extruded away from the weld into the flash, leading to a defect-free solid weld. This phenomenon is known as 'self-cleaning effect', which prevents the retention of the contaminants within the weld, consequently improving the structural integrity of the weld.

2.3.1 Phases of Welding

The LFW process can be split into four distinct phases [124, 125]: initial, transition, equilibrium, and deceleration phases, as demonstrated in Figure 2.42 (b). In the initial phase, the two workpieces are brought together in contact by the applied pressure. Due to the surface roughness and asperities, the initial true contact area is smaller than the surface area of the workpieces. Linear oscillation is applied on one of the workpieces to generate friction and heat at the interface. If the rubbing velocity is not sufficient for a given applied pressure, the generated frictional heat would be insufficient to soften the material and cannot initiate the next phase. With sufficient frictional heat, the welding process moves into a transition phase, where the asperities wear out and begin to be expelled from the weld. It is considered that the true contact area becomes the same as the surface area of the workpieces. The thickness of the HAZ is expanding during this phase for the next phase to follow.

In equilibrium phase, the plasticised material is no longer able to support the compressive pressure, thus stable extrusion of the plasticised material and axial shortening begins. The frictional heat generated at the interface is conducted away into the flash and the base material, leading to a thermal equilibrium in this phase. Consequently, the temperature does not further increase beyond this point. Once the desired axial shortening is achieved, the process moves on to the deceleration phase, where the oscillation motion is terminated, while the compressive pressure is still applied to consolidate the weld. Figure 2.42 (c) is an example of the variation of shear force and axial displacement during each phase in LFW.

A modern definition of phases in LFW [126, 127] introduces a conditioning phase before the initial phase, and split the deceleration phase into two phases: forge phase and release phase, as illustrated in Figure 2.43. In this definition, the initial, transition, and equilibrium phases are included in the frictional phase. The conditioning phase involves the ramp-up process of the oscillation until it stabilised, in this phase the compressive pressure (friction force) has not been applied yet. The forge phase is introduced to emphasis the effect of forge pressure, which is usually has greater magnitude than the compressive pressure. In the release phase, the forge pressure is removed, this causes a slight expansion of the workpiece, the total upset (axial shortening) is therefore slightly reduced.

2.3.2 Key Process Variables

There are three key process variables which predominantly determines the properties of LFW'd joints, namely oscillation frequency (f), oscillation amplitude (a), and compressive friction pressure (P). Specific power input (w) has been introduced by many researchers [125, 128, 129] to characterise the process parameters as

$$w \propto \mu \frac{afP}{2\pi} \tag{2.20}$$

where μ is the coefficient of friction. The power input can be used as the first estimation for the weldability of the process variables, low power input indicates poor weldability or even failure to weld. The power input is an indication of the energy density generated during LFW. Increasing power input will heat up the weld interface more rapidly, and result in higher temperature at the weld interface. This in turn affects the microstructure of the weld zone. Other key process variables include forge pressure, forge time, ramp-up time, ramp-down time, and burn-off distance (a certain axial shortening that triggers the start of the forge phase). All key process variables can be controlled directly through the welding machine.

There are several variables that cannot be controlled directly during the process, nevertheless, they are still of importance to the integrity of the LFW'd joints. These variables are referred to as secondary process variables, as they are considered as consequences of the key process variables. Secondary process variables include upset (total axial shortening), upset rate, shear force, and welding time [127, 130–132].

2.3.3 Temperature Distribution

Experimentally measuring the temperature distribution in LFW'd joints is technically challenging, nevertheless, Turner *et al.* [133] managed to embedded thermocouples into the workpiece at different distance away from the interface to measure the temperature distribution in the axial direction. The results are used to validate their finite element model and shows a good agreement with the model prediction. As finite element method appears to be a robust method for the thermal analysis of LFW process, many researchers adopted this method to investigate the temperature distribution in the weld. McAndrew *et al.* [128, 134, 135] used finite element model to predict the thermal profile in LFW'd Ti-64 with different welding velocity, friction pressure, and in-plane width, as shown in Figure 2.44. The results indicate that higher welding velocity, lower friction pressure, and thicker workpiece can increase the temperature at the weld interface. Greater welding velocity also increases the gradient of the thermal profile, this helps reducing the size of HAZ.

Vairis and Frost [125] established a finite element model to predict the temperature variation at the interface over time. Although their model predicts that the interfacial temperature does not exceed 900 ℃ during the entire welding process, which is opposed to the metallurgical observation, their method still demonstrates the versatility of finite element analysis. Li *et al.* [136] provides an improved model which predicts that the temperature at the interface rises rapidly within the first second to approximately 970 ℃, then the temperature keeps increasing to approximately 1000℃ at two seconds and maintains at the same level before the forging phase starts, as shown in Figure 2.45 (a). Their temperature

profile also indicates a rapid cooling rate at approximately 160℃/s during the forging phase, this correlates well with metallurgical observation of martensitic transformation.

Finite element analysis can also predict the cross-sectional temperature distribution at the weld interface, as demonstrated by Sorina-Muller *et al.* [137] and Grujicic *et al.* [138]. Figure 2.46 illustrates the temperature distribution at the interface when desired upset is achieved for different workpiece geometries. Great temperature difference at the interface, ~475K (177℃) at the edges and ~1200K (927℃) in the centre of the body, was observed. The low temperature at the edges of the weld interface can be explained by the short time of overlap and heat losses through thermal convection.

Although developing a reliable predictive model for the welding process is challenging due to the variability of input parameters like friction coefficients and the non-equilibrium conditions in LFW, the existing modelling efforts focusing on heat generation and transient temperature distribution serve as a valuable guideline for gaining a deeper understanding of the welding process and the resulting microstructure development [10].

2.3.4 Metallurgy of the Welds

Figure 2.47 illustrates typical sections of titanium alloy after LFW. There are four distinct zone across the weld interface: central weld zone (CWZ), thermo-mechanically affected zone (TMAZ), heat-affected zone (HAZ), and parent material (PM). Each zone has unique microscopic feature and mechanical properties, which is discussed as follow.

CWZ is a narrow region located near by the weld interface. As this region is the closest region to the interface, where the heat is generated during LFW, the temperature in CWZ usually exceeds the β transus of the base alloys, therefore, the microstructure achieves 100% β phase and dynamic recrystallisation occurs in this region. The temperature in this region drops rapidly after the oscillation movement is terminated, this results in martensitic transformation which forms fine acicular α' phase [131, 139]. Texture is significantly

developed in this region due to the asymmetric nature of LFW, leading to a strong anisotropy of its mechanical properties.

TMAZ is a region located next to CWZ further away from the interface. The temperature in this region is slightly lower than CWZ, and it generally does not exceed the β transus of the titanium alloys. Hence, the microstructure in this region exhibits certain similarity with the microstructure in the base material, except from the severe grain distortion resulting from the plastic deformation during the welding process due to the compressive pressure and oscillation. As the temperature in this region is still close to the β transus, phase transformation and recrystallisation may partially occur in this region.

HAZ is located further away from the interface next to TMAZ. By definition, HAZ is a region only affected thermally but not mechanically, thus no grain distortion appears in this region. The temperature in this region is significantly lower than the β transus, hence the material can well withstand the compressive pressure. The thermal effects in HAZ includes grain coarsening and the formation of secondary phases. However, the size of HAZ is small or is difficult to be identified in materials with poor thermal conductivity, for example, Ti-64 [12]. The PM is the rest of the material which does not affected by LFW process at all, therefore it consists of the exact same microstructure as the base alloys.

It is worth noting that different terminology has been used to describe each weld zone in LFW'd joints. Some use 'plastic section' to describe CWZ, and some use 'partially deformed section' to describe TMAZ [124], whilst some use 'plastic affected zone' for both CWZ and TMAZ [139], others may use HAZ for the entire weld zone [140]. The reader is advised to be cautious when comparing different terminology used in the papers.

There are numerous studies on the mechanical properties of LFW'd titanium [62, 131, 141–143]. Wanjara *et al.* [131] and Romero *et al.* [143] both reported that LFW'd Ti-64 with appropriate process parameters have superior hardness and tensile strength to their parent materials. In both studies, from the hardness profile across the weld, the maximum value

occurs at the weld interface for its fine martensitic microstructure. The exact shape of the profile varies with the applied process parameters and the employed alloys. In traditional welding, HAZ with reduced strength tends to be the weakness of the welds. However, the HAZ in the welds generally maintain similar hardness compared to the base material. The results from the previous studies suggest that LFW can provide improved strength in the weld without having weakness in HAZ.

2.3.5 Residual Stress

During the process of LFW, residual stress is introduced to the workpieces and the fracture toughness of CWZ is usually reduced compared to the PM. Consequently, it is essential to carry out a post-weld heat treatment (PWHT) to relieve the residual stress and recover the fracture toughness of the welds. The two main variables of PWHT, temperature and processing time, have huge influence on the resulting microstructure and material properties. A previous study [144] investigated the effect of three different PWHT temperatures to Ti-17 similar welds. It is reported that higher temperature facilitates the recrystallisation of α phase, which disperses uniformly in the recrystallised β phase. This results in a lower level of residual stress as well as helps to recover ductility and tensile properties to the extent that even better than PM. However, increasing the PWHT temperature also coarsen the grains and affect the properties of the PM, hence, the PWHT temperature for titanium alloys after LFW is usually below its annealing temperature. Table 2.3 lists some recommended PWHT process for titanium and selected $\alpha + \beta$ alloys.

2.3.6 Dissimilar Welds

Modern jet engines usually have large by-pass ratio, which means most of the hot air passes by blades but not by the disc. This results in different operating temperature between blades and the disc, especially in the compressor and turbine stages. Moreover, the stress state of blades is also different from the disc: during high-speed rotation, blades only need to withstand the centrifugal force to support themselves, whereas the disc is required to support

itself and all blades attached to it. Therefore, it is reasonable to use different materials for blades and discs to match the different requirements in service. LFW offers an advantage that it is possible to produce dissimilar welds with dual material properties, which is useful for optimising blisks. There has been numerous studies on LFW of dissimilar titanium alloys or nickel-base superalloys [63, 145–149]. Nonetheless, welding dissimilar materials also introduce several new issues which do not appear in similar welds.

First, greater residual stress may result from joining materials with different thermal expansion coefficients, and this may lead to potential cracking in the weld [150]. Second, dissimilar materials have different strength at welding temperature. It is easier for the softer side to deform and to be extruded, leading to an uneven extrusion behaviour, which has been observed in several studies on LFW of dissimilar materials [151–155]. For self-cleaning effect to take place properly, sufficient extrusion from both sides of workpieces is required, otherwise inclusions may retain in the weld and compromise the structural integrity of the weld. The uneven extrusion behaviour in LFW of dissimilar materials effectively requires more material burn-off on the softer side, if the relative burn-off ratio is too large, such dissimilar welding would be impractical.

Furthermore, when welding different metals, depending on the material combinations, intermetallic phases may form during welding. Since intermetallic phases are generally brittle, their existence deteriorates the performance of the weld, hence they are undesirable. Intermetallic phases have been found in LFW of aluminium to copper [152, 154], as well as aluminium to magnesium [153]. Nevertheless, Wanjara *et al.* [155] studied LFW of Ti-64 to IN718 (workhorse nickel-base superalloy). They found limited interaction between the two materials at the interface, and particularly no intermetallic layer between the two material was formed.

There is also a potential issue on the PWHT of dissimilar welds. As mentioned previously, the PWHT temperature should be lower than the annealing temperature of the PMs to avoid

affecting their properties. It could be more difficult to find an PWHT temperature which relieves enough residual stress while meets the temperature requirements for both sides of materials in dissimilar welds (see Table 2.3). Therefore, it is crucial to find an optimised PWHT procedure for dissimilar welds.

2.3.7 Blisk Repair

Application of blisks in jet engines brings new challenges in terms of repair and maintenance. After the blisks have been in service for certain period of time, damage and wear on the blades will be noticeable. Once the damage surpasses the threshold set by the authority, repairing the blades is necessary. For traditional mechanically assembled blades, engine manufacturers can simply swap the damaged parts with a new one. However, for integrated blisks, swapping the blades requires more sophisticated process. Adaptive machining [156] is required to remove the damaged blades. This technique involves acquiring the 3D representation of the blisks, either by optical geometry measurement or tactile coordinate measuring machines [157]. Once the 3D representation is obtained, the STL file can be passed to a CNC code generator to generate milling tool paths that suits the measured geometry for blades removal. After the damaged blades was removed by adaptive machining, new blades can be welded back to original places on the disc by LFW [158] before final machining to the original dimensions.

2.4 Fracture and Fatigue

2.4.1 Linear Elastic Fracture Mechanics

Linear elastic fracture mechanics (LEFM) is regarded as the fundamental principle of fracture mechanics, it describes the fracture of materials when they perform elastic deformation with linear material behaviour [159–164]. The definition of linear elastic materials is illustrated in Figure 2.48. LEFM is ideal to characterise the fracture behaviour of brittle materials, nevertheless, with several modifications, it can also be applied to ductile materials as long as overall they exhibit linear elastic deformation.

2.4.2 Fracture Toughness

A. A. Griffiths [165] proposed the first study on fracture mechanics which demonstrates the fracture stress σ_f of brittle materials with a known crack size a. However, Griffith's criterion does not work well for ductile materials. G. R. Irwin [166] extended Griffith's method with consideration of the plastic work required to create surface in ductile materials, as

$$\sigma_f = \sqrt{\frac{2E(\gamma_s + \gamma_p)}{\pi a}} \tag{2.21}$$

where E is Young's modulus, γ_s and γ_p are the surface energy of brittle and ductile materials, respectively. H. M. Westergaard [167] analysed the stress state of a cracked body and derived its closed-form expression using airy stress functions. Irwin simplified his solution for the stress near a crack tip as [164]

$$\sigma_{ij} = \frac{K}{\sqrt{2\pi r}} f_{ij}(\theta) \tag{2.22}$$

where σ_{ij} is the stress tensor, r and θ is the polar coordinates, as shown in Figure 2.49. Note that Equation (2.22) implies a stress singularity when $r \to 0$. Here, Irwin introduced K as stress intensity factor to characterises the stress singularity as $K \propto \sigma_{ij}$. K is commonly expressed as

$$K = Y\sigma\sqrt{\pi a} \tag{2.23}$$

where σ is the applied stress, and Y is a dimensionless function related to the crack length (a) and the width of specimen (W). Equation (2.23) implies that the fracture of a material occurs when its stress intensity factor K (resulting from the applied stress and the existing crack length) reaches a critical value, fracture toughness (K_c).

2.4.3 Crack Tip Plasticity

The stress analysis in Equation (2.22) predicts infinite stress at crack tips, which is not realistic. Real materials show plasticity when they are subjected to a stress greater than their yield stress σ_{YS}. As the stress approaches infinity at a crack tip, this implies that there is a plastic zone around the crack tip, where the local stress is greater than σ_{YS}, as illustrated in Figure 2.50.

On the crack plane ($\theta = 0$), Irwin suggested that yielding occurs at $\sigma_{yy} = \sigma_{YS}$, the stress singularity is truncated by yielding at the crack tip. Besides, the exceeded stress must redistribute to satisfy equilibrium [164]. The estimated plastic zone size r_p is expressed as

$$r_p = \frac{1}{\pi}\left(\frac{K_I}{\sigma_{YS}}\right)^2 \tag{2.24}$$

On account of the plastic zone, the relationship of singularity zone and plastic zone is illustrated in Figure 2.51. The exact three-dimensional shape of plastic zone can be calculated by finite element analysis (FEA), as presented in Figure 2.52. Notice that the shape of cross-sectional area on the surface of the specimen is different from the shape in the core since their stress states are different. On the surface, there is no stress in z direction, thus the material is subjected to a plane stress condition. Whereas in the core, the strain in z direction is constrained by the surrounding material, resulting in a plane strain condition. The difference in stress state is important as it affects the measurement of fracture toughness.

2.4.4 Fatigue Crack Growth

Fatigue is a common type of in-service failure where material is subjected to cyclic loading, even when the applied stress is less than the yield stress of the material. Paris *et al.* [168, 169] demonstrated that fracture mechanics is a useful tool for analysing the crack growth behaviour induced by fatigue. Maximum stress σ_{max} and minimum stress σ_{min} are the two main parameters in fatigue testing, we can derive several useful parameters as follows

$$\sigma_{mean} = \frac{\sigma_{max} + \sigma_{min}}{2} \tag{2.25}$$

$$\Delta\sigma = \sigma_{max} - \sigma_{min} \tag{2.26}$$

$$R = \frac{\sigma_{min}}{\sigma_{max}} \tag{2.27}$$

where σ_{mean} is the mean stress, $\Delta\sigma$ is the stress range, and R is the stress ratio. With regards to stress intensity factor, we can incorporate Equation (2.23) into Equation (2.26), which gives

$$\begin{aligned} \Delta K &= K_{max} - K_{min} \\ &= Y\sigma_{max}\sqrt{\pi a} - Y\sigma_{min}\sqrt{\pi a} \\ &= Y\Delta\sigma\sqrt{\pi a} \end{aligned} \tag{2.28}$$

where ΔK is the stress intensity range. Equation (2.28) describes the stress states near crack tip in fatigue testing, as demonstrated in Figure 2.53(a). The variation in stress intensity factor promotes the crack growth in each cycle and introduces a continuously enlarging plastic zone around the crack, as illustrated in Figure 2.53(b).

The rate of crack growth is expressed as da/dN, where N is the number of cycles. It has been discovered that da/dN is dependent on ΔK, and their relationship is illustrated in Figure 2.54. There are three regimes in fatigue crack growth: threshold regime, Paris regime, and static fracture regime (as regime I, II, III indicated in Figure 2.54, respectively). Each regime has a unique fatigue crack growth mechanism, which will be discussed in the following sections.

2.4.4.1 Threshold Regime

When materials are loaded in a low ΔK condition, the crack growth is dominated by shear force in the direction of the primary slip system. This results in a zigzag crack path, as shown in Figure 2.55(a), which is often accompanied by flat fracture surfaces.

If we keep decreasing ΔK, the crack growth rate eventually approaches to zero. The minimal stress intensity range can be defined as fatigue crack growth threshold ΔK_{th}. In threshold regime, the extension of the crack growth in each cycle and the generated plastic zone size are normally on the scale of grain size. Therefore, the value of ΔK_{th} is highly dependent on the microstructural features (e.g. grain boundary). Figure 2.56 illustrates the micro-mechanism of crack growth in this regime. When a crack propagates though a grain, the crack growth stops by the grain boundary, which acts as a barrier for crack growth. The applied stress range causes dislocations pile-up in the adjacent grain, leading to crack initiation and crack coalescence, consequently allowing the crack propagates across the grain [170].

Generally, materials with coarse grains and increased ductility have larger ΔK_{th}, since the crack need more dislocation pile-up to propagate through a coarse grain. However, large grains are usually unfavourable since they reduce the strength of materials. To optimise the microstructural dimensions for ΔK_{th}, a compromise in strength is necessary in the choice of grain size [163].

2.4.4.2 Paris Regime

From the threshold regime, the increase of ΔK results in the enlargement of the plastic zone. Once the plastic zone is large enough, the crack is no long sensitive to microstructural features, and it starts to grow perpendicularly to the applied load, as shown in Figure 2.55(b). This indicates the magnitude of ΔK is large enough, and da/dN starts to move into the Paris regime. In this regime, there is a linear relationship between ΔK and da/dN on a log-log scale in Figure 2.54, which is expressed as

$$\frac{da}{dN} = A \cdot \Delta K^m \tag{2.29}$$

where A and m are material properties.

The crack growth in the Paris regime generates fatigue striations on the fracture surface, as illustrated in Figure 2.57. The formation mechanism of striations is proposed and illustrated in Figure 2.58. In each cycle, the crack opens along with two shear planes when the applied stress is increasing and then blunts when the stress is decreasing. After crack opening and crack blunting, the crack extends by a distance and leaves a striation behind the crack front. The width of striations is dependent on the applied stress range, and it is considered as the physical representation of da/dN [163].

2.4.4.3 Static Fracture Regime

With the increase of ΔK and as K_{max} approaches to K_c, da/dN increases rapidly until the fracture occurs. Since fracture is related to K_{max}, the stress ratio R shown in Equation (2.27) can have a great influence on the crack growth in this regime. Forman extended Equation (2.29) as

$$\frac{da}{dN} = \frac{C \cdot \Delta K^m}{(1-R) \cdot K_c - \Delta K} \tag{2.30}$$

which is widely used in industry as it describes the fatigue behaviour in both regime II and III.

2.4.5 Short Fatigue Cracks

The above introduction about fatigue crack growth is based on a well-developed long crack, in other words, the crack length is significantly longer than microstructural features such as grain size. Short fatigue cracks behave quite differently from long fatigue cracks, for example, the concept of fatigue crack growth threshold ΔK_{th} is not applicable to short cracks. If short cracks had threshold behaviour, there would be no crack initiation from a smooth surface, since according to Equation (2.28) ΔK would always be zero when crack length is zero [164]. The behaviour of fatigue crack initiation and short fatigue crack growth is introduced in the following sections.

2.4.5.1 Crack Initiation

Fatigue crack initiation are found to take place at defects, either on the surface or internally. Typical surface initiation sites include scratches, dents, and threads, as they all suffer from local stress concentration. Typical internal initiation sites include pores, inclusions, phase boundaries, and grain boundaries [163]. Cracks tend to nucleate at pores for stress concentration, similar to those surface initiation sites. Inclusions, either non-metallic inclusions such as oxides or intermetallic inclusions, are typically brittle compared to the matrix. They tend to fracture under low stress, forming internal microcrack which facilitates local stress concentration [164]. Fatigue cracks can initiate at second phase boundaries and grain boundaries due to discontinuous slip system across the boundaries. At elevated temperatures, sliding and cavitation are also promoted at boundaries, allowing environmental embrittlement to further assistant crack initiation [171].

Within defect-free alloys, cyclic loading can generate persistent slip bands (PSBs) on the smooth surface. These PSBs are found to be the initiation sites of fatigue cracks. Figure 2.59 illustrates the formation of PSBs under cyclic loading. The alternate tensile and compressive stress causes the material to slip along the slip systems with maximum critical resolved shear stress, which is usually 45° from the loading axis. The slip bands near surface leads to the formation of extrusion and intrusion on the free surface. The intrusions are particularly harmful as they act like sharp notches with high stress concentration, consequently result in crack initiation [159].

2.4.5.2 Short Fatigue Crack Growth

When the length of a short fatigue crack is only on the order of the grain size, the crack growth behaviour is significantly influenced by microstructural features. At such microscopic scale, the material does not behave as a homogeneous isotropic continuum anymore. Short cracks usually grow irregularly, they may be arrested when they encounters grain boundaries or inclusions, or they may grow rapidly for certain period of time [164].

Figure 2.60 illustrates the stage I short fatigue crack growth behaviour compared to long cracks. After a crack is initiated from PSBs on the surface, the crack can grow along the active slip system with the assistant of resolved shear stress. Once the crack grows across the grain boundary into an adjacent grain, since the next grain is crystallographically oriented differently from the original grain, the Schmid factor of each slip system in the next grain is different, the crack path is required to reorient to meet the critical slip system with minimum critical resolved shear stress in the next grain. If the applied stress is insufficient to meet the critical resolved shear stress, the crack may be arrested at the grain boundary. Alternatively, if the local stress concentration induced by the crack is sufficient to introduce an internal crack within the next grain, then that internal crack may be able to grow backward and join the first crack. To sum up, the crack growth mechanism of short cracks is primarily dominated by shear along the active slip systems, hence short cracks is often referred to as shear cracks (see Figure 2.60). The plastic zone size at the tip of a short crack is only a few grain diameters.

If the short crack overcomes all the microstructural barriers and successfully developed to a stage II long crack, the plastic zone size at the crack tip becomes significantly larger than the microstructural features, the crack growth behaviour now becomes independent to microstructure, instead it is rather dependent on the external loading. Therefore, the stage II cracks are also referred to as tensile cracks (see Figure 2.60). The crack growth mechanism of stage II cracks is introduced in Section 2.4.4. It is considered that the fatigue resistance is primarily determined by the difficulty of a stage I crack growth [172], as a specimen with smooth surface would have significantly longer fatigue life compared to a notched specimen under the same loading condition.

Chapter 3

Materials and Methodology

3.1 Materials

3.1.1 Base Alloys

The linear friction welded (LFW'd) joints studied in this thesis consist of two commercial $\alpha + \beta$ alloys, Ti-6Al-4V (Ti-64) and Ti-5.3Al-7.7V-0.5Si (Ti-575). Their chemical compositions are listed in Table 3.1, their selected physical properties are listed in Table 3.2. The welded samples and test pieces are produced, extracted, and supplied by Rolls-Royce plc.

3.1.2 Pre-Weld Heat Treatment

Pre-weld heat treatments were applied to the alloys prior to the LFW process, as listed in Table 3.3. For Ti-64, a solution heat treatment for 1 hour at 965℃ was applied, followed by an annealing for 2 hours at 700℃. For Ti-575, it first went through a solution heat treatment for 1 hour at 910℃, then followed by an ageing process for 8 hours at 500℃. Air cooling was

applied after all the heat treatment processes mentioned above. All pre-weld heat treatments were carried out by Rolls-Royce plc.

3.1.3 Linear Friction Welding

The alloys were joined by LFW to simulate the blisk joint, where Ti-64 served as the disc material and Ti-575 served as the blade material.

Trapezoidal geometry with flat-to-flat contact and 50° chamfer were used for all welds in this study, as illustrated in Figure 3.1. The direction of friction pressure and oscillation, as well as the weld thickness (T_{max}) and upset are also indicated. The oscillation stroke and the upset were recorded during LFW, their variation against time is shown in Figure 3.2. From the oscillation and upset curves, four phases in LFW can be identified, namely ramp-up, transition, equilibrium, and ramp-down phases.

A total of 8 types of welds were studied in this research, each weld was produced by a distinct combination of T_{max}, upset, and friction pressure. The frequency and amplitude of oscillation for all welds were the same. Processing variables used for each weld are listed in Table 3.4. All welds were produced by Rolls-Royce plc using a LF60 welding machine.

3.1.4 Post-Weld Heat Treatment

The samples and test pieces were sent in as-welded condition from Rolls-Royce, and the post-weld heat treatment (PWHT) was performed using a Camco High Vacuum Cold Wall Furnace at the University of Birmingham. A two-step heating process was used: first, heating from room temperature to 100 ℃ below the desired temperature at a rate of 10℃/minute, then a slower rate of 5℃/minute to reach the desired temperature. After reaching the target temperature, it was held for a desired period before initiating furnace cooling. A schematic diagram of the temperature profile during PWHT is illustrated in Figure 3.3. The tolerance of the desired temperature was controlled within ±5℃, and the

operating vacuum was controlled under 1×10^{-5} Torr. After PWHT, the surface layer with 1 mm depth was removed to eliminate the effect of oxidation.

3.2 Characterisation Methods

3.2.1 Sample Extraction

Micro-slice samples were extracted from the welds by Electrical Discharge Machining (EDM) along the X-Z plane, as illustrated in Figure 3.4. The thickness of the micro-slices is 2 mm. Note that there is a 19° angle between the oscillation direction and the leading edge of the weld. The 19° angle was introduced to resemble the stagger angle of the blades (aerofoil). As texture in the welds is usually dependent on the oscillation direction, this would affect the texture characterisation detailed in Section 3.2.7.

3.2.2 Metallographic Sample Preparation

After extraction, a part of samples underwent designated PWHT conditions while the others stayed in the as-welded condition. All the samples then underwent metallographic preparation before being used in microscopy examination, hardness measurements, and texture analysis. During the preparation, the samples were firstly mounted in conductive Bakelite or non-conductive resin, and then underwent grinding and polishing procedures using a Struers automatic polisher, as shown in Table 3.5. After each grinding step, hand grinding for 1 minute was applied to ensure a flat surface was obtained.

Hardness measurement and texture analysis were performed on samples in the polished condition for better quality of the results. Samples for microscopy examination were etched by Kroll's reagent for 10-15 seconds [173] after polishing. Note that the duration of etching in this study is notably longer than the usual etching duration for titanium alloys, since the microstructural features in weld region is much finer than the parent materials (PMs), it takes longer for the etchant to remove enough α phase and reveal the contrast.

3.2.3 Optical Microscopy (OM)

OM was carried out using a Keyence VHX-6000 digital optical microscope. Generally, a low magnification image at 20x was taken for each sample to give an overview of the weld. High magnification images at 1500x of the samples were used for grain size analysis of the PMs. In the optical images, the α phase appear brighter whereas the β phase appears darker, because the etchant preferably erodes the α phase, leading to a flat surface to reflect more light from a co-axial light source.

3.2.4 Scanning Electron Microscopy (SEM)

SEM was performed using Jeol 6060, Jeol 7000F and Philips XL-30 FEG ESEM to observe the microstructure of the welds at high magnification. The accelerating voltage used in this study is 20 kV, and the working distance is 10 mm. For samples mounted in non-conductive resin, a layer of gold particles was coated on the samples using a sputter coater.

High magnification secondary electron images (SEI) from 2,000x to 20,000x were taken to observe fine microstructural features in the weld, including martensitic α' laths, secondary and tertiary α within β phase, and precipitates in PWHT'd samples. On the contrary to OM, the β phase appears brighter in comparison with the α phase in SEI, as more α phase was etched away by the etchant, less secondary electron would be emitted from α phase.

3.2.5 Image Processing and Analysis

Images of microstructures taken by both OM and SEM were used for grain size analysis and phase fraction analysis. The image analysis was performed using ImageJ and MATLAB®. Several image processing techniques (e.g. gaussian filter [174], adaptive thresholding [175], morphological operations [176], and image region analysis [177]) were adopted to remove the noise signals in the images and better extract the desired features. Although the image processing techniques are sufficient to analyse the majority of the images in this study,

manual tracing was performed if those image processing techniques fail to extract the features.

3.2.6 Energy-Dispersive X-ray Spectroscopy (EDS)

EDS was performed using Oxford Inca EDS attached onto Jeol 6000, Jeol 7000F, and Philips XL-30 FEG ESEM for chemical composition analysis.

The accelerating voltage used in EDS depends on the area of interests, as the interaction volume generated by the X-ray is proportional to the accelerating voltage. The depth of the interaction volume (z_m) can be estimated by Castaing's formula [178], and the radius of the interaction volume (r_X) is given by Anderson-Hasler range [179]:

$$z_m = 0.033(E_0^{1.7} - E_c^{1.7})\frac{A}{\rho Z} \tag{3.1}$$

$$r_X = 0.064(E_0^{1.68} - E_c^{1.68})\frac{1}{\rho} \tag{3.2}$$

where E_0 is the accelerating voltage (kV), E_c is the minimum emission voltage (keV); A is the atomic mass, ρ is the density (kg/m^3), and Z is the atomic number of the material.

The spatial resolution of EDS analysis is primarily determined by r_X. For titanium, the interaction radius resulting from an accelerating voltage at 20 kV for usual examination is approximately 2.12 μm, which is sufficient for characterising the composition of α phase and β phase, as the average grain size of primary α grains is approximately 10 μm. However, such resolution is not enough to analyse the chemical composition of fine microstructural features in the welds, such as martensitic laths and precipitates, whose size is usually submicron. For the chemical analysis of fine features, the accelerating voltage was reduced to 10 kV, which reduces the interaction radius down to approximately 0.53 μm.

3.2.7 Electron Backscatter Diffraction (EBSD)

EBSD was performed using Jeol 7000F FEG-SEM with Oxford AZtec software. Data analysis was carried out by AZtec and Channel 5 HKL software, as well as MTEX – a MATLAB toolbox [180].

Polished samples were used for EBSD measurements, sample preparation methods are described in Section 3.2.1. After inserting the samples into the SEM, the working distance was set to 20 mm, and the samples were tilted to 70º facing toward the EBSD detector. The EBSD mapping was carried out using an accelerating voltage at 20 kV and a probe current at $1.2 \cdot 10^{-8}$ Å. The step size used for each map was chosen depending on the mapping area and the minimum size of the microstructural features, the value ranged from 0.1 to 0.5 μm.

For each Electron Backscatter Pattern (EBSP) recognition, at least 4 Kikuchi bands were required for a pattern solution, and the allowance between the detected Kikuchi band and the ideal solution band was set to be 2.5º. The lattice parameters of all phases for indexing EBSPs in this study are listed in Table 3.6.

The indexing rates for the EBSD maps taken at the PMs were nearly 100%. However, due to the fine features found in Ti-575 CWZ, it is naturally difficult to get a good indexing rate there. In this study, the indexing rates in Ti-575 CWZ are at least larger than 70%. Data cleaning technique provided by AZtec software was used to improve the quality of the EBSD maps, after the application of data cleaning, the solved indexed rate in Ti-575 CWZ can be improved to nearly 100%.

EBSD was used for texture analysis in the current study. Pole figures and inverse pole figures (orientation maps) were generated using AZtec and Channel 5 software to identify the texture component in each zone of the dissimilar welds. EBSD mapping can also be used for grain size and phase fraction analysis, as the EBSP can be utilised to determine crystal structure . Since the requirement of spatial resolution for these kinds of analyses is not so

strict, as the average primary α grain size is approximately 10 μm, a larger step size (0.3-0.5 μm) was used in these kinds of analyses.

Figure 3.5 illustrates the sample coordination used in EBSD measurements, where the sample normal direction is parallel to the sample Y direction, the forge direction (FD) is parallel to the sample Z direction, and the oscillation direction (OD) lies on the sample X-Y plane with a 19° stagger to the sample X direction. The raw EBSD measurements were all initially aligned with sample coordinates (i.e. X, Y, and Z directions), however, for oscillation-dependent textures, their pole figures would not be symmetrical as their texture components does not align with sample coordinates. To better visualise the pole figures for oscillation-dependent textures, in the current study, these pole figures were rotated −19° by the Z-axis and plotted in FD-OD coordinates, this makes the pole figures symmetrical and shows the most texture components. The pole figures presented in this study are plotted using equal area projection in default, except for those with a specific type of projection mentioned in the captions.

3.2.8 β Reconstruction

β reconstruction was carried out to analyse the $\beta \rightarrow \alpha$ phase transformation occurred during LFW, especially within CWZ and TMAZ. β reconstruction was performed using MTEX [180], which is a MATLAB® toolbox for analysing EBSD data. In the reconstruction process, Burgers orientation relationship [34], as shown in Equation (2.1) and (2.2) is applied. The angular threshold to differentiate the α grains was set to 1.5°, which is deliberately small to avoid α orientations that belong to different β grains get merged into the same α grain. The variant graph was calculated using a 1.5° threshold with three iterations. β grains with misorientation less than 5° were considered as the same grain, therefore are merged into a single grain. After merging the prior β grains, normally there are still numerous discrete

'inclusions' within the β grains where the reconstructor fails to assign a prior orientation. Those poorly indexed inclusions were merged into the surrounding grain if they consist of fewer pixels than a certain threshold. The MATLAB® script used to perform β reconstruction can be found in Appendix C.1.

3.2.9 Transmission Electron Microscopy (TEM)

TEM was used to analyse the chemical composition, the crystal structure, and the orientation of the fine microstructural features in the CWZ and TMAZ.

The samples for TEM examination were prepared by the twin-jet polishing method. Samples were firstly thinned down to 300 μm thick, and then discs with 3 mm in diameter were extracted by a Disc Punch System. These discs were further thinned down to 150 μm before twin-jet polishing. Twin-jet polishing was performed on a Struers TenuPol-3 polishing machine with an electrolyte containing 60% methanol, 35% butanol and 5% perchloric acid (in volume fraction) at 20 V and -35℃. The twinjet polishing electrolyte punched a hole through each disc and made the surrounding area of the hole electron transparent (less than 100 nm thick). Although the twin-jet polishing method can prepare lots of TEM samples quickly, there is no control to the location of the electron transparent area. For LFW'd Ti-64:Ti-575 joints, it turns out that the hole tends to locate at the CWZ on Ti-64 side. Hence it is not suitable to prepare TEM samples for Ti-575 using the twin-jet polishing method.

For site-specific TEM samples, focused ion beam method was used to extract the foils at the desired location. This method was performed on a FEI Quanta-3D FEG FIB-SEM. After locating the region of interest on a micro-slice, a layer of platinum was deposited on the surface as a protection before milling out the surrounding material. An undercut was performed to extract a thin foil perpendicular to the surface of the micro-slice. The thin foil was then attached to an I-shaped post on a copper grid by platinum deposition on both sides of an edge. Note that the usage of V-shaped post was avoided as it affects the results of EDS analysis. Normally this

method is able to produce a 10 x 10 x 2 μm^3 thin foil at this stage. Finally, the thin foil was then carefully thinned and polished down to about 100-200 nm thick to be electron transparent for TEM examination.

Selected area diffraction (SAD) analysis was carried out to determine the crystal structure of the microstructure in the welds. For small features that are difficult to analyse, convergent beam electron diffraction (CBED) was taken instead of SAD patterns. All microstructural features were analysed by a combination of dark field images (DFI), bright field images (BFI), and the corresponding diffraction pattern. The lattice parameters of the phases listed in Table 3.6 were used to index the SAD patterns obtained from TEM under multiple zone axes. Tilt experiment [181] was performed to further confirm the uniqueness of the result. The diffraction pattern analysis was carried out with the assistance of CrysTBox software [182] to measure the d-spacings and angles from the diffraction patterns. A program developed by the author using MATLAB® was used to automatically index the input patterns and perform tilt experiment, the source code of the program can be found in Appendix C.2. Note that the code is only partially presented here, it only takes two crystal structures (`Hcp-Ti` and `Bcc-Ti`) into consideration, whereas in the current study all crystal structures listed in Table 3.6 were considered. Other crystal structures can be included by creating new classes which inherit the `CrystalStructure` class and implement the abstract properties and methods.

3.3 Mechanical Testing

3.3.1 Hardness Measurement

The microhardness variation across the weld interface of samples with polished surface was measured by a Struers DuraScan-5 micro-hardness tester with 0.5 kg load and 10 second holding time. The indent pattern used in this study was designed to have more indents in the weld zone to characterise its sudden change of hardness values. Meanwhile, the minimum distance between individual indents was at least three times of the indent diameter according

to British Standard BS 6507-1 [183]. The indent pattern was carefully aligned to ensure that it's perpendicular to the weld line.

After the application of the indents, a stitched image covering all indents across the weld interface was taken at 500x magnification using an optical microscope, this image was then processed by a MATLAB® script to automatically determine the size and the location of the indents using image processing techniques described in Section 3.2.5. The script can be found in Appendix C.3. This script has been validated with manual measurement, and the error was ensured to be less than 3%, as shown in Figure 3.6. With the diameters of the indents, the corresponding Vickers hardness value (HV) is given by

$$HV = \frac{2F \sin\left(\frac{\theta}{2}\right)}{\bar{d}^2} \tag{3.3}$$

where F is the applied load, θ is the angle at the vertex of the pyramidal indenter (nominally is 136°), and $\bar{d}$ is the average of the two diagonal lengths of the indent.

The hardness values and their corresponding location can be utilised to produce hardness maps for the samples. Natural neighbour interpolation [184] was used to smoothly interpolate the hardness values in-between the indents. The programming script to plot hardness maps can be found in Appendix C.4. Additionally, hardness profiles can also be extracted by averaging the hardness values with the same distance to the weld interface. The indent pattern used in this study was designed to have at least five indents sharing the same distance to the weld interface. The error bar of each data point in the hardness profiles indicates one standard deviation of the hardness values, as demonstrated in Figure 3.6.

The average macrohardness of both PMs and the weld interface was also measured using the same hardness tester with 10 kg load and 10 second holding time. Note that larger load was used to cover more grains in order to better approach the true mean hardness value. At least three indents were used for each sample, if the deviation of the initial three indents had been larger than 10 HV, more indents were then be applied.

The measured hardness values are useful for predicting the strength of the materials. The relationship between HV and yield stress (σ_y) for titanium alloys is given by

$$\sigma_y = \frac{HV \cdot g}{3} \cdot 0.1^n \tag{3.4}$$

where $g = 9.81$ m/s^2 is gravitational constant, and n is the strain hardening exponent. For Ti-64, $n = 0.176$ [185]. Equation (3.4) was utilised to estimate the strength of the PMs as well as the strength of the welds for each weld zone.

3.3.2 Ageing Behaviour

In order to investigate the optimal condition of PWHT, a series of PWHT were performed on the samples at different temperatures (450/500/550/600/650/700 ℃) and different holding time (0.5/1/2/4 hours). After PWHT, the hardness of the PMs and the weld interface was measured to produce the ageing curves. With the ageing behaviour in respect of duration and temperature, over-ageing can be avoided, and the optimal PWHT condition, which gives the sufficient hardness for the weld and for the PMs, can be determined. It is worth noting that a practical PWHT requires also considering the degree of stress relief for the residual stress. Hence, the PWHT conditions were downselected depending on the hardness values, then residual stress measurement was performed for the test pieces after selected PWHT.

3.3.3 Test Piece Extraction

Test pieces for mechanical testing were firstly extracted from the welds by Electrical Discharge Machining (EDM), followed by a high precision machining to their final dimensions. Figure 3.4 illustrates the orientation of the test pieces. Two types of test pieces were extracted, either cylindrical test pieces or single-edge-notched bending (SENB) test pieces. Cylindrical test pieces were used in testing in axial loading condition, such as tensile testing and high cycle fatigue testing. SENB test pieces were used in three- or four-point bending configuration in fatigue crack propagation testing. Note that there is a 19° stagger

between the oscillation direction and the leading edge of the weld. The extraction of SENB test pieces was aligned with the oscillation direction, to assure that the crack propagation direction is either parallel or perpendicular to the oscillation direction in this study. The full-sized extracted SENB test pieces have a 10×9 mm^2 cross-sectional geometry. Further cutting of the SENB test pieces were applied to produce half-sized test pieces for a greater degree of stress relief. The half-sized test pieces have either 10×4.5 or 9×5 mm^2 cross-sectional geometry.

3.3.4 Tensile Testing

Tensile tests were carried out using a Zwick 1484 screw-driven testing machine with a 200 kN load cell at room temperature in accordance with BS 6892-1:2019 [186]. A Zwick clip on macro extensometer was used to monitor the gauge length extension during the test, and a digital system, Zwick Test Expert 2, was used to control the machine and record data.

All the geometry of specimens were cylindrical tension-tension threaded test piece with two ridges for mounting the extensometer. The gauge diameter is 5 mm, and the gauge length is 25.3 mm (i.e. the distance between the two ridges).

The specimens were monotonically loaded in stroke control at a speed of 0.2 mm/minute until the ultimate fracture of the test piece. During the test, the applied load and the distance between the ridges were recorded. Engineering stress-strain curves can be produced by the collected data., and the engineering strain is given by

$$\varepsilon = \frac{\Delta L}{L_0} \tag{3.5}$$

where ΔL is the total elongation of the gauge length, and L_0 is the initial gauge length. The engineering stress is given by

$$\sigma = \frac{P}{A} \tag{3.6}$$

where A is the cross-sectional area of the specimen. For a cylindrical geometry, $A = \pi\left({}^{d}/_{2}\right)^2$.

From the stress-strain curve, several useful information can be obtained. The yield stress (σ_y) can be determined from the result by calculating the intersection between the stress-strain curve and the 0.2% offset of the elastic region; the ultimate tensile stress (UTS) can be determined from the maximum stress appeared in the stress-strain curve; the Youngs' modulus (E) can be determined by the slope of the elastic region; and the plastic strain (ε_p) can either be determined by the total elongation subtracted by the elastic elongation, or be measured from the total length of the fractured specimen.

Note that for dissimilar weld specimens, the data obtained from the tensile testing may not be representative for either of the PMs nor the weld, since the test pieces are not homogeneous, thus the deformation of each material may not be equivalent. Generally, the material with lower strength would have more deformation. Therefore, the measured properties result from all materials within the test piece.

3.3.5 High Cycle Fatigue Testing

High cycle fatigue (HCF) tests were carried out according to the British Standards BS 3987:2009 [187], BS 3518-1:1993 [188], and BS 1099:2017 [189]. All the tests were performed using an Amsler Vibrophore resonant test machine with a 20 kN load cell at room temperature. The applied waveform was sinusoidal with a natural frequency at approximately 80 Hz. All specimens were machined to a cylindrical tension-tension geometry with 4.5 mm diameter (d) and 12 mm gauge length. The applied stress (σ) was calculated by Equation (3.6).

The maximum stress $\sigma_{\max}$ used in the HCF tests ranges from 450 to 800 MPa with a stress ratio $R = 0.1, 0.3, \text{and } 0.7$. For each test, the applied $\sigma_{\max}$ and R were kept constant during the entire test. The HCF tests were terminated either when a catastrophic failure occurred, or when it achieved 1.5×10^7 cycles, which is considered as run-out. In each test, the applied maximum stress, the stress ratio, and the number of cycles was recorded. Additionally, in

the HCF tests with dissimilar weld, the failure location – in terms of the distance to the weld interface – was also recorded. After all tests have been done, a S-N curve was generated from the data.

3.3.6 Fatigue Crack Growth Testing

3.3.6.1 Fatigue Threshold Testing

The fatigue crack growth threshold ΔK_{th} of the test pieces was tested according to the British Standard BS 12108:2018 [190]. Different crack orientations (parallel or perpendicular to the oscillation direction) and crack locations (at the weld interface, CWZ, TMAZ, or PM) were used in the tests to investigate their effect. Every test was carried out at room temperature using Amsler Vibrophore resonant testing machine with a 20 kN load cell, and a sinusoidal waveform with frequency approximately 65 Hz.

Single-edge-notched bending (SENB) specimens and four-point bending configuration were used in pre-cracking and the following fatigue crack growth threshold testing, as shown in Figure 3.7. The specimens were received with smooth machined surfaces without a notch initially, they were firstly etched to reveal the weld interface, before introducing a 1 mm notch at a desired location by EDM. A reverse bending, where the notch of SENB sample is placed upward rather than downward in Figure 3.7, was applied before pre-cracking. The load magnitude was intentionally selected to ensure that the crack tip experienced a stress level close to yielding. The reverse bending can create a tensile residual stress at the notch tip so as to facilitate pre-cracking with a straight crack front.

Pre-cracking was then performed with stress ratio $R = 0.1$ at about 80 Hz to introduce a 0.5 mm crack ahead of the notch tip. To minimise the effect of pre-cracking, load-shedding method was adopted during the pre-cracking process. The crack length was monitored by the Direct Current Potential Difference (DCPD) method during both pre-cracking and the actual testing. The details of this method can be found in Section 3.3.6.3.

After pre-cracking, the fatigue crack growth threshold testing was carried out with a starting ΔK. The starting ΔK was chosen to yield a crack growth rate $da/dN \geq 10^{-5}$ mm/cycle. For a SENB specimen in four-point bending configuration, ΔK is given by

$$\Delta K = \frac{\Delta P \cdot S}{BW^{1.5}} f\left(\frac{a}{W}\right) \tag{3.7}$$

where S is the loading span, ΔP is the load range, B and W is the thickness and width of the specimen, respectively. ΔP is related to the maximum applied load $P_{\max}$ and the stress ratio R, their relationship is given by

$$\Delta P = P_{\max}(1 - R) \tag{3.8}$$

$f(a/W)$ is a dimensionless function related to specimen geometry, for SENB it is given by

$$f\left(\frac{\mathrm{a}}{\mathrm{W}}\right) = 3(2\tan\theta)^{0.5}\left[\frac{0.923 + 0.199(1 - \sin\theta)^4}{\cos\theta}\right] \tag{3.9}$$

where

$$\theta = \frac{\pi a}{2W} \tag{3.10}$$

Equation (3.9) is valid for $0 \leq a/W \leq 1$.

K-decreasing method was used for all fatigue crack growth threshold tests. The stress ratio R was held constant during the entire test, while the applied load was kept reducing at each 5 μV increment, which is equivalent to about 0.1 mm increment of crack length Δa, to achieve a reduction in ΔK. The reduction in ΔK obey the following equation:

$$\Delta K_{i+1} = \Delta K_i \exp(C_k \Delta a) \tag{3.11}$$

where i indicates each increment of crack growth, C_k is the normalised gradient of ΔK. For every test, C_k was fixed at -0.35 mm^{-1} to achieve a final a/W between 0.45 to 0.55.

The crack growth rate da/dN was determined by a three-point secant for data smoothing, as

$$\frac{da}{dN} = \frac{a_{i+1} - a_{i-1}}{N_{i+1} - N_{i-1}} \tag{3.12}$$

The test was terminated once da/dN satisfies the following criteria

$$\frac{da}{dN} \leq 10^{-8} \text{ mm/cycle} \tag{3.13}$$

After the test was completed, fracture toughness testing was carried out to break open the specimen. Then the actual crack length was measured from the fracture surface to calibrate the crack length estimated by the DCPD method. Details of crack length measurement is described in Section 3.3.6.3. Finally, the corrected ΔK corresponding to Equation (3.13) was regarded as the fatigue crack growth threshold ΔK_{th}.

The location of the crack tip when it reached the fatigue crack growth threshold was estimated by the side views of the crack taken by an optical microscope. The distance between the crack tip and the weld interface can be measured from the side views. By comparing this distance with the thickness of each weld zone, the location of the crack tip (in terms of which weld zone it is located in) can be determined.

If a crack is located in the Ti-64 CWZ when viewed from one side, and in the Ti-575 CWZ when viewed from the other side, it evidently suggests that the crack spans across the weld interface somewhere in the specimen. The location of such cracks is labelled as 'interface'.

3.3.6.2 Fatigue Crack Propagation Testing

The fatigue crack growth resistance of the welds and the PMs was tested by fatigue crack propagation testing according to the British Standard BS 12108:2018 [190]. Every test was carried out at room temperature using ESH servo-hydraulic testing machine with a sinusoidal waveform and a frequency approximately 10 Hz.

Similar to the fatigue crack growth threshold testing, SENB specimens and four-point bending configuration were used for fatigue crack propagation testing, as shown in Figure 3.7. The specimens initially went through a reverse bending and a pre-cracking process before the actual testing. DCPD method was also used here for crack length monitoring, as described in Section 3.3.6.3.

K-increasing method was used for all fatigue crack propagation tests, where the applied load was remained constant, and thus the applied stress intensity factor would increase along with the increment of the crack length. The initial ΔK was chosen to give a starting $da/dN \approx 10^{-5}$ mm/cycle, and the test was terminated at $da/dN \approx 2 \times 10^{-3}$ mm/cycle to capture the crack growth behaviour in both Paris regime and static fracture regime.

After the crack propagation testing was completed, similar to the fatigue crack growth threshold testing, the specimen was broken by performing fracture toughness testing, then the actual crack length was measured from the fracture surface for crack length calibration. The location of the crack was also determined by the side views. Finally, the Paris law constants A and m, as derived from Equation (2.29), were obtained through a linear regression in log-log scale on the calibrated da/dN against ΔK curves within the Paris regime. The Paris regime was determined by the highest number of consecutive data points that result in the optimal linear fit (or statistically, minimum regression coefficient).

3.3.6.3 Direct Current Potential Difference (DCPD) Method

The variation of crack length during the fatigue tests was monitored by DCPD method. The advantage of DCPD method is that it is an *in-situ* monitoring technique, thus manual interruption for crack measurement can be reduced.

Two lead wires were spot welded on both sides of the notch, the distance between the spot-welding location was 2 mm. A direct current was provided by a voltage box through crocodile clips at each end of the specimen. The apparatus was left for ten minutes before testing to obtain the initial stabilised potential difference V_0. As the crack length increases, the cross-

sectional area of the specimen decreases, and thus the resistance of the material increases. Consequently, by Ohm's law, the potential difference V between the two lead wires increases, hence it can be utilised to estimate the crack length. The relationship between normalised crack length a/W and normalised potential drop V/V_0 for SENB specimens is given by an in-house calibrated function as

$$\frac{a}{W} = -0.21395 + 0.59859\left(\frac{V}{V_0}\right) - 0.15197\left(\frac{V}{V_0}\right)^2 + 0.01733\left(\frac{V}{V_0}\right)^3 \tag{3.14}$$

Note that the crack length measured by DCPD method may not be the actual crack length, it will be calibrated after breaking open the specimen and measuring the actual crack length on the fracture surface.

The actual crack length was measured from the fracture surface using an optical microscope, as demonstrated in Figure 3.8. The average crack length was calculated using nine-point average value as

$$\bar{a} = \frac{(a_1 + a_9)/2 + \sum_{i=2}^{8} a_i}{8} \tag{3.15}$$

On the fracture surface, only the pre-crack length (or notch length if the pre-crack was not clear on the fracture surface) and the final crack length were measured for the calibration, all other values were calculated by linear interpolation, as

$$a^c = a_0^c + (a - a_0)\frac{a_f^c - a_0^c}{a_f - a_0} \tag{3.16}$$

where a^c is the corrected crack length, a is the estimated crack length; a_0^c is the measured pre-crack length, a_0 is the estimated pre-crack length; a_f^c is the measured final crack length, and a_f is the estimated final crack length.

3.3.6.4 Fracture Toughness Testing

Fracture toughness tests of the welds and the PMs were carried out according to the British Standard BS 7448-1:1998 [191]. A portion of the tests was carried out using a DMG screw-driven test machine with a 100 kN load cell at room temperature.

The fracture toughness testing was carried out after either fatigue crack growth threshold testing or fatigue crack propagation testing – the final crack length for these tests serves as the initial crack length for the fracture toughness test, and the normalised crack length a/W was between 0.45 and 0.55 for majority of the test pieces.

Before testing, 2 mm outward pointing knife edges were attached to both sides of the notch tip, and a DG-40 clip gauge was mounted on the knife edges to monitor the notch tip opening displacement during the testing. Similar to the fatigue testing, SENB specimens and four-point bending configuration were used for fracture toughness tests, as shown in Figure 3.7. The test piece was then loaded monotonically on the testing machine in stroke control at a constant rate of 0.5 mm/minute until a catastrophic failure occurred. During each test, the applied load and the notch tip opening displacement are recorded, and a load against displacement curve can be produced from the collected data.

Figure 3.9 illustrates three typical loads against notch tip displacement curves and the definition of tentative fracture load P_Q, which is denoted as F_Q in Figure 3.9. For all tests in the weld, the obtained curves only show linear elastic behaviour before fracture, which is the case I in Figure 3.9. This implies that the maximum load P_{max} during the fracture toughness testing can be treated as the tentative fracture load P_Q for all tests in the weld, as there's nearly no plastic deformation occur during the test. After realising this fact, the rest of the fracture toughness testing was done by ESH servo-hydraulic testing machine without clip gauge.

Similar to Equation (3.7), for a SENB specimen in four-point bending configuration, the tentative stress intensity factor K_Q is given by

$$K_Q = \frac{P_Q S}{BW^{1.5}} f\left(\frac{a}{W}\right) \tag{3.17}$$

where $f(a/W)$ is given by Equation (3.9), S is the loading span, P_Q is the tentative fracture load, B and W is the thickness and width of the specimen, respectively.

The validity of K can be justified if all the following criteria are satisfied

$$2.5\left(\frac{K_Q}{\sigma_y}\right)^2 < \begin{Bmatrix} a_0 \\ B \\ W - a_o \end{Bmatrix} \tag{3.18}$$

where a_0 is the initial crack length, σ_y is the yield stress of the material. σ_y can be either measured by tensile testing or estimated by Equation (3.4) from the hardness measurement. In addition, all nine-point measurements of crack length in Equation (3.15) must not exceed $0.1\sqrt{(W-a_0)B}$. There are several other criteria to be checked for valid usage of K, they can be found in the British standard [191]. If K-validity test is passed, the tentative stress intensity factor K_Q is equivalent to the plane strain fracture toughness K_{Ic}.

If Equation (3.18) is not satisfied, then the obtained K_Q is not sufficient to describe the plane strain fracture toughness of the material, elastic-plastic fracture toughness (J_{Ic}) testing may be needed to characterise this kind of behaviour.

3.3.6.5 Residual Stress Measurement

The residual stress within the SENB specimens was measured by Stresscraft Ltd. using hole drilling method. A schematic diagram of the locations of residual stress measurements can be found in Figure 3.10. Before the hole drilling, Stresscraft type EA-06-031UMG1360-120 strain gauges were attached by the hole. The holes were drilled at the heat-affected zone in both Ti-575 and Ti-64, which is about 1 mm to the weld interface. The holes were drilled

incrementally with 16 increments, given a final diameter of about 1 mm, and a final depth of 704 μm. As the material removed by the drilling process, the relaxation of the residual stress around the holes would cause the surrounding material to deform. This deformation was measured by the strain gauges, the residual stress can be calculated from the measured strain based on generalised Hooke's law in two dimensions; the details of residual stress calculation can be found in American Society for Testing and Materials (ASTM) standard E837-20 [192]. The relevant material properties used for strain-to-stress data conversion are listed in Table 3.2. For both alloys, holes were drilled on two surfaces to ensure that residual stresses along both the forge direction and the oscillation direction were obtained.

3.3.7 Fractography

The fracture surfaces from the specimens after mechanical testing were examined using both optical microscopy and electron microscopy. An overview of each fracture surface was taken at 20x magnification using an optical microscope. For single edge notched bending specimens, the optical images of the fracture surfaces were used for crack length measurement and calibration, as demonstrated in Figure 3.8. Both front view and back view of the cracks were also taken to measure the distance of the crack relative to the weld interface, which is useful for determining the location of the crack. Secondary electron images were used to inspect the details of the fracture surfaces for determination of fatigue crack propagation mechanisms and fracture mechanisms.

3.4 Processing Assessment

3.4.1 Flash Characterisation

The microstructure in the flash was studied to obtain more information during LFW process, as the flash preserves the same microstructure when it was extruded. It is considered that the entire flash contains the whole history of the LFW process. A cross-section of the flash was machined from the weld carcass by electrical discharge machining (EDM), then it went

through a standard metallographic sample preparation procedure as described in Section 3.2.1.

A stitched image covering the whole flash was taken at 30x magnification, as shown in Figure 3.11. The thickness of the flash particularly extruded from each alloy was measured from the optical images of the flash, as shown in Figure 3.12. Notice that ridges on the Ti-64 side of the flash can be observed from Figure 3.11, each ridge was formed by each oscillation cycle during LFW process, as illustrated in Figure 3.13. Thanks to the correlation between the ridges and the oscillation cycles, the exact time when each ridge was extruded can be identified through counting the cycles on the oscillation stroke in Figure 3.2. The flash thickness measurement can then be correlated to the oscillation stroke, leading to an insight of flash thickness variation throughout the welding process, as shown in Figure 3.14. The flash thickness can be seen as an indication of the extrusion rate, higher flash thickness corresponds to higher extrusion rate. By calculating the ratio of flash thickness between the two alloys, the relative extrusion rate and/or relative upset can be estimated.

The microstructure in the flash was investigated using SEM with the machines and the procedures described in Section 3.2.4. As mentioned above, by correlating the ridges in the flash to each oscillation cycle, it is possible to identify the microstructure at a specific time during the welding process. For instance, the end of the flash, where the flash attached to the weld, is considered to have the microstructure resulting from the final deceleration stage. On the other hand, the tip of the flash is regarded to be firstly extruded during the transition stage. In the middle of the flash, the thickest part is reckoned to be extruded during the equilibrium stage. The observation of the microstructure at different locations of the flash can give indications of the temperature distribution and weld zones sizes at any given time during LFW process.

3.4.2 Flow Stress Testing

The flow stress testing was performed using a closed loop servo-hydraulic testing machine (Instron 8850) by the University of Oxford. The machine was equipped with a 100 kN load

cell and a digital system control using Instron's Wavematrix software. The experimental setup is illustrated in Figure 3.15.

Cylindrical specimens with 4 mm in diameter and 4.5 mm in height was used in the flow stress testing, they were held between tungsten carbide anvils inside a vacuum chamber. The contact surface of the anvils was lubricated with a thin film of Boron Nitride spray as a high-temperature lubricant.

Specimens were heated to the desired testing temperature in the range of 800-1200℃ by an induction coil powered by 10 kW Ambrell EasyHeat Induction system. A K-type thermocouple with 0.15 mm diameter was spot-welded at the central region of the cylindrical specimens with a special limit of error ±1.1℃ or 0.4%, whichever is greater. An Eurotherm 2704 PID controller was used to control the temperature, it is capable of using thermocouple for feedback in the closed loop control system. It is worth noting that the anvils and the contact surfaces were also inside the induction field of the coil and hence were heated to the desired temperature as well. This greatly reduced the thermal gradient in the specimens.

After reaching the desired testing temperature, the compression of the specimens was initiated immediately. The servo-hydraulic machine was operated under displacement control to achieve a constant strain rate at 1/s until achieving a total engineering strain at 0.55. Rapid quenching was followed by the compression through the thermal conduction to the anvils at approximately 100℃/s, in an attempt to minimise any change of the recovered microstructure.

3.4.3 Dynamic Beta Approach

As LFW process only takes approximately three seconds to complete, it is known to have an extremely fast heating rate and cooling rate. In order to understand the phase content of the weld in such dynamic condition, a series of heat treatments was performed to establish a dynamic beta approach curve for both Ti-64 and Ti-575.

The samples were used in the heat treatments, and they were machined to a small size approximately $5 \times 2 \times 2$ mm^2 to minimise the thermal gradient in the samples. A Carbolite STF & TZF horizontal tube furnace was used for this study, it was pre-heated to 50℃ above the desired temperature before inserting the sample in order to achieve fast heating rate. The samples were firstly attached to a N-type thermocouple with a Fluke 60 Hz thermometer, and then inserted to the pre-heated furnace. Once the temperature reaches the desired temperature, water quenching was carried out immediately. The duration of the samples at the desired temperature was controlled within one second, to limit any diffusional phase transformation.

The reading of the thermometer during the whole process was recorded to establish the temperature profile, as shown in Figure 3.16. From the temperature profile, we can work out the average heating rate and cooling rate. For all samples, the achieved heating rate is approximately 25℃/s, and the achieved cooling rate is approximately 500℃/s.

After the heat treatment, the samples went through the standard metallographic preparation procedures, and their microstructure were examined by SEM. An example of the micrograph of the samples is shown in Figure 3.17 (a), it is clear to see that numerous α grains retained in the microstructure. EBSD mapping was used to characterise these grains, and it has been confirmed that they are retained primary alpha grains α_p, as shown in Figure 3.17 (b)(c). EBSD phase map was also utilised to automatically quantify the phase fractions of the retained α_p in the microstructure, and by plotting the phase fractions against the peak temperature in heat treatment, the dynamic beta approach curves can be established.

Chapter 4

Microstructure Characterisation

4.1 Characterisation of Weld Zones

Linear friction welding (LFW) results in a narrow weld region which undergoes a rapid heating and cooling treatment together with thermo-mechanical deformation. This process modified the microstructure significantly. The weld zones can be distinguished from the optical micrographs by the high contrast between each zone, as shown in Figure 4.1. The thermo-mechanically affected zone (TMAZ) appears to be the dark region, whereas the central weld zone (CWZ) appears to be the bright region within TMAZ. The heat-affected zone (HAZ) cannot be easily distinguished from the parent material (PM) in optical macrographs as they share similar morphology.

The optical macrographs of two etched Ti-64:Ti-575 welds with different T_{max} are shown in Figure 4.2. Notice that the zone size of the CWZ and TMAZ is not uniform along the weld interface on both Ti-64 and Ti-575 sides. The sizes of the CWZ and TMAZ were measured from Figure 4.2 and presented in Figure 4.3. At the bifurcation point, where the flow of the material diverges, both alloys have thinner CWZ and thicker TMAZ compared to the edges.

Additionally, notice that at the bifurcation point, Ti-575 has a slightly thinner CWZ compared to Ti-64, however, on the edges the Ti-575 CWZ is obviously larger than the Ti-64 CWZ. Comparing Figure 4.3 (a) and (b), we can see that larger T_{max} yields larger zone sizes (e.g. the maximum Ti-575 CWZ size for 18 mm and 32 mm welds is 0.34 mm and 0.77 mm, respectively). This indicates that the weld with a larger T_{max} achieved higher temperature at the weld interface during welding, as the zone sizes correlate with the temperature distribution in the weld.

It is also worth mentioning that the bifurcation point is not at the centre of the welds. This phenomenon can be observed in both Figure 4.3 (a) and (b) for both T_{max}. Vairis and Frost [124] analysed the frictional heat generated during LFW, they discovered that instead of symmetrically distribution throughout the whole cycle, the heat input is concentrated during the same one half of each cycle, resulting in an uneven temperature distribution along the weld interface. The half of the weld with higher temperature has a thicker plasticised layer, hence more material can be extruded. Consequently, this leads to a rotation of the weld interface from the original contact plane, as can be observed in Figure 4.2 (a) and (b), both weld interfaces are slightly rotated clockwise, indicating that the right halves of the welds have greater heat input. Coincidentally, in Figure 4.3 (a) and (b), both right halves of the welds have thicker CWZ, which can be seen as the plasticised layer.

4.2 As-Welded Microstructures

Detailed examinations for each weld zone in the as-welded condition were carried out using SEM in this study. The observations of microstructural features and the proposed formation mechanism are summarised as follows:

4.2.1 Ti-575

4.2.1.1 Parent Material

The microstructure of the Ti-575 PM is shown in Figure 4.4. In the secondary electron images (SEI), α phase appears dark whereas β phase appears bright. Ti-575 has a typical

bi-modal microstructure with equiaxed primary α grains and transformed β region. The microstructure of the PM is largely determined by their pre-weld heat treatment, which is listed in Table 3.3. The high-magnification secondary electron image of Ti-575 is shown in Figure 4.4 (b). Fine secondary and tertiary α laths can be seen in the image; their width is approximately 300 nm for secondary α and 50 nm for tertiary α. The tertiary α laths can only be found in Ti-575 due to their additional ageing treatment (see Table 3.3), they are suspected to be the main contributor to the superior hardness of Ti-575, which is discussed in Section 6.2.

Electron backscatter diffraction (EBSD) mapping was utilised to analyse the primary α grain size in Ti-575, as shown in Figure 4.5. The measured primary α grain size is 11.9 ± 3.9 μm, and the primary α content is 68%. However, according to Thomas *et al.* [13], with the same heat treatment trials, the resulting primary α content of Ti-575 is only 15-18%. A possible reason for such discrepancy may be the introduction of pre-weld heat treatment in this study. The mechanical properties of the Ti-575 alloy may have a huge difference to the one used in the literature because of the large deviation in the α phase fraction, this will be discussed later in Section 6.4. Notice that in the orientation map as shown Figure 4.5 (a) a macrozone [179, 193, 194] coloured in red can be recognised at the bottom left corner. The texture of this macrozone can be identified through pole figures shown in Figure 4.5 (d), as a $\{0001\}_\alpha$ is concentrated with a maximum intensity of 4.63 multiple uniform distributions (MUD).

Energy-dispersive X-ray spectroscopy (EDS) was used to carry out chemical composition analysis for the PM. The chemical composition of α and β phase in Ti-575 is listed in Table 4.1. It can be seen that there is more aluminium content in α phase, and there is more vanadium content in β phase, as aluminium serves as an α stabiliser element, whereas

vanadium serves as an β stabiliser element. In comparison with the average alloy compositions listed in Table 3.1, the amount of aluminium in α phase appears to be more than the average composition, and the same thing happens for vanadium in β phase as well. It can be concluded that α and β phases both contain a larger amount of their own stabiliser element.

Titanium silicides were found particularly in Ti-575 as can be seen in Figure 4.4 (b). The existence of silicides can be rationalised by the nominal chemical composition of Ti-575 (see Table 3.1), as 0.5 wt.% of silicon was included in Ti-575. It is possible that the silicon was introduced during polishing from the oxide polishing suspension (OPS), hence, efforts have been made to exclude such possibility by chemical analysis using EDS on a sample polished without OPS. However, it turns out that silicon signals were still detected particularly in Ti-575, but not in Ti-64 at all. This further confirms that the silicon signals came from the alloying element rather than external contamination during metallurgical preparation. Knowing the existence of titanium silicides in Ti-575 PM is important, as these silicides also appear in the weld zones on the Ti-575 side, whose microstructure will be illustrated in the following section.

4.2.1.2 Heat-Affected Zone

The microstructure in the HAZ of the Ti-575 side is shown in Figure 4.6. In comparison with the microstructure of its PM (Figure 4.4 (a)), most of the secondary and tertiary α laths within the transformed β were dissolved into the β phase. The dissolution of fine α laths may result from the heat generated during LFW. The temperature in HAZ during welding undeniably did not exceed the β transus, but it may be higher than the temperature at which these fine α laths were formed. For instance, the ageing temperature (500℃) during pre-weld heat treatment, as listed in Table 3.3; such temperature shall be sufficient to transform these fine α laths back to β phase. This can be confirmed by performing some

heat treatment trials with a rapid induction heating to several elevated temperatures below the β transus, and then observe at what temperature these fine α laths dissolve. The overall shape of the primary α grains remain equiaxed, and no dislocation was found in this region. These indicate that the heat was not able to soften the material enough for any deformation to occur.

4.2.1.3 Thermo-Mechanically Affected Zone

The TMAZ of the Ti-575 side can be further divided into two regions: outer TMAZ and inner TMAZ. The microstructure of the outer TMAZ of Ti-575 is shown in Figure 4.7. The majority of the primary α grains remain equiaxed, which indicates that not much deformation occurs here. Dark stripes appear within the primary α grains in outer TMAZ as can be seen in Figure 4.7 (b). In the high magnification secondary electron image (Figure 4.7 (b)), notice that the primary α seems to segregate from the retained β phase, forming a groove about 1 μm in width. Within the groove, fine laths emerge with about 100 nm in width. These laths seem to be well oriented as most of them are parallel to each other.

The microstructure of the inner TMAZ of Ti-575 is shown in Figure 4.8. Within inner TMAZ, the shape of primary α grains is severely compressed by the friction pressure and elongated along the oscillation direction, presumably due to the sufficient softening effect owing to the heat experienced here. Acicular laths were formed inside primary α grains, and they cover all over the grains. A highly deformed β phase was retained in this region around primary α grains.

4.2.1.4 Central Weld Zone

Figure 4.9 shows the microstructure of the CWZ in Ti-575. The microstructure appears to be homogenous as there are no distinguishable bimodal α and β regions. Dark acicular α

laths dominate this zone, surrounding by a few bright boundaries, which is considered to be the grain boundaries of recrystallised prior β grains formed during LFW. The width of the acicular α laths is approximately 40 nm. The laths in CWZ are much thinner than the laths found in the inner TMAZ (Figure 4.8), as the microstructure in CWZ experienced a faster cooling rate (as cooled from higher temperature). Note that the width of the extremely fine acicular α laths in CWZ is comparable to the tertiary α in Ti-575 parent (Figure 4.4), hence they both contribute to their superior hardness.

4.2.2 Ti-64

4.2.2.1 Parent Material

The microstructure of the Ti-64 PM is shown in Figure 4.10. Ti-64 has a fully equiaxed microstructure with equiaxed primary α grains and intergranular β. The high-magnification secondary electron images of Ti-64 are shown in Figure 4.10 (b). Unlike Ti-575, the secondary α laths can only be found occasionally in Ti-64, the majority of the β phase is intergranular. The chemical composition of α and β phase in Ti-64 is listed in Table 4.2.

The primary α grain size of Ti-64 is 15.3 ± 5.1 μm, and the volume fractions of α phase is 84%, measured by EBSD mapping as shown in Figure 4.11. Compared to the grain size analysis of Ti-575 in Figure 4.5, the microstructure of Ti-64 consists of larger primary α grains as well as more α phase fraction, presumably due to a slower cooling rate experienced during pre-weld heat treatment. As opposed to Ti-575, there is no noticeable macrozone that can be seen in Figure 4.11 (a). The pole figures in Figure 4.11 (d) also illustrate weaker texture in Ti-64 as there is no strongly concentrated texture component, and the maximum intensity is only 2.48 MUD.

4.2.2.2 Heat-Affected Zone

The microstructure in the HAZ of the Ti-64 side is shown in Figure 4.12. Similar to the HAZ of Ti-575, the overall shape of the primary α grains remains equiaxed, and no dislocation

was found in this region. These indicate that the heat was not able to soften the material enough for any deformation to occur. However, unlike the HAZ of Ti-575, the dissolution of fine α is not obvious even though the temperature could be approximately 500℃ (as discussed in Section 4.2.1.2), since there is not much secondary α to dissolve in its PM (Figure 4.4 (b)).

4.2.2.3 Thermo-Mechanically Affected Zone

The microstructure of Ti-64 TMAZ in as-welded condition is shown in Figure 4.13. As mentioned above, in TMAZ the temperature is high enough to soften the material, allowing grains to be compressed by the friction pressure and elongated along the oscillation direction by the shear stress. Notice that unlike in HAZ and PM, the primary α in TMAZ is not flat and smooth within a single grain. Acicular laths seem to penetrate through the α grains from the retained β region. Furthermore, flat blocky plateaus form within α grains with slightly different contrasts due to the difference in altitude after etching.

4.2.2.4 Central Weld Zone

Figure 4.14 shows the microstructure of the CWZ in Ti-64. Similar to the CWZ in Ti-575, the microstructure here appears to be homogenous as there are no distinguishable bimodal α and β regions. As Ti-575 CWZ, acicular α laths dominate this region. The width of these α laths is approximately 300 nm, which is notably thicker than the ones on the Ti-575 side.

4.3 Post-Weld Heat-Treated Microstructures

The combination of rapid heating and cooling treatment during LFW generates metastable martensitic microstructures with limited diffusion. Post-weld heat treatment (PWHT) at 600℃ for 1 hour provides enough energy and time for the elements to diffuse and modify the microstructure even further.

4.3.1 Ti-575

4.3.1.1 Heat-Affected Zone

Figure 4.15 shows the micrographs of the PWHT'd HAZ for Ti-575. Compared to the as-welded condition (Figure 4.6), where the fine secondary and tertiary α are dissolved into intergranular β phase, lots of α precipitates formed inside the β phase after PWHT. Those fine α precipitates are regarded as the main reason for the recovery of the hardness of Ti-575 HAZ.

4.3.1.2 Thermo-Mechanically Affected Zone

Figure 4.16 shows the microstructure of Ti-575 outer TMAZ in the PWHT'd condition. Similar to HAZ, α precipitates formed in the retained β phase. Furthermore, in comparison with the microstructure in as-welded condition (see Figure 4.7), it is observed that β precipitates also formed along the 'dark strips' and within the 'grooves'. This indicates that those microstructural features in as-welded condition, although located within the primary α grains, are either chemically or crystallographically more inclined to β phase, allowing β precipitates preferably to form along these microstructural features.

Figure 4.17 depicts the microstructure of PWHT'd inner TMAZ on the Ti-575 side. In the inserted image of Figure 4.17, there are α precipitates in the intergranular β phase, and there are β precipitates in α phase. This indicates that both α and β phases in Ti-575 were metastable in the as-welded condition, and PWHT helps segregate the two phases. Besides, note that the width of laths becomes thicker compared to as-welded condition (Figure 4.8). This suggests that PWHT also facilitate coarsening the acicular laths, which indicates that these acicular laths may have α phase crystal structure, as the PWHT temperature is far below the β transus of the alloy.

4.3.1.3 Central Weld Zone

Figure 4.18 illustrates the microstructure of Ti-575 CWZ in PWHT'd condition. It can be seen that the extra fine martensitic α' laths in as-welded condition (Figure 4.9) completely disappeared after PWHT, instead, intertwined α and β laths dominate the microstructure. The martensitic α' laths segregated into α and β phase due to diffusion. The width of these α and β laths is approximately 80 nm, which is thicker compared to the martensitic α' laths (~40 nm), however, they are still a lot thinner than the laths found in Ti-64 CWZ and Ti-575 TMAZ (~300 nm), therefore the microstructure here still possesses the highest level of hardness of the weld. The β phase fraction in Ti-575 CWZ is 52%, as measured by image analysis of Figure 4.18. Notice that the amount of β phase is significantly higher here compared to Ti-64 CWZ (see Section 4.3.2.3), likely due to a higher amount of β stabiliser (vanadium) in the alloying element. The α phase fraction after PWHT is lower than the β phase fraction, resulting in a microstructure that appears to consist of α laths embedded in a β matrix. However, in reality, β precipitates formed at the boundaries of α' laths, and due to the excessive β stabiliser content, these β precipitates were able to coarsen to a size even larger than the remaining α laths decomposed from the α' laths.

4.3.2 Ti-64

4.3.2.1 Heat-Affected Zone

Similarly to the HAZ on the Ti-575 side, as shown in Figure 4.19, the fine α precipitates also formed in the intergranular β in Ti-64 HAZ, they help increase the hardness of Ti-64 HAZ as well.

4.3.2.2 Thermo-Mechanically Affected Zone

The TMAZ on the Ti-64 side, as shown in Figure 4.20, we can also see the α precipitates in β phase, but no β precipitates in α phase. In as-welded condition, the α phase in Ti-64 TMAZ mainly retained primary α grains, as shown in Figure 4.13. The absence of β precipitates in retained primary α for Ti-64 implies that the retained α phase is chemically more stable than the α laths in Ti-575 TMAZ, and there was not sufficient β stabiliser in retained α phase to form β precipitates in Ti-64 TMAZ.

4.3.2.3 Central Weld Zone

In the CWZ on the Ti-64 side, as shown in Figure 4.21, fine β precipitates formed at the boundary of α laths, with approximately 50 nm in width and 700 nm in length. Those small precipitates help increase the hardness in CWZ. Due to the segregation of β stabiliser, the α' laths in as-welded condition should now be transformed into α laths with α phase composition. The width of those α laths remains the same as the prior α' laths, approximately 300 nm. Notice that the amount of β precipitates in Ti-575 is noticeably more than in Ti-64, as there is more β stabiliser (vanadium) as an alloying element in Ti-575. The β phase fraction in Ti-64 CWZ is 11%, as measured by image analysis of Figure 4.21.

4.4 Discussion

4.4.1 Phase Identification in As-Welded Microstructures

4.4.1.1 Ti-575 Parent Material

As discussed in Section 4.2.1.1, titanium silicides exist in Ti-575 PM, as shown in Figure 4.4. To confirm the nature of these titanium silicides, further investigation was carried out using TEM. Figure 4.22 (a) shows the bright field image of a titanium silicide. The size of the titanium silicide can be measured as 800 nm, which is distinguishably larger than the size of

silicon particles in OPS polishing suspension (250 nm). EDS analysis was carried out within the bounded area in Figure 4.22 (a), the X-ray spectrum and the chemical composition are shown in Figure 4.22 (b). The EDS results indicate that the atomic ratio between titanium and silicon is 5:3, which suggests that the titanium silicide has a chemical formula of Ti_5Si_3.

TEM diffraction analysis was carried out to confirm the crystal structure of the titanium silicide. Figure 4.22 (c)-(e) shows the diffraction patterns obtained from the titanium silicide in three different beam directions. All the phases listed in Table 3.6 were included to index the diffraction patterns, it turns out that all diffraction patterns can be successfully indexed as Ti_5Si_3. Additionally, the three beam directions of the diffraction patterns also pass the tilt experiment [181], which further confirms that Ti_5Si_3 with HCP crystal structure is the only possible solution for the given set of diffraction patterns.

According to Zhao *et al.* [195], Ti_5Si_3 is a common type of titanium silicides formed within titanium alloys when the silicon content is higher than 0.1 wt.%. Titanium silicides are most likely formed during the ageing stage of the pre-weld heat treatment (Table 3.3) as precipitation, hence it is able to strengthen the alloy through precipitation hardening. Surprisingly, the existence of silicon particles was not specifically reported by the previous studies on Ti-575 [13, 15–17]. Nevertheless, the existence of silicon particles can be found in one of their scanning electron micrographs [15].

4.4.1.2 Ti-575 Outer Thermo-Mechanically Affected Zone

As discussed in Section 4.2.1.3, dark 'stripes' within primary α grains and 'grooves' (segregation between α and β phase) were observed in Figure 4.7. EBSD mapping was carried out to investigate the crystal structures and the orientations of the microstructural features within as-welded Ti-575 outer TMAZ, as presented in Figure 4.23. From the phase map in Figure 4.23 (b), three phases (α-Ti, β-Ti, and Ti_5Si_3) were identified. Similar to the HAZ, the microstructure is composed of primary α phase and retained intergranular β phase. The orientation map in Figure 4.23 (c) illustrates that the orientation within a single

primary α grain remains well aligned even though multiple stripes penetrated through the grain.

To investigate the nature of these stripes, EDS and EBSD line scans were carried out to analyse their chemical composition and crystal structure. EDS line scan in Figure 4.24 suggests that those stripes have a similar chemical composition to the primary α, as the aluminium content in Figure 4.24 (c) is relatively stable across the stripe at approximately 6%, which is coincident with the aluminium content of α phase in Ti-575 (see Table 4.1). Note that even though the vanadium content in Figure 4.24 (b) seems to fluctuate a lot, the average weight per cent is approximately 4%, which is also close to the average vanadium content of α phase in Ti-575. Besides, the vanadium weight per cent is far below the typical vanadium content in Ti-575 β phase, this indicates that there is no $\alpha \rightarrow \beta$ phase transformation occurring within the stripes. EBSD line scan in Figure 4.24 (e) shows that the stripe has a hcp crystal structure, which is the same crystal structure of α phase. In addition, the stripe also shares the same orientation with the primary α grain it resides in, as the pole figures suggest a dominant orientation, and the misorientation profile in Figure 4.24 (e) also indicates there is less than one degree of misorientation between the stripe and the primary α grain. It is suspected that those stripes are dislocation bands generated by the combination of compressive and shear stresses along with sufficient softening by the heat.

EDS line scan was carried out to investigate the diffusion across a groove whose secondary electron image is shown in Figure 4.25 (a). The obtained vanadium and aluminium profiles in Figure 4.25 (c) and (d) show that vanadium diffuses from the retained β phase to primary α phase, while aluminium diffuses in the opposite direction. More importantly, both vanadium and aluminium content changes smoothly across the groove for approximately 2.5 μm. A similar EDS line scan was also carried out to investigate the diffusion at the

boundary of primary α grains and intergranular β phase in Ti-575 PM, as shown in Figure 4.26. The vanadium content profile in Figure 4.26 (b) indicates that the diffusion of vanadium is limited as vanadium content changes sharply within 0.2 μm; the diffusion of aluminium occurs more but is still limited as the aluminium content profile in Figure 4.26 (c) shows that aluminium content varies within 0.5 μm. The results from the EDS line scan suggest that the diffusion zone in outer TMAZ is significantly larger than that of Ti-575 PM at α-β phase boundary. This indicates that the diffusion of these elements was able to occur in outer TMAZ at a much higher degree than in the PM, which is reasonable given the heat experienced in this region during LFW.

It is suspected that the original phase boundary was located at the boundary of retained β phase, and then with the heat generated during LFW, vanadium was able to diffuse into α phase. With the increase in vanadium content, these vanadium-rich α was able to transform into metastable β phase at elevated temperatures. After the LFW process is finished, rapid cooling then forces the metastable β phase to undergo a martensitic transformation, forming acicular α' laths in the groove.

4.4.1.3 Ti-575 Inner Thermo-Mechanically Affected Zone

As discussed in Section 4.2.1.3, acicular laths were observed within primary α grains, as shown in Figure 4.8. EBSD mapping was carried out to investigate the crystal structures and the orientations of these acicular laths. The EBSD phase map presented in Figure 4.27 (b) shows that the acicular laths observed in Figure 4.8 have α-Ti crystal structure. EBSD orientation map shown in Figure 4.27 (c) illustrated that each of these acicular laths has a different orientation, whereas as shown previously in Figure 4.23 (c) there is only a single orientation throughout the entire primary α grain at outer TMAZ.

Reconstruction of prior β phase was carried out to investigate the relationship between these acicular α laths, the orientation map of prior β phase is shown in Figure 4.27 (d). Note that the region of interest was chosen to have less distortion so as to improve the quality of the maps. By comparing Figure 4.27 (b) and (d), notice that all the pixels within the same primary α grain in the phase map share the same prior β orientation. This indicates that the primary α grains were transformed into β phase during the heating stage of LFW, then after the oscillation ceased, the heat accumulated at the interface rapidly conducted away through the PM, this results in a fast-cooling rate that resembles water quenching. Consequently, the β phase went through a martensitic transformation, resulting in the acicular α laths inside the primary α grains. The amount of the transformed α laths depends on the temperature experienced, as inner TMAZ is closer to the weld interface, the accumulated heat within this region raises the temperature up enough to make such phase transformation possible. On the contrary, outer TMAZ is further away from the weld interface, the temperature here was not high enough to facilitate the phase transformation.

The proposed phase transformation mechanism was later found contradictory to findings from the study of dynamic β transus, further discussion is provided in Section 7.5.4.

4.4.1.4 Ti-575 Central Weld Zone

The microstructure within Ti-575 CWZ is shown in Figure 4.9. The chemical composition in CWZ was measured using EDS, listed in Table 4.3. It was found that all the elements are distributed uniformly in CWZ. Comparing the chemical composition in CWZ to that of the PMs shown in Table 4.1, notice that the composition of CWZ is closer to the average alloy composition of Ti-575. This shows that the chemistry of CWZ is homogenised, indicating that the temperature of CWZ once raised above β transus during LFW for the heat generated from the weld interface. The rapid cooling afterwards happens fast enough to prevent any elemental diffusion, hence the chemistry stays homogenised.

EBSD was used to characterise the crystal structure of the acicular laths in Ti-575 CWZ, as shown in Figure 4.28. The phase map in Figure 4.28 (b) indicates that the majority of the microstructure consists of HCP crystal structure, with no BCC indexed, hence the acicular laths contain α phase structure. β reconstruction was performed as shown in Figure 4.28 (d), it is confirmed that the orientations of adjacent laths follow Burgers' orientation relationship, which indicates that these laths underwent $\beta \rightarrow \alpha$ phase transformation. Taking the EDS results shown in Table 4.3 into consideration, as the chemistry stays homogenised, the phase transformation is considered diffusionless, which suggests that martensitic phase transformation occurred.

It is possible to form two types of martensite in the CWZ: α' with HCP structure and α'' with orthorhombic structure. It has been studied that α' exists in the CWZ of Ti-64, the hardness of α' is significantly higher than Ti-64 parent [5, 23]. On the other hand, Guo *et al.* [62] discovered α'' in the CWZ of Ti-6246, however, the hardness of α'' is lower than the PM. As the EBSD mapping suggests that the acicular laths consist of HCP structure, plus the microhardness measurement shown in Figure 6.3 also confirms superior hardness in CWZ to the PMs, it is concluded that these acicular laths can be identified as martensitic α' laths.

Figure 4.29 shows another EBSD map in Ti-575 taken at 50 µm away from the weld interface. Notice that in Figure 4.29 (b) BCC structure can be found even though it is only 50 µm away from the weld interface. This indicates that β phase in Ti-575 is stable enough to retain after rapid cooling. As the presence of retained β phase is a sign of entering TMAZ, these stable retained β results in a narrow CWZ as measured in Figure 4.3.

As the dark acicular laths in Figure 4.9 can be identified as martensitic α' laths transformed from prior β phase, the surrounding bright boundaries are considered as prior β phase boundaries. These prior β phase boundaries can be seen as the outline of the prior β grains

at elevated temperatures. From the shape of the prior β grains, one can realise that they are primarily equiaxed, as opposed to the highly distorted grains in TMAZ. The same indication can also be found in the reconstructed β grains shown in Figure 4.28 (d). Both pieces of evidence suggest that recrystallisation occurred within CWZ.

4.4.1.5 Ti-64 Thermo-Mechanically Affected Zone

As discussed in Section 4.2.2.3, acicular laths appeared to penetrate through the primary α grains from the retained β phase, as shown in Figure 4.13. EBSD point & ID is utilised to identify the crystal structure and orientation of these acicular laths, the results are shown in Figure 4.30. The point & ID at locations A, B, and C demonstrated that the acicular laths have a HCP crystal structure, which is the same as the crystal structure of primary α phase. However, the orientation of the acicular laths is not the same as the orientation of the primary α grain where they reside. Location D, E, and F reveal that the flat plateaus also consist of HCP structure, each plateau has its unique orientation. Location G, H, and I identified the retained intergranular β phase as the long stripes distorted along the oscillation direction and compressed along the forge direction.

Similar to the TMAZ in Ti-575, it is regarded that primary α grains were able to partially transform into β phase during LFW. The rapid cooling rate after the termination of the oscillation was fast enough to force the metastable β phase to transform back to α phase through a diffusionless transformation. The acicular α laths and flat α plateaus are suspected to have formed through this process.

Note that in Figure 4.13, there are some retained primary α in the TMAZ of Ti-64. Those retained primary α cannot be found in Ti-575 TMAZ. This may be explained by the difference in β transus, as Ti-64 has a higher β transus (996ºC) than Ti-575 (965ºC), it is more difficult for $\alpha \rightarrow \beta$ phase transformation to occur in Ti-64 at the same temperature,

assuming the specific heat capacity and the thermal conductivity of Ti-64 and Ti-575 are similar, hence the temperature at a certain distance away from the interface is the same for the two alloys.

4.4.1.6 Ti-64 Central Weld Zone

As in Ti-575 CWZ, the chemical composition in CWZ of Ti-64 is also found to be homogenised and resembles to its nominal alloy composition, as shown in Table 4.4. Therefore, it is considered that the temperature here exceeded β transus during LFW, hence the microstructure was fully transformed into β phase with homogeneous composition. The rapid cooling afterwards forced β phase to undergo a martensitic phase transformation, consequently α' laths were formed. EBSD results in Figure 4.31 also agree with this explanation as these acicular laths are composed of HCP crystal structure, plus the β reconstruction can successfully merge the adjacent laths into prior β grains as shown in Figure 4.31 (d), indicating that a $\beta \rightarrow \alpha'$ phase transformation occurred.

The width of α' laths in CWZ Ti-64 is approximately 300 nm, which is considerably thicker than the α' laths in Ti-575 CWZ. This indicates the α phase is much more stable in Ti-64 thus the α' laths grow faster in Ti-64, which is reasonable as Ti-64 indeed has a higher amount of α stabiliser (aluminium). The same conclusion can be drawn from the EBSD phase map. As shown in Figure 4.31 (b), there is no noticeable retained β phase found in the proximity to the weld interface, however, such retained β can be seen on the Ti-575 side close to the weld interface as shown in Figure 4.28 (b). This indicates that β phase in Ti-575 is more stable to retain after rapid cooling, which is reasonable as Ti-575 indeed has a higher amount of β stabiliser (vanadium). α' laths are beneficial to the hardness of the weld as they are much smaller in size compared to the microstructural features in PM, however, the hardness of Ti-64 CWZ is not as high as the hardness of Ti-575 CWZ due to the thicker α'

laths on the Ti-64 side. Further details about the hardness measurement are discussed in Section 6.2.

4.4.2 Phase Identification in Post-Weld Heat Treated Microstructures

4.4.2.1 Ti-575 Central Weld Zone

EDS mapping was carried out using TEM to analyse the chemical composition of the α and β laths in PWHT'd Ti-575 CWZ. As shown in Figure 4.32, vanadium (β stabiliser) and aluminium (α stabiliser) both are clearly segregated into α phase and β phase. The chemical compositions measured at α phase (aluminium-rich region) and β phase (vanadium-rich region) are listed in Table 4.5. Compared to the chemical composition of α and β phase measured in the Ti-575 PM (Table 4.1), the α phase here has more α stabiliser, and the β phase here also has more β stabiliser. The chemical composition measured here reflects the equilibrium chemical composition at the PWHT temperature (600℃), whereas the chemical composition measured in PM reflects the composition at the PWHT temperature (500℃).

A selected area diffraction pattern has been taken at the same region as in Figure 4.32 to confirm the crystal structure of α phase and β phase, as shown in Figure 4.33 (b). Here, multiple diffractions originating from both phases were superimposed. Figure 4.33 (c) illustrates a schematic diagram of the diffraction pattern, specifically differentiating the diffraction spots generated from each phase. Three sets of diffraction spots were identified, their beam directions are respectively $[1\bar{1}\bar{1}]_\beta$, $[\bar{1}2\bar{1}0]_\alpha$, and another $[\bar{1}2\bar{1}0]_\alpha$ with different orientation. Dark field images obtained from $[1\bar{1}\bar{1}]_\beta$ diffraction patterns are shown in Figure 4.33 (d)-(f), the illuminated region matches with the vanadium-rich region in Figure 4.32. Similarly, dark field images obtained from the two sets of $[\bar{1}2\bar{1}0]_\alpha$ diffraction patterns are presented in Figure 4.33 (g)-(i), the illuminated region matches with the

aluminium-rich region in Figure 4.32. The observation from the dark field images confirms that the β phase (vanadium-rich region) is composed of BCC crystal structure, and the α phase (aluminium-rich region) is composed of HCP crystal structure.

As the α diffraction patterns superimposed onto the β diffraction pattern with a specific misorientation, one can deduce the orientation relationship between α and β phase from the diffraction patterns. From Figure 4.33 (c), notice that $\{0002\}_\alpha$ spots are always coincident with one of the $\{110\}_\beta$ spots, which suggests that

$$\{0002\}_\alpha \parallel \{110\}_\beta \tag{4.1}$$

Furthermore, the beam directions of all diffraction patterns must be parallel to each other, in other words,

$$[\bar{1}2\bar{1}0]_\alpha \parallel [1\bar{1}\bar{1}]_\beta \tag{4.2}$$

Taking symmetry into consideration, Equation (4.2) can be written as

$$\langle 11\bar{2}0\rangle_\alpha \parallel \langle 1\bar{1}1\rangle_\beta \tag{4.3}$$

The observation above coincident with the well-known Burgers orientation relationship, as described in Equation (2.1) and (2.2). This suggests that Burgers orientation relationship also applies to Ti-575.

4.4.2.2 Ti-64 Central Weld Zone

The microstructure of PWHT'd Ti-64 CWZ was examined by TEM. A twin-jet polished sample with a hole located 35-85 μm away from the weld interface was prepared, as shown in Figure 4.34. The area around the hole is electron transparent to be observed using TEM. Figure 4.35 shows the bright field images taken from the bounded area in Figure 4.34 (b). Compared with the secondary electron image (Figure 4.21), the α laths are clearly visible, while the bright β precipitates cannot be found easily within the bright field images.

Efforts have been made to find the β precipitates using TEM, and some small β precipitates have been found, as shown in Figure 4.36. These β precipitates are confirmed to have a BCC crystal structure by their diffraction pattern, as shown in Figure 4.36 (b). However, these β precipitates are in a spherical shape, and their size are only approximately 50 nm, which is much less than the β precipitates observed under SEM. It is considered that only the smallest β precipitates found in the secondary electron image are actually having β phase crystal structure, whereas the majority of the large precipitates are merely chemical agglomerations of β stabilisers. They are visible under SEM since the sample has a chemically etched surface, and the etchant is highly sensitive to the composition, therefore the β-stabiliser-rich region preferentially remained, consequently resulting in higher contrast in the secondary electron image. On the other hand, the twin-jet polished sample was evenly polished, thus there is no contrast for the β-stabiliser-rich region. Furthermore, the bright field image represents the contrast from the diffraction, clearly, there is no obvious contrast for the β-stabiliser-rich region, therefore it can be concluded that the β-stabiliser-rich region still consists of α-Ti (HCP) crystal structure, but their chemical composition is more inclined with β phase.

EDS mapping was carried out to measure the chemical composition of the spherical small β precipitates, as shown in Figure 4.37 and Table 4.6. It is clear that these β precipitates have a similar chemical composition as the β phase measured in the Ti-64 PM (Table 4.2). The observation from TEM confirms that the small β precipitates are both crystallographically and chemically β phase. The chemical composition measured at location G shown in Figure 4.37 and Table 4.5 indicates the content of the laths, it is similar to the α phase content measured from the Ti-64 PM (Table 4.2). This indicates that the martensitic α'

laths with nominal alloy composition have been transformed into α laths with α phase composition.

Apart from the α laths and the β precipitates, large α grains approximately 3 μm in size were also found in this region, as shown in Figure 4.38. It has been confirmed that these α grains have HCP crystal structure due to their diffraction patterns. These α grains may either be primary α retained in CWZ after LFW or were grown during PWHT.

4.5 Conclusions

1. LFW with a chambered trapezoidal geometry and flat-to-flat contact surfaces results in a narrower CWZ and larger TMAZ at the bifurcation point of the welds compared to the edges. The size of Ti-575 CWZ is thinner than Ti-64 CWZ at the bifurcation point, but thicker at the edges. The uneven zone size between Ti-575 and Ti-64 implies the differences in their thermal responses at different heating rates.
2. Ti-575 parent material has a bi-modal microstructure with primary α grains and transformed β phase. Fine secondary and tertiary α laths can be found in the β regions. Ti-64 parent material has equiaxed microstructure with primary α grains and intergranular β phase. No tertiary α laths have been found in Ti-64.
3. Titanium silicides were found in Ti-575 parent material. The titanium silicides are confirmed chemically and crystallographically to be Ti_5Si_3 by TEM, they are suspected to originate from the 0.5 wt.% of silicon incorporated in the alloying element. The HAZ and TMAZ on the Ti-575 side inherit the parent material and therefore also have titanium silicides.
4. In Ti-575 HAZ, the fine secondary and tertiary α laths dissolved into the β phase due to the heating experienced during LFW. Ti-64 HAZ does not have a notable difference from the parent material, because there are few secondary α laths in the intergranular

β phase in the parent material microstructure, therefore the dissolution of fine α laths is not obvious.

5. The microstructure of the as-welded Ti-575 TMAZ is very different from the as-welded Ti-64 TMAZ. In Ti-575 TMAZ the primary α grains fully transformed into lamellar α laths, whereas in Ti-64 TMAZ the majority of primary α grains remain, with partially transformed lamellar α laths at the α/β phase boundaries.
6. In as-welded CWZ, the microstructure on both Ti-575 and Ti-64 sides fully transformed into martensitic acicular α' laths. The width of α' laths in Ti-575 (40 nm) is thinner than the ones in Ti-64 (300 nm).
7. In PWHT'd HAZ and TMAZ, fine α precipitates form in β phase on both Ti-575 and Ti-64 sides. In Ti-575 TMAZ, fine β precipitates also formed at the boundaries of lamellar α laths inside the original primary α grains. The formation of precipitates after PWHT indicates the metastable nature of these phases in the as-welded condition.
8. In PWHT'd condition, the martensitic α' laths in both Ti-575 and Ti-64 CWZ decomposed into $\alpha + \beta$ region. In Ti-64, fine β precipitates formed at the boundaries of α laths. Whereas in Ti-575, the volume fraction of β precipitates is more than 50%, which makes the microstructure more like α precipitates in β matrix.

Chapter 5

Texture Development Analysis

5.1 Central Weld Zone of Ti-575 and Ti-64

The α texture measured from the central weld zone (CWZ) on both Ti-575 and Ti-64 sides is shown in Figure 5.1. Both alloys exhibit similar texture which is dominated by a transverse texture component $\{10\bar{1}0\}\langle 11\bar{2}0\rangle_{\alpha}$ (T) with respect to the forge direction (FD) and the oscillation direction (OD). There are several basal (B) and rolling (R / R') texture components with intermediate intensity, their misorientation angle from the transverse texture is either 60° or 90°, which is commonly seen in the misorientation profile of transformation textures. Similar textures have also been found in CWZ of self-similar linear friction welded (LFW'd) Ti-64 from the literature [10, 63, 139, 199].

5.1.1 β Reconstruction

As previously discussed in Section 4.2, the CWZ contains martensitic microstructure resulting from the $\beta \rightarrow \alpha'$ phase transformation. Given the well-established Burgers

orientation relationship governing phase transformation in titanium, it becomes feasible to reconstruct the former β phase and, subsequently, investigate the texture development that occurred within the CWZ. To demonstrate this concept, Ti-64 CWZ is taken as an example. Figure 5.2 presents the orientation maps and inverse pole figures measured from Ti-64 CWZ, alongside those of the reconstructed prior β phase. The reconstructed β orientation map in Figure 5.2 (c) shows that the reconstructed prior β phase mainly comprises similar orientations, as indicated by the similar colours. This observation is better elucidated in the inverse pole figures (IPF) shown in Figure 5.2 (d). Specifically, the pole concentrates at [112] in IPF-FD and at [111] in IPF-OD, suggesting that the prior β phase mainly consists of $\{11\bar{2}\}\langle 111\rangle_\beta$ orientation. The textures of the reconstructed prior β phase in CWZ for both Ti-575 and Ti-64 are visualised by the pole figures shown in Figure 5.3. Based on the observation of the inverse pole figures, it can be deduced that Figure 5.3 primarily represents $\{11\bar{2}\}\langle 111\rangle_\beta$ texture.

5.1.2 Texture Simulation

Texture simulation using MTEX can be used to verify this hypothesis. The pure $\{11\bar{2}\}\langle 111\rangle_\beta$ texture is simulated and shown in Figure 5.4 (c), along with two representative orientations in $\{11\bar{2}\}\langle 111\rangle_\beta$ family: $(11\bar{2})[111]_\beta$ and $(112)[\bar{1}\bar{1}1]_\beta$, which are illustrated in Figure 5.4 (a) and (b), respectively. Notice that Figure 5.4 (c) resembles the reconstructed prior β texture displayed in Figure 5.3, thus confirming that the prior β phase predominantly comprises $\{11\bar{2}\}\langle 111\rangle_\beta$ orientation. Furthermore, texture simulation following the Burgers orientation relationship can generate α texture inherited from $\{11\bar{2}\}\langle 111\rangle_\beta$ texture, as presented in Figure 5.4 (d). Comparing the simulated texture with the measured α texture shown in Figure 5.1, it is observed that the locations of all texture components align, despite the measured transverse component being notably stronger.

5.2 Ti-64 Thermo-Mechanically Affected Zone

The texture measured in CWZ is generally consistent throughout the entire weld. However, the texture in TMAZ is affected by the material flow direction. The spatial variation of the texture in LFW'd Ti-64 joints in the centre and on the edges was studied previously [139, 200]. The following investigation in TMAZ is focused on the texture at the bifurcation point. Figure 5.5 illustrates the α and β texture measured from Ti-64 inner TMAZ at the bifurcation point. The texture here shares similar texture components with the CWZ texture, despite having lower intensity. The β texture resembles the simulated $\{11\bar{2}\}\langle 111\rangle_\beta$ texture shown in Figure 5.4 (b), which indicates that the retained β in Ti-64 TMAZ was deformed and oriented to $\{11\bar{2}\}\langle 111\rangle_\beta$ during welding. The α texture also resembles the inherited texture shown in Figure 5.4 (c), although the transverse texture T and a pair of rolling textures R are notably stronger due to variant selection. It can be inferred from the inherited α texture that $\beta \rightarrow \alpha$ phase transformation occurred in this region. However, since the β was only partially transformed, plus the existence of retained primary α phase, the maximum texture intensity (9.3x) is considerably lower than the maximum texture intensity measured in CWZ (25x), where β phase was fully transformed into α phase.

5.3 Ti-575 Thermo-Mechanically Affected Zone at Bifurcation Point

On the other hand, the Ti-575 inner TMAZ at the bifurcation point exhibits a completely different texture from the Ti-64 inner TMAZ, as shown in Figure 5.6. For $\{0001\}_\alpha$ pole figure, a basal texture B appears with a transverse texture T and a few rolling-type textures R', all with a similar level of intensity. Note that the coordinates of these pole figures are not aligned with forging and oscillation directions, but with X and Z directions, which are associated with the weld geometry. This indicates that the texture here is independent of

the oscillation direction, but is dependent on the weld geometry. The misorientation angle from the transverse texture to the rolling and basal texture are respectively 60° and 90°, again, this is a sign of transformation texture. Notice that the $\{110\}_\beta$ pole figure in Figure 5.6 (b) resembles the $\{0001\}_\alpha$ pole figure, as from the Burgers relationship it is known that $\{0001\}_\alpha \parallel \{110\}_\beta$, the similarity between the α and β pole figures indicates that the α and β phase follows the Burgers relationship, which implies that $\beta \rightarrow \alpha$ phase transformation occurred locally. This observation suggests that the α phase in TMAZ is potentially inherited from the β phase.

Figure 5.7 shows the orientation maps and inverse pole figures of α and β phase at the bifurcation point of Ti-575 inner TMAZ. The α orientation map depicts acicular microstructure with neighbouring laths having different orientations, this suggests the occurrence of rapid $\beta \rightarrow \alpha$ phase transformation. In the β orientation map shown in Figure 5.7 (c), notice that the majority of the β phase shares a similar orientation, as indicated by the similar colour. The inverse pole figures in Figure 5.7 (d) demonstrate a [011] pole parallel to the sample Z direction and a strong [001] pole parallel to the sample X direction, suggesting that the β phase comprises primarily $\{110\}\langle001\rangle_\beta$ orientation.

5.3.1 β Reconstruction

It was suspected that the α phase underwent $\beta \rightarrow \alpha$ phase transformation from the retained β phase. A possible way to validate this speculation is to apply β reconstruction to the α phase, and see if those acicular α laths can be successfully reconstructed into β matrix that is coherent with the retained β phase. Figure 5.8 (a) presents the reconstructed β orientation map, it can be seen from the figure that the majority of the α phase was successfully

reconstructed into prior β phase. In addition, by comparing Figure 5.7 (c) and Figure 5.8 (a), one can see that the reconstructed β orientation conforms with the retained β orientation. Therefore, it is reasonable to suggest that in Ti-575 TMAZ, the α phase was fully transformed into β phase during welding, however, the transformed β phase was relatively metastable compared to the β phase presented in the parent material, hence it transformed back to α phase due to rapid cooling in the ramp-down and consolidation stage.

In Figure 5.8 (a) there are a few areas coloured in red which means $\{001\}_\beta$ planes are parallel to the sample Y direction, instead of $\{011\}_\beta$ planes coloured in green. However, it is worth noting that when viewing the map with respect to the sample Z direction, as shown in Figure 5.8 (b), almost the entire map is coloured green, indicating that the $\{011\}_\beta$ planes of the prior β phase are well aligned with the sample Z direction, or equivalently, forge direction. This implies that the orientation of the prior β phase is predominantly affected by the compressive forge pressure, and is less dependent on the oscillation direction.

The inverse pole figures of the prior β phase in Figure 5.8 (c) indicates the prior β orientation is primarily $\{110\}\langle001\rangle_\beta$, for the similar reason discussed in Figure 5.7 (c). The textures of the prior β phase at the bifurcation of Ti-575 inner TMAZ are visualised by the pole figures shown in Figure 5.8 (d). Again, as discussed in Section 5.1.1, based on the observation of the inverse pole figures, it can be deduced that the pole figures primarily represent $\{110\}\langle001\rangle_\beta$ texture.

5.3.2 Texture Simulation

Similarly, simulated texture can be used to demonstrate texture development here as well. As shown in Figure 5.9, a $\{110\}\langle001\rangle_\beta$ texture (with respect to the weld geometry) resembles the reconstructed prior β texture (see Figure 5.8 (d)) and the measured retained β texture

(see Figure 5.6 (b)), besides, the inherited α texture also resembles the measured α texture (see Figure 5.6 (a)). Notice that there is no specific component with outstanding intensity in the measured α texture, both basal texture B and rolling texture R' are strong, although the transverse texture T shown in Figure 5.6 (a) is notably weaker, strong transverse texture was also measured at a different region of interest. This implies that little or no variant selection occurred in Ti-575 TMAZ. Furthermore, the fact that the measured β texture resembles the simulated β texture indicates that the β phase here retains its orientations at elevated temperatures, whereas the α phase was formed via a phase transformation from the β matrix.

5.3.3 Scope of Bifurcation Texture

The Z-orientation map of the prior β phase shown in Figure 5.8 (b) is a good example of showing that the $\{110\}_\beta$ planes of the prior β phase are well aligned with the forge direction. By extending the measured area, it is possible to reveal the size of the region with $\{110\}\langle001\rangle_\beta$ texture. Figure 5.10 shows the prior β orientation map stitched and reconstructed from six EBSD mappings at the bifurcation point of Ti-575 inner TMAZ. This map covers an area of approximately 300×500 μm^2, which is large enough to reveal the territory of the $\{110\}\langle001\rangle_\beta$ texture. It can be seen from the map that at the bifurcation point a region of area approximately 300×300 μm^2 is primarily coloured in green, which indicates that $\{110\}_\beta$ planes are aligned with the forge direction. As the $\{110\}_\beta$ planes are so well-aligned in this region, strong $\{110\}\langle001\rangle_\beta$ texture can be measured from both the retained β phase and the reconstructed prior β phase locally. Further away from the bifurcation point, the material tended to flow toward the edges, therefore the texture there

was affected by the oscillation direction and hence the $\{110\}\langle 001\rangle_\beta$ texture at bifurcation diminished.

5.4 Discussion

5.4.1 Texture Development Mechanism

5.4.1.1 Central Weld Zones

The α pole figures of the CWZs textures shown in Figure 5.1 show peak-type texture components, no fibre texture (e.g. Figure 2.38) can be found. To study the texture development mechanism, comparing the measured texture with the well-known ideal textures is a decent approach to start with. The ideal texture components found in the measured texture may imply that the measured texture may share a similar texture development mechanism to the ideal textures.

Figure 5.11 shows a comparison between the α texture measured in Ti-64 CWZ and the simple shear textures of HCP materials, by overlaying Figure 2.40 onto Figure 5.1 (b), where the forge direction (FD) is parallel to the shear plane normal (SPN) and the oscillation direction (OD) is parallel to the shear direction (SD). Note that Figure 2.40 is presented in equal angle projection, while Figure 5.1 (b) is presented in equal area projection. For ease of comparison, both pole figures in Figure 5.11 are presented in equal angle projection. Notice that the P_1 simple shear texture component is coincident with the measured transverse texture component T, both having the same orientation $\{10\bar{1}0\}\langle 11\bar{2}0\rangle$. Furthermore, the C_1 and C_2 peak-type texture components (not C_1- and C_2-fibre textures) are also coincident with the measured texture component R.

It has been demonstrated in Figure 5.3 and Figure 5.4 that the prior β phase in CWZ has a strong $\{11\bar{2}\}\langle 111\rangle_\beta$ texture. Notice that this type of texture is one of the simple shear textures of BCC materials. Figure 5.12 shows the pole figures of the reconstructed prior β

texture overlaying with Figure 2.39, in a similar fashion to Figure 5.11. Notice that all the prior β texture components coincide with D_1 and D_2 type simple shear texture, together they form $\{11\bar{2}\}\langle 111\rangle_\beta$ texture.

The observations presented above suggest that the stress condition in CWZ during LFW is similar to the simple shear condition, where FD // SPN and OD // SD. During welding, the subjected shear stress and temperature caused deformation and recrystallisation, forcing the recrystallised β grain to deform via $\{11\bar{2}\}\langle 111\rangle_\beta$ slip systems, consequently resulting in D_1 and D_2 $\{11\bar{2}\}\langle 111\rangle_\beta$ simple shear texture. Upon ramp-down and forging stages, $\beta \rightarrow \alpha'$ phase transformation took place in line with the Burgers orientation relationship, leading to the α texture inherited from the β texture, as shown in Figure 5.4 (d), assuming all 12 α variants have an equal probability to grow from a single β grain.

However, the simulated α texture inherited from ideal $\{11\bar{2}\}\langle 111\rangle_\beta$ texture shown in Figure 5.4 (d) does not exhibit the strong transverse component $T\{10\bar{1}0\}\langle 11\bar{2}0\rangle$ in the measured CWZ textures (see Figure 5.1). One possible reason for this may be that the simple shear stress condition was still prevalent in the ramp-down stage, hence the α' grains may be re-oriented via grain rotation by the shear stress to P_1, C_1, and C_2 orientations (see Figure 5.11). This explains the intensity of components T and R is superior to R' components in the measured CWZ textures (see Figure 5.1), whereas in the solely inherited α texture they should have similar intensity (see Figure 5.4 (d)).

Another possible reason is variant selection. Variant selection may occur due to the stress induced by anisotropic thermal contraction [115], or lattice strain of β phase induced by plastic deformation [118], leading to the preferential selection of the transverse texture $\{10\bar{1}0\}\langle 11\bar{2}0\rangle_\alpha$. A similar variant selection mechanism has also been observed in the texture

of titanium sheets after hot rolling. It is known that strong transverse texture arises from unidirectional rolling at near or above β transus for $\alpha + \beta$ alloys [70], as shown in Figure 2.41. In LFW, when the temperature starts decreasing during the ramp-down stage for $\beta \rightarrow \alpha$ phase transformation to occur, the oscillation motion resembles the hot rolling action, therefore it is reasonable that LFW shares a similar variant selection mechanism with the hot-rolled titanium sheet. A similar texture development mechanism in the CWZ of Ti-64 self-similar welds can also be found in the literature [139].

5.4.1.2 Ti-575 Thermo-Mechanically Affected Zone at Bifurcation Point

Similar to the texture in CWZ, the texture in Ti-575 TMAZ at the bifurcation point shown in Figure 5.6 exhibits peak-type texture components. One can also study the texture development mechanism by comparing the measured texture with the ideal textures. Figure 5.13 shows a comparison between the α texture in Ti-575 TMAZ at bifurcation (see Figure 5.6 (a)) and the simple shear textures of HCP materials (see Figure 2.40), where the sample Z direction (also parallel to the forge direction) is parallel to the shear plane normal (SPN) and the sample X direction is parallel to the shear direction (SD). Note that both pole figures in Figure 5.13 are presented in equal angle projection. The measured texture exhibits a strong basal texture component B, which is coincident with B $\{0001\}\langle uvtw\rangle$ in simple shear texture. The transverse component T is also coincident with the P_1 texture component, both having the same orientation $\{10\bar{1}0\}\langle 11\bar{2}0\rangle$. However, it is important to note that the transverse texture here is different from the transverse texture in CWZ, since the transverse direction here is with respect to the sample geometry, whereas the transverse direction in CWZ is with respect to the oscillation direction. The measured component R' does not correlate to any simple shear component.

It has been demonstrated by Figure 5.6 (b) and Figure 5.9 that the β phase and the reconstructed prior β phase in Ti-575 TMAZ at bifurcation both have a strong $\{110\}\langle 001\rangle_\beta$

texture. Notice that this type of texture is coincident with the texture component F in the simple shear textures of BCC materials. Figure 5.14 shows the pole figures of the measured β texture overlaying with Figure 2.39, in a similar fashion to Figure 5.13. Notice that all the measured β texture components coincide with the simple shear texture component F $\{110\}\langle001\rangle$.

The results suggest that the bifurcation point in Ti-575 TMAZ also experienced a simple shear stress condition during LFW, where the shear direction is parallel to the sample X direction. It is a rather counter-intuitive observation since the shear stress during LFW is generated by oscillation, and the SD should be parallel to the OD, as discussed in 5.4.1.1. The dependency of the texture on the weld geometry in Ti-575 TMAZ at the bifurcation point can be attributed to the material extrusion. On both sides of the bifurcation point, the material was extruded along the $\pm$X direction toward the edges, whereas at the bifurcation point, the material is restricted to flow along the $\pm$Z direction toward the weld interface. Furthermore, it is known that upon flowing the longitudinal axis of $(1\bar{1}0)$ plane as illustrated in Figure 5.9 (a) tends to align with the flowing direction [139]. Consequently, the longitudinal axis of $(1\bar{1}0)$ plane is aligned with the Z direction, resulting in a strong basal texture.

5.4.1.3 Ti-64 Thermo-Mechanically Affected Zone

Although the intensity of the texture in Ti-64 TMAZ is not as strong as that in CWZ, the major texture components in Ti-64 TMAZ are located at similar locations on the pole figures to the texture components in CWZ, as shown in Figure 5.5. This suggests that the transformational texture development mechanism described in Section 5.4.1.1 also occurs in Ti-64 TMAZ.

Basal texture can also be found in Ti-64 TMAZ in Figure 5.5, although its intensity is weak but is still distinguishable, unlike the texture measured in CWZ (see Figure 5.1), no basal

texture is found at all. This suggests that the same texture development mechanism at bifurcation in Ti-575 TMAZ may also occurred in Ti-64 TMAZ, despite the influence of the CWZ texture being much stronger. As discussed in Section 4.4.1.5, the observation on the microstructure in Ti-64 TMAZ suggests that primary α grains were able to partially transform into β phase during LFW, before transform back to α phase due to the rapid cooling rate. The partially transformed β phase may slip along the $\{110\}\langle001\rangle$ slip system, which contributes to its weak basal texture components.

5.4.1.4 Texture Development in Thermo-Mechanically Affected Zone of Ti-575 and Ti-64

The difference between the texture in Ti-575 TMAZ and Ti-64 TMAZ may arise from the occurrence of phase transformation. Ti-575 has a higher amount of β stabiliser in its alloying elements, the α phase was able to transform into β phase at a lower temperature, hence almost all α phase in Ti-575 TMAZ was transformed. Once the whole microstructure contains mostly β phase, its deformation follows the material flow line. Away from the bifurcation point, the material flows side way toward the edges. However, right at the bifurcation point, the material is constrained at the bifurcation, therefore the longitude of the (110) plane is aligned with the forge direction. In Ti-64, there are less β stabiliser in its alloying elements, so it is more difficult for $\alpha \rightarrow \beta$ phase transformation to occur in Ti-64 TMAZ, therefore only partial transformation is observed. Since the microstructure still contains mostly α phase during welding, the deformation does not follow the bcc slip system, therefore the crystals do not align with the forge direction that well. In short, the difference in texture can be attributed to the difference in phases between the two alloys.

5.4.2 Spatial Variation of Texture

Based on the results presented in Chapter 5 and the understanding of texture in self-similar LFW'd Ti-64 from the literature [139, 200], the spatial variation of the texture in LFW'd

Ti-64:Ti-575 joints can be summarised and illustrated by a schematic diagram shown in Figure 5.15. In CWZ of both materials, strong $\{11\bar{2}\}\langle 111\rangle_\beta$ texture was exhibited in the prior β phase during welding, however, during the consolidation stage, a combination of $\beta \rightarrow \alpha$ phase transformation and variant selection resulted in a strong transverse $\{10\bar{1}0\}\langle 11\bar{2}0\rangle_\alpha$ texture. In Ti-64 TMAZ, regardless of bifurcation point, $\{11\bar{2}\}\langle 111\rangle_\beta$ texture also appeared in the prior β phase, despite having much lower intensity compared to the one reconstructed in CWZ. Upon cooling, the metastable β phase transformed back to α phase with a transverse texture T and one of the rolling textures R were preferentially selected. The selected rolling texture is dependent on the material flow direction. At the bifurcation point, both rolling textures are possible to be selected. The texture in Ti-575 TMAZ exhibits similar behaviour as the texture in Ti-64 TMAZ, except at the bifurcation point, instead of the $\{11\bar{2}\}\langle 111\rangle_\beta$ texture, strong $\{110\}\langle 001\rangle_\beta$ dominate this region during welding. Upon cooling, variant selection is less effective in this region, resulting in a combination of transverse $\{10\bar{1}0\}\langle 11\bar{2}0\rangle_\alpha$ texture, basal $\{0001\}\langle 11\bar{2}0\rangle_\alpha$ texture, and a few rolling-type texture components R'.

Note that except for the oscillation-independent texture at the bifurcation point of Ti-575 TMAZ, all the other textures are dependent on the oscillation direction. The oscillation-dependent texture is affected by the material flow direction, this would change the actual texture nominated. For instance, in CWZ the material flows horizontally toward the edges, hence the $\langle 111\rangle_\beta$ slip directions align with the horizontal flow. However, in TMAZ close to the bifurcation point, the material flow is slightly rotated around the transverse direction. The slip directions still tend to align with the material flow, this results in a rotation of the $\{11\bar{2}\}\langle 111\rangle_\beta$ texture and therefore the inherited α texture.

5.5 Conclusions

1. The texture of the weld was investigated. In the CWZ of both Ti-64 and Ti-575, a strong transverse α texture was found. Such texture is dependent on the oscillation direction. β reconstruction and texture simulation results indicate that the CWZ texture is derived from the $\{11\bar{2}\}\langle 111\rangle_\beta$ texture. The notably strong transverse texture component can be attributed to variant selection, which may be induced by the anisotropic stress due to thermal contraction or lattice strain of β phase due to plastic deformation. Such arguments are supported by the literature.
2. By comparing the measured and reconstructed texture with the ideal simple shear textures, the results suggest that the stress condition in CWZ during LFW is close to the ideal simple shear condition, where the forge direction is parallel to the shear plane normal, and the oscillation direction is parallel to the shear direction. The recrystallised β grains were forced to deform via $\{11\bar{2}\}\langle 111\rangle_\beta$ slip systems, therefore resulting in $\{11\bar{2}\}\langle 111\rangle_\beta$ texture.
3. In Ti-575 TMAZ at the bifurcation point, a strong basal α texture was found. This texture is not dependent on the oscillation direction, but on the weld geometry, which has not been documented in the literature. β reconstruction and texture simulation results indicate that the TMAZ texture is derived from the $\{110\}\langle 001\rangle_\beta$ texture.
4. The stress condition in Ti-575 TMAZ at the bifurcation point is close to the ideal simple shear condition, where the weld plane normal (sample Z direction) is parallel to the shear plane normal, and the longitudinal direction (sample X direction) is parallel to the shear direction. The dependency of the texture on the weld geometry in Ti-575 TMAZ at the bifurcation point can be attributed to the material extrusion, as on both sides of the bifurcation point, the material was extruded along the X

direction toward the edges, whereas at the bifurcation point, the material is restricted to flow along Z direction toward the weld interface.

5. Ti-64 TMAZ at bifurcation point does not exhibit the same texture as Ti-575 TMAZ at bifurcation point. The difference between the texture in Ti-575 TMAZ and Ti-64 TMAZ can be attributed to the amount of retained primary α grains. Compared to the Ti-575 side, there are more primary α retained on the Ti-64 side, therefore during welding the local deformation does not follow the $\{110\}\langle 001\rangle_\beta$ slip system. Consequently, the effect of restricted material flow along the bifurcation line is not significant on the Ti-64 side.
6. The scope of the geometry-dependent texture in Ti-575 TMAZ at the bifurcation point was found to be a $300 \times 300\ \mu m^2$ area. Within this area, prior β texture $\{110\}\langle 001\rangle_\beta$ is pronounced. Outside this area, the texture is influenced by the material flow direction towards the edges.
7. Based on results in the present study, and with an understanding of texture in self-similar LFW'd Ti-64 from the literature, the spatial variation of the texture within the entire LFW'd Ti-64:Ti-575 joint has been captured.

Chapter 6

Mechanical Behaviour

6.1 Introduction

This chapter presents a thorough evaluation of the structural integrity of linear friction welded (LFW'd) Ti-64 and Ti-575. The investigation covers both the as-welded and the post-weld heat treated (PWHT) condition. To assess strength distribution, microhardness measurements were conducted across the entire section of the weld. Exploring the ageing behaviour, macrohardness of the welds was measured following a series of PWHTs, aimed at determining the optimal PWHT condition. Among the candidate PWHT conditions, two were selected for further comprehensive mechanical testing. This encompassed evaluating residual stress, tensile strength, high cycle fatigue strength, fatigue crack growth threshold, fatigue crack growth resistance, and fracture toughness subsequent to the two PWHT processes. Additionally, the effect of processing variables, texture, and PWHT on these properties, along with the microstructure-property correlation, are discussed at the end of this chapter.

6.2 Microhardness Distribution

A microhardness map covering the entire weld in the as-welded condition is shown in Figure 6.1. The diameter of the indents is approximately 40-60 μm . The hardness distribution well reflects the zone size measurement, as one can correlate each weld zone to the microhardness map. Generally, the weld possesses superior hardness to both parent materials (PMs), with the maximum hardness value of 500 HV at the central weld zone (CWZ) of Ti-575 on the edges of the weld. At the bifurcation point, the CWZ is not only thinner but also softer than the edges. The thermo-mechanically affected zone (TMAZ) is slightly harder than the PMs. The heat-affected zone (HAZ) in Ti-64 is barely distinguishable from the PM in terms of macrographs and the microhardness map, whereas the HAZ on Ti-575 side is noticeably weaker than its parent.

Microhardness profiles at the bifurcation point and the right edge extracted from the microhardness map are shown in Figure 6.2. At the bifurcation point, the hardness of the weld is reduced compared to the edge. The reduction at the weld interface is notably larger for Ti-575 (-50 HV) compared to Ti-64 (-10 HV). Such reduction results in a narrower CWZ for both alloys and a hardness trough in the HAZ of Ti-575, whereas the size of the TMAZ remains roughly the same at about 1 mm for both alloys across the entire weld.

As Figure 6.1 reveals that the Ti-64:Ti-575 weld is weaker in the core compared to the edges, the following microhardness profile measurements focus on the middle thickness of the weld. To investigate the effect of processing variables listed in Table 3.4 on the microhardness of the welds, a series of microhardness profiles across the weld interface were measured at the middle thickness (approximately 4 mm to the right of the bifurcation point, see Figure 6.1) for all the welds in as-welded condition, as shown in Figure 6.3. Welds with different thicknesses (T_{max}) does have noticeably different microhardness profiles. To better illustrate the most significant difference among the microhardness profiles, the profiles of thick welds (where T_{max} is large) are coloured in black, whereas the profiles of thin welds (where T_{max}

is small) are coloured in blue. From the microhardness profiles, it is clear to see the effect of T_{max}, where thick welds have superior hardness (450 HV) at the weld interface to the thin welds (420 HV). The microhardness at the interface of the thin welds is roughly 30 HV lower than the thick welds. This is possibly due to different temperature and cooling rate experienced during the welding process. According to the study on the effect of weld thickness on the interface temperature [128], thick weld experience higher temperature during LFW. As higher temperatures are usually followed by a higher cooling rate given the process environment is the same, the resulting microstructure should contain finer martensitic α' laths.

The difference in T_{max} does not affect the overall shape of the microhardness profile, as all welds show higher hardness in the TMAZ and CWZ, and hardness trough in the HAZ. However, it is clear that the thin weld has a narrower weld than the thick weld as it has thinner microhardness peak, which indicates the width of TMAZ. This can be related to the weld zone size measurement in Figure 4.3, which shows that the thick weld has thicker weld zone than the thin weld. As the size of the weld zone is affected by T_{max}, the microhardness profile evidently has to change with the size of the weld.

For pressure and upset, there is no obvious impact on the microhardness distribution, as profiles with different pressure or upset collapse together as long as they share the same T_{max}. It is most likely that the variation of pressure and upset is too little to make significant changes in the microhardness, as the variation of pressure in the current study is only $110 \pm 20\%$ MPa. In comparison, T. Webster [11] studied the effect of KPVs in detail, the variation of pressure is much higher than the variation in the current study. His results show that a pressure at 180 MPa yields a thicker weld zone compared with a pressure at 50 MPa, nevertheless, such variation in pressure does not seem to have much effect on the peak hardness at the weld interface.

Figure 6.4 presents the microhardness profiles for all welds after PWHT at 600℃ for 1 hour. It illustrated that PWHT is beneficial to the microhardness distribution as the microhardness slightly increased across the whole weld zones for all welds regardless of their processing variables, presumably due to the formation of fine precipitates. In addition, the difference in microhardness between the thick welds and thin welds in as-welded condition is mitigated after PWHT, again as a result of fine precipitates, which will be discussed in Section 6.10.1.5.

To better compare the microhardness profiles between as-welded and PWHT'd conditions, the microhardness profiles of the same weld (ID: 473-01) in both conditions are presented in Figure 6.5. In the as-welded condition, the measured hardness values of PMs were approximately 350 and 310 HV for Ti-575 and Ti-64, respectively. Moving inward to the interface, Ti-575 has a noticeable HAZ with an inferior hardness value of 320 HV, however, there is no distinguishable weak spot on the Ti-64 side. Starting from the TMAZ, the hardness values gradually rise up to about 370 HV for both alloys. Entering the CWZ, Ti-575 has a sharp increase in hardness to 450 HV, while there is no dramatic change in the hardness of the Ti-64 CWZ. In PWHT'd condition, there is no obvious change in hardness of the Ti-575 PM, whereas the hardness of Ti-64 PM is slightly increased by 10 HV. However, the hardness trough in the Ti-575 HAZ is recovered to 350 HV, which is similar to its parent. Within the TMAZ and the CWZ, PWHT at 600ºC for 1 hour seems to be beneficial, as there is up to 50 HV increase in hardness there, although the maximum hardness at the weld interface stays the same.

6.3 Ageing Behaviour

It is of interest to optimise the PWHT process for the LFW'd dissimilar joint in terms of temperature and duration. A series of PWHTs were performed on the samples extracted from the same weld (with the same KPVs). The temperature used in these PWHTs ranges from 400 to 700℃, and duration ranges from 0.5 to 4 hours. Macrohardness was measured

at the weld interface and at both PMs to estimate the effect of temperature and duration on the mechanical property of the weld.

Figure 6.6 (a) shows the ageing curve of the weld interface with respect to various temperature for 1 hour. Values shown in the ageing curves were measured by macrohardness indents with a load of 10 kg. The size of the indents was approximately 200-250 μm, which is significantly larger than the microhardness indents. This results in a reduction in macrohardness values at the weld interface, as the large indents covered a good amount of softer Ti64 CWZ. The macrohardness values reflect the average hardness of the entire area covered by the indents, whereas the microhardness values can better capture the local spike of hardness at the weld interface.

As discussed in Section 4.2.1.4 and 4.3.1.3, the weld interface consists of metastable α' which is supersaturated. PWHT allows the elemental diffusion to occur and forms fine β precipitates which strengthen the material. Peak-aged hardness value occurs at 400-550℃. Over-ageing occurs at temperatures over 600℃ as the hardness drops significantly at a rate of approximately 24 HV/100℃. Under-ageing may occur at a temperature below 400℃, which was not explored in the current study. For the effect of duration at 600℃, as shown in Figure 6.6 (b), peak hardness occurs for 0.5-1 hour. Over-ageing does occur for longer duration, however, the negative impact is not as severe as over-ageing by temperature since the hardness drops at a lower rate.

Figure 6.7 (a) presents the ageing curves of PMs with respect to temperature for 1 hour. Unlike weld interface, the PM does not consist of supersaturated phase, thus precipitation hardening does not take place here. The hardness changes mainly due to the dissolution of secondary and tertiary α phase. For Ti-64, it seems that the change in temperature does not affect the hardness much within the range of temperatures studied, presumably due to the lack of secondary and tertiary α phase. On the other hand, for Ti-575, the hardness is lower

after PWHT for all temperatures studied, as Ti-575 contains large amount of transformed β phase. Note that for temperatures at 400-550℃, the hardness values stay at the same level before it drops further at temperatures between 550-650℃. At temperature above 650℃, the hardness values remain at the same level again. This two-step reduction of hardness in Ti-575 may associate with the dissolution of tertiary and secondary α laths at each step. After reaching over 650℃, when all fine α laths was fully dissolved, further increase in temperature has no effect on the hardness values. Figure 6.7 (b) shows the ageing curves of PMs with respect to duration at 600℃. Both PMs are less sensitive to the duration of PWHT as changing the duration from 0.5 to 4 hours does not make noticeable impact on their hardness.

The ageing curves serve as the first estimate on the effect of PWHT to the hardness of the welds. However, this is far from sufficient to optimise PWHT of the welds for aerospace applications. To ensure the integrity of the welds, further investigation on mechanical properties such as fatigue life and fatigue crack growth threshold is needed. The following mechanical testing in the current study focuses on two PWHT procedures: 1 hour at 500℃ and 1 hour at 600℃. Both durations are fixed for 1 hour as the ageing curves suggests that longer duration has a negative impact on the hardness of the weld interface, even though it has negligible impact on the hardness of PMs. 500℃ was chosen as it is the highest temperature that yields the maximum hardness for the weld and the PMs, whereas 600℃ was chosen as a comparison for the extra stress relief at the weld without extensively compromising the strength of Ti-575.

6.4 Tensile Strength

Tensile testing was carried out to investigate the room-temperature tensile strength of the LFW'd Ti-64:Ti-575 joints after PWHT for 1 hour at 600℃. A total of four tests was performed, the obtained engineering stress-strain curves are shown in Figure 6.8. HT001,

HT002, and HT004 were tested using a constant strain rate through the entire test, whereas HT003 used a different strain rate after yielding, hence resulting in a sharp increase in stress when strain is approximately 4%. The results are listed in Table 6.1. A typical fracture surface of the tensile specimens taken by optical microscope after testing is shown in Figure 6.9. The full set of fracture surfaces can be found in Appendix D.1.

The four test specimens were extracted from welds with different processing parameters (T_{max}, pressure, and upset). However, the measured Young's Modulus (E), 0.2% proof stress ($\sigma_{0.2\%}$), ultimate tensile stress (UTS), and plastic elongation (ε_{pl}) are fairly uniform among all tests. The average E is 93±4 GPa, the average $\sigma_{0.2\%}$ is 897±4 MPa, the average UTS is 960±2 MPa, and the average ε_{pl} is 12.5±1.2%. Note that HT003 is excluded from these values as different strain rate was used.

In all four test pieces, the final fracture occurred in Ti-64 PM. This indicates that the weld zone and Ti-575 has a higher tensile strength than Ti-64. It can be deduced that the measured proof stress (~900 MPa) is solely attributed to Ti-64, as the material with the lowest tensile strength starts yielding first. The measured Young's Modulus (~93 GPa), however, is considered the average modulus of the entire joint, as a result of non-uniform elastic deformation among Ti-64 and Ti-575 parent materials, as well as the weld zones.

The gauge diameter of the test pieces was measured before and after testing, as listed in Table 6.2. Notice that the diameter measured at the interface after testing is mostly identical to the initial gauge diameter, whereas the diameter measured in Ti-575 is noticeably reduced. This indicates that plastic deformation occurred in Ti-575, while the weld interface only experienced elastic deformation. As UTS is the maximum engineering stress achieved during the testing, one can deduce that the measured UTS is higher than the yield stress of Ti-575, yet it is still lower than the yield stress of the weld interface.

However, according to the tensile properties of Ti-64 and Ti-575 from the literature (see Table 3.2), the proof stress of Ti-575 (1050 MPa) is actually greater than the measured UTS (~960 MPa) in this study. Such contradiction can be rationalised by the discrepancy in observed microstructure between this study and the literature. As mentioned in Section 4.2.1.1, the primary α phase fraction in Ti-575 was 68% measured in this study, whereas the α content in Ti-575 measured by Thomas *et al.* [13] (with the same heat treatment procedures) was only 15-18%. This significant increase in primary α content (equivalently, reduction in transformed β content) potentially have a great impact on the mechanical properties of the alloy. As discussed later in Section 6.10.1.2, the microhardness results show that the transformed β region is the main strengthening phase in Ti-575, the loss of transformed β phase suggests that the tensile strength of Ti-575 in this study is lower than the one measured in the literature. Combined with the observation on the gauge diameter, the proof stress of Ti-575 used in this study is reduced to a value less than the measured UTS (~960 MPa).

6.5 High Cycle Fatigue

High cycle fatigue (HCF) testing was carried out to investigate the room-temperature fatigue strength of the LFW'd Ti-64:Ti-575 joints after PWHT for 1 hour at 500 and 600℃. HCF testing was completed at maximum stress (σ_{max}) range from 450 to 800 MPa and stress ratios (R) at 0.1, 0.3, and 0.7. The results are listed in Table 6.3. S-N curves plotted using maximum stress and stress range are shown in Figure 6.10 and Figure 6.11, respectively. Fractography of all test pieces taken by optical microscope can be found in Appendix D.2.

Notice that all HCF specimens failed at Ti-64 PM, therefore the properties measured from HCF testing is more relevant to Ti-64 PM, instead of the weld. Nevertheless, as there was no failure occurred in the weld and Ti-575 PM, the results still suggest that the weld and

Ti-575 generally have better fatigue life compared to Ti-64. Residual stress may also have an impact on the measured fatigue life, as discussed later in Section 6.6, Ti-575 and Ti-64 has different degree of residual stress in SENB specimens. However, measurement of residual stress in HCF specimens is beyond the scope of this study.

Figure 6.12 shows a typical fracture surface of the HCF test pieces. Since the test pieces failed at Ti-64 parent, which has higher toughness compared to the weld, the fracture surface is generally rough. Looking at the S-N curves, the tests carried out at $R = 0.3$ generally follow the same trend, no matter the T_{max}, pressure, upset, and PWHT temperature. This indicates that the aforementioned welding parameters do not have a noticeable impact on HCF life of Ti-64 PM within the investigated range.

The test performed at $\sigma_{max} = 600$ MPa at $R = 0.1$ (HF009) exhibits a similar fatigue life to the tests performed at the same maximum stress at $R = 0.3$ (HF005-HF008). This suggests that changing R from 0.1 to 0.3 barely has any effect on the fatigue life. However, increasing R to 0.7 significantly increases the fatigue life. The test with maximum stress at 600 MPa (HF010) was shown to run out after 5.26×10^7 cycles; the same test piece was then tested at 800 MPa, failing after a further 1.83×10^6 cycles.

The average and minimum HCF life for a disc material from Rolls-Royce internal data are also shown in Figure 6.10. The HCF life of Ti-64:Ti-575 welds is above their average HCF life below 1×10^7 cycles. Above 1×10^7 cycles, the test at 450 MPa exhibits a similar HCF life to the average HCF life. This suggest that the Ti-64:Ti-575 welds generally have better HCF life than the typical disc material used in Rolls-Royce.

From the microhardness profiles shown in Figure 6.5, along with the hardness-yield stress relationship in Equation (3.4), one can deduce that the weld zone has superior strength to the PMs. The lowest strength in the dissimilar weld occurs at Ti-64 PM. During HCF testing with a machined smooth test piece geometry, the HCF life is dominated by the formation of

persistent slip bands (PSBs) as discussed in Section 2.4.5.1 and illustrated in Figure 2.59. Plasticity develops primarily in regions with lower strength, hence the majority of PSBs forms in Ti-64 PM, consequently leading to the final failure.

6.6 Residual Stress

The residual stress of the single-edge notched bending (SENB) specimens after PWHT for 1 hour at 500℃ was measured in both forge direction and oscillation direction by hole drilling at the HAZ in both Ti-64 and Ti-575. The results are presented in a residual stress vs. depth chart as shown in Figure 6.13. For both alloys in both directions, there is a strong compressive residual stress with a value greater than -150 MPa near the surface, the maximum value was measured at Ti-575 in the forge direction at -244 MPa. The compressive residual stress gradually decreases as depth increases, and even turn into tensile stress in nature, due to the self-equilibrating character of residual stresses. The maximum tensile residual stress was measured at Ti-64 in the oscillation direction at 115 MPa.

The residual stress of the SENB specimens after PWHT for 1 hour at 600℃ was also measured, and the results are shown in Figure 6.14. In comparison with Figure 6.13, both the compressive residual stress near surface and the tensile residual stress in the core are reduced, showing the effectiveness of stress relief by increasing PWHT temperature. After PWHT at 600℃, the maximum compressive stress was measured at Ti-64 in the forge direction at -167 MPa, and the maximum tensile stress was measured also at Ti-64 in the oscillation direction at 78 MPa.

The maximum principal residual stress occurred in a direction close to the oscillation direction, and the minimum principal residual stress occurred in a direction close to the forge direction, as an example shown in Figure 6.15. The direction of the principal residual stresses maintains mostly unchanged throughout the depth measured, although it is compressive in nature near surface while it becomes tensile in nature in the core.

The residual stress would affect the results obtained from the SENB specimens, including fatigue threshold, fracture toughness, and fatigue crack growth resistance, as the external subjected stress may be facilitated or inhibited by the residual stress within the specimens.

6.7 Fatigue Crack Growth Threshold

The fatigue crack growth threshold testing in this study was all performed with a stress ratio (R) of 0.1 at room temperature. The effect of upset, friction pressure, crack location, crack propagation orientation and PWHT temperature on fatigue crack growth threshold were investigated. All testing conditions and results are listed in Table 6.4. Figure 6.16 shows the fatigue crack growth curves down to a threshold value. Fractography of the fracture surfaces of all SENB specimens after testing was taken by optical microscope, the full set of images can be found in Appendix D.3.

6.7.1 Effect of Upset

The effect of upset on the fatigue crack growth threshold can be seen from CP001L and CP009R. Both test pieces were PWHT'd at 500℃ and tested with crack located in Ti-575 CWZ and propagated along the oscillation direction. The upsets of CP001L and CP009R are 4.2 and 3.6 mm, respectively. The measured ΔK_{th} were 5.6 and 5.7 MPa$\sqrt{\text{m}}$ for CP001L and CP009R, respectively. The similar threshold values measured from the test pieces suggest that the difference in upset from 3.6 to 4.2 mm has barely any effect on the fatigue crack growth threshold in the given testing condition. Having different upset values generally does not change the microstructure that much, as long as the upset value is large enough for the completion of self-cleaning effect. Once a solid weld is obtained, further upset should not have much effect on the microstructure nor the mechanical properties of the weld. Therefore, the upset value of 3.6 and 4.2 mm are considered the same in the following discussion.

6.7.2 Effect of Friction Pressure

The effect of friction pressure on the fatigue crack growth threshold can be seen from CP002 and CP017. Both test pieces were PWHT'd at 600℃ and tested with crack located in Ti-575 CWZ growing parallel to the oscillation direction. The friction pressure of CP002 is 110 MPa while that of CP017 is 130 MPa. The measured threshold ΔK_{th} were 4.8 and 4.2 MPa$\sqrt{\text{m}}$ respectively for CP002 and CP017. The results seem to suggest that the welds with higher friction pressure have a marginally lower fatigue crack growth threshold in Ti-575 CWZ. However, without more repeated testing, conclusions cannot be drawn based on just two set of test results.

6.7.3 Effect of Crack Location

The effect of crack location on the fatigue crack growth threshold can be seen from CP002, CP010, CP012, and CP014. All four test pieces have similar geometry, the same friction pressure during LFW, PWHT'd at 600℃, and crack propagate parallel to the oscillation direction. Note that CP010 has an upset value of 3.6 mm, whereas the rest of the test pieces all have an upset value of 4.2 mm. As discussed in Section 6.7.1, the effect of upset within the range is negligible, hence CP010 is considered to have the same testing condition as the others. Cracks were located at Ti-575 CWZ, weld interface, Ti-575 parent, and Ti-64 parent respectively for CP002, CP010, CP012, and CP014. The measured threshold ΔK_{th} values were 4.8, 4.6, 5.0, 5.5 MPa$\sqrt{\text{m}}$, respectively. Similar analysis can be done for test pieces PWHT'd at 500℃ from CP001L and CP001R. Both test pieces were tested at the same conditions except the crack location is at Ti-575 CWZ and weld interface for CP001L and CP001R, respectively. The measured values of ΔK_{th} were 5.6 and 5.7 MPa$\sqrt{\text{m}}$, respectively.

The results suggest that the PMs generally have higher threshold values than the weld. Specifically, Ti-64 seems to have higher threshold than Ti-575. This is reasonable as the grain size of Ti-64 is larger, and the threshold value is dependent on the grain size, as

discussed in Section 2.4.4.1, larger grain requires more dislocation pile-up to break through the grain boundary. Within the weld region, the difference in threshold value between Ti-575 CWZ and weld interface is subtle, as only 0.2 MPa$\sqrt{\text{m}}$ difference was measured for test pieces PWHT'd at 600℃ and only 0.1 MPa$\sqrt{\text{m}}$ difference was measured for test pieces PWHT'd at 500℃. For PWHT at 600℃, the weld interface has slightly lower threshold than Ti-575 TMAZ, whereas for PWHT at 500℃, the weld interface has slightly higher threshold than Ti-575 CWZ. It is not entirely clear which one has higher threshold, but generally within weld zone, the threshold for Ti-575 CWZ and weld interface is pretty much the same for both PWHT temperatures.

6.7.4 Effect of Crack Orientation

The effect of crack orientation has been investigated through cracks propagated either parallel or perpendicular to the oscillation direction. Such effect at 500℃ in Ti-575 CWZ can be seen from CP003 and CP007. The crack in CP003 propagated parallel to the oscillation direction, while the crack in CP007 propagated perpendicular to the oscillation direction. The achieved ΔK_{th} values were 7.6 and 8.3 MPa$\sqrt{\text{m}}$ for CP003 and CP007, respectively. The results suggest that cracks propagated perpendicularly in Ti-575 CWZ would achieve higher fatigue crack growth threshold values when PWHT'd at 500℃.

For PWHT at 600℃ in Ti-575 CWZ, the effect of crack orientation can be seen from CP002, CP004 and CP006. The crack in CP002 and CP004 propagated parallel to the oscillation direction, while the crack in CP006 propagated perpendicular to the oscillation direction. The measured ΔK_{th} values were 4.8, 4.5 and 4.3 MPa$\sqrt{\text{m}}$ for CP002, CP004 and CP006, respectively. Interestingly, as opposed to the results obtained from 500℃, the results here appear to suggest that cracks propagated perpendicularly in Ti-575 CWZ would achieve slightly lower fatigue crack growth threshold values when PWHT'd at 600℃. However, this

argument is merely based on a single test repetition and marginal differences, more tests are needed for a solid conclusion to be drawn.

It appears that PWHT temperatures has a great influence on the effect of crack orientation. At 500℃, the perpendicularly propagated crack showed higher resistance to fatigue crack growth, hence achieving higher threshold values. However, when PWHT temperature is raised up to 600℃, the resistance to fatigue crack growth of perpendicularly propagated crack seems to be reduced.

6.7.5 Effect of Post-Weld Heat Treatment Temperature

From the fatigue crack growth curves shown in Figure 6.16, it is clear that PWHT temperature has a significant effect on fatigue threshold. As all specimens PWHT'd at 600℃ have threshold values that range from 4.2 to 4.8 MPa$\sqrt{\text{m}}$, whereas specimens PWHT'd at 500℃ have threshold values that range from 7.6 to 8.3 MPa$\sqrt{\text{m}}$, which is nearly twice the value of specimens PWHT'd at 600℃. The results seem to suggest that specimens PWHT'd at 500℃ are able to achieve higher fatigue crack growth threshold values.

However, as PWHT is associated with stress relief, specimens with lower PWHT temperature generally have higher degree of residual stress. The measured high fatigue crack growth threshold may be attributed to the residual stress rather than other factors such as changes in microstructural features or fracture mechanisms. To verify this hypothesis, one can look into the fracture surfaces of the specimens. For instance, CP006 and CP007 were respectively PWHT'd at 600 ℃ and 500 ℃, their fracture surfaces are shown in Figure 6.17 and Figure 6.18, respectively. Both test pieces underwent the same procedure during fatigue crack growth threshold testing, more specifically, the applied cyclic load for pre-cracking and the rate of load shedding are the same for all tests listed in Table 6.4. However, notice that the crack front of CP007 is significantly bowed, to an extent that the crack has never penetrated the surface of the test piece. On the other hand, although the crack front of

CP006 is also bowed, it is less severe than the crack in CP007. It was observed that all test pieces PWHT'd at 500℃ have severely bowed crack front, whereas test pieces PWHT'd at 600℃ all have moderately bowed crack front. As the crack length is measured by the nine-point average according to Equation (3.15), such bowed crack front would obviously underestimate the crack length and break the validity of stress intensity factor. Nevertheless, the current study still provides the calculated ΔK_{th} as a preliminary estimation. Compared to PWHT temperature, all other factors including upset, friction pressure, crack location, and crack orientation do not have a notable effect on the shape of the crack front.

It is suspected that the difference in residual stress between the PWHT temperature at 500 and 600℃ resulted in the difference in the crack propagation behaviour. As discussed in Section 6.6, PWHT at 500℃ was not sufficient to relieve the residual stress in the SENB specimens. Although the residual stress was measured in HAZ, one can expect that the magnitude of residual stress in TMAZ and CWZ should be even greater than the measured values, as they underwent a more severe thermo-mechanical condition during LFW. Consequently, a strong compressive residual stress was retained at the near surface region. The compressive residual stress near surface effectively restricts the crack propagation during fatigue crack growth threshold testing.

Efforts have been made to investigate the effect of PWHT on the fatigue threshold values excluding the effect of residual stress. This will be discussed in more detail later in Section 6.10.2.

6.7.6 Fractography

Fractography of selected fatigue crack growth threshold test specimens was taken by a scanning electron microscope (SEM) at the near threshold region. Figure 6.19 shows the fractography of specimen CP002 whose fatigue threshold ΔK_{th} is 4.8 MPa$\sqrt{\text{m}}$. A relatively smooth, featureless, and flat fracture surface was observed, which suggests that transgranular

fracture is the dominant mechanism in this region. The microstructure of CP002, whose crack was located in Ti-575 CWZ, is shown in Figure 4.18. Fine α and β laths with widths of approximately 80 nm are observed; these were segregated from martensitic α' laths during PWHT. Due to the existence of such fine microstructural features, the distance for the transgranular crack to advance is reduced. As discussed in Section 2.4.4.1 and illustrated in Figure 2.56, small microstructural features allow less dislocation pile-up for the crack to break through, consequently a low fatigue threshold ΔK_{th} values can be achieved.

Figure 6.20 shows the fractography of specimen CP003 whose fatigue threshold ΔK_{th} is 7.6 MPa$\sqrt{\text{m}}$. Similar to Figure 6.19, a featureless and flat fracture surface can be observed in this specimen, suggesting the same fracture mechanism, transgranular crack propagation, occurred in CP003. The major difference between CP002 and CP003 is their PWHT temperature, respectively at 600 and 500°C. Even through there is a significant difference in the fatigue threshold values between CP002 and CP003, however, the similarity in their fracture surfaces suggests that changes in PWHT temperature does not change the fatigue crack growth mechanism. This further confirms aforementioned hypothesis that the difference in fatigue threshold values should result from the residual stress, as suggested in Section 6.7.5, because the crack propagation mechanism is the same for both PWHT temperatures.

Figure 6.21 shows the fractography of specimen CP012 whose fatigue threshold ΔK_{th} is 5.0 MPa$\sqrt{\text{m}}$. Transgranular crack propagation with round granular features can be observed on the fracture surface of this specimen, presumably since the crack is located at Ti-575 PM. The size of the facets on the fracture surface appears to be similar to the primary α grain size (~10 μm). Compared to cracks located at the weld, the fracture surfaces at the PMs appear to be rougher, which may contribute to the higher fatigue threshold values.

Figure 6.22 shows the fractography of specimen CP014 whose fatigue threshold ΔK_{th} is 5.5 MPa$\sqrt{\text{m}}$. Similar to Figure 6.21, grain-like features are observed, as the crack is located at Ti-64 PM. Compared to Ti-575, the granular features in Ti-64 is notably larger, as the average grain size of Ti-64 is larger (as discussed in Section 4.2.1.1 and 4.2.2.1). Larger microstructural features require more dislocation pile-up for the crack to break through, consequently higher fatigue threshold ΔK_{th} values can be achieved.

6.8 Fatigue Crack Growth Resistance

The fatigue crack growth resistance was measured by carrying out fatigue crack propagation testing in this study. All tests were performed using specimens sliced in half (10×4.5 mm^2) with a stress ratio (R) of 0.1 at room temperature with K-increasing method until the specimens approached final fracture. The range of ΔK in the Paris regime was determined by the consecutive data points that result in the optimal linear fit, which was then used to calculate the Paris law constant A and m. The effect of upset, friction pressure, crack location and PWHT temperature on fatigue crack growth resistance were investigated. All testing conditions and results are listed in Table 6.5. Figure 6.23 and Figure 6.24 show the fatigue crack growth curves in the Paris regime and static fracture regime.

6.8.1 Effect of Upset

The effect of upset can be seen between CP011L and CP013L, whose upset are 3.6 and 4.2 mm, respectively. However, the crack growth resistance (in terms of Paris law constants A and m) and maximum stress intensity factor (K_{max}) of the two test pieces are all almost identical, meaning that the difference in upset within the studied range has nearly no effect on fatigue and fracture properties.

6.8.2 Effect of Friction Pressure

The effect of friction pressure on the fatigue crack growth resistance can be seen from Figure 6.23. It appears that specimens with lower friction pressure (CP011R, CP013L, and CP013R) all have a higher intercept A, ranging from 1.8×10^{-7} to 3.3×10^{-7} mm/cycle, whereas specimens with higher friction pressure ($P = 130$ MPa) usually have intercept A an order of magnitude lower. The measured exponent m of the specimens with lower pressure ranges from 2.0 to 2.3, whereas that of specimens with higher pressure ranges from 2.6 to 3.0. It appears that lower friction pressure yields larger A and lower m. However, the variance in A and m is considered insignificant, since similar degree of variance can also be found in repeated tests. Details will be discussed in Section 6.8.3. On the other hand, in terms of K_{max}, all four specimens shown in Figure 6.23 have values ranges within a narrow range, from 30.5 to 31.2 MPa$\sqrt{\text{m}}$. Such difference is negligible, thus it can be considered that friction pressure barely has any effect on K_{max}.

6.8.3 Effect of Crack Location

The effect of crack location on the fatigue crack growth resistance can be seen from Figure 6.24. The fatigue crack growth resistance within the Paris regime for all specimens within the figure lies in similar trend with A ranges from 1.2×10^{-8} to 3.4×10^{-7} mm/cycle and m ranges from 2.0 to 3.0. The variation in A and m is considered not significant, since similar degree of variation can also be seen from a few repeated tests with the exact same condition. For instance, CP016R and CP022R both were PWHT'd at 600℃ with crack located at Ti-64 PM, however, their respective measured A were 2.7×10^{-8} and 3.4×10^{-7} mm/cycle, with an order of magnitude difference. Additionally, their respective measured m were 2.6 and 2.0, where the difference is over half of the range of all tests.

Hence, it is considered that the crack location has little effect on the fatigue crack growth resistance.

However, within static fracture regime, difference in crack location shows significant influence on the K_{max}. For CP015L, CP021R, CP016L, and CP022R, where the crack was respectively located at Ti-575 CWZ, Ti-64 CWZ, Ti-575 PM, and Ti-64 PM, the measured K_{max} were 31.0, 54.4, 50.3, and 67.7 MPa$\sqrt{\text{m}}$, respectively. The results suggest that Ti-64 PM has the greatest K_{max}, followed by Ti-64 TMAZ, Ti-575 PM, and finally Ti-575 CWZ has the lowest K_{max} among all locations. The value of K_{max} is closely related to the critical stress intensity factor K_{Ic}, as K_{max} was measured at the moment when the specimens were nearly fractured.

6.8.4 Effect of Post-Weld Heat Treatment Temperature

The effect of PWHT temperature can be seen from CP015L and CP021L, whose PWHT temperatures are 600 and 500 ℃, respectively. As discussed in Section 6.8.3, PWHT temperature also has little effect on the fatigue crack growth resistance in terms of Paris law constants A and m. However, the difference between the two test pieces is observed in K_{max}, where the value for CP015L and CP021L are 31.0 and 34.9 MPa$\sqrt{\text{m}}$, respectively. The results seem to suggest that lower PWHT temperatures would yield higher K_{max}. The effect of PWHT may associate with to residual stress and the change in microstructure. As will be discussed later in Section 6.8.5, both test pieces were sliced in halves, and the crack fronts on both fracture surfaces appear fairly straight. It is considered that the effect of residual stress is not prominent for halved test pieces. The effect of microstructure will be discussed in more details later in Section 6.10.1.5.

6.8.5 Fractography

Fractography of the fracture surfaces of all SENB specimens after testing was taken by optical microscope. An example of the typical fracture surfaces after fatigue crack

propagation testing is shown in Figure 6.25. The full set of images can be found in Appendix D.4. As the crack fronts appear fairly straight on all fracture surfaces, it is considered that the residual stress in the specimens has little effect on the measured crack growth resistance.

Fractography of selected fatigue crack propagation test pieces was taken by a SEM at low and high ΔK in the Paris regime, as shown in Figure 6.26 to Figure 6.31. In general, at low ΔK, transgranular crack propagation is observed for all test pieces. For crack located in the CWZ (CP015L in Figure 6.26), the fracture surface is flat and featureless; for crack located in the PMs (CP016L in Figure 6.28 and CP022R in Figure 6.30), granular boundary features can be observed. The fracture surfaces of crack propagation test pieces at low ΔK are much similar to the fracture surfaces of fatigue threshold test pieces near threshold region (see Section 6.7.6).

At high ΔK, the fracture surfaces generally become rougher, with microvoids appearing occasionally at grain boundaries, as shown in Figure 6.27, Figure 6.29, and Figure 6.31. In this region the test pieces were very close to static fracture regime, it is considered that a mixed mode crack propagation mechanism with transgranular crack growth and microvoids coalescence occurred. The existence of microvoids on the fracture surfaces indicates that fatigue testing of titanium alloys and welds at room temperature exhibits ductile fracture behaviour.

Figure 6.32 illustrates the fracture surface of CP022R taken at the end of static fracture regime, right before the final fracture. Fatigue striations can be observed in this region. The largest striation spacing measured in Figure 6.32 (2.3 μm) is close to the measured crack growth rate at this ΔK (2.5 μm/cycle). This can be seen as evidence of the validity of the testing results.

6.9 Fracture Toughness

The fracture toughness testing was all performed at room temperature after completing fatigue crack growth threshold testing or fatigue crack propagation testing, as the crack length to width ratio (a/W) after threshold testing was controlled within 0.45-0.55, which is ideal to perform a fracture toughness testing. However, there are a few tests with a/W exceeding the ideal range, hence those test results should be treated carefully. All testing conditions and results are listed in Table 6.4. The measured load-displacement curves are shown in Figure 6.33. Fractography of the fracture surfaces of all SENB specimens after testing was taken by optical microscope, the full set of images can be found in Appendix D.3 and D.4. The effect of friction pressure, crack location, crack propagation orientation and PWHT temperature on fracture toughness were investigated.

6.9.1 Effect of Friction Pressure

The effect of friction pressure on the fracture toughness can be seen from CP002 and CP017. In Table 6.4, the friction pressure of both CP002 is 110 MPa, whereas that of CP017 is 130 MPa. All other testing conditions are the same. The measured K_Q for CP002 and CP017 were 29.8 and 24.5 MPa$\sqrt{\text{m}}$, respectively. The results suggest that test pieces with higher friction pressure have a notably lower K_Q. Note that CP004 was tested in the exact same condition as CP002, its measured K_Q was 29.9 MPa$\sqrt{\text{m}}$, which is very close to that of CP002. This gives more credits on the measured fracture toughness of CP002.

6.9.2 Effect of Crack Location

The effect of crack location on the fracture toughness can be seen from CP002, CP010, CP012, and CP014, as the crack was located respectively at Ti-575 CWZ, weld interface, Ti-575 PM, and Ti-64 PM. As listed in Table 6.4, the measured K_Q for CP002, CP010, CP012, and CP014 is 29.8, 28.6, 44.8, 66.8 MPa$\sqrt{\text{m}}$, respectively. The result suggests that

both PMs have higher fracture toughness compared to the weld. It appears that the fracture toughness can be associated with the size of the microstructural features. As Ti-64 PM has the largest primary α grain size among all four locations, its measured fracture toughness is also the largest. Meanwhile, the weld interface has the finest microstructural feature, the martensitic α' laths, it also had the lowest measured fracture toughness.

6.9.3 Effect of Crack Orientation

The effect of crack orientation on fracture toughness for crack located at Ti-575 CWZ and PWHT'd at 500℃ can be seen from CP003 and CP007, whose cracks respectively propagated parallel and perpendicular to the oscillation direction. The measured K_Q were respectively 25.0 and 26.3 MPa$\sqrt{\text{m}}$ for CP003 and CP007. The crack which grew perpendicular to the oscillation direction has a slightly higher fracture toughness compared to the parallel one.

For PWHT temperature at 600℃ at the weld interface, the effect of crack orientation on fracture toughness can be seen from CP008 and CP010. The crack in CP008 grew perpendicular to the oscillation direction, while the crack in CP010 grew parallel to the oscillation direction. The measured K_Q were respectively 26.3 and 28.6 MPa$\sqrt{\text{m}}$ for CP008 and CP010. In this case, the crack which grew perpendicularly has a slightly lower fracture toughness compared to the parallel one. It appears that the effect of crack orientation reverses at a higher PWHT temperature.

However, the effect of crack orientation is almost negligible when compared to the effect of the crack location. For instance, as discussed in Section 6.9.2, the fracture toughness of Ti-64 parent is 66.8 MPa$\sqrt{\text{m}}$, whereas that of weld Ti-575 CWZ is only 29.8 MPa$\sqrt{\text{m}}$. Hence, it should be considered that crack orientation barely has any effect on the fracture toughness after PWHT at both 500 and 600℃.

6.9.4 Effect of Post-Weld Heat Treatment Temperature

The effect of PWHT temperature on fracture toughness can be seen from CP002 and CP003, where CP002 was PWHT'd at 600℃ and CP003 was PWHT'd at 500℃. All other testing conditions are the same. The measured K_Q were 29.8 and 25.0 MPa$\sqrt{\text{m}}$ for CP002 and CP003, respectively. The results suggest that the test pieces with higher PWHT temperatures have higher values of fracture toughness. From the microhardness profiles shown in Figure 6.5, it is clear that the weld PWHT'd at 500℃ is much hardness than the weld PWHT'd at 600℃. Generally, hardness (which correlates with strength) has inverse relationship with toughness. Therefore it is expected that harder weld would have lower fracture toughness. In metallurgical point of view, PWHT temperature has direct influence on the number and the size of the precipitates form in the weld. Different PWHT temperatures lead to different degrees of precipitation hardening effect, which will be discussed in Section 6.10.1.5.

6.9.5 Fractography

Fractography of selected fatigue threshold test pieces and fatigue crack propagation test pieces at final fracture region was taken using SEM. Generally, for all test pieces with a crack located in the weld region, microvoids coalescence is observed in the final fracture region, indicating a ductile fracture behaviour. Figure 6.34 illustrates the fracture surface of CP005L, showing a typical fracture surface taken in the fracture region when crack is located in the weld zone. Changes in friction pressure, crack orientation, and PWHT temperature do not affect the fracture mechanism of the test pieces. However, granular features appear on the fracture surfaces where cracks located at the PMs, for instance, CP014 shown in Figure 6.35. This type of features also appears in the fatigue regions as discussed in Section 6.7.6 and 6.8.5. It is considered that mixed mode fracture mechanism occurred when cracks are located at the PMs with larger grains. The changes in fracture mechanism may also give

rise to the higher measured fracture toughness K_Q. A full set of fractographs taken in the fracture regions of the selected test pieces can be found in Appendix D.5.

6.10 Discussion

6.10.1 Microstructure and Microhardness

The microhardness has a strong relationship with the observed microstructure in LFW'd Ti-64:Ti-575 joints. The microhardness profile of the weld in as-welded condition is shown in Figure 6.5. The relationship between microstructure and microhardness in as-welded condition for each weld zone in the welds is elaborated as follows.

6.10.1.1 Parent Materials

The microhardness of Ti-575 PM is approximately 350 HV, which is slightly higher than that of Ti-64 PM (~310 HV). This can be rationalised by looking at their microstructure. As shown in Figure 4.4, the microstructure of Ti-575 consists of transformed β phase, which contains fine secondary and tertiary α laths. Conversely, as shown Figure 4.10, Ti-64 only consist of intergranular β phase where secondary α laths can only be found occasionally, and no tertiary α laths can be found at all. The width of the tertiary α laths found in Ti-575 is extremely fine, only approximately 40 nm. Such fine microstructural feature helps strengthen the material and increase the microhardness values.

The difference in microhardness between the two alloys may be also attributed to the difference in other microstructural features, such as the size of the primary α grains and the phase fractions. The primary α grain size in Ti-575 ($\sim$11.9 μm) is slightly smaller than that in Ti-64 ($\sim$15.3 μm). Smaller grain size indicates more grain boundary strengthening effect, therefore this also helps Ti-575 to gain higher microhardness values. In terms of phase fractions, Ti-575 has lower α phase fraction (68%) compared to Ti-64 (84%). Lower α phase fraction generally suggests lower hardness values, since in titanium α phase is stronger than

β phase, as α phase consists of closed-packed crystal structure (HCP), whereas β phase consists of non-closed-packed structure (BCC). However, since the β phase in Ti-575 is transformed β phase with fine α laths, it is considered much stronger than all other phases as the size of the fine α laths is 3 orders of magnitude smaller. Therefore, even though Ti-64 has slightly higher amount of α phase, the hardening effect from the fine α laths in Ti-575 is significant, hence resulting in higher microhardness values in Ti-575.

6.10.1.2 As-Welded Heat-Affected Zone

Focusing on the HAZ, Figure 6.5 illustrates that the microhardness of HAZ in Ti-575 drops slightly to approximately 320 HV compared to its PM, whereas the microhardness of HAZ in Ti-64 maintains a similar level of microhardness to its PM. From the microstructure of Ti-575 HAZ in Figure 4.6, it is evident that the fine α laths dissolved into β phase, presumably due to the heat experienced in this region. This also reflects subtle differences in its visual appearance compared with Ti-575 PM, as can be seen in Figure 4.1. By comparing Figure 4.4 and Figure 4.6, there is no major change in grain size and phase fractions in this region compared to Ti-575 PM, it can be deduced that the 30 HV drop in microhardness is attributed to the dissolution of the fine α laths. On the other hand, the microhardness of Ti-64 HAZ is maintained at a similar level to Ti-64 PM. This supports the fact that the microstructure of Ti-64 HAZ in Figure 4.12 shows a similar microstructure to Ti-64 PM, as originally very few fine α laths are observable, hence the heat experienced during welding does not significantly modify the microstructure. The heat may marginally assist the growth of β phase, but the effect is not sufficient to have notable impact on its hardness values.

6.10.1.3 As-Welded Thermo-Mechanically Affected Zone

Within TMAZ on the Ti-575 side, the microhardness gradually increases as shown in Figure 6.5. The microstructure of Ti-575 outer TMAZ shown in Figure 4.7 suggests that the

fine laths formed within the groove between the α/β phase boundary act as strengthening features. The dark strips are suspected to be the cumulated dislocation bands resulting from deformation; they may also contribute to the higher microhardness values. The microstructure of Ti-575 inner TMAZ shown in Figure 4.8 showing higher degree of deformation, which leads to work hardening and strengthen the material. Besides, the formation of fine α laths in the primary α grains also act as strengthening features. Similarly on the Ti-64 side, as shown in Figure 4.13, a high degree of deformation is presented, and the formation of fine α laths also occurs. However, the number of fine α laths on the Ti-64 side is fewer than the Ti-575 side, hence the amount of increase in microhardness in Ti-64 TMAZ is also less than in Ti-575 TMAZ.

6.10.1.4 As-Welded Central Weld Zone

In CWZ on both sides, the microhardness increases even further until the maximum value is reached at the weld interface, as shown in Figure 6.5. The microstructure observed in CWZ on the Ti-575 and Ti-64 sides, respectively shown in Figure 4.9 and Figure 4.14, both suggest that the formation of fine martensitic α' laths with 100% coverage over the entire CWZ is the dominant reason for the high microhardness values. Note that the microhardness values on the Ti-575 side is slightly higher than on the Ti-64 side when comparing at the same distance to the weld interface. This can be explained by the difference in width of the martensitic α' laths formed on both sides. As the width of the α' laths on Ti-575 side is constantly approximately 40 nm, whereas the width on the Ti-64 side varies from 40 to 300 nm, the microhardness in Ti-575 CWZ maintains at a higher level, while the microhardness in Ti-64 CWZ drops abruptly away from the weld interface.

6.10.1.5 Weld Zones in Post-Weld Heat Treated Condition

From Figure 6.5, it can be seen that the microhardness trough in Ti-575 HAZ is recovered after the application of PWHT, additionally, the microhardness in Ti-64 PM/HAZ also exhibited a slight increase after PWHT. Figure 4.15 illustrates the microstructure of HAZ

on both sides of the weld; the increase in local microhardness can be attributed to the formation of α precipitates within the β phase. As those α precipitates are at a similar scale to the fine tertiary α laths in Ti-575 PM, they help recover the microhardness back to the same level. The β phase fraction of Ti-64 is less than that of Ti-575, therefore the strengthening effect from the α precipitates in Ti-64 is not as effective as in Ti-575. Consequently, the increase in microhardness on the Ti-64 side is less significant.

The formation of α precipitates can also be observed in TMAZ and CWZ in PWHT'd condition on both sides, as shown in Figure 4.17, Figure 4.18, and Figure 4.21. Those α precipitates in TMAZ and CWZ all act as strengthening phase, hence increasing the microhardness in TMAZ and CWZ compared to as-welded condition, as shown in Figure 6.5.

The observation on the microstructure in Ti-575 CWZ after PWHT at different temperatures, as shown in Figure 6.36, shows that PWHT at 500℃ yields a microstructure with finer precipitates, which strengthen the material further than PWHT at 600℃. The precipitation hardening effect is also evident by the microhardness profiles shown in Figure 6.5, as PWHT at 500℃ yields significantly greater hardness values than PWHT at 600℃.

6.10.2 Effect of Residual Stress on Fatigue Crack Growth Threshold

As discussed in Section 6.7.5, it was observed that test pieces PWHT'd at lower temperatures can achieve a higher fatigue threshold. To investigate the reason for this, one can consider the fractography of the specimens and the relevant residual stresses. Figure 6.37 and Figure 6.38 illustrate the effect of residual stress on the shape of the crack front by overlaying the residual stress vs. depth curve onto the fracture surfaces of the specimens. For CP006 (PWHT'd at 600℃), strong compressive residual stresses only existed within 50 μm below

the side surfaces of the test specimens, which is a very narrow region that can barely affect the shape of the crack front. Over 250 μm below the surface, the residual stress becomes tensile in nature, which facilitates crack propagation. Therefore the crack in CP006 propagated faster in the core while receiving little resistance close to the edge, resulting in a slightly bowed crack front. For CP007 (PWHT'd at 500℃), much stronger compressive residual stresses existed near surface and further into the core. Although the magnitude of the compressive residual stress gradually becomes smaller further into the core, the residual stress remained compressive throughout the entire depth of measurement, as can be seen from Figure 6.13. Such strong compressive stresses completely prohibited the crack propagation near the edges of the specimen, resulting in a significant bowed crack front. As the crack propagation was restricted dramatically in CP007 and all other specimens PWHT'd at 500℃, it is highly suspected that the strong residual stress resulted in the higher measured fatigue crack growth threshold values. Furthermore, it was observed that the largest compressive residual stress measured near surface (-244 MPa) is greater than the applied bending stress at the beginning of pre-cracking process (128 MPa). Hence, it can be deduced that the strong compressive residual stress near surface significantly impeded the local crack propagation, hence, the crack never breaks through the surface of the test pieces for CP003 and CP007. Consequently, the cracks produced in these test pieces were not ideal through-thickness cracks, therefore yielding much higher threshold values. Admittedly, there is no residual stress data measured in the as-welded condition to serve as a reference point for estimating the degree of stress relief. Plus the residual stress was measured before pre-cracking, which may further alter the residual stress during fatigue crack growth testing. With these limitations, the measured residual stress can only serve as a preliminary estimation.

Another series of tests were performed with test pieces sliced in half by electrical discharge machining (EDM) to achieve further stress relief and to see whether superior fatigue crack growth threshold can still be achieved. The sliced specimens are labelled with a postfix 'L'

or 'R', their dimensions are either 10 by 4.5 or 9 by 5 mm. The testing conditions and results for the sliced specimens are listed in Table 6.4, and the corresponding fatigue crack growth curves down to a threshold value are shown in Figure 6.39. Fractography of the fracture surfaces of all SENB specimens after testing was taken by optical microscope, the full set of images can be found in Appendix D.3.

A typical fracture surface obtained from the sliced specimens is shown in Figure 6.40, where a relatively straighter crack front is observed. This suggests that slicing the specimens in half can effectively further relief the residual stress and mitigate the effects of compressive residual stresses on the shape of the crack front. Hence, the measured fatigue crack growth threshold values from the sliced specimens should reflect the intrinsic mechanical property without the influence of residual stress.

CP001L, CP001R, and CP009R are all sliced specimens with PWHT temperature at 500℃ and crack located within Ti-575 CWZ; their measured ΔK_{th} were 5.6, 5.7, and 5.7 MPa$\sqrt{\text{m}}$, respectively. Compared to the threshold values of the specimens in the same conditions without slicing (CP003 and CP007 with threshold at 7.6 and 8.3 MPa$\sqrt{\text{m}}$, respectively), the further stress relief achieved by slicing indeed mitigated the restriction from the residual stress and thus reducing the threshold values. However, when compared to the threshold values of the specimens PWHT'd at 600 ℃ (CP002, CP004, CP010, and CP017 with threshold at 4.8, 4.5, 4.6, and 4.2 MPa$\sqrt{\text{m}}$, respectively), the specimens PWHT'd at 500℃ still achieved notably higher threshold values. This indicates PWHT at 500℃ would give better fatigue crack growth threshold resistance even without considering its strong compressive residual stress near surface. To eliminate any side effects that may arise from slicing the specimens, a fatigue crack growth threshold testing was performed on a sliced specimen PWHT'd at 600℃ (CP011L), and the measured ΔK_{th} was 4.6 MPa$\sqrt{\text{m}}$, which is pretty much similar to the values measured from the specimens without slicing. As further stress relief from slicing the specimens in half did not have much effect on fatigue threshold

of CP011L, it is suggested that PWHT at 600℃ can effectively relieve the residual stress and remove its impact on fatigue crack growth threshold.

The effect of crack orientation on fatigue crack growth threshold was also re-investigated excluding the influence of residual stress. CP005L and CP005R were both sliced specimens with crack propagated perpendicular to the oscillation direction. Their measured ΔK_{th} were 8.1 and 8.6 MPa$\sqrt{\text{m}}$, respectively. Compared to the cracks propagated parallel to the oscillation direction with the same conditions (CP001L, CP001R and CP009R, whose measured threshold were 5.6, 5.7, and 5.7 MPa$\sqrt{\text{m}}$, respectively), the perpendicularly propagated cracks show much higher fatigue threshold values. The results obtained from the sliced specimens are consistent with the results obtained from the specimens without slicing, as discussed in Section 6.7.4. The fractography of CP005L shown in Figure 6.41 appears similar to Figure 6.20, which suggests that the fracture mechanism does not change.

One of the possible reasons for this observation is the difference in texture intensity between PWHT'd at 500℃ and 600℃. Figure 6.36 illustrates the microstructure of Ti-575 CWZ after PWHT'd at 500℃ and 600℃. Image analysis of the Figure 6.36 (a) and (b) yields α phase volume fraction at 70% and 83%, respectively. Since PWHT at 600℃ reduces the volume fraction of α phase, this effectively reduces intensity of the α texture and reduces the anisotropy originating from the HCP crystal structure, consequently, reduces the effect of texture on the mechanical properties. Another possible reason is the effect of anisotropic residual stress relief resulting from slicing the specimen in different orientations. The specimens with cracks propagated parallel to the oscillation direction may gained a higher degree of compressive stress relief, resulting in a lower threshold.

The crack in CP009L propagated into Ti-575 TMAZ when reaching its fatigue crack growth threshold at 7.1 MPa$\sqrt{\text{m}}$, which is notably higher than the threshold achieved in Ti-575 CWZ and at the weld interface in the same conditions (CP001L, CP001R and CP009R,

whose measured threshold were 5.6, 5.7, and 5.7 MPa$\sqrt{\text{m}}$, respectively). This suggests that Ti-575 TMAZ has a higher resistance in fatigue crack growth threshold than CWZ. The fractography of CP009L shown in Figure 6.42 appears to be rougher than Figure 6.41, which suggests that the microstructural features in Ti-575 TMAZ are larger than Ti-575 CWZ. The higher threshold value of CP009L can be attributed to the same reason discussed in Section 6.7.3, as the microstructural features in Ti-575 TMAZ (i.e. α lath and retained β phase) are larger than the microstructural features in Ti-575 CWZ (i.e. martensitic α laths).

6.10.3 Fatigue Crack Path Deviation in Weld Zones

From the side view of the fracture surfaces, it was observed that most of the cracks do not propagate in a straight line. For instance, in Figure 6.17 the crack deviate from the weld interface. The side views of all fracture surfaces of test pieces after fatigue crack growth threshold testing (see Appendix D.3) and fatigue crack propagation testing (see Appendix D.4) were used to observe the crack path for all cracks located in the welds. The observations are listed in Table 6.6, and the crack deviation behaviour is summarised in Table 6.7. It was observed that cracks located in Ti-575 CWZ and TMAZ tend to deviate away from the weld interface, with 14 observations from the threshold testing and 10 observations from the crack propagation testing. Nevertheless, there are two exceptions where the cracks located in Ti-575 CWZ deviated toward the weld interface. For cracks located in Ti-64 CWZ, they all tend to deviate toward the weld interface, which is evident by six observations. Specifically, two of them even grew across the weld interface into Ti-575 CWZ.

The crack deviation behaviour is generally associated with the uneven plastic zone size around the crack tip. According to Equation (2.24), the plastic zone size depends on the yield stress σ_{YS} of the material. For a given applied stress intensity factor, materials with lower yield stress would have a larger plastic zone size, which facilitates crack propagation. Therefore, generally the crack tends to deviate toward the region with lower yield stress.

This behaviour has been observed in a study on dissimilar inertia friction welding of RR1000 to IN718 [201], where cracks tend to grow from the hard material (RR1000) to the soft one (IN718). Crack deviation from HAZ to PM with lower strength has also been observed [202].

The yield stress can be estimated by the hardness via Equation (3.4). Hence, the microhardness profile shown in Figure 6.5 is useful for estimating the plastic zone size around the crack tip located in the welds. From all microhardness profiles, the peak hardness values occur at the weld interface. As generally the weld interface is harder, with a larger yield stress, following the theory of uneven plastic zone size, the crack should deviate away from the weld interface. Residual stresses may also play an important role on crack path deviation, especially when asymmetric residual stresses present on both sides of the weld. However, as shown in Figure 6.13 and Figure 6.14, the residual stresses around the crack tip consist of both compressive and tensile components at different depth, plus the fact that only subsurface residual stress was measured, further study is needed to fully appreciate its effect on crack path deviation.

This theory based on yield stress can explain the observations that cracks located in Ti-575 CWZ and TMAZ deviated away from the weld interface. However, the cracks that deviated from Ti-575 CWZ and Ti-64 CWZ toward the weld interface, along with two cracks that even grew from Ti-64 CWZ across the interface to Ti-575 CWZ, effectively grew towards material with larger yield stress, which does not follow this theory.

There are several possible reasons that can explain such behaviour which contradicts the theory. Firstly, PWHT temperature can affect the crack growth behaviour as the microhardness profile changes significantly after different PWHT (see Figure 6.5). For test pieces PWHT'd at 600℃, such as CP015R, since the weld interface, Ti-575 CWZ, and Ti-64 CWZ all share similar hardness values, the uneven plastic zone size phenomenon is not prominent, and therefore it is possible for the cracks grow freely. Secondly, the crack is not an ideal two-dimensional plane, it is a curved surface, it may be tilted towards the loading direction, and it may be located across multiple weld zones. As an example, the crack in

CP001R was located across the weld interface, one side in Ti-575 CWZ and another in Ti-64 CWZ, as shown in Figure 6.43. The deviation behaviour of such complicated crack is influenced by the tendency of both sides of the crack, in this case, both sides tend to deflect away from the weld interface, as the PWHT temperature is 500℃ and the difference in hardness between Ti-575 CWZ and Ti-64 CWZ is significant. However, from Figure 6.43, at the location where the crack length is around 1.5 mm, approximately 80% of the crack is located on the Ti-575 side, which indicates that its influence is much stronger than the partial crack on the Ti-64 side. Consequently, the crack path was dominated by most of the crack located in Ti-575 CWZ, which forces the partial crack located in Ti-64 CWZ to grow toward and even across the weld interface. Interestingly, initially the crack on the Ti-64 side tends to grow away from the weld interface, which follows the theory of uneven plastic zone size. Nevertheless, this portion of crack cannot grow against the majority and soon yielded to the overall crack growth tendency.

6.10.4 Full Fatigue Crack Growth Curves

As the current study performed both fatigue crack growth threshold testing and fatigue crack propagation testing, full fatigue crack growth curve can be established by combining the results from both testing, as shown in Figure 6.44. Since all fatigue crack propagation test pieces are half-sized specimens, only half-sized fatigue threshold test pieces are included in Figure 6.44. Even though the frequency used in both testing is quite different (65 Hz was used in fatigue threshold testing while 10 Hz was used in fatigue crack propagation testing), the data points connect well in the Paris regime, especially for CP011L and CP015L.

6.10.5 Hardness and Fracture Toughness

As Rolls-Royce has established many years of experience in research on the mechanical properties of titanium alloys joined by LFW, with a large amount of data, a strong relationship between hardness and fracture toughness is observed. This relationship is applicable to various types of $\alpha + \beta$ titanium alloys, as well as to both PMs and LFW'd joints. The data obtained in the current study along with dataset previously obtained by

Rolls-Royce have been used to correlate hardness and fracture toughness, as shown in Figure 6.45. Generally, hardness is inversely proportional to fracture toughness. Ti-6246 welds possess high hardness close to 500 HV, which yields low fracture toughness only approximately 20 MPa$\sqrt{\text{m}}$. On the other hand, parent titanium alloys generally have lower hardness compared to the welds. For Ti-64 and Ti-575, their hardness values range from 300 to 350 HV, which yields higher fracture toughness values ranging from 45 to 80 MPa$\sqrt{\text{m}}$. Ti-64 and Ti-575 welds have moderate hardness values, which also gives moderate fracture toughness values. With all data included, the linear fit of the hardness to fracture toughness relationship can be expressed as

$$K_Q = -0.25HV + 140 \tag{6.1}$$

Admittedly, this linear fit was obtained from multiple titanium alloys in a variety of weld zones with different microstructures, the regression coefficient (R^2) is only 0.78. Equation (6.1) can be used as a preliminary estimation of fracture toughness for a titanium alloy with known hardness, rather than a precise prediction.

6.11 Conclusions

1. The zone size and microhardness distribution were investigated. At the bifurcation point, the CWZ is thinner and the HAZ is larger compared to the edges. The overall hardness of the weld at the bifurcation point is lower than on the edges.
2. The weld zone is found to have superior hardness to both parent materials. The maximum hardness is found at the weld interface on the Ti-575 side with a value of 500 HV due to the formation of exceptionally fine martensitic α' laths.
3. A hardness trough was found at Ti-575 HAZ due to the dissolution of fine tertiary α laths. This hardness trough can be recovered by applying appropriate PWHT, such as 1 hour at 600 or 500℃.

4. The PWHT temperature has a more significant effect on the ageing behaviour of the weld interface and both parent materials compared to the duration. Ti-64 is less sensitive to PWHT temperature compared to Ti-575 and the weld interface, which both exhibit over-ageing at temperatures over 600℃. Two PWHT procedures, 1 hour at 500 and 600℃, are chosen for further investigation on mechanical testing.
5. The residual stresses after the two PWHT in SENB test pieces were measured. The surface exhibits strong compressive residual stresses, whereas the core exhibits tensile residual stresses. PWHT at 500℃ yields greater residual stresses, the maximum value was measured in the forge direction at -244 MPa, the maximum tensile residual stress was measured in the oscillation direction at 115 MPa.
6. Compared to both parent materials, the weld exhibits better tensile strength and high cycle fatigue strength, lower fracture toughness, and a similar fatigue crack growth resistance.
7. The fatigue crack growth threshold of test pieces PWHT'd at 500 and 600℃ is approximately 8.0 and 4.5 MPa$\sqrt{\text{m}}$, respectively. The notably high threshold of test pieces PWHT'd at 500℃ results from the effect of residual stress. After further stress relief by slicing the test pieces in half, the threshold of test pieces PWHT'd at 500℃ is reduced to approximately 5.5 MPa$\sqrt{\text{m}}$.
8. Process variables, upset and friction pressure, as well as crack orientation do not have significant effect on fatigue and fracture properties investigated in the current study.
9. Cracks located on the Ti-575 side tend to deviate away from the weld interface, whereas cracks located on the Ti-64 side tend to deviate toward the weld interface. Two cracks located in Ti-64 CWZ even grew across the weld interface into Ti-575 CWZ.

10. Hardness of the weld appears to be inversely correlated with fracture toughness. Such relationship has been observed in parent materials and the weld of Ti-64, Ti-575, and Ti-6246.

Chapter 7

Processing and Relative Upset

7.1 Introduction

In linear friction welding (LFW), the term 'upset' denotes the axial shortening between the two workpieces resulting from the applied compressive pressure and the material being extruded away from the weld. When welding similar materials, the degree of upset contributed from both workpieces is generally similar, as a similar amount of material is extruded from the two workpieces due to similar material properties. However, when welding dissimilar materials, the amount of extruded material from each workpiece is uneven. This uneven extrusion behaviour arising from welding dissimilar materials is termed 'relative upset', defined as the ratio of the partial upsets of the dissimilar materials. The partial upset can be measured as the distance between each side of the machine datum and the weld interface.

In the current study, the relative upsets for all the welds were measured and are presented in Figure 7.1. The relative upset of the LFW'd Ti-64:Ti-575 joints ranges from 2.1 to 3.2, depending on the friction pressure and weld thickness (T_{max}). A relative upset value greater

than one indicates that Ti-575 is generally more difficult to weld than Ti-64. The chart shows that welds with higher T_{max} exhibit higher relative upset. Additionally, for both large and small T_{max}, the relative upset is inversely proportional to the friction pressure. The reasons for the relationship between relative upset and T_{max}, as well as the reasons for the inversely proportional relationship between relative upset and friction pressure, are currently unclear. To the author's knowledge, no previous study has investigated relative upset in LFW of dissimilar materials. It is of interest to understand the nature of relative upset, identify what material properties and process parameters contribute to the relative upset, and find ways to reduce the relative upset when manufacturing dissimilar welds.

This chapter focuses on the studies related to the relative upset of the welds. To investigate the relative upset, the flash was analysed as it preserves the entire history of the welding process. The thickness of the flash was measured in Section 7.2.1, and its microstructure was characterised in Section 7.2.2. The relative upset is believed to be linked to the flow stress at elevated temperatures. Flow stress testing was conducted using both fast and slow heating rates, and the results are presented in Section 7.3. In Section 7.4, the microstructure at a high heating rate at elevated temperatures was examined, and the dynamic beta approach curves were established. The concept of dynamic β transus is introduced, which helps explain the results of the flow stress testing. Moreover, taking the dynamic β transus into account helps optimise the dissimilar welds.

7.2 Flash Characterisation

To investigate relative upset in dissimilar welds, studying flash is a useful starting point. Flash contains the extruded materials throughout the entire welding process, making it a proxy for studying the history of the welding process. By examining the ridges on the flash, it is possible to determine which cycle of oscillation it corresponds to. The thickness of the flash at a certain location can provide an estimate of the amount of material being extruded at that moment. Additionally, the microstructure of the flash can provide insight into its

local thermal history. The information obtained from flashes is valuable for understanding the nature of relative upset in the welds.

7.2.1 Flash Thickness Measurements

Optical images of flashes with different processing parameters are shown in Figure 7.2. The ridges observed on the flash were formed due to the extrusion motion during welding, with each ridge corresponding to one cycle of oscillation. It is evident from the images that the extruded flash thickness was non-uniform during the welding process. To measure the flash thickness, several locations were selected and correlated with the welding curves by counting the cycles and the number of ridges. The results, shown in Figure 7.3 to Figure 7.7, indicate that Ti-64 began to extrude in the middle of the transition stage while Ti-575 had not yet started. During the equilibrium stage, the extrusion of Ti-575 began, and the thickness of Ti-64 flash increased abruptly. During the equilibrium stage, the flash thickness of both materials continued to increase until the ramp-down stage. However, the flash thickness in the ramp-down stage was not included in the analysis due to the large curvature of the flash, which made the measurements inaccurate.

The delay in the extrusion of Ti-575 is a significant characteristic that affects the relative upset, and is defined as the 'conditioning time'. To investigate this, the conditioning time was measured for welds with various process parameters, and the results are presented in Figure 7.8. The data show that the conditioning time is inversely proportional to the friction pressure for both thick and thin welds, and that larger T_{max} values tend to increase the conditioning time. Extrapolating the lines to the point where the conditioning time equals zero indicates a friction pressure of approximately 184 MPa, which implies that it may be possible to eliminate the conditioning time by applying 184 MPa of pressure. This would enable Ti-575 to be extruded simultaneously with Ti-64, which would increase the upset of Ti-575 and thus help to reduce the relative upset. Admittedly, the extrapolation for the thick welds ($T_{max} = 32$ mm) only has two data points. More flash thickness measurements is required to further gain confidence on this interpretation.

7.2.2 Flash Microstructure

Figure 7.9 displays the microstructure of the flash at different locations, including the flash tip (Figure 7.9 (b)) and the middle of the flash close to the weld interface on both sides of the materials (Figure 7.9 (c) and (d)). The microstructure at all three locations shows martensitic microstructures, indicating a temperature above β transus during welding followed by rapid cooling. Such microstructure is similar to the CWZ microstructures, as shown in Figure 4.9 and Figure 4.14. The flash tip represents the beginning of the extrusion, which occurred in the transition stage, where only Ti-64 was extruded. The middle of the flash represents the equilibrium stage, where both Ti-64 and Ti-575 were stably extruded. The microstructure at the flash tip has thicker laths than the microstructure in the middle of the flash, indicating that the flash tip experienced a slower cooling rate. This is reasonable since upon cooling, the heat in the weld had to dissipate through the parent materials (PMs), and the flash tip is the farthest location from the PMs. Therefore, the heat remained there for the longest period, allowing the martensitic laths to grow for a longer time.

Figure 7.10 illustrates the microstructure in the flash at different locations away from the flash interface: the conditioning stage (Figure 7.10 (h) and (i)), the stable extrusion stage (Figure 7.10 (f) and (g)), the ramp-down stage (Figure 7.10 (d) and (e)), and the end of the weld (Figure 7.10 (b) and (c)). For both materials, the microstructure observed in the conditioning, stable extrusion, and ramp-down stages appears to be martensitic, exhibiting similar characteristics to the microstructure shown in Figure 7.9. At the end of the weld, highly deformed α grains and intergranular β phase were observed in the microstructure, indicating that the local temperature did not exceed β transus.

7.3 Flow Stress Testing

Flow stress, defined as the minimum stress required for a material to initiate flow, is crucial in assessing the ease of extrusion during LFW, specifically for dissimilar joints. The flow stress of a material can be found in its stress-strain curve as any value of stress between the

yield point and final fracture. The ratio of flow stress between the two materials may also be indicative of the relative upset. Flow stress tests have been conducted under conditions simulating those of the actual welding process, including a nominal strain rate of 1/s and a heating rate of 50°C/s over a temperature range of 800-1200°C. It should be noted that the actual heating rate during LFW was estimated to be approximately 2000°C/s [136], which is significantly higher than the heating rate used in this study. Therefore, additional flow stress tests were performed using a slow heating rate of 2°C/s while maintaining the same strain rate and temperature range to investigate the dependency of flow stress on heating rate. In addition, note that the strain rate during LFW was estimated to be approximately 3.5/s [124], which is also higher than the strain rate used in this study. As it is known that Ti-64 is sensitive to strain rate [124], the effect of strain rate on the flow stress is worth investigating but beyond the scope of this study.

7.3.1 Flow Stress at Elevated Temperatures

Figure 7.11 (a) presents the true stress-strain curves obtained for Ti-64, which show that the yield strength and post-yield hardening/softening behaviour are strongly influenced by the peak test temperature, with the yield strength increasing with heating rate. The true stress-strain curves are characterised by an initial rapid rise in stress, followed by work hardening up to a peak stress at a threshold strain. This initial work hardening is then followed by slight softening and a plateau in flow stress, where there is little hardening or softening response with increasing strain. Figure 7.11 (b) presents an equivalent set of true stress-strain curves for Ti-575, obtained over the same temperature range and heating rates. The true stress follows broadly the same trends observed for Ti-64, although Ti-575 appears to demonstrate more significant softening immediately following the peak stress.

The flow stress is determined as the maximum true stress from the curves and is plotted as a function of temperature for Ti-64 and Ti-575 with both slow and fast heating rates in Figure 7.12 (a) and (b). Both materials demonstrate a drop in flow stress with increasing

temperature. The flow stress appears independent of heating rate above 1000°C and 1100°C for Ti-64 and Ti-575, respectively. Figure 7.12 (c) shows the flow stress curves for both alloys at a heating rate of 2°C/s. At this heating rate, the flow stress of Ti-575 is slightly lower than that of Ti-64 below 1000°C. Conversely, the flow stress of Ti-575 is slightly higher than that of Ti-64 above 1000°C. However, the difference in flow stress measured at this heating rate is only approximately 20 MPa. It should be noted that at a slow heating rate, the flow strength of both alloys is quite similar. Figure 7.12 (d) illustrates the flow stress curves for both alloys at a heating rate of 50°C/s. Here, the flow stress relationship between the two alloys clearly reverses at a temperature between 950-1000°C. This indicates that at elevated temperatures above 1000°C, with a heating rate of 50°C/s, Ti-575 has a higher flow stress compared to Ti-64.

7.3.2 Microstructures in Flow Stress Test Pieces

The microstructures of all flow stress test pieces were examined by scanning electron microscopy, as shown in Figure 7.13 to Figure 7.16. Figure 7.13 shows the microstructures of Ti-575 tested at 800-1200℃ at a heat rate of 50℃/s. The microstructures in the specimens tested at lower temperatures remain similar to the PM microstructures. For instance, Ti-575 tested at 800℃ as shown in Figure 7.13 (a) exhibits a bi-model microstructure with equiaxed primary α grains, transformed β, and intergranular β regions, similar to the as-welded Ti-575 parent microstructures shown in Figure 4.4. As the testing temperature increases, the volume fraction of primary α grains gradually decreases, while the amount of β phase becomes higher, and its morphology becomes more uniform, as illustrated in Figure 7.13 (b)-(d). Over 1100℃, β phase transformed into $\alpha + \beta$ region with fine α and β laths. It is suspected that α laths formed from the relatively fast cooling rate from the air quenching after compression. There seem to be few primary α grains left in the microstructure, and the

α/β phase boundary becomes a zigzag shape, as β laths grew into the primary α grains, as shown in Figure 7.13 (e)-(f).

Figure 7.14 shows the microstructures of Ti-575 tested at 800-1200℃ at a heat rate of 2℃/s. Again, at 800℃, as shown in Figure 7.14 (a), the microstructures are similar to the as-welded Ti-575 PM microstructures. As the testing temperature increases, the volume fraction of primary α grains gradually decreases, while the amount of β phase becomes higher, and its morphology becomes more uniform, as shown in Figure 7.14 (b)-(c). Over 1000℃, almost no primary α grain remains, $\alpha+\beta$ region dominates the microstructures, as shown in Figure 7.14 (d)-(f). Notice that in Figure 7.14 (d), there is a combination of darker and brighter regions, while in Figure 7.14 (e)-(f), the microstructure appears to be more uniform. It is considered that in Figure 7.14 (d), with the testing temperature at 1000℃, the chemical composition has not yet stabilised due to the lack of time for diffusion to occur at elevated temperatures. The original primary α region still possesses chemical composition closer to α phase, while the original β region still possesses chemical composition closer to β phase, therefore resulting in different degree etching by the Kroll's reagent, consequently leading to different contrast in the secondary electron image. On the other hand, in Figure 7.14 (e)-(f) with higher testing temperatures, the specimens experience longer time at elevated temperatures, allowing more diffusion to occur, hence the overall chemical composition of the $\alpha+\beta$ region is more homogeneous, and uniform etching was achieved.

Figure 7.15 shows the microstructures of Ti-64 tested at 800-1200℃ at a heat rate of 50℃/s. Similarly, at low temperatures, the microstructures are similar to the as-welded PM microstructures, as can be seen in Figure 7.15 (a). As the testing temperature increases, the volume fraction of primary α grains gradually decreases, while the amount of β phase becomes higher, as shown in Figure 7.15 (b)-(d). Over 1100℃, almost all primary α grains

dissolved into β phase at elevated temperatures, and the β phase transformed back into fine martensitic α' laths after cooling, presumably due to the relatively fast cooling rate from the air quenching, as shown in Figure 7.13 (e)-(f). Similar chemical segregation can also be observed in Ti-64.

Figure 7.16 shows the microstructures of Ti-64 tested at 800-1200℃ at a heat rate of 2℃/s. All the aforementioned microstructure evolution mechanisms can also be observed here. Except less chemical segregation occurred, presumably due to a slower heating rate and longer time at elevated temperatures for diffusion to take place.

Note that the primary α phase in Figure 7.14 was fully dissolved at a lower temperature (1000℃), in comparison with Figure 7.13 (1100℃). The temperature at which the primary α phase fully dissolves is defined as β transus in titanium alloys. It is considered that a higher heating rate effectively limits the time for diffusion to occur at elevated temperatures, consequently resulting in a delay in reaching the β transus. In other words, the β transus is a function of heating rate, the traditional definition of β transus on the phase diagram is in equilibrium condition at an extremely slow heating rate. In thermal processing with a high heating rate such as LFW, the temperature required to fully dissolve α phase would be higher than the traditional β transus. Such temperature is defined as dynamic β transus in the current study.

Dynamic β transus may have a significant impact on the flow stress of titanium alloys since it alters the α and β phase fractions in the microstructure, besides, the flow strength of the hexagonal close-packed (HCP) α phase and body-centred cubic (BCC) β phase is different. The equilibrium β transus of Ti-575 and Ti-64 can be found in the literature, and they are listed in Table 3.2. However, it is not feasible to estimate the β transus from the microstructures of the flow stress test pieces, since the cooling rate from air quenching is not

fast enough to completely eliminate microstructure modification after testing, as evident from the zigzag α/β phase boundary shown in Figure 7.13 (e). To estimate the dynamic β transus of Ti-575 and Ti-64 during LFW, heat treatment trials with a high heating rate followed by water quenching were performed. Details of the results will be discussed in Section 7.4.

7.4 Dynamic β Transus

Upon examining the flow stress curves in Figure 7.12 (d), it is evident that the flow stress of Ti-64 drops dramatically at a temperature close to 1000℃ at a high heating rate, while the flow stress of Ti-575 does not drop as much. This reversal in the flow stress relationship between the two alloys is of great interest. It is important to understand why such distinct behaviour occurs near 1000℃ as this temperature is close to the β transus of both alloys. It is suspected that this dramatic drop in flow stress may be related to the β transus of the alloys.

Typically, the β transus temperature of titanium alloys is determined under thermodynamic equilibrium conditions, or a quasi-static process [203]. In this process, samples are heated at a slow and controlled rate to predetermined temperatures, held for a few minutes to achieve thermodynamic equilibrium, and then rapidly quenched in water. The volume fraction of the β phase present at the soak temperature is then quantified through microstructural analysis. The lowest temperature at which 100% of the β phase is achieved is then determined as the β transus temperature. However, the heating rate in LFW is extremely fast, making such a quasi-static process unsuitable for determining the β transus. Instead, the β transus in a rapid heating condition, defined as 'dynamic β transus', is more relevant for the welding process. It is important to understand the behaviour of the alloys at high heating rates, such as those experienced in LFW, to determine the dynamic β transus and its impact on the

flow stress. The drop in flow stress observed in Ti-64 near 1000℃ may be linked to the dynamic β transus of the alloy.

To determine the dynamic β transus for Ti-64 and Ti-575, the samples of the alloys were subjected to rapid heating at a rate of 25℃/s to the predetermined temperatures. Detailed methods are described in Section 3.4.3. After reaching the desired temperature, the samples were immediately quenched into water. This process limited the diffusional phase transformation as the time at elevated temperatures was restricted, similar to the actual situation during LFW. The β phase fraction in the samples was analysed using electron backscatter diffraction (EBSD) mapping, which allowed for easy distinction of the retained primary alpha grains from the martensite transformed from the β phase. As noted in the flow stress tests, the heating rate achieved in this experiment is not representative of the actual heating rate during LFW due to instrumental limitations. Nevertheless, the dependency of the β transus on the heating rate can be made by comparing the measured dynamic β transus to the equilibrium β transus.

Figure 7.17 depicts the microstructures of both alloys after the heat treatment at various predetermined temperatures. The retained alpha grains, which appear as bright equiaxed shapes embedded in the darker martensite matrix, can be seen to decrease in amount as the temperature increases. At temperatures above 1060℃, there is virtually no retained alpha phase present in either alloy. The β phase fraction at elevated temperatures for both alloys was measured under dynamic conditions and presented in Figure 7.18, alongside the beta approach curves measured under equilibrium conditions from the literature [13, 203]. The temperature at which 100% of the β phase is achieved was used to determine the β transus of the alloys. In equilibrium conditions, the β transus of Ti-575 and Ti-64 are 965 and 996℃, respectively. However, under dynamic conditions with a heating rate of 25℃/s, the β transus

of both alloys is increased to approximately 1060℃. It is reasonable for the dynamic β transus to be higher than the equilibrium β transus for both alloys because diffusional phase transformation is restricted in dynamic conditions, resulting in less β phase transformation occurring compared to equilibrium conditions at the same temperature.

7.5 Discussion

7.5.1 Nature of Relative Upset

Based on the relative upset measurements presented in Figure 7.1, a relative upset value greater than one indicates that Ti-64 is generally more weldable than Ti-575. More specifically, Ti-64 demonstrates superior ease of extrusion during LFW. The ease of extrusion can be linked to flow stress as it is a characteristic parameter that describes the minimum stress required for a material to initiate flow. In the context of LFW, material extrusion is essentially the flow of material in shear mode. Therefore, the flow stress of a material can be a useful indicator of its ease of extrusion during LFW. Thus, the superior ease of extrusion observed for Ti-64 suggests that it has a lower flow stress.

Flow stress is influenced by microstructure features, including grain size and β phase fraction. During LFW, extrusion mainly occurs at elevated temperatures close to or above the β transus. At these temperatures, most of the alpha grains have transformed into the β phase, making the original alpha grain size less significant in affecting the flow stress. The β phase fraction, on the other hand, predominantly influences the flow stress at elevated temperatures. In titanium, the alpha phase is composed of a HCP structure, whereas the β phase is composed of a BCC structure. The HCP structure generally possesses higher strength than the BCC structure due to its higher packing density. Thus, a lower flow stress indicates a higher β phase fraction in the microstructure.

Furthermore, the β phase fraction is correlated with the β transus, which is defined as the temperature at which the alpha phase fully transforms into the β phase. The β transus can serve as an estimation of the amount of β phase present in titanium alloys. At a specific elevated temperature, titanium alloys with lower β transus would exhibit a higher amount of β phase than alloys with higher β transus. Therefore, a higher β phase fraction in the microstructure indicates a lower β transus.

Based on the aforementioned discussion, it may be inferred that Ti-64 has a lower β transus than Ti-575. However, upon comparing the literature values for the β transus of Ti-575 (965℃) and Ti-64 (996℃), the opposite trend is observed. The issue lies in the fact that the β transus values from the literature were measured in equilibrium conditions, which involve an extremely slow heating rate. In contrast, during LFW, the heating rate is incredibly rapid, reaching a rate of approximately 2000℃/s [136]. Consequently, it is necessary to consider the β transus under dynamic conditions with fast heating rates.

According to the dynamic beta approach curves illustrated in Figure 7.18, there is a difference in the extent of increase in dynamic β transus between Ti-575 and Ti-64. Ti-575 exhibits a +95℃ increase in dynamic β transus compared to its equilibrium β transus, whereas Ti-64 shows only a +64℃ increase. This suggests that the impact of heating rate on β transus is more pronounced for Ti-575 than for Ti-64. Furthermore, the heating rate used in this study is only 25℃/s, which is far from the estimated heating rate of 2000℃/s in LFW. It is expected that the effect of heating rate on β transus would be even more significant during actual LFW. Therefore, it is likely that the dynamic β transus of Ti-575 during LFW is higher than that of Ti-64.

Furthermore, based on the flow stress curves presented in Figure 7.12, the flow stress appears to be insensitive to heating rates above 1000 and 1100℃ for Ti-64 and Ti-575, respectively. This suggests that the amount of β phase at these temperatures is high enough to eliminate the hardening effect from the retained alpha phase. Although these temperatures may not exactly correspond to their dynamic β transus, they suggest that Ti-64 has a higher amount of β phase compared to Ti-575. As previously discussed, a higher amount of β phase indicates a lower β transus. Therefore, it can be deduced that at a heating rate of 50℃/s, the β transus of Ti-64 is reduced to a level below that of Ti-575. This further confirms that in the actual LFW process, the dynamic β transus of Ti-64 is lower than that of Ti-575 since the estimated heating rate is even higher than the heating rate employed in this study.

In conclusion, this study compares the weldability of Ti-64 and Ti-575 during LFW. Ti-64 is found to be more weldable due to its superior ease of extrusion, which is related to its lower flow stress. The flow stress is influenced by microstructure features, including grain size and β phase fraction, with the latter being the predominant factor at elevated temperatures. Lower flow stress indicates a higher β phase fraction in the microstructure, which is correlated with lower dynamic β transus. The evidence from the dynamic beta approach experiment and flow stress tests confirms that the dynamic β transus of Ti-64 is lower than that of Ti-575 during LFW, which confirms the higher weldability of Ti-64.

7.5.2 Effect of Heating Rate on the Zone Size

By considering the dynamic effect resulting from different heating rates, it is possible to observe this effect in the zone size measurements presented in Figure 4.3. The boundary between the central weld zone (CWZ) and the thermo-mechanically affected zone (TMAZ) can be seen as the contour of the β transus, since the microstructure in the CWZ consists of 100% martensite transformed from the β phase at elevated temperatures, indicating that the

temperature in this region was above the β transus during welding. In contrast, the presence of only partial martensite in the TMAZ implies that the temperature here is below the β transus.

It is noteworthy that at the bifurcation point, the CWZ in Ti-575 is thinner than that of Ti-64, while the opposite is observed at the edges. Assuming that the thermal conductivity of Ti-575 and Ti-64 are comparable, the temperature distribution across the weld interface is expected to be similar on both sides. Alloys with higher β transus typically exhibit a thinner CWZ, whereas those with a lower β transus tend to have a thicker CWZ.

The difference in the size of the CWZ between Ti-575 and Ti-64 can be explained by the difference in heating time. At the bifurcation region, the material was pushed sideways immediately after reaching the weld interface, leaving little time for the material to heat up fully and complete the $\alpha \rightarrow \beta$ phase transformation. This can be considered as a fast-heating condition. Conversely, at the edges, the material first travelled from the PMs to the weld interface before being pushed sideways to the edges. Consequently, it was heated up once it reached the weld interface and had more heating time while it was pushed to the edges, allowing more time to complete the $\alpha \rightarrow \beta$ phase transformation. This can be interpreted as a slow heating condition.

In the slow heating condition, the β transus of the alloys is closer to their equilibrium β transus. Ti-64 has a higher equilibrium β transus (996ºC) than Ti-575 (965ºC), which explains why Ti-64 has thinner CWZ at the edges than Ti-575. In contrast, in the fast-heating condition, the β transus of the alloys is closer to their dynamic β transus. The dynamic beta approach experiments and flow stress tests showed that Ti-64 has a lower dynamic β transus than Ti-575, which explains why Ti-64 has a thicker CWZ at the bifurcation point than Ti-575.

7.5.3 Effect of Flow Stress on Conditioning Time

The underlying mechanism behind the conditioning time (i.e. the delay in extrusion of Ti-575) can be attributed to the flow stress curves. As depicted in Figure 7.19 (a), which presents the measured flash thickness of weld 473-03 with a friction pressure of 110 MPa and a maximum weld thickness (T_{max}) of 32 mm, the start of extrusion for Ti-64 and Ti-575 is marked by annotations 'A' and 'B', respectively. The duration between these two points represents the conditioning time of the weld. Figure 7.19 (b) displays the measured flow stress curves for Ti-64 and Ti-575 under rapid heating conditions (50℃/s) that are analogous to the rapid heating rate during LFW (2000℃/s). The red dashed line represents the friction pressure of weld 473-03 (110 MPa), while annotations 'C' and 'D' indicate where the flow stress equals the friction pressure for Ti-64 and Ti-575, respectively.

The conditioning time, as observed from the flash thickness curves in Figure 7.19 (a), can be correlated to the flow stress curves depicted in Figure 7.19 (b). The following detailed explanations are presented. Throughout the LFW process, the applied pressure remained constant, whereas the initial temperature started at room temperature and rapidly increased due to the oscillation and friction, exceeding the β transus temperature of both alloys during welding. This is evident by the martensitic microstructure observed in the flash.

In the ramp-up stage, the temperature was still below the β transus of both alloys, causing their flow stress to be above the friction pressure. Consequently, there was no extrusion of material during this stage, as observed in Figure 7.19 (a). In the transition stage, as the temperature increased and reached above 990℃, the flow stress of Ti-64 dropped below the friction pressure, which initiated the extrusion of Ti-64, as indicated by the annotation 'A' in Figure 7.19 (a) and 'C' in Figure 7.19 (b). However, Ti-575 had not been extruded yet since its flow stress was still higher than the friction pressure at this temperature. The oscillation and friction in the transition stage continued to generate power and heat, causing the temperature to increase further. When the temperature exceeded 1030℃, the flow stress

of Ti-575 reduced below the friction pressure, initiating the extrusion of Ti-575, as indicated by the annotation 'B' in Figure 7.19 (a) and 'D' in Figure 7.19 (b). In summary, the difference in flow stress of Ti-64 and Ti-575 with respect to the friction pressure (denoted by annotations 'C' and 'D') is the main factor responsible for the discrepancy in their extrusion time (denoted by annotations 'A' and 'B').

Based on the discussion above, it can be inferred that the relative upset arises due to the difference in flow stress between the two alloys and the resulting conditioning time. To eliminate the conditioning time observed in the welding process, increasing the pressure to approximately 173 MPa, as indicated by annotation 'E' in Figure 7.19 (b), can be considered as a potential solution. This increase in pressure can lead to simultaneous extrusion of both alloys, as the flow stress of both alloys would drop below 173 MPa at the same time, thereby reducing the relative upset. Therefore, the minimum pressure required to achieve zero conditioning time ($P_{t=0}$) can be seen as a valuable process variable to be considered when welding dissimilar materials. The value of $P_{t=0}$ is expected to depend on the dynamic β transus and flow stress of the welding alloys.

While the method described above to estimate $P_{t=0}$ involves conducting flow stress tests on the welding materials, there is a quicker way to estimate $P_{t=0}$ through flash thickness measurement. As seen in the conditioning time vs. pressure chart in Figure 7.8, $P_{t=0}$ can be estimated by extrapolating the trend to where the conditioning time equals zero. This method yields a $P_{t=0}$ value of 184 MPa for a T_{max} of 32 mm, which is the same thickness of the weld 473-03. This $P_{t=0}$ value is in good agreement with the value obtained from the flow stress curves (173 MPa), indicating the reliability of both methods. Note that while the flow stress curves involve interpolating data to estimate $P_{t=0}$, the flash thickness measurement involves extrapolating data, in either case, a more precise estimation can be achieved by reducing the intervals of the data or increasing the number of data points. The flash thickness

measurement method is more cost-effective, as it only requires producing several dissimilar welds and examining them using optical microscopes.

In practice, the increase of friction pressure may impose some technical challenges, such as breaking the limitation of the capability of the equipment. Another thing worth considering would be the change in welding temperature. As can be seen in Figure 7.19, if one increases the friction pressure to 173 MPa, the material will start to be extruded at approximately 965℃, which is well below the β transus of both alloys. The drop in extrusion temperature implies a significant change in the microstructure of the weld, as no $\beta \rightarrow \alpha'$ martensitic phase transformation will occur, consequently, this may result in a softer weld interface. Besides, as the peak temperature at the weld interface is decreased, the temperature distribution of the weld will change accordingly, leading to a narrower weld zone.

7.5.4 Phase Transformations in Thermo-Mechanically Affected Zone Respecting Dynamic β Transus

The results obtained by dynamic beta approach presented in Section 7.4 suggest that in comparison with Ti-64, Ti-575 has a higher dynamic β transus, especially at a heating rate of approximately 2000℃ during LFW. However, as discussed in Section 4.4.1.3 and Section 4.4.1.5, the observation on the microstructure of as-welded Ti-575 TMAZ and Ti-64 TMAZ seems to suggest that Ti-575 has a lower dynamic β transus, since Ti-575 TMAZ was able to achieve a complete phase transformation into β phase during LFW, whereas Ti-64 TMAZ still retained some primary α grains after LFW. These findings appear contradictory to each other.

Nevertheless, this contradiction can possibly be resolved by reevaluating the mechanism of the formation of acicular α laths in the as-welded Ti-575 TMAZ, since it is possible that those acicular α laths form without surpassing the dynamic β transus. The first possible

mechanism is martensitic transformation during rapid heating. Although generally it is known that martensitic phase transformation occurs during cooling, this kind of martensitic phase transformation during heating has previously been observed by Seward *et al.* [196] using a scanning electron microscope with an *in-situ* heating stage, and acicular β laths can be observed at a heating rate of 10℃/min in pure titanium. If this phase transformation mechanism was to occur in Ti-575 TMAZ during LFW, the acicular β laths formed during heating would also undergo another martensitic phase transformation upon cooling. In this case, it is suspected that the α laths inherited the shape of the acicular β laths, while the crystallographic orientation of the α phase follows Burgers' orientation relationship with the prior β laths, each individual β lath was transformed randomly into one of the 12 possible α variants. Although the mechanism of martensitic transformation during rapid heating seems plausible, it has only been observed in pure titanium, and the heating rate during LFW was estimated to be approximately 2000°C/s [136], which is much faster than the heating rate used in the study of Seward *et al.*

Another possible mechanism would be 'massive transformation', defined as a type of phase transformation involving diffusional nucleation and growth by means of short-range diffusional jumps across the massive/matrix interface [197]. Pilchak and Broderick [198] observed a similar type of microstructure (acicular α laths inside the prior primary α grains) in a solid-state weld of Ti-64 near the boundary of HAZ and TMAZ. Their investigation using chemical and crystallographic analysis excluded the possibility of that the microstructure was formed by diffusional transformation or by martensitic transformation, instead they proposed that massive transformation is a possible mechanism for the formation of such microstructure. The material and its thermo-mechanical history in their study appear be similar to ones in the current study, as both studies use $\alpha + \beta$ titanium alloys joined by solid-state welding. In addition, the microstructural features, acicular β laths extending into

the primary α grains, observed in the study of Pilchak and Broderick can also be seen from the microstructure of flow stress specimens, see Figure 7.13 (e) as an example. The massive transformation mechanism seems to be a plausible solution to the contradiction. However, they did not provide any welding parameters nor temperature profiles, hence it is difficult to resolve why such microstructure was not observed on the Ti-64 side in this current study. Further investigation on the criteria of massive transformation is needed to fully understand the conditions for this mechanism to occur.

7.6 Conclusions

1. The high relative upset in LFW'd Ti-64 to Ti-575 joints is found to originate from the delay in the extrusion of Ti-575. Such delay is a significant characteristic in LFW'd dissimilar joints, and is defined as the 'conditioning time'.
2. The flash consists of a fine martensitic microstructure, which is similar to the microstructure observed in CWZ. This observation indicates that the flash underwent similar thermal mechanical processing during LFW as the CWZ, and that the temperature of the material exceeded β transus before being extruded into the flash.
3. The flow stress testing results show that the flow stress is dependent on the heating rate. A higher heating rate yields higher flow stress for both Ti-64 and Ti-575. The results also indicate that at a high heating rate, the flow stress of Ti-64 is higher than Ti-575 at temperatures lower than 950℃. However, at temperatures above 1000℃, Ti-575 has higher flow stress. This increase in flow stress of Ti-575 at a high heating rate and high temperature is considered to control the conditioning time.
4. The measurement of dynamic β transus shows that a high heating rate also increases the β transus of both alloys, and that the amount of increase in β transus of Ti-575 is greater than that of Ti-64. Furthermore, the heating rate investigated in the current study is much lower than the actual heating rate in LFW. Therefore, it can be deduced

that during LFW the dynamic β transus of Ti-575 is much higher than that of Ti-64, leading to higher flow stress.

5. The conditioning time can be reduced by increasing friction pressure. From the flash measurement, it is predicted that the conditioning time can be eliminated by applying 184 MPa. Coincidently, the flow stress results predict that by applying 173 MPa, Ti-64 and Ti-575 will have the same flow stress, effectively leading to zero conditioning time. The prediction made from flash measurement has good agreement with the prediction made from the flow stress results.

Chapter 8

Summary and Future Work

8.1 Summary

The current study concentrates on microstructural characterisation, crystallographic texture analysis, fatigue and fracture evaluation, and processing assessment of linear friction welded (LFW'd) Ti-64:Ti-575 joints. This section provides a concise summary of the main findings from this study. For more detailed conclusions on each topic, please refer to the respective sections in Chapter 4 to Chapter 7.

Several key conclusions emerge from the research are listed below:

1. Ti-575 parent material has a bi-modal microstructure with fine secondary and tertiary α laths in the transformed β phase. The fine α laths act as a strengthening phase, contributing to the superior hardness of Ti-575 compared to Ti-64. However, in heat-affected zone (HAZ), such fine α laths dissolved into β phase due to the heat experienced during LFW, leading to a reduction in local hardness. Post-weld heat

treatment (PWHT) at 600℃ for 1 hour can recover the hardness in HAZ due to the formation of fine α precipitates inside the β phase.

2. Fast cooling rate after LFW results in martensitic phase transformation in the central weld zone (CWZ) on both Ti-575 and Ti-64 sides, resulting in the formation of fine acicular α' laths. This transformation significantly increased the hardness of the weld, surpassing the hardness of both parent materials. PWHT causes the decomposition of α' laths. On the Ti-64 side, little amount of fine β precipitates formed at the boundaries of α laths. In contrast, a significant volume fraction of β precipitates formed on the Ti-575 side, as if α precipitates formed in β matrix.
3. The as-welded CWZ exhibits an oscillation-dependent transverse α texture. Texture development analysis indicates that the CWZ texture is derived from the $\{11\bar{2}\}\langle 111\rangle_\beta$ texture. The stress condition in CWZ during LFW is similar to the ideal simple shear condition, which allows the recrystallised β grains to deform via $\{11\bar{2}\}\langle 111\rangle_\beta$ slip systems. The notably strong transverse texture component can be attributed to variant selection induced by thermal contraction during cooling after LFW.
4. In thermo-mechanically affected zone (TMAZ) on the Ti-575 side, specifically at the bifurcation point, a geometry-dependent basal α texture was discovered. Texture development analysis indicates that this texture is derived from the $\{110\}\langle 001\rangle_\beta$ texture. The dependency of the texture on the weld geometry in Ti-575 TMAZ at bifurcation point can be attributed to the material extrusion, as at the bifurcation point, the material is restricted to flow along Z direction toward the weld interface. The scope of the geometry-dependent texture in Ti-575 TMAZ at bifurcation point was found to be a 300×300 μm^2 area. Ti-64 TMAZ at bifurcation point does not exhibit the same texture due to higher amount of retained primary α grains, which prohibit the local deformation of β phase via $\{110\}\langle 001\rangle_\beta$ slip system.

5. The PWHT temperature has significant ageing effect on the weld. The hardness at the weld interface increased from 380 HV in as-welded condition to 430 HV after PWHT at temperatures below 600℃. Over-ageing occurs when the weld is PWHT'd at higher temperatures.
6. The residual stress after PWHT at 500℃ yields a strong compressive stress near the surface of the SENB test pieces. The compressive residual stress is beneficial to fatigue crack growth as it increases the fatigue crack growth threshold values to approximately 8.3 MPa$\sqrt{\text{m}}$ by creating a bowed crack front. In comparison, test pieces PWHT'd at 600℃ have much weaker compressive residual stress, and their fatigue crack growth threshold values are only approximately 4.5 MPa$\sqrt{\text{m}}$.
7. Compared to the parent materials, the weld exhibits superior tensile strength and high cycle fatigue strength, reduced fracture toughness, and similar fatigue crack growth resistance. Process variables, upset and friction pressure, as well as crack orientation do not have significant effects on the fatigue crack growth resistance, fatigue crack growth threshold, and fracture toughness of the Ti-575 CWZ.
8. The high relative upset in LFW of dissimilar titanium alloys is found to originate from the conditioning time, the delay in extrusion of one of the alloys. The conditioning time is associated with the discrepancy in flow stress and dynamic β transus.
9. Increasing friction pressure is an effective way to reduce the conditioning time. It is predicted that the conditioning time can be completely eliminated by applying approximately 180 MPa of pressure, evident by both flow stress results and flash measurement.

8.2 Future Work

1. In the microstructural characterisation study, uncertainty in the phase identification of Ti-575 TMAZ remains due to the limited resolution of chemical and

crystallographic analyses using scanning electron microscopes. To fully understand the microstructural evolution in Ti-575 TMAZ during LFW, further investigation using transmission electron microscopes is needed.

2. In the crystallographic texture development study, a unique geometry-dependent texture was discovered in Ti-575 TMAZ, exclusively at the bifurcation point. However, the effect of such texture on fatigue and fracture resistance and other mechanical properties remains unclear. Fatigue crack growth testing with cracks located precisely at this region of interest is required.
3. In the study of fatigue and fracture, all mechanical testing was performed at room temperature for fan blisk applications. It is known that the service temperature of titanium alloys ranges from 300 to 600℃, which allows blisk applications in the low and intermediate pressure compressor. To certify the validity of such applications and expand the applicability of Ti-64:Ti-575 welds, an assessment of fatigue and fracture resistance at elevated temperatures is needed.
4. In the processing study, the nature of relative upset in LFW'd dissimilar joints was investigated. It was proposed that the relative upset is associated with conditioning time, flow stress, and dynamic β transus. Although the proposed theory is able to explain accurately the relative upset in Ti-64:Ti-575 welds, its applicability to other titanium alloys remains unclear. A systematic study on relative upset over a wide range of titanium alloys is required to further confirm the validity of the proposed theory.

Tables

Chapter 2

Table 2.1 Slip systems in α-Ti [204, 205].

Burgers vector type	Slip direction	Slip plane	No. of slip systems	
			Total	Independent
$\vec{a}$	$\langle 11\bar{2}0 \rangle$	$\{0002\}$	3	2
$\vec{a}$	$\langle 11\bar{2}0 \rangle$	$\{10\bar{1}0\}$	3	2
$\vec{a}$	$\langle 11\bar{2}0 \rangle$	$\{10\bar{1}1\}$	6	4
$\vec{c}+\vec{a}$	$\langle 11\bar{2}3 \rangle$	$\{11\bar{2}2\}$	6	5

Table 2.2 Influence of microstructure on selected properties of titanium alloys [22].

Fine	Coarse	Property	Lamellar	Equiaxed
○	○	Elastic modulus	○	+/− (texture)
+	−	Strength	−	+
+	−	Ductility	−	+
−	+	Fracture toughness	+	−
+	−	Fatigue crack initiation	−	+
−	+	Fatigue crack propagation	+	−
−	+	Creep strength	+	−
+	−	Superplasticity	−	+
+	−	Oxidation behaviour	+	−

Table 2.3 Recommended PHWT (follow with air cooling) for several titanium alloys [206].

Alloy	Temperature (℃)	Time (hour)
CP-Ti	480 - 595	1/4 - 4
Ti-6Al-4V	480 - 650	1 - 4
Ti-6Al-6V-2Sn (Cu+Fe)	480 - 650	1 - 4
Ti-3Al-2.5V	540 - 650	1/4 - 2
Ti-6Al-2Sn-4Zr-6Mo	595 - 705	1/4 - 4
Ti-5Al-2Sn-2Zr-4Mo-4Cr	480 - 650	1 - 4

Chapter 3

Table 3.1 Chemical composition of the Ti-64 and Ti-575 alloys.

(wt.%)	Ti	Al	V	Si	Fe	C	N	O	H
Ti-64 [207]	Base	5.5-6.75	3.5-4.5	-	<0.40	<0.08	<0.05	<0.20	<0.015
Ti-575 [13]	Base	5.3	7.7	0.5	<0.25	<0.01	<0.01	<0.018	-

Table 3.2 Selected material properties of the titanium alloys, where T_β is β transus, T_m is melting point, E is Young's modulus, $\sigma_{0.2\%}$ is proof stress, UTS is ultimate tensile stress, and μ is Poisson's ratio. *The melting point of Ti-575 was calculated using Thermo-Calc software.

	Density (g/cm^3)	T_β (℃)	T_m (℃)	E (GPa)	$\sigma_{0.2\%}$ (MPa)	UTS (MPa)	μ
Ti-64 [207]	4.42	996	1655	115.0	913	1002	0.32
Ti-575 [13]	4.47	965	1696*	110.6	1050	1176	0.30

Table 3.3 Pre-weld heat treatments of the titanium alloys.

Alloy	Solution Heat Treatment	Annealing / Ageing
Ti-64	1hr@965℃+AC	2hr@700℃+AC
Ti-575	1hr@910℃+AC	8hr@500℃+AC

Table 3.4 Processing parameters for each weld.

Weld ID	T_{max} (mm)	Pressure (MPa)	Upset (mm)	Frequency (Hz)	Amplitude (mm)
473-01	32	110	3.6	45	2
473-02	32	110	4.2	45	2
473-03	32	110	4.2	45	2
473-04	32	130	4.2	45	2
473-05	18	110	4.2	45	2
473-06	18	110	4.2	45	2
473-07	18	130	4.2	45	2
473-08	18	90	4.2	45	2

Table 3.5 Grinding and polishing procedure used in the current study.

Disc	Suspension	Load (N)	RPM	Duration (min)
MD-Piano	Water	40	300	Until Plain
SiC P1200	Water	40	150	5
SiC P2500	Water	40	150	5
MD-Chem	OPS	15	100	45

Table 3.6 Lattice parameters used in indexing EBSPs and diffraction patterns. (Unit: Å)

Phase	Crystal Structure	Space group	a	b	c
α/α'-Ti	HCP	$P6_3/mmc$	2.95	2.95	4.68
β-Ti	BCC	Im3m	3.31	3.31	3.31
α''-Ti	Orthorhombic	Cmcm	3.01	4.97	4.68
Ti_5Si_3	HCP	$P6_3/mcm$	7.47	7.47	5.12

Chapter 4

Table 4.1 Chemical composition of α and β phase in Ti-575 measured by EDS. (unit: wt.%)

Phase	Ti	Al	V	Si	Fe
α	88.5	6.6	4.3	0.7	
β	77.5	3.7	17.7	0.5	0.6

Table 4.2 Chemical composition of α and β phase in Ti-64 measured by EDS. (unit: wt.%)

Phase	Ti	Al	V	Si	Fe
α	89.1	7.6	3.3		
β	82.1	4.1	12.9		0.9

Table 4.3 Chemical composition of as-welded CWZ in Ti-575 measured by EDS. (unit: wt.%)

Ti	Al	V	Si	Fe
86.0	5.2	7.7	0.8	0.3

Table 4.4 Chemical composition of as-welded CWZ in Ti-64 measured by EDS. (unit: wt.%)

Ti	Al	V	Si
88.7	5.9	3.7	0.0

Table 4.5 Chemical composition of α and β phase in Ti-575 CWZ in PWHT'd condition, measured from the labelled location in Figure 4.32.

(wt.%)	Ti	Al	V	Si	Fe
α phase	88.2	5.8	5.3	0.7	0.1
β phase	65.9	2.0	30.1	1.5	1.6

Table 4.6 Chemical composition of Ti-64 CWZ in PWHT'd condition, measured from the labelled location in Figure 4.37.

Location	Ti	Al	V	Fe
A	77.6	6.0	14.0	2.5
B	78.2	5.9	13.5	2.4
C	78.6	6.4	12.7	2.2
D	83.8	7.5	7.7	1.0
E	79.8	7.1	11.0	2.1
F	81.6	6.7	10.1	1.7
G	88.3	8.6	3.0	0.1

Chapter 6

Table 6.1 Tensile testing results. *A change in strain rate was employed during the test of HT003, resulting in a notably higher UTS.

Sample ID	T_{max} (mm)	Pressure (MPa)	Upset (mm)	PWHT	E (GPa)	$\sigma_{0.2\%}$ (MPa)	UTS (MPa)	ε^{pl}	Failure location
HT001	32	110	3.6	1hr@600°C	90	893	957	11.0%	Ti-64 Parent
HT002	32	110	3.6	1hr@600°C	99	903	963	14.3%	Ti-64 Parent
HT003	18	130	4.2	1hr@600°C	91	897	980*	12.3%	Ti-64 Parent
HT004	18	130	4.2	1hr@600°C	92	896	959	12.6%	Ti-64 Parent

Table 6.2 Diameter of tensile specimens before/after testing.

Sample ID	Before Testing	After Testing	
	Gauge Diameter (mm)	Interface Diameter (mm)	Ti-575 Diameter (mm)
HT001	4.98	4.989	4.964
HT002	5.00	5.001	4.986
HT003	5.00	4.998	4.986
HT004	5.00	4.999	4.985

Table 6.3 High cycle fatigue testing results.

Sample ID	T_{max} (mm)	Pressure (MPa)	Upset (mm)	PWHT	R	σ_{max} (MPa)	Cycles	Failure Location
HF001	32	110	4.2	1hr@600°C	0.3	450	1.80×10^7	Ti-64 Parent
HF002	32	110	3.6	1hr@600°C	0.3	600	1.18×10^6	Ti-64 Parent
HF003	32	110	3.6	1hr@600°C	0.3	500	4.62×10^6	Ti-64 Parent
HF004	32	110	3.6	1hr@600°C	0.3	550	2.05×10^6	Ti-64 Parent
HF005	32	110	4.2	1hr@600°C	0.3	600	7.67×10^5	Ti-64 Parent
HF006	32	110	4.2	1hr@600°C	0.3	600	8.11×10^5	Ti-64 Parent
HF007	32	110	4.2	1hr@500°C	0.3	600	9.21×10^5	Ti-64 Parent
HF008	32	110	4.2	1hr@500°C	0.3	600	6.33×10^5	Ti-64 Parent
HF009	32	110	4.2	1hr@500°C	0.1	600	8.19×10^5	Ti-64 Parent
HF010	32	110	4.2	1hr@500°C	0.7	600	5.26×10^7	Run out
HF010	32	110	4.2	1hr@500°C	0.7	800	1.83×10^6	Ti-64 Parent
HF011	32	110	4.2	1hr@500°C	0.3	525	4.19×10^6	Ti-64 Parent
HF012	32	110	4.2	1hr@500°C	0.3	575	2.36×10^6	Ti-64 Parent
HF013	18	130	4.2	1hr@600°C	0.3	600	8.51×10^5	Ti-64 Parent
HF014	18	130	4.2	1hr@600°C	0.3	800	1.53×10^5	Ti-64 Parent
HF015	18	130	4.2	1hr@600°C	0.3	750	3.21×10^5	Ti-64 Parent
HF016	18	130	4.2	1hr@500°C	0.3	800	1.00×10^5	Ti-64 Parent
HF017	18	130	4.2	1hr@500°C	0.3	700	4.26×10^5	Ti-64 Parent
HF018	18	130	4.2	1hr@500°C	0.3	775	2.76×10^5	Ti-64 Parent

Table 6.4 Fatigue crack growth threshold testing results. All specimens have $T_{max} = 32$ mm. All tests were performed with stress ratio $R = 0.1$ at room temperature. Crack orientation denoted by // and ⊥ represent crack propagated parallel and perpendicular to the oscillation direction, respectively. Crack location denotes the region where the crack reached its fatigue threshold.

Sample ID	Pressure (MPa)	Upset (mm)	W (mm)	B (mm)	PWHT	Crack Orientation	Crack Location	a/W	ΔK_{th} (MPa$\sqrt{\text{m}}$)	K_Q (MPa$\sqrt{\text{m}}$)	K-Validity
CP002	110	4.2	10.07	9.08	1hr@600°C	//	Ti-575 CWZ	0.42	4.8	29.8	Invalid
CP003	110	4.2	9.10	10.10	1hr@500°C	//	Ti-575 CWZ	0.59	7.6	25.0	Invalid
CP004	110	4.2	10.09	9.08	1hr@600°C	//	Ti-575 CWZ	0.57	4.5	29.9	Invalid
CP006	110	4.2	9.09	10.08	1hr@600°C	⊥	Ti-575 CWZ	0.51	4.3		Invalid
CP007	110	4.2	10.10	9.08	1hr@500°C	⊥	Ti-575 CWZ	0.55	8.3	26.3	Invalid
CP008	110	4.2	9.07	10.08	1hr@600°C	⊥	Interface	0.45	4.4	26.3	Invalid
CP010	110	3.6	10.10	9.09	1hr@600°C	//	Interface	0.45	4.6	28.6	Invalid
CP012	110	3.6	10.06	9.07	1hr@600°C	//	Ti-575 Parent	0.50	5.0	44.8	Invalid
CP014	110	4.2	10.06	9.07	1hr@600°C	//	Ti-64 Parent	0.56	5.5	66.8	Invalid
CP017	130	4.2	10.06	9.06	1hr@600°C	//	Ti-575 CWZ	0.43	4.2	24.5	Invalid
CP001L	110	4.2	9.10	4.97	1hr@500C	//	Ti-575 CWZ	0.57	5.6	25.8	Valid
CP001R	110	4.2	9.10	4.91	1hr@500C	//	Ti-575 CWZ	0.65	5.7	30.7	Invalid
CP005L	110	4.2	10.08	4.45	1hr@500C	⊥	Ti-575 CWZ	0.50	8.1	33.7	Invalid
CP005R	110	4.2	10.08	4.43	1hr@500C	⊥	Interface	0.55	8.6	33.8	Invalid
CP009L	110	3.6	9.10	4.98	1hr@500C	//	Ti-575 TMAZ	0.47	7.1	30.5	Invalid
CP009R	110	3.6	9.10	4.91	1hr@500C	//	Ti-575 CWZ	0.57	5.7	30.3	Invalid
CP011L	110	3.6	10.06	4.46	1hr@600C	//	Ti-575 CWZ	0.52	4.6	22.2	Invalid

Table 6.5 Fatigue crack propagation testing results. All specimens have $T_{max} = 32$ mm. All tests were performed with stress ratio $R = 0.1$ at room temperature. All cracks propagated parallel to the oscillation direction. Crack location denotes the region where the crack propagated during the test. The ΔK range indicates the measured crack growth rate within the linear Paris regime. The data within ΔK range was used to calculate the Paris law constants A and m.

Sample ID	Pressure (MPa)	Upset (mm)	W (mm)	B (mm)	PWHT	Crack Location	A (mm/cycle)	m	ΔK range (MPa$\sqrt{\text{m}}$)	a/W	K_{max} (MPa$\sqrt{\text{m}}$)	K_Q (MPa$\sqrt{\text{m}}$)	K-Validity
CP011R	110	3.6	10.06	4.40	1hr@600°C	Ti-575 CWZ	2.24×10^{-7}	2.2	13.3−23.4	0.55	31.2		Valid
CP013L	110	4.2	10.08	4.42	1hr@600°C	Ti-575 CWZ	1.77×10^{-7}	2.3	13.0−23.2	0.49	31.2	30.5	Valid
CP013R	110	4.2	10.07	4.48	1hr@600°C	Ti-575 CWZ	3.28×10^{-7}	2.0	13.3−22.0	0.51	30.5	29.4	Valid
CP015L	130	4.2	10.06	4.44	1hr@600°C	Ti-575 CWZ	1.77×10^{-8}	3.0	8.6−20.1	0.70	31.0		Valid
CP015R	130	4.2	10.06	4.42	1hr@600°C	Ti-64 CWZ	3.44×10^{-8}	2.6	6.1−33.6	0.58		60.6	Invalid
CP016L	130	4.2	10.06	4.42	1hr@600°C	Ti-575 Parent	1.18×10^{-8}	3.0	12.7−32.9	0.70	50.3		Valid
CP016R	130	4.2	10.07	4.47	1hr@600°C	Ti-64 Parent	2.71×10^{-8}	2.6	20.4−50.4	0.66		73.4	Invalid
CP021L	130	4.2	10.06	4.41	1hr@500°C	Ti-575 CWZ	1.57×10^{-8}	3.0	13.2−27.1	0.46	34.9	33.6	Valid
CP021R	130	4.2	10.06	4.41	1hr@600°C	Ti-64 CWZ	1.39×10^{-7}	2.3	19.6−40.0	0.48	54.4	60.7	Invalid
CP022L	130	4.2	10.06	4.46	1hr@600°C	Ti-575 Parent	5.96×10^{-8}	2.6	25.7−31.1	0.31		49.3	Invalid
CP022R	130	4.2	10.06	4.43	1hr@600°C	Ti-64 Parent	3.40×10^{-7}	2.0	27.9−48.8	0.48	67.7	80.4	Invalid

Table 6.6 List of all fatigue crack growth path in the weld zones.

Sample ID	Crack Location	Side	Crack Path
CP001L	Ti-575 CWZ	Front	Straight crack in Ti-575
		Back	Crack in Ti-575 deviate away from the interface
CP001R	Ti-575 CWZ	Front	Crack in Ti-575 deviate away from the interface
		Back	Crack initiated in Ti-64, went across interface to Ti-575
CP002	Ti-575 CWZ	Front	Straight crack in Ti-575
		Back	Crack in Ti-575 deviate away from the interface
CP003	Ti-575 CWZ	Front	Crack in Ti-575 deviate away from the interface
		Back	Crack didn't break through the surface
CP004	Ti-575 CWZ	Front	Crack initiated in Ti-64, went across interface to Ti-575
		Back	Crack in Ti-575 deviate away from the interface
CP005L	Ti-575 CWZ	Front	Straight crack in Ti-575
		Back	Crack in Ti-575 deviate toward the interface
CP005R	Interface	Front	Straight crack in Ti-575
		Back	Crack in Ti-575 deviate toward the interface, then grow along the interface
CP006	Ti-575 CWZ	Front	Straight crack in Ti-575
		Back	Crack in Ti-575 deviate away from the interface
CP007	Ti-575 CWZ	Front	Crack didn't break through the surface
		Back	Straight crack in Ti-575
CP008	Interface	Front	Crack in Ti-64 deviate toward the interface
		Back	Crack in Ti-575 deviate away from the interface
CP009L	Ti-575 TMAZ	Front	Crack in Ti-575 deviate away from the interface
		Back	
CP009R	Ti-575 CWZ	Front	Crack in Ti-575 deviate away from the interface
		Back	Crack in Ti-575 deviate away from the interface
CP010	Interface	Front	Straight crack at the interface
		Back	Crack in Ti-575 deviate away from the interface
CP011L	Ti-575 CWZ	Front	Crack in Ti-575 deviate away from the interface
		Back	Crack in Ti-575 deviate away from the interface
CP011R	Ti-575 CWZ	Front	Crack in Ti-575 deviate away from the interface
		Back	Crack in Ti-575 deviate away from the interface
CP013L	Ti-575 CWZ	Front	Crack in Ti-575 deviate away from the interface
		Back	Crack in Ti-575 deviate away from the interface
CP013R	Ti-575 CWZ	Front	Crack in Ti-575 deviate away from the interface
		Back	Crack in Ti-575 deviate away from the interface
CP015L	Ti-575 CWZ	Front	Crack in Ti-575 deviate away from the interface
		Back	Crack in Ti-575 deviate away from the interface
CP015R	Ti-64 CWZ	Front	Crack in Ti-64 deviate toward the interface
		Back	Crack in Ti-64 deviate toward the interface
CP021L	Ti-575 CWZ	Front	Crack in Ti-575 deviate away from the interface
		Back	Crack in Ti-575 deviate away from the interface
CP021R	Ti-64 CWZ	Front	Crack in Ti-64 deviate toward the interface
		Back	Crack in Ti-64 deviate toward and away from the interface

Table 6.7 Summary of all fatigue crack growth path deviation in weld zones. The '=' symbol denotes that the destination is the same as the initiation.

Test	Initiation	Deviation	Destination	Count
Threshold	Ti575 CWZ	Away from interface	=	12
Threshold	Ti575 TMAZ	Away from interface	=	2
Threshold	Ti575 CWZ	Toward interface	=	2
Threshold	Ti64 CWZ	Toward interface	=	1
Threshold	Ti64 CWZ	Toward interface	Ti575 CWZ	2
Threshold		No deviation		7
Crack Prop	Ti575 CWZ	Away from interface	=	10
Crack Prop	Ti64 CWZ	Toward interface	=	3

Figures

Chapter 1

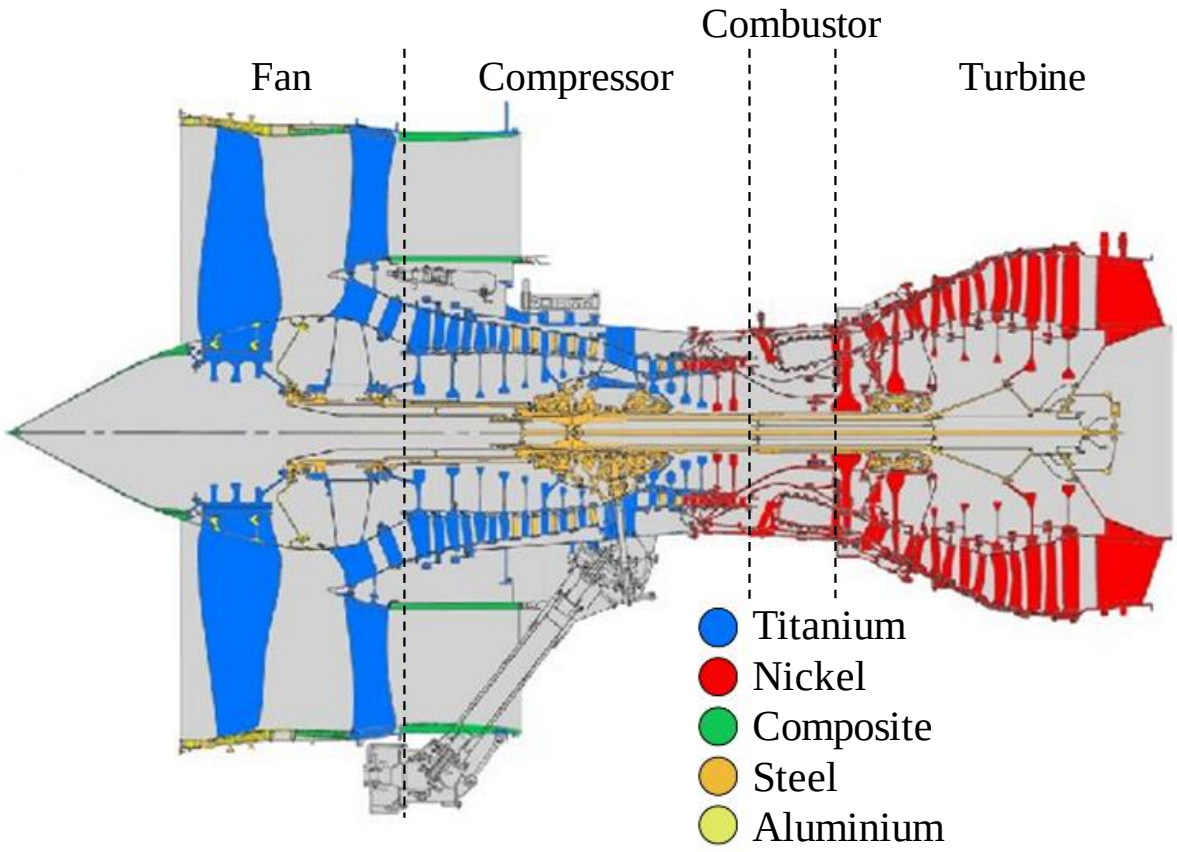

Figure 1.1 The materials usage in different parts of Trent engines (image courtesy: Rolls-Royce plc).

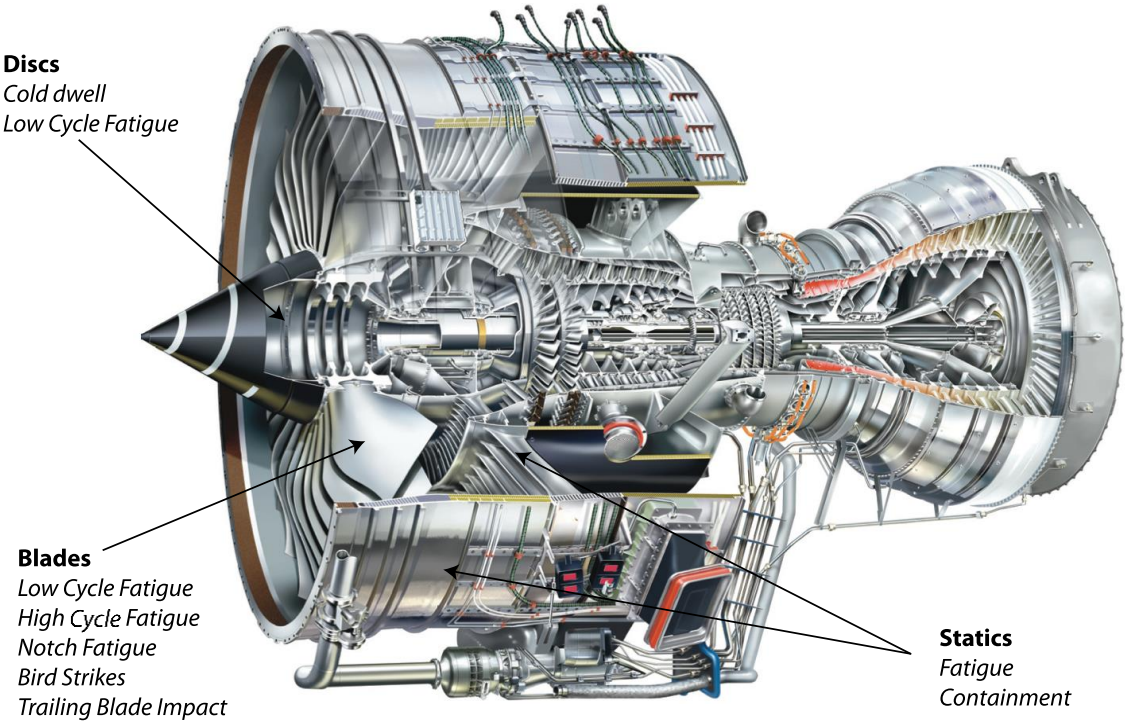

Figure 1.2 Render of a Rolls-Royce Trent engine. Figure highlights regions of titanium use and common load regimes [95].

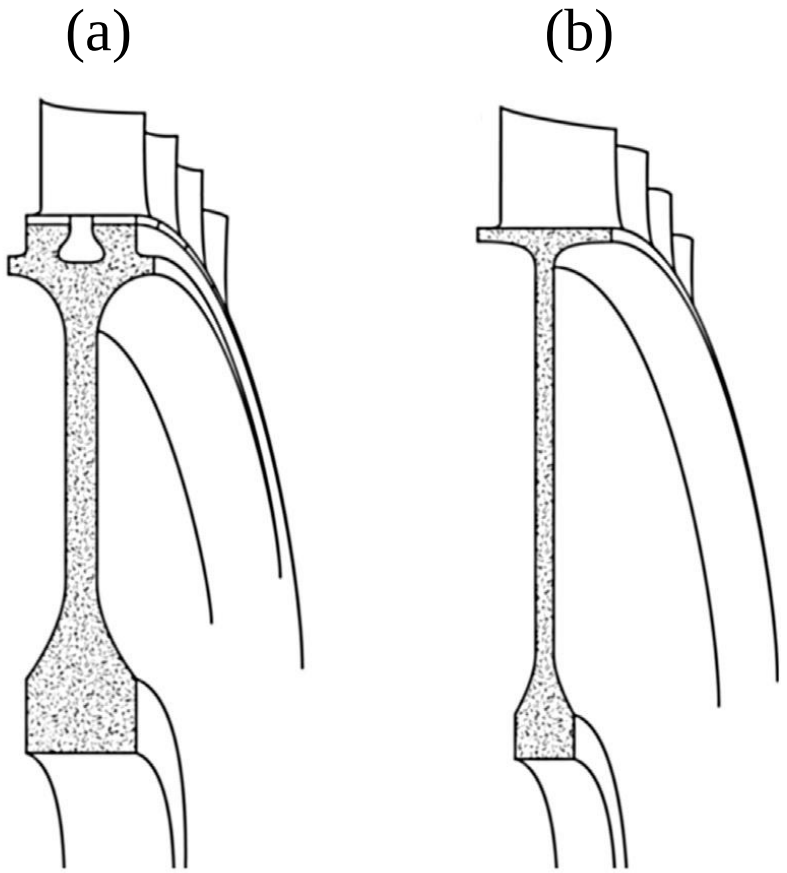

Figure 1.3 (a) Mechanically assembled blades and disc. (b) Integrally bladed disc (Blisk) [128].

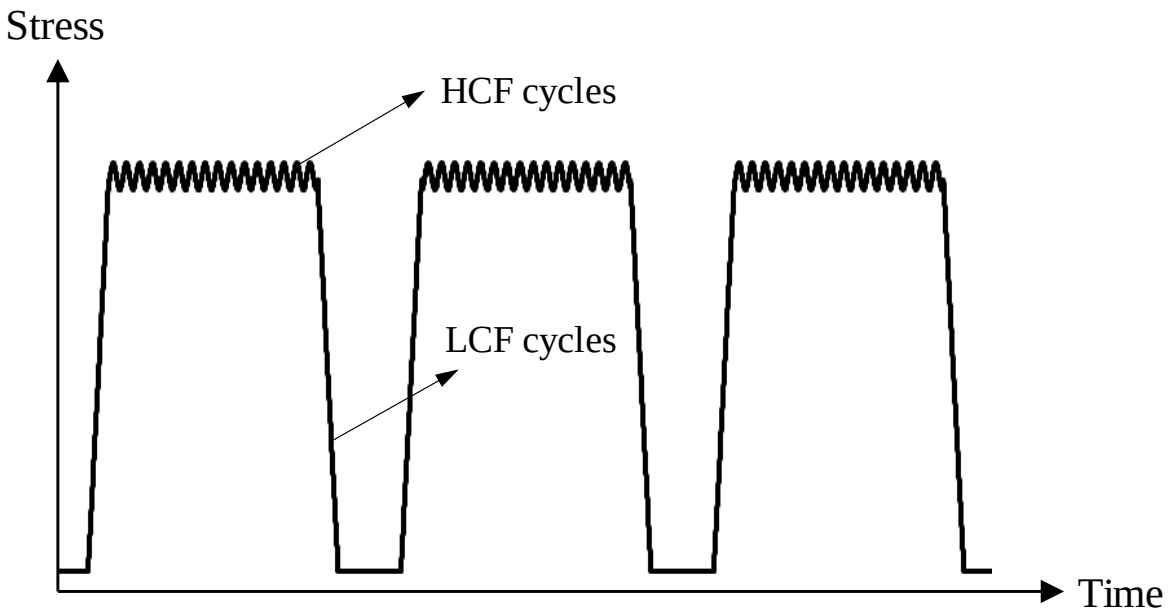

Figure 1.4 Typical loading condition for turbine blades. (Modified from [208])

Chapter 2

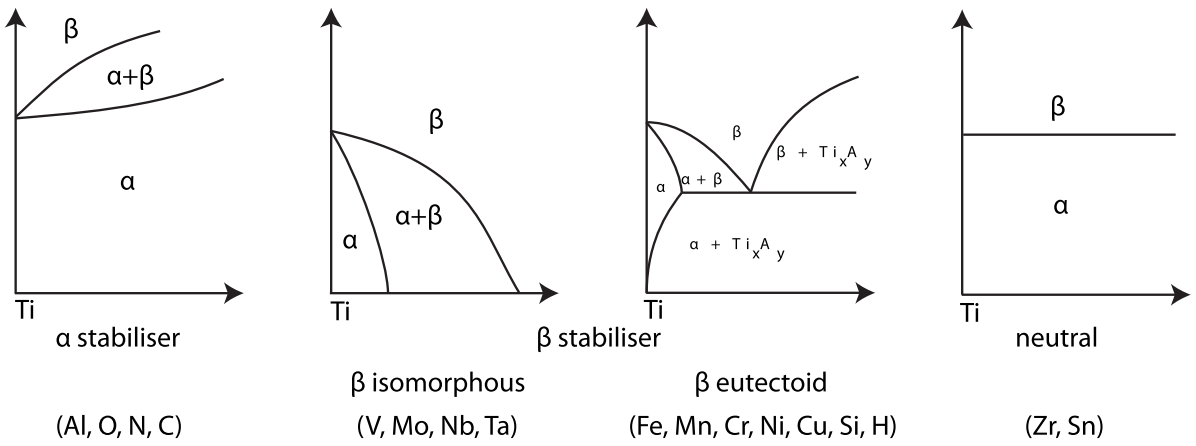

Figure 2.1 Schematic phase diagram of titanium alloys with various alloying elements [23].

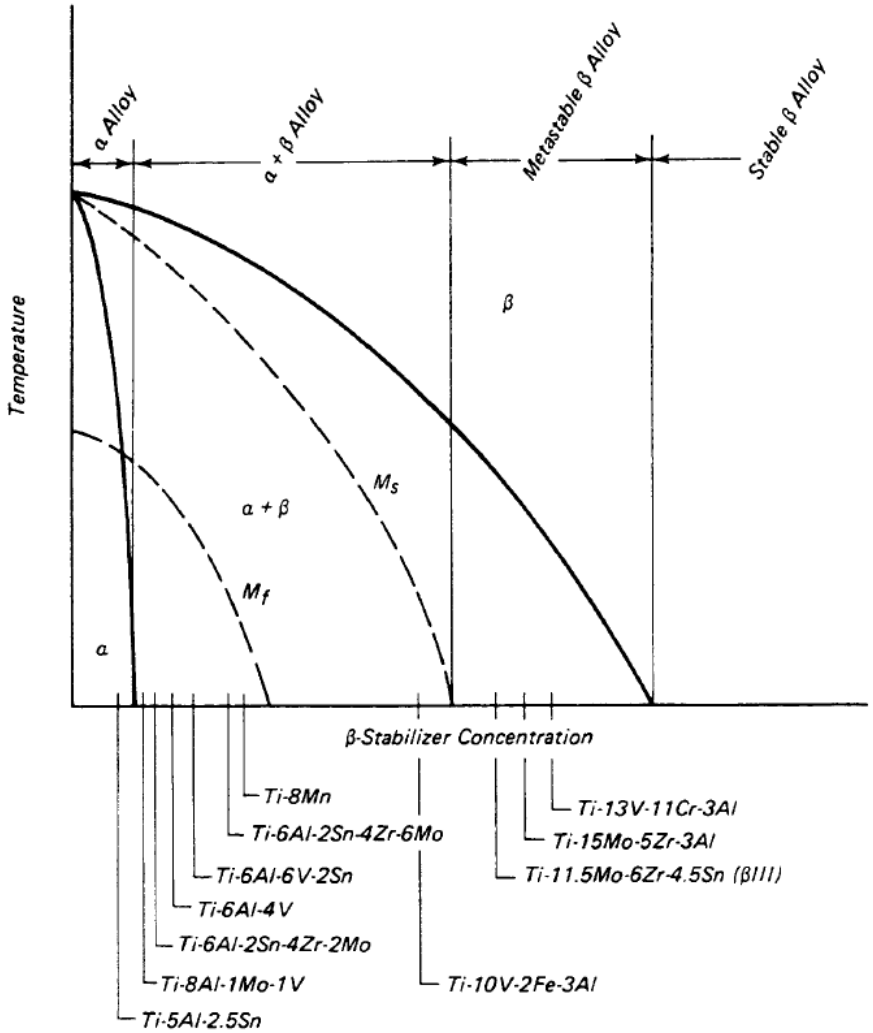

Figure 2.2 Pseudo-binary section through a β-isomorphous phase diagram [27].

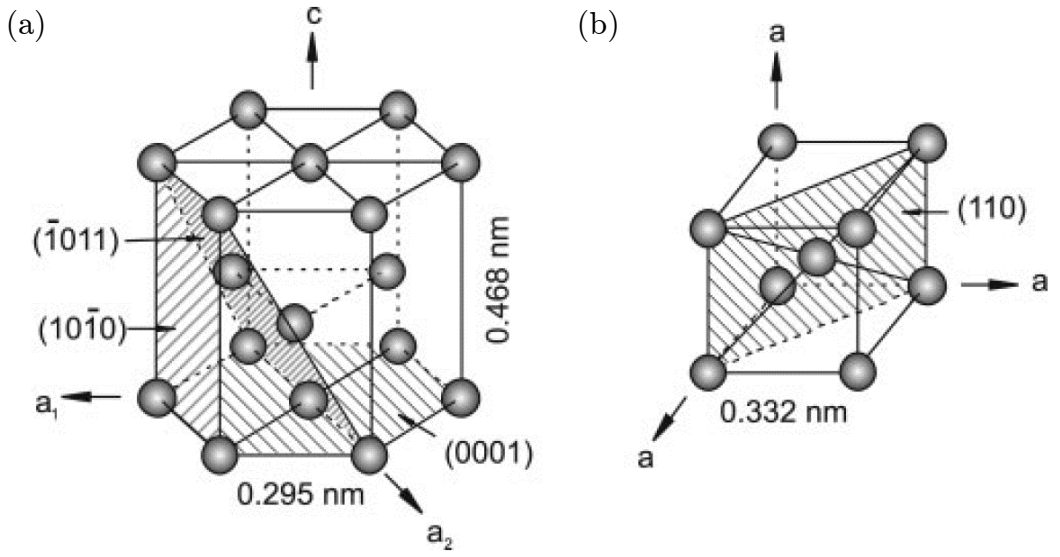

Figure 2.3 Schematic diagrams of (a) HCP and (b) BCC crystal structures in titanium [22].

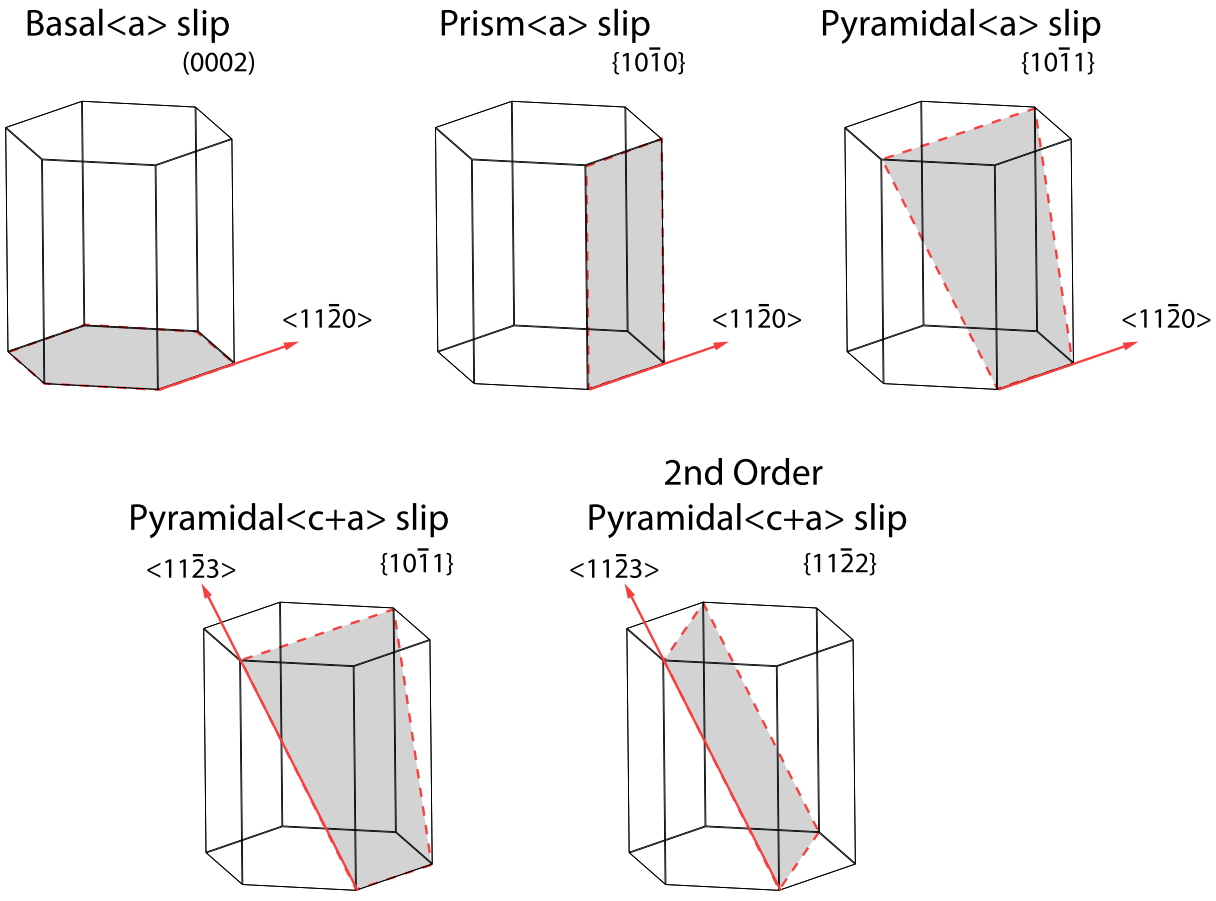

Figure 2.4 Slip planes and slip directions in hexagonal α phase [95].

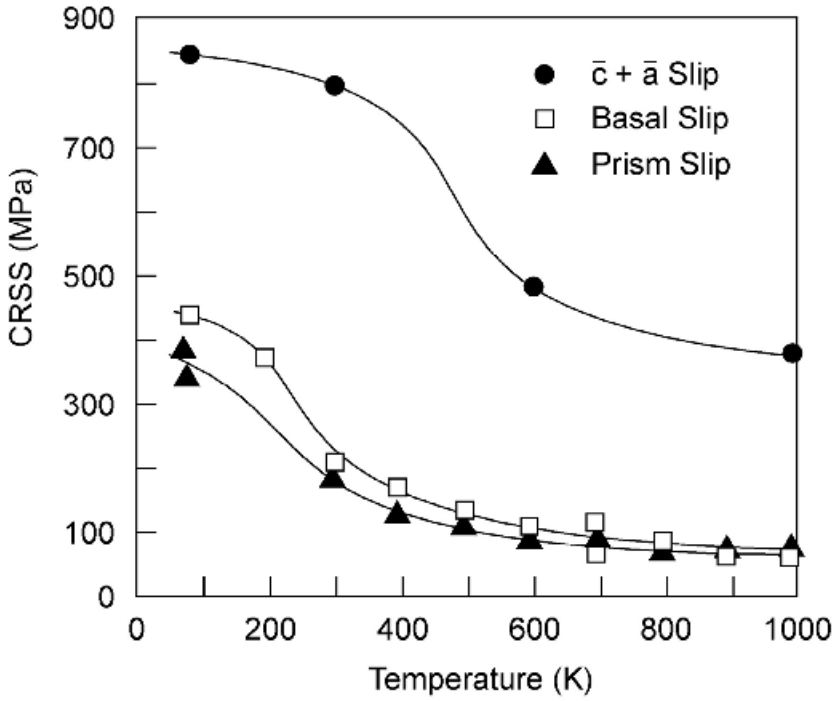

Figure 2.5 Temperature dependence of CRSS for slip with $\vec{a}$ and $\vec{c}+\vec{a}$ Burgers vectors in single crystals of Ti-6.6Al [209].

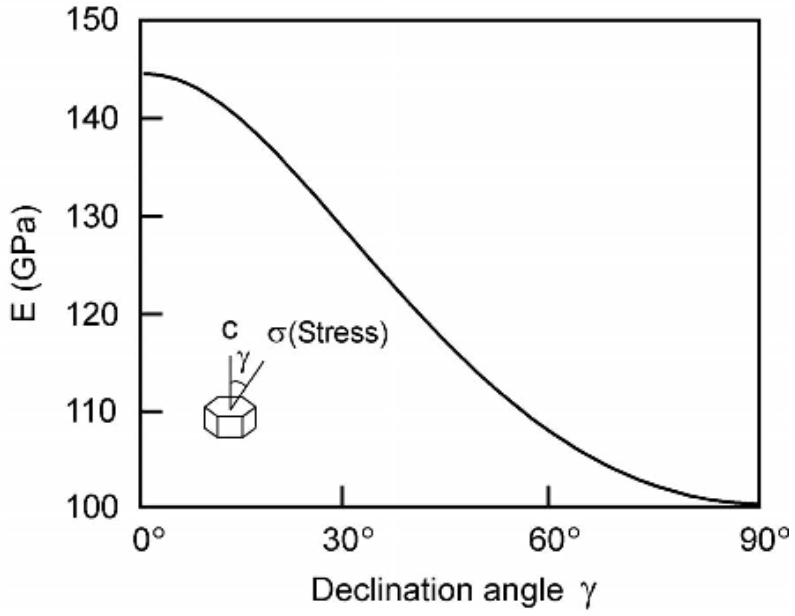

Figure 2.6 Modulus of elasticity E of α-Ti single crystals as a function of declination angle γ [210].

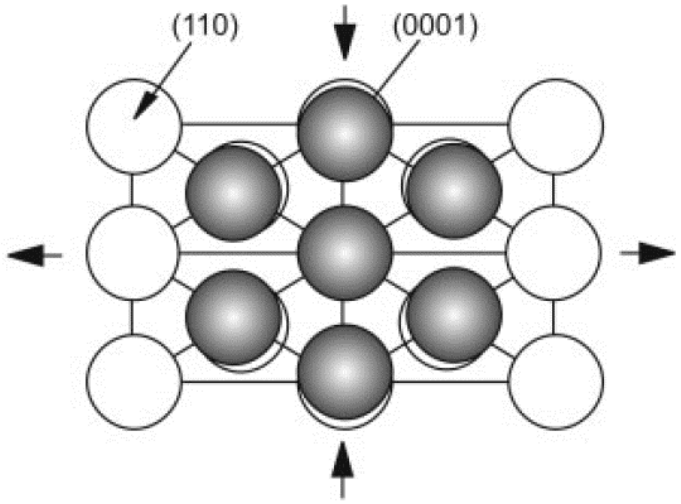

Figure 2.7 Schematic diagram of atomic distortion resulting from $\alpha \leftrightarrow \beta$ phase transformation [22].

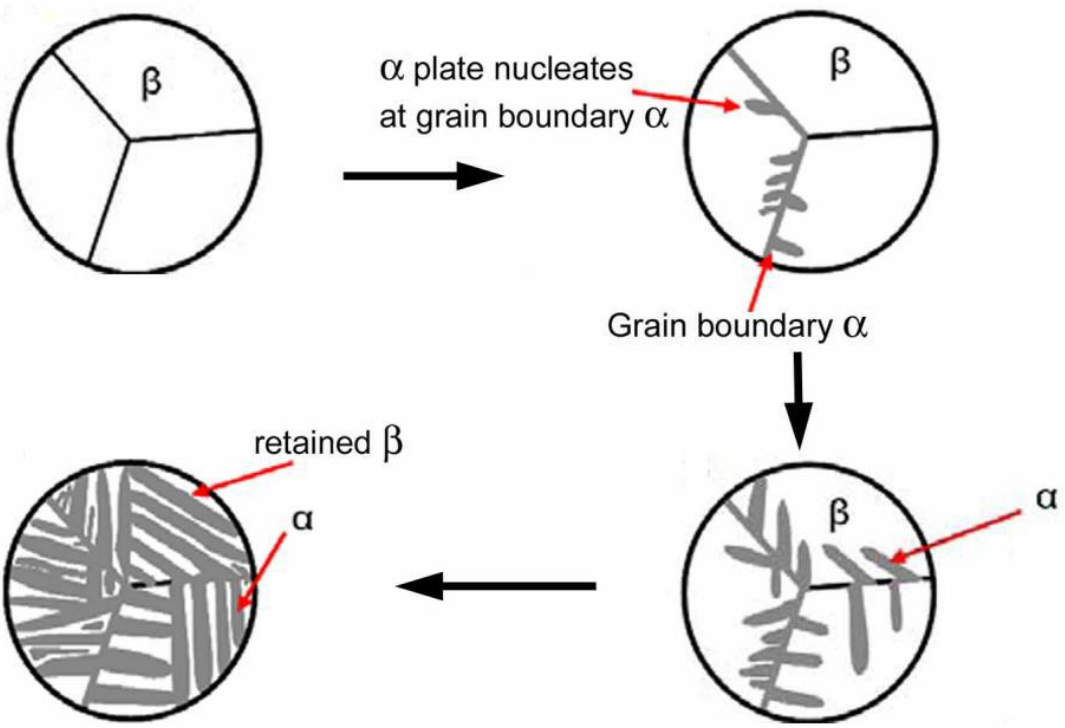

Figure 2.8 Schematic diagram of the diffusional phase transformation process during cooling from β phase [46].

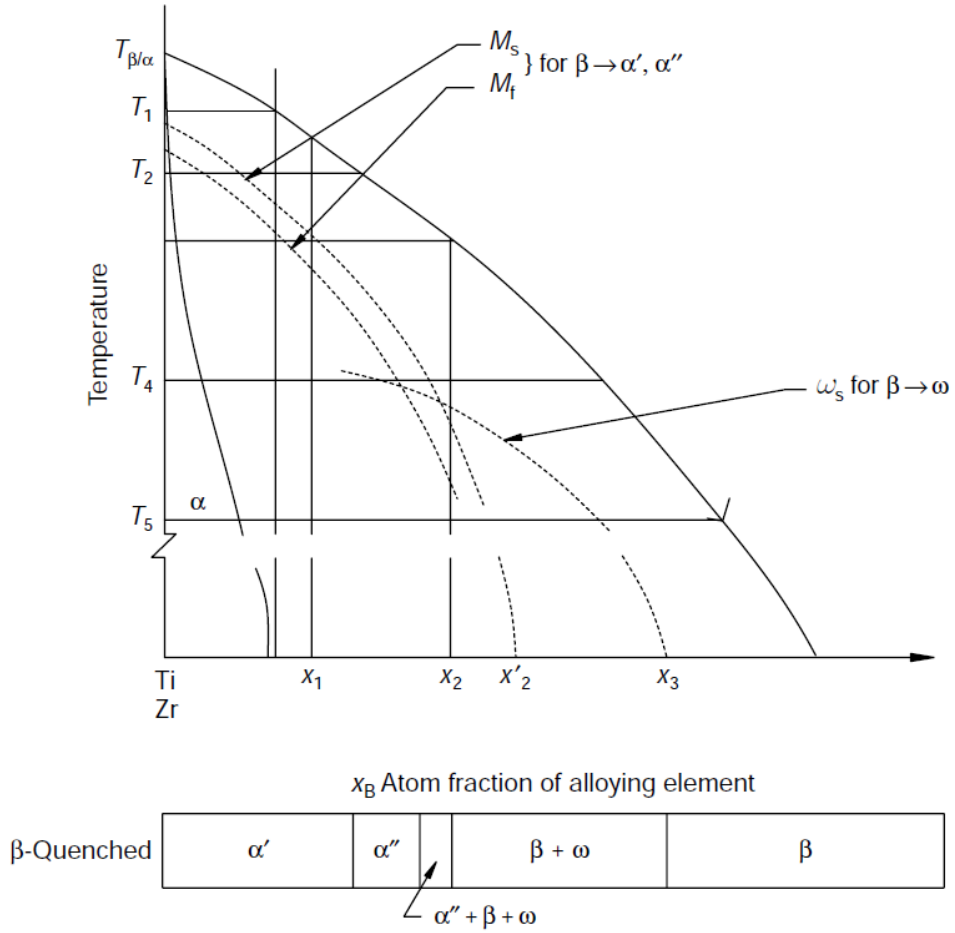

Figure 2.9 Schematic β isomorphous phase diagram showing the quenched products in titanium and zirconium alloys. X_B denotes the atomic fraction of the β stabiliser [24].

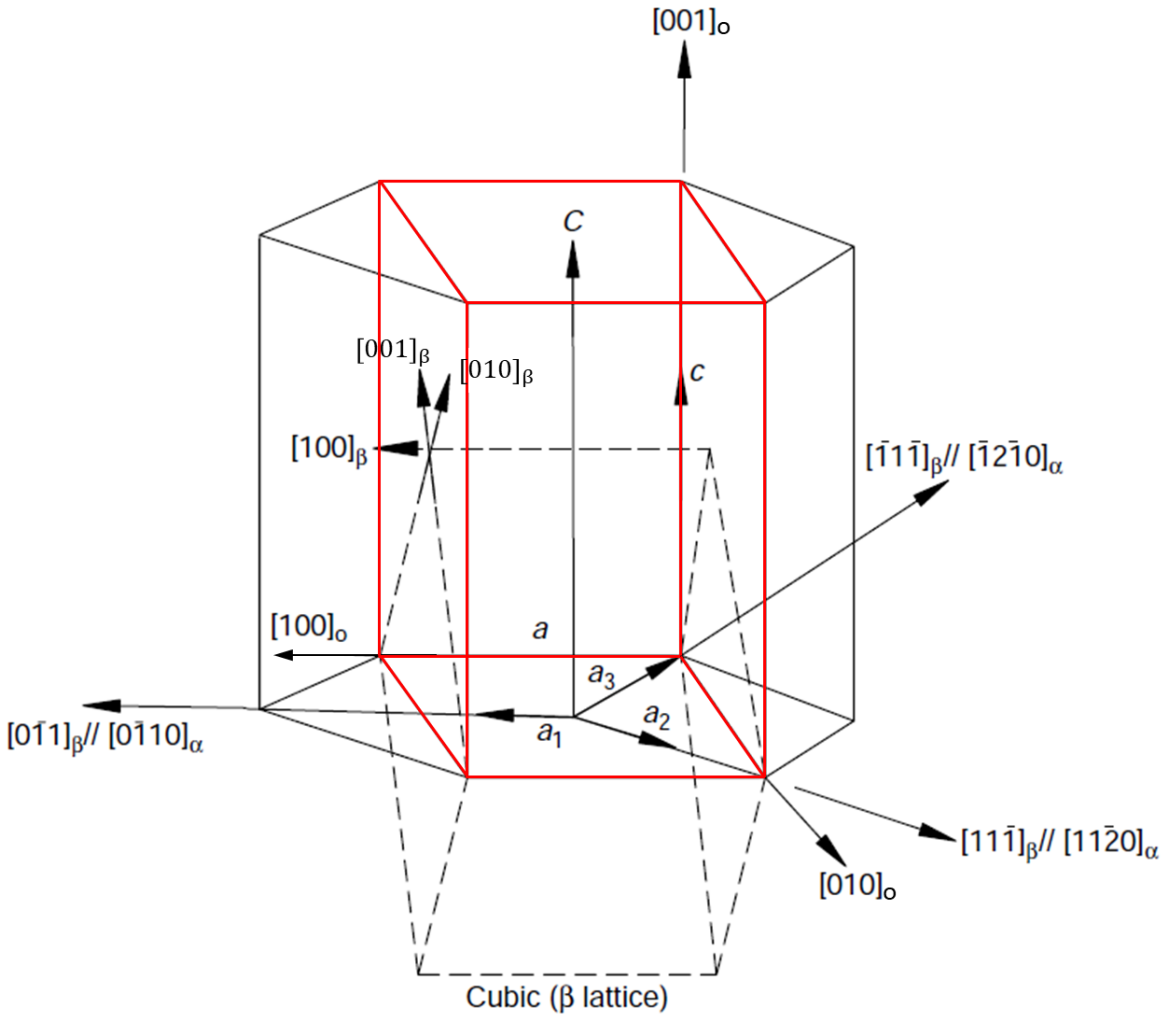

Figure 2.10 The lattice correspondence between BCC, HCP, and orthorhombic unit cells in titanium alloys. The BCC unit cell is indicated by the black dashed lines and denoted by 'β'; the HCP unit cell is indicated by the black solid lines and denoted by 'α'; the orthorhombic unit cell is indicated by the red solid lines and denoted by 'o'. (Modified from [10])

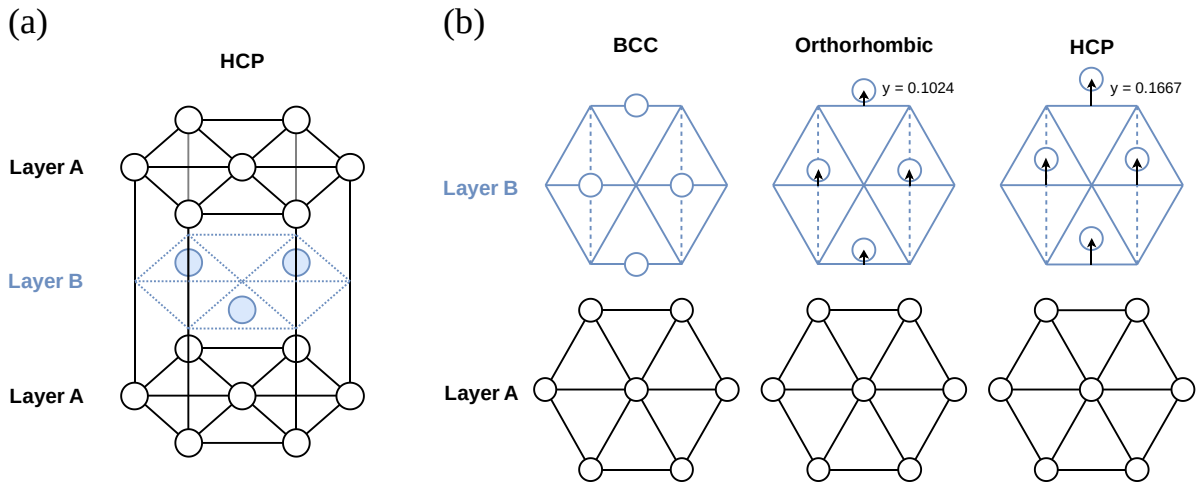

Figure 2.11 Schematic diagram of (a) HCP unit cell and atomic layers; (b) atomic shearing process during martensitic transformation from BCC to orthorhombic or HCP structures. The dotted lines indicate the outline of orthorhombic unit cell. 'y' denotes the normalised displacement of atoms.

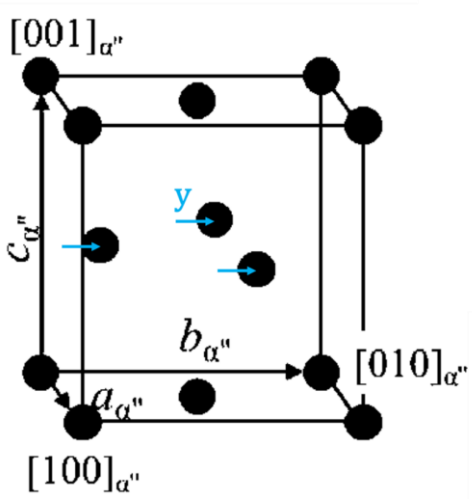

Figure 2.12 Orthorhombic unit cell of α'' phase in titanium. 'y' denotes the displacement of atoms from the face-centred positions. (Modified from [44])

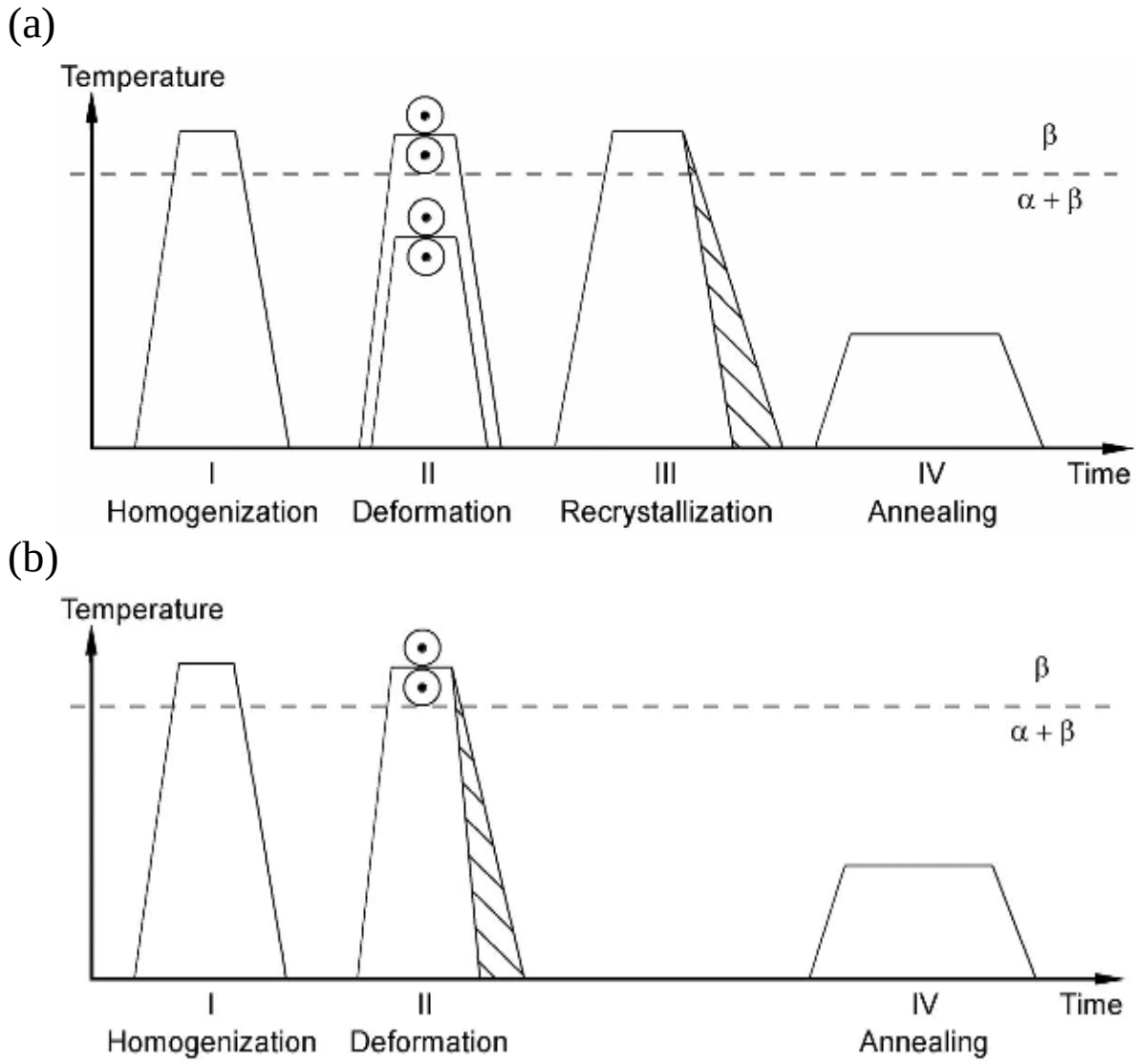

Figure 2.13 (a) β annealed and (b) β processed processing routes for fully lamellar microstructure [23].

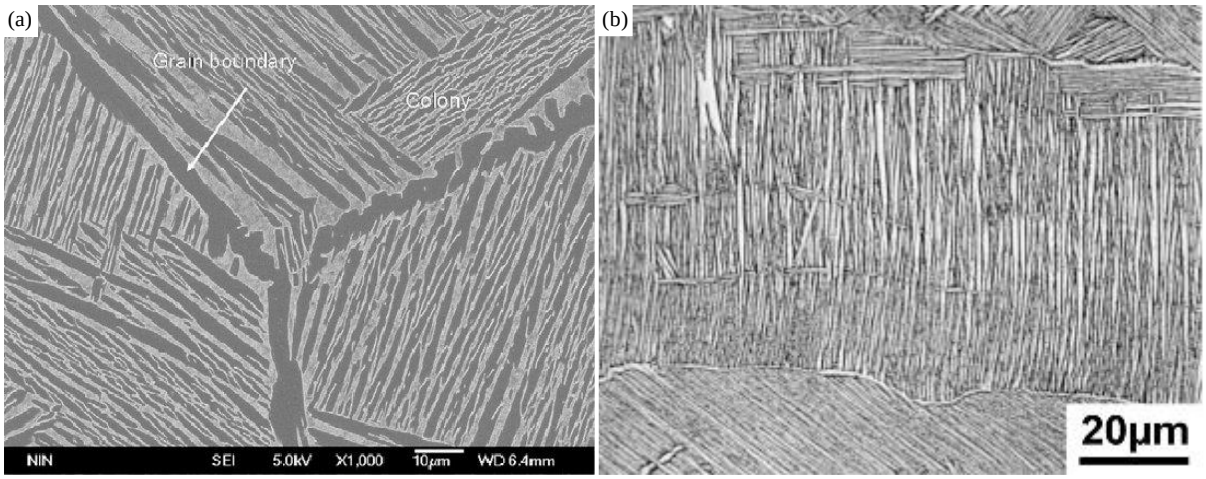

Figure 2.14 Fully lamellar microstructures of (a) TC-21 alloy in the β annealed condition [211] and (b) Ti-6246 in the β processed condition [23].

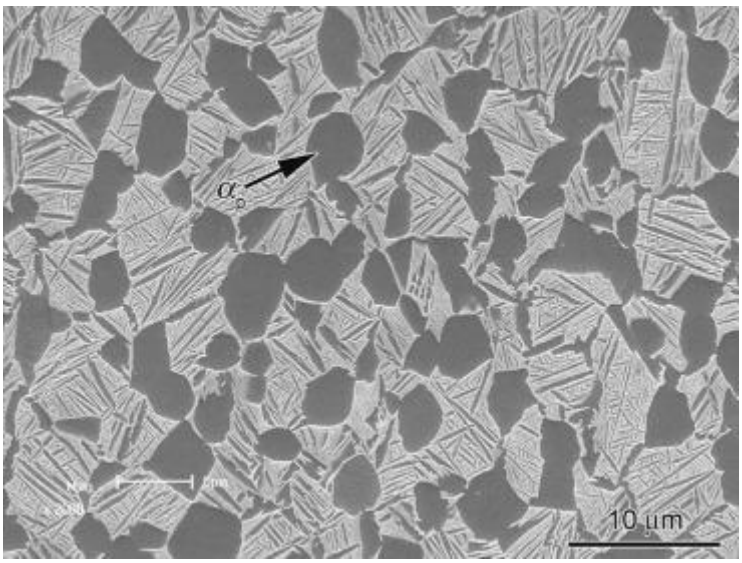

Figure 2.15 Typical bi-modal microstructure in $\alpha + \beta$ titanium alloys [212].

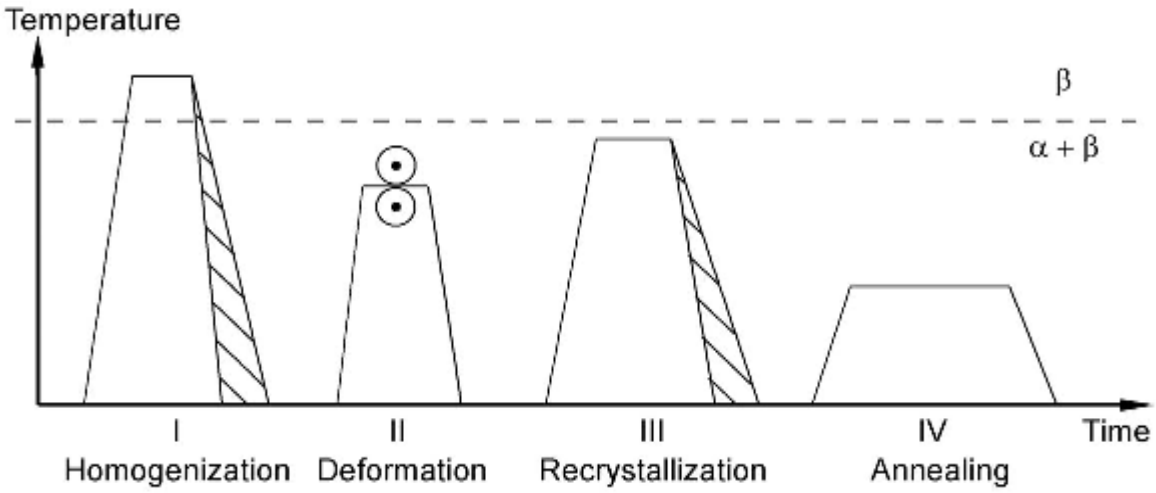

Figure 2.16 Processing route for bi-modal microstructure [23].

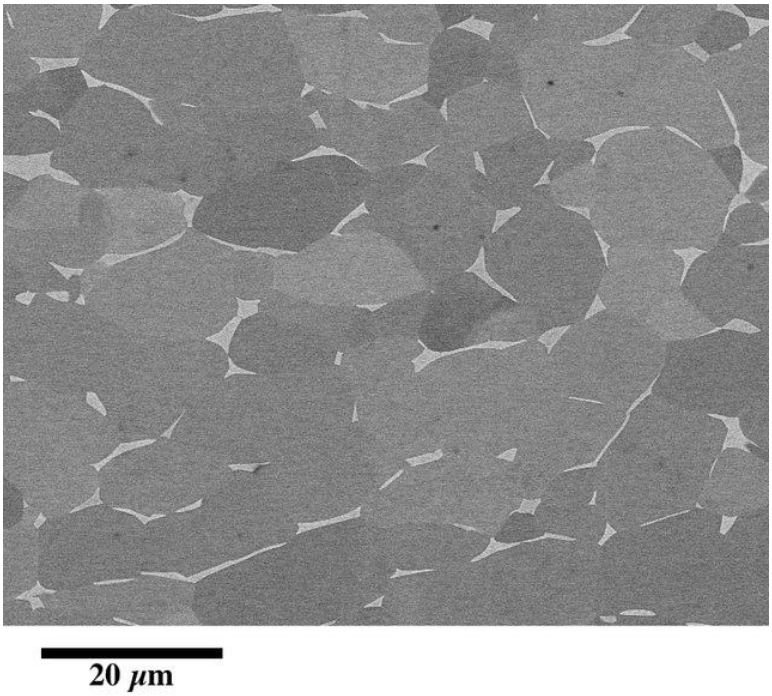

Figure 2.17 Typical fully equiaxed microstructure in $\alpha + \beta$ titanium alloys [213].

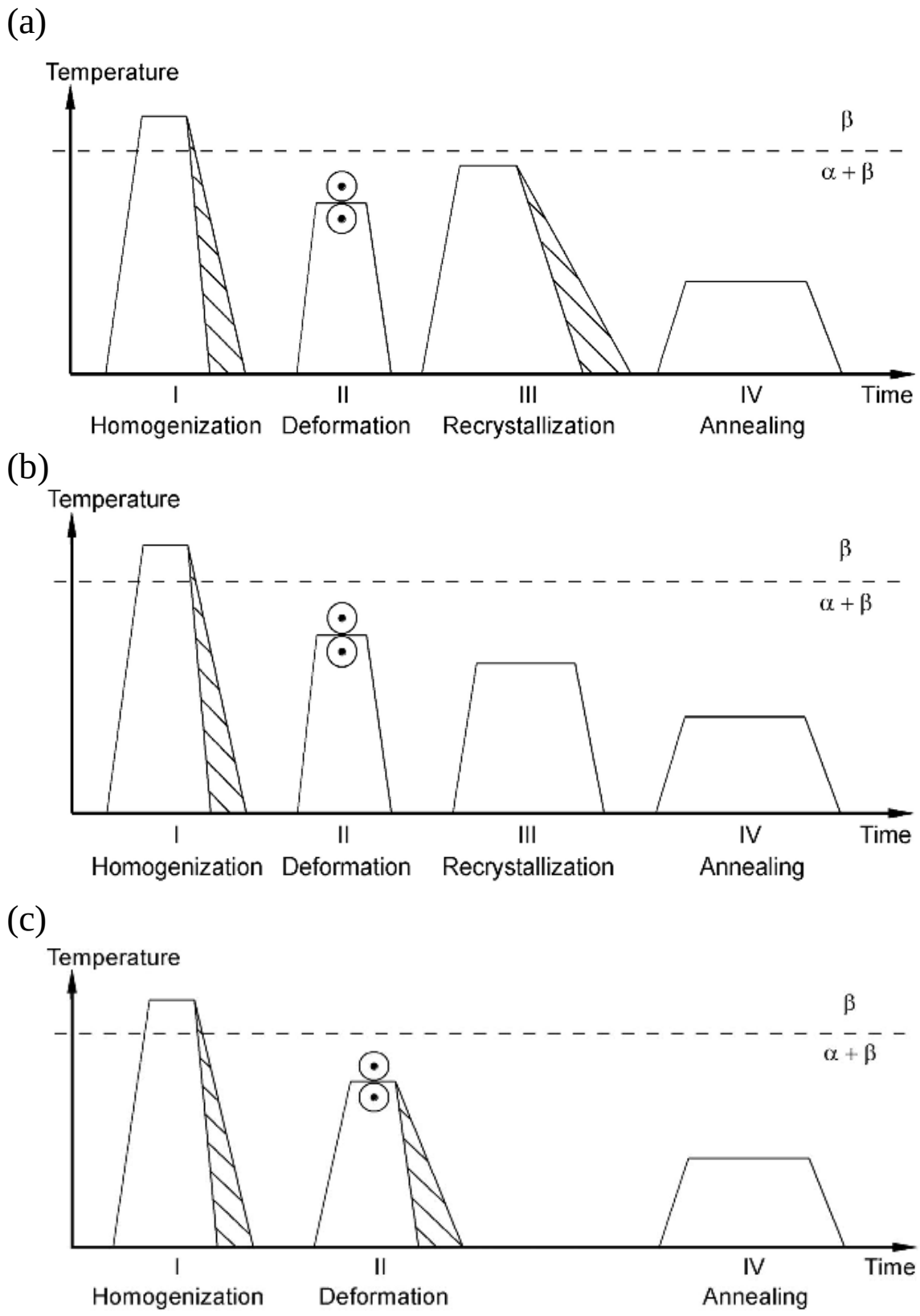

Figure 2.18 Processing routes for fully equiaxed microstructure. (a) Slow cooling from bimodal recrystallisation temperature; (b) recrystallise at low temperature; (c) mill-annealed condition [23].

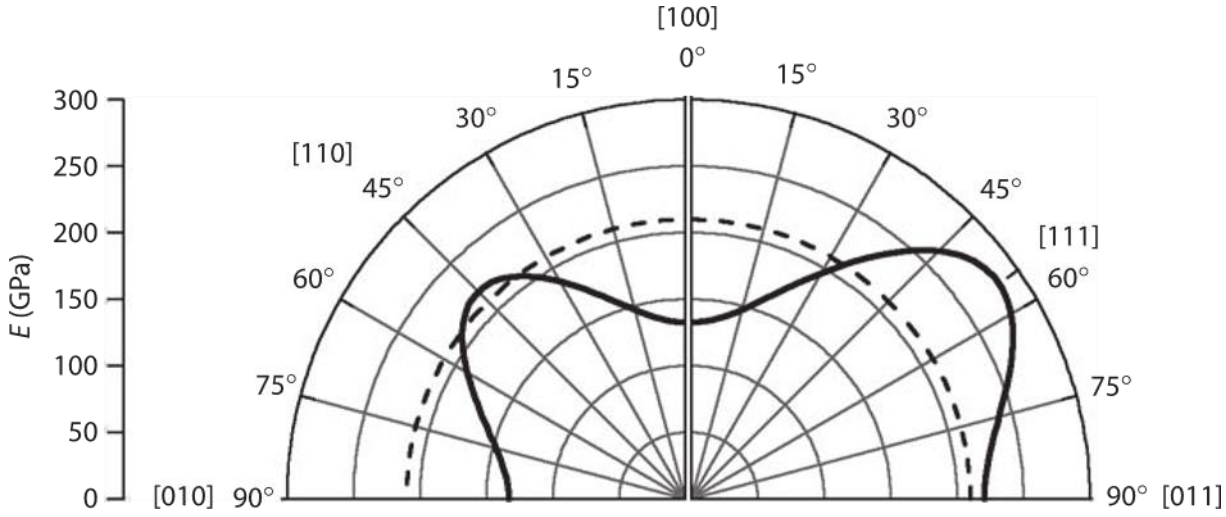

Figure 2.19 Elastic (Young's) modulus E of single-crystalline iron as a function of crystal direction. Clearly, the values strongly differ from the well-known bulk modulus of 210 GPa (dotted line), which is only obtained in isotropic, that is, texture-free material [89].

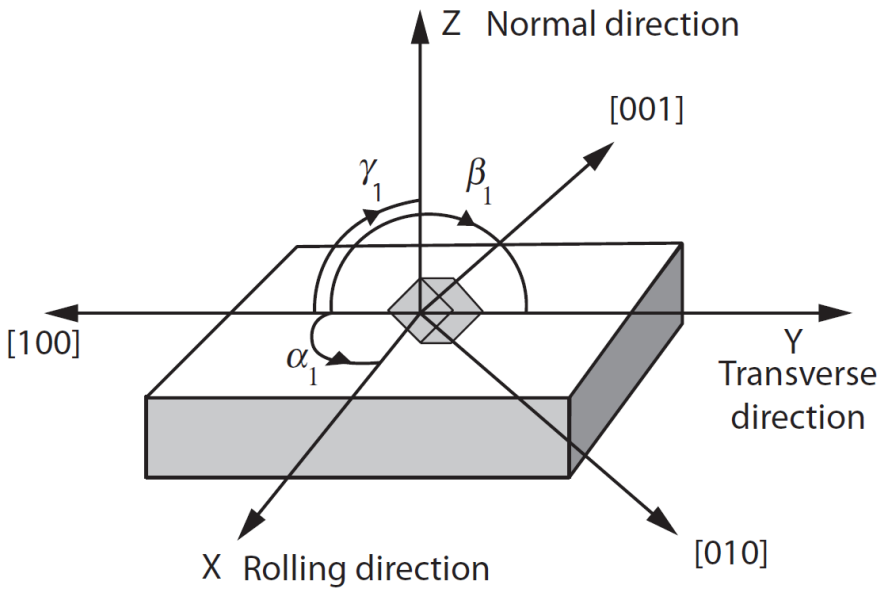

Figure 2.20 Relationship between the specimen coordinate system X, Y, Z (or RD, TD, ND for a rolled product) and the crystal coordinate system [100], [010], [001] where the cubic unit cell of one crystal in the specimen is depicted. The cosines of the angles α_1, β_1, γ_1 give the first row of the orientation matrix [89].

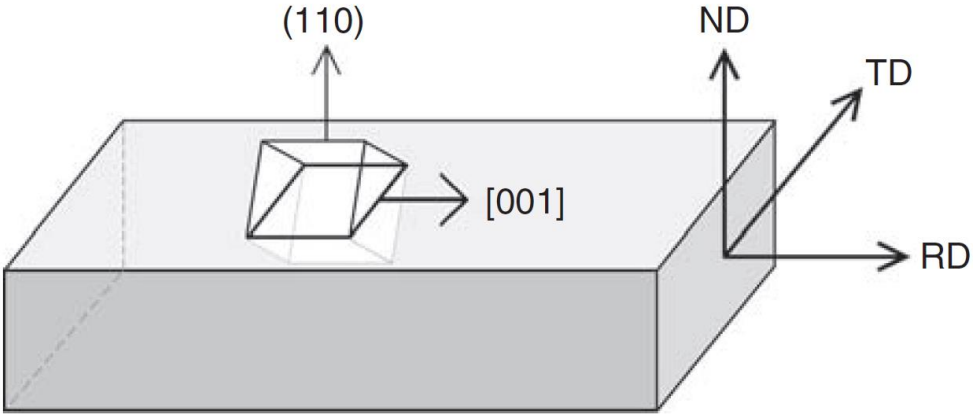

Figure 2.21 Schematic illustration of the relationship between the crystal and specimen axes for the (110)[001] Goss orientation, that is, the normal to (110) is parallel to the specimen ND, or Z axis and [001] is parallel to the specimen RD, or X axis [89].

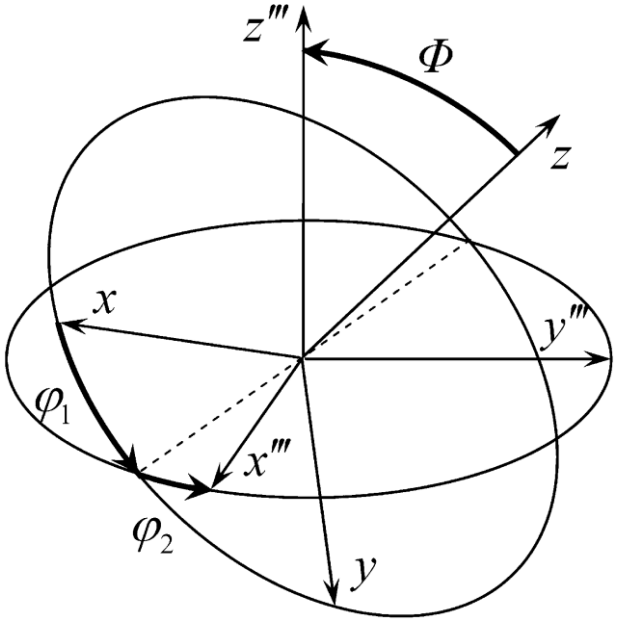

Figure 2.22 Definition of the orientation of a coordinate system, following the conventional interpretation of the Euler angles. The orientation is determined as the result of three consecutive rotations, performed about the z, x', and z'' axes by the angles φ_1, Φ, and φ_2, respectively [100].

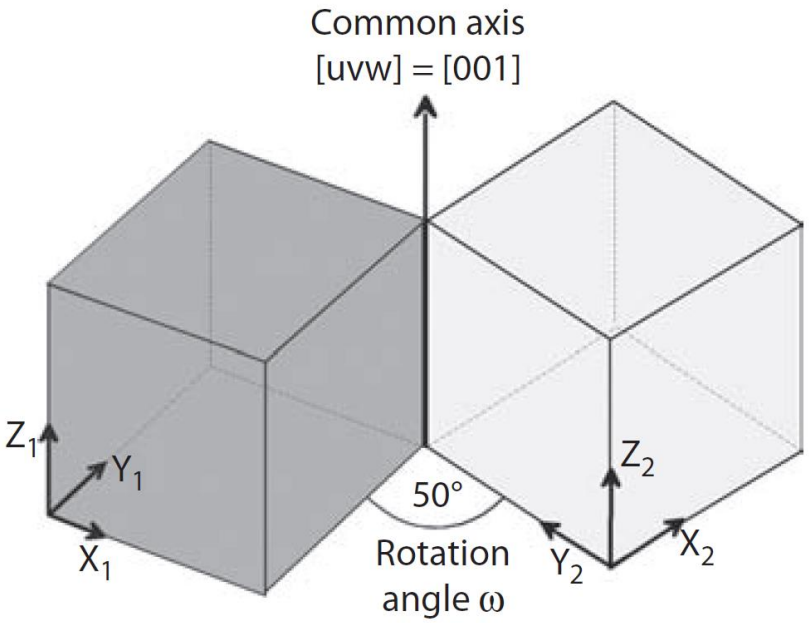

Figure 2.23 Diagram showing the angle/axis of rotation.

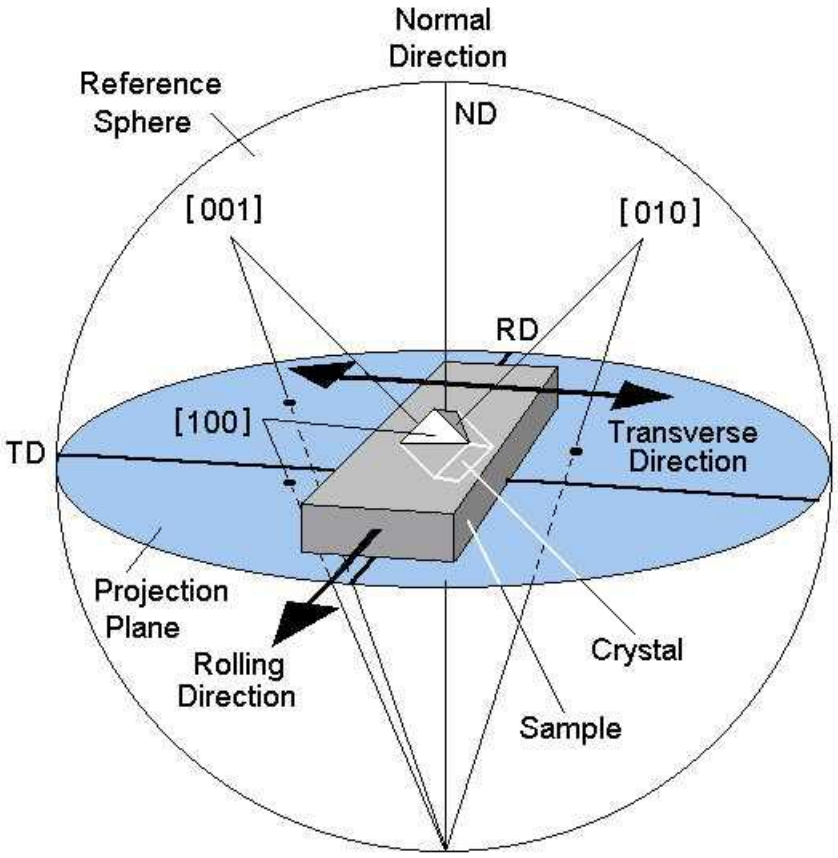

Figure 2.24 Schematic diagram illustrating the construction of a pole figure and the relationship between crystal orientation and sample frame [214].

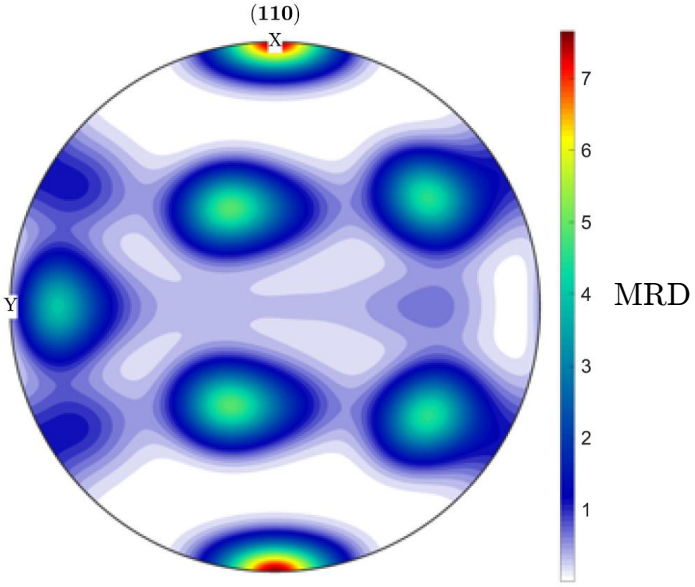

Figure 2.25 An example of contour pole figure. The intensity of texture components is indicated as multiple of random distribution (MRD). [215]

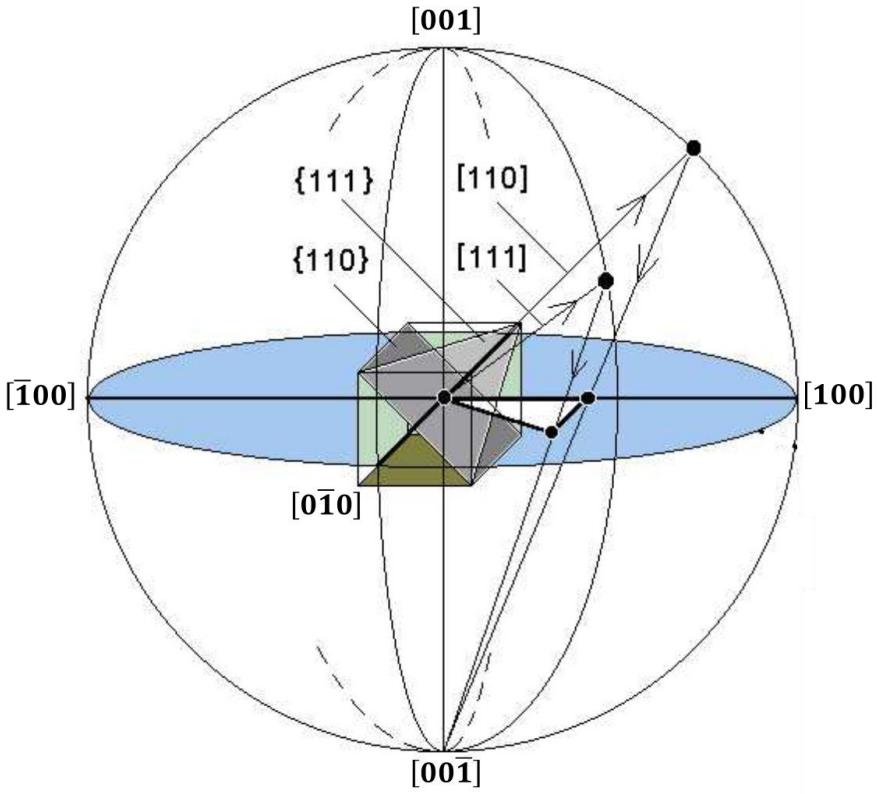

Figure 2.26 Schematic diagram illustrating the generation of inverse pole figures [214].

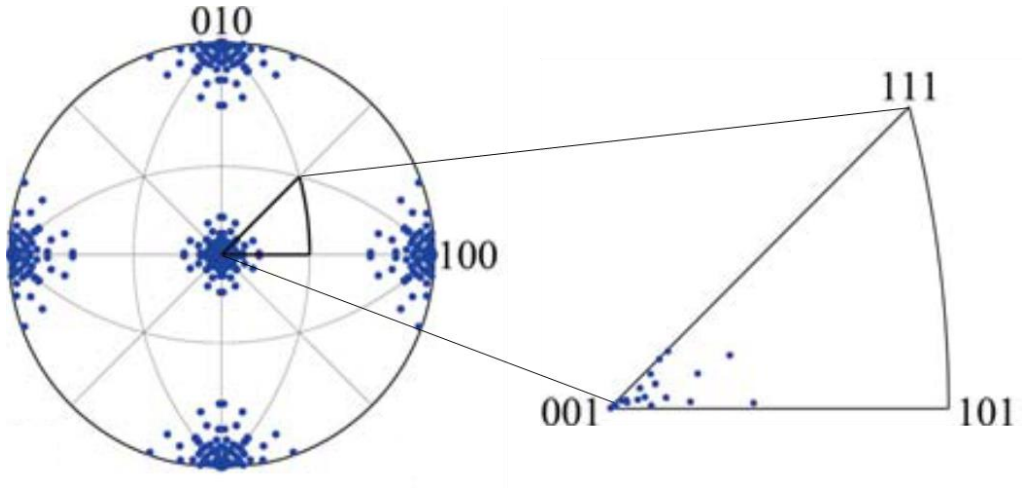

Figure 2.27 An example of inverse pole figure. The inverse pole figure on the left is divided into stereographic triangles. Due to the symmetry of the crystal, it is common to extract and display a reduced portion of the whole figure, shown on the right. Miller indices in the figure refer to directions in the local crystallographic frame [100].

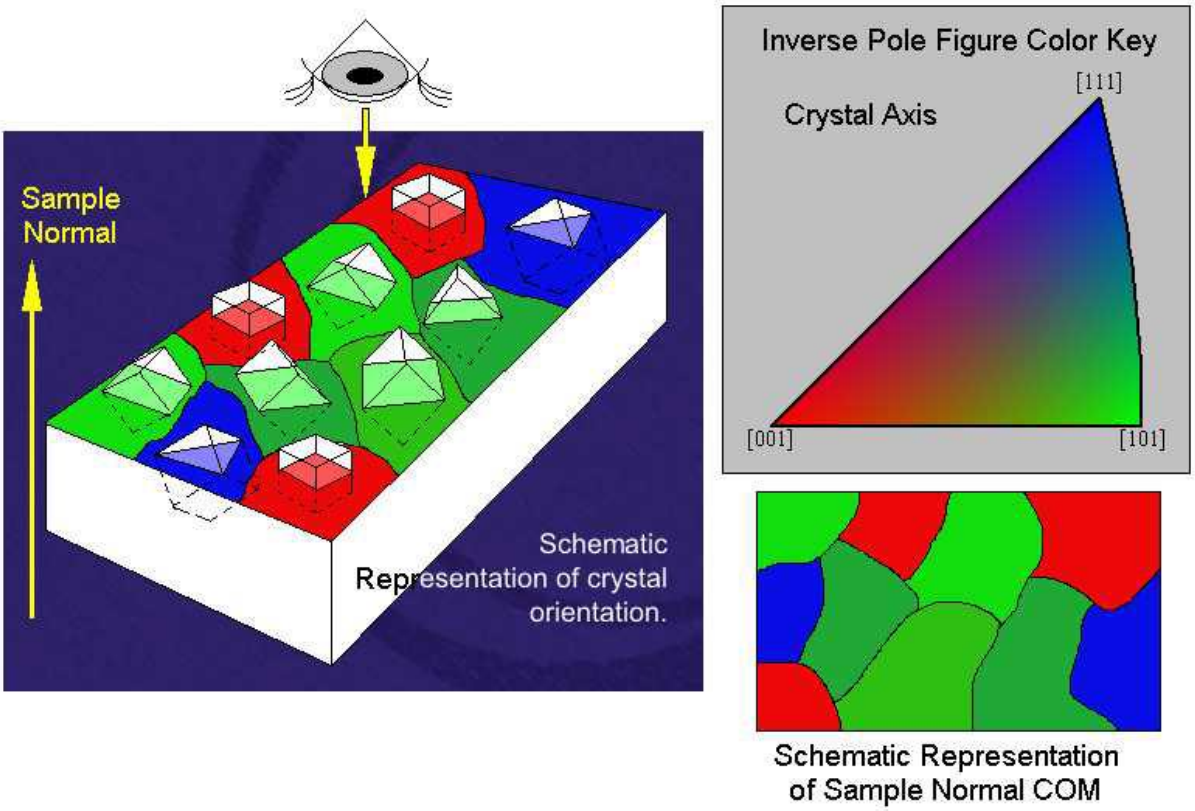

Figure 2.28 Schematic diagram of crystal orientation, inverse pole figure, and orientation map [214].

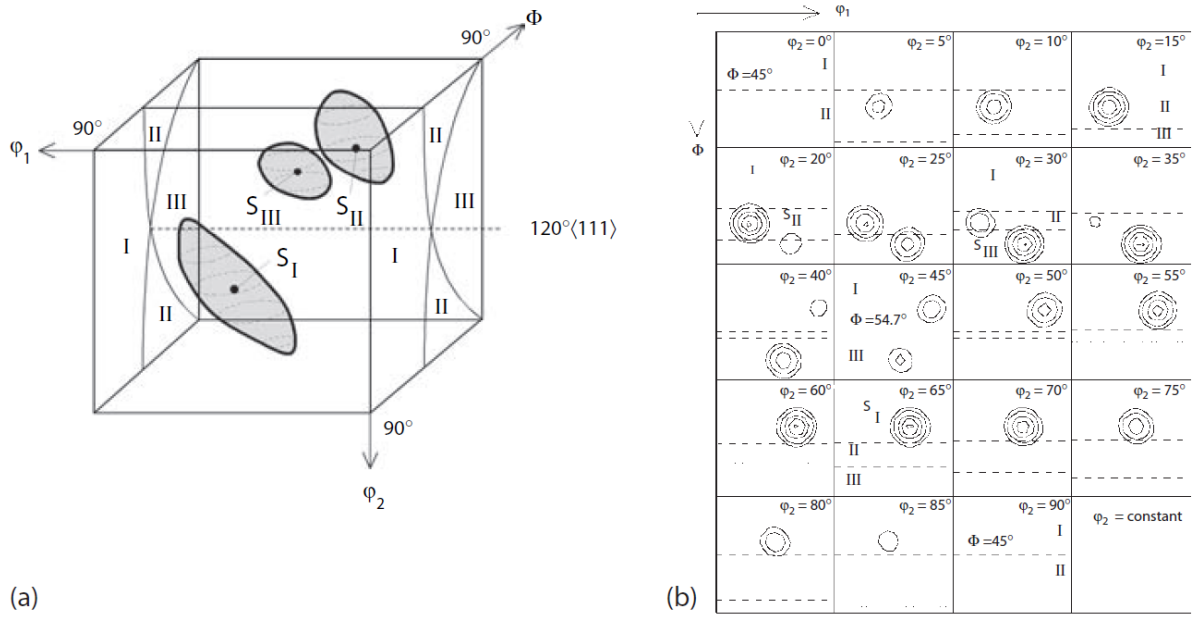

Figure 2.29 Examples of ODF visualised in (a) the three-dimensional Euler space and in (b) a series of φ_2 sections through the Euler space. [89].

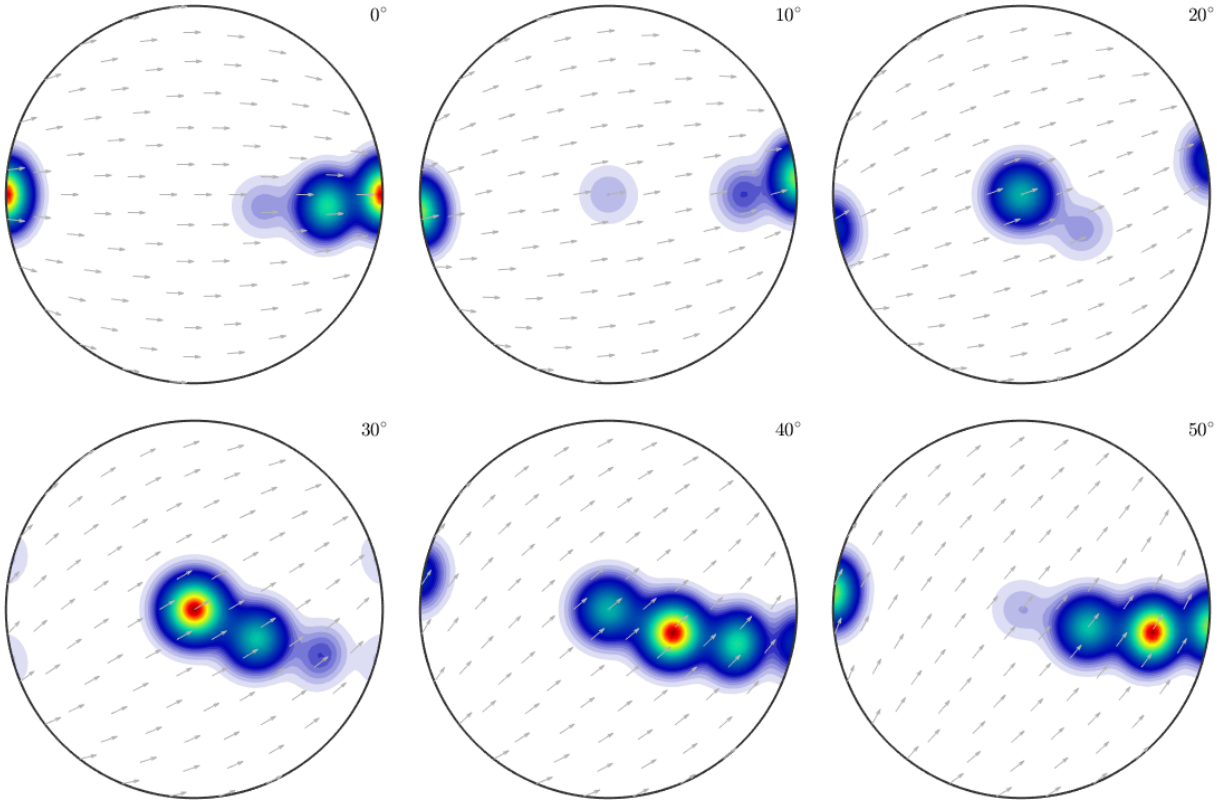

Figure 2.30 Examples of ODF visualised in sigma sections for hexagonal crystals (Courtesy of MTEX). Each section is visualised as c-axis pole figure with arrows indicating the direction a-axis.

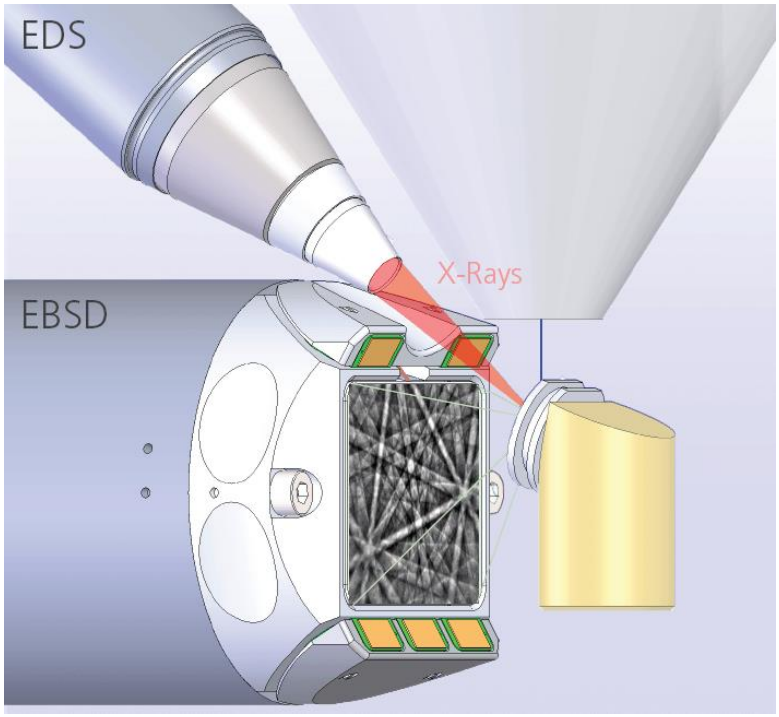

Figure 2.31 A typical geometry for EBSD, showing the tilted sample and the EBSP projected onto a phosphor screen at the end of the EBSD detector [216].

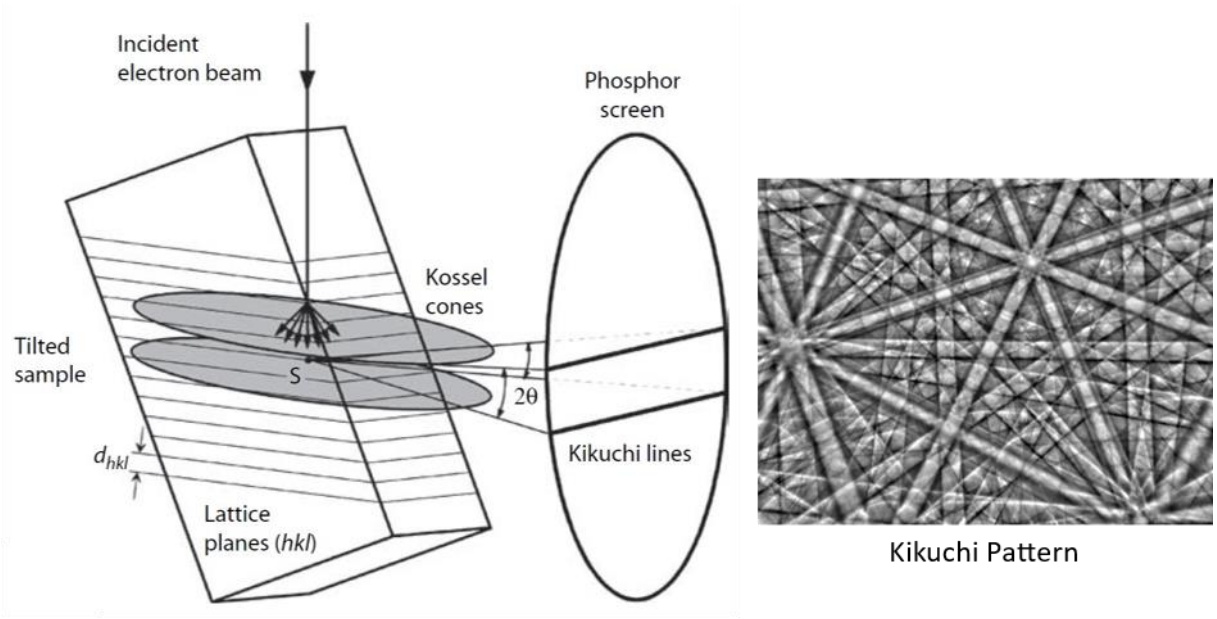

Figure 2.32 Formation of backscatter Kikuchi patterns by EBSD. [89].

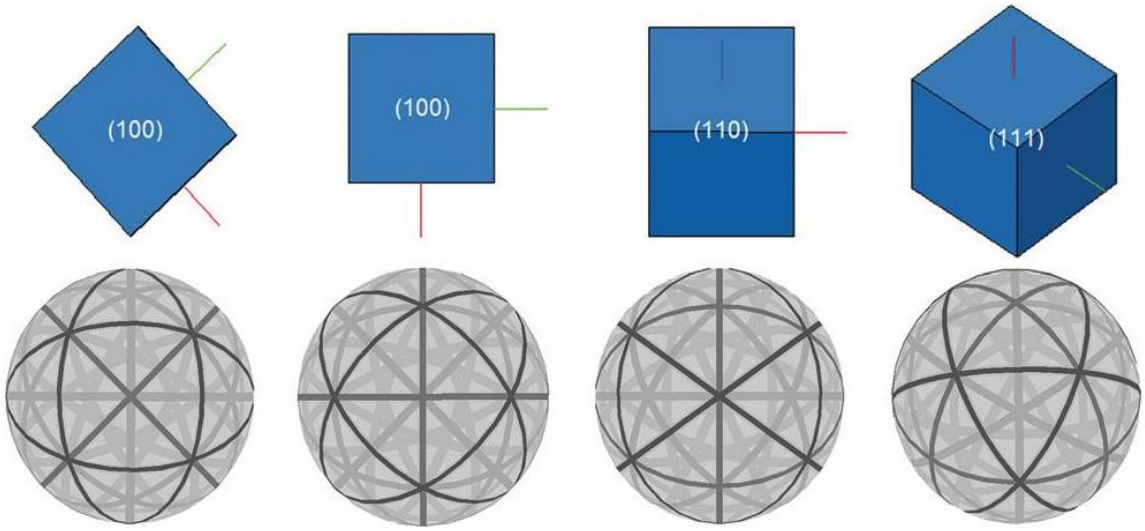

Figure 2.33 Spherical diffraction patterns generated by different orientations of a cubic structure [216].

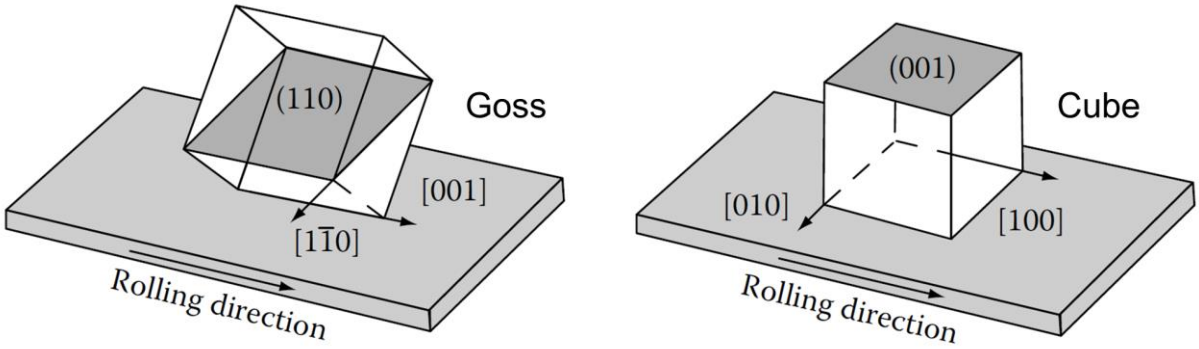

Figure 2.34 Schematic illustration of ideal Goss $\{110\}\langle 001\rangle$ and cube $\{001\}\langle 100\rangle$ texture [217].

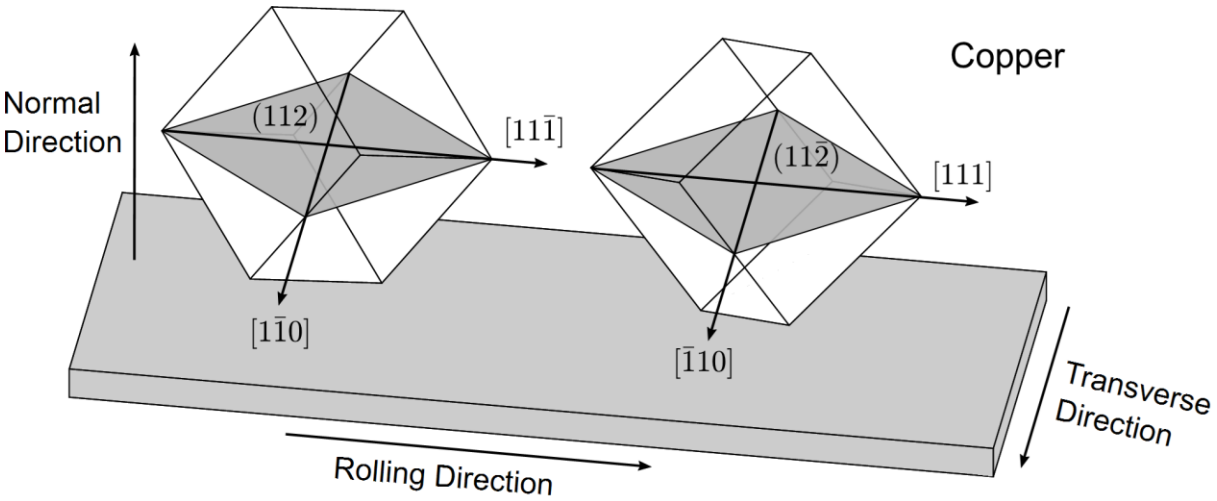

Figure 2.35 Schematic illustration of ideal copper $\{112\}\langle 11\bar{1}\rangle$ texture.

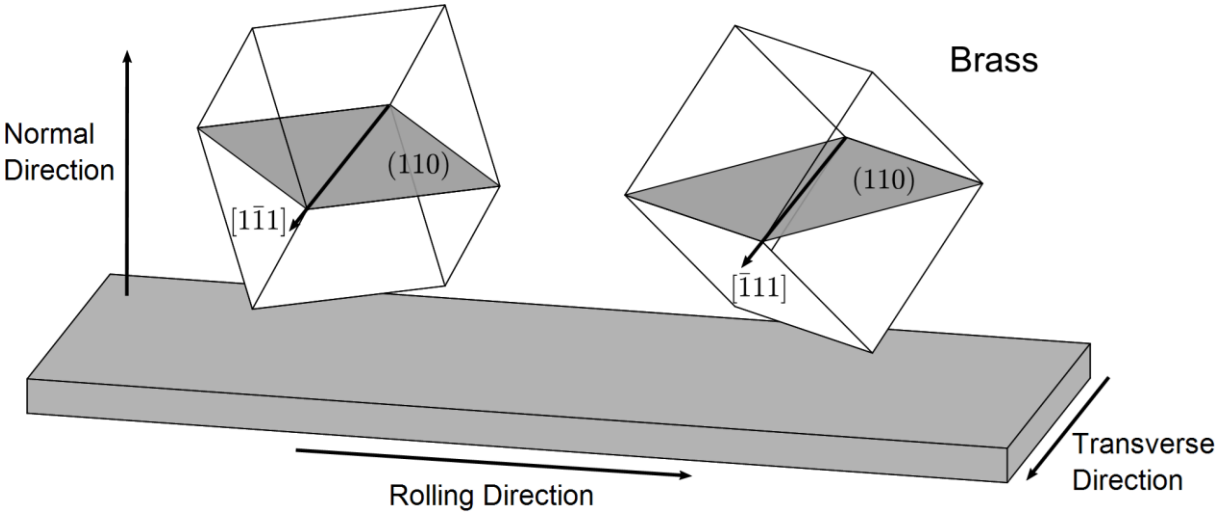

Figure 2.36 Schematic illustration of ideal brass $\{110\}\langle 1\bar{1}2\rangle$ texture.

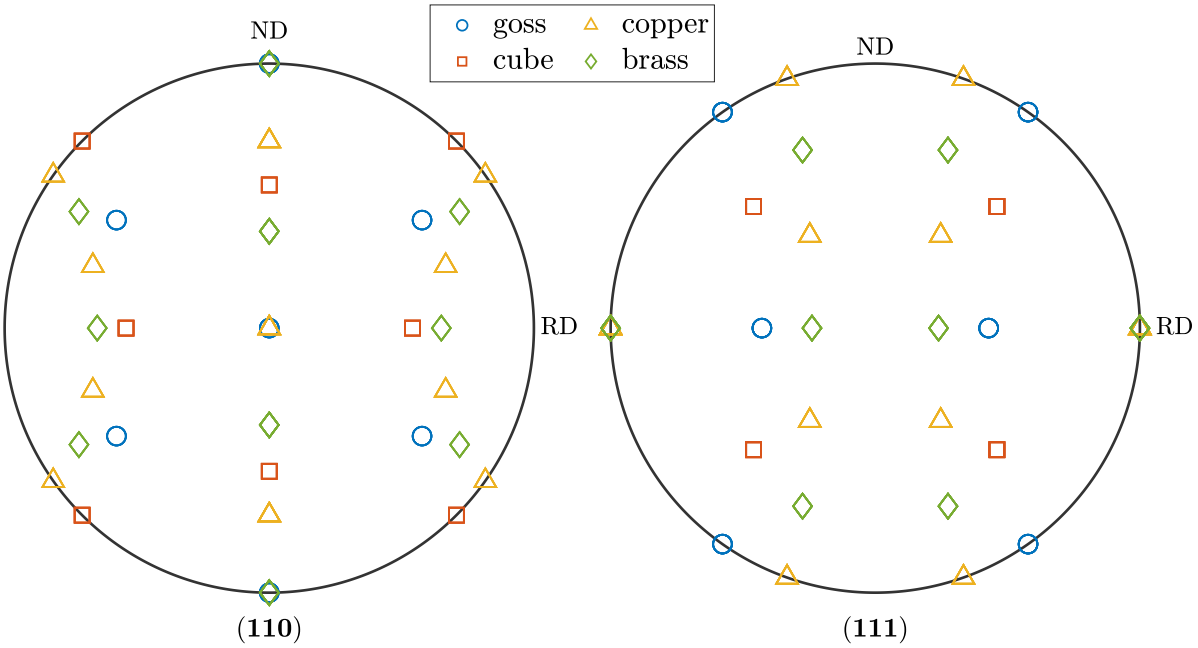

Figure 2.37 Standard (110) and (111) pole figures showing ideal texture components.

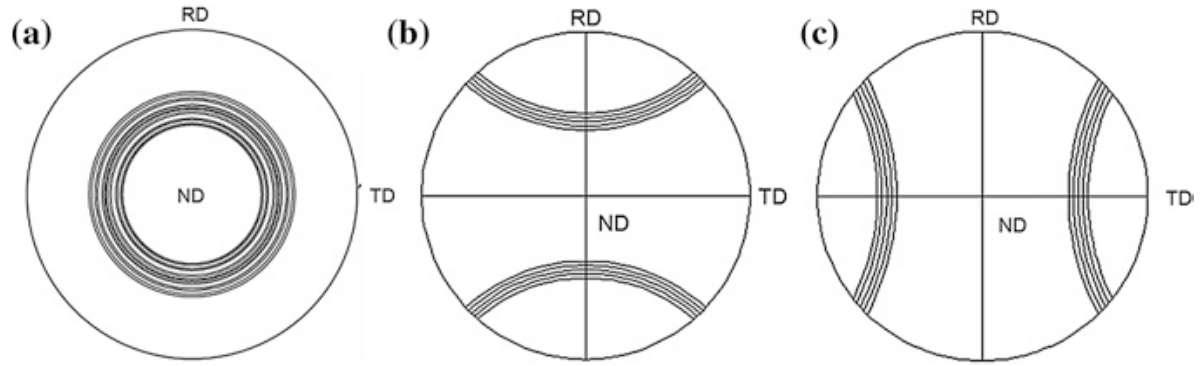

Figure 2.38 (001) Pole figure showing (110) fiber along (a) ND, (b) RD, and (c) TD [218].

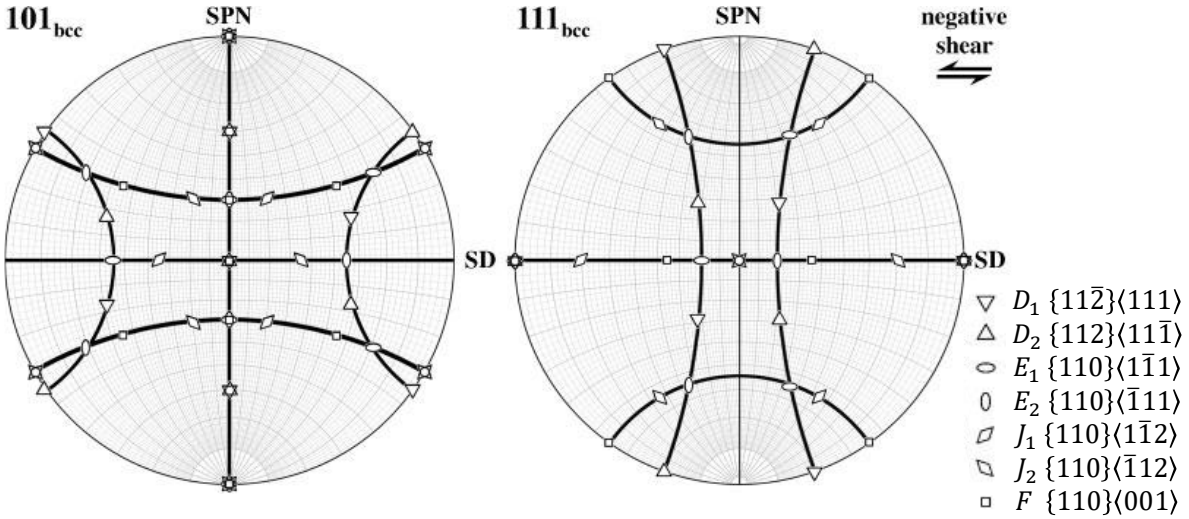

Figure 2.39 (110) and (111) pole figures showing important ideal orientations associated with simple shear deformation of bcc materials. SPN denotes shear plane normal, and SD denotes shear direction. Note that these pole figures are presented as equal angle projection. (Modified from [105])

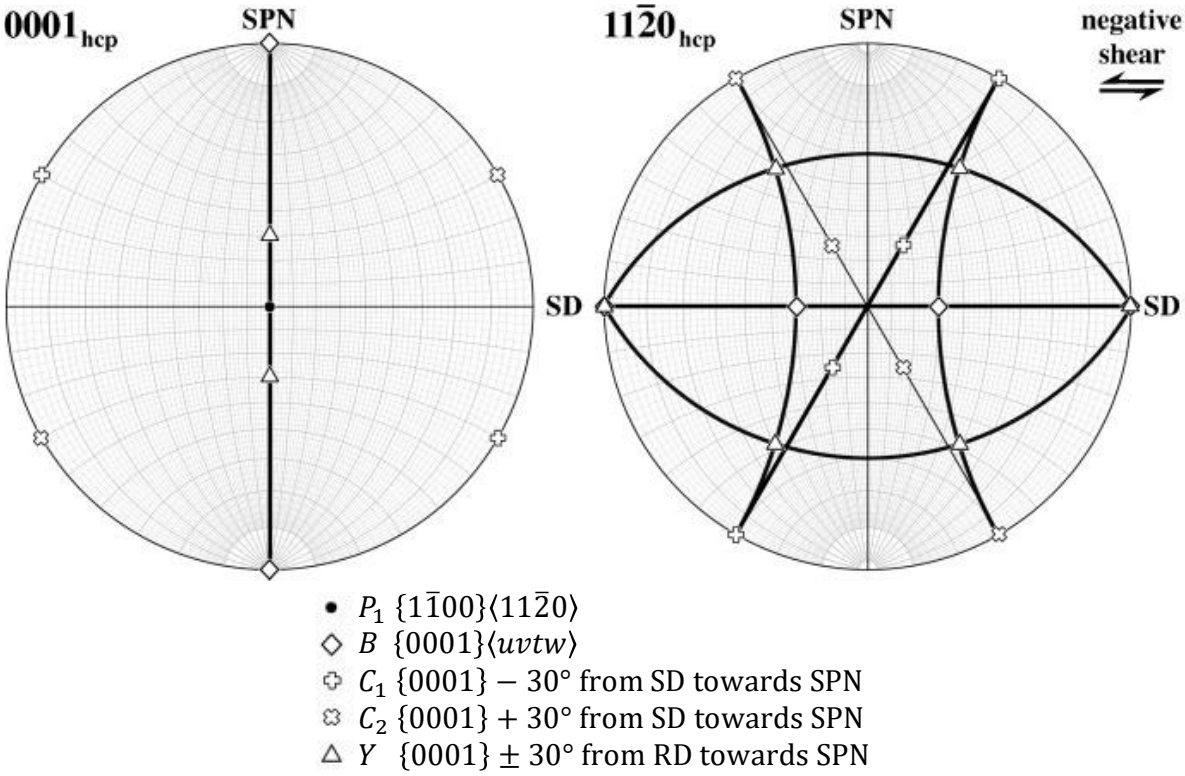

Figure 2.40 (0001) and (11$\bar{2}$0) pole figures showing important ideal orientations associated with simple shear deformation of hcp materials. SPN denotes shear plane normal, and SD denotes shear direction. Note that these pole figures are presented as equal angle projection. (Modified from [105])

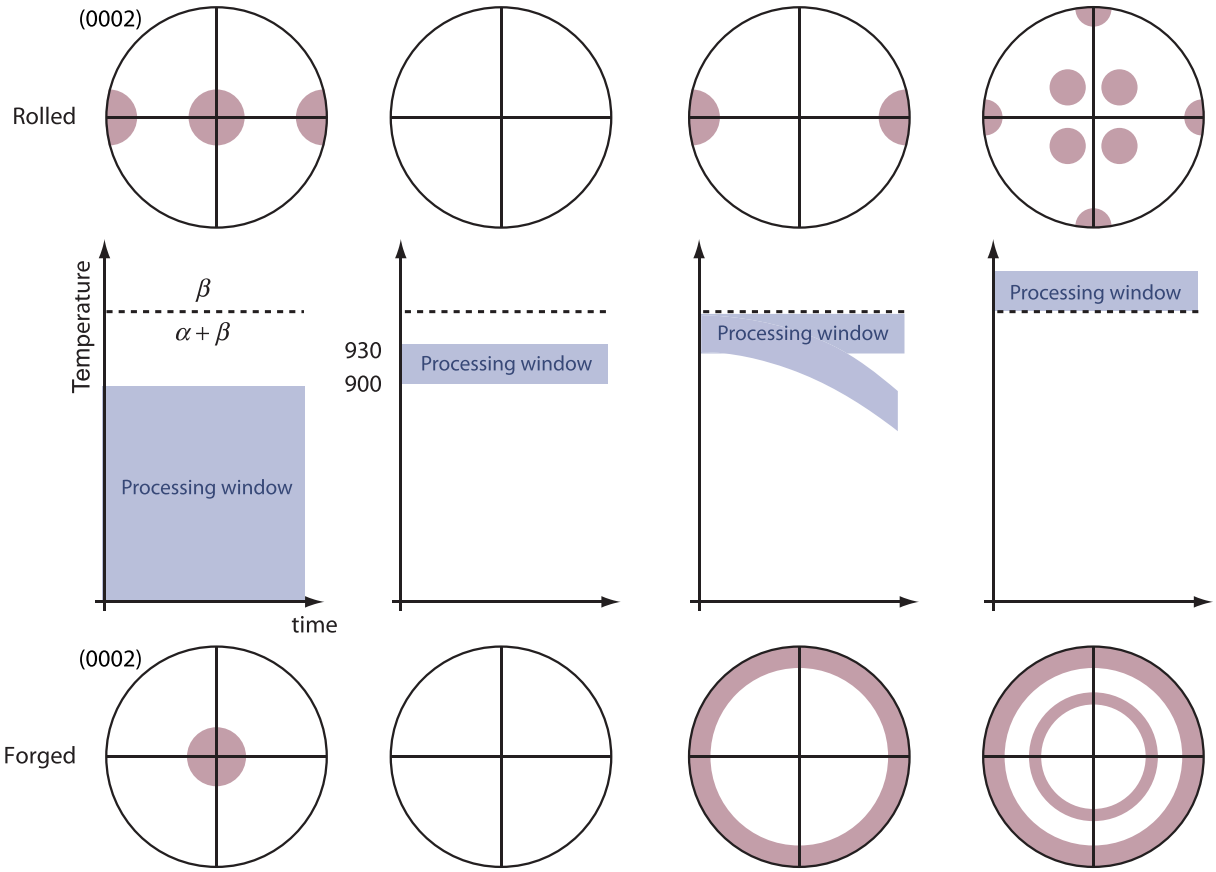

Figure 2.41 $(0002)_{\alpha}$ pole figures formed during rolling and forging within the indicated temperatures in $\alpha + \beta$ titanium alloys (schematically). (Modified from [95, 23])

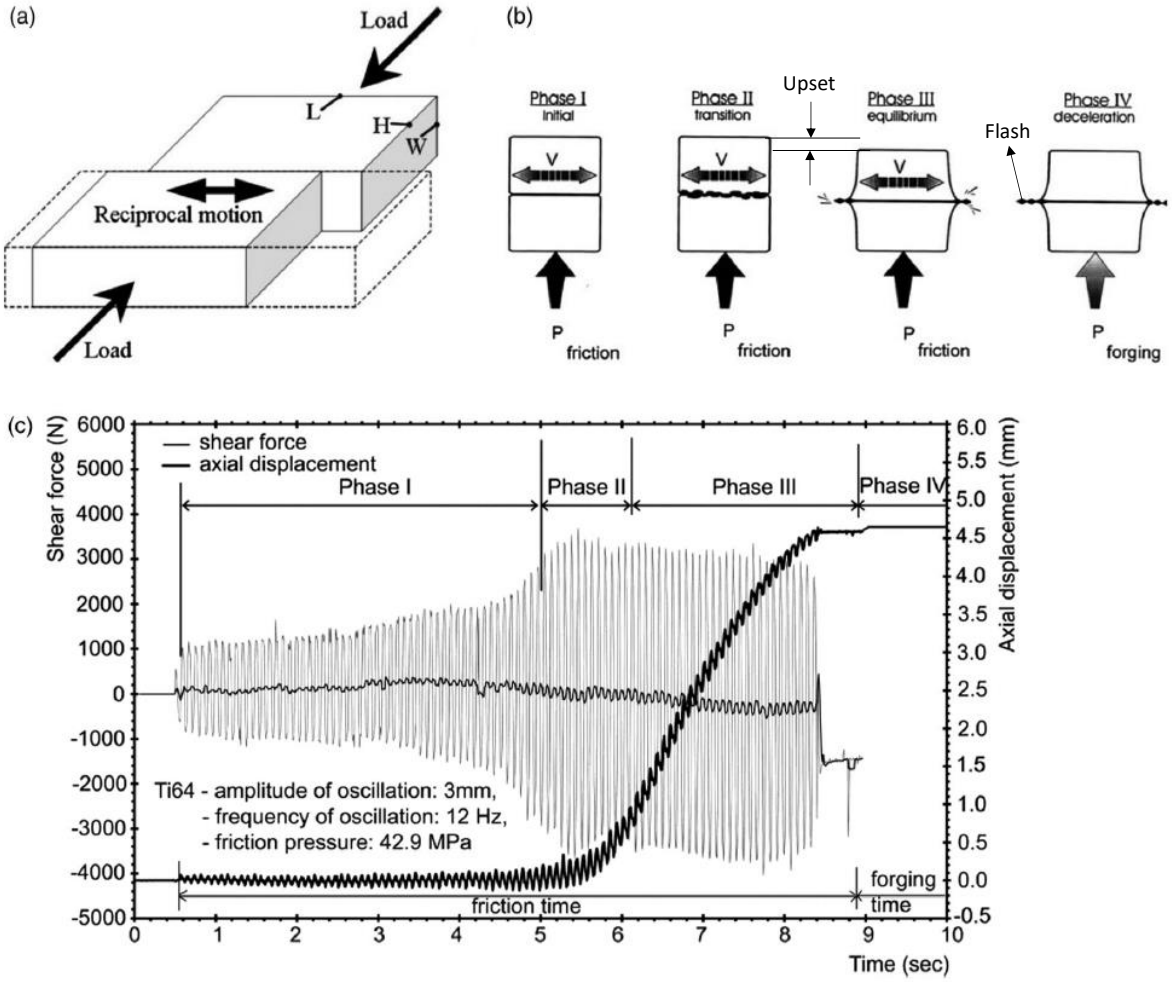

Figure 2.42 Schematic diagram of (a) LFW process and (b) its process phases. (c) The variation of process variables during LFW process [123–125].

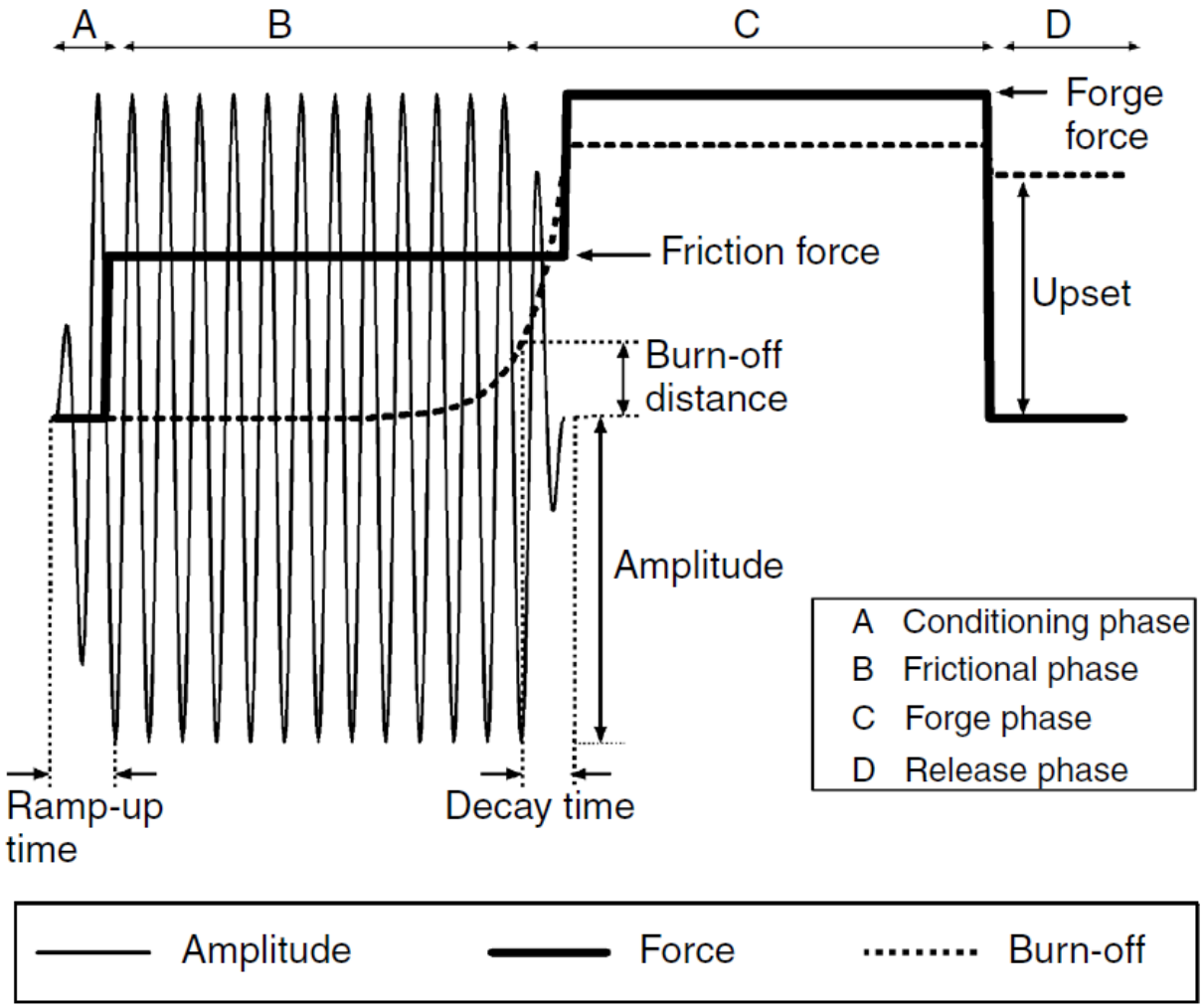

Figure 2.43 Schematic diagram of the parameter traces that are obtained during the LFW process [127].

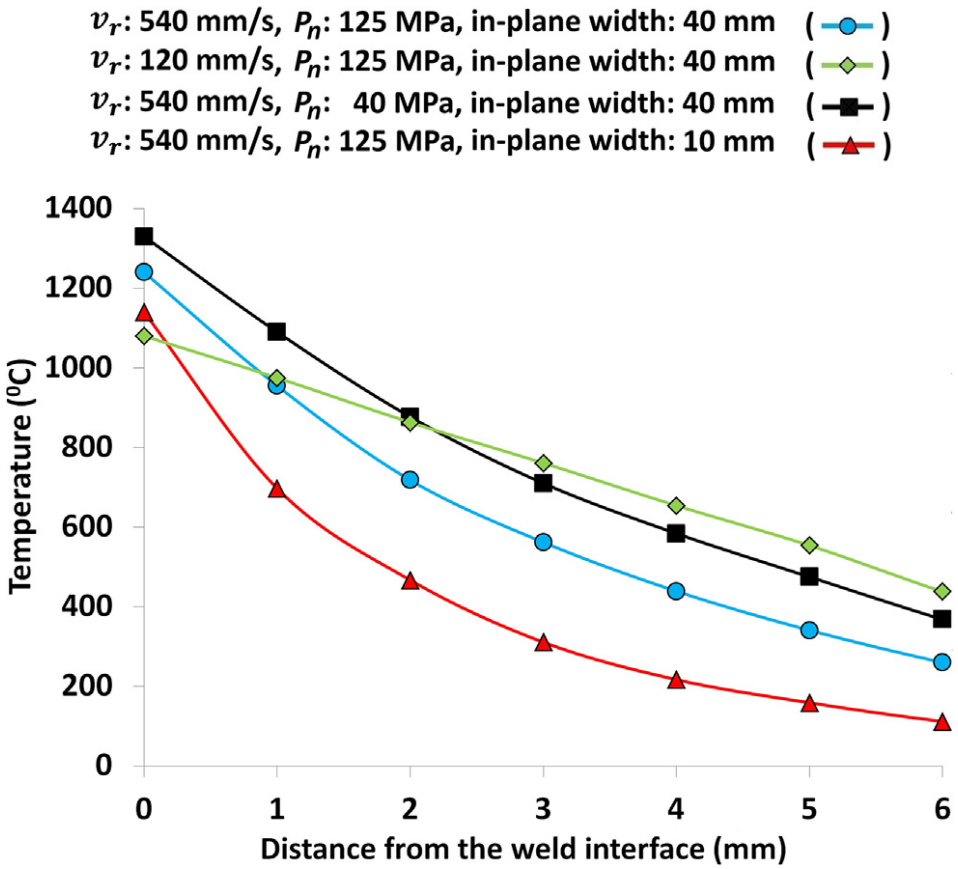

Figure 2.44 Thermal profiles in Ti-6Al-4V linear friction welds showing the effects of the rubbing velocity, v_r, pressure, P_n, and in-plane width. These profiles were obtained from FEA [128].

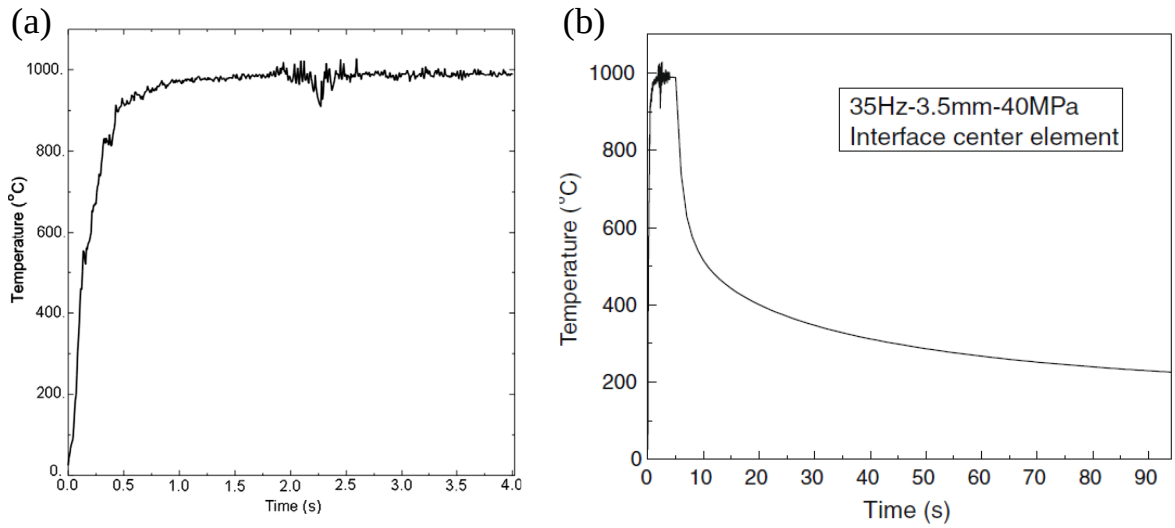

Figure 2.45 Simulated temperature profiles at the interface (a) before the forging phase; (b) during the whole linear friction welding process. [136].

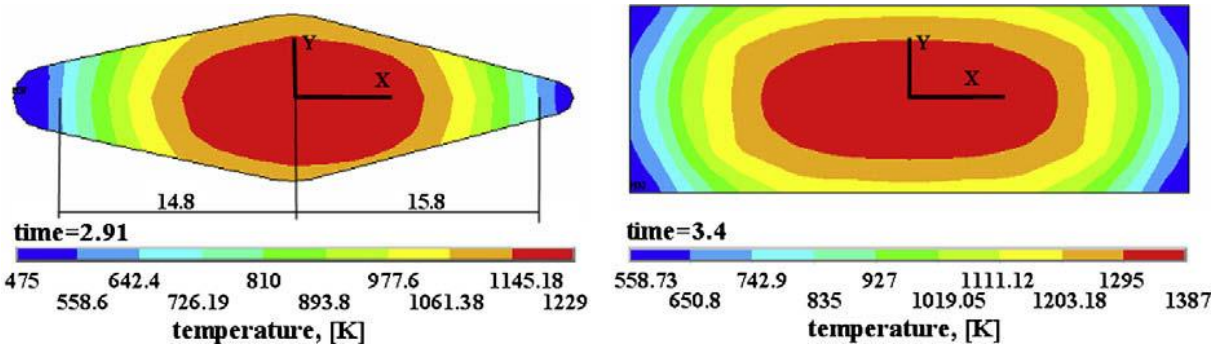

Figure 2.46 Temperature distribution in the rubbing interface of the stationary part. The temperature is showed at the time when the desired upset is reached and the relative movement starts slowing down [137].

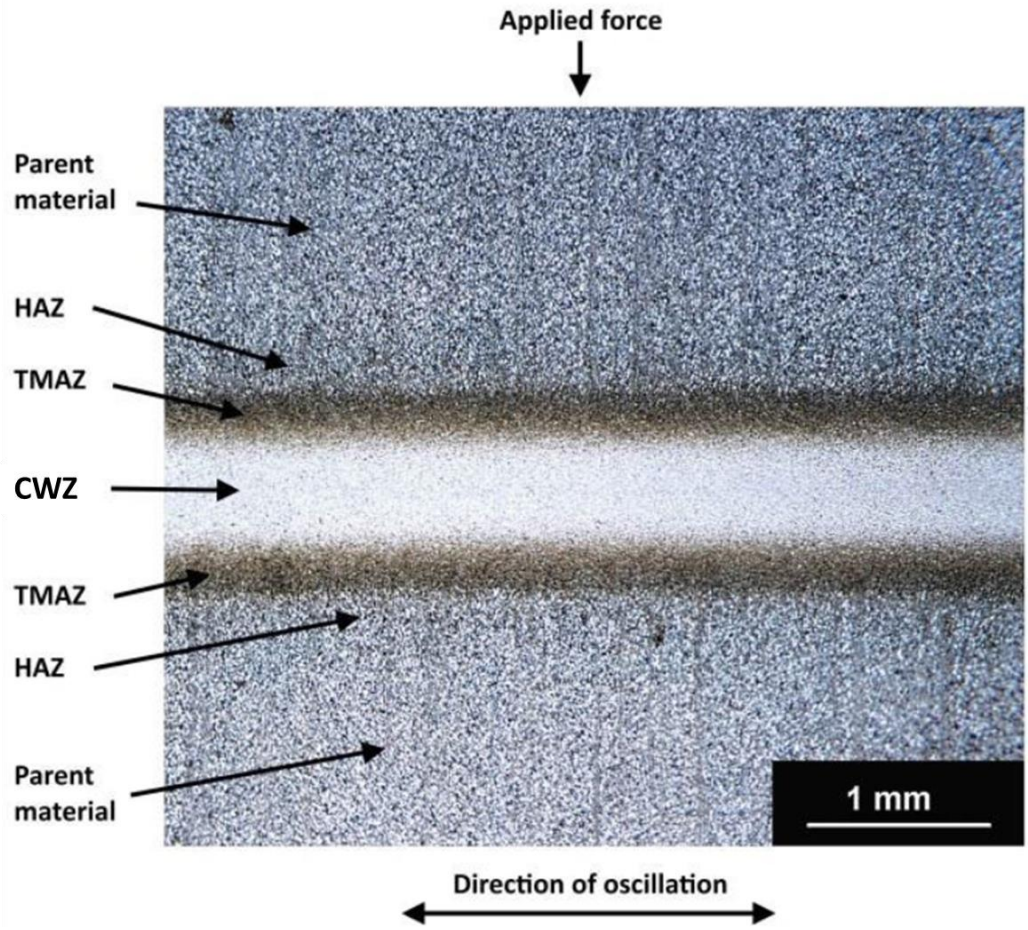

Figure 2.47 An optical micrograph of Ti-64 after linear friction welding [2].

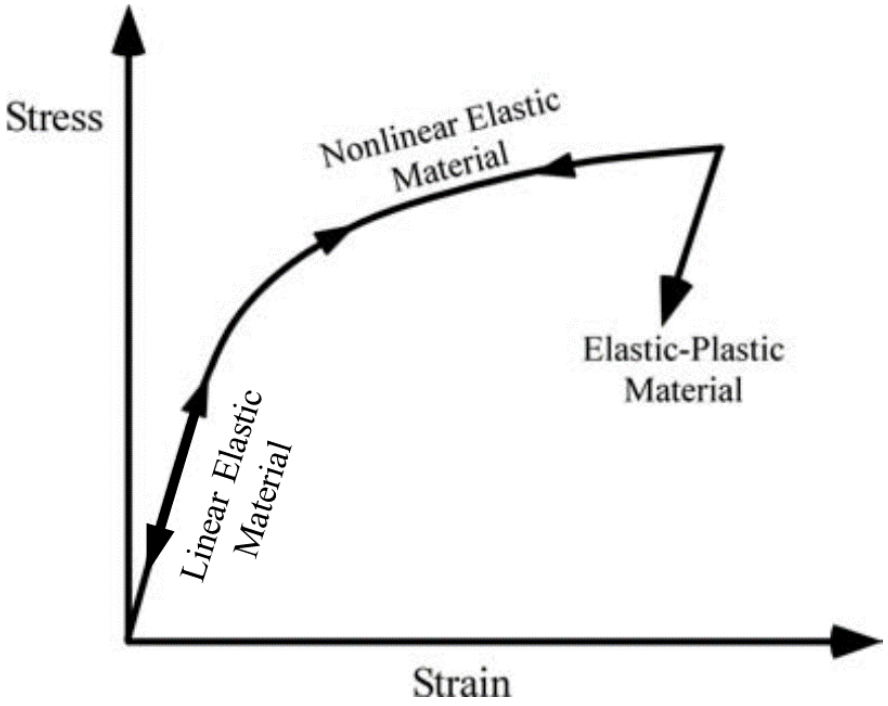

Figure 2.48 Schematic comparison of the stress-strain behaviour between linear elastic, elastic-plastic and nonlinear elastic materials [164].

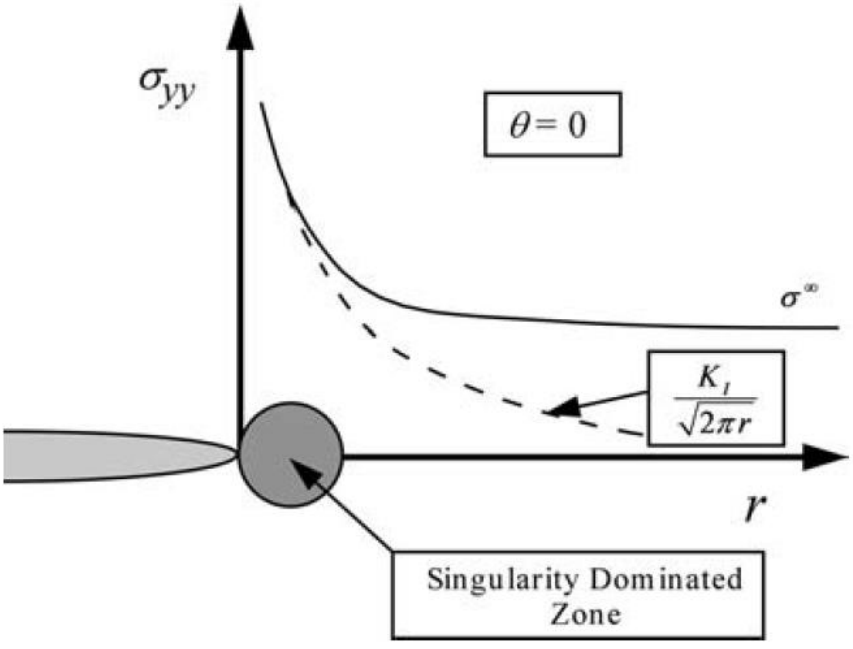

Figure 2.49 Stress normal near a crack tip and the singularity zone. [164]

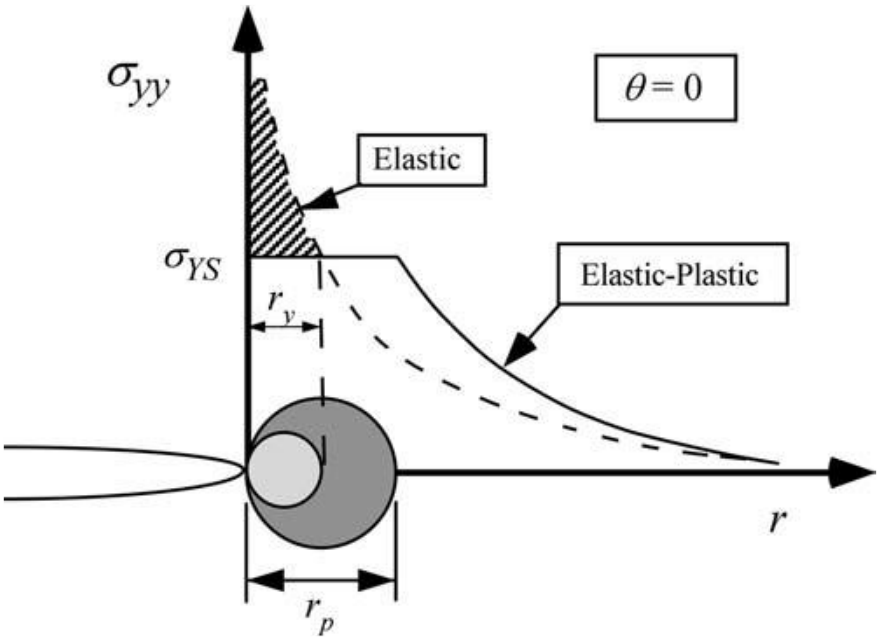

Figure 2.50 Estimation of the plastic zone size. The slashed area indicates the stress must be redistributed, resulting in a larger plastic zone. [164]

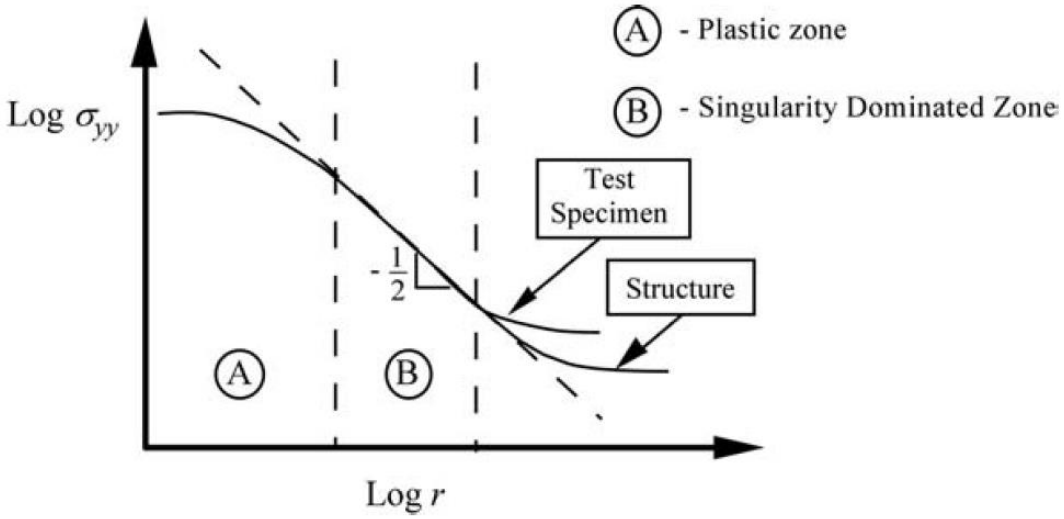

Figure 2.51 Schematic diagram of the stress normal, plastic zone, and singularity dominated zone. [164]

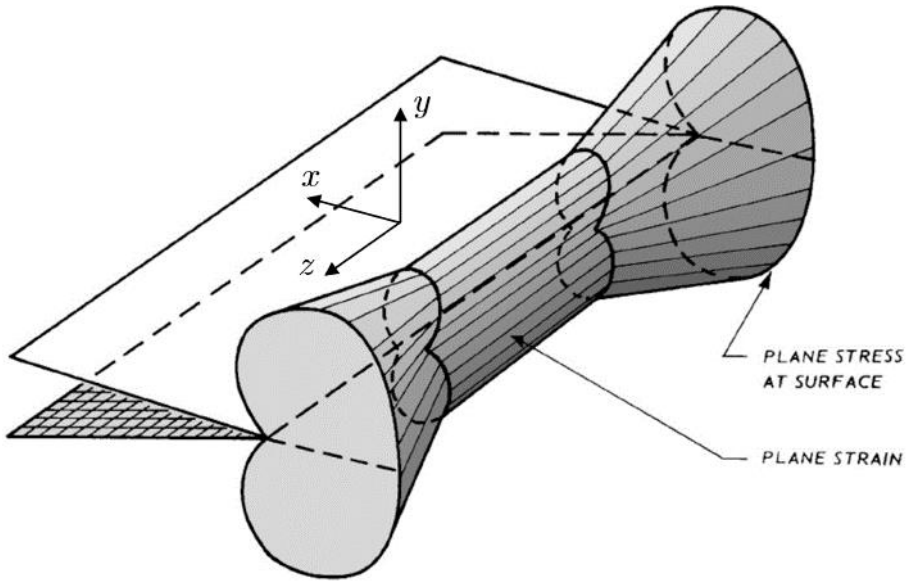

Figure 2.52 The shape of plastic zone around a through-thickness crack. [159]

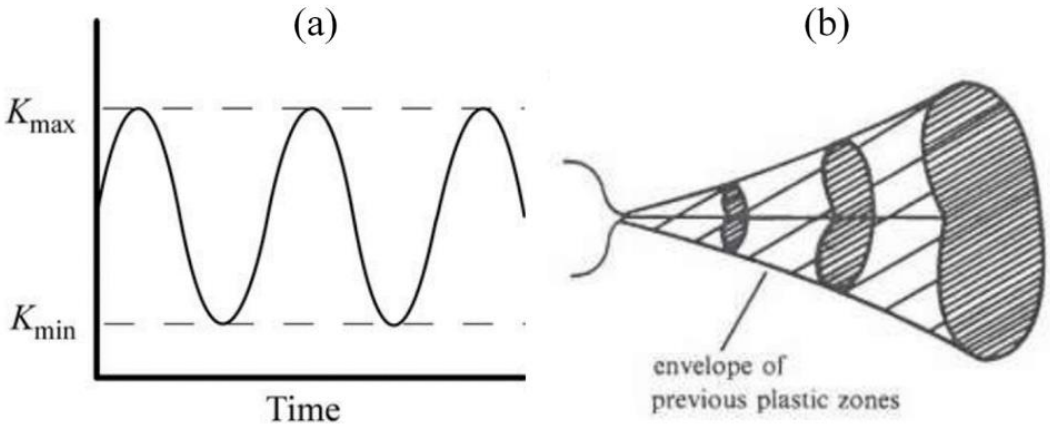

Figure 2.53 (a) Constant amplitude fatigue crack growth under small-scale yielding conditions. (b) The plastic zones introduced by fatigue crack growth. [164].

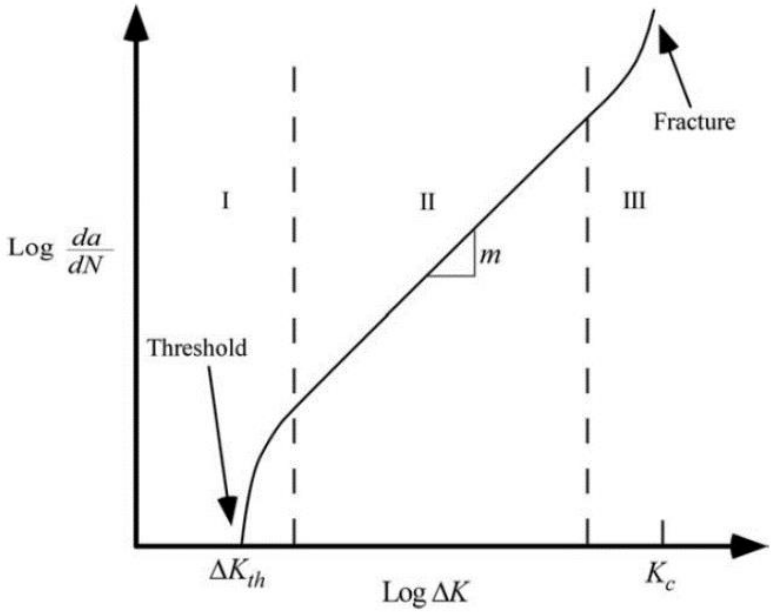

Figure 2.54 Typical fatigue crack growth behaviour composed of three distinct regimes in da/dN vs. ΔK curve in metals [219].

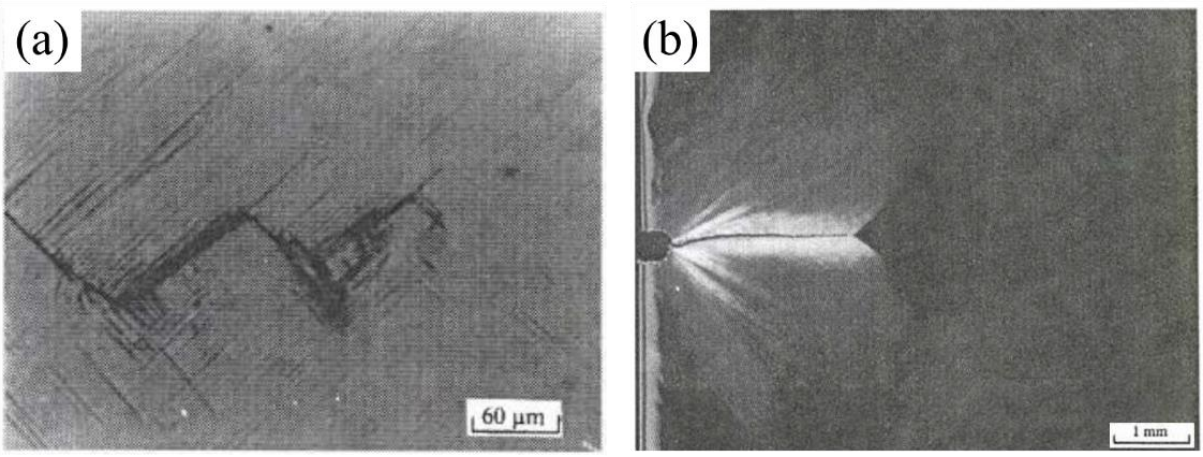

Figure 2.55 Fatigue crack growth in the (a) threshold regime and (b) Paris regime. [163]

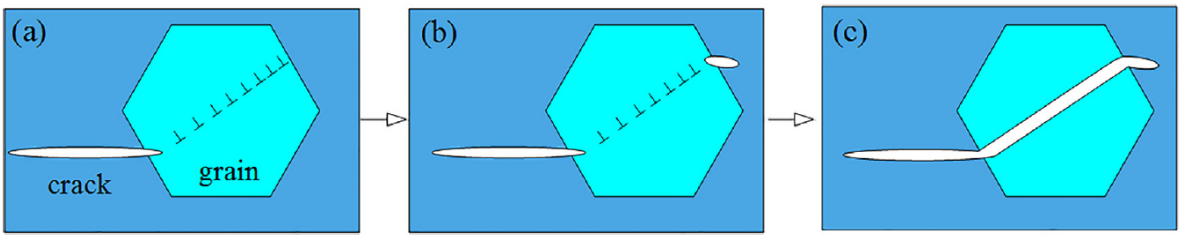

Figure 2.56 Micro-mechanism of crack propagation in threshold regime [170].

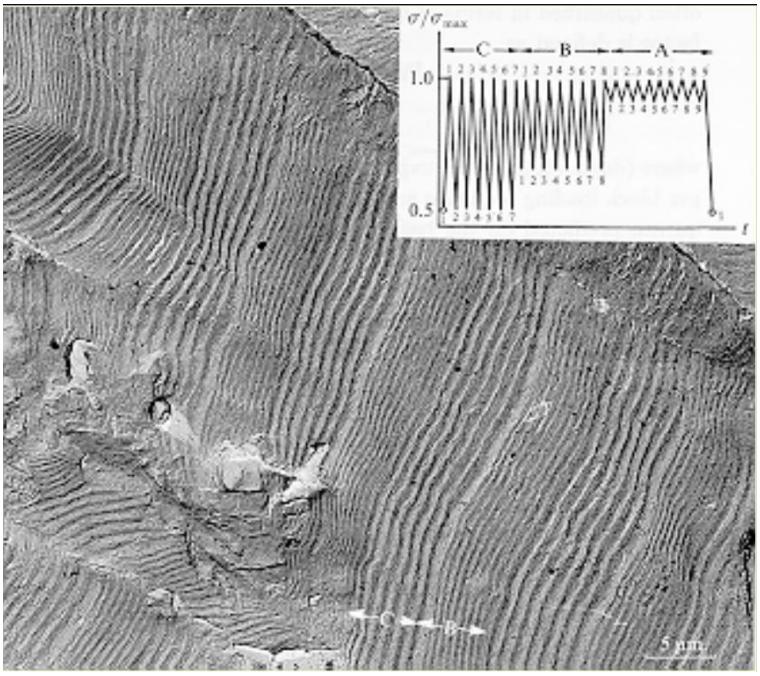

Figure 2.57 Fatigue striations resulting from different stress range [163].

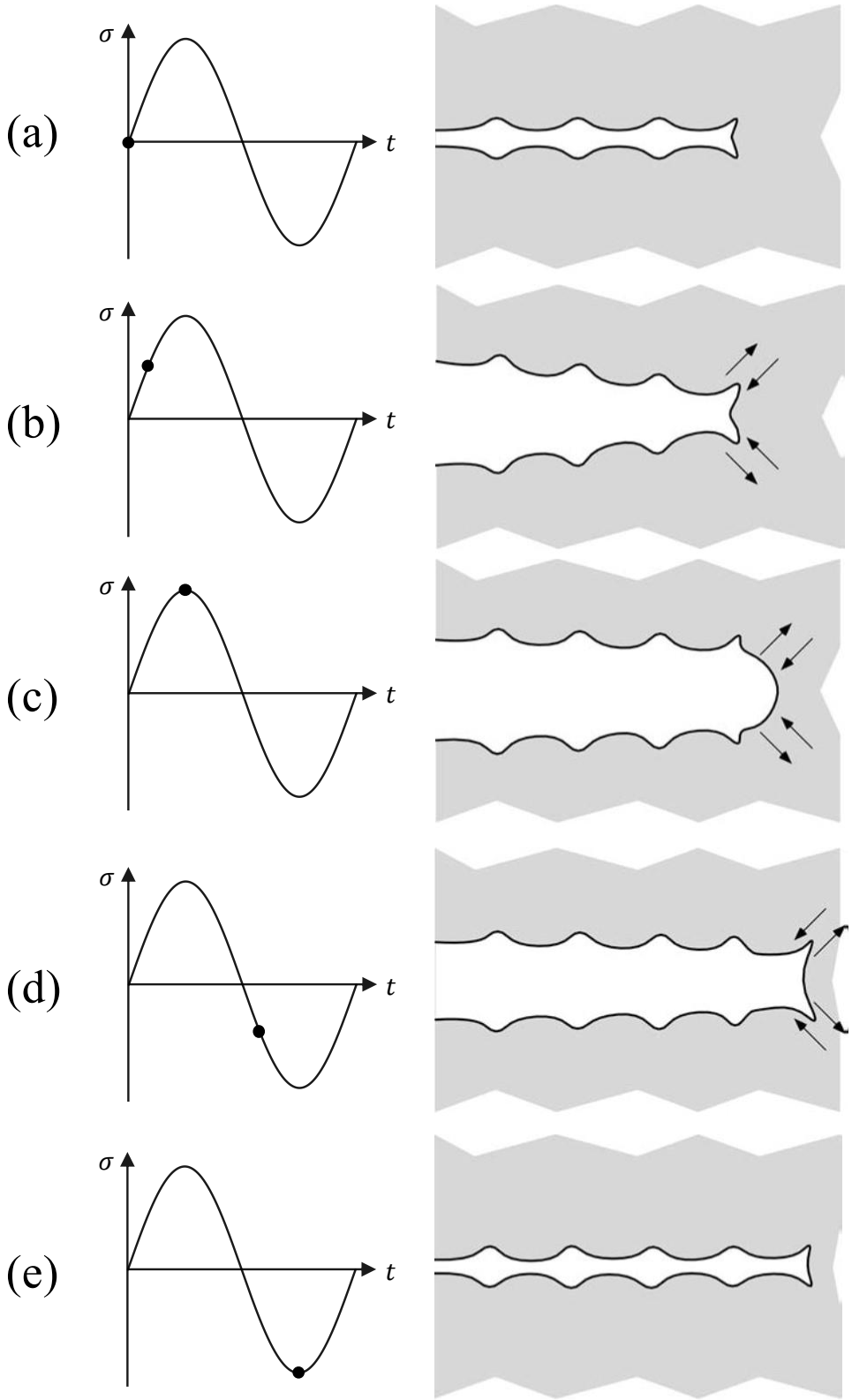

Figure 2.58 Micro-mechanism of fatigue crack growth in the Paris regime [220]. (a) under zero stress; (b) under small tensile stress; (c) under maximum tensile stress; (d) onset of compressive stress; (e) under maximum compressive stress.

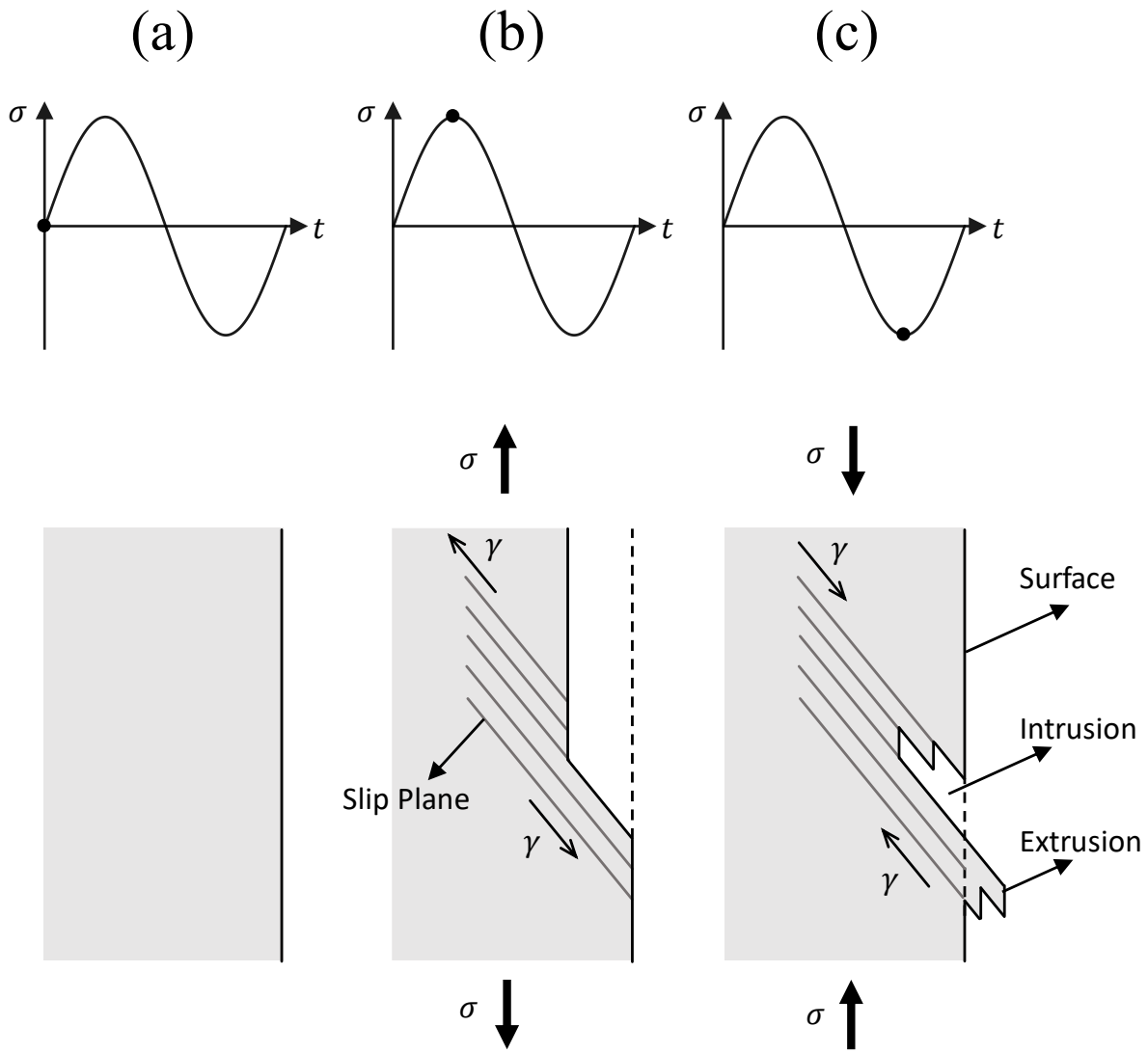

Figure 2.59 Micro-mechanism of the formation of persistent slip bands and the resultant extrusion and intrusion on the surface. (a) under zero stress; (b) under maximum tensile stress; (c) under maximum compressive stress. (Adapted from [221])

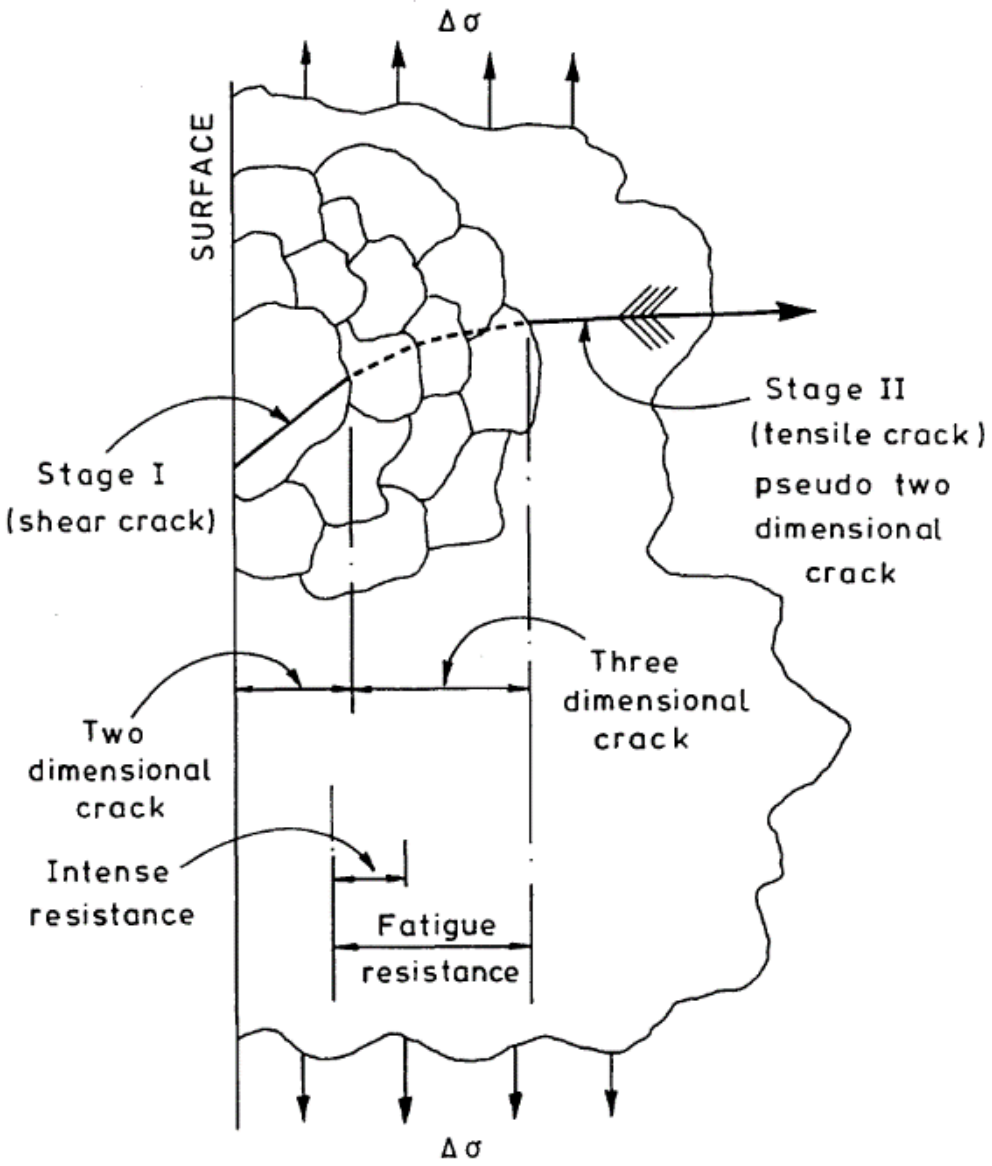

Figure 2.60 Schematic illustration of short fatigue crack growth [172].

Chapter 3

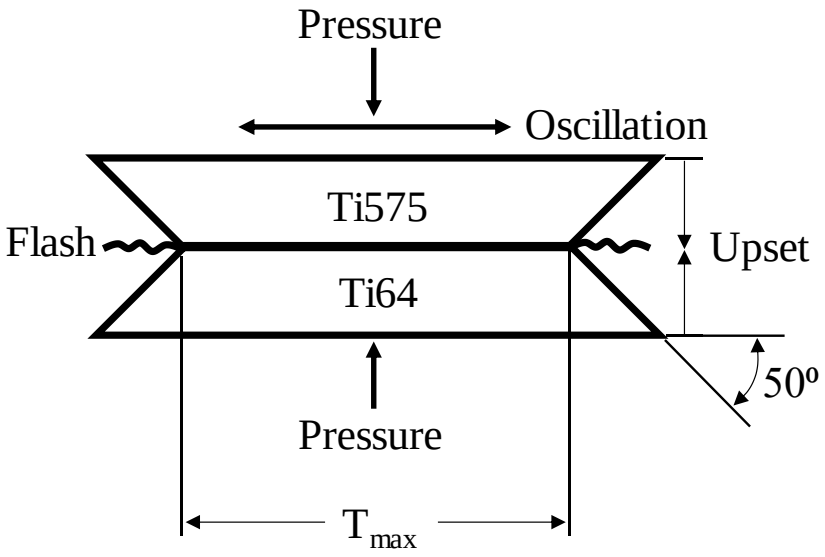

Figure 3.1 Schematic illustration of linear friction welding process and the weld geometry used in this study.

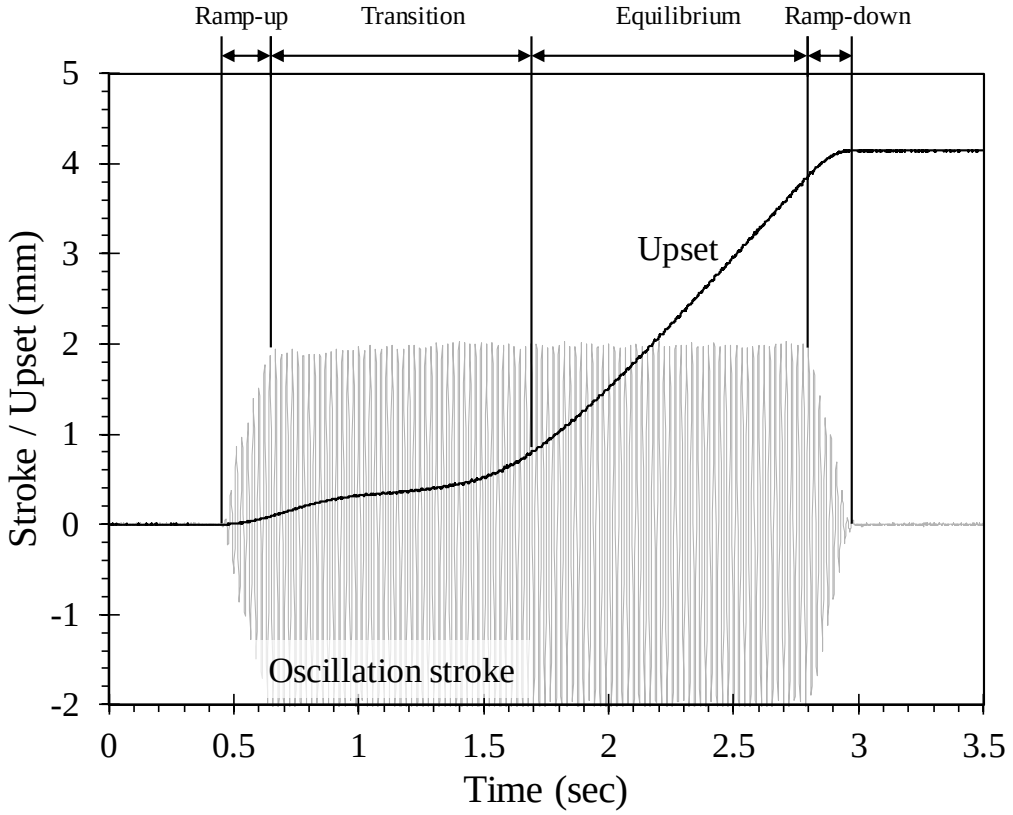

Figure 3.2 The oscillation stroke and upset curves during LFW process. Four distinct phases in LFW can be identified from these curves.

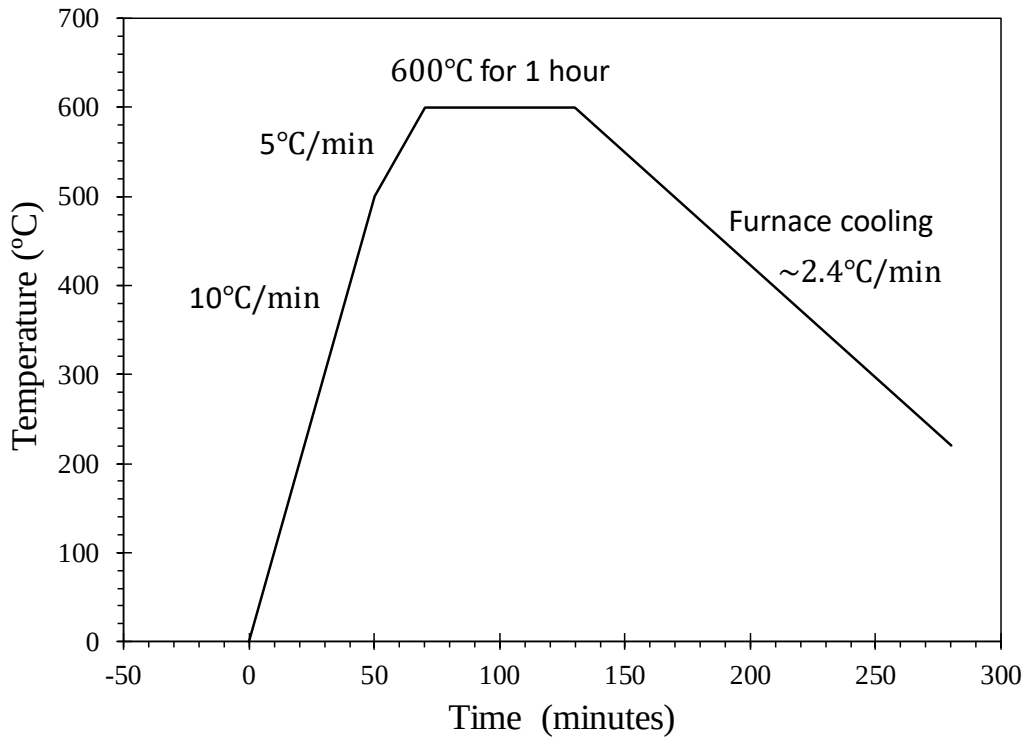

Figure 3.3 Schematic temperature profile of a PWHT at 600°C for 1 hour.

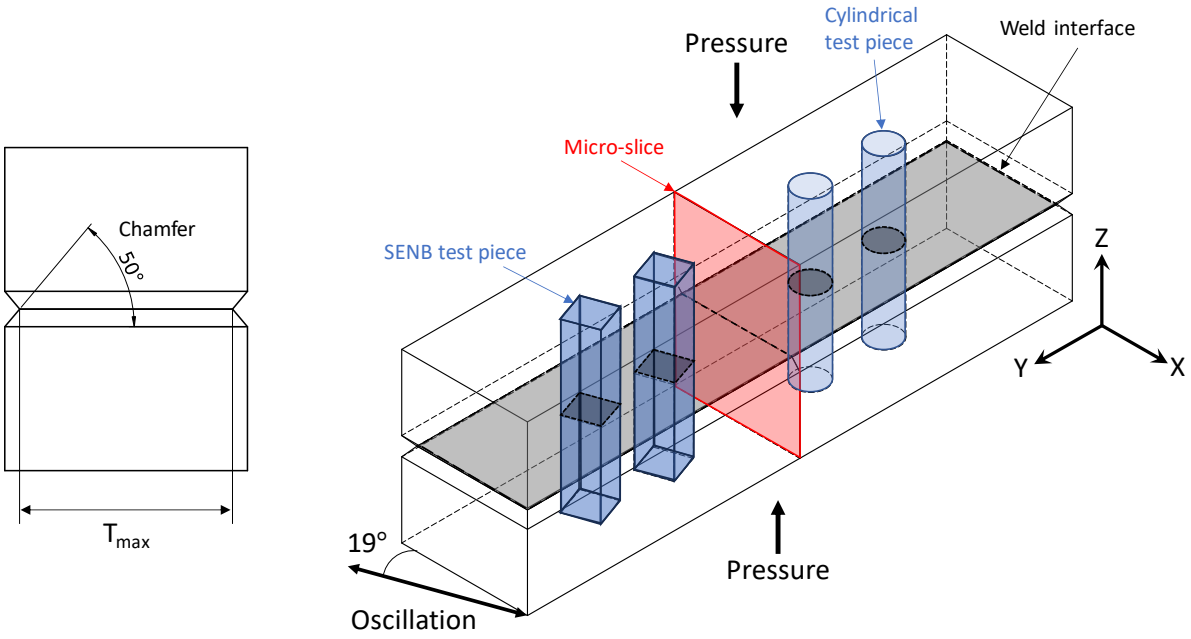

Figure 3.4 Schematic illustration of the orientation of test pieces and samples extraction with respect to the oscillation direction.

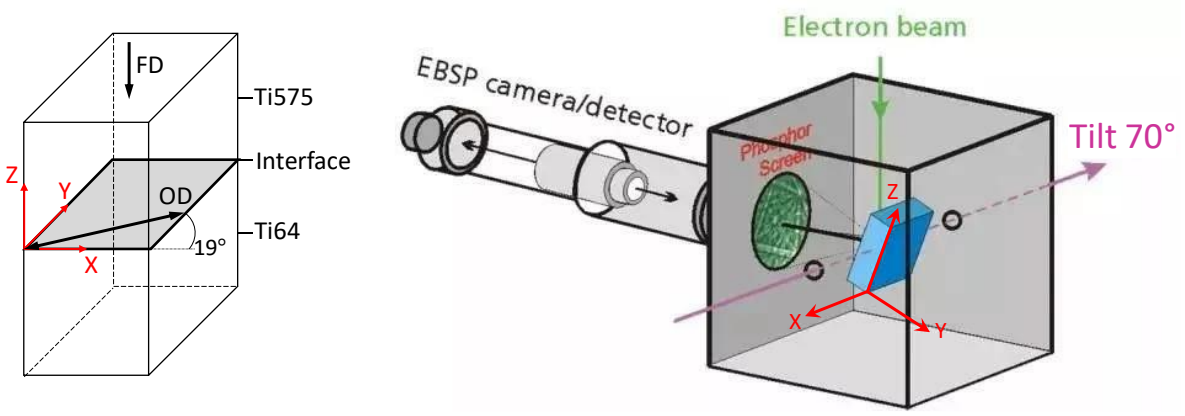

Figure 3.5 Schematic illustration of the sample coordination used in EBSD measurements. (FD: forge direction, OD: oscillation direction)

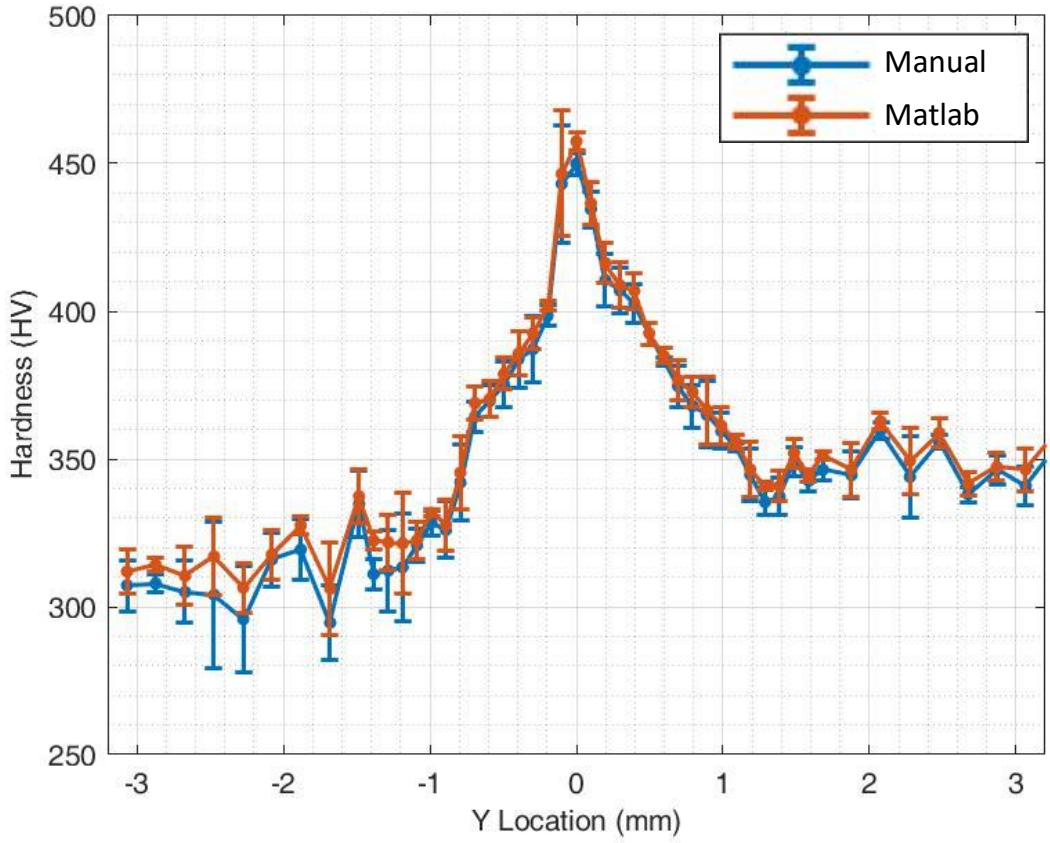

Figure 3.6 Validation result for automatic indent size recognition MATLAB® script. The maximum difference between manual measurement and the script is less than 3%.

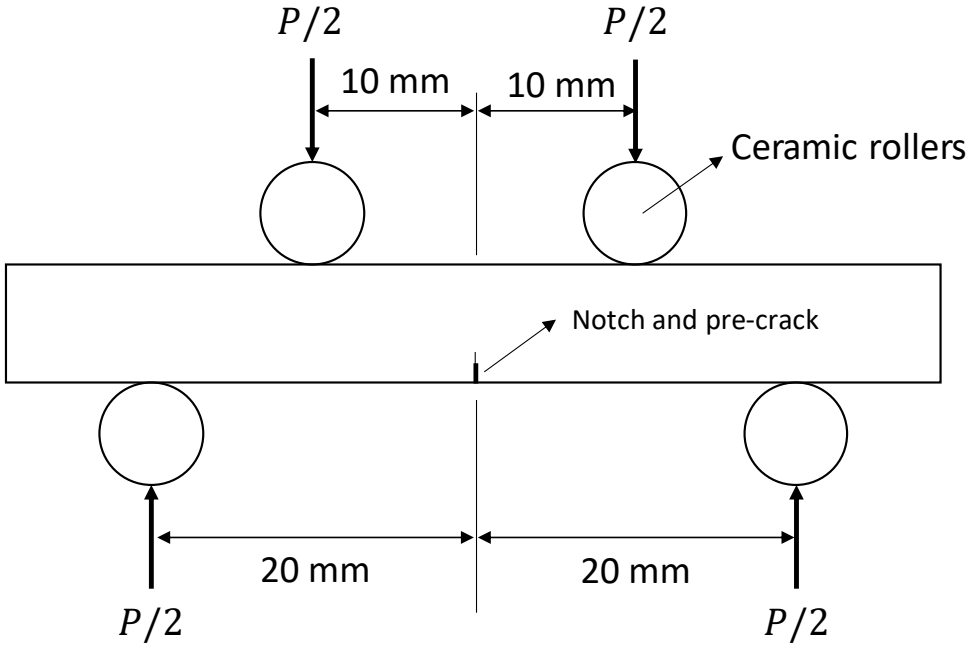

Figure 3.7 Four-point bending test configuration (Modified from [12]).

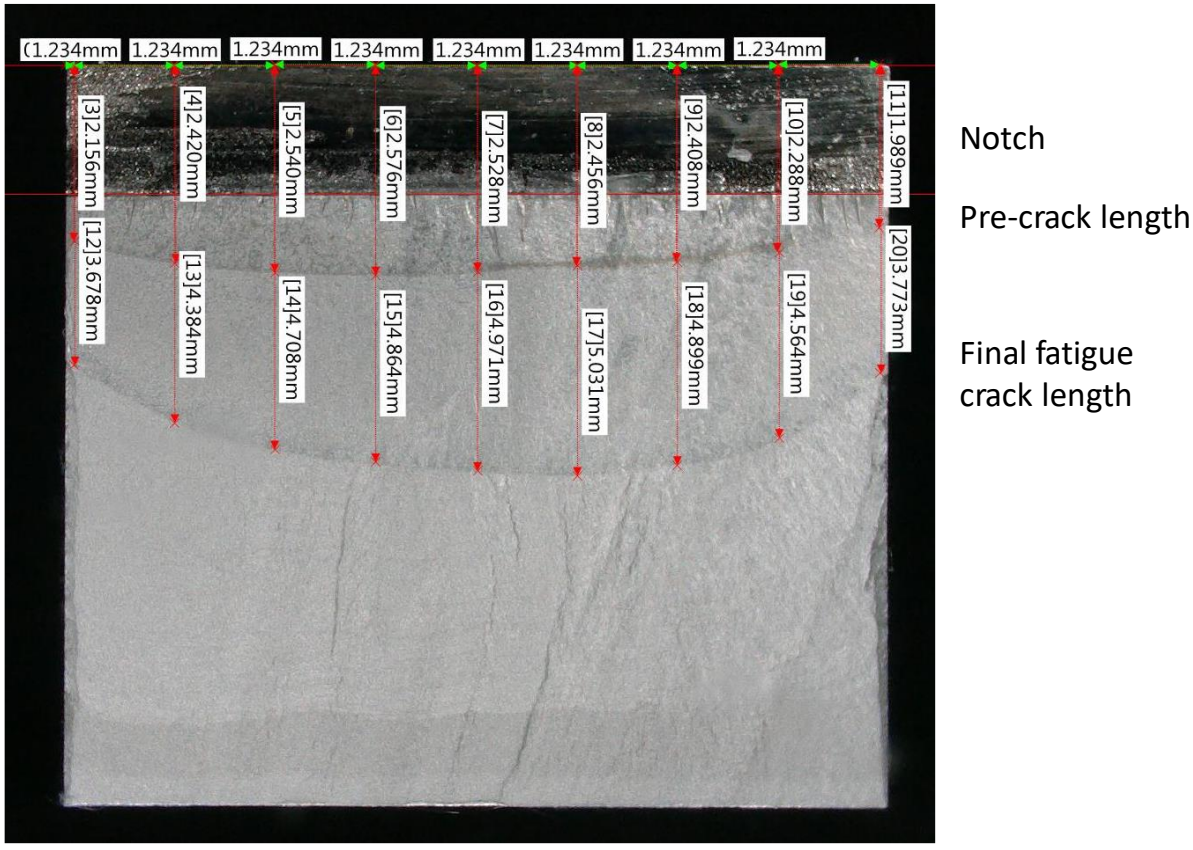

Figure 3.8 An example of the crack length measurement on the fracture surface.

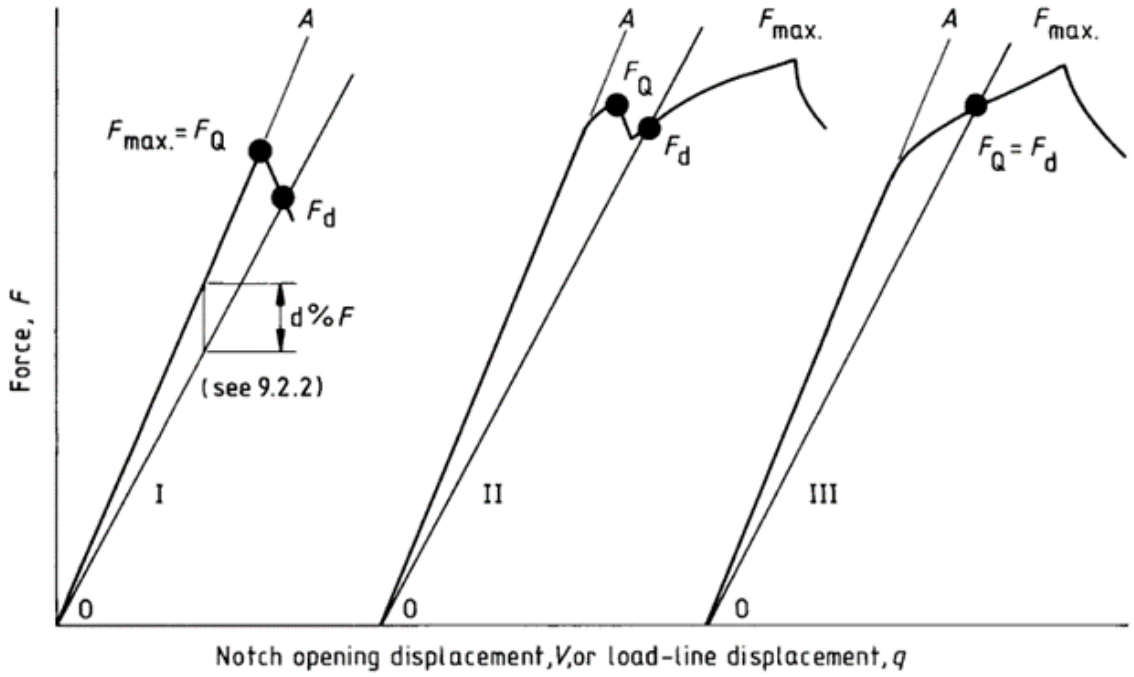

Figure 3.9 Schematic diagram of 95% secant method and the definition of P_Q (Denoted as F_Q in the diagram) [191].

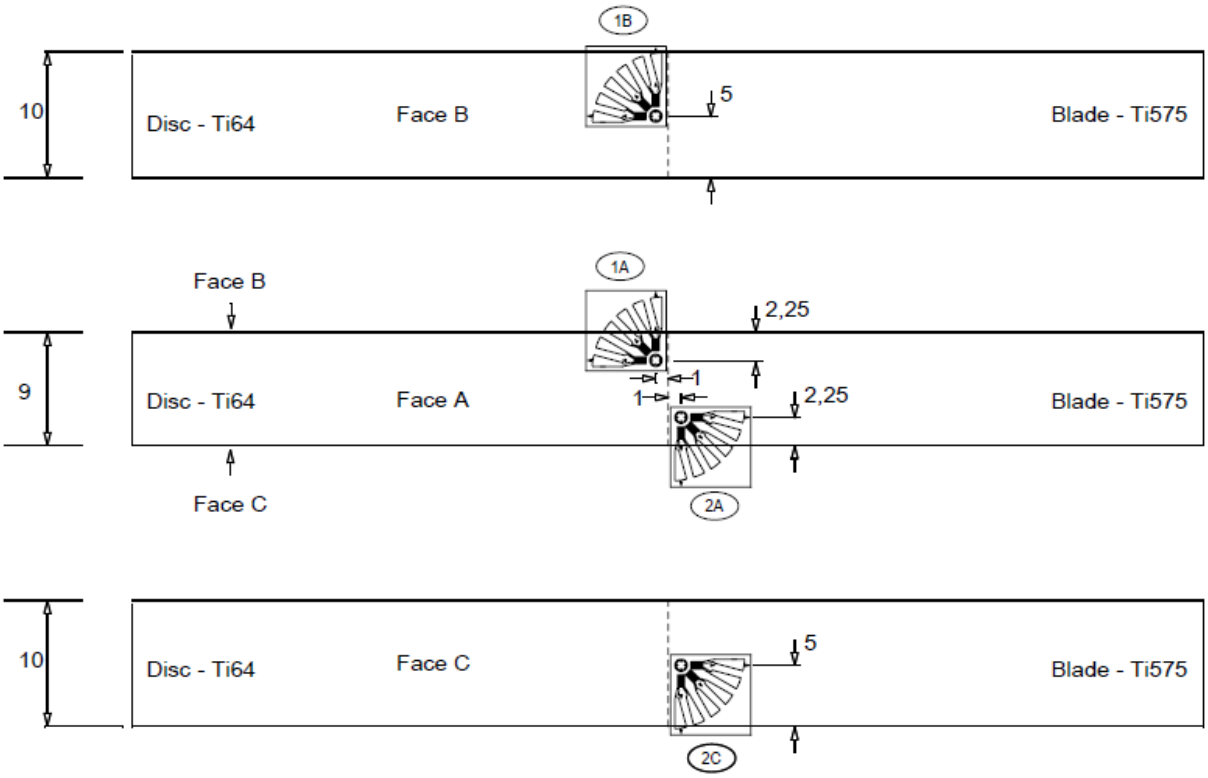

Figure 3.10 Schematic diagram of the location of residual stress measurements. The dashed line denotes the weld interface. (Unit: mm)

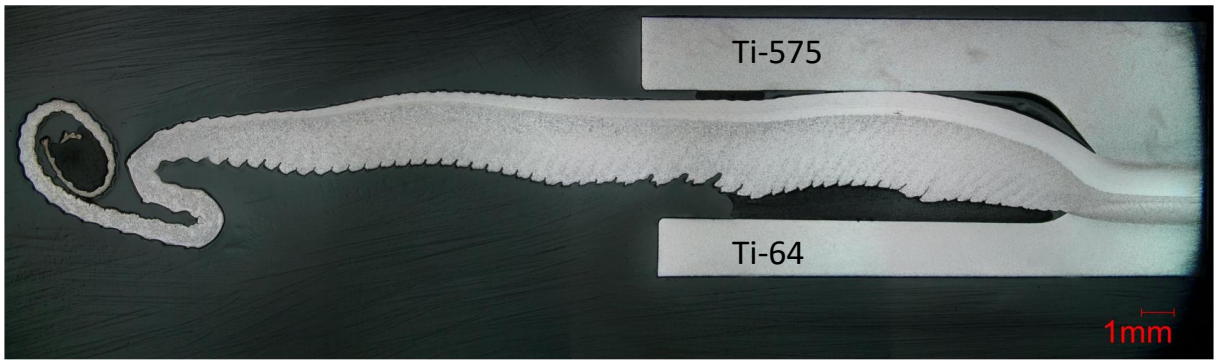

Figure 3.11 An optical macrograph of the flash.

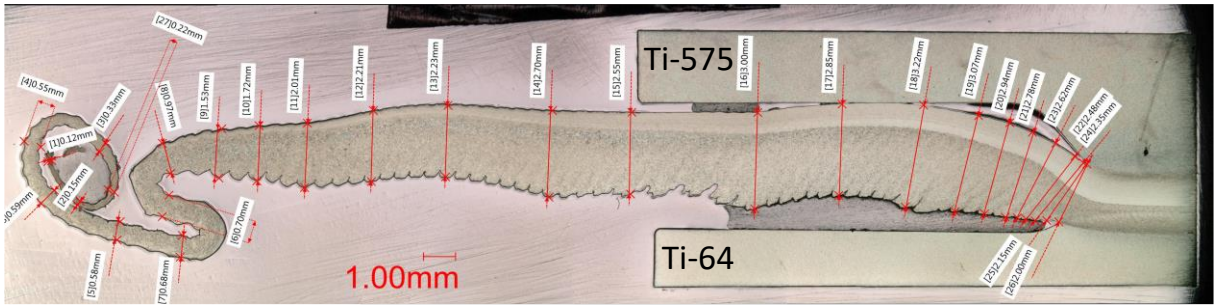

Figure 3.12 An example of flash thickness measurement of Figure 3.11.

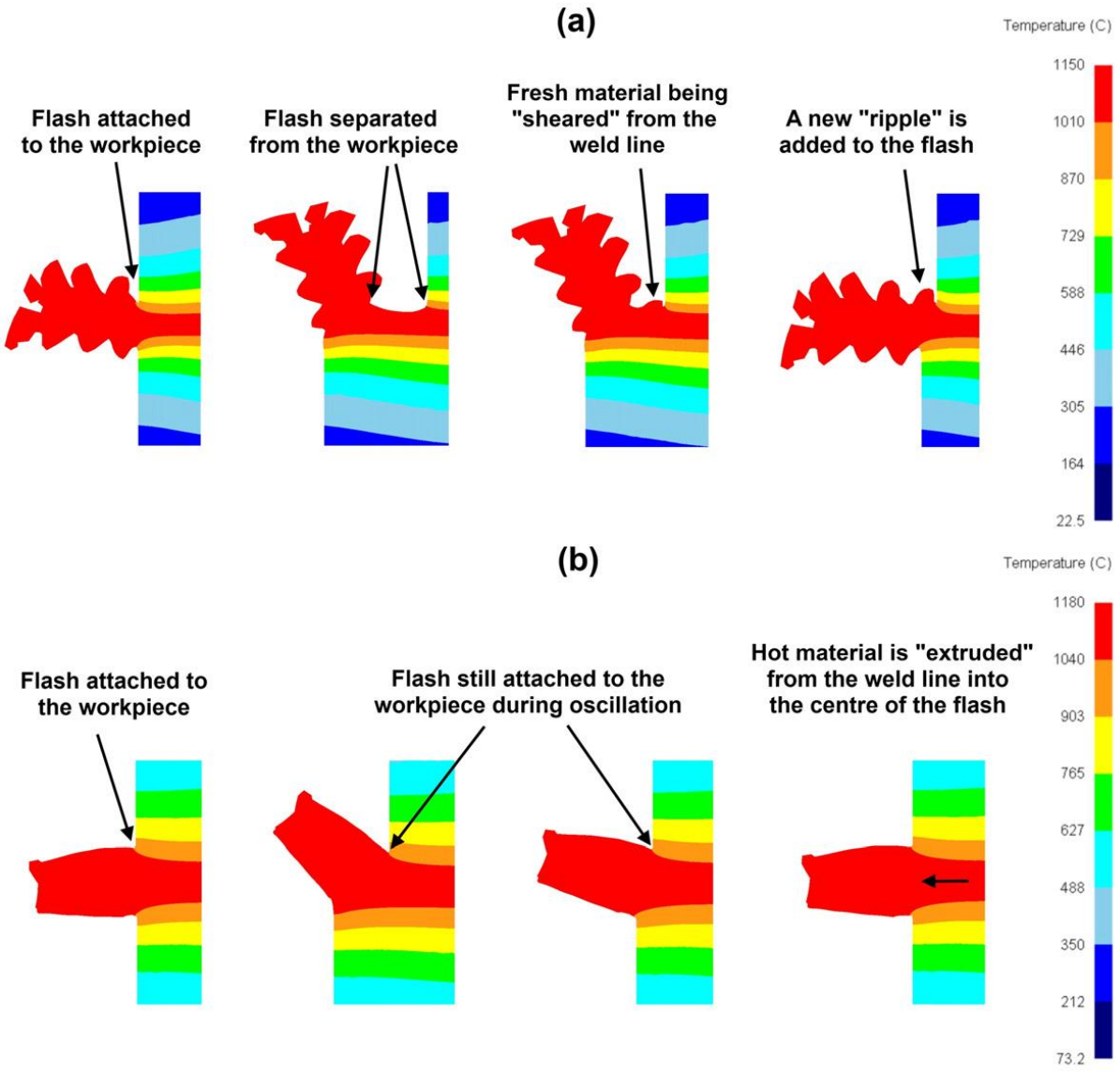

Figure 3.13 Ridge formation mechanism simulated by finite element analysis [135].

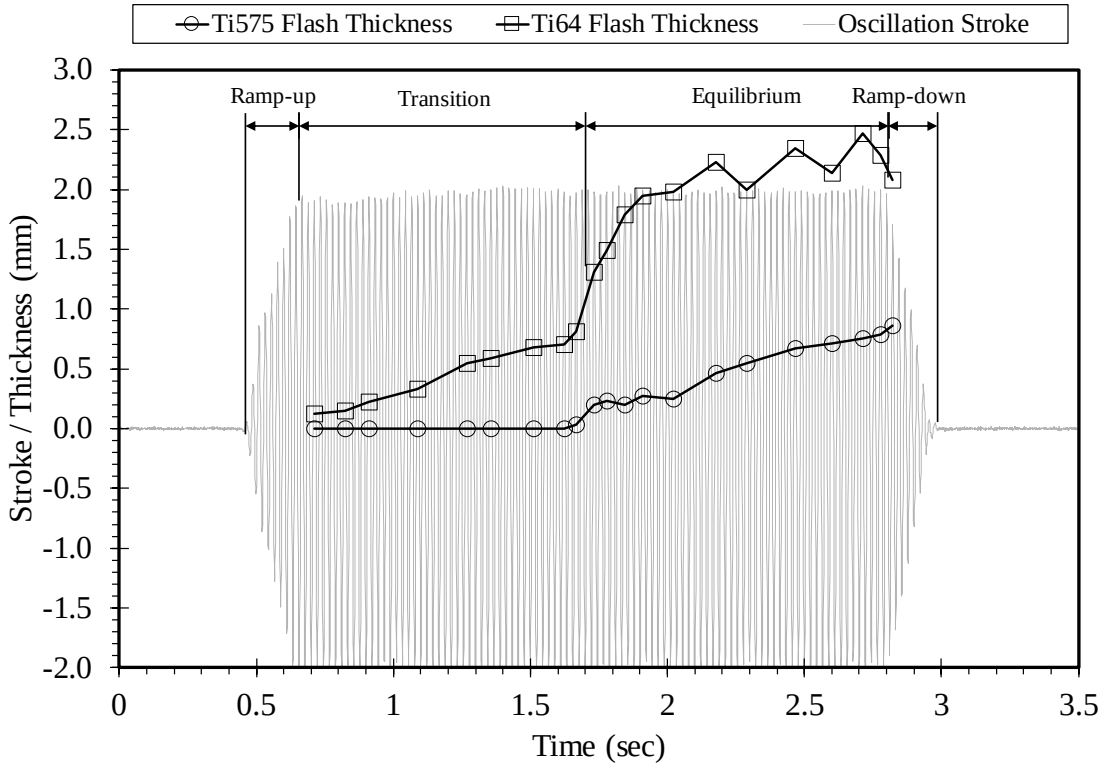

Figure 3.14 An example of flash thickness measurement overlaps onto the oscillation stroke by correlating the ridges and cycle count.

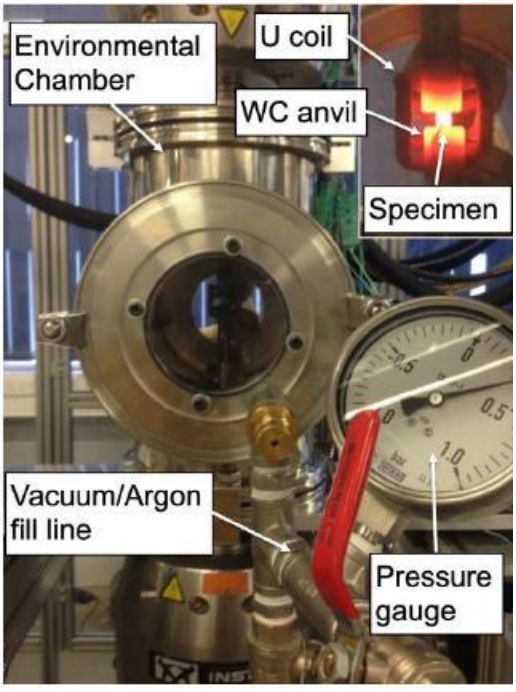

Figure 3.15 Photograph of the experimental setup of flow stress testing.

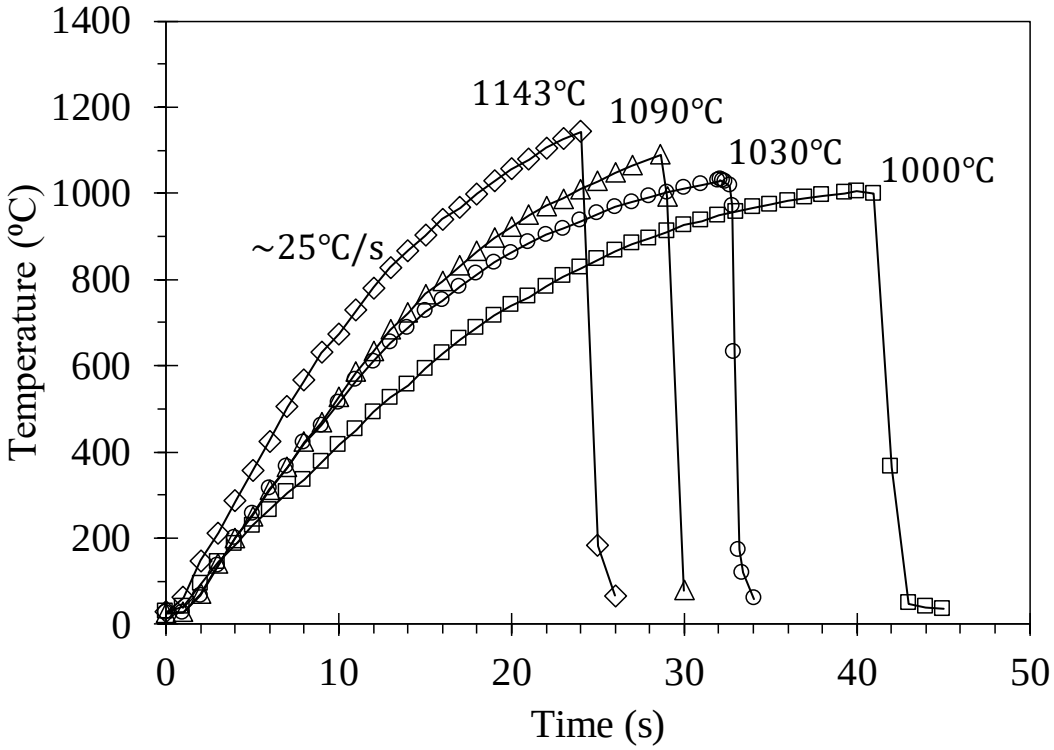

Figure 3.16 Temperature profiles of dynamic beta approach heat treatments.

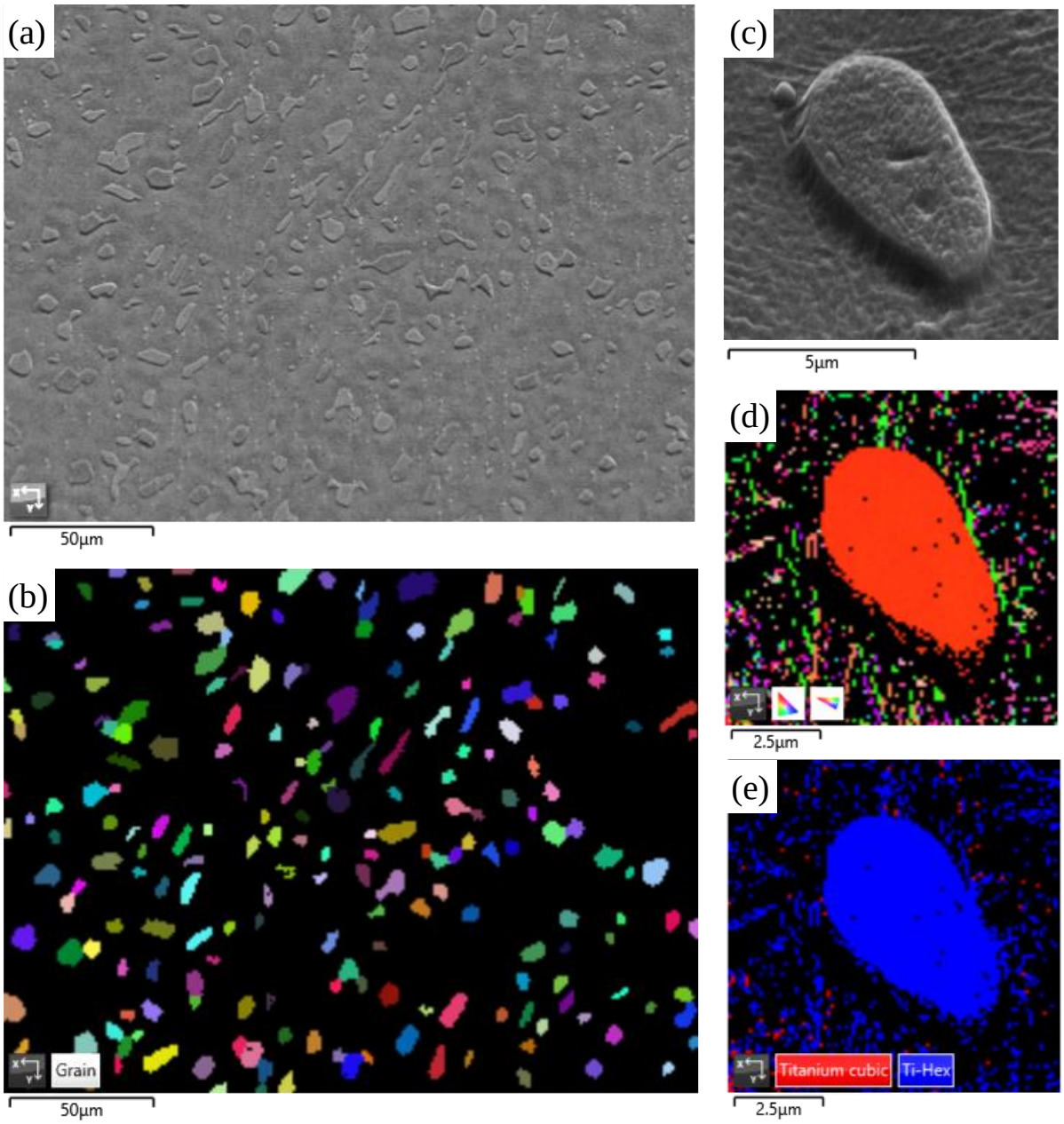

Figure 3.17 (a) A SEI of Ti-575 after dynamic beta approach heat treatment at 1000°C. (b) The corresponding EBSD grain map. (c) A high magnification SEI of one retained α_p grain. (d) The corresponding EBSD orientation map of the retained α_p grain. (e) The corresponding EBSD phase map of the retained α_p grain.

Chapter 4

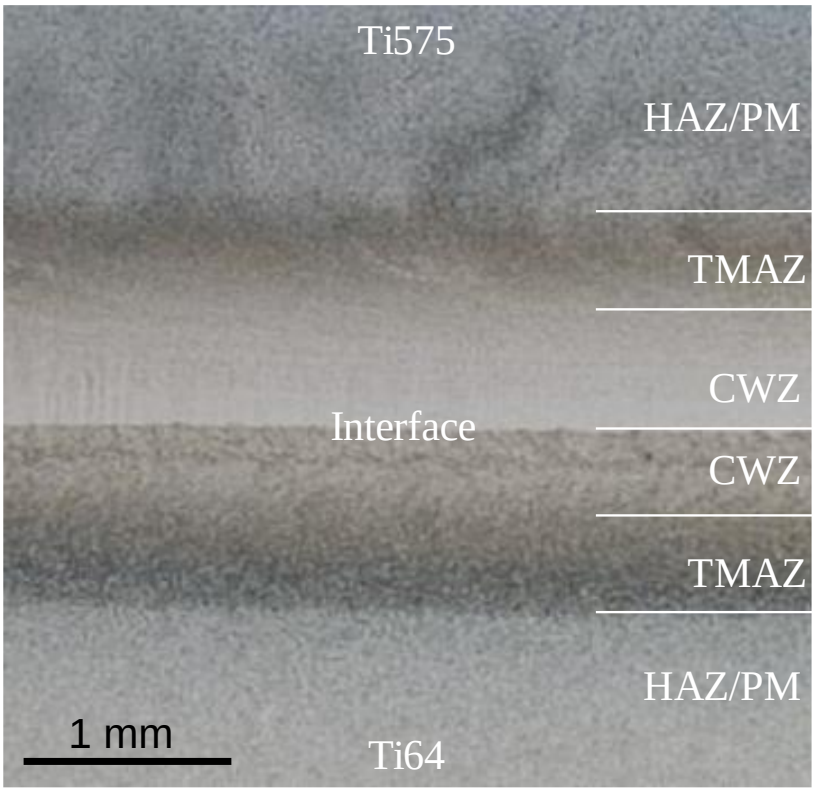

Figure 4.1 Optical micrograph of a Ti-64:Ti-575 linear friction weld in as-welded condition. Each weld zone can be distinguished by its appearance in the micrograph.

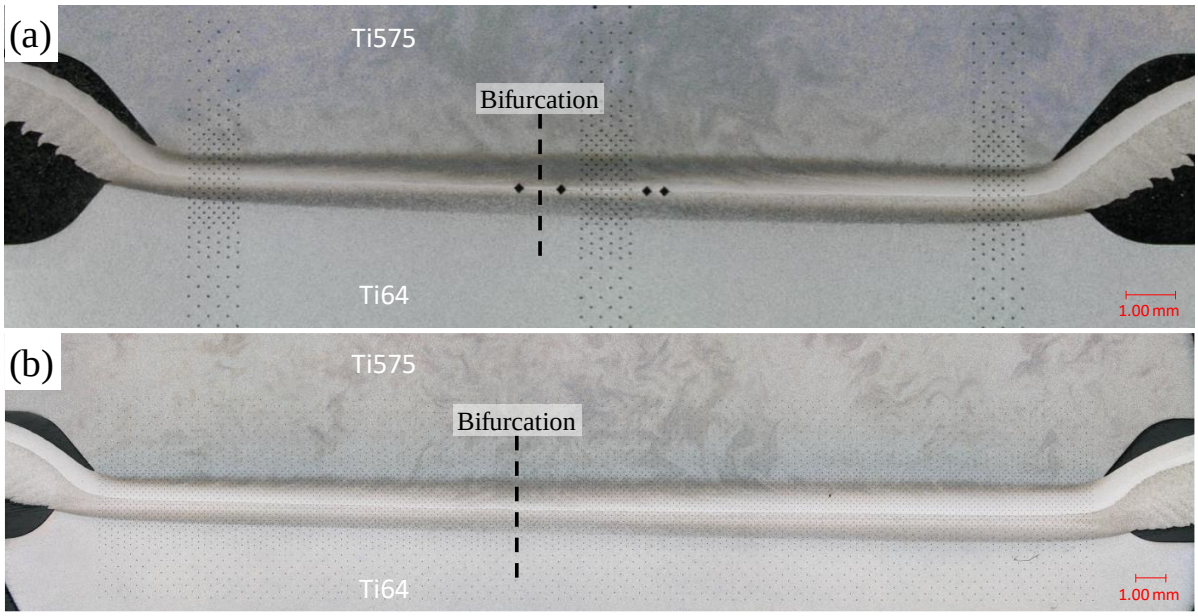

Figure 4.2 Macro images of as-welded Ti-64:Ti-575 linear friction welds. (a) T_{max} = 18 mm, Weld ID = 473-05; (b) T_{max} = 32 mm, Weld ID = 473-03.

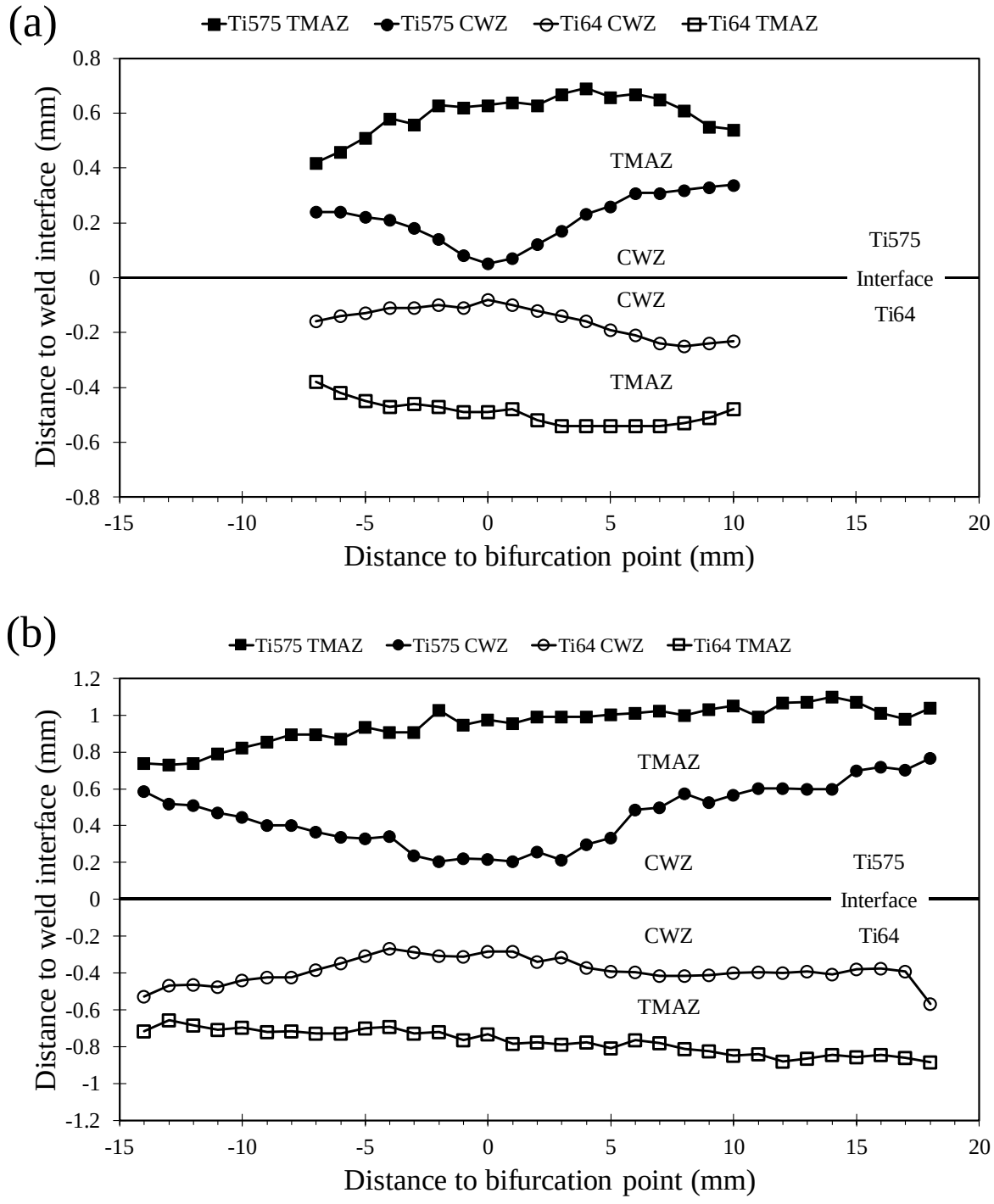

Figure 4.3 Zone size measurement for Ti-64:Ti-575 linear friction welds. (a) $T_{max} = 18$ mm, Weld ID = 473-05; (b) $T_{max} = 32$ mm, Weld ID = 473-03.

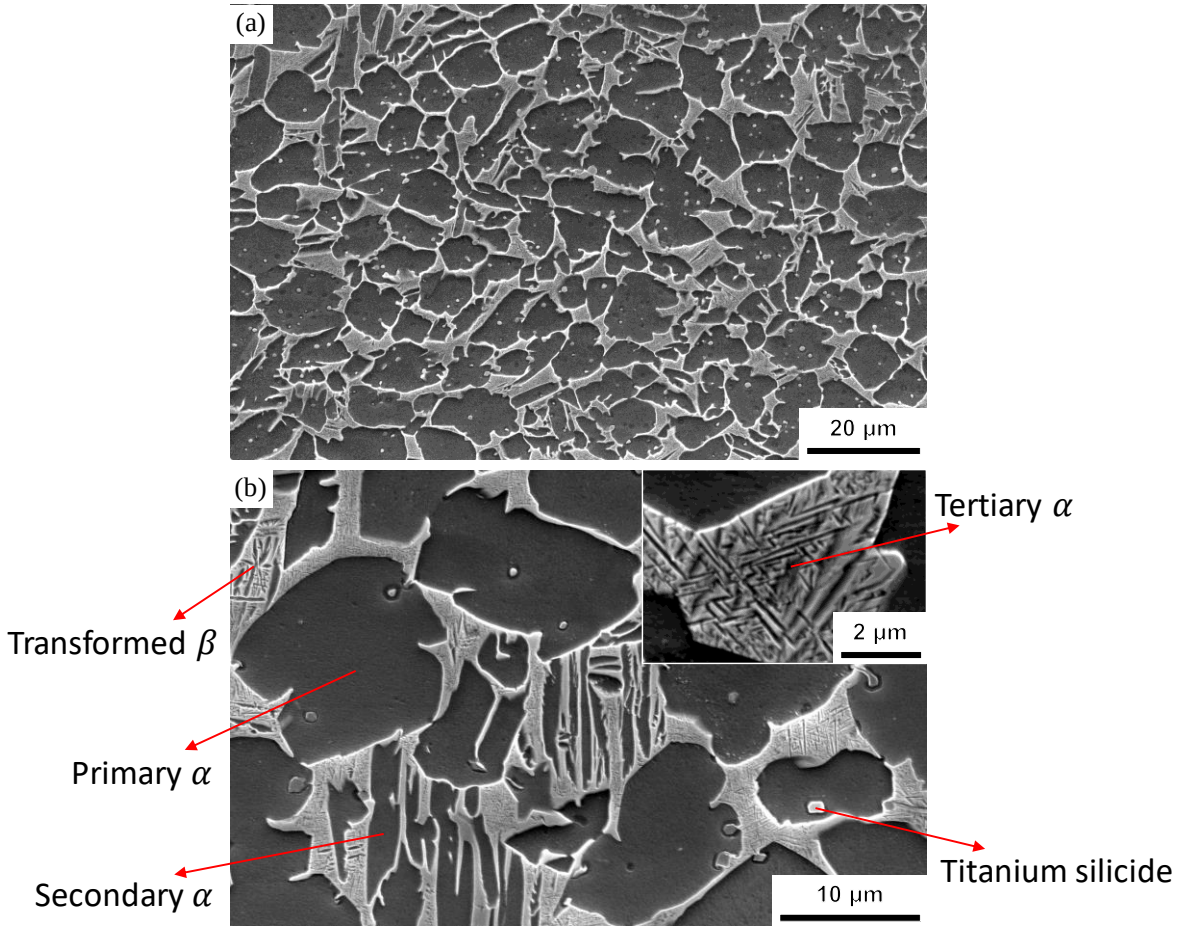

Figure 4.4 (a) Low and (b) high magnification secondary electron images of Ti-575 parent material. α and β phase in SEI appears dark and bright, respectively.

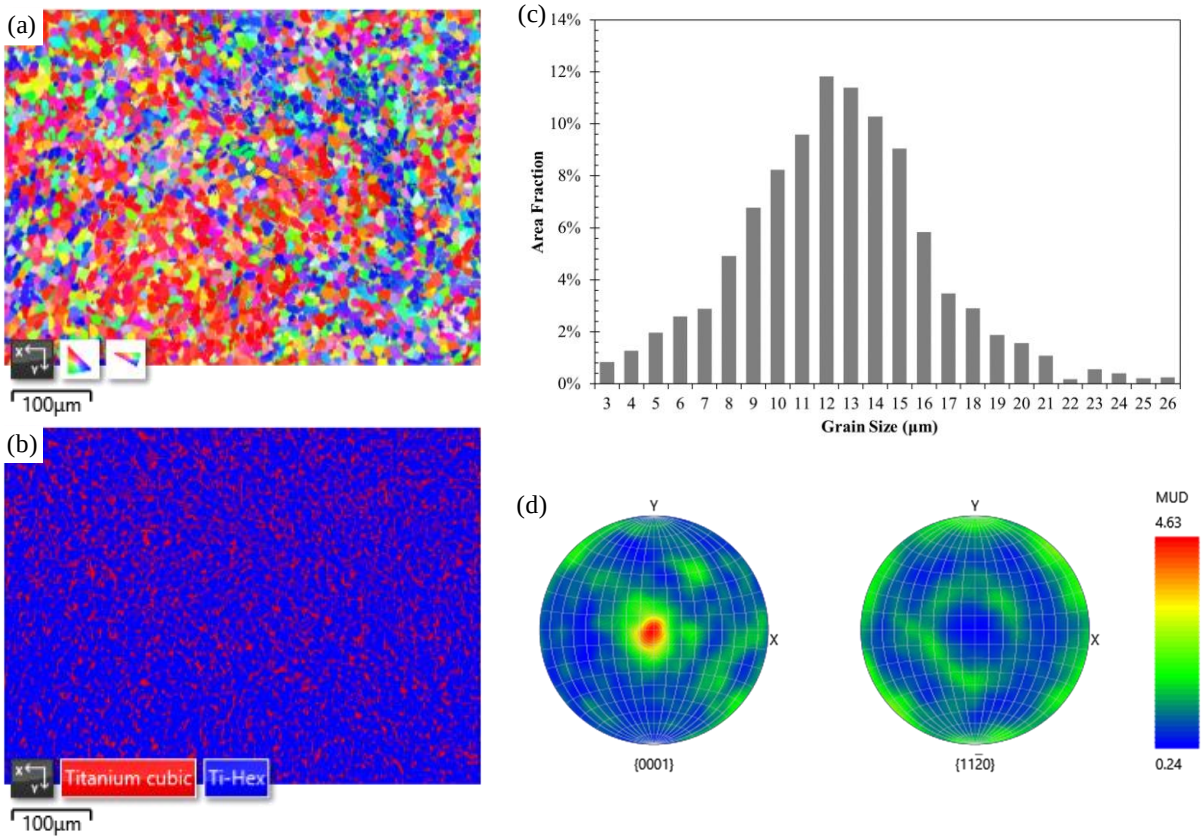

Figure 4.5 EBSD mapping for grain size analysis for Ti-575. (a) Orientation map. (b) Phase map. (c) Primary α grain size distribution. (d) Pole figures of $\{0001\}$ and $\{11\bar{2}0\}$ planes.

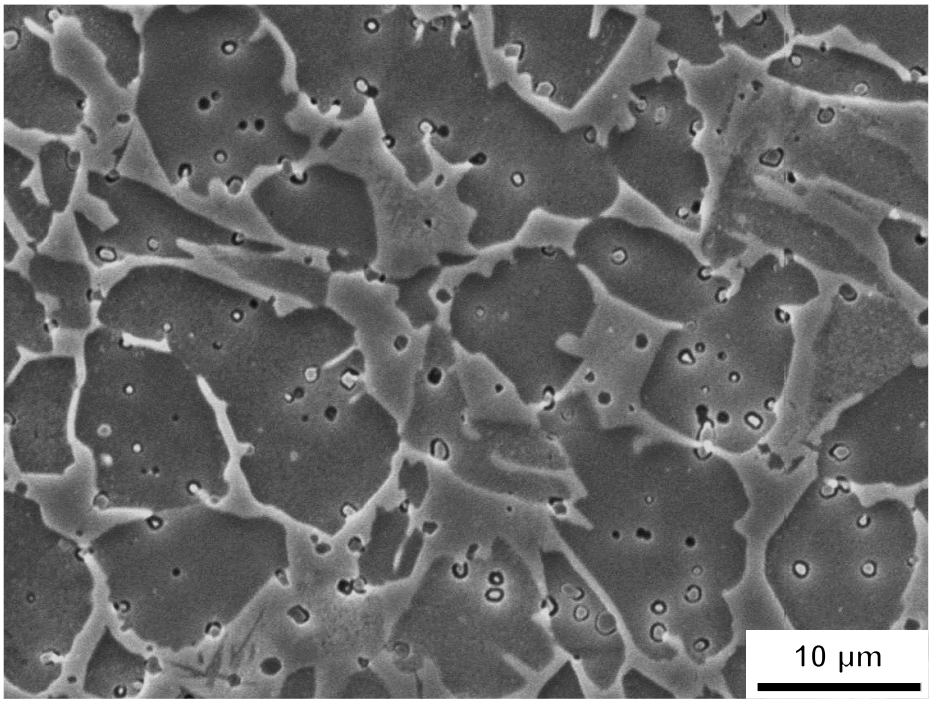

Figure 4.6 Secondary electron image of the HAZ of Ti-575 side in as-welded condition.

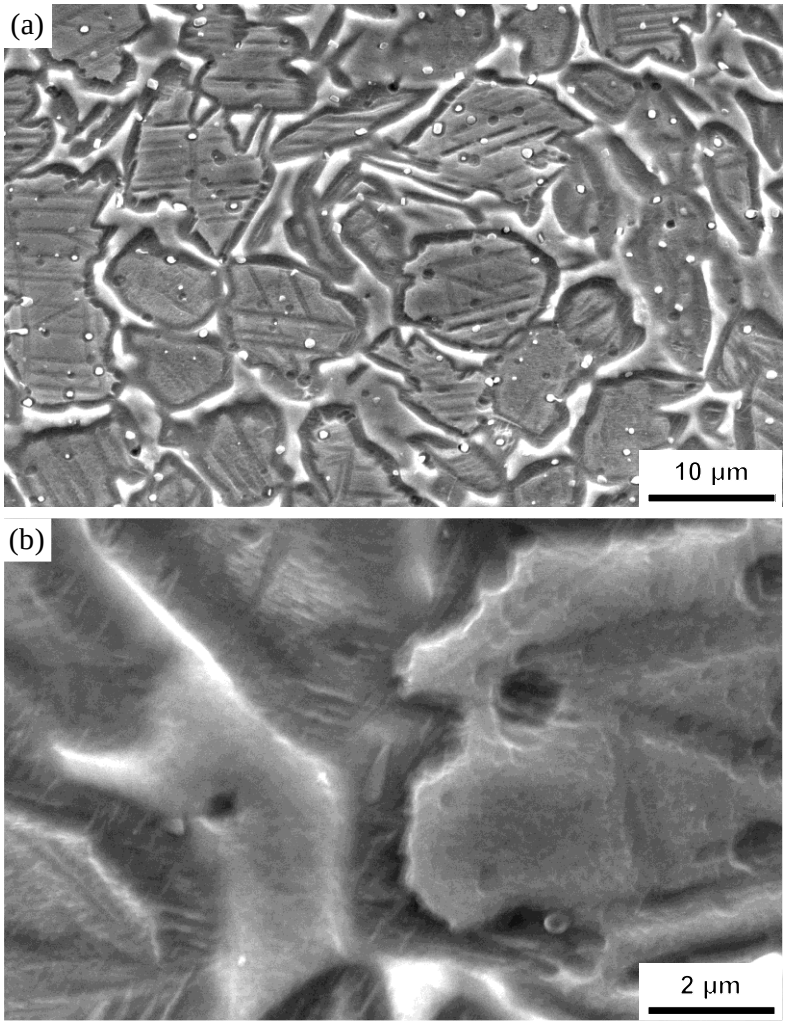

Figure 4.7 (a) Low magnification and (b) high magnification secondary electron image of outer TMAZ of Ti-575 in as-welded condition.

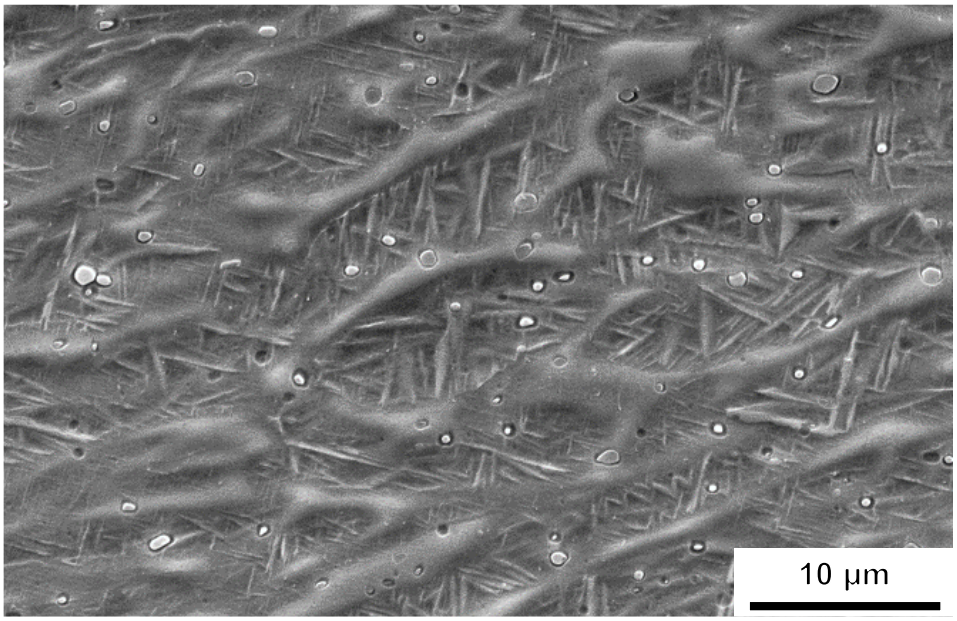

Figure 4.8 Secondary electron image of inner TMAZ in Ti-575 in as-welded condition.

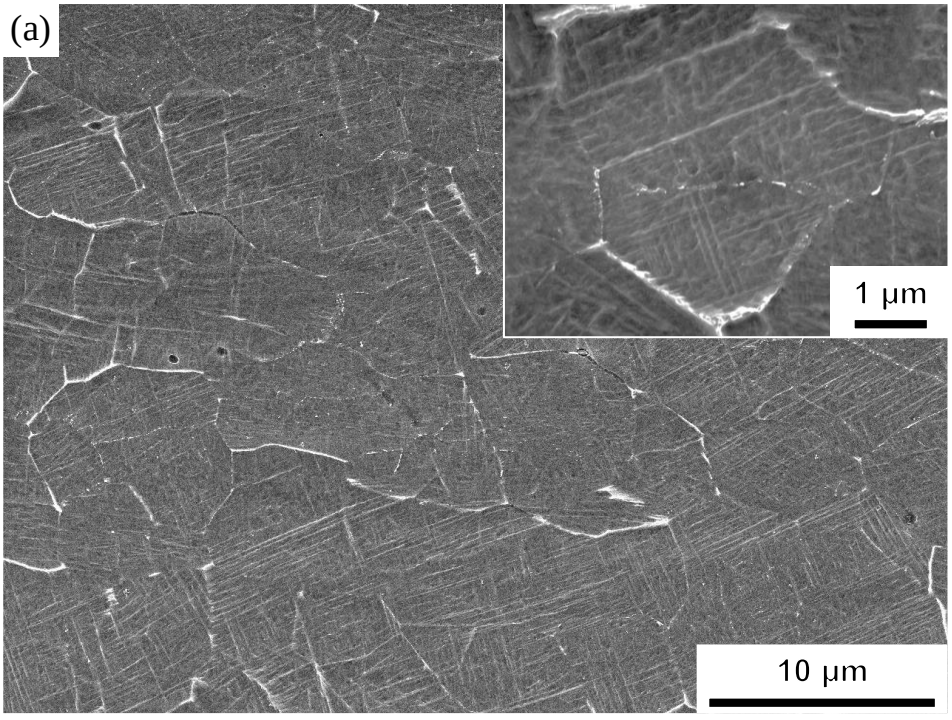

Figure 4.9 Secondary electron image of CWZ in Ti-575 in as-welded condition.

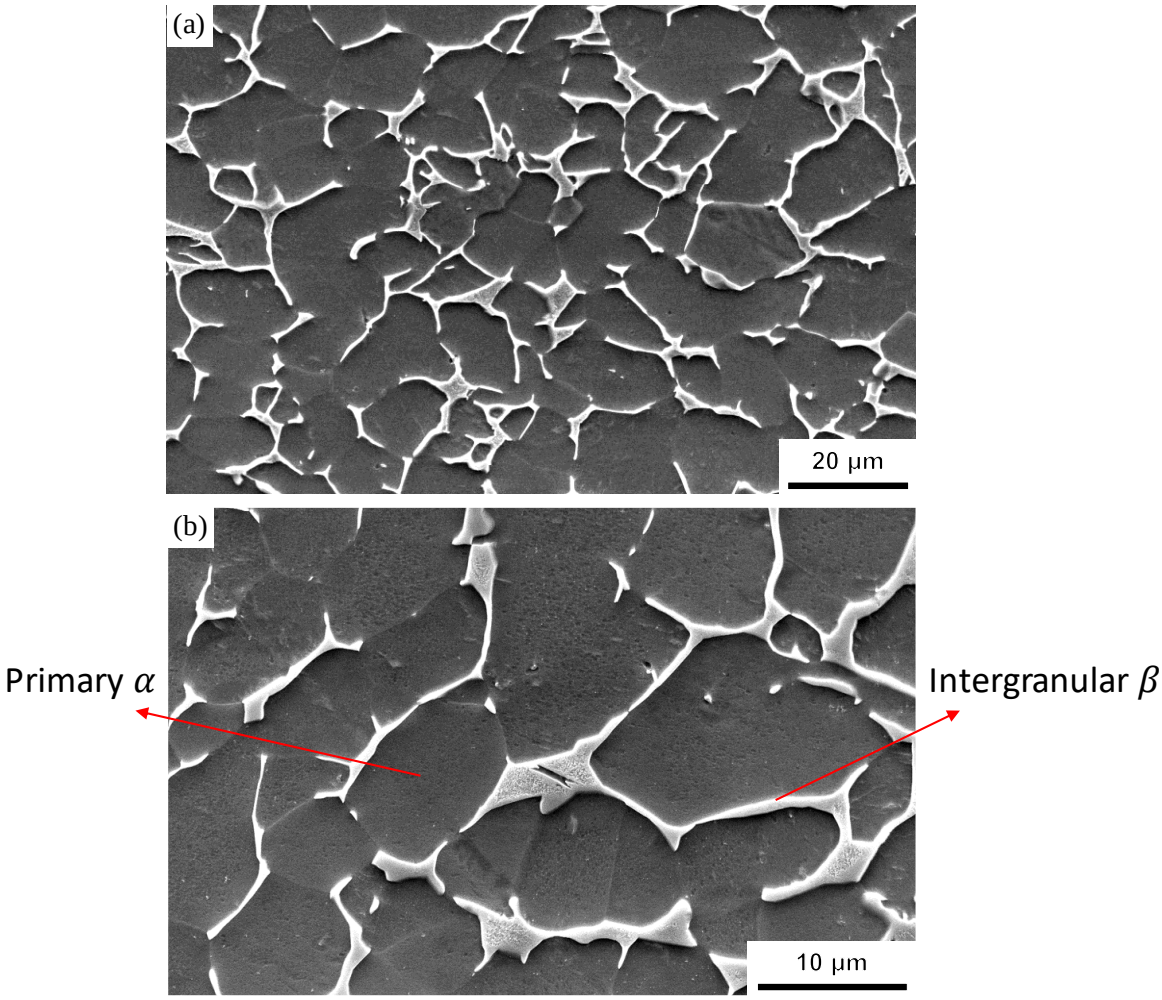

Figure 4.10 (a) Low and (b) high magnification secondary electron images of Ti-64 parent material. α and β phase in SEI appears dark and bright, respectively.

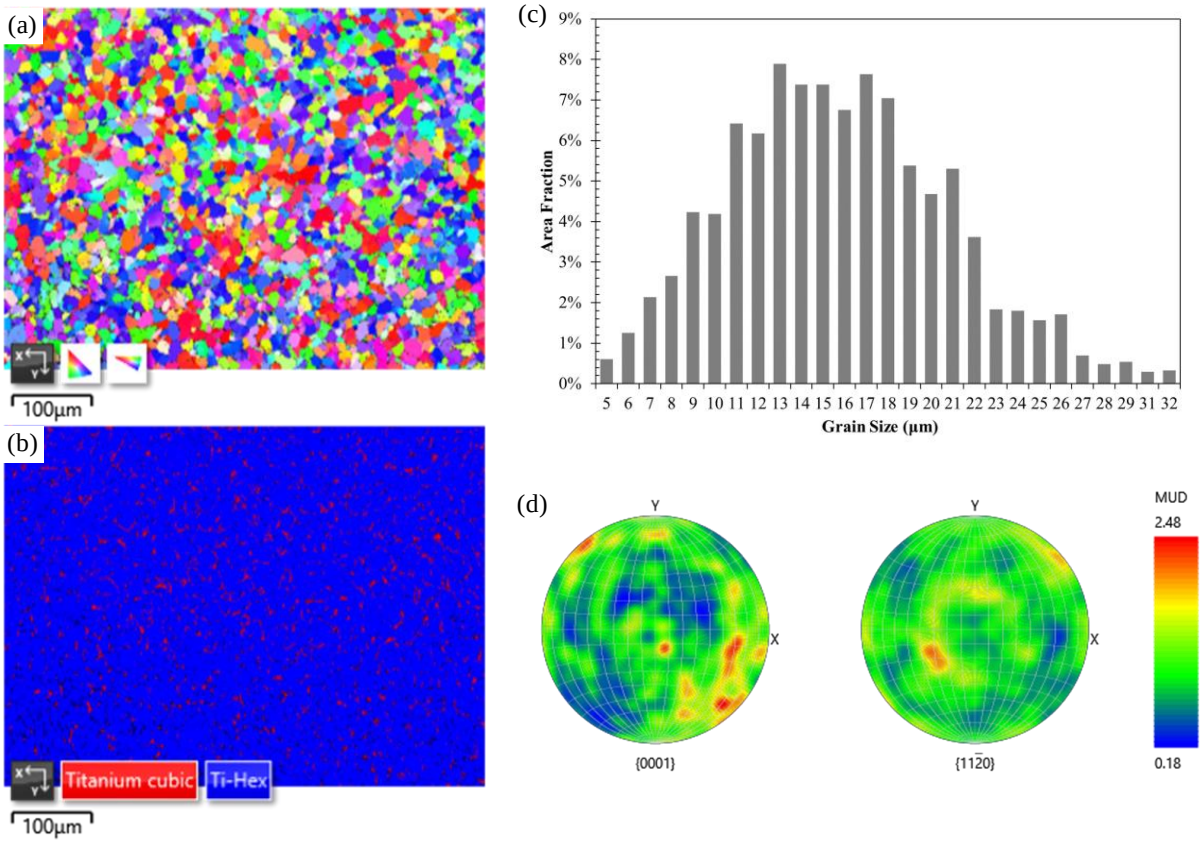

Figure 4.11 EBSD mapping for grain size analysis for Ti-64. (a) Orientation map. (b) Phase map. (c) Primary α grain size distribution. (d) Pole figures of $\{0001\}$ and $\{11\bar{2}0\}$ planes.

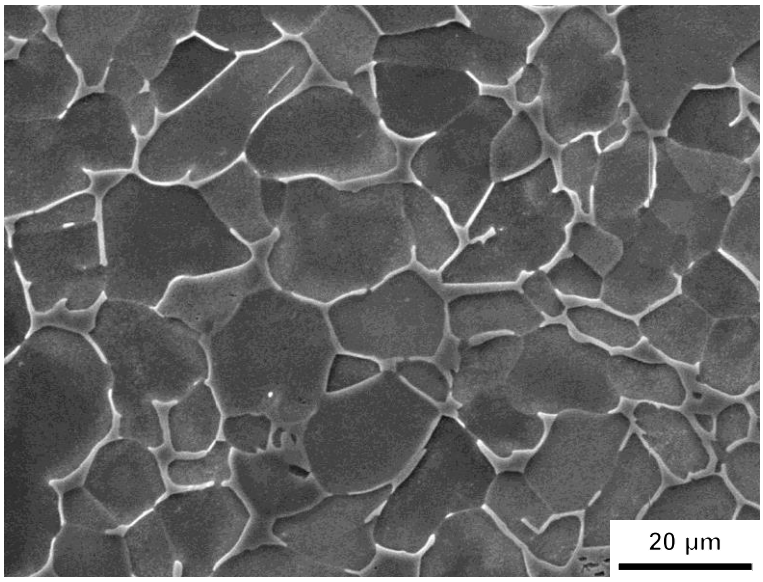

Figure 4.12 Secondary electron image of the HAZ of Ti-64 side in as-welded condition.

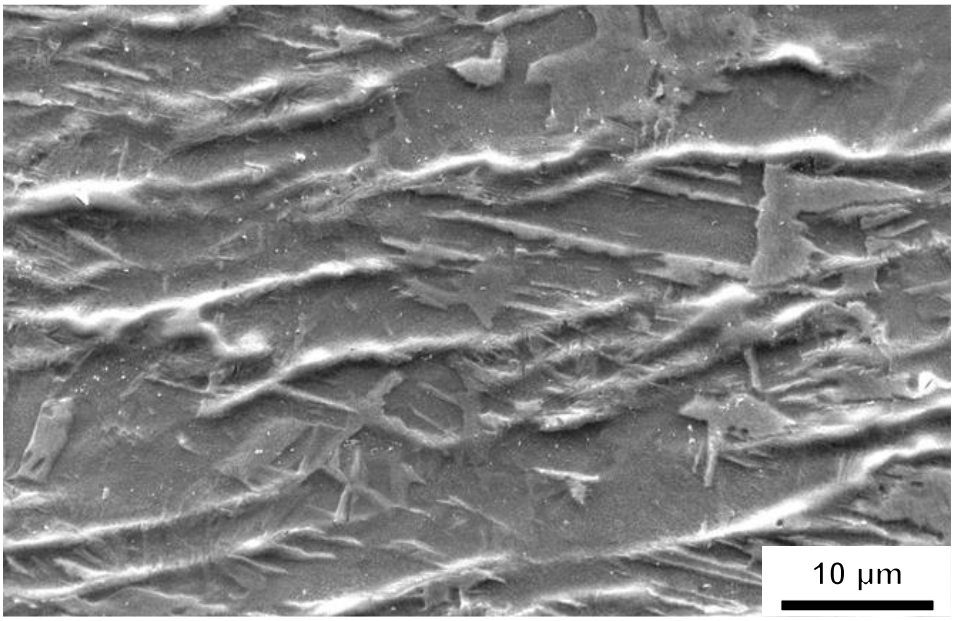

Figure 4.13 Secondary electron image of TMAZ in Ti-64 in as-welded condition.

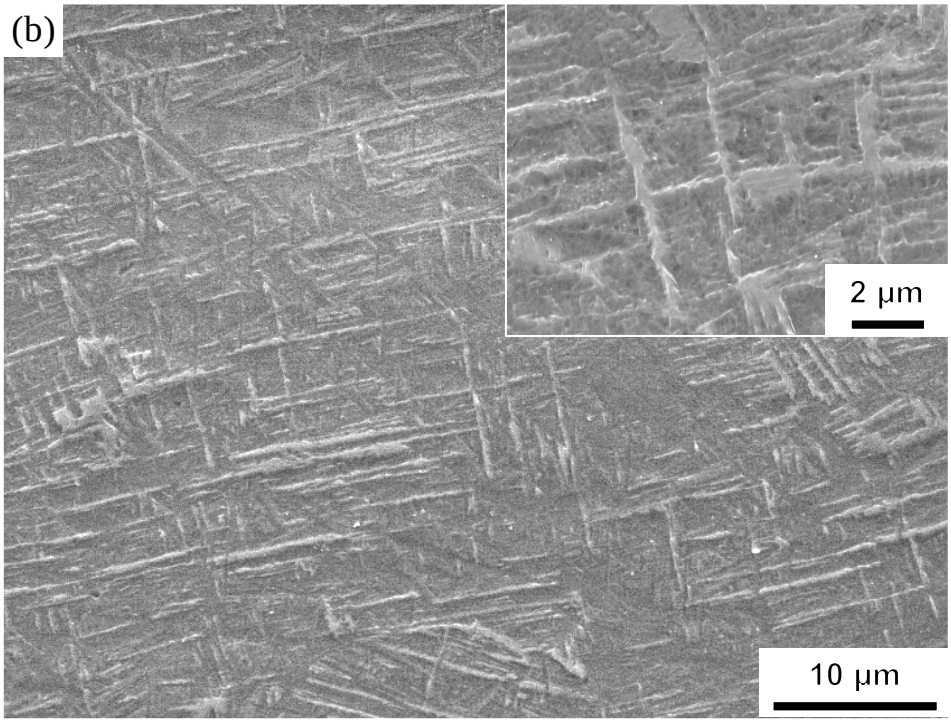

Figure 4.14 Secondary electron image of CWZ in Ti-64 in as-welded condition.

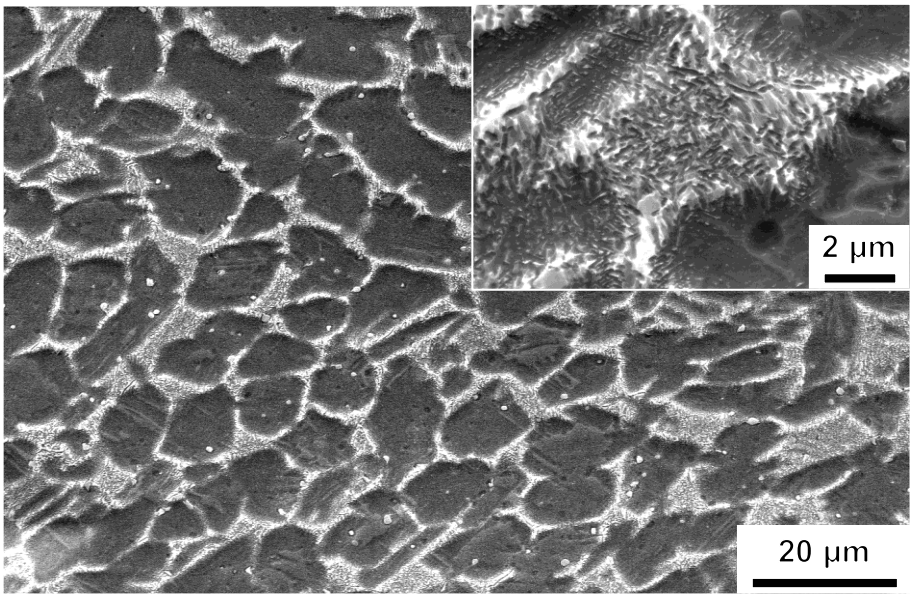

Figure 4.15 Secondary electron images of Ti-575 HAZ in PWHT'd condition.

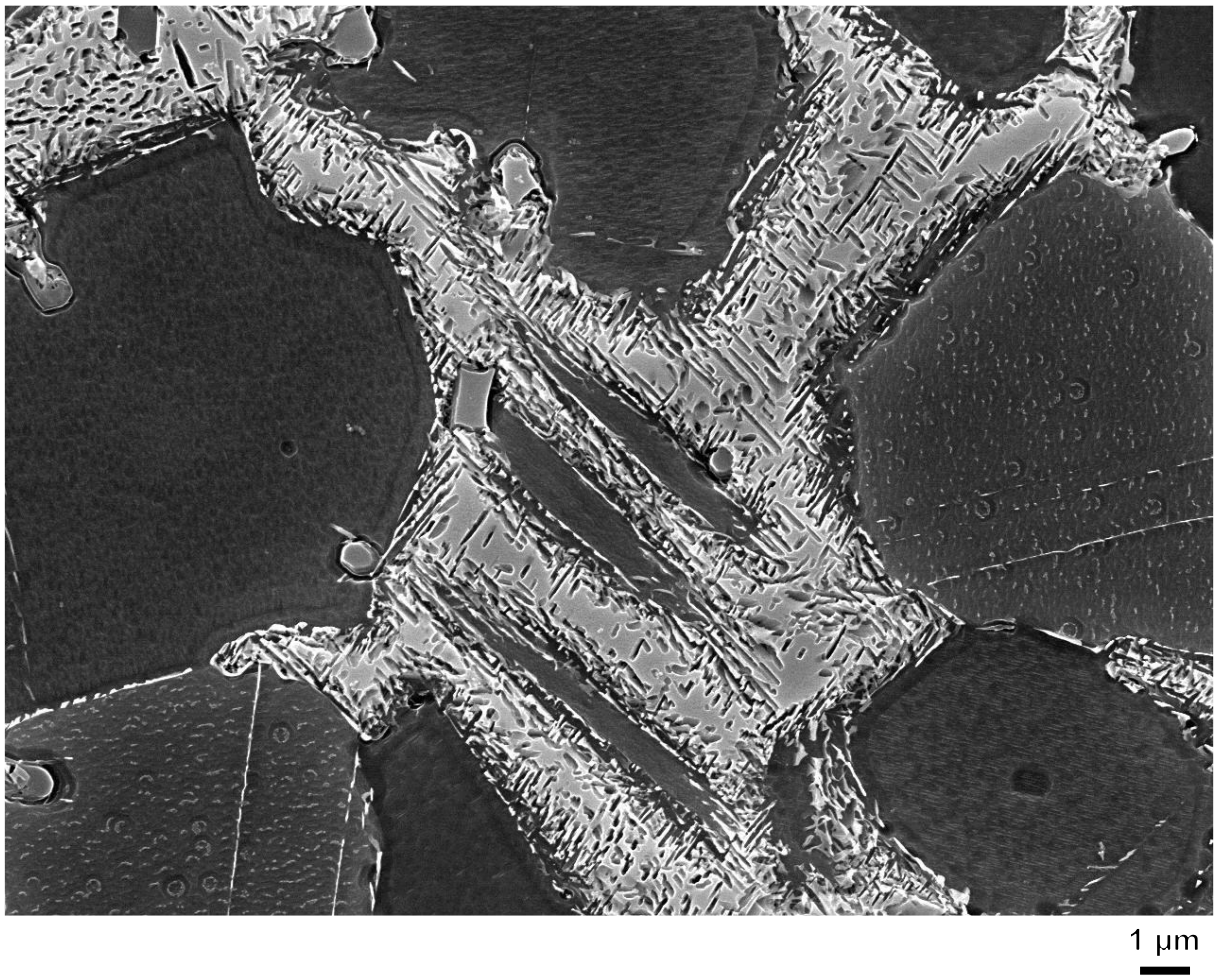

Figure 4.16 Secondary electron image of Ti-575 outer TMAZ in PWHT'd condition.

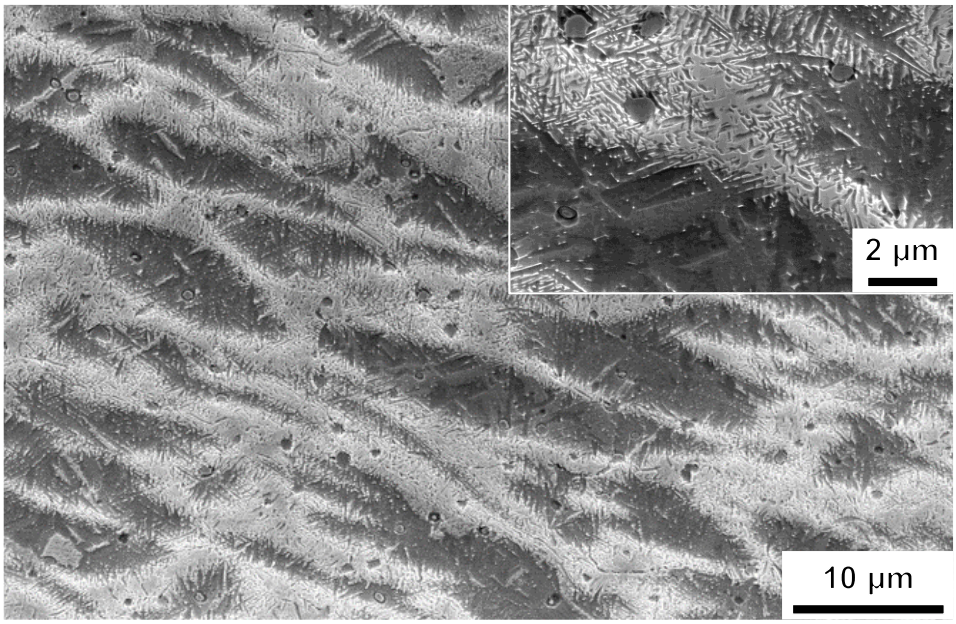

Figure 4.17 Secondary electron images of Ti-575 inner TMAZ in PWHT'd condition.

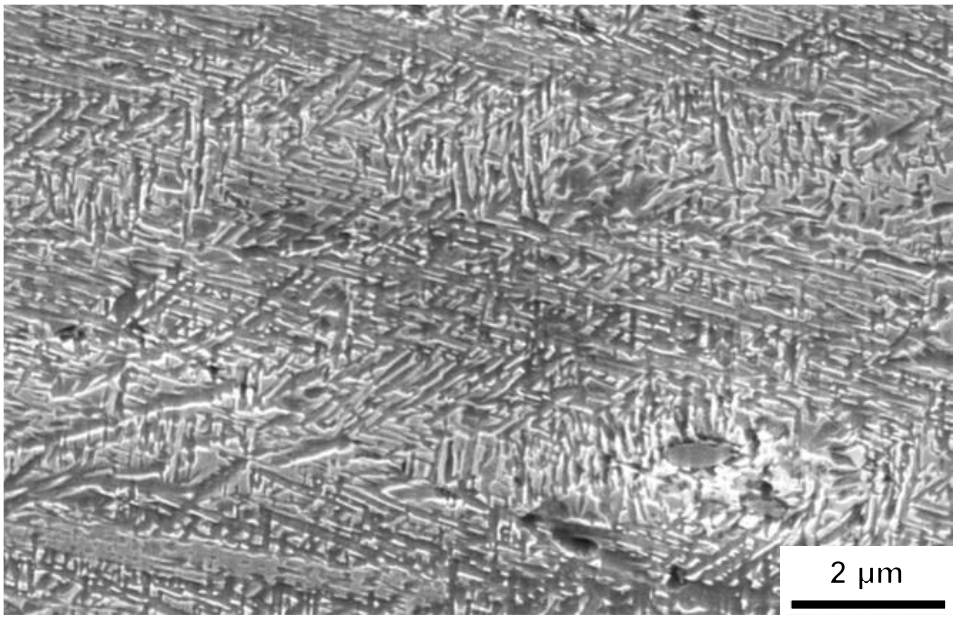

Figure 4.18 Secondary electron image of CWZ in Ti-575 in PWHT'd condition.

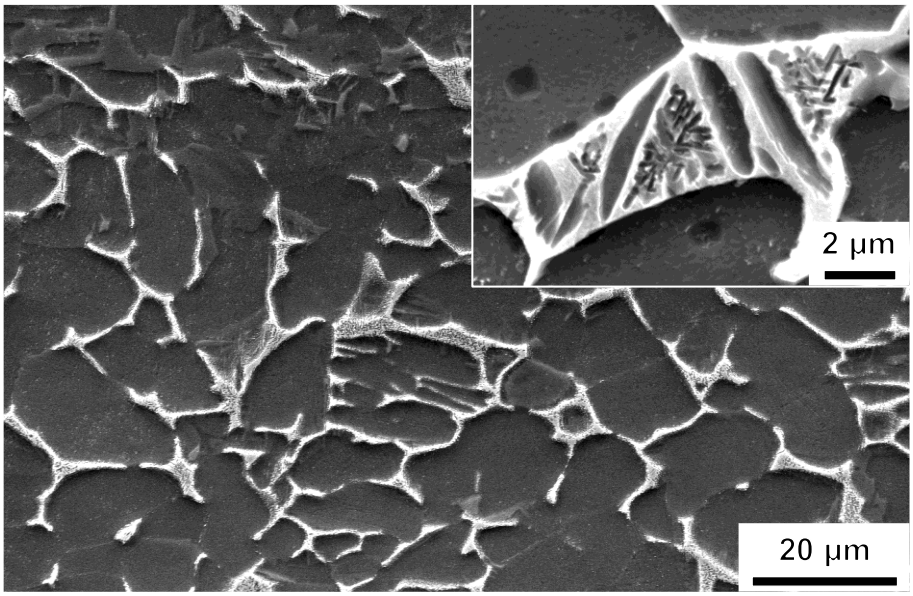

Figure 4.19 Secondary electron images of Ti-64 HAZ in PWHT'd condition.

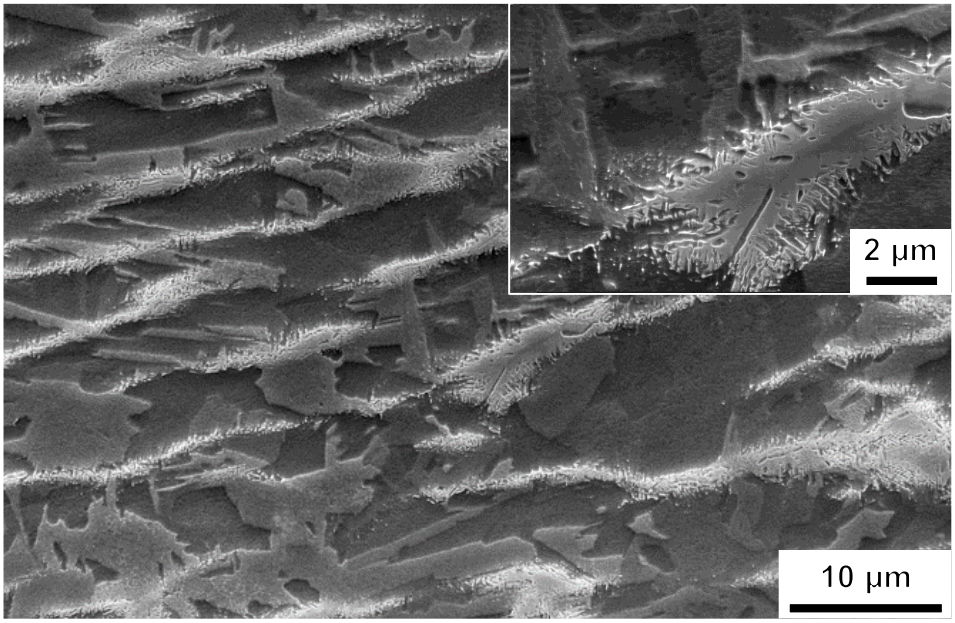

Figure 4.20 Secondary electron images of Ti-64 TMAZ in PWHT'd condition.

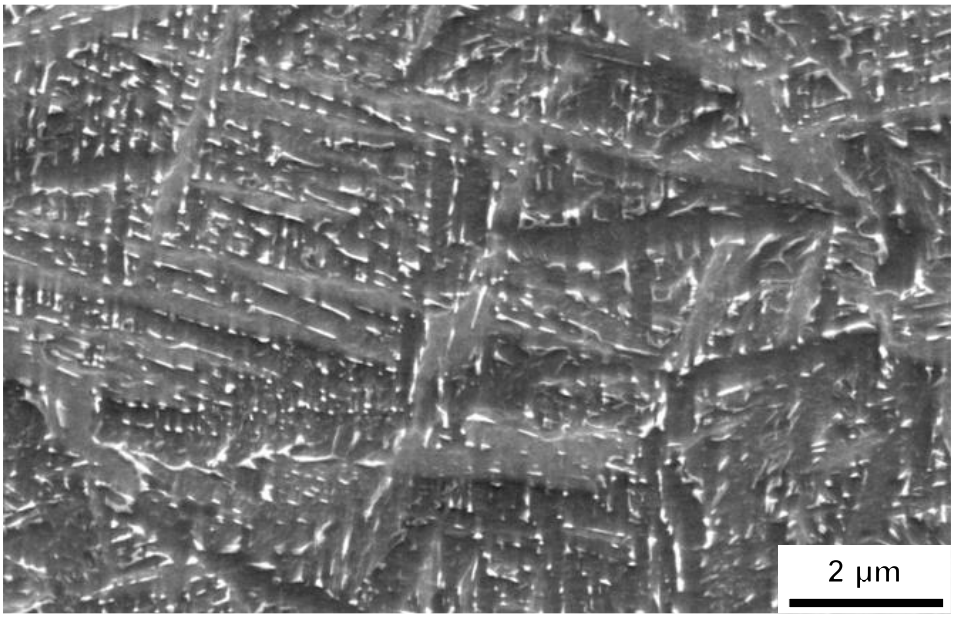

Figure 4.21 Secondary electron image of CWZ in Ti-64 in PWHT'd condition.

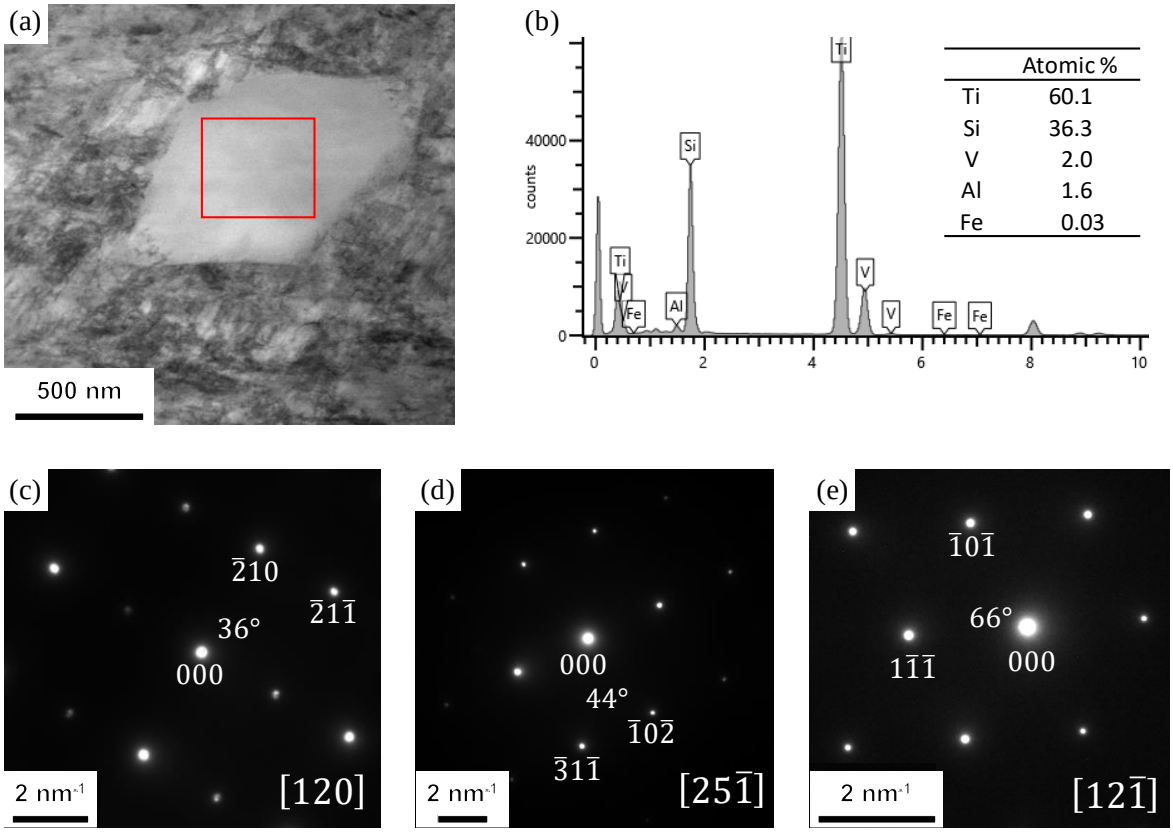

Figure 4.22 (a) Bright field image of Ti_5Si_3. (b) EDS spectrum obtained from the bounded region in Figure (a) and the corresponding table of chemical composition. (c)-(e) Selected area diffraction patterns with beam direction (c) [120], (d) [25$\bar{1}$], and (e) [12$\bar{1}$].

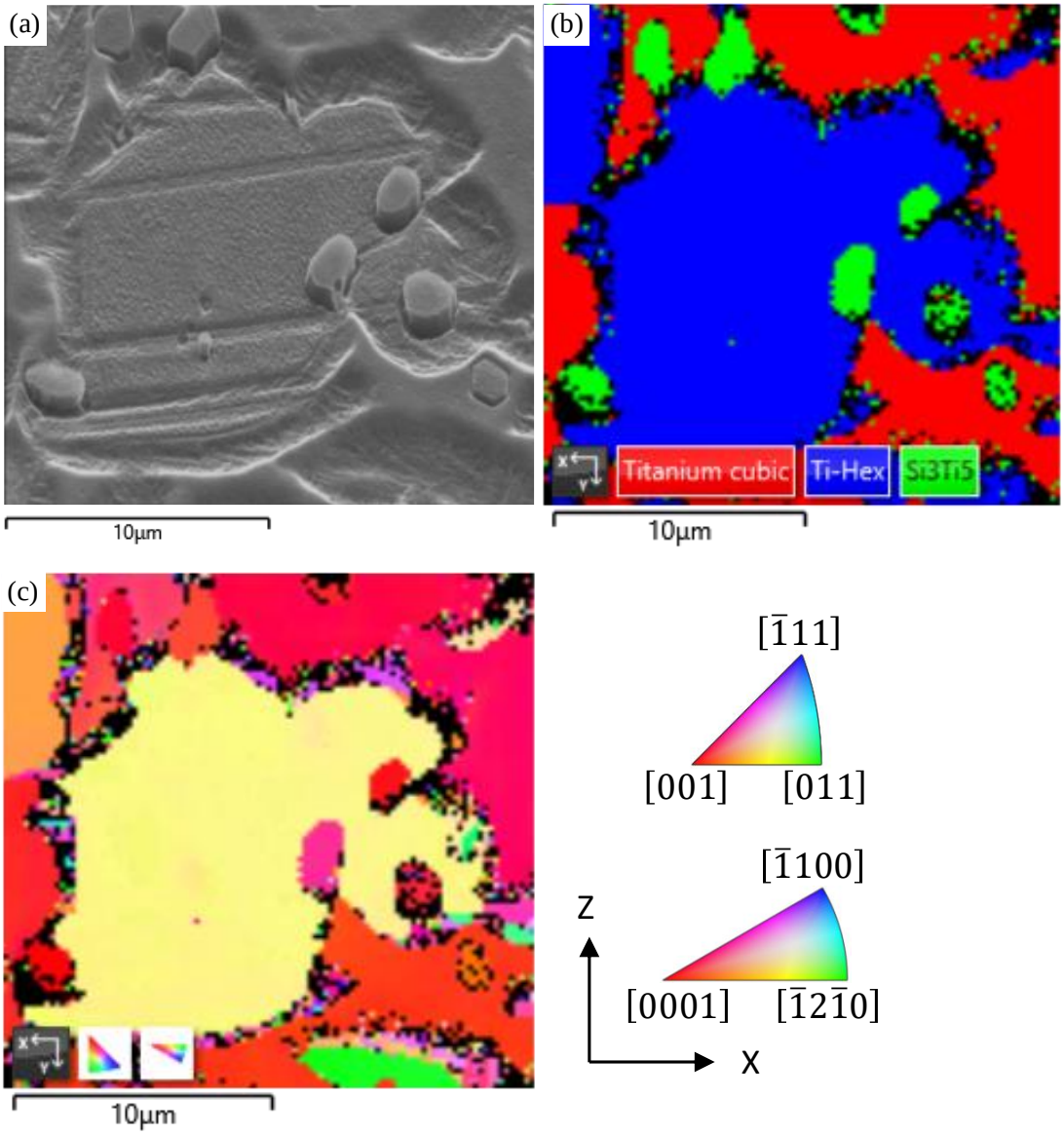

Figure 4.23 (a) Secondary electron image, (b) EBSD phase map, and (c) EBSD orientation map of outer TMAZ of Ti-575 in as-welded condition. Step size = 0.2 µm.

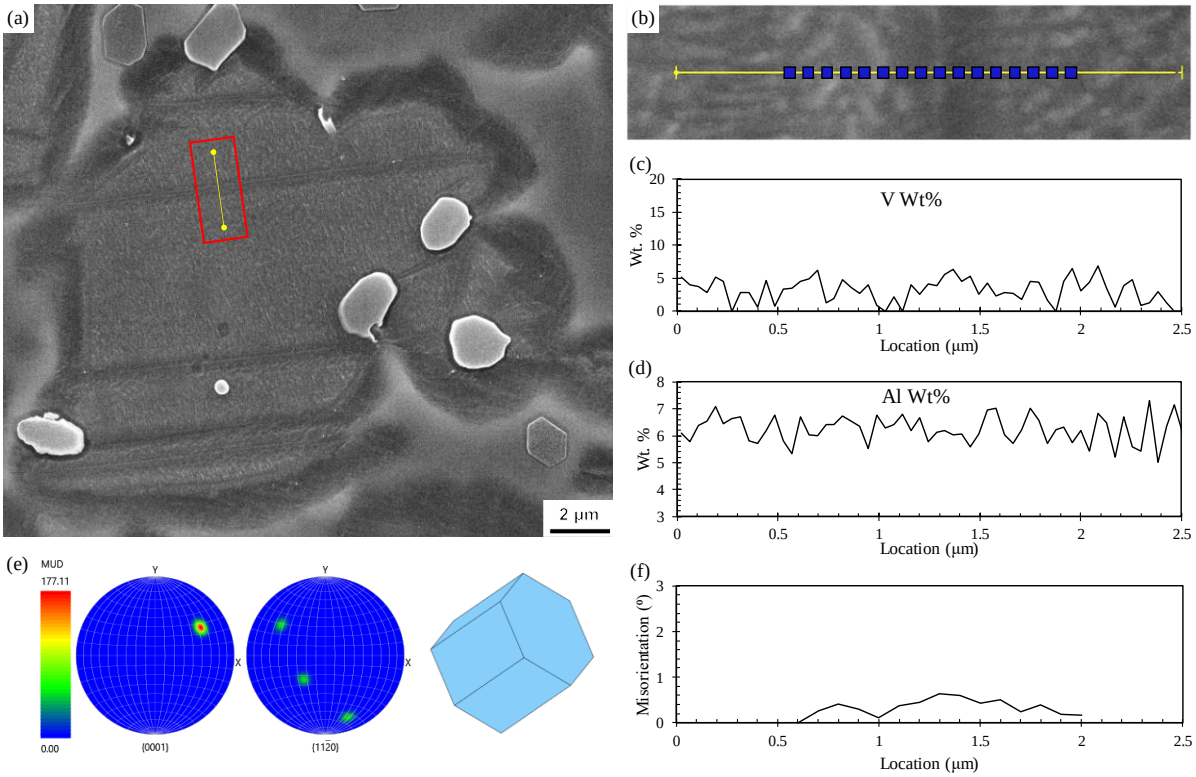

Figure 4.24 EDS and EBSD line scan of the stripe within Ti-575 outer TMAZ in as-welded condition. (a) Low magnification secondary electron image. (b) High magnification electron image at the bounded area of figure (a). The yellow line indicates the location of EDS line scan. The blue squares indicate the location of EBSD line scan. (c) Vanadium and (d) aluminium wt. % profile obtained from the EDS line scan. (e) Pole figures of $\{0001\}$ and $\{11\bar{2}0\}$ planes, the visualisation of the dominant crystal orientation, and (f) misorientation profile obtained from the EBSD line scan.

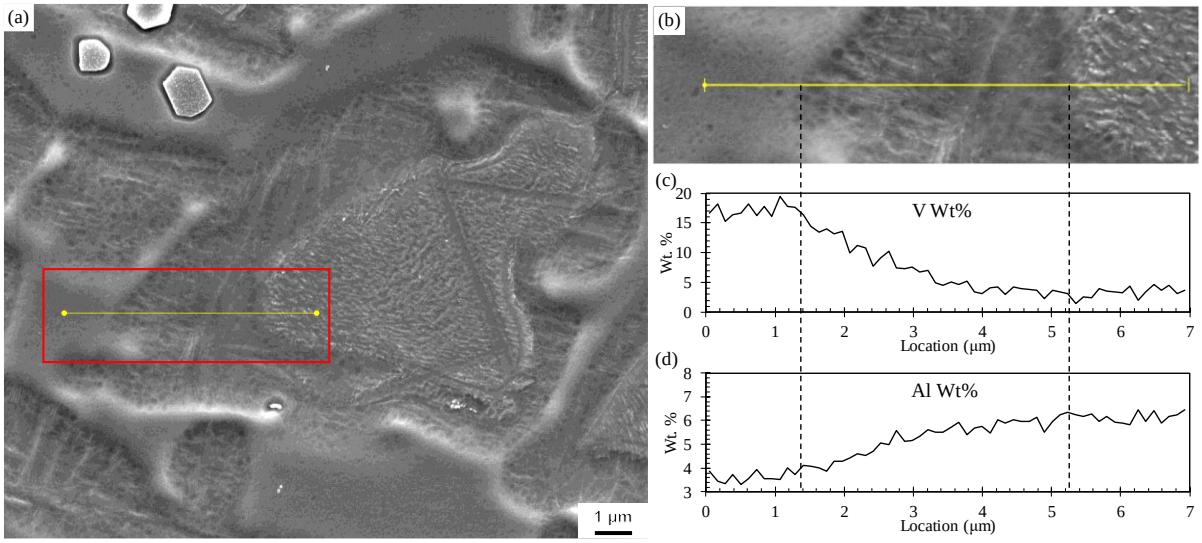

Figure 4.25 EDS line scan of the boundary between primary α and retained β phase in outer TMAZ of Ti-575 in as-welded condition. (a) low magnification and (b) high magnification secondary electron images. (c) Vanadium wt. % profile. (d) Aluminium wt. % profile.

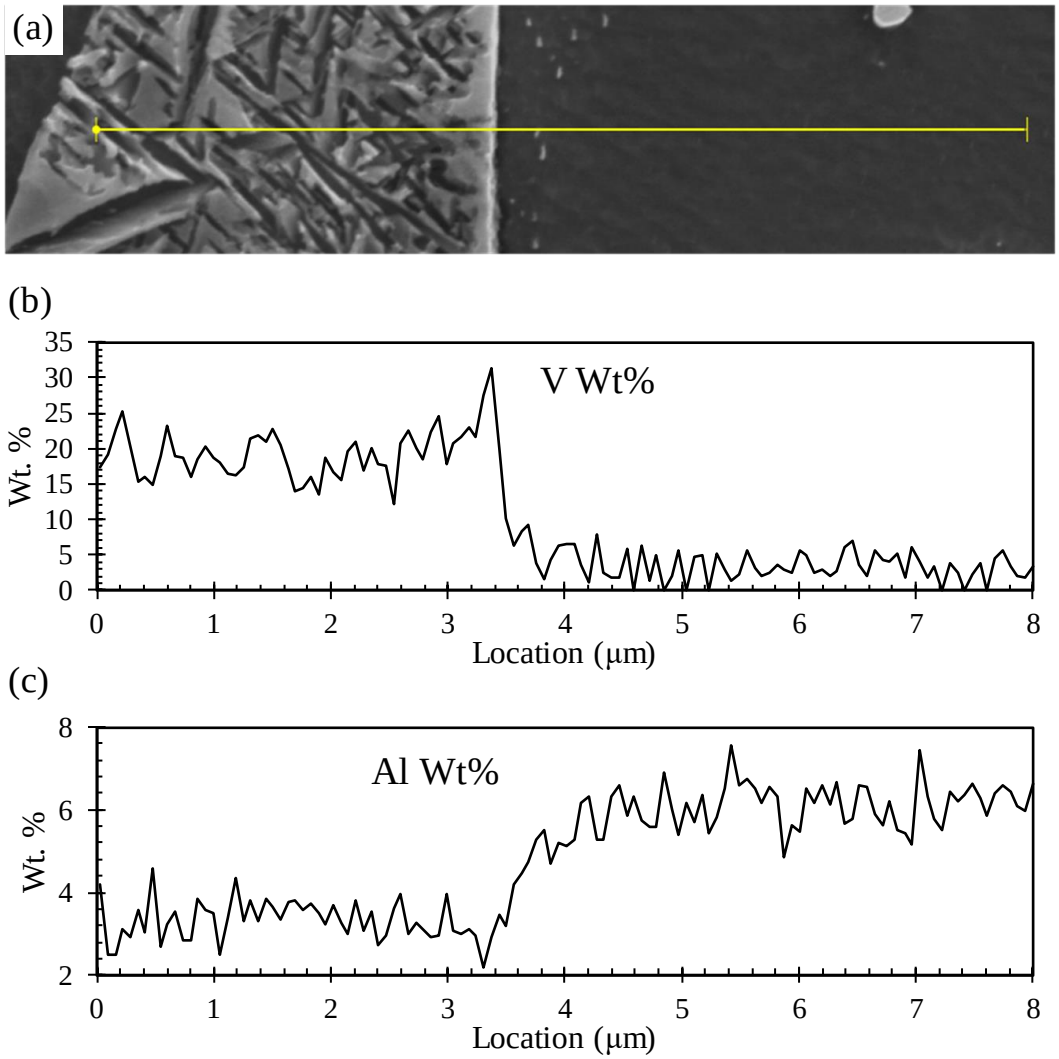

Figure 4.26 EDS line scan across the α and β phase boundary in Ti-575 parent material. (a) Secondary electron image with yellow line indicating the location of the line scan. (b) Vanadium wt.% profile. (c) Aluminium wt.% profile.

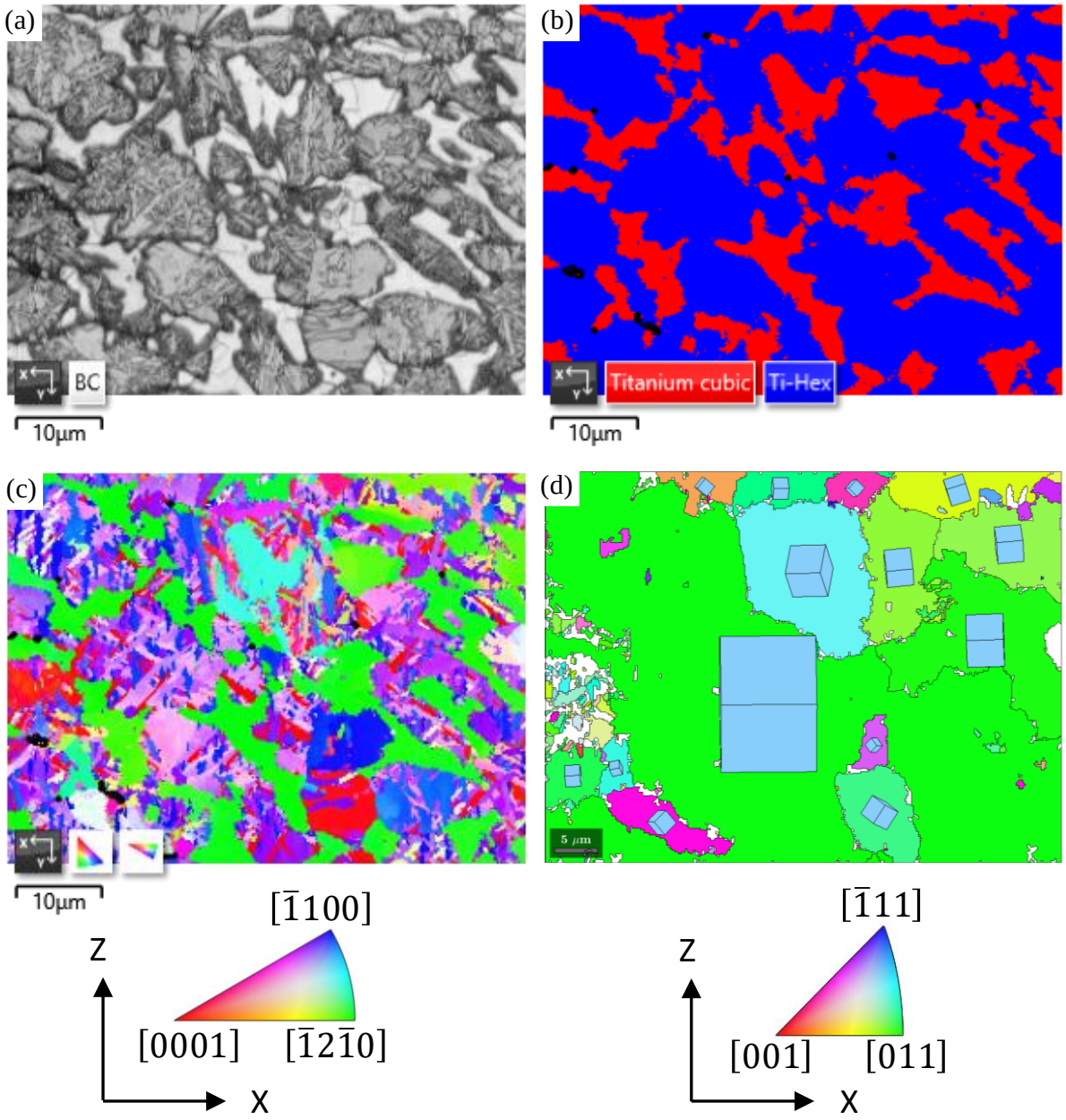

Figure 4.27 EBSD maps of inner TMAZ in Ti-575 in as-welded condition. (a) Band contrast. (b) Phase map. (c) Orientation map. (d) Reconstructed prior β orientation map. (Step size: 0.2 µm)

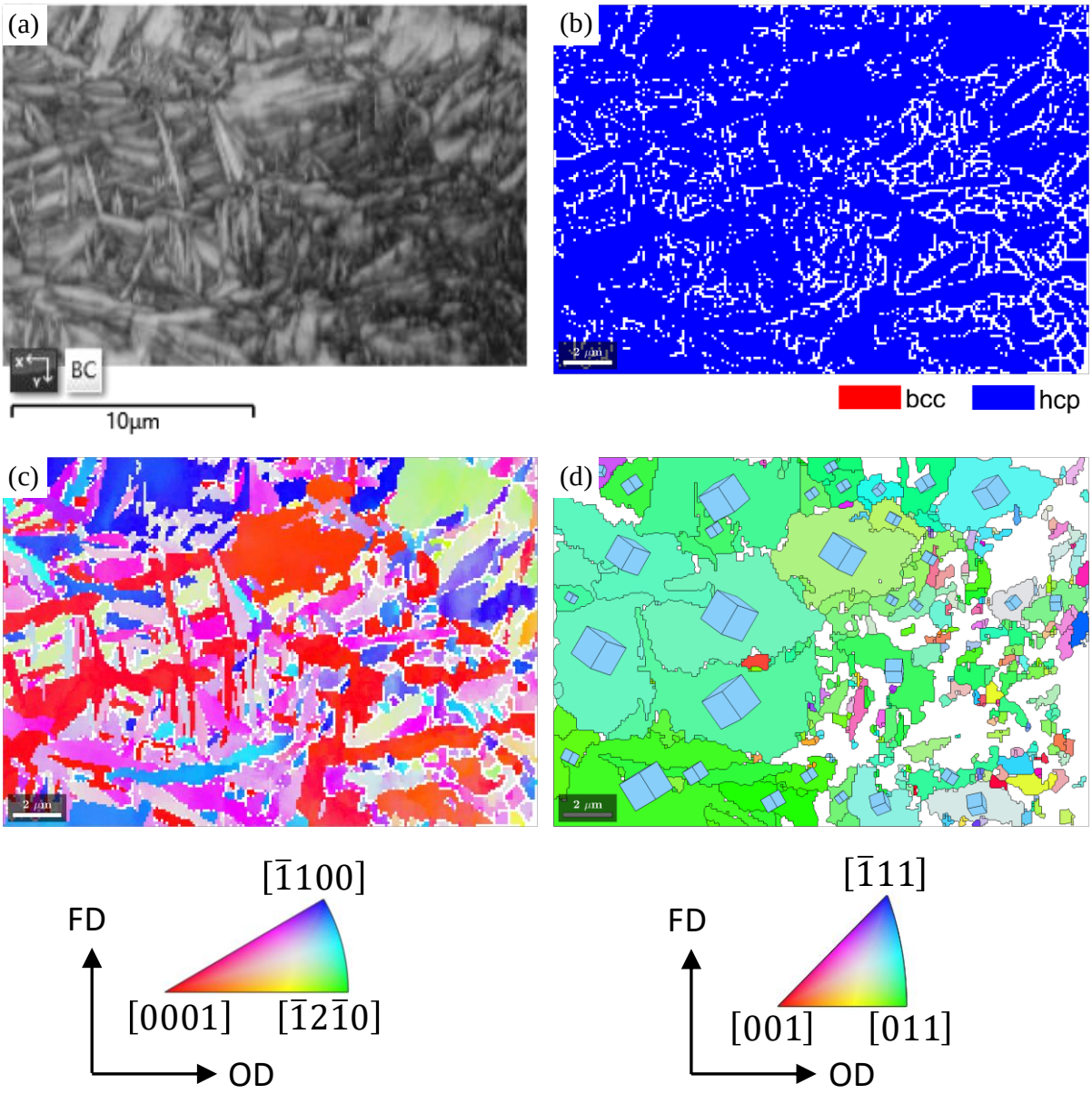

Figure 4.28 EBSD maps of CWZ in Ti-575 in as-welded condition. (a) Band contrast. (b) Phase map. (c) Orientation map. (d) Reconstructed prior β orientation map. (Step size: 0.2 μm)

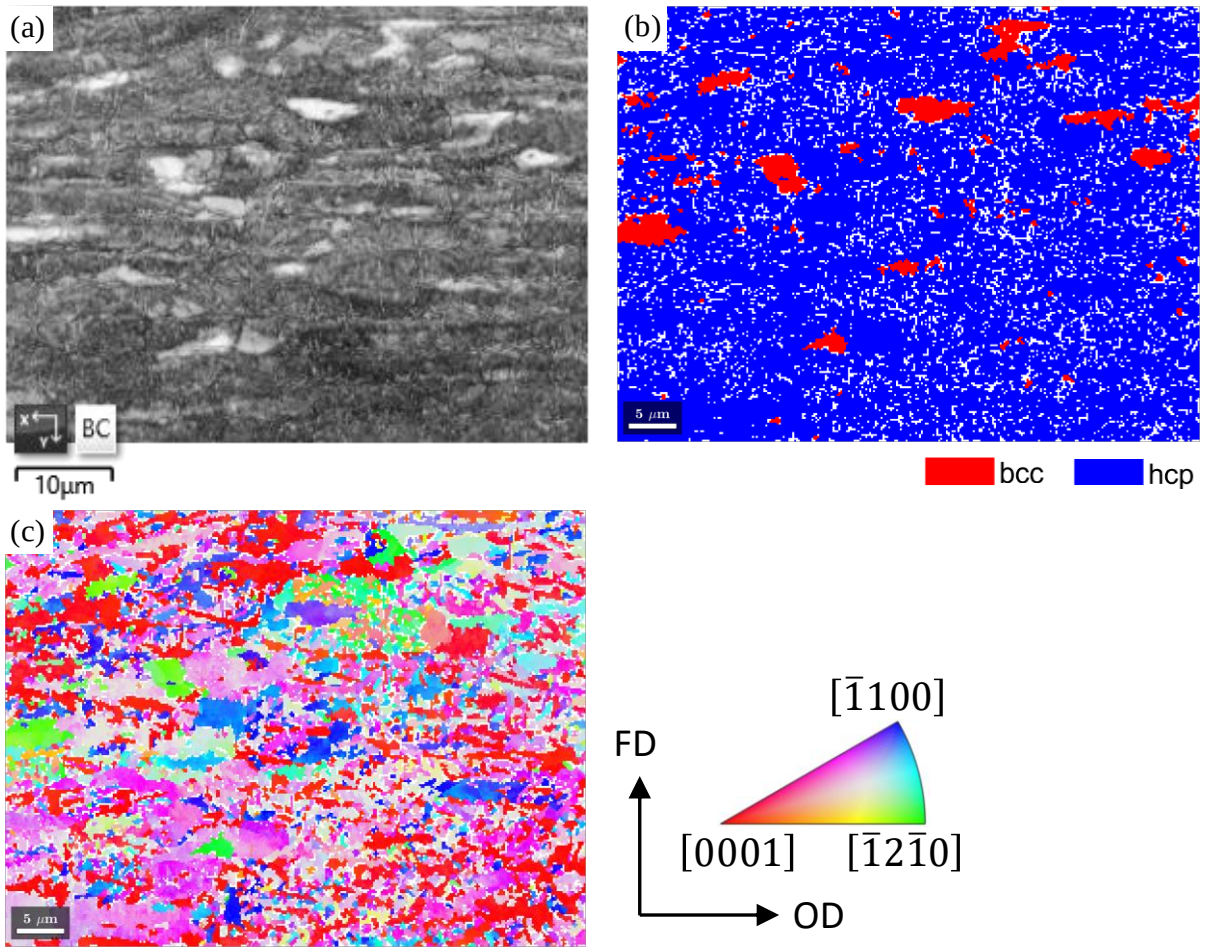

Figure 4.29 EBSD maps of the boundary between CWZ and TMAZ in Ti-575 in the as-welded condition, taken at 50 μm away from the weld interface. (a) Band contrast. (b) Phase map. (c) Orientation map. (Step size: 0.2 μm)

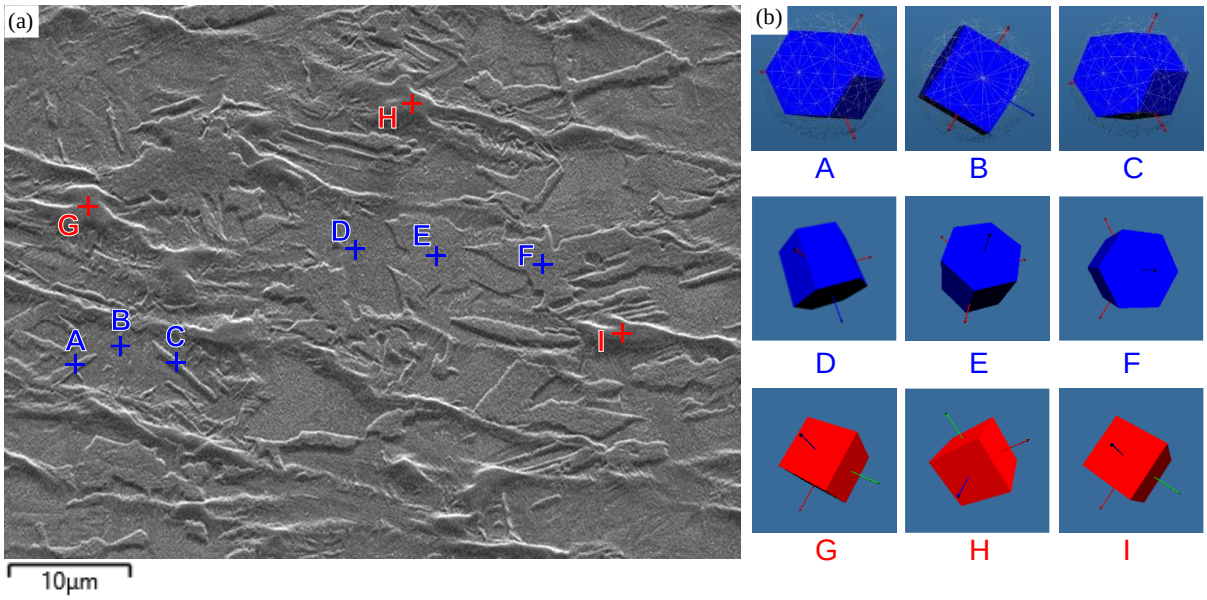

Figure 4.30 (a) Secondary electron image of Ti-64 TMAZ in as-welded condition. (b) Visualisation of the orientation and the crystal structure measured by EBSD point & ID at the labelled location.

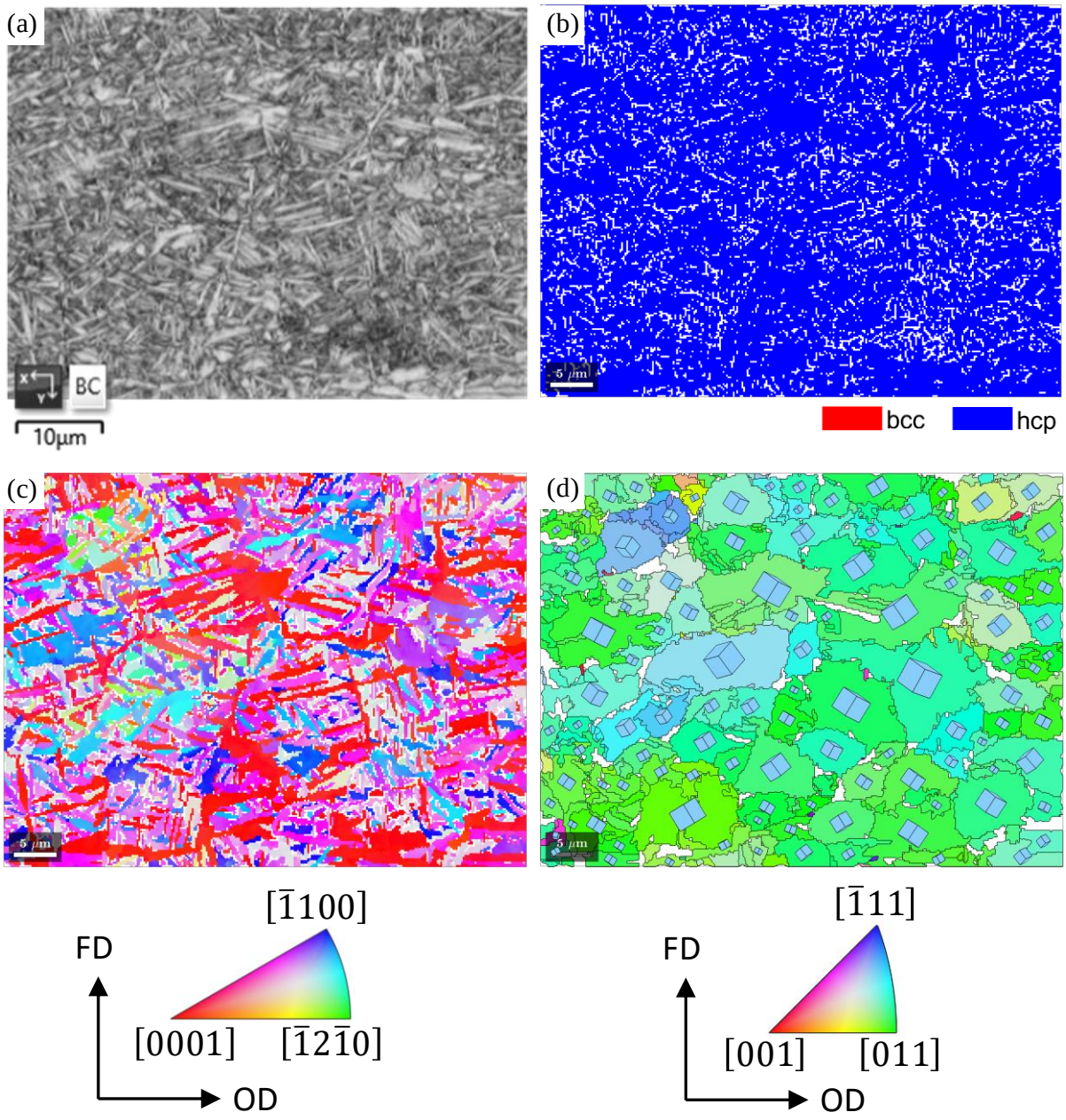

Figure 4.31 EBSD maps of CWZ in Ti-64 in as-welded condition. (a) Band contrast. (b) Phase map. (c) Orientation map. (d) Reconstructed prior β orientation map. (Step size: 0.2 μm)

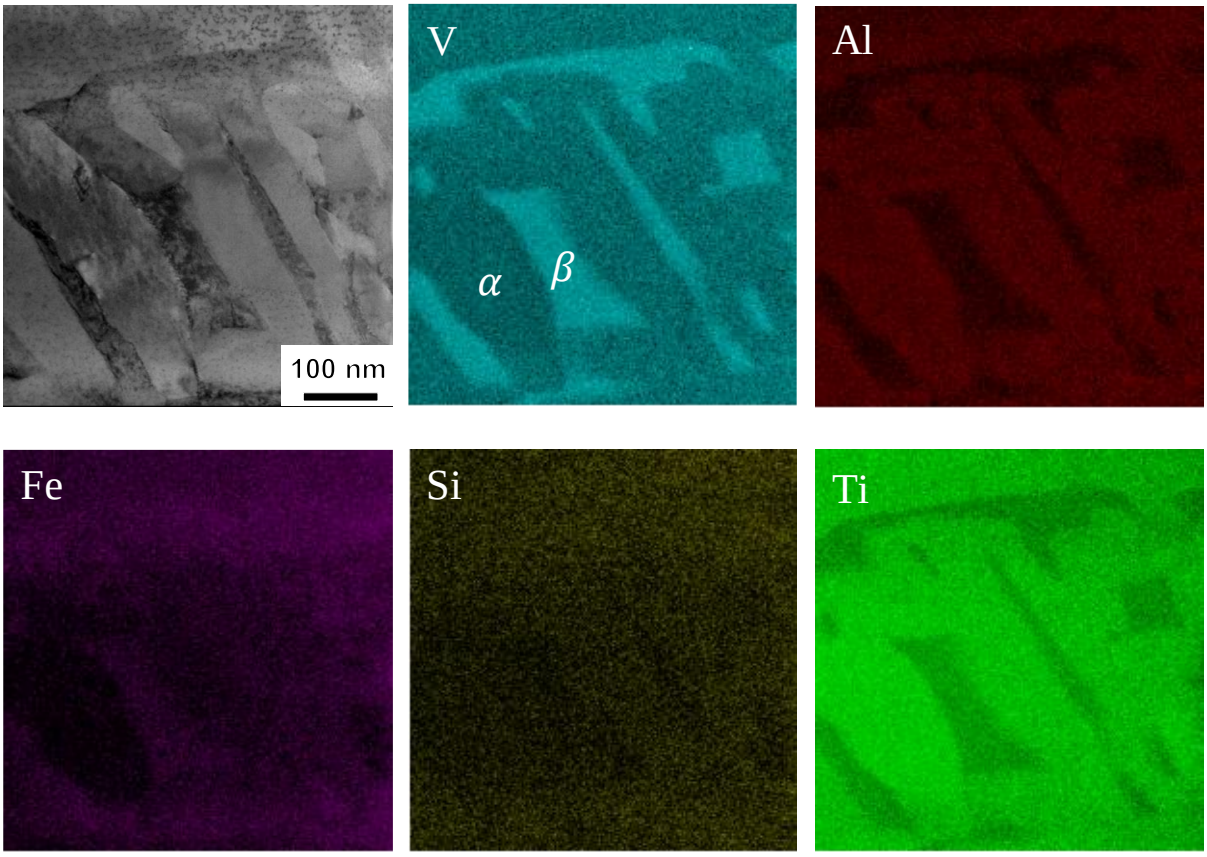

Figure 4.32 A bright field STEM image and EDS maps taken from the CWZ of Ti-575 in PWHT'd condition.

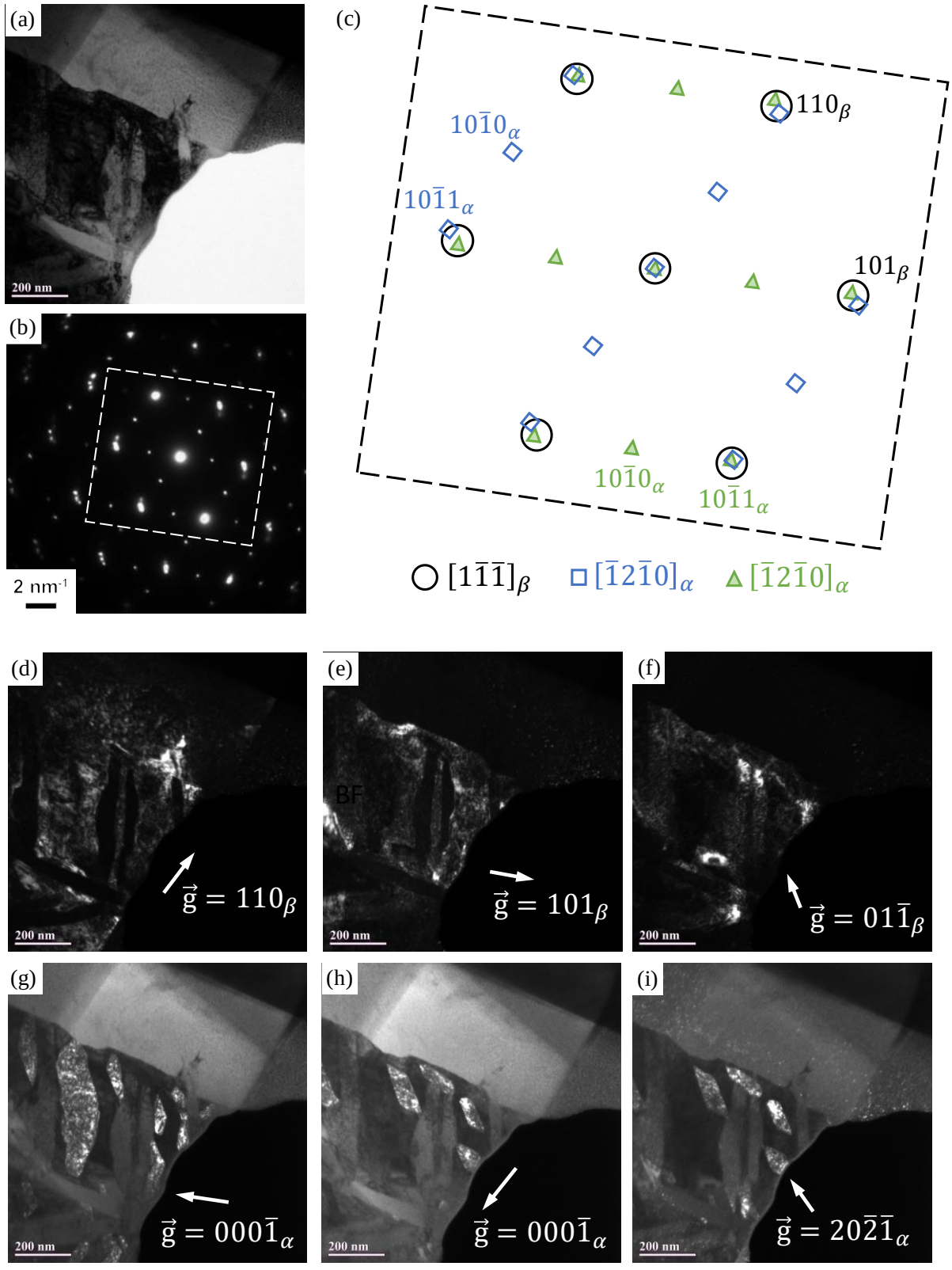

Figure 4.33 A bright field STEM image and EDS maps taken from the CWZ of Ti-575 in PWHT'd condition.

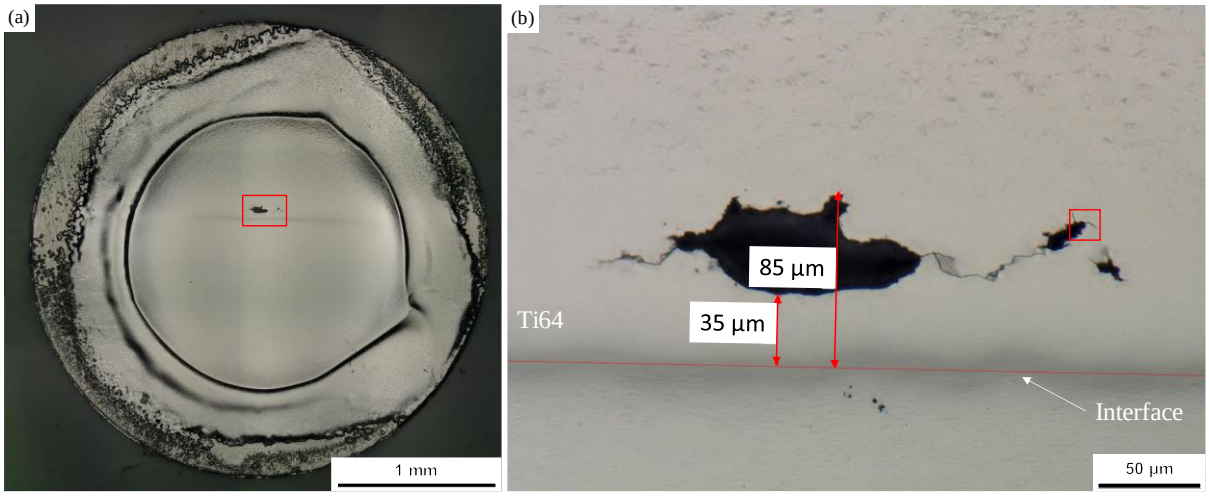

Figure 4.34 (a) Optical macrograph of a twin-jet polished sample. (b) High magnification view of the bounded area in Figure (a). The region surrounding the hole is electron transparent.

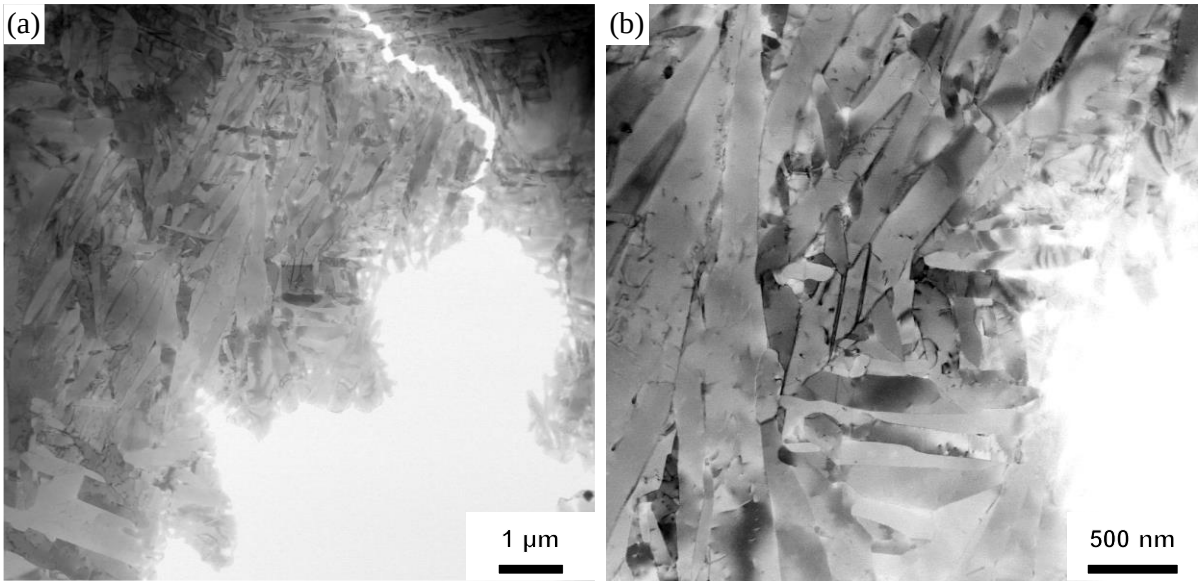

Figure 4.35 (a) Low and (b) high magnification bright field images of CWZ in Ti-64 in PWHT'd condition.

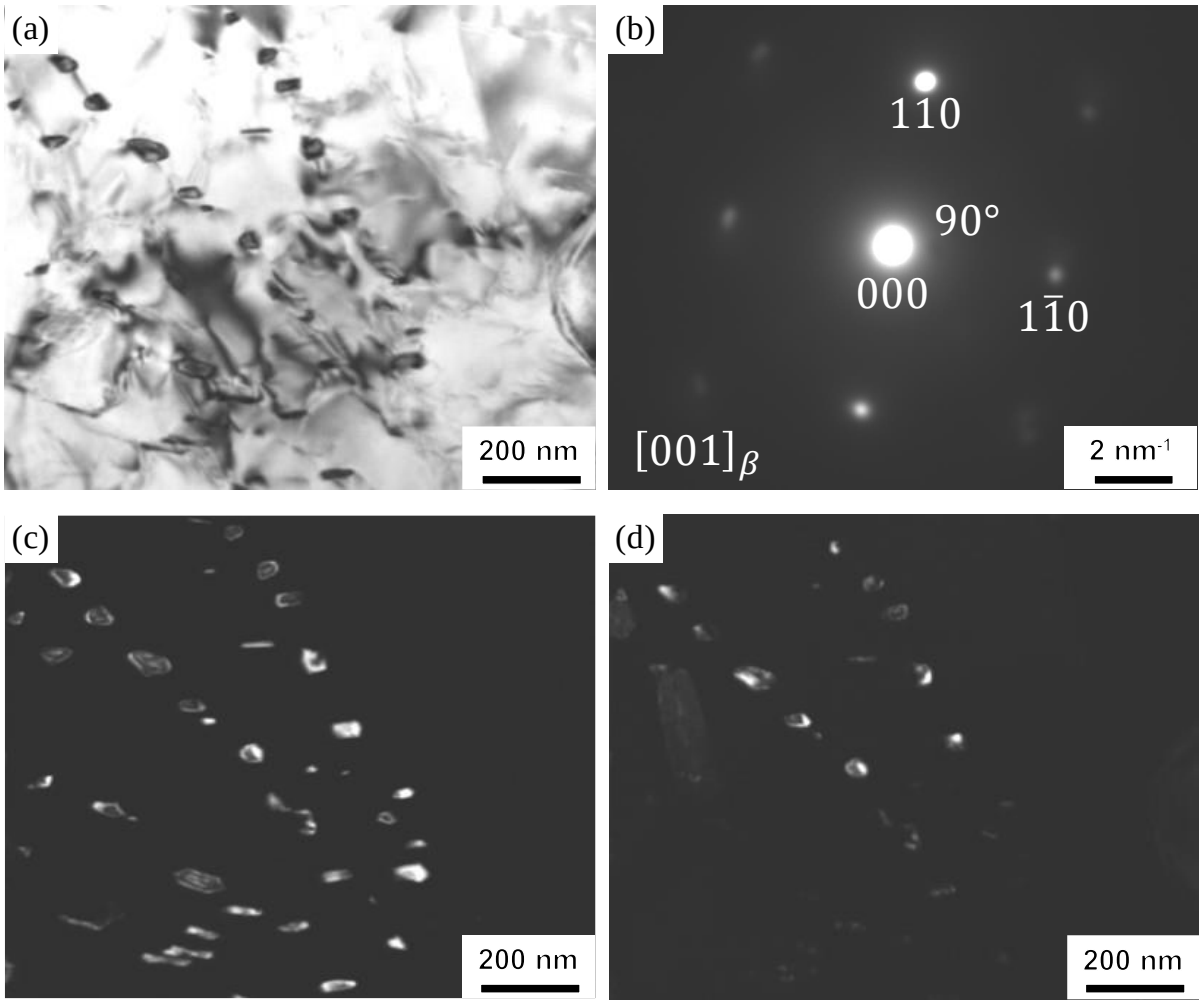

Figure 4.36 TEM images taken from the CWZ of Ti-64 in PWHT'd condition, specifically illustrating the β precipitates. (a) Bright field image. (b) $[001]_\beta$ selected area diffraction pattern. (c) and (d) Dark field images.

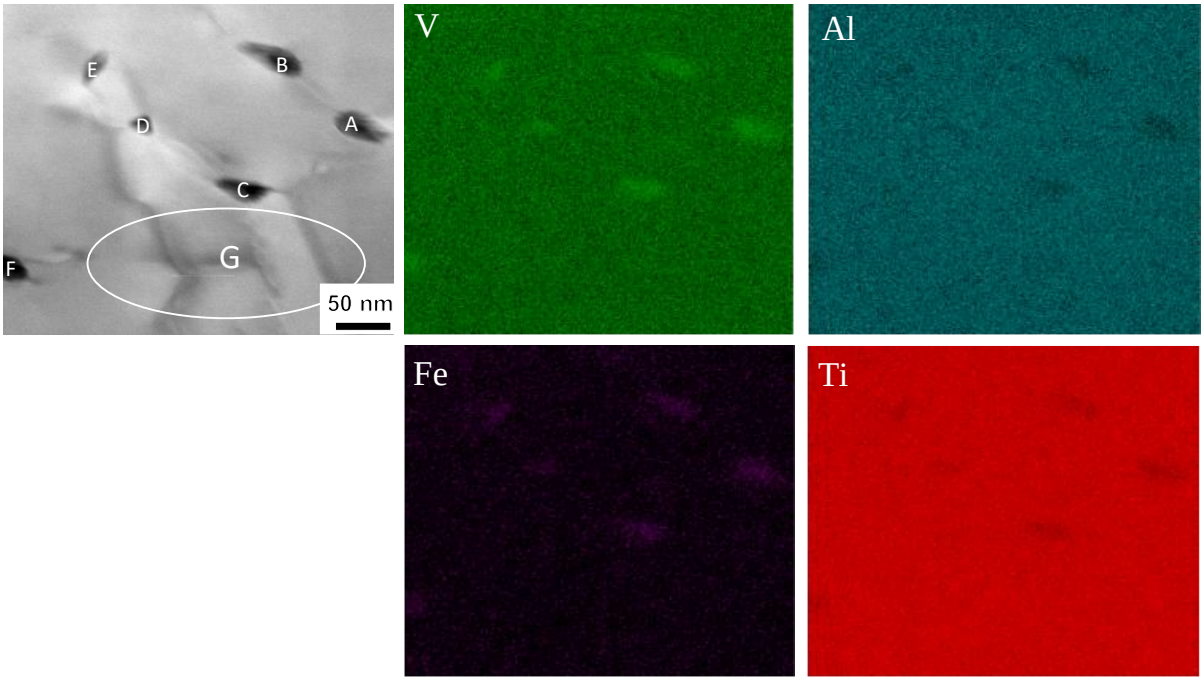

Figure 4.37 A bright field STEM image and EDS maps taken from the CWZ of Ti-64 in PWHT'd condition.

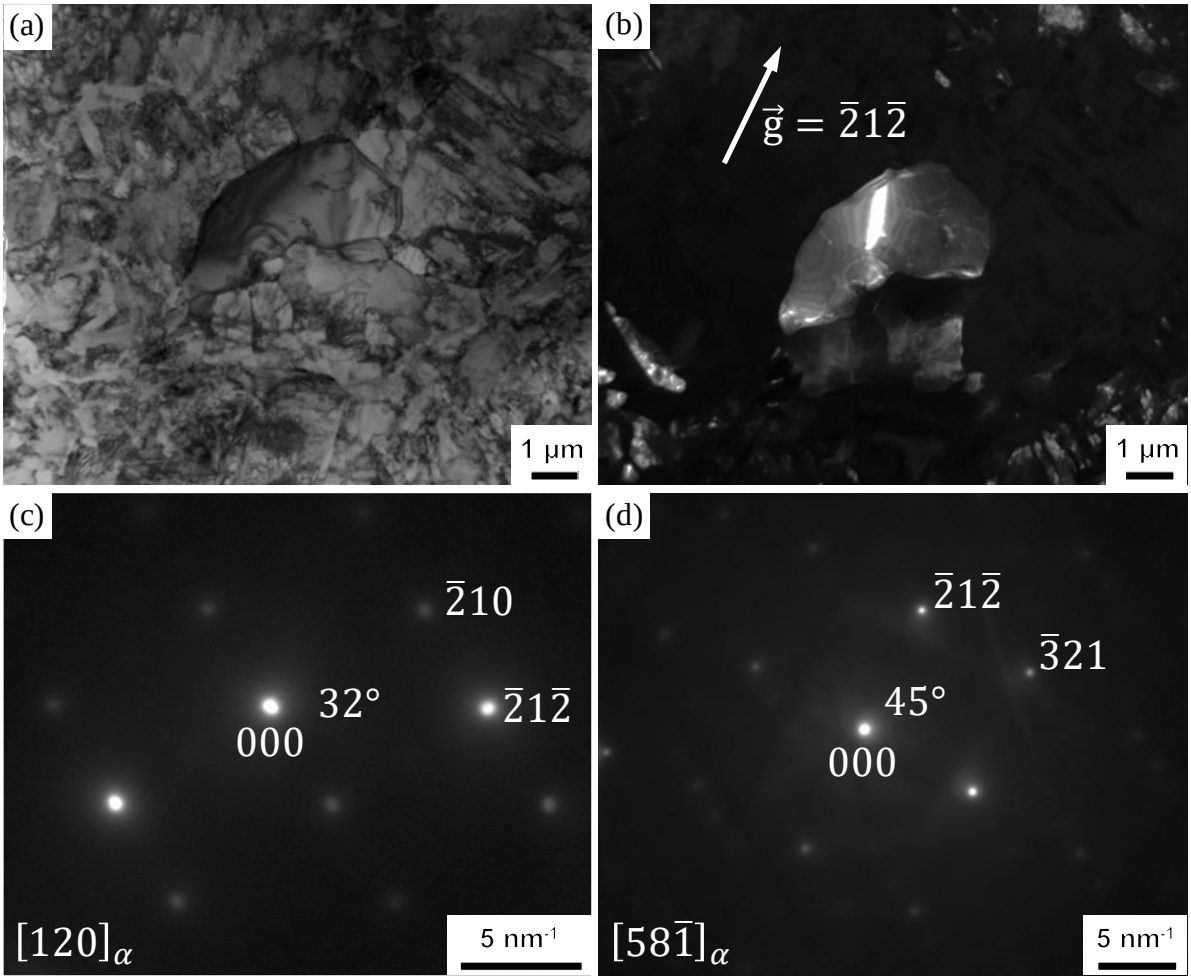

Figure 4.38 TEM images taken from the CWZ of Ti-64 in PWHT'd condition, specifically illustrating the α grain. (a) Bright field and (b) dark field images. (c) $[120]_\alpha$ and (d) $[58\bar{1}]_\alpha$ selected area diffraction pattern.

Chapter 5

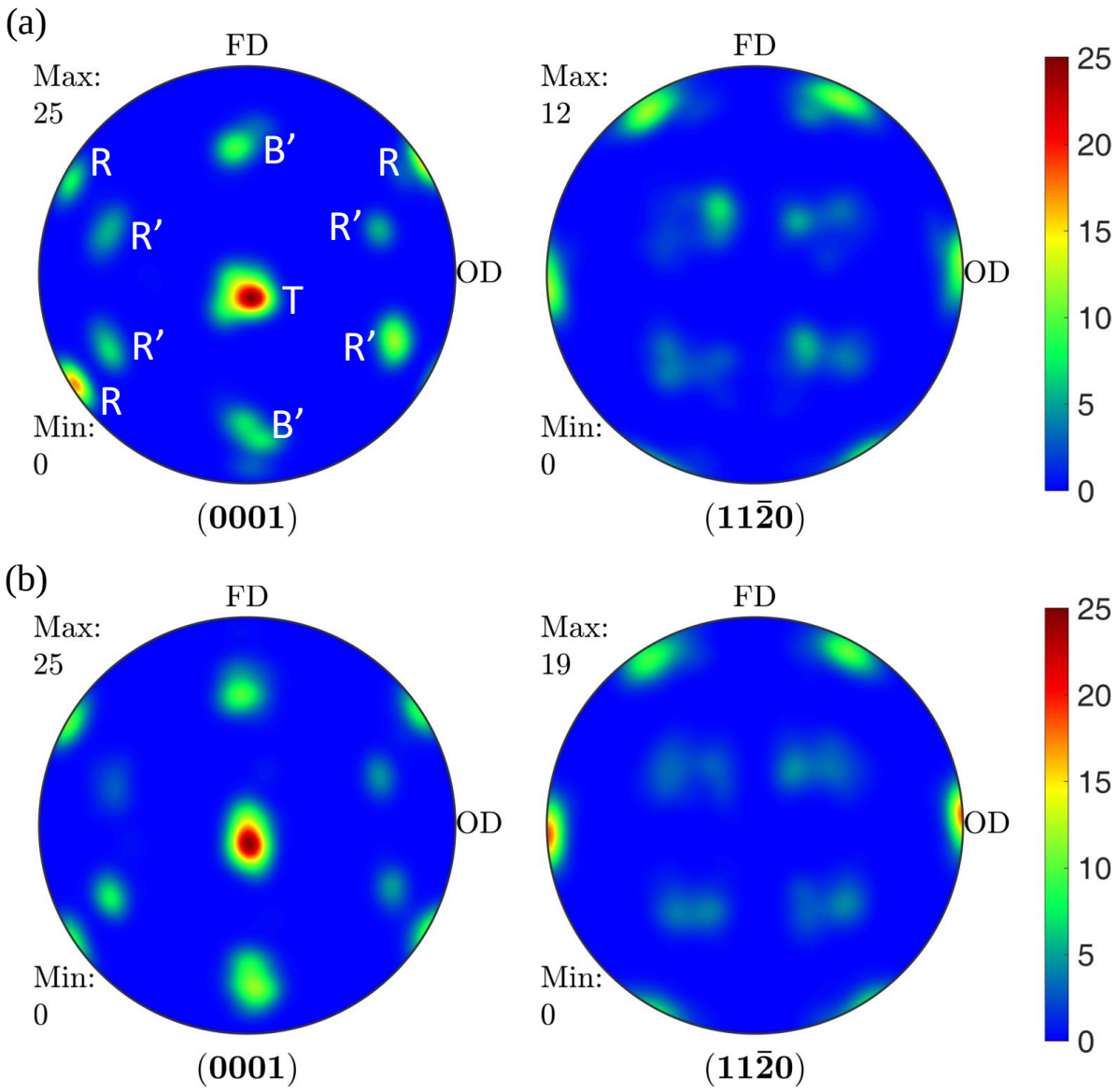

Figure 5.1 α texture measured in CWZ of (a) Ti-575 and (b) Ti-64. Pole figures are aligned with FD and OD.

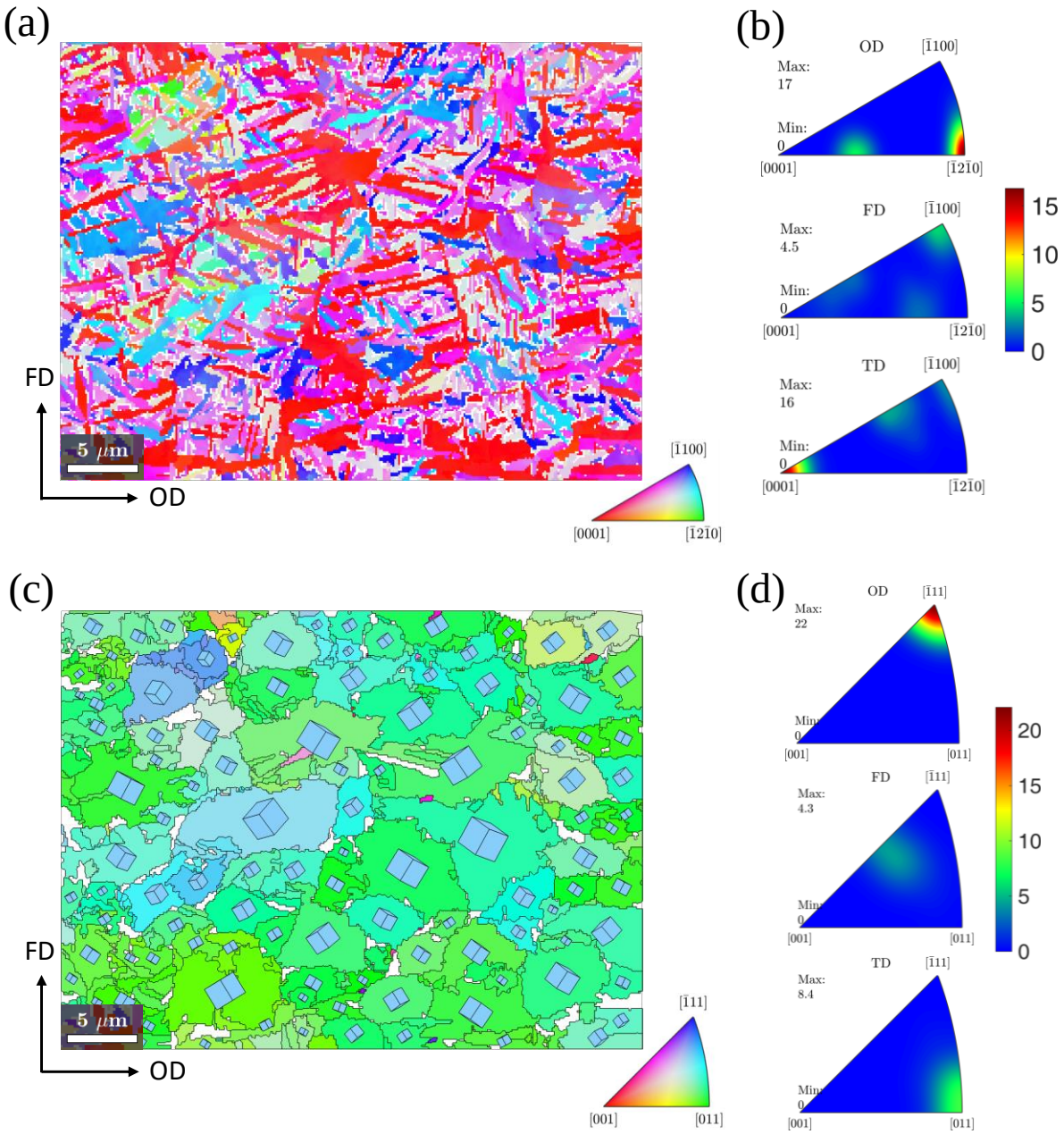

Figure 5.2 (a) Orientation map and (b) inverse pole figures measured in Ti-64 CWZ. (c) Prior β orientation map and (d) inverse pole figures reconstructed from Figure (a)(b). Note that the inverse pole figures are aligned with OD, FD, and TD.

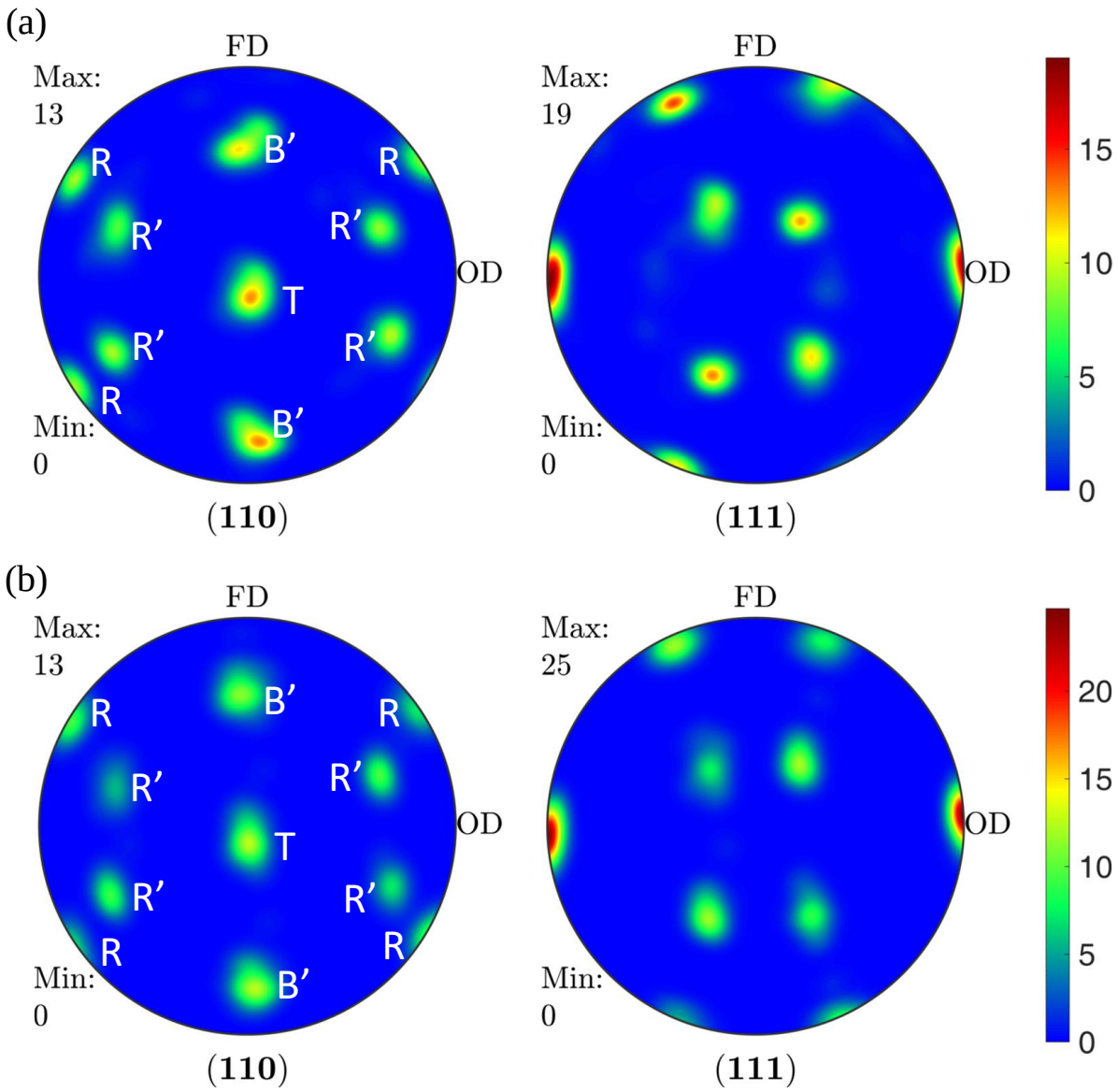

Figure 5.3 Pole figures of the reconstructed prior β phase in the CWZ of (a) Ti-575 and (b) Ti-64. Note that the pole figures are aligned with FD and OD.

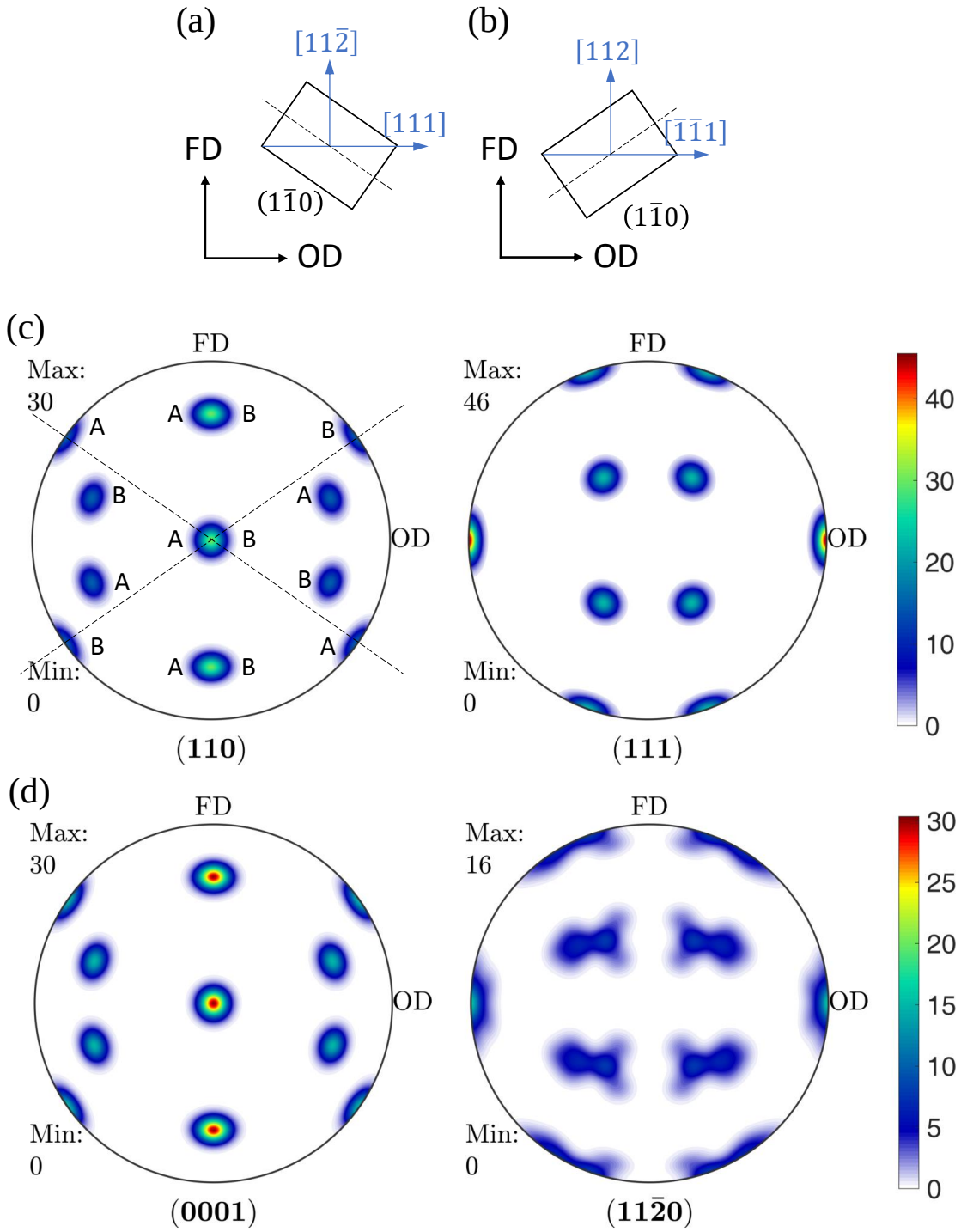

Figure 5.4 Schematic visualisation of (a) $(11\bar{2})[111]_\beta$ and (b) $(112)[\bar{1}\bar{1}1]_\beta$ orientations, along with their (c) simulated β texture. The texture components labelled as 'A' were inherited from $(11\bar{2})[111]_\beta$, while the components labelled as 'B' were inherited from $(112)[\bar{1}\bar{1}1]_\beta$. The dashed line associated with the longitudinal axis of $(1\bar{1}0)$ plane correlates to the texture components marked in Figure (c). (d) Simulated α texture inherited from the β textures following Burgers orientation relationship without variant selection.

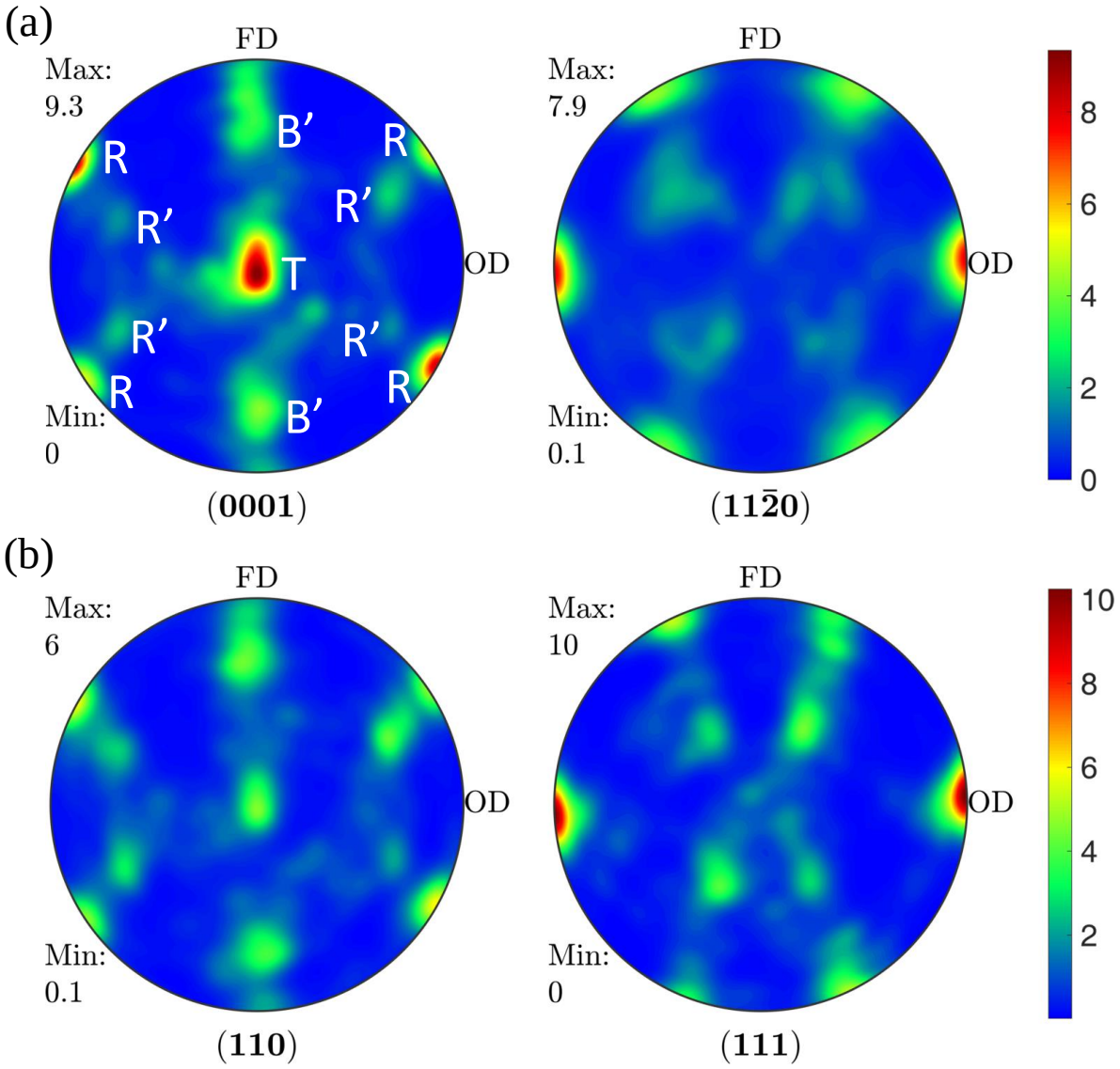

Figure 5.5 (a) α and (b) β texture measured in Ti-64 TMAZ at the bifurcation point. Pole figures are aligned with FD and OD.

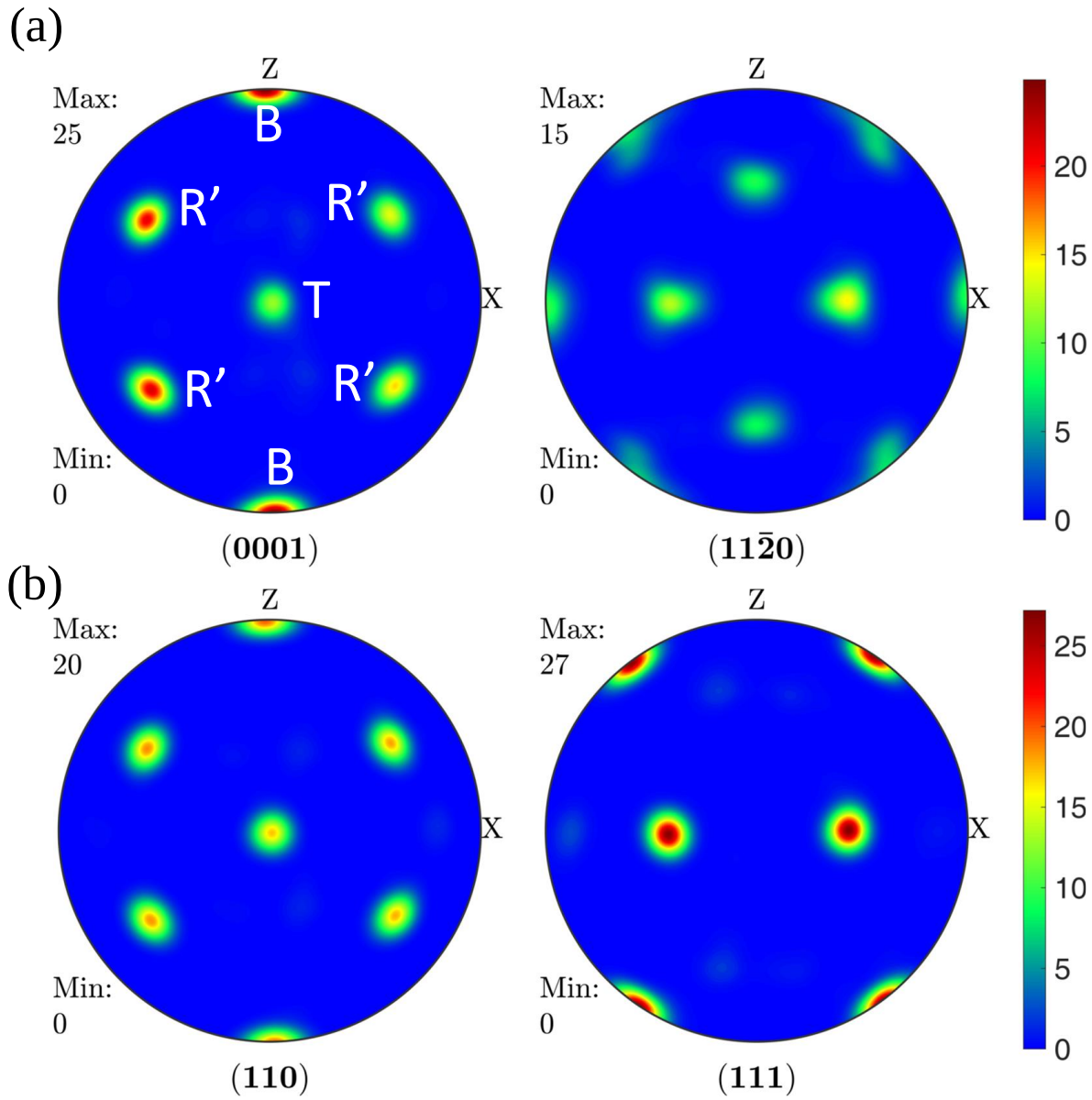

Figure 5.6 (a) α and (b) β texture measured in Ti-575 TMAZ at the bifurcation point. Pole figures are aligned with X and Z directions.

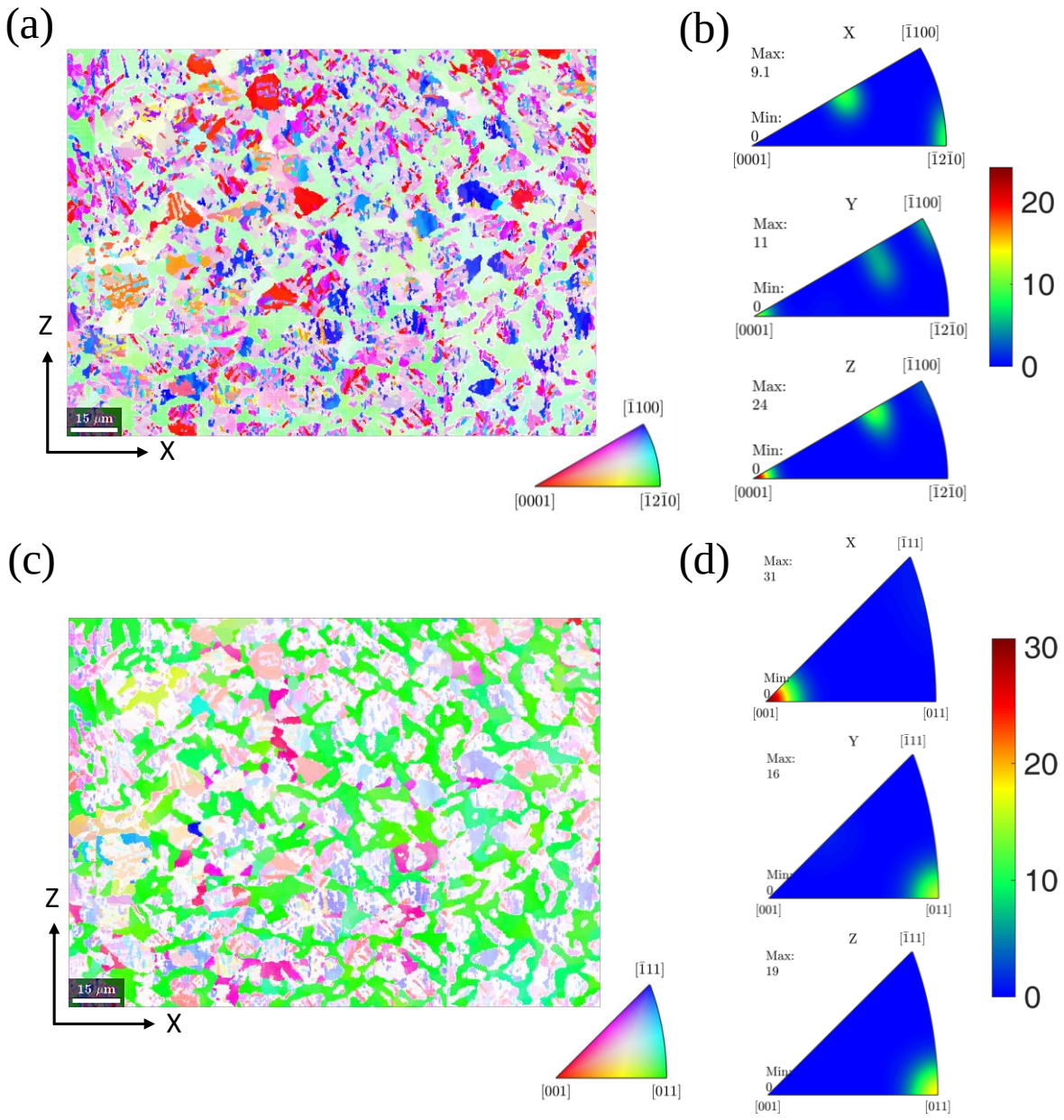

Figure 5.7 (a) α phase orientation map with corresponding (b) inverse pole figures, and (c) β phase orientation map with corresponding (d) inverse pole figures, all measured at bifurcation point of Ti-575 TMAZ. Note that the inverse pole figures are aligned with X, Y, and Z directions.

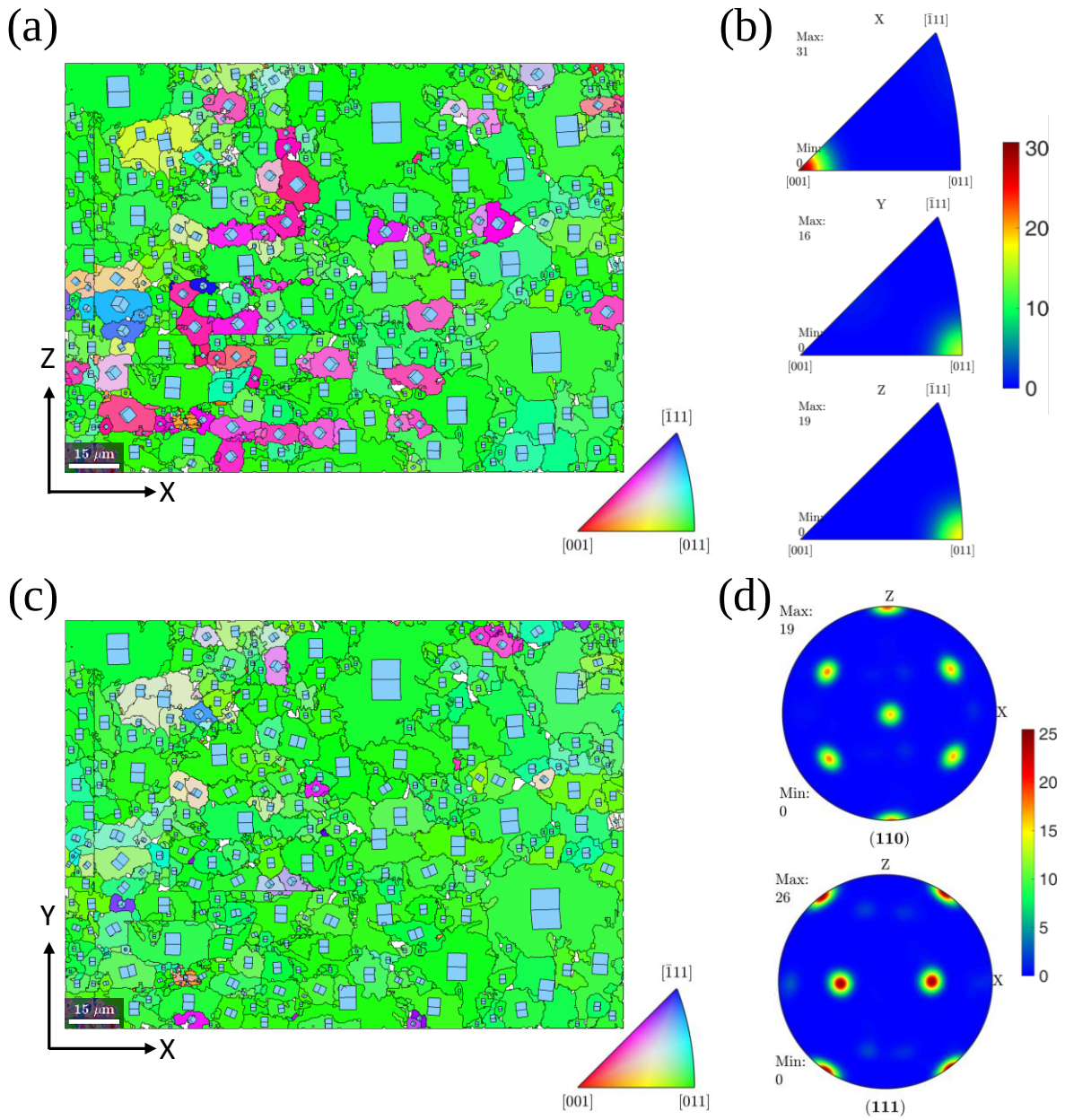

Figure 5.8 (a) Y-orientation map, (b) inverse pole figures, (c) Z-orientation map, and (d) pole figures of prior β phase reconstructed from Figure 5.7. Note that the pole figures are aligned with X and Z directions.

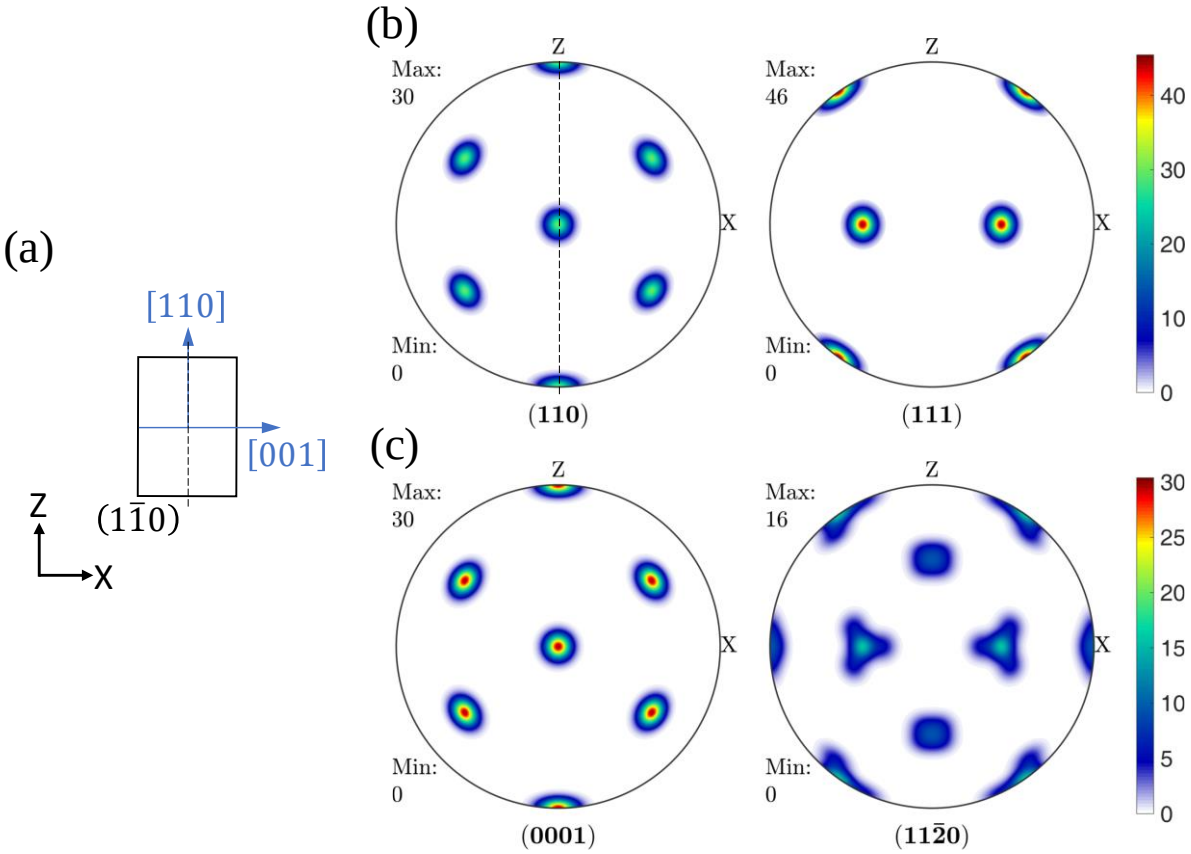

Figure 5.9 (a) Schematic visualisation of $\{110\}\langle 001\rangle_{\beta}$ texture and its (b) simulated β texture. The dashed line associated with longitudinal axis of $(1\bar{1}0)$ plane correlates to the texture components marked in Figure (b). (c) Simulated α texture inherited from the β texture following the Burgers orientation relationship without variant selection.

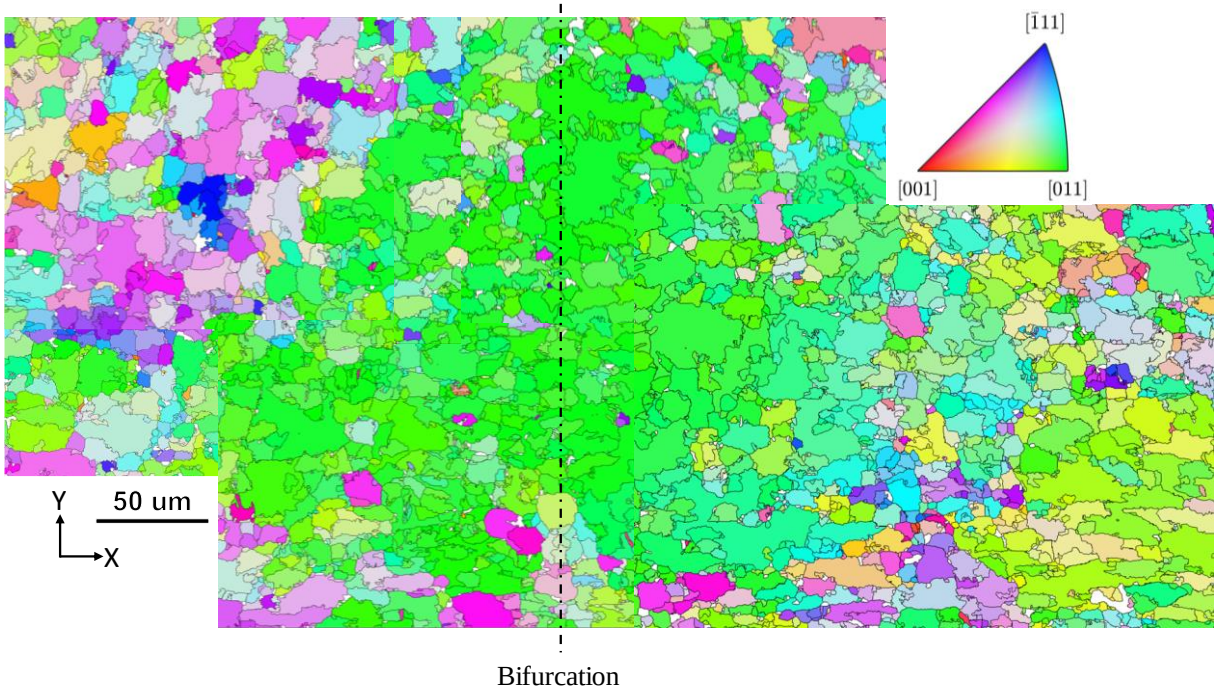

Figure 5.10 Prior β orientation map along sample Z direction (equivalently forge direction) at the bifurcation point of Ti-575 TMAZ. This map was stitched and reconstructed from six EBSD mappings.

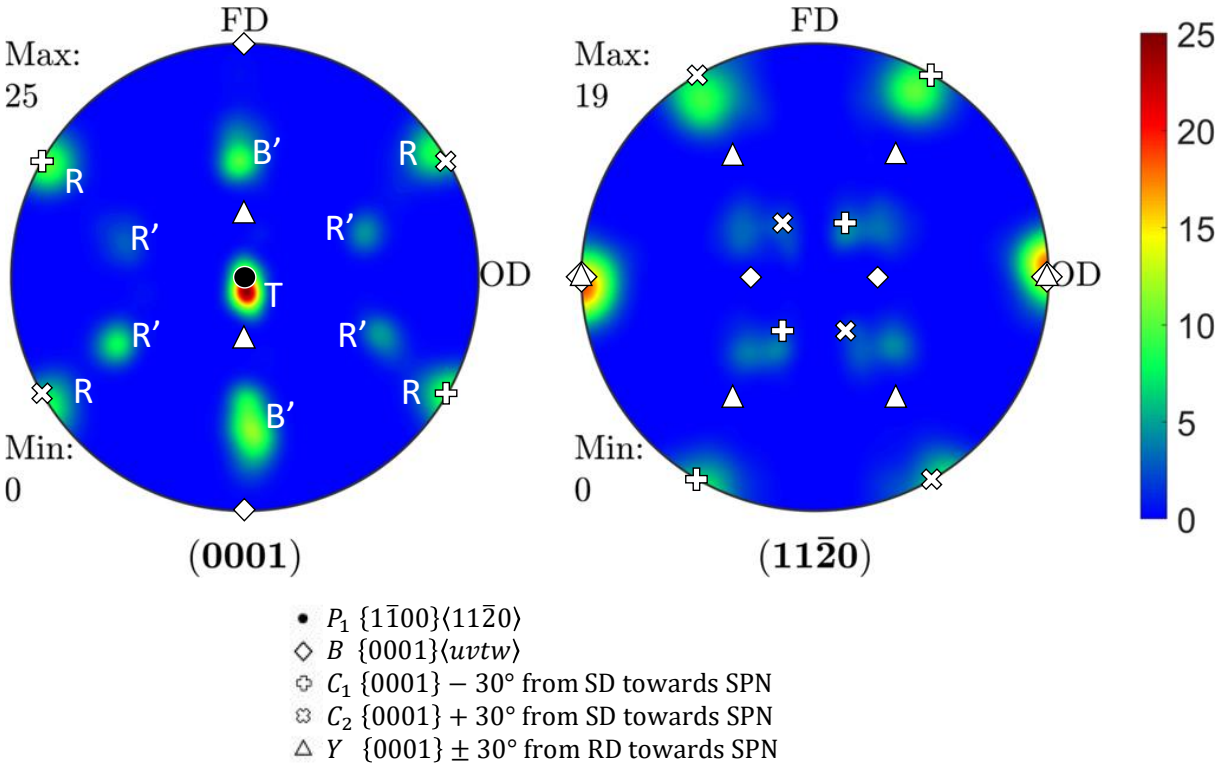

Figure 5.11 $(0001)_\alpha$ and $(11\bar{2}0)_\alpha$ pole figures measured in Ti-64 CWZ presented in equal angle projection. Note that these pole figures are the same as Figure 5.1 (b), except from different type of projection. Simple shear textures of HCP materials (see Figure 2.40) are overlaid onto the pole figures, where FD // SPN and OD // SD.

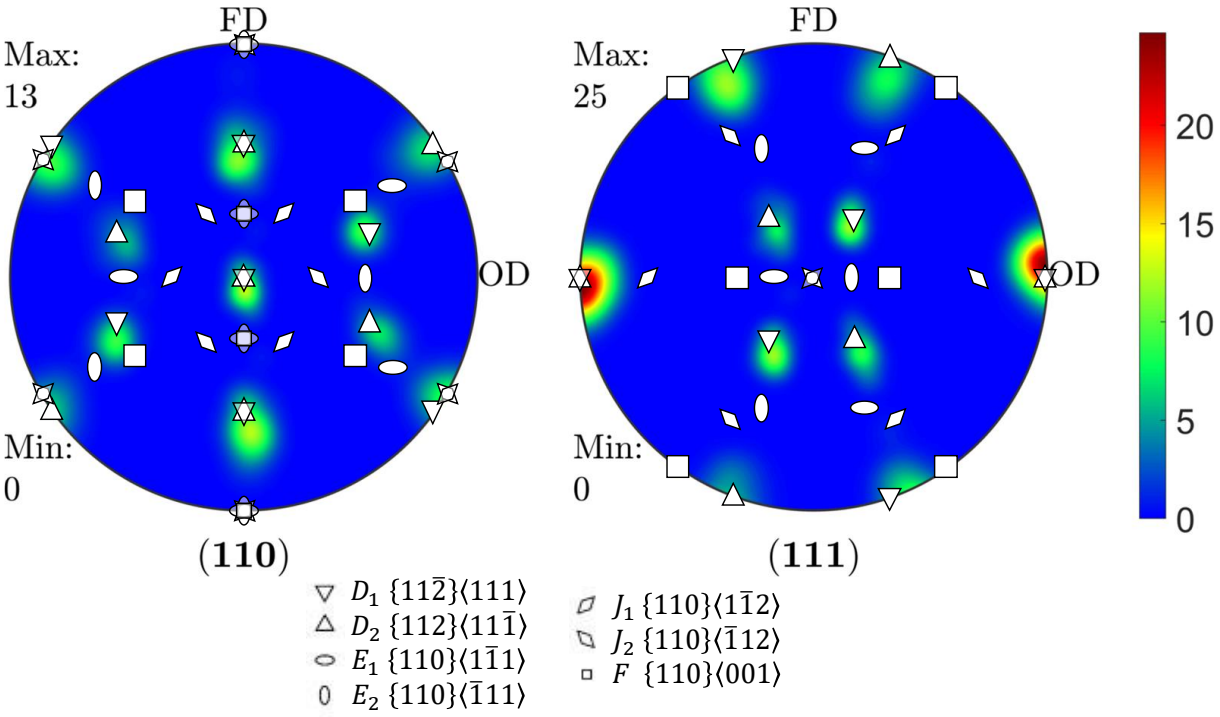

Figure 5.12 $(110)_\beta$ and $(111)_\beta$ pole figures of reconstructed prior β texture in Ti-64 CWZ presented in equal angle projection. Note that these pole figures are the same as Figure 5.3 (b), except from different type of projection. Simple shear textures of BCC materials (see Figure 2.39) are overlaid onto the pole figures, where FD // SPN and OD // SD.

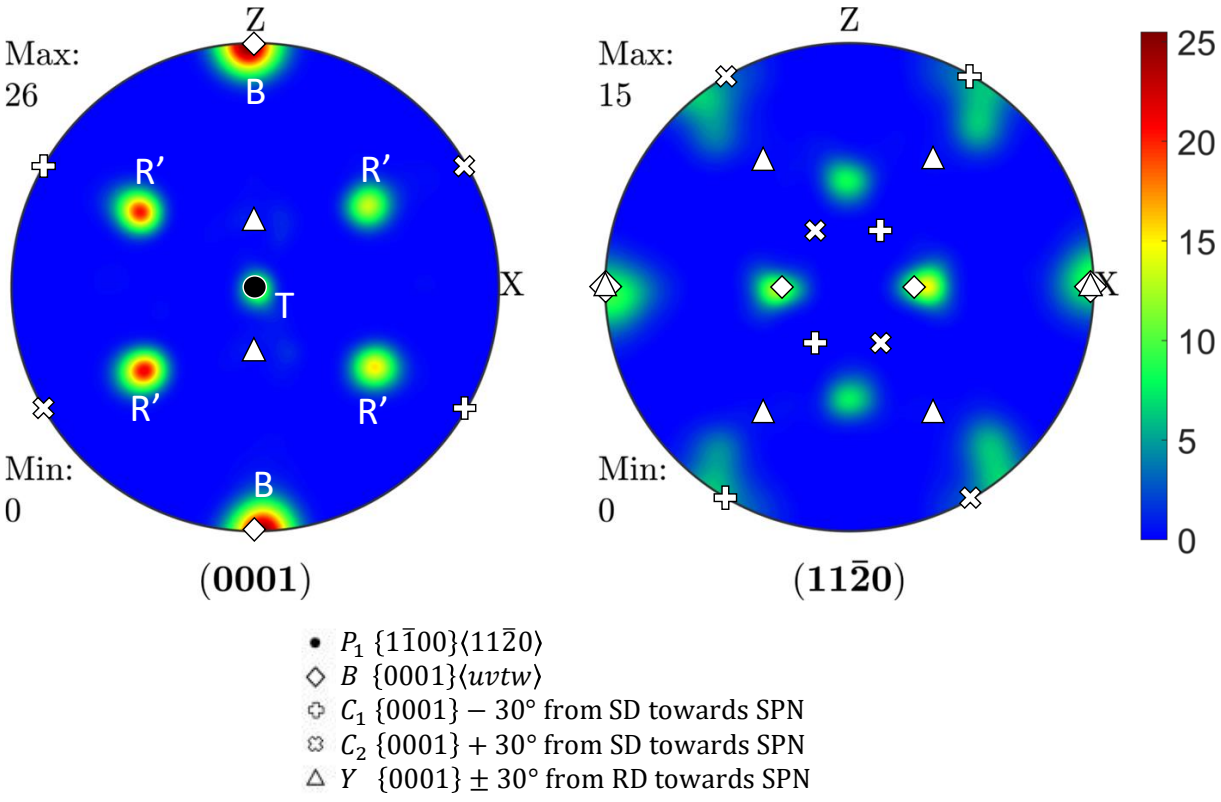

Figure 5.13 $(0001)_\alpha$ and $(11\bar{2}0)_\alpha$ pole figures measured in Ti-575 TMAZ at bifurcation point presented in equal angle projection. Note that these pole figures are the same as Figure 5.6 (a), except from different type of projection. Simple shear textures of HCP materials (see Figure 2.40) are overlaid onto the pole figures, where Z // SPN and X // SD.

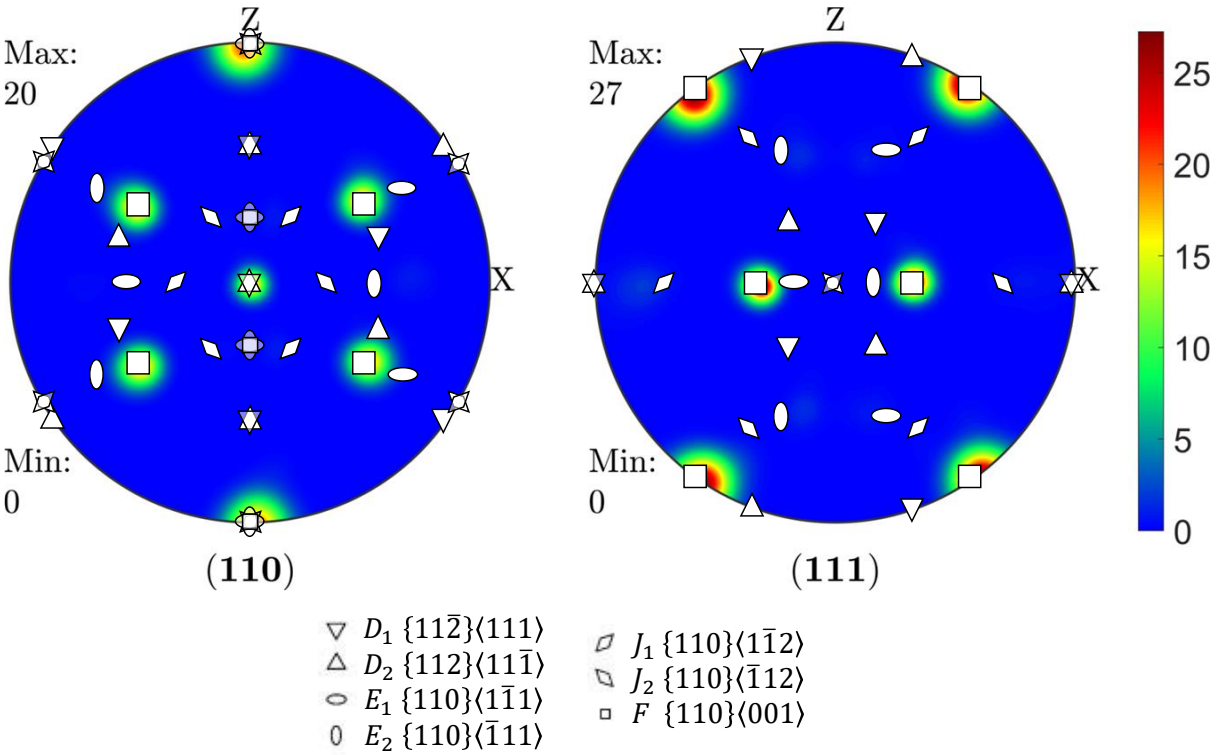

Figure 5.14 $(110)_\beta$ and $(111)_\beta$ pole figures of β texture in Ti-575 TMAZ at bifurcation point presented in equal angle projection. Note that these pole figures are the same as Figure 5.6 (b), except from different type of projection. Simple shear textures of BCC materials (see Figure 2.39) are overlaid onto the pole figures, where Z // SPN and X // SD.

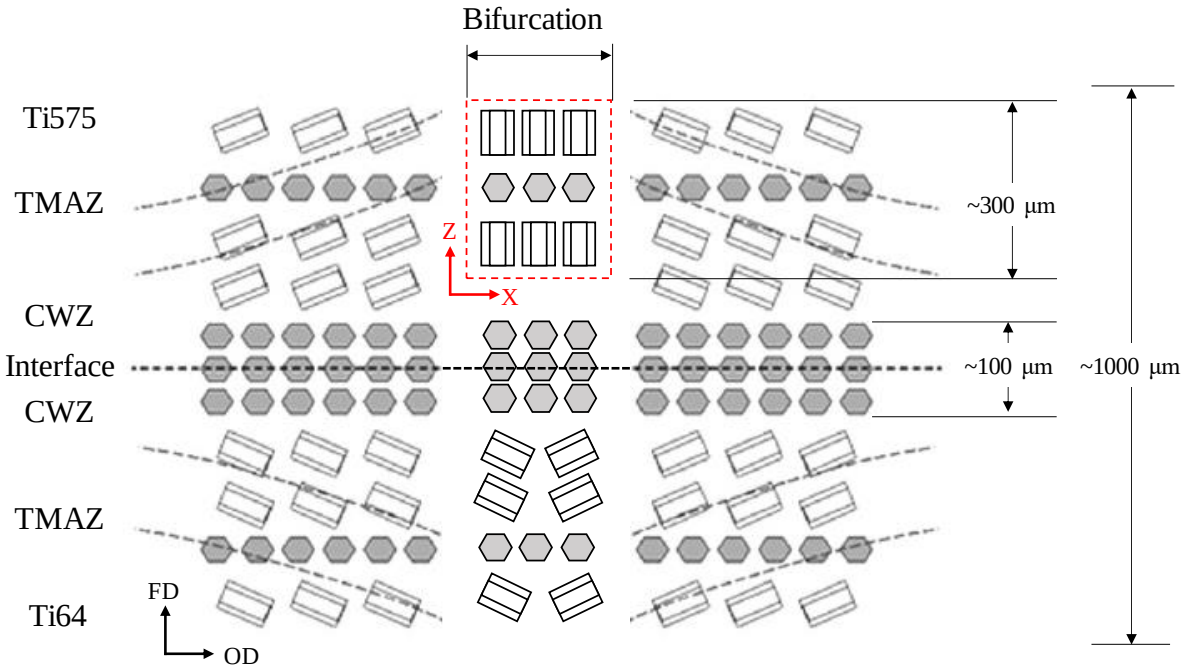

Figure 5.15 Schematic diagram of the spatial variation of texture in Ti-64:Ti-575 linear friction welds. (Modified from [139])

Chapter 6

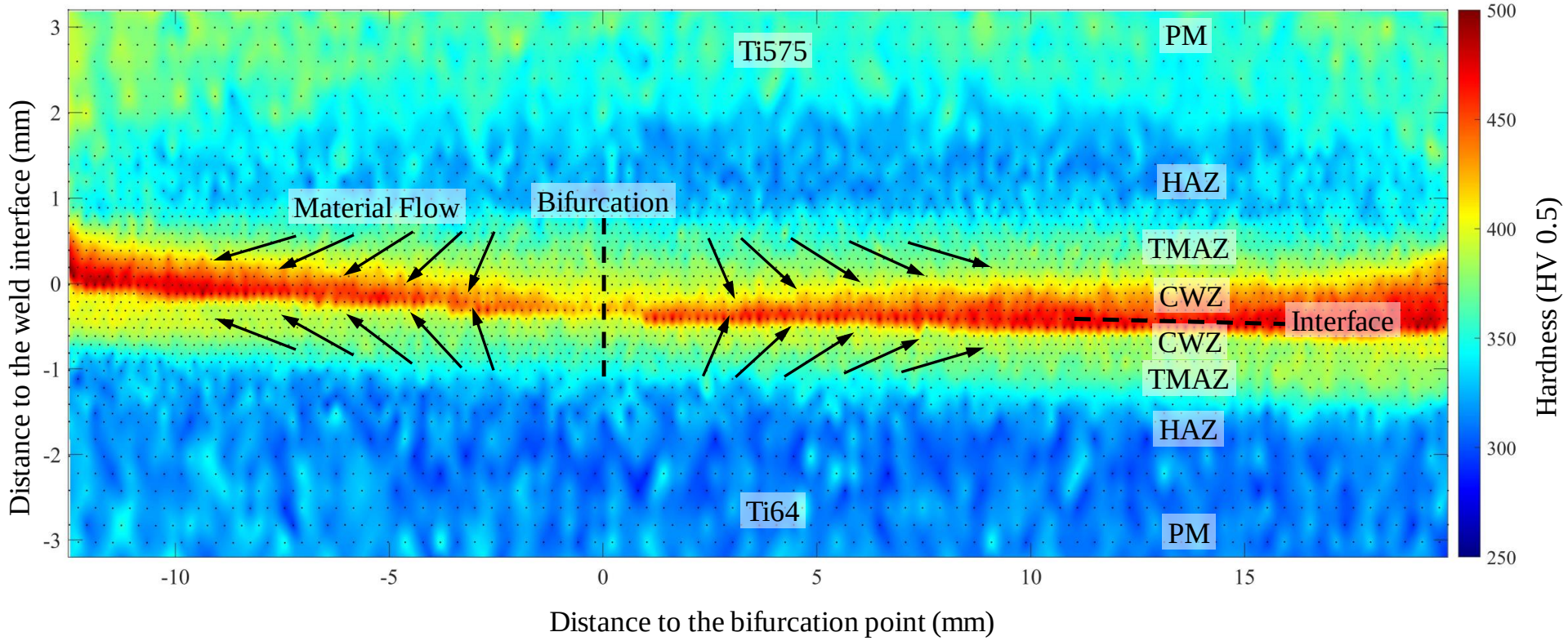

Figure 6.1 A microhardness map of a Ti-575:Ti-64 linear friction weld (Weld ID: 473-03) in as-welded condition. The small black dots represent the actual locations of the indents. The values in between the indents are calculated by natural neighbour interpolation.

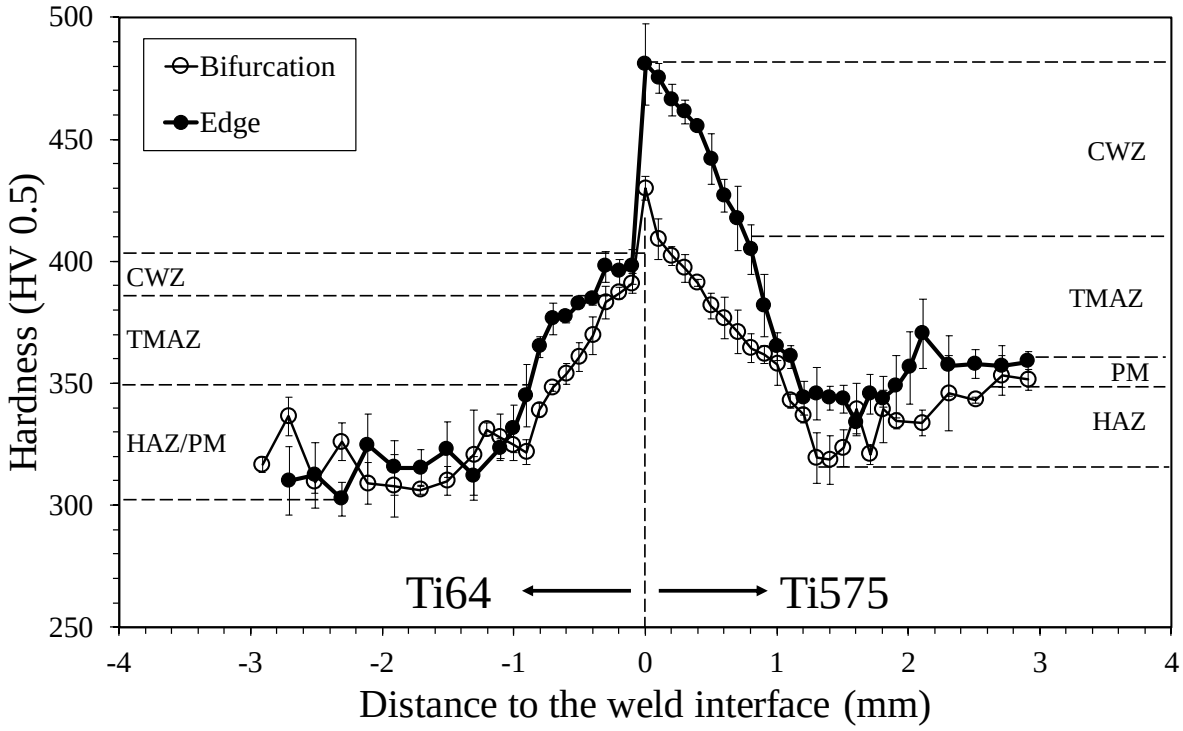

Figure 6.2 Microhardness profiles measured across the weld interface at the bifurcation point of the Ti-64:Ti-575 weld (ID: 473-03) in as-welded condition.

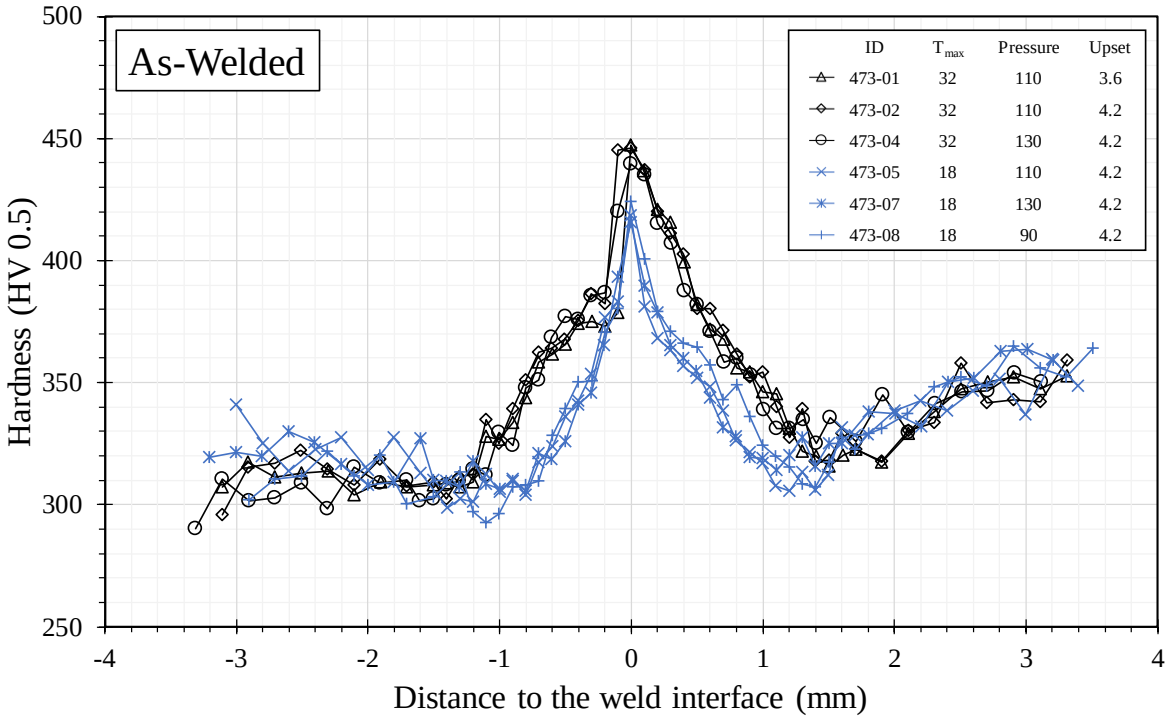

Figure 6.3 Micro-hardness profiles measured across the weld interface at the middle thickness of all Ti-64:Ti-575 welds with different processing variables in as-welded condition. Ti-575 is located on the positive distance side to the weld interface.

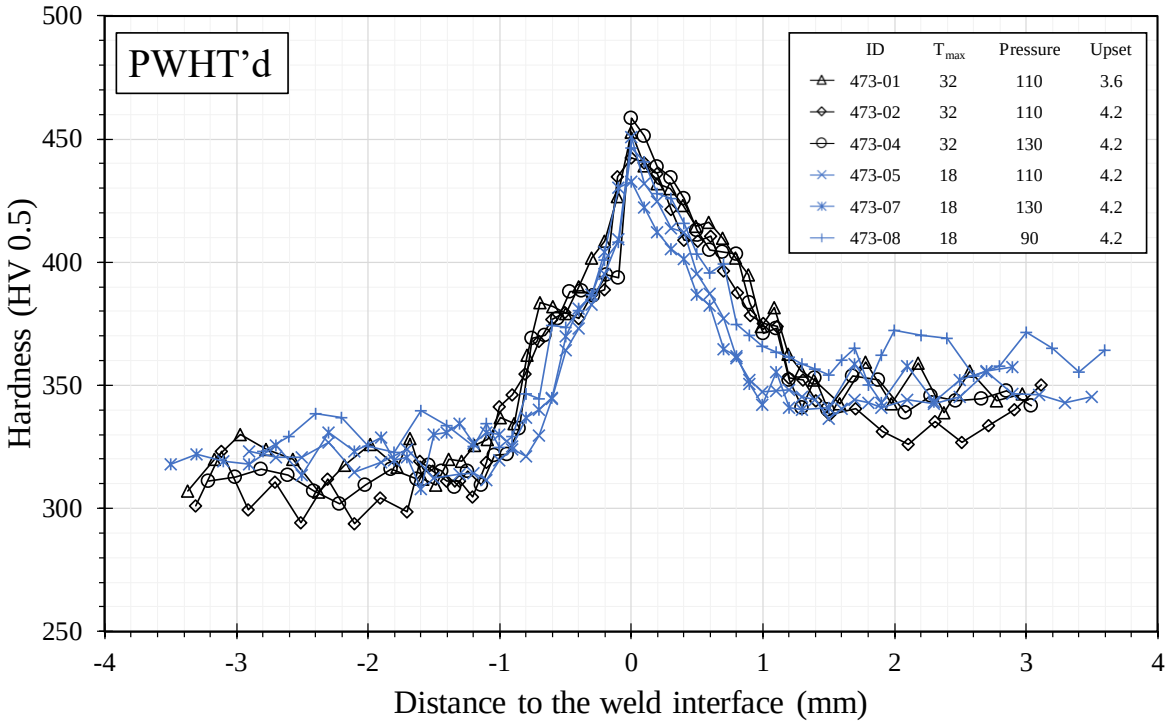

Figure 6.4 Micro-hardness profiles measured across the weld interface at the middle thickness of all Ti-64:Ti-575 welds with different processing variables after PWHT'd at 600℃ for 1 hour. Ti-575 is located on the positive distance side to the weld interface. The hardness reduction in as-welded Ti-575 HAZ can be recovered.

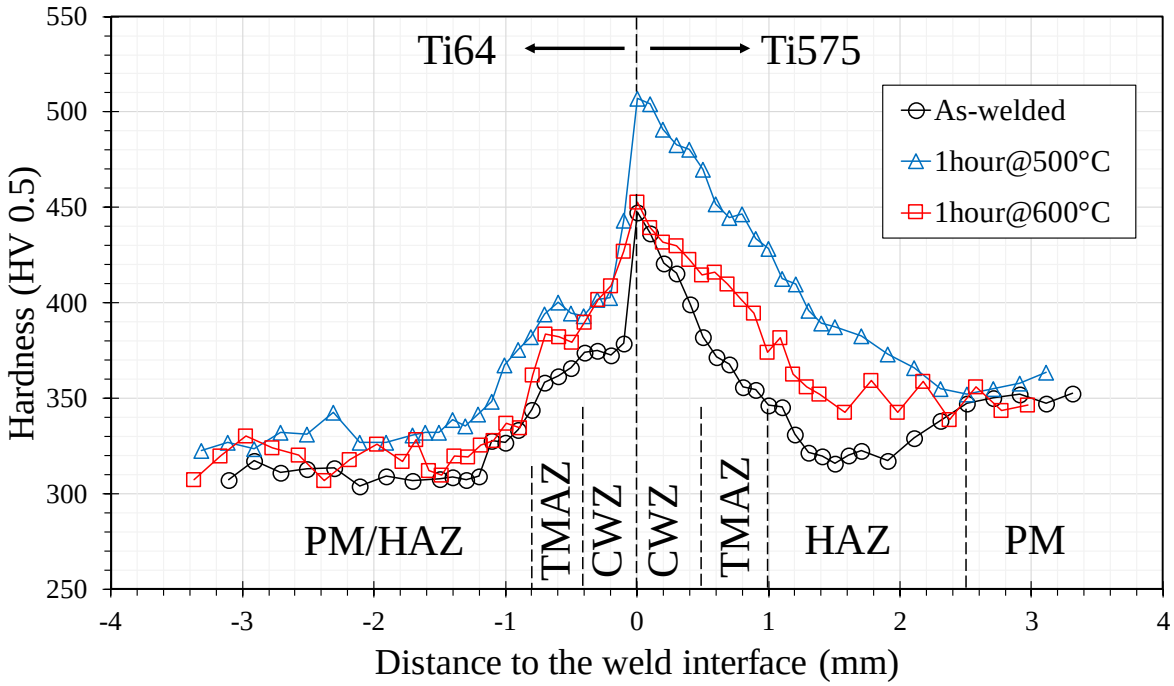

Figure 6.5 Microhardness profiles measured across the weld interface at the middle thickness of the Ti-64:Ti-575 weld (ID: 473-01) in as-welded and PWHT'd conditions.

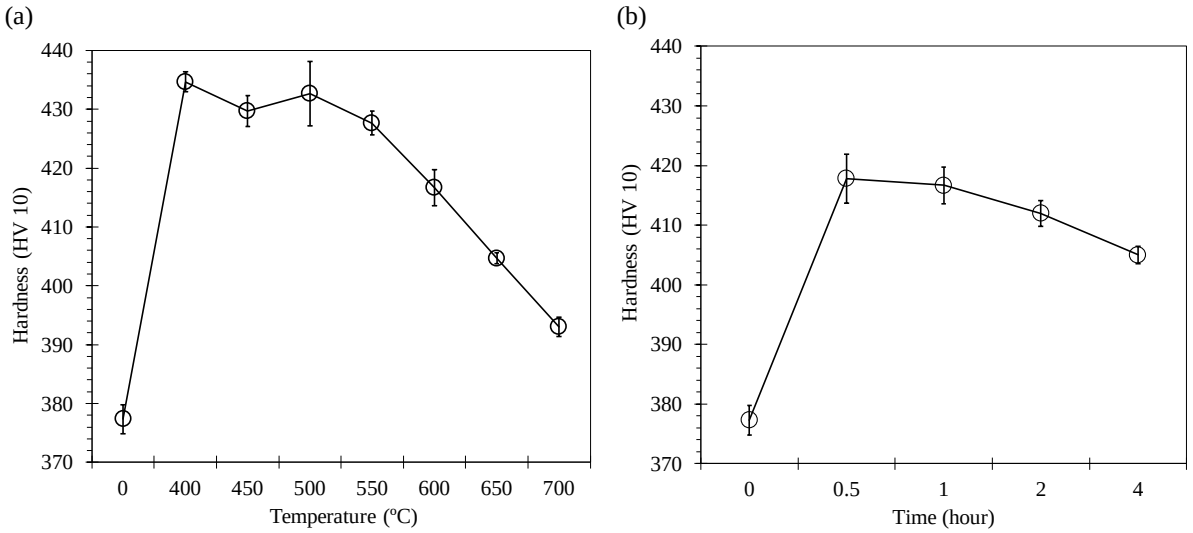

Figure 6.6 Ageing curves of the Ti-64:Ti-575 weld interface. (a) For 1 hour at various temperatures; (b) At 600℃ for various duration.

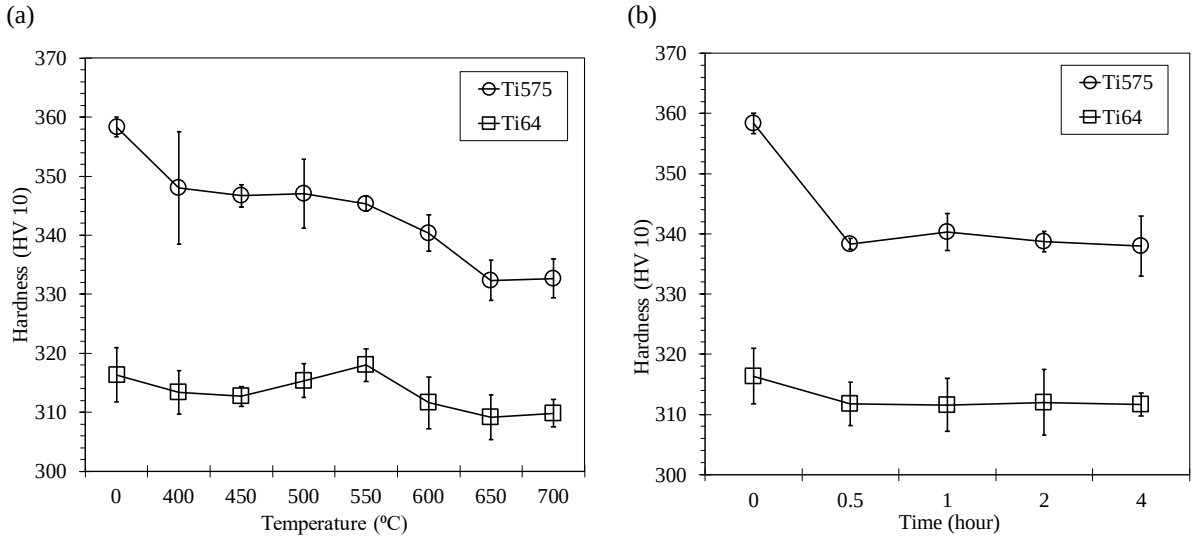

Figure 6.7 Ageing curves of parent materials (Ti-575 and Ti-64). (a) For 1 hour at various temperatures; (b) At 600℃ for various duration.

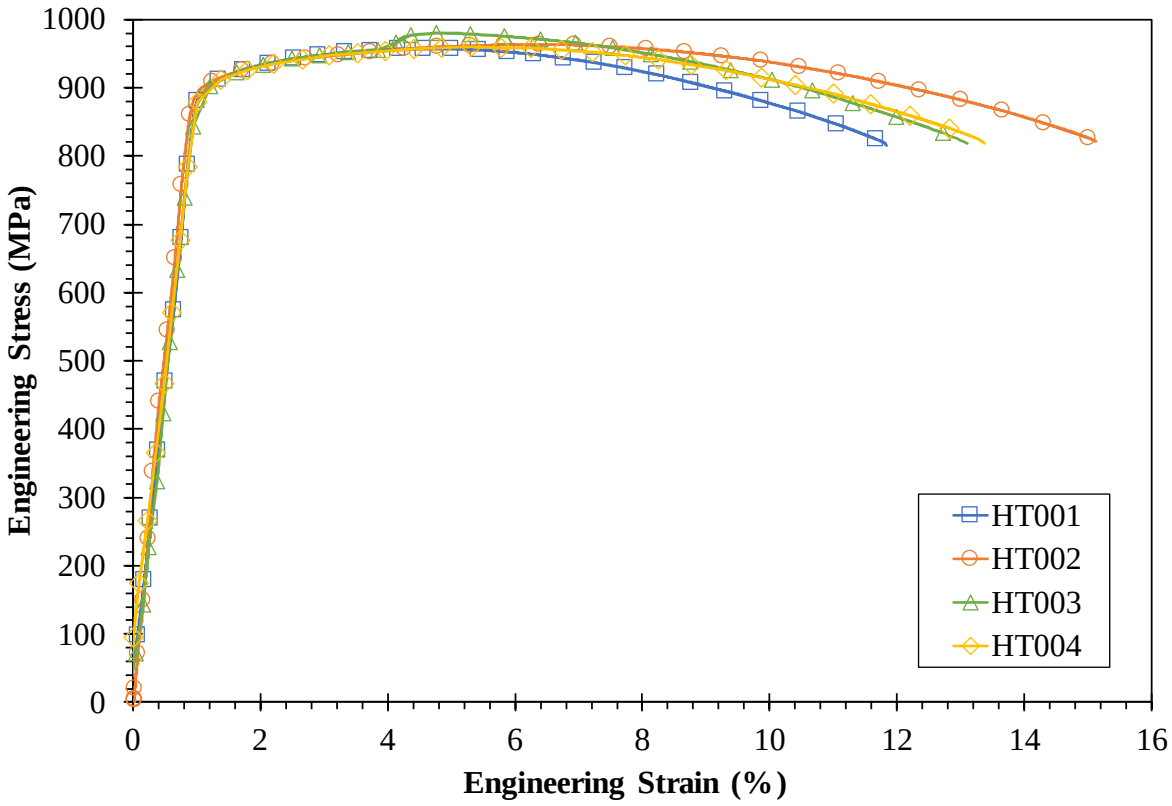

Figure 6.8 Stress-strain curves obtained from the tensile testing at room temperature.

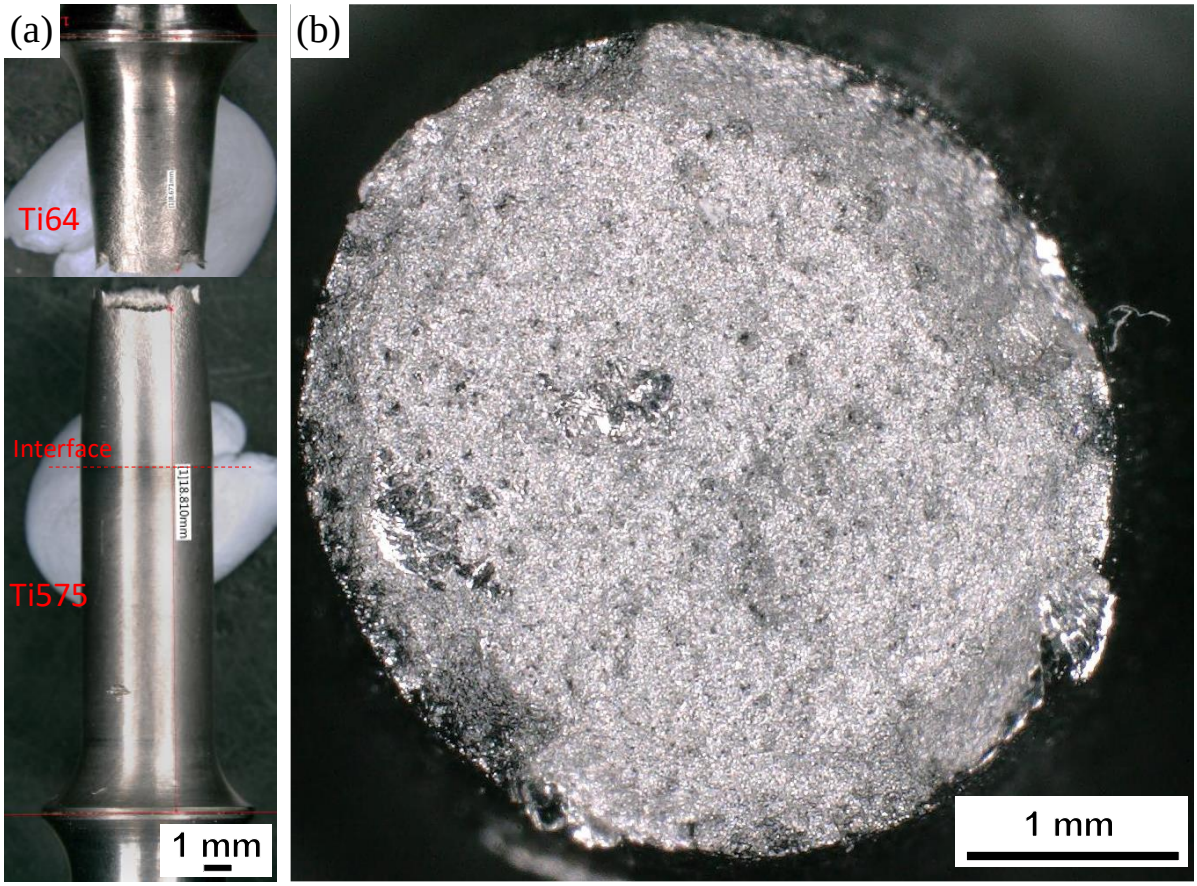

Figure 6.9 Typical optical images of (a) side view and (b) front view of the fracture surface of a specimen failed at Ti-64 parent material after tensile testing. (Specimen ID: HT001)

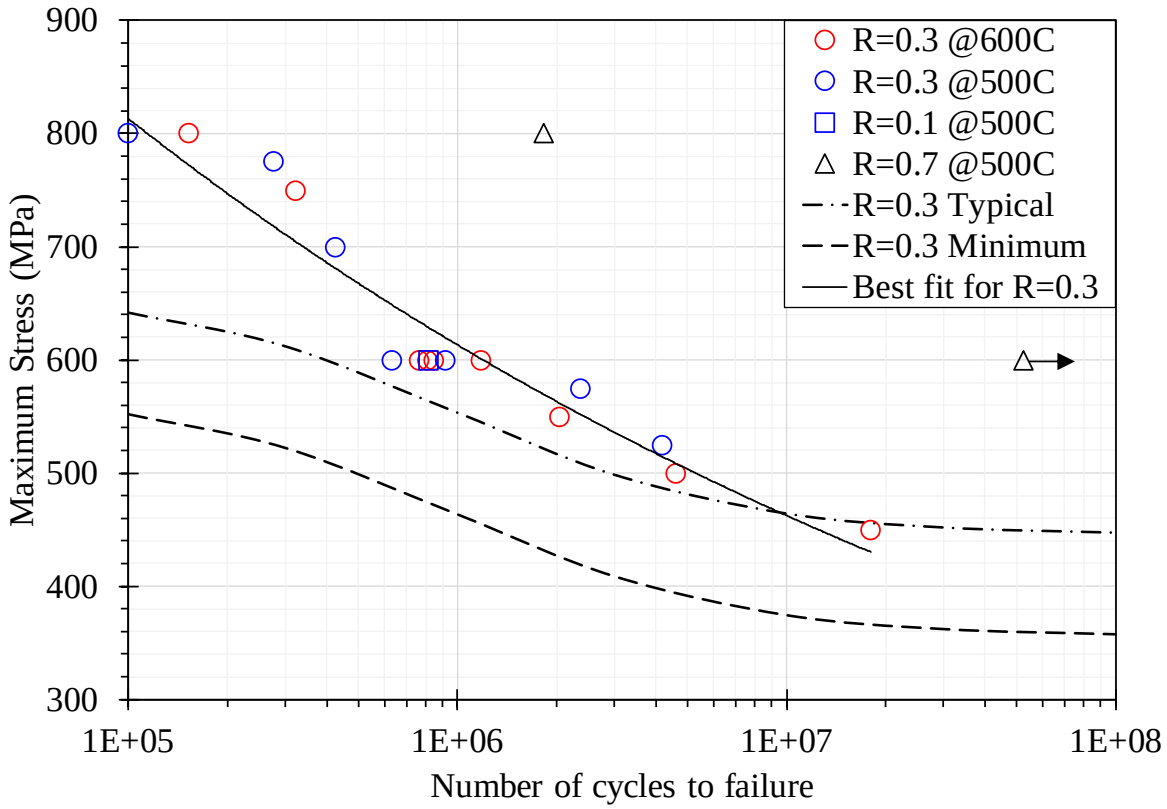

Figure 6.10 Maximum stress S-N curve for high cycle fatigue testing for specimens after PWHT for 1 hour at 500 and 600℃ at $R = 0.3$. Typical and minimum S-N curves of Ti-64 at $R = 0.3$ provided by Rolls-Royce are indicated by the dashed lines. Additional results for samples after PWHT for 1 hour at 500℃ at $R = 0.1$ and 0.7 are also included. The data with an arrow indicates run out (no failure) occurred. All other specimens failed at Ti-64 parent material.

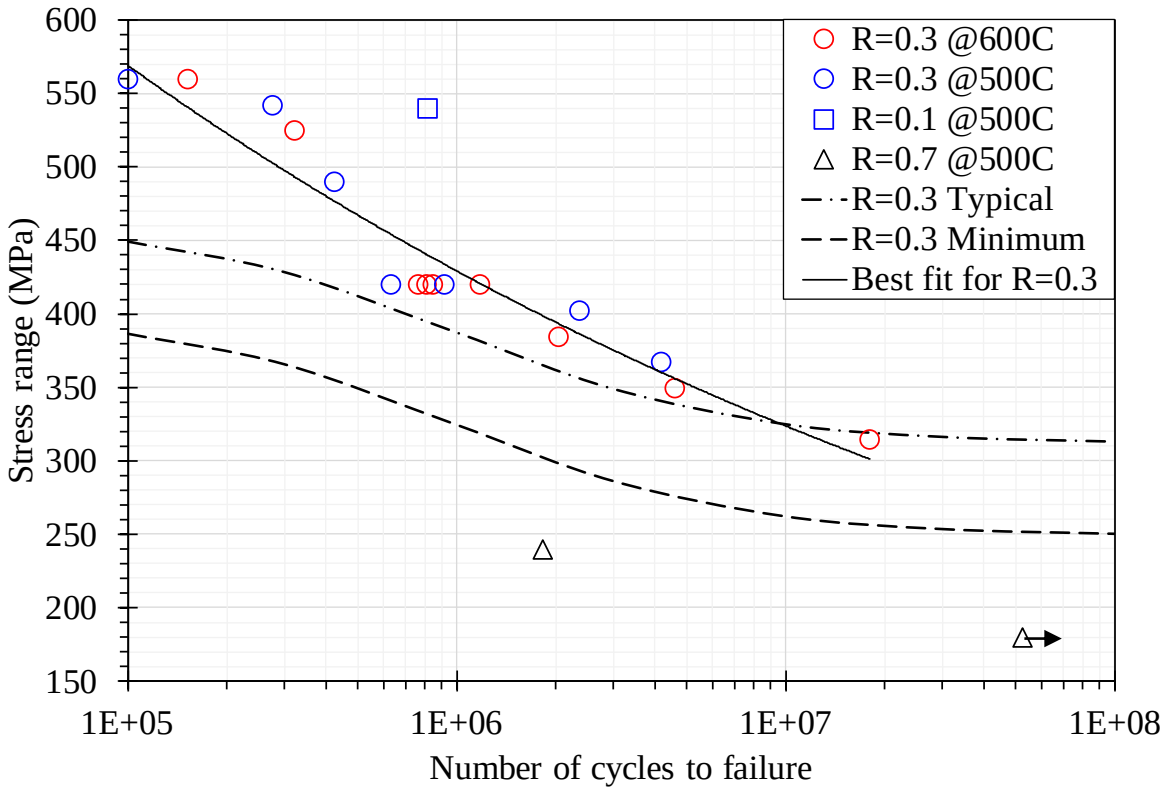

Figure 6.11 Stress range S-N curve for high cycle fatigue testing for specimens after PWHT for 1 hour at 500 and 600℃ at $R = 0.3$. Typical and minimum S-N curves of Ti-64 at $R = 0.3$ provided by Rolls-Royce are indicated by the dashed lines. Additional results for samples after PWHT for 1 hour at 500℃ at $R = 0.1$ and 0.7 are also included. The data with an arrow indicates run out (no failure) occurred. All other specimens failed at Ti-64 parent material.

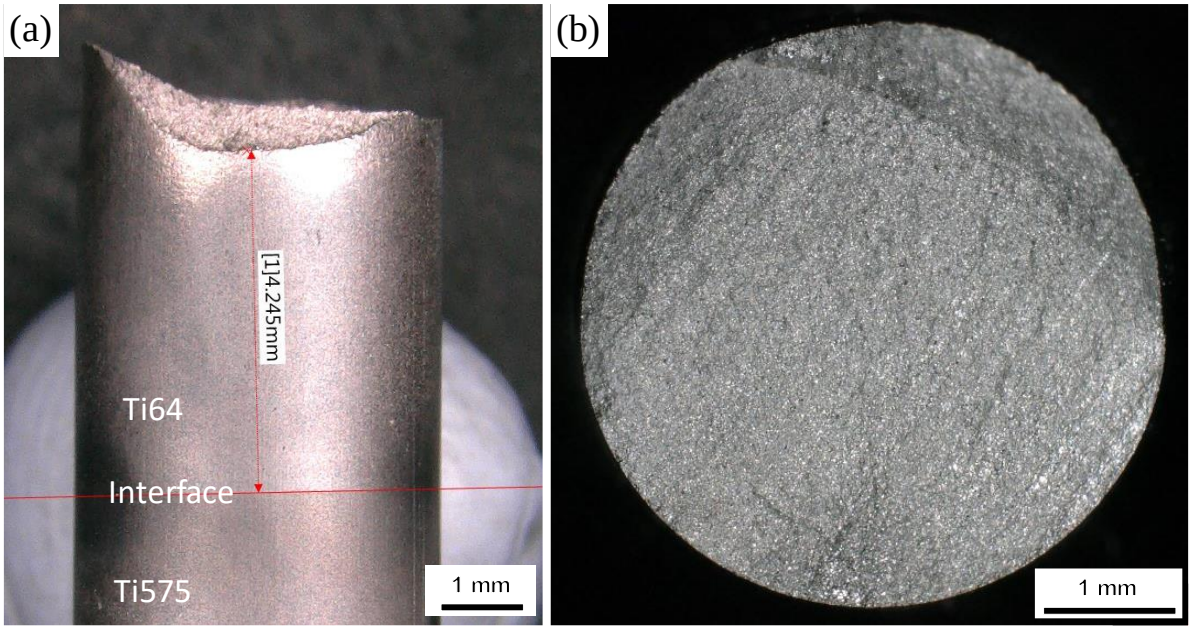

Figure 6.12 Typical optical images of (a) side view and (b) front view of the fracture surface of a specimen failed at Ti-64 parent material after high cycle fatigue testing. (Specimen ID: HF001)

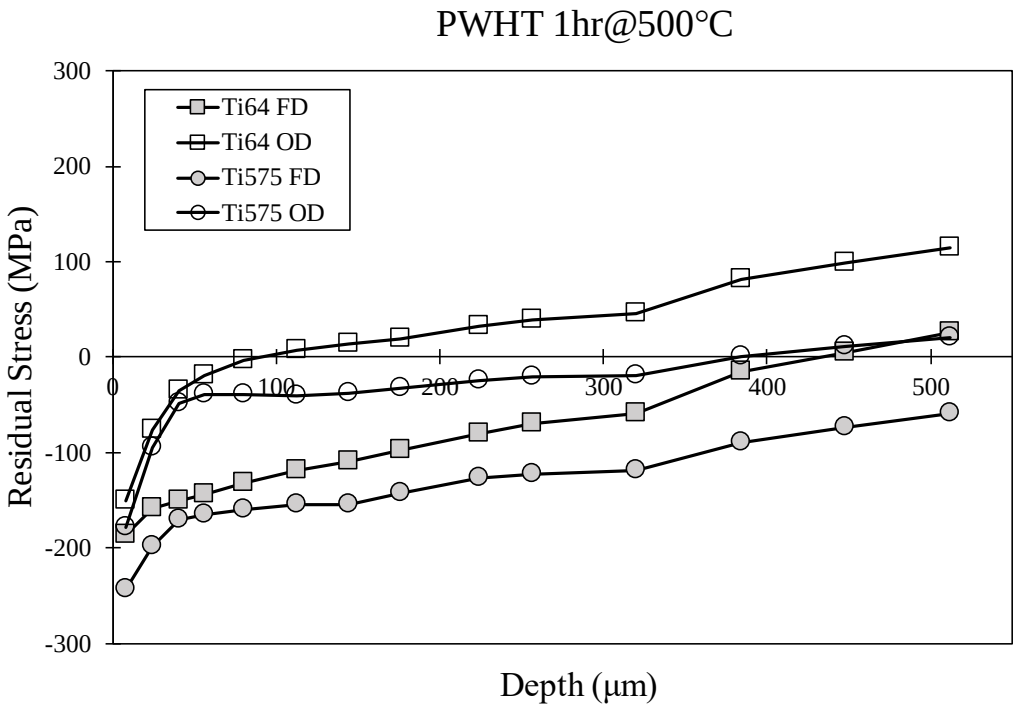

Figure 6.13 Residual stress distributions of specimen after PWHT for 1 hour at 500ºC. FD denotes forge direction; OD denotes oscillation direction. (Specimen ID: CP009)

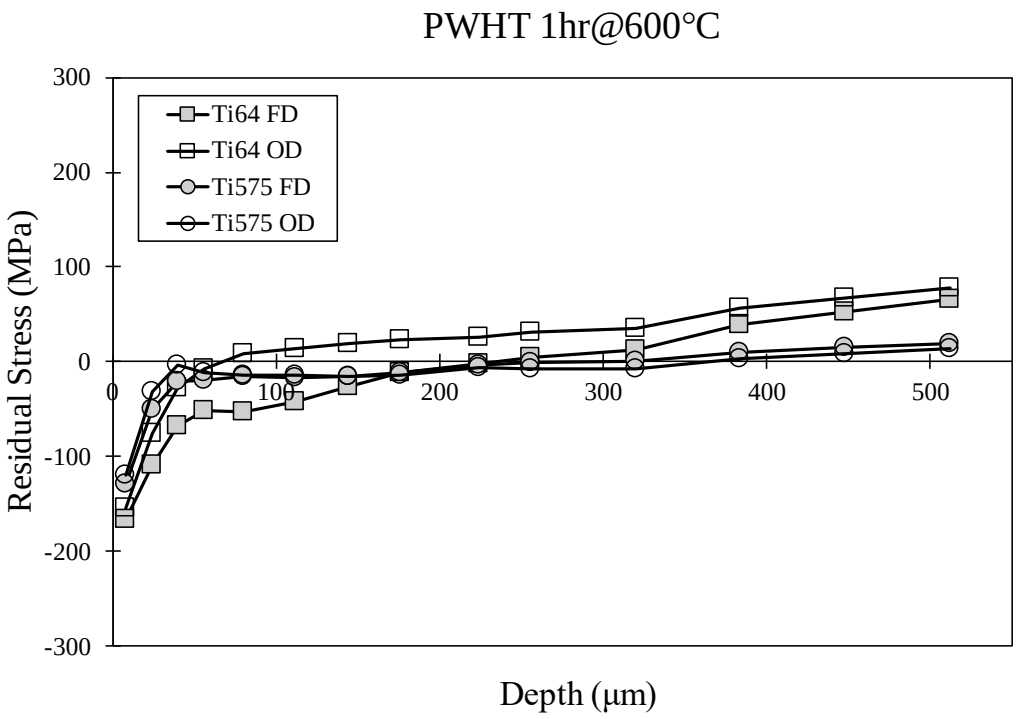

Figure 6.14 Residual stress distributions of specimen after PWHT for 1 hour at 600ºC. FD denotes forge direction; OD denotes oscillation direction. (Specimen ID: CP010)

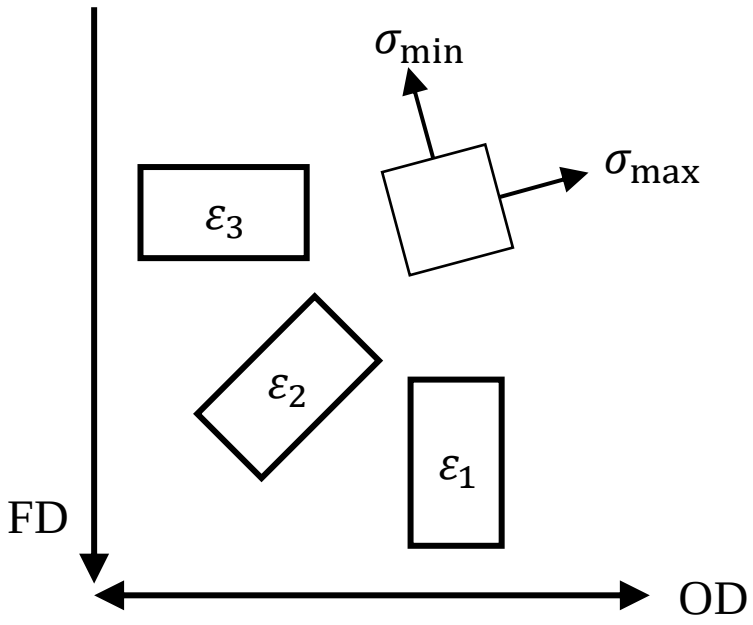

Figure 6.15 Schematic diagram of the principal residual stresses (σ_{max} and σ_{min}) measured at Ti-64 HAZ at depth 512 μm with respect to the oscillation direction (OD), forge direction (FD), and orientation of the strain gauges (ε_1, ε_2, and ε_3).

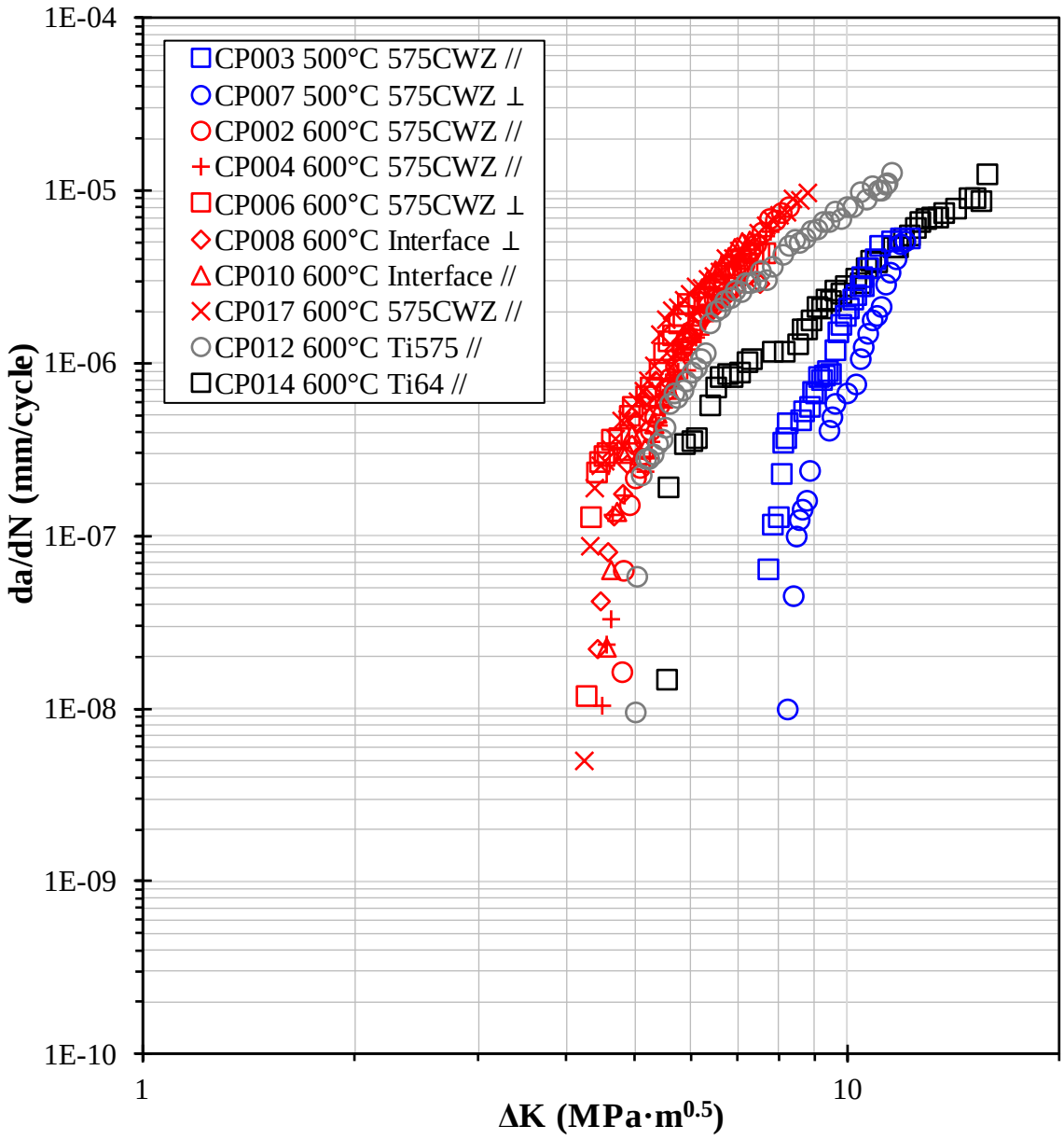

Figure 6.16 Fatigue crack growth curves down to a threshold value tested at room temperature with $R = 0.1$. The geometry of all specimens is 10×9 mm^2. Cracks propagated parallel and perpendicular to the oscillation direction are denoted by // and ⊥, respectively.

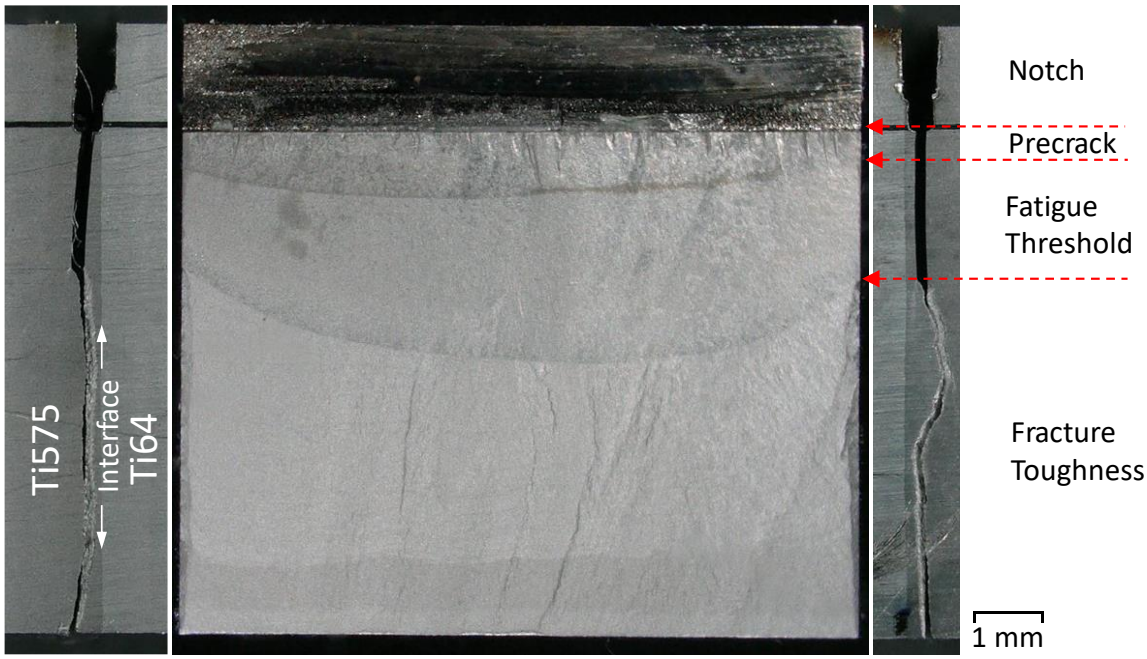

Figure 6.17 Optical micrographs of the front and side views of the fracture surface of specimen CP006 after fatigue crack growth threshold testing and fracture toughness testing. Each stage of the testing is indicated by the red dashed arrows.

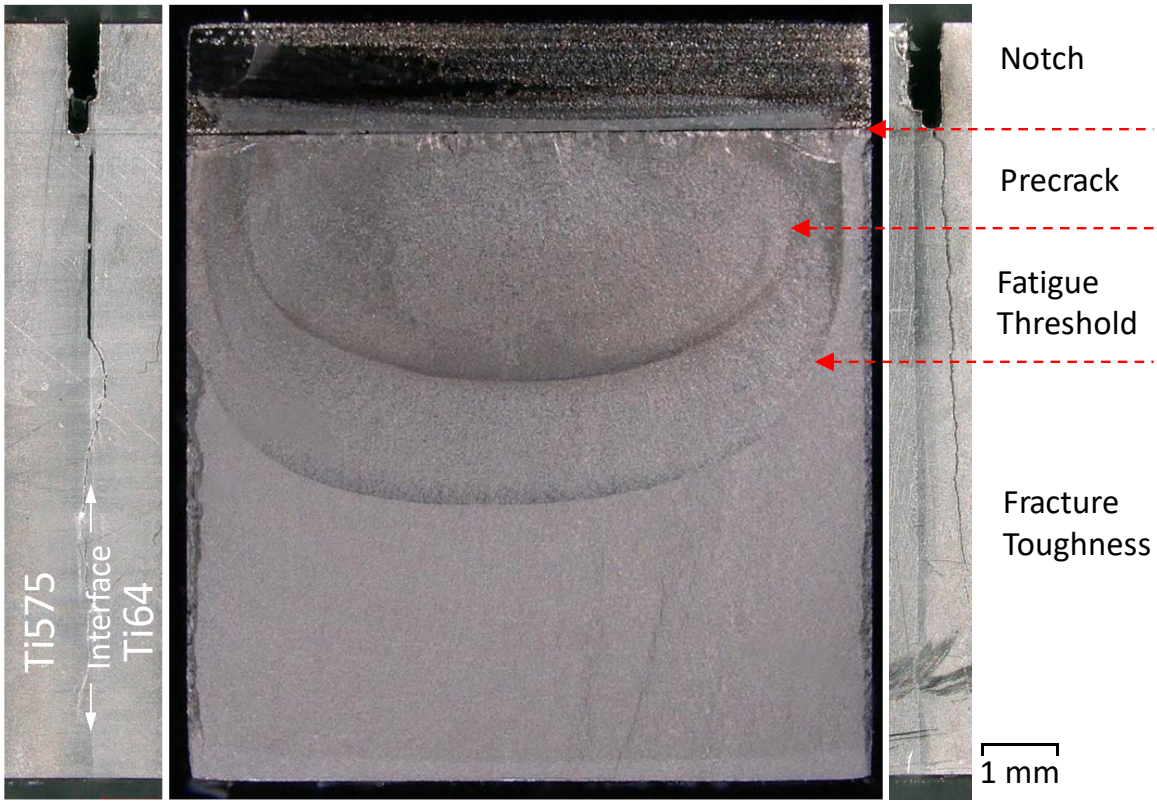

Figure 6.18 Optical micrographs of the front and side views of the fracture surface of specimen CP007 after fatigue crack growth threshold testing and fracture toughness testing. Each stage of the testing is indicated by the red dashed arrows.

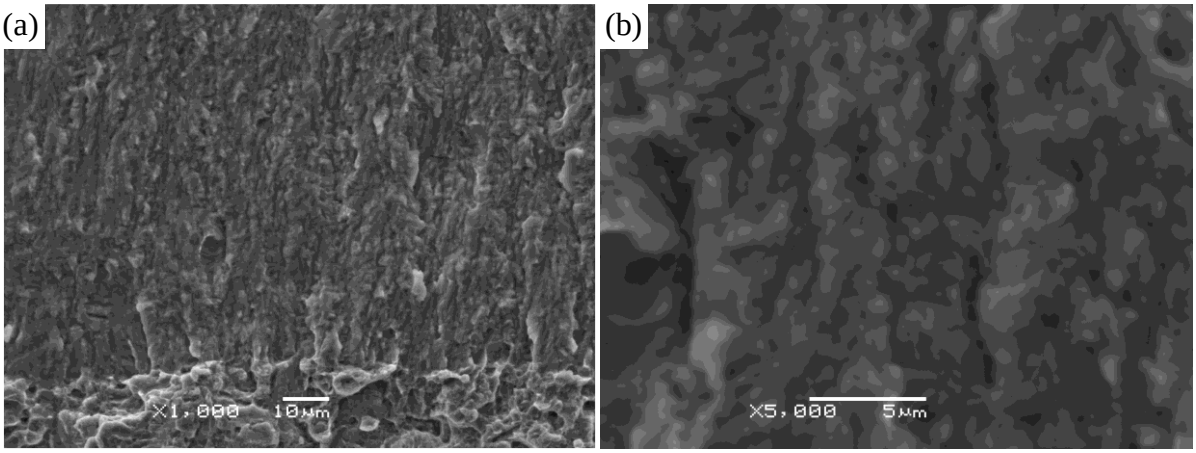

Figure 6.19 (a) Low and (b) high magnification secondary electron images of the fracture surface of CP002 in near threshold region. ($\Delta K_{th} = 4.8$ MPa$\sqrt{\text{m}}$)

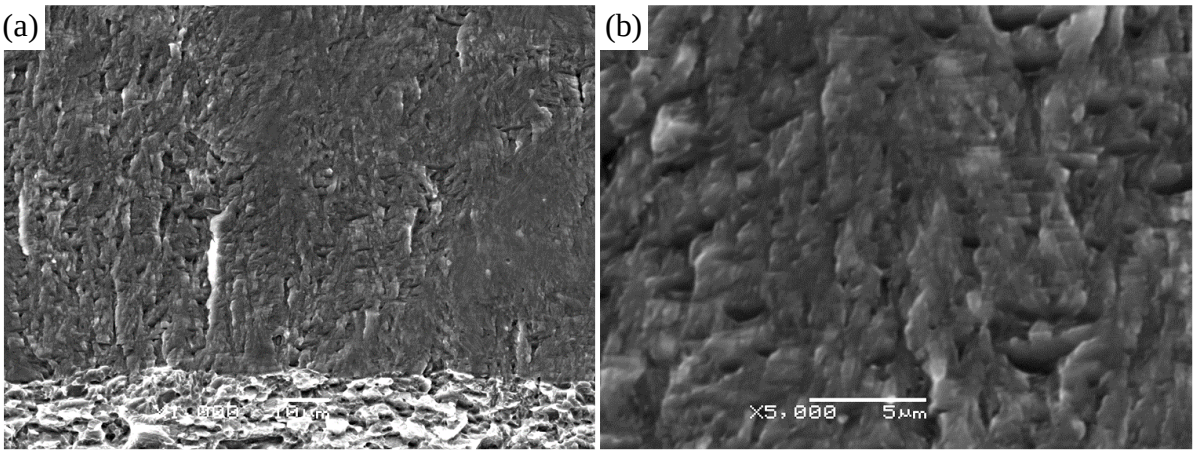

Figure 6.20 (a) Low and (b) high magnification secondary electron images of the fracture surface of CP003 in near threshold region. ($\Delta K_{th} = 7.6$ MPa$\sqrt{\text{m}}$)

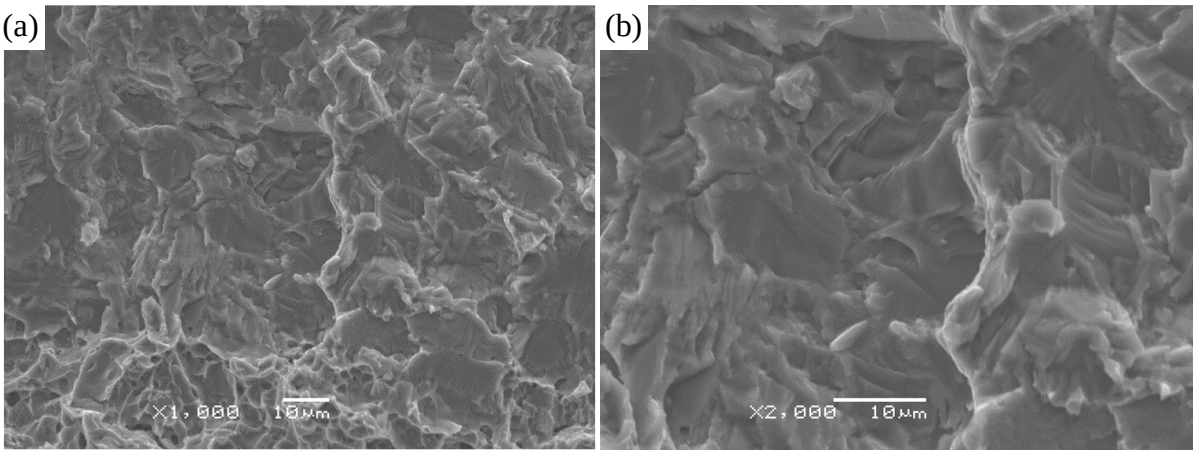

Figure 6.21 (a) Low and (b) high magnification secondary electron images of the fracture surface of CP012 in near threshold region. ($\Delta K_{th} = 5.0$ MPa$\sqrt{\text{m}}$)

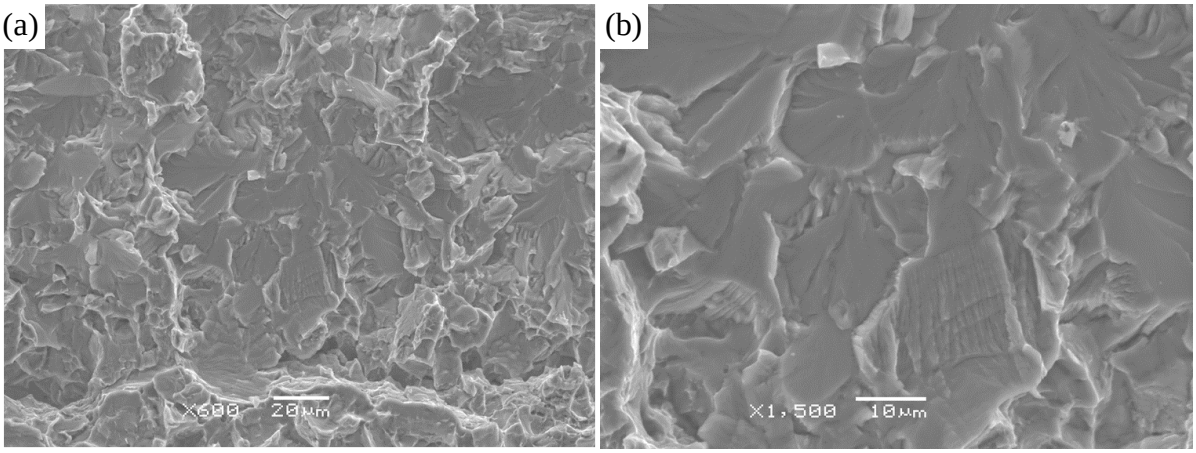

Figure 6.22 (a) Low and (b) high magnification secondary electron images of the fracture surface of CP014 in near threshold region. ($\Delta K_{th} = 5.5$ MPa$\sqrt{\text{m}}$)

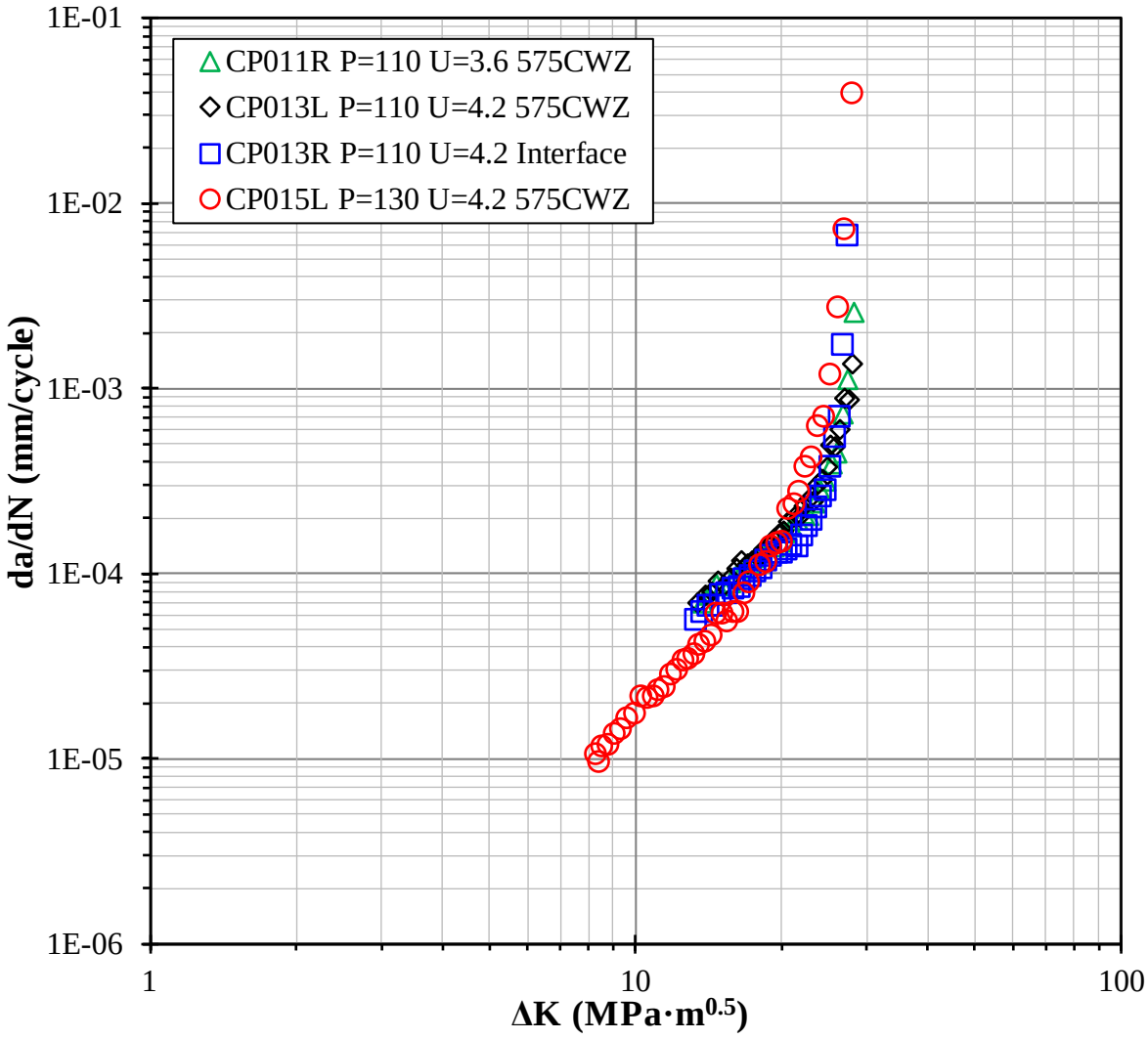

Figure 6.23 Fatigue crack growth curves tested at room temperature with $R = 0.1$ and crack parallel to the oscillation direction. Specimens all PWHT'd for 1 hour at 600°C before testing. The friction pressure and upset of the specimens are denoted by P and U, respectively.

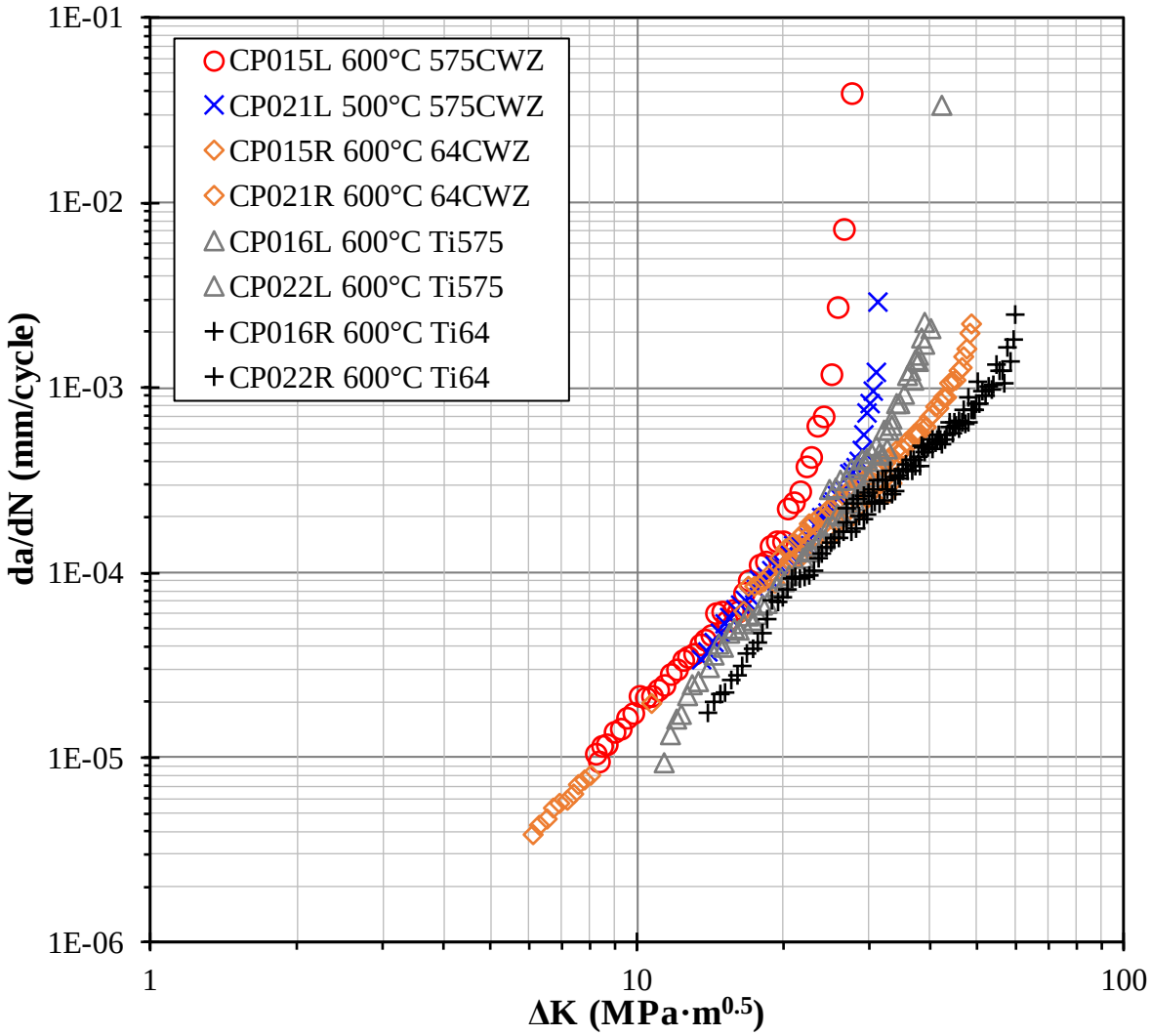

Figure 6.24 Fatigue crack growth curves tested at room temperature with $R = 0.1$ and crack parallel to the oscillation direction. The friction pressure and upset for all specimens are 130 MPa and 4.2 mm, respectively. Specimens all PWHT'd for 1 hour at 500 or 600°C before testing.

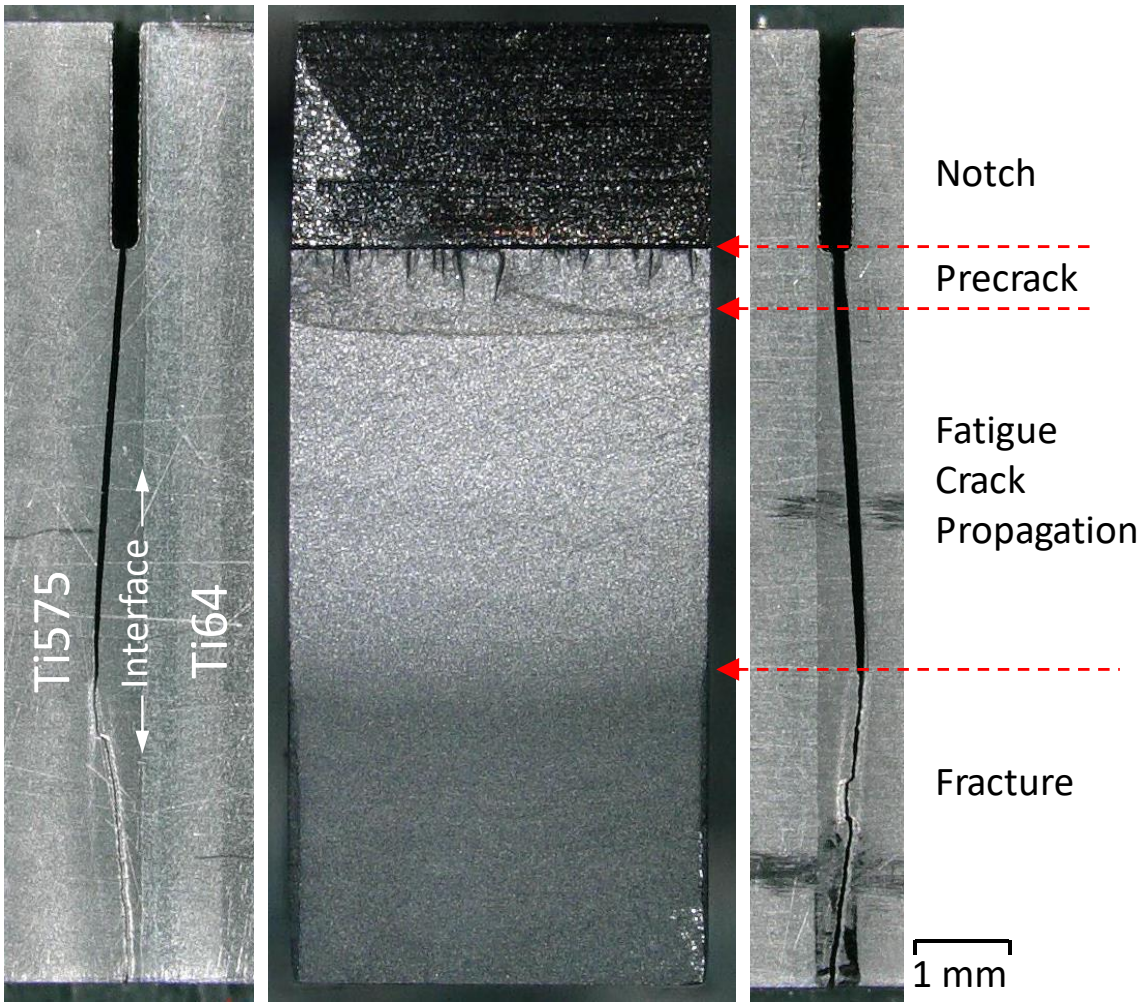

Figure 6.25 Typical optical micrographs of the front and side views of the fracture surface of a specimen after fatigue crack propagation testing. Each stage of the testing is indicated by the red dashed arrows. (Specimen ID: CP011R)

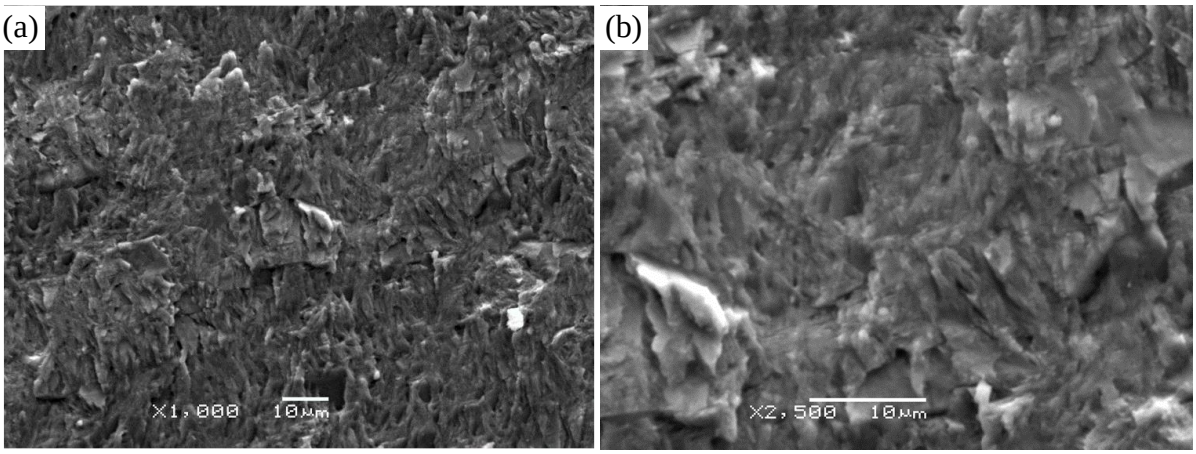

Figure 6.26 (a) Low and (b) high magnification secondary electron images of the fracture surface of CP015L in low ΔK region. ($\Delta K = 8.4$ MPa$\sqrt{\text{m}}$)

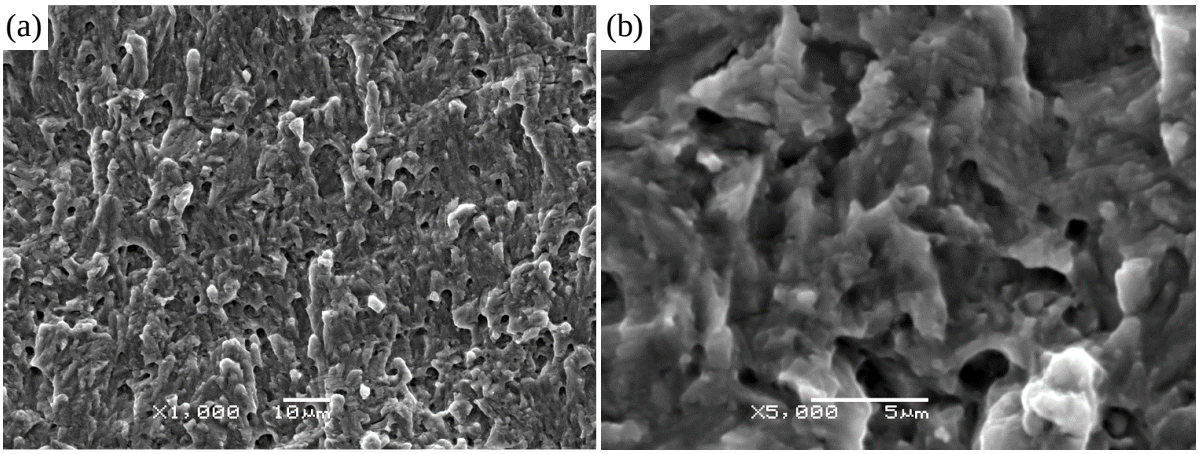

Figure 6.27 (a) Low and (b) high magnification secondary electron images of the fracture surface of CP015L in high ΔK region. ($\Delta K = 20.1$ MPa$\sqrt{\text{m}}$)

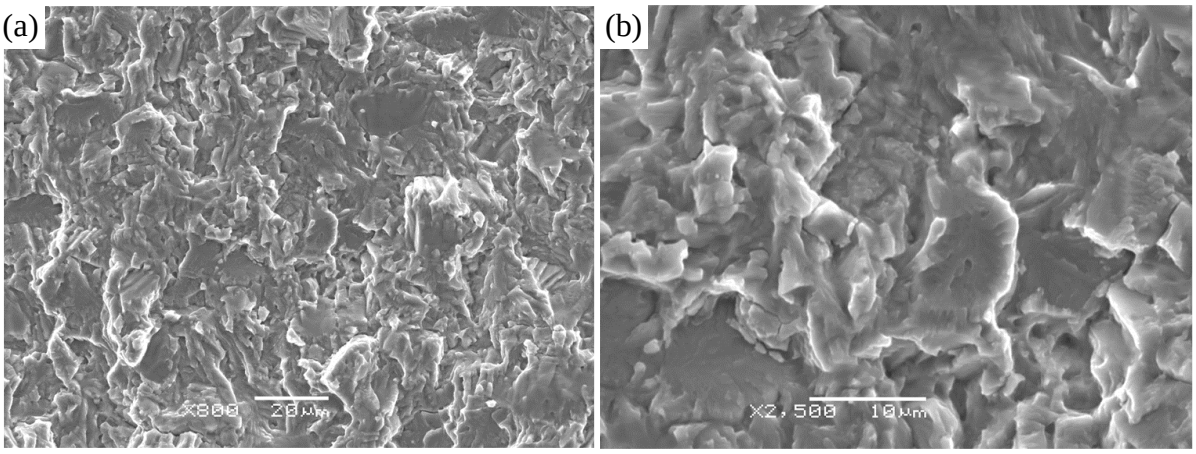

Figure 6.28 (a) Low and (b) high magnification secondary electron images of the fracture surface of CP016L in low ΔK region. ($\Delta K = 13.1$ MPa$\sqrt{\text{m}}$)

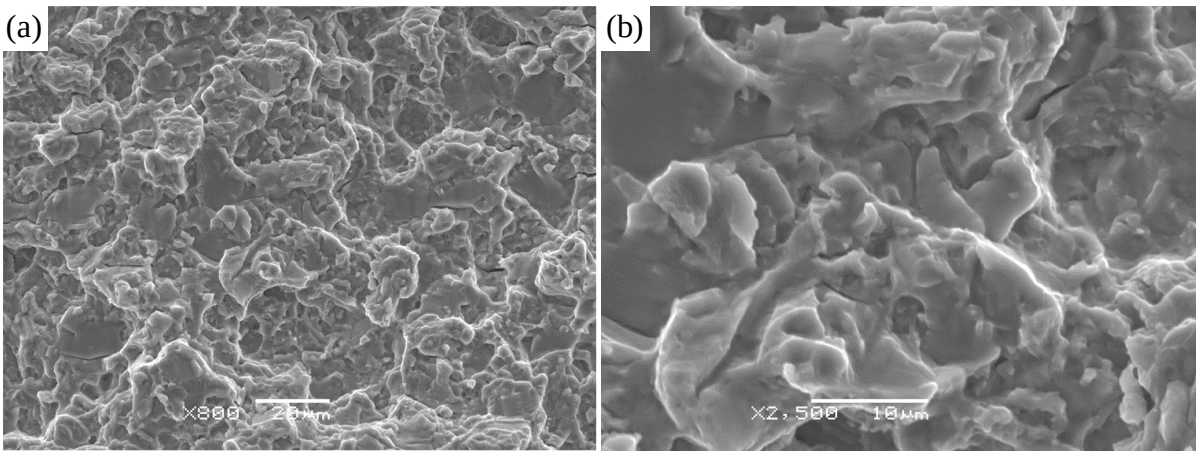

Figure 6.29 (a) Low and (b) high magnification secondary electron images of the fracture surface of CP016L in high ΔK region. ($\Delta K = 32.9$ MPa$\sqrt{\text{m}}$)

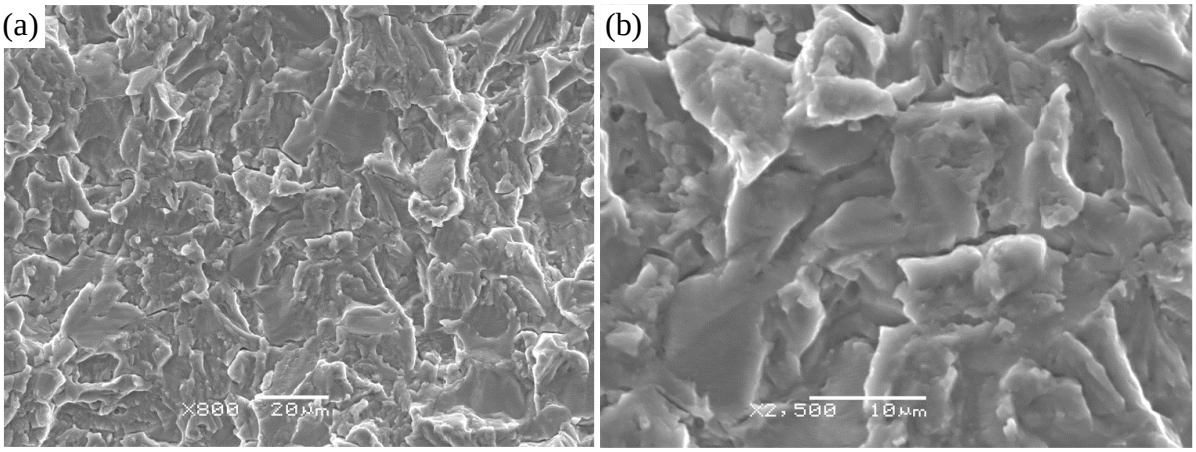

Figure 6.30 (a) Low and (b) high magnification secondary electron images of the fracture surface of CP022R in low ΔK region. ($\Delta K = 27.9$ MPa$\sqrt{\text{m}}$)

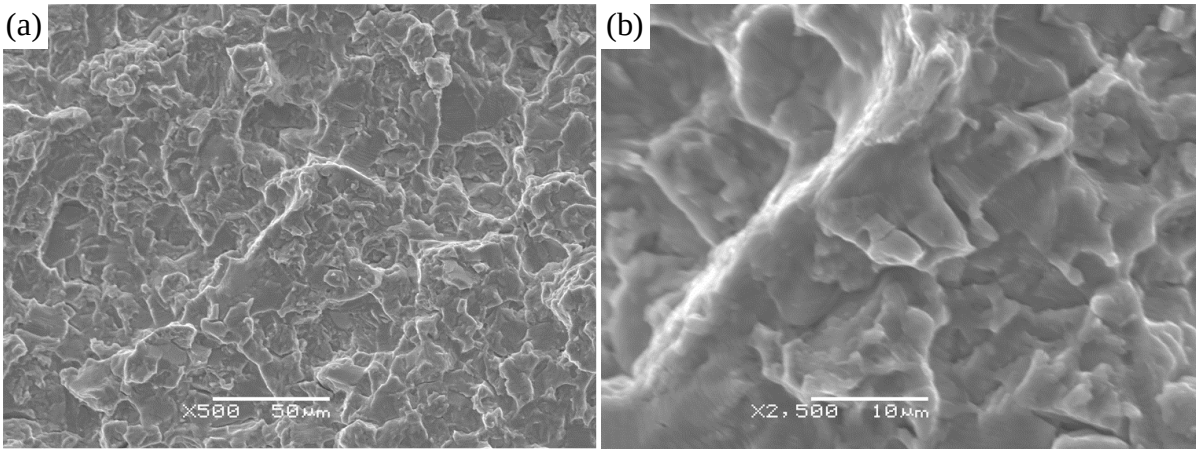

Figure 6.31 (a) Low and (b) high magnification secondary electron images of the fracture surface of CP022R in high ΔK region. ($\Delta K = 48.8$ MPa$\sqrt{\text{m}}$)

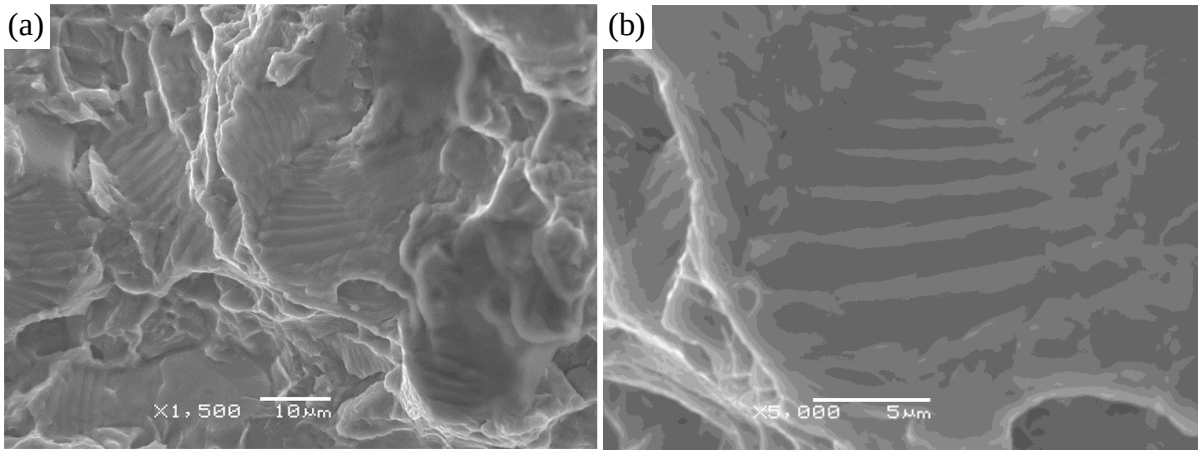

Figure 6.32 (a) Low and (b) high magnification secondary electron images of the fracture surface of CP022R right before fracture. Fatigue striations were observed in this region. ($\Delta K = 60.9$ MPa$\sqrt{\text{m}}$)

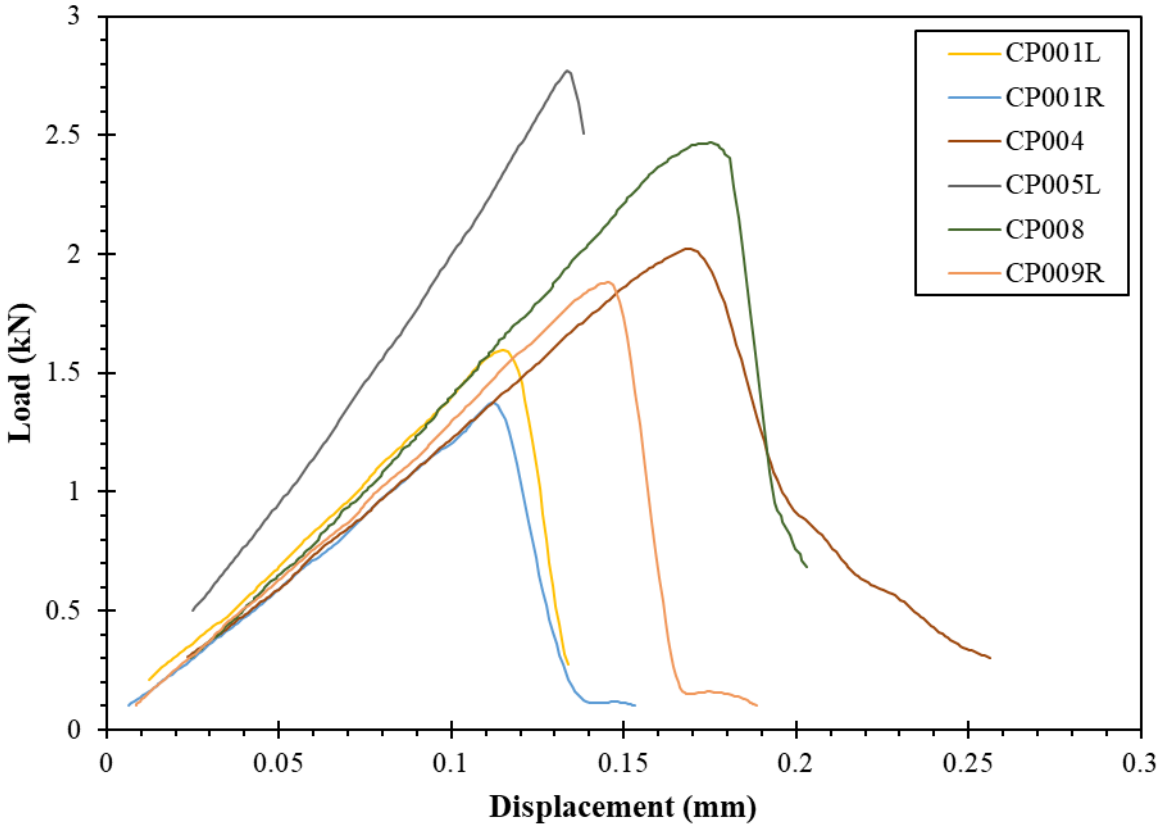

Figure 6.33 Examples of typical fracture toughness load-displacement curves obtained in this study.

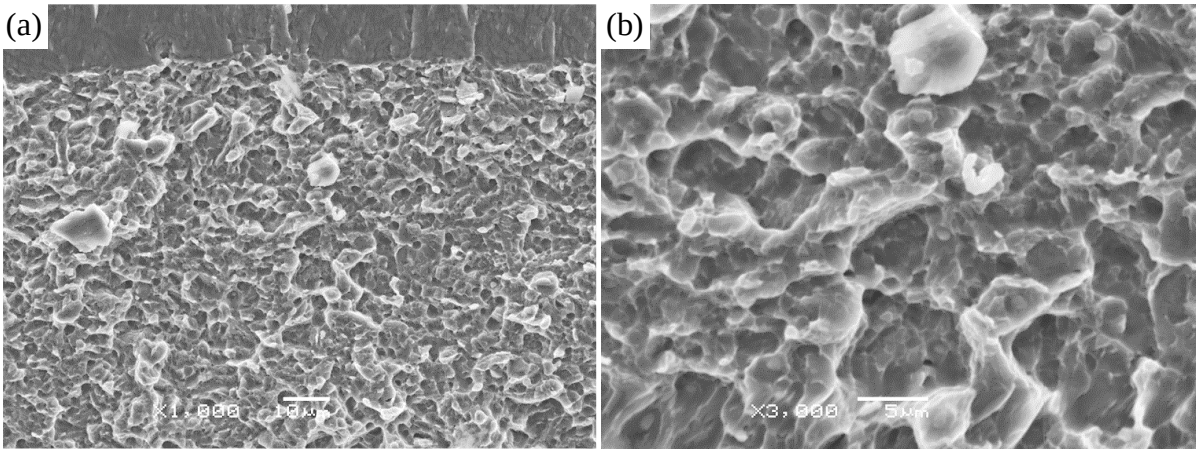

Figure 6.34 (a) Low and (b) high magnification secondary electron images of the fracture surface of CP005L in fracture region. ($K_Q = 33.7$ MPa$\sqrt{\text{m}}$)

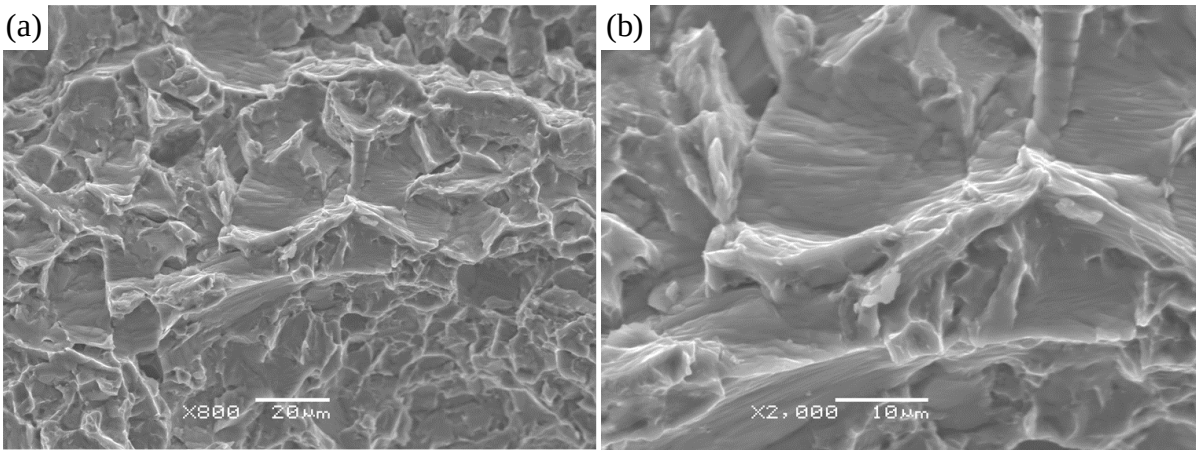

Figure 6.35 (a) Low and (b) high magnification secondary electron images of the fracture surface of CP014 in fracture region. ($K_Q = 66.8$ MPa$\sqrt{\text{m}}$)

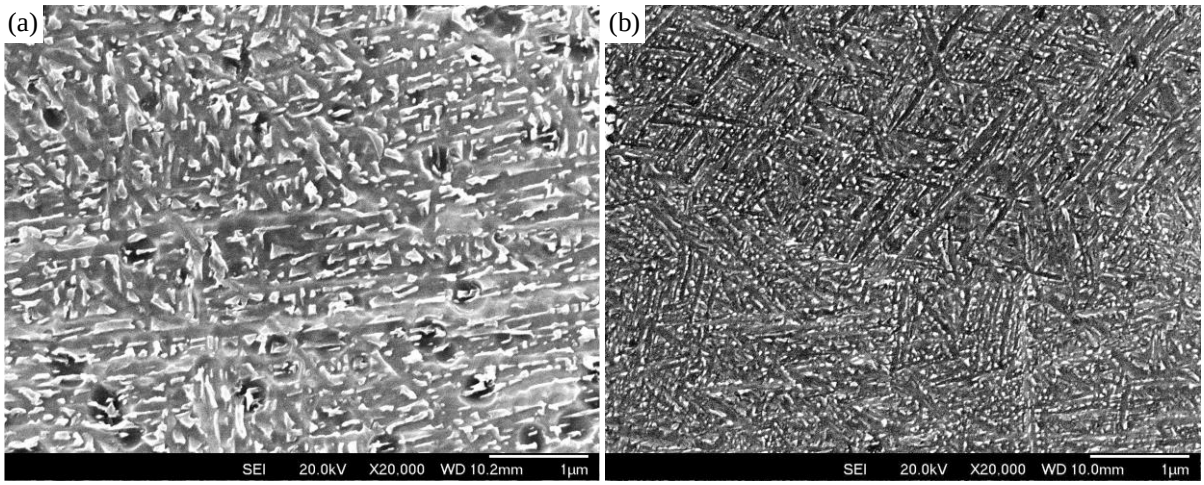

Figure 6.36 Secondary electron images of Ti-575 CWZ after PWHT for 1 hour at (a) 600℃ and (b) 500℃.

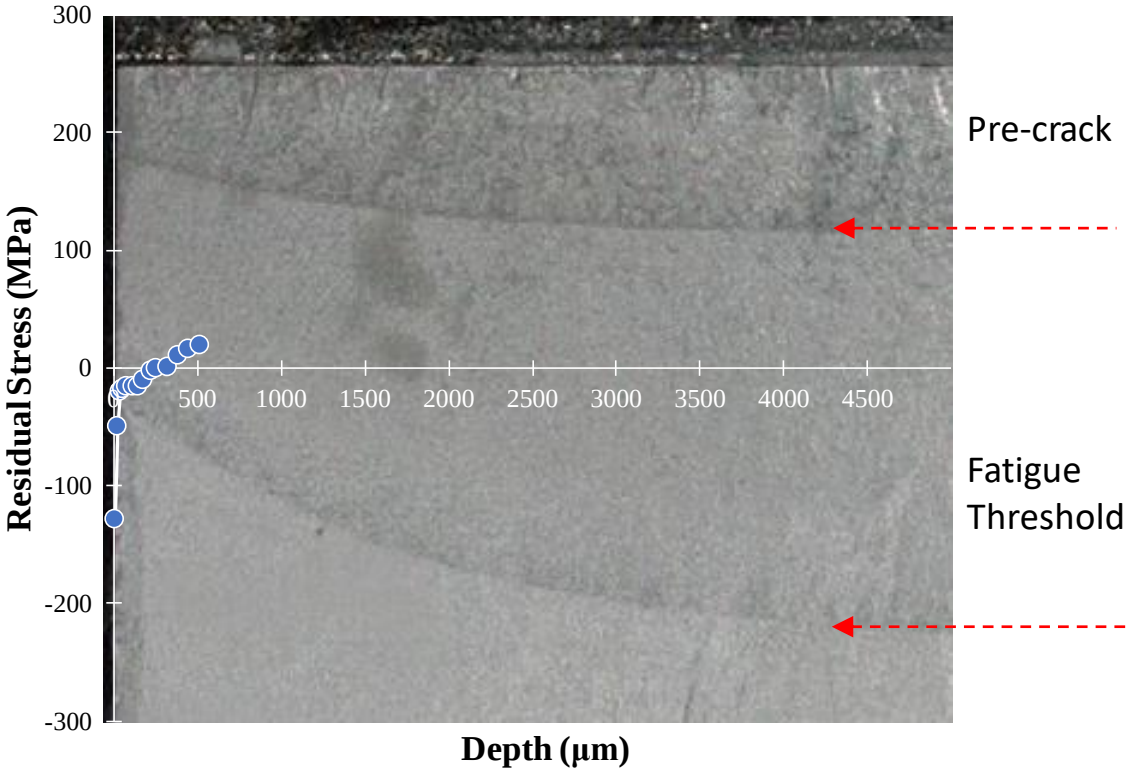

Figure 6.37 Residual stress measurement overlaid onto the fracture surface of CP006 (PWHT'd at 600℃), showing the effect of residual stress on the shape of the crack front.

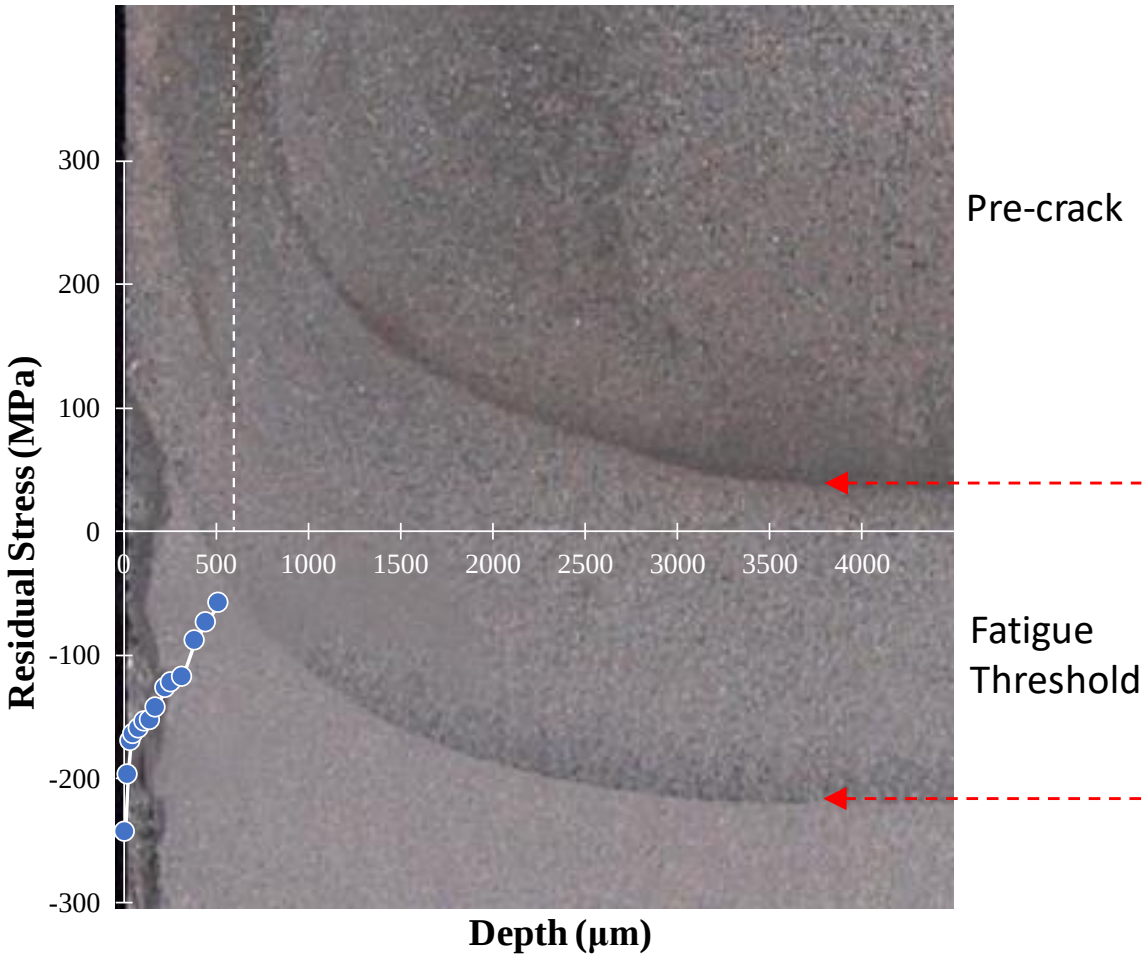

Figure 6.38 Residual stress measurement overlaid onto the fracture surface of CP007 (PWHT'd at 500℃), showing the effect of residual stress on the shape of the crack front.

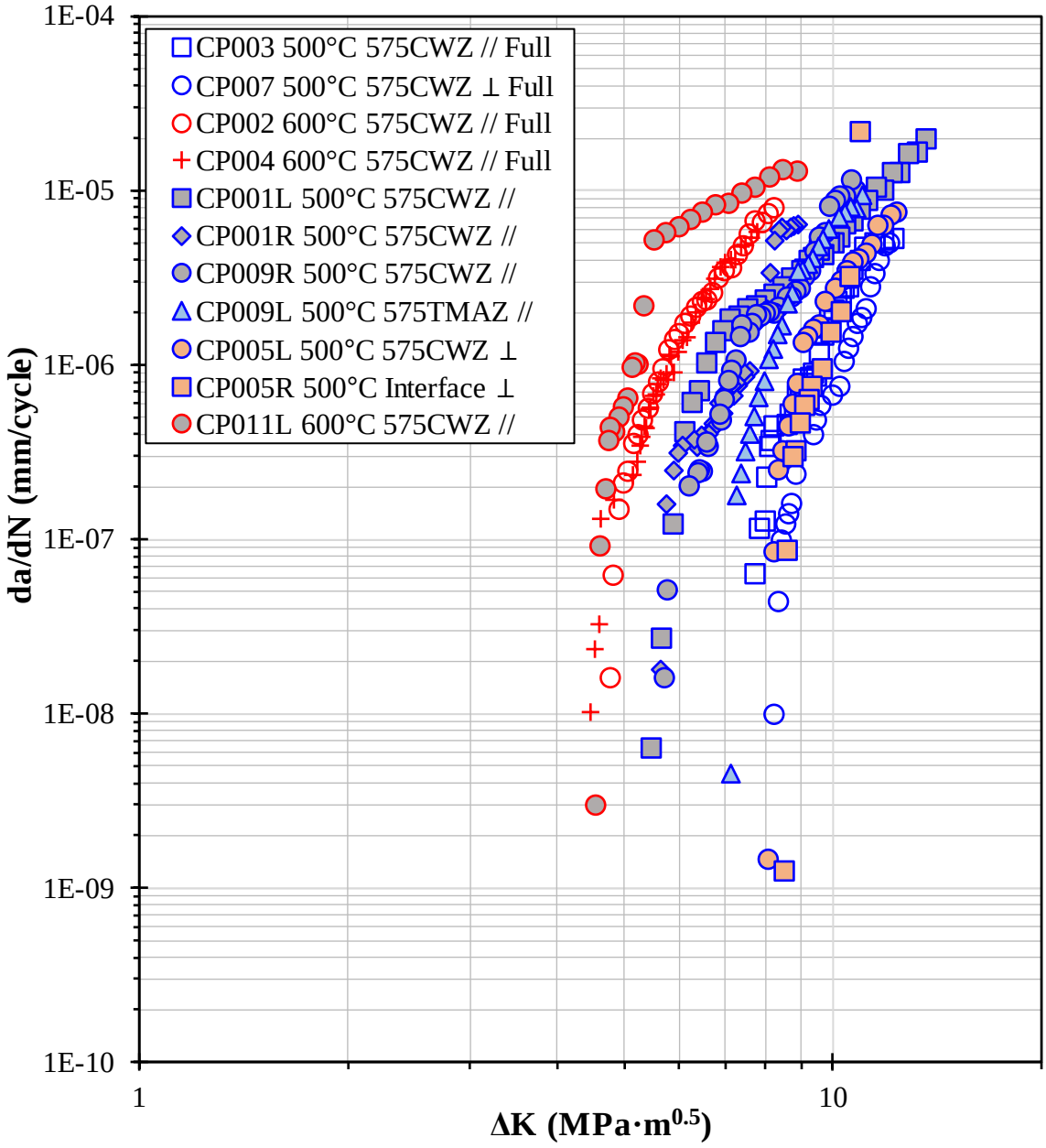

Figure 6.39 Fatigue crack growth curves down to a threshold value tested at room temperature with $R = 0.1$. All specimens were sliced in half to achieve further relief of residual stress except for those who denoted by 'Full'. Cracks propagated parallel and perpendicular to the oscillation direction are denoted by // and ⊥, respectively.

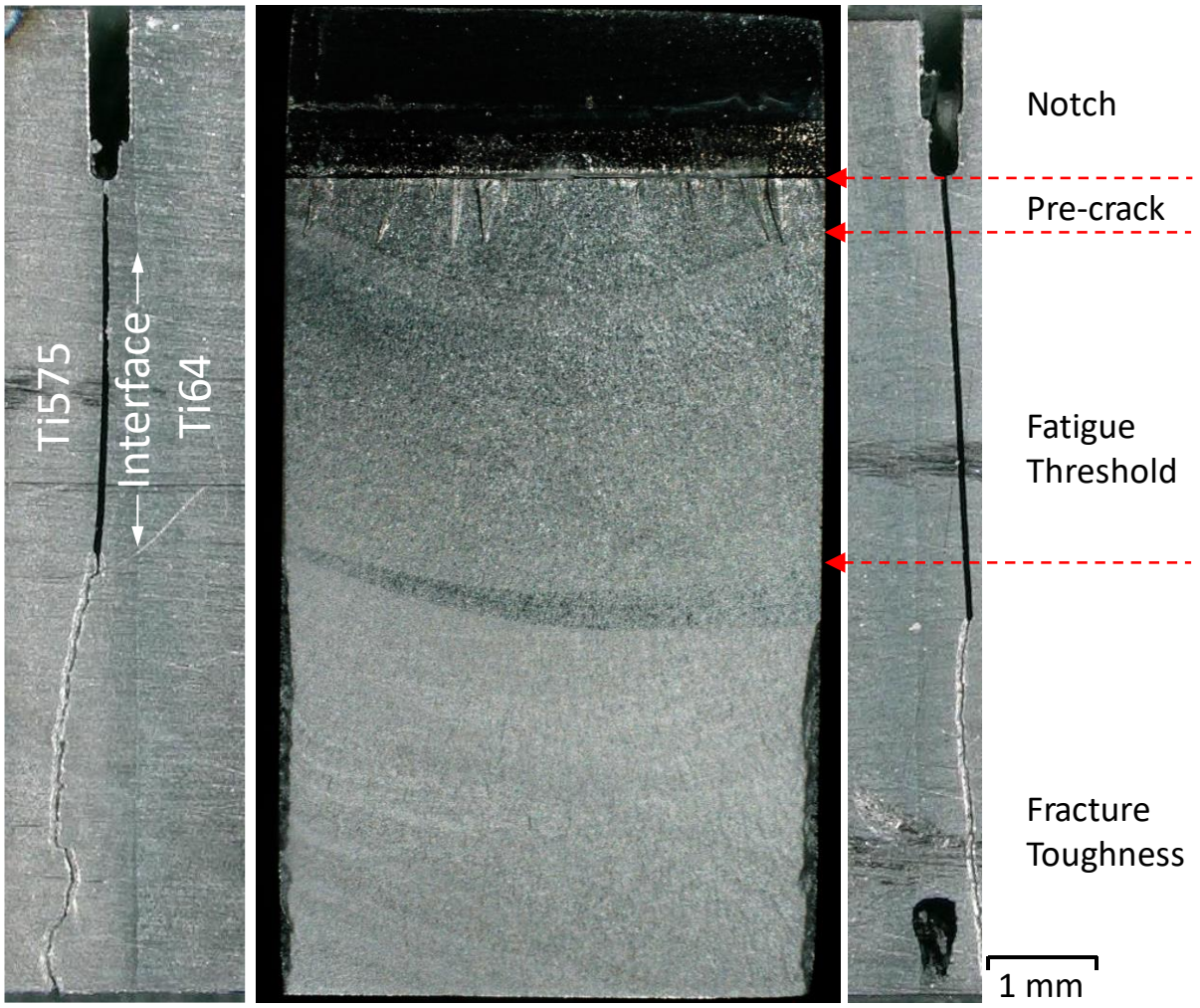

Figure 6.40 Optical micrographs of the front and side views of the fracture surface of specimen CP001L after fatigue crack growth threshold testing and fracture toughness testing. Each stage of the testing is indicated by the red dashed arrows.

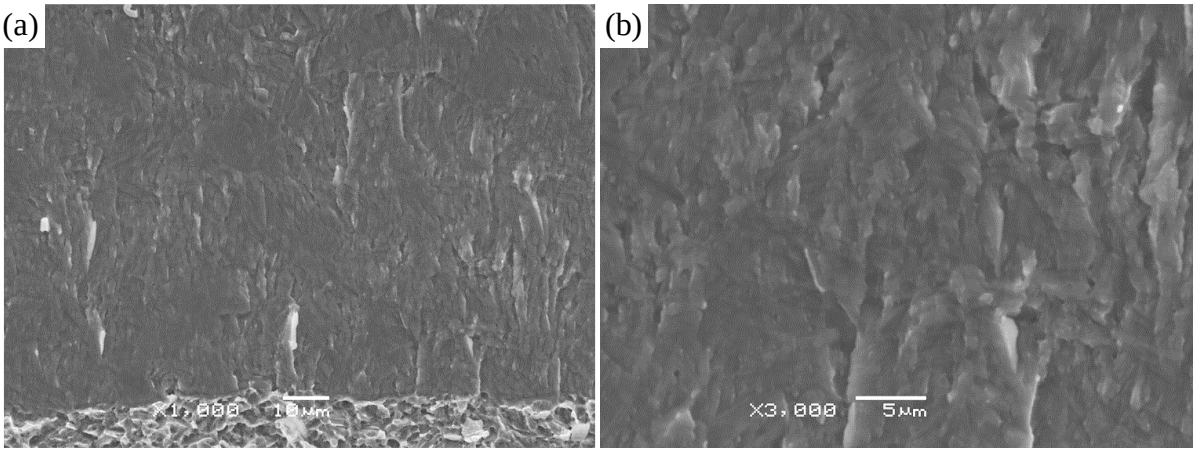

Figure 6.41 (a) Low and (b) high magnification secondary electron images of the fracture surface of CP005L in near threshold region. ($\Delta K_{th} = 8.1$ MPa$\sqrt{\text{m}}$)

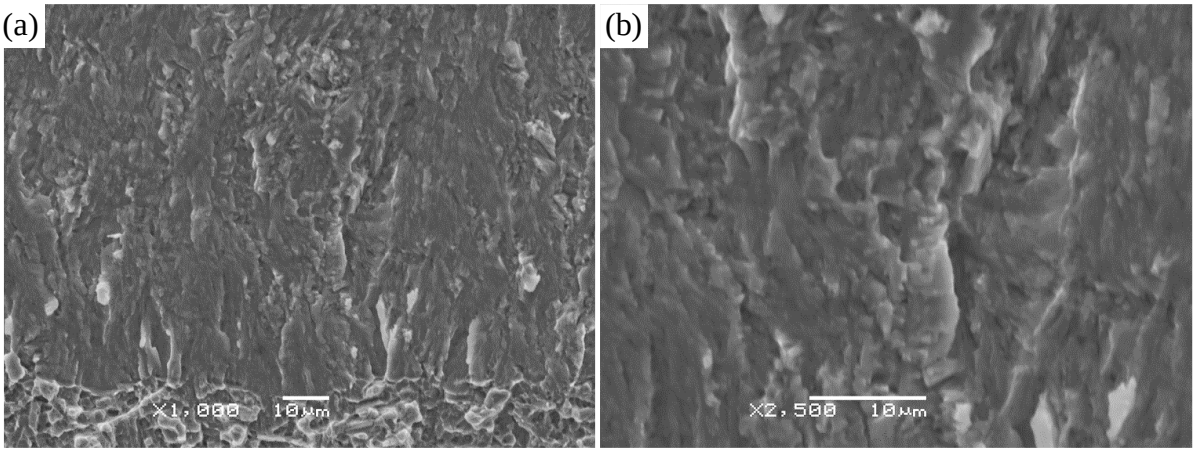

Figure 6.42 (a) Low and (b) high magnification secondary electron images of the fracture surface of CP009L in near threshold region. ($\Delta K_{th} = 7.1$ MPa$\sqrt{\text{m}}$)

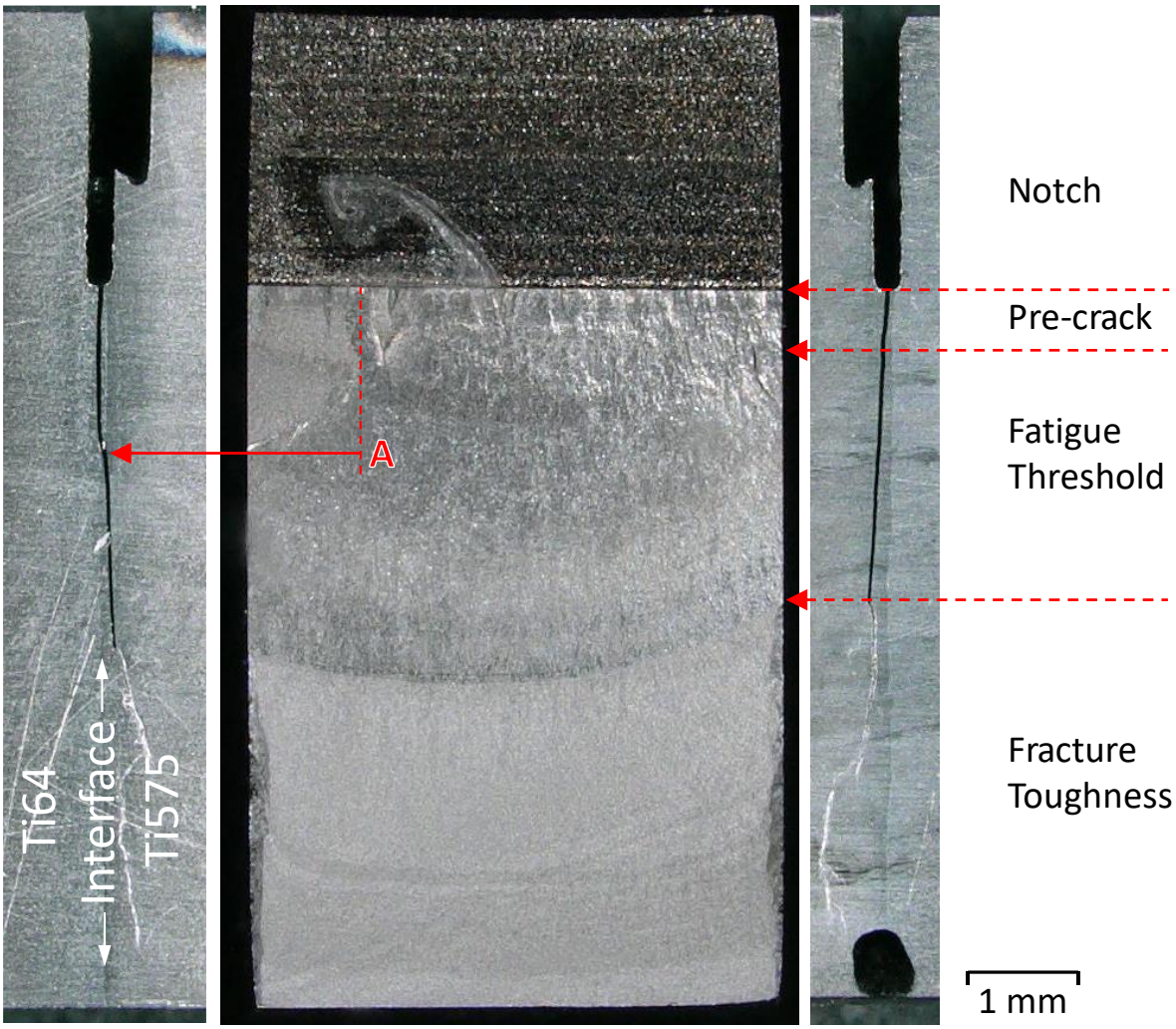

Figure 6.43 Optical macrographs of the front and side views of the fracture surface of specimen CP001R after fatigue crack growth threshold testing and fracture toughness testing. Each stage of the testing is indicated by the red dashed arrows. Annotation 'A' indicates the location where crack went across the weld interface.

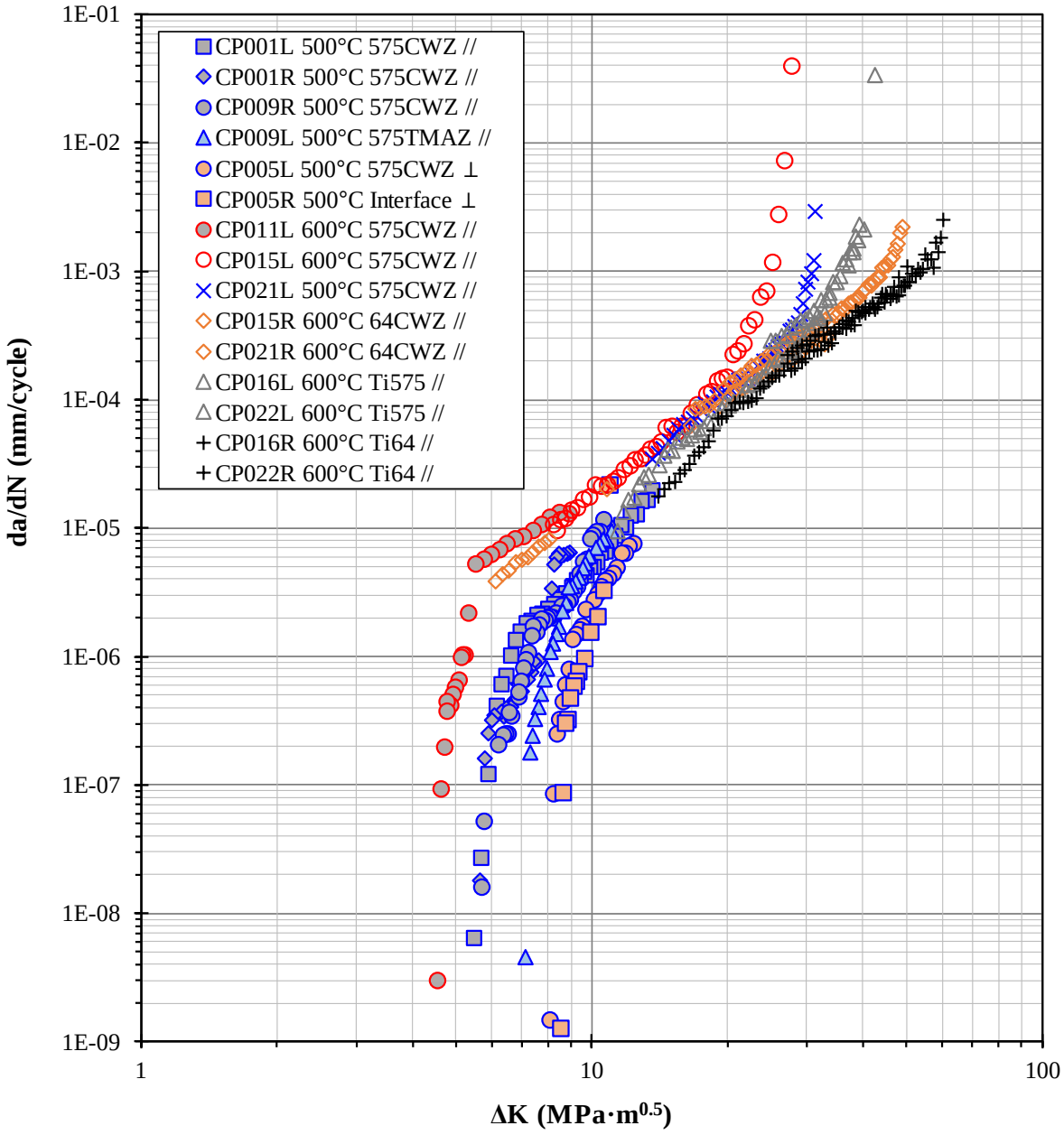

Figure 6.44 Full fatigue crack growth curves including threshold, stable crack growth, and static fracture regimes. All specimens were sliced in half and tested at room temperature with $R = 0.1$. Specimens PWHT'd for 1 hour at 500 and 600℃ are shown in blue and red, respectively.

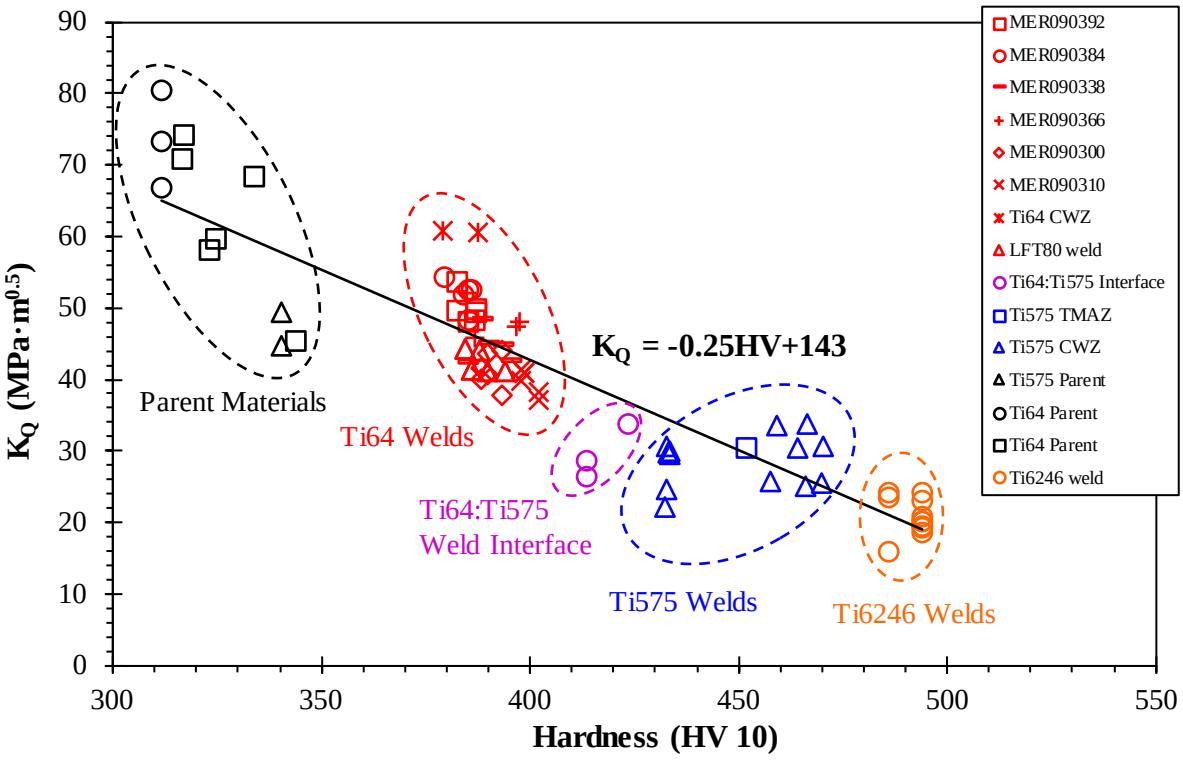

Figure 6.45 Correlation between hardness and fracture toughness measured from various dissimilar linear friction welds at a variety of locations. This chart includes data from the previous works on Ti-64 [222] and Ti-6246 [11]. It is observed that fracture toughness is generally inversely proportional to the hardness values.

Chapter 7

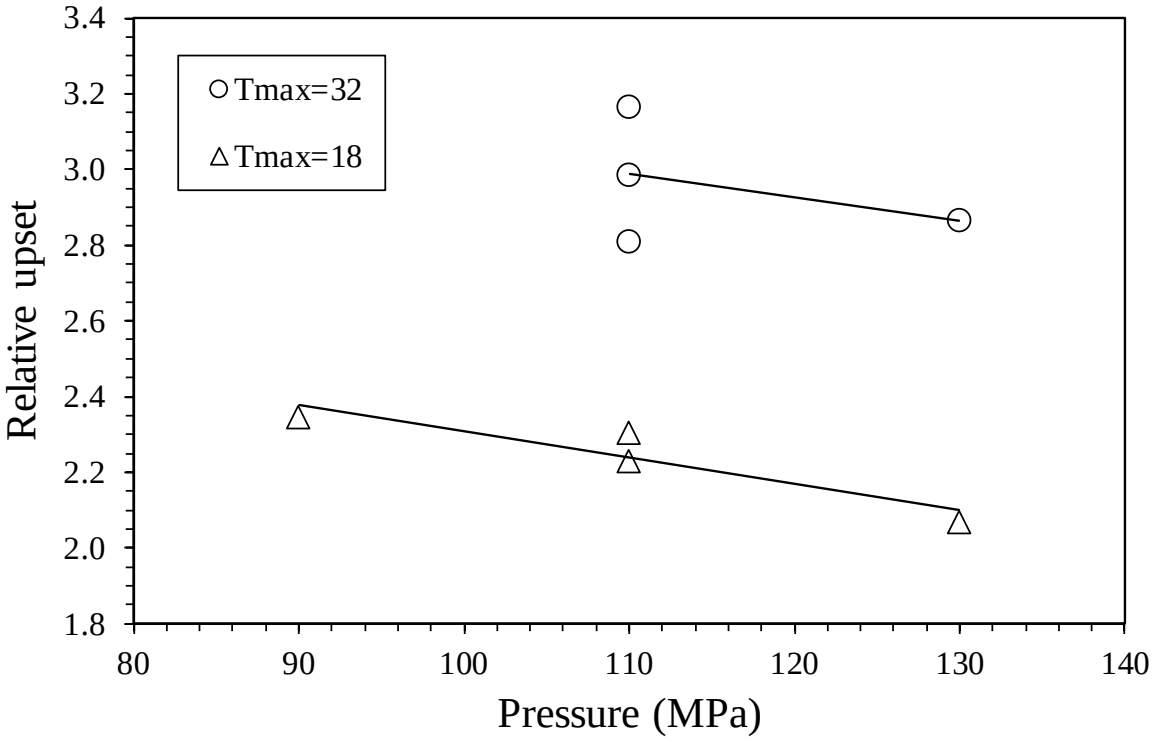

Figure 7.1 Relative upset (Ti-575/Ti-64) measured from the welds 473-01 to 473-08 with respect to the friction pressure and T_{max}.

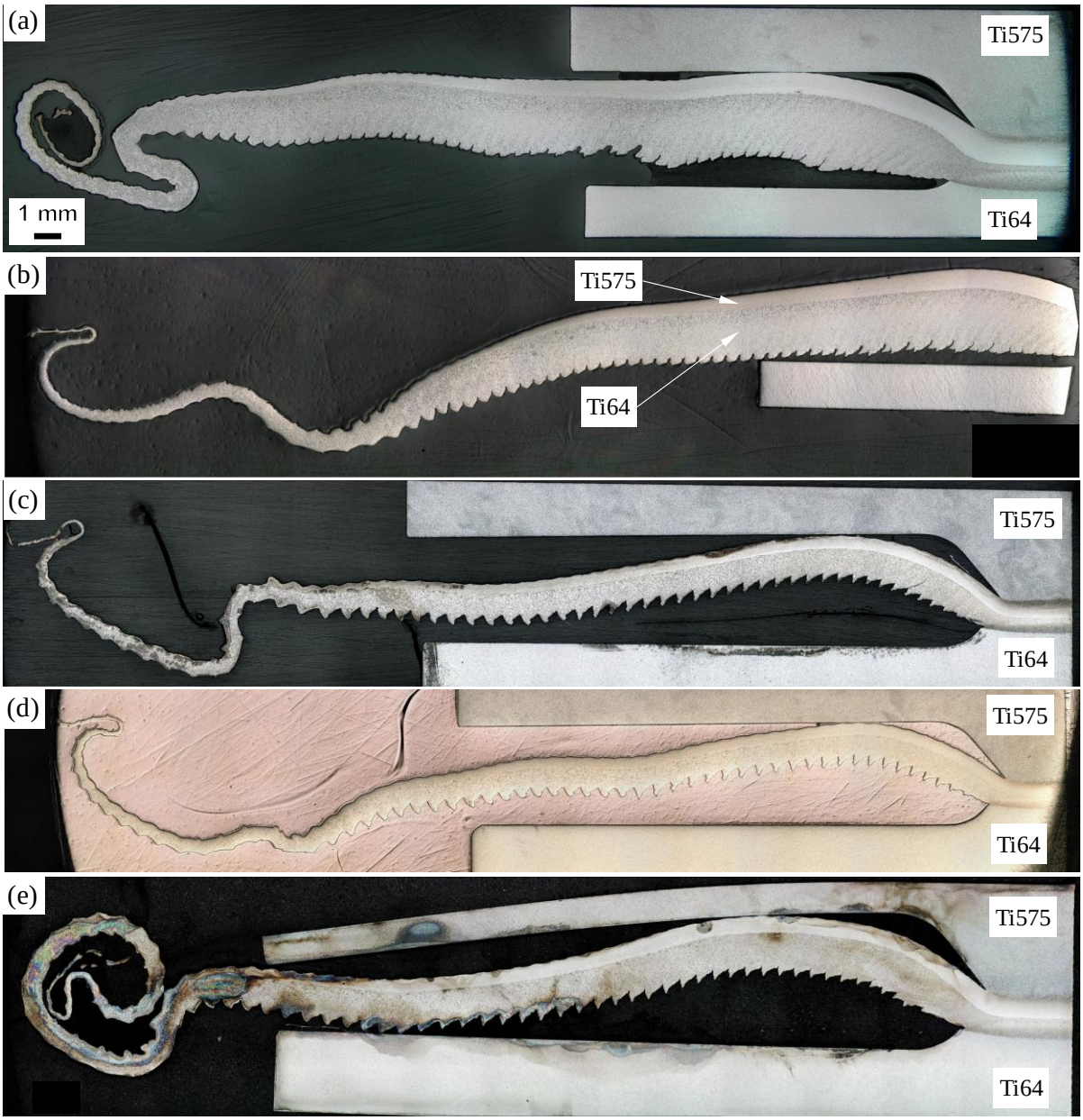

Figure 7.2 Optical micrographs of the flash of the welds. Weld ID: (a) 473-03, (b) 473-04, (c) 473-06, (d) 473-07, (e) 473-08.

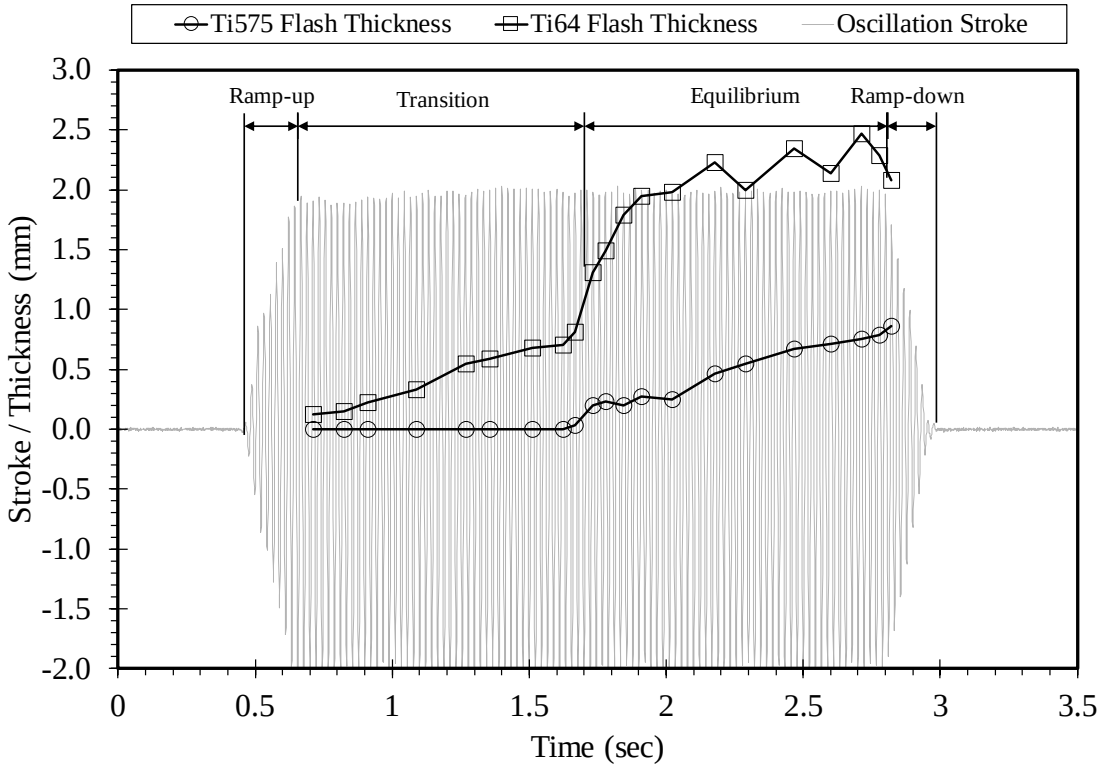

Figure 7.3 Flash thickness curve with respect to the oscillation stroke and welding time. (Weld ID: 473-03).

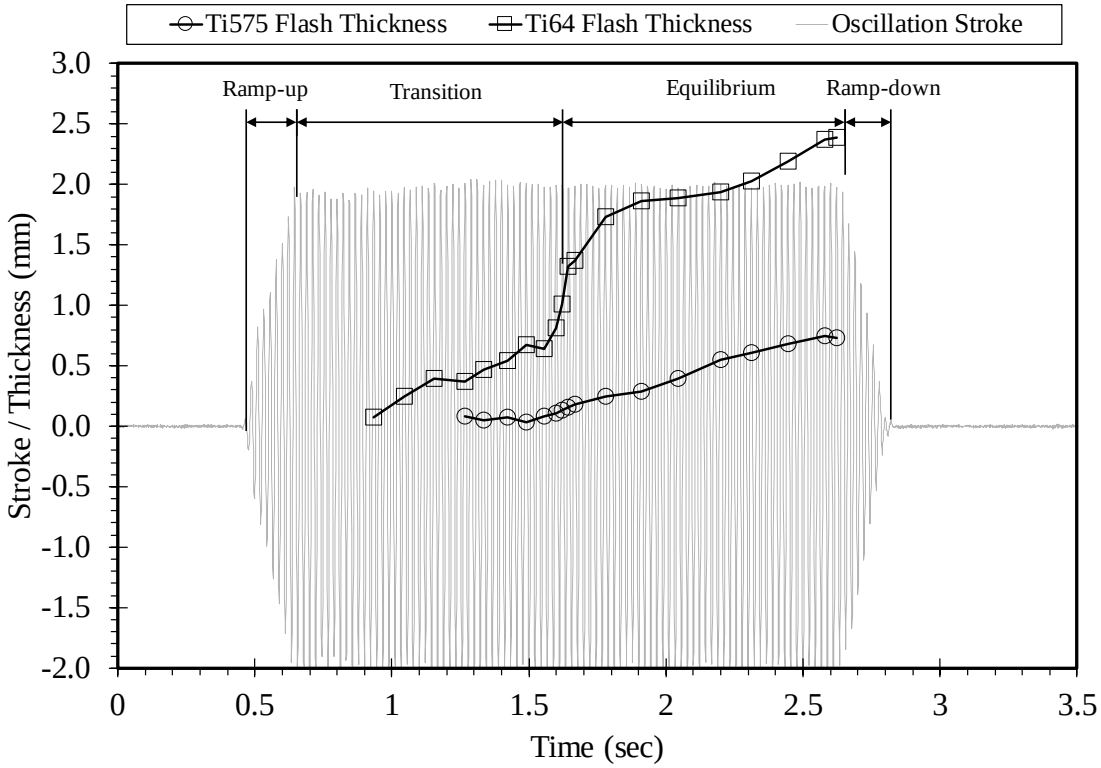

Figure 7.4 Flash thickness curve with respect to the oscillation stroke and welding time. (Weld ID: 473-04).

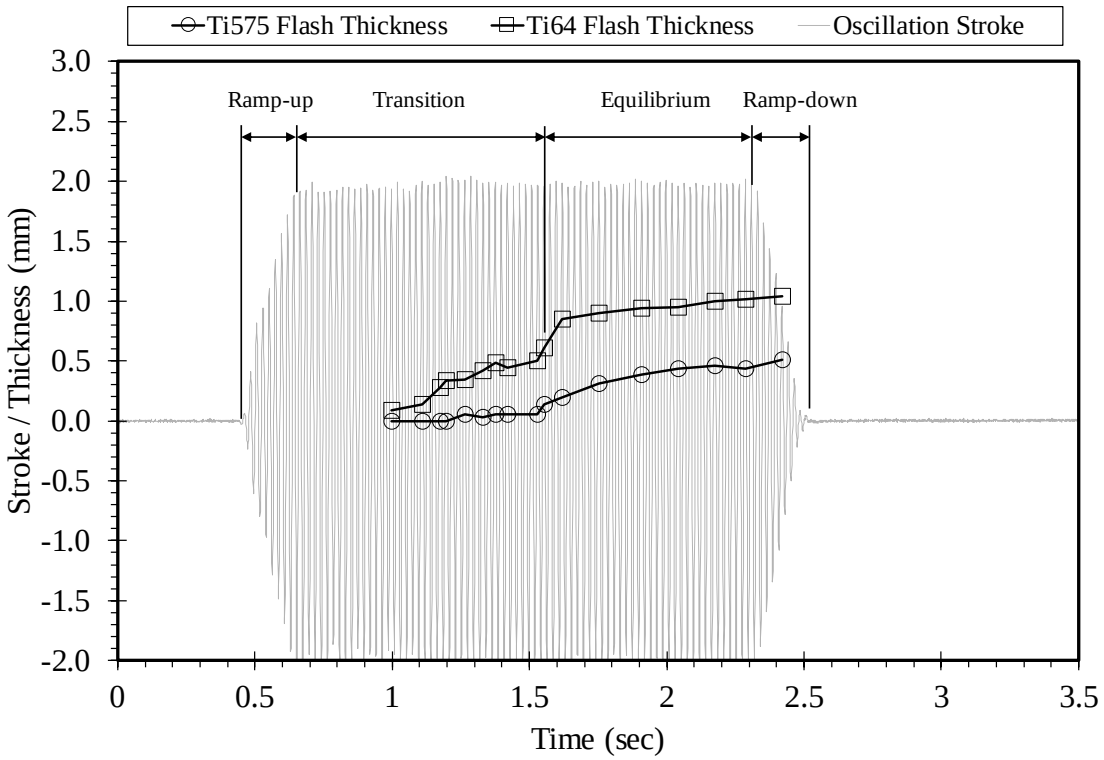

Figure 7.5 Flash thickness curves with respect to the oscillation stroke and welding time. (Weld ID: 473-06).

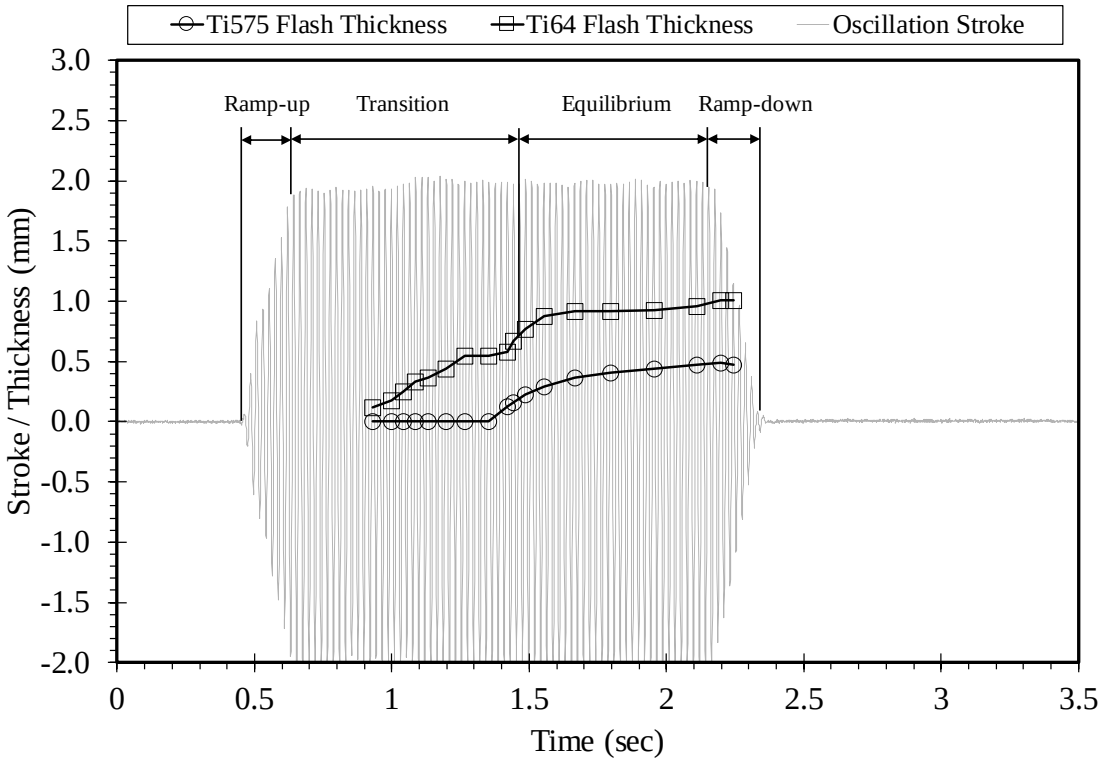

Figure 7.6 Flash thickness curves with respect to the oscillation stroke and welding time. (Weld ID: 473-07).

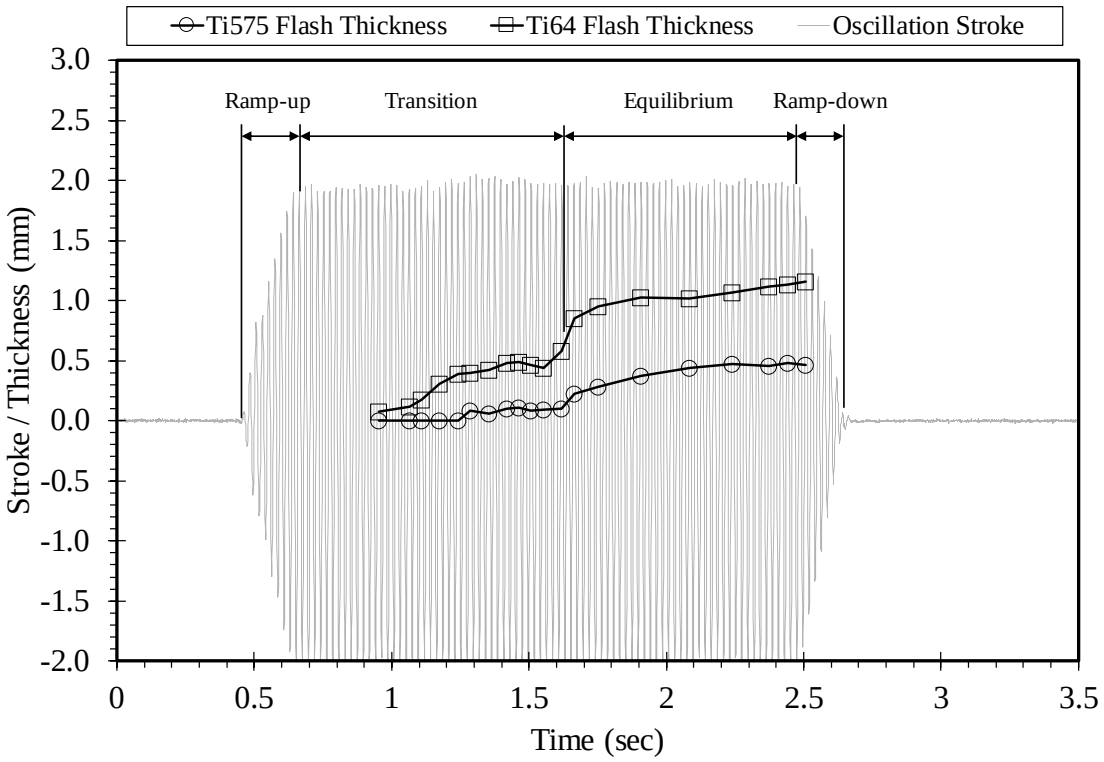

Figure 7.7 Flash thickness curves with respect to the oscillation stroke and welding time. (Weld ID: 473-08).

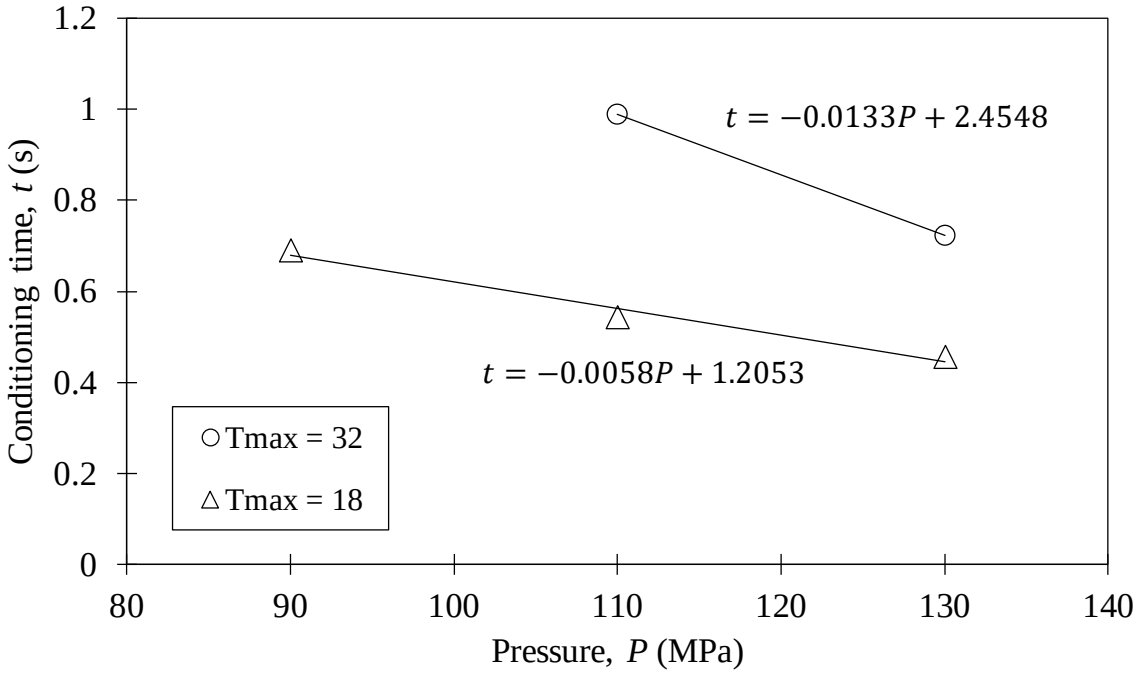

Figure 7.8 Conditioning time measured from the flash thickness curves with respect to the friction pressure and weld thickness (T_{max}).

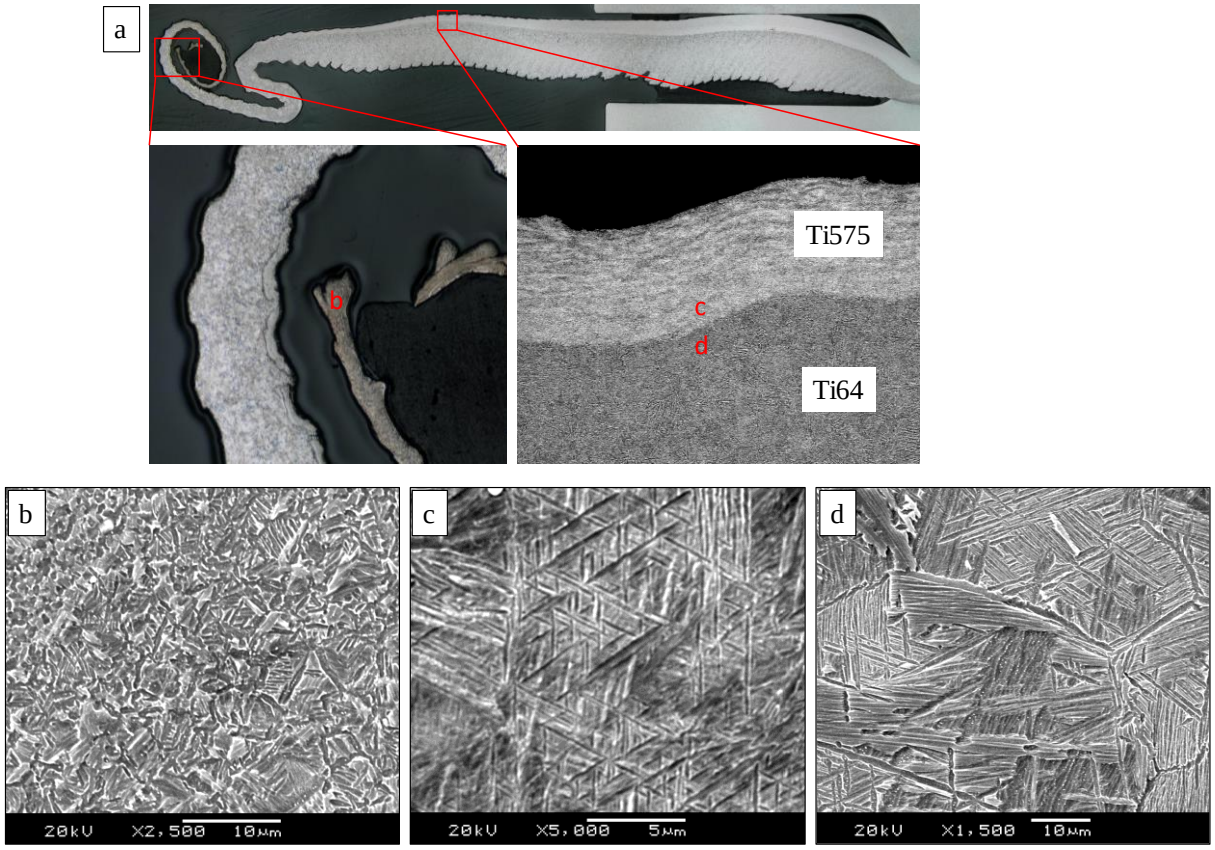

Figure 7.9 Secondary electron micrographs of (b) Ti-64 flash tip, (c) Ti-575 flash interface (d), and Ti-64 flash interface, observed at the labelled location in subfigure (a).

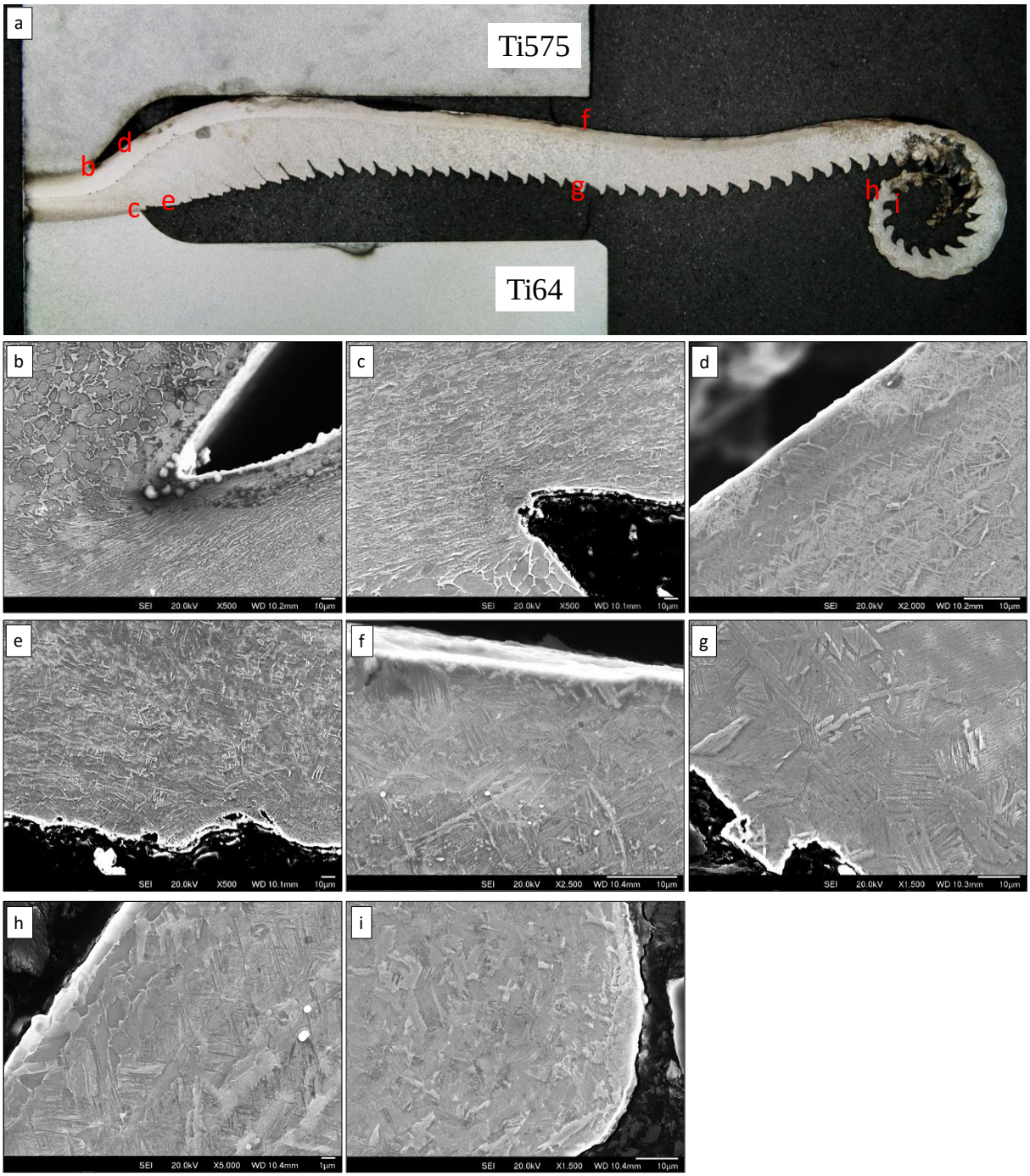

Figure 7.10 (a) Optical micrograph of the overview of the flash (Weld ID: 473-03) and (b)-(i) secondary electron micrographs of the detailed microstructure observed at the labelled location in subfigure (a).

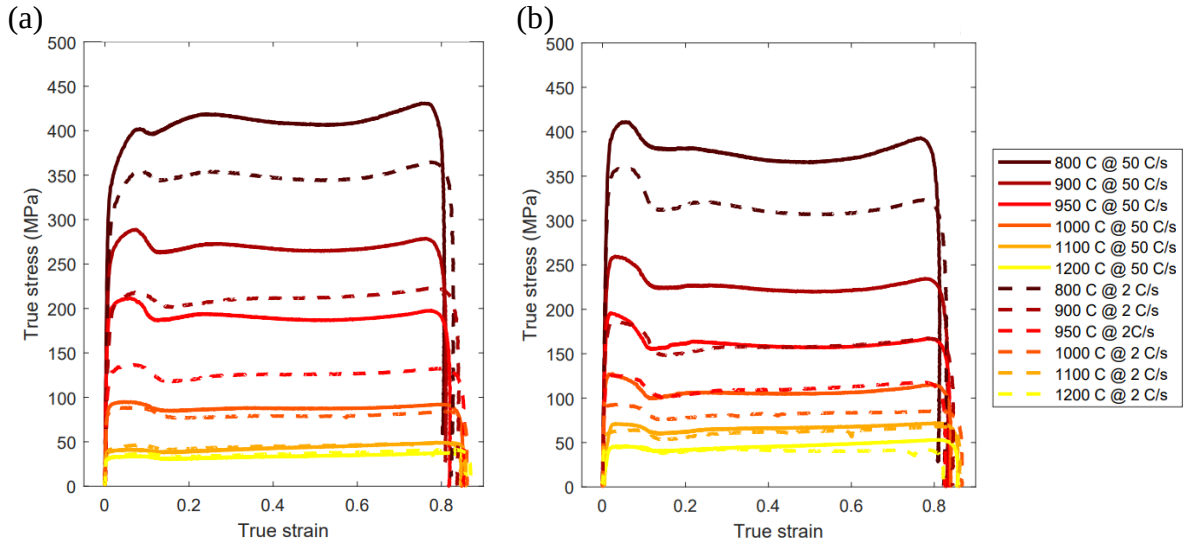

Figure 7.11 True stress-strain curves obtained from the flow stress tests at elevated temperatures with different heating rates for (a) Ti-64 and (b) Ti-575.

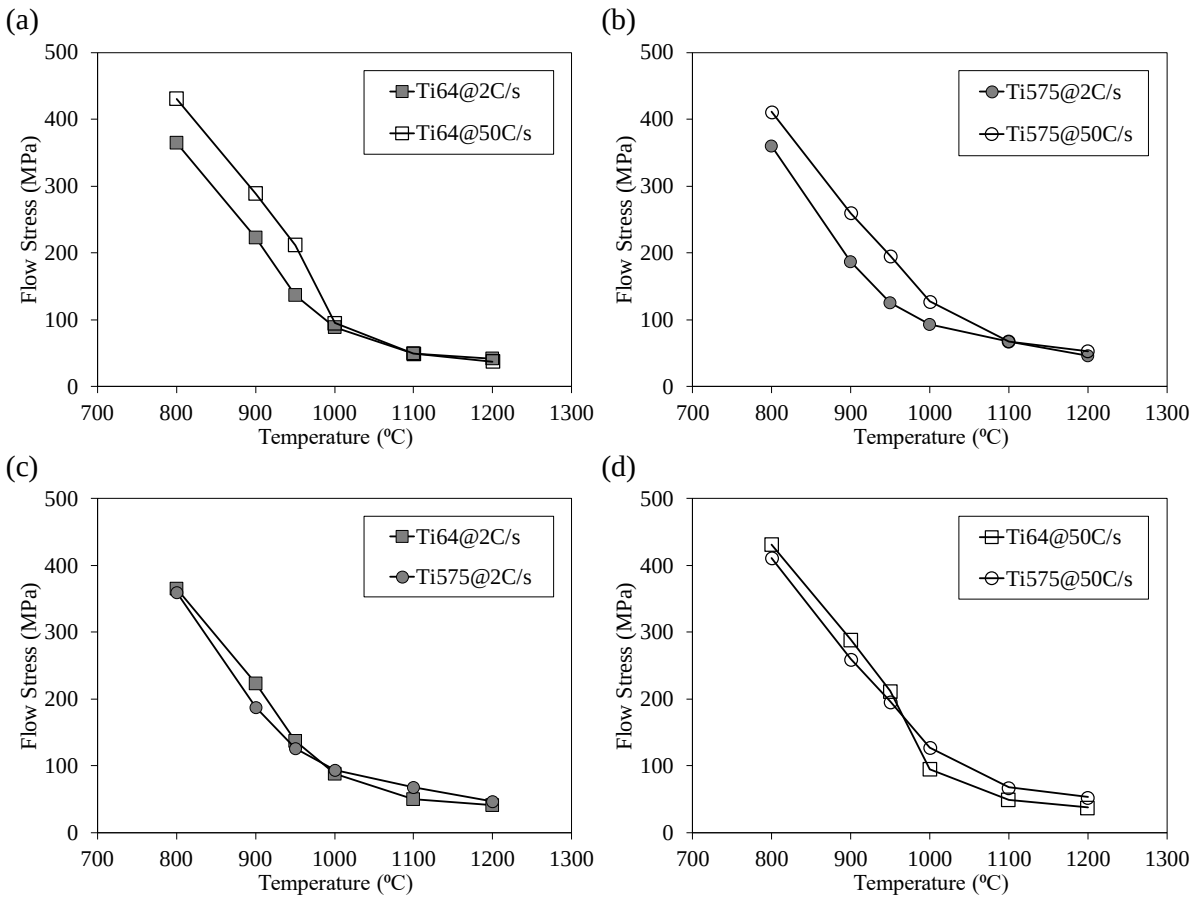

Figure 7.12 Flow stress curves with respect to the testing temperatures.

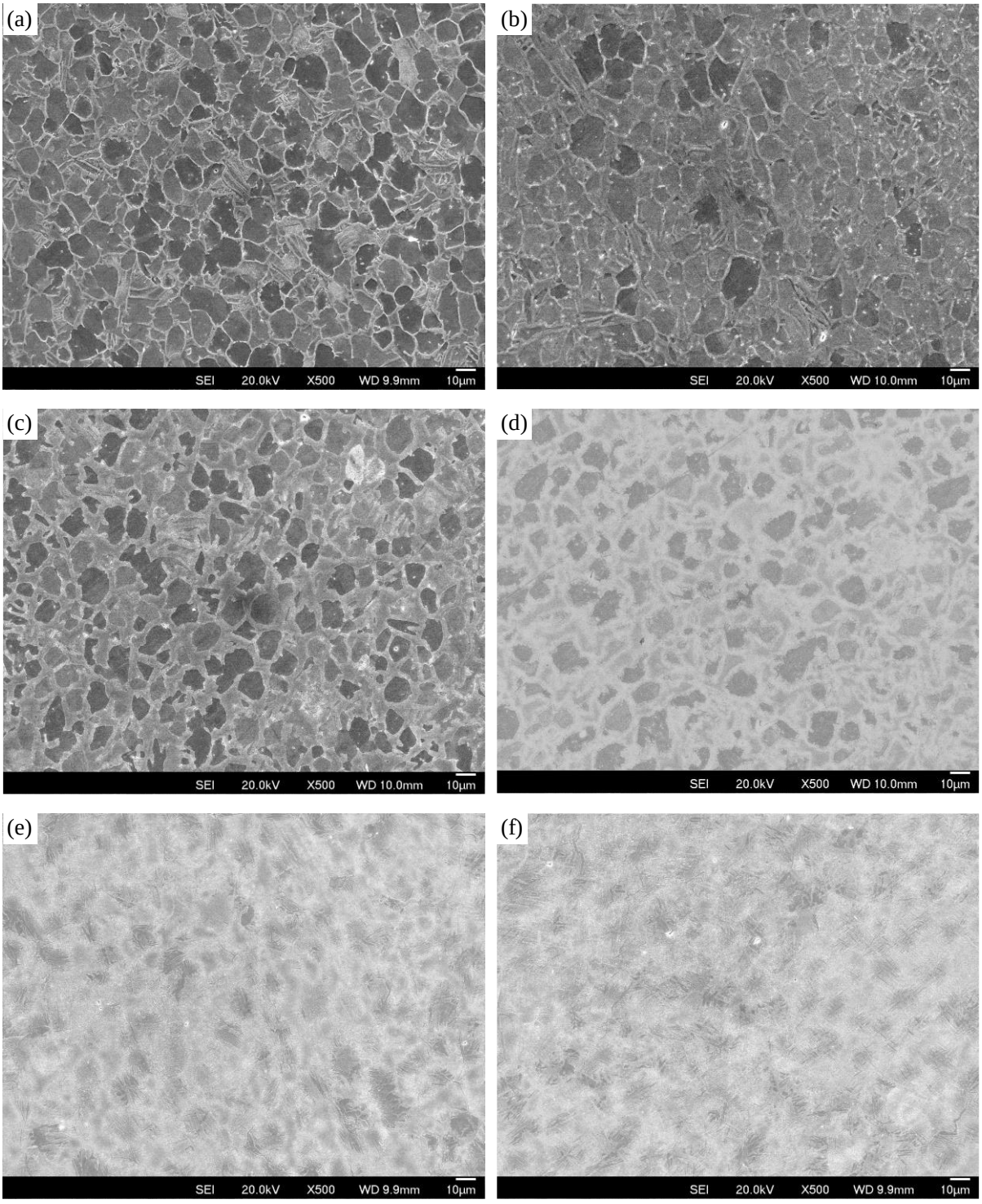

Figure 7.13 Secondary electron images of Ti-575 flow stress test pieces with heating rate at 50℃/s tested at (a) 800, (b) 900, (c) 950, (d) 1000, (e) 1100, and (f) 1200℃.

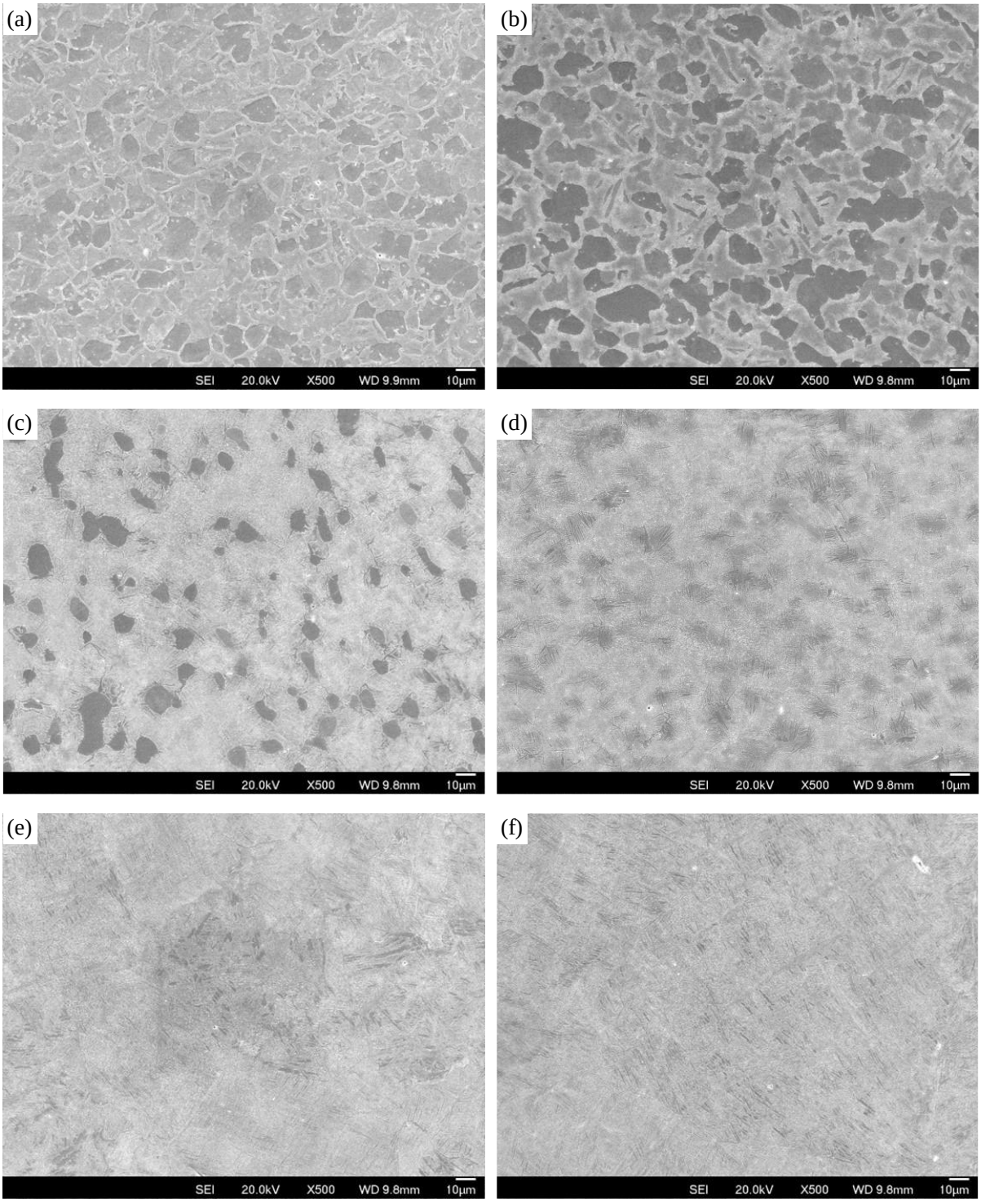

Figure 7.14 Secondary electron images of Ti-575 flow stress test pieces with heating rate at 2℃/s tested at (a) 800, (b) 900, (c) 950, (d) 1000, (e) 1100, and (f) 1200℃.

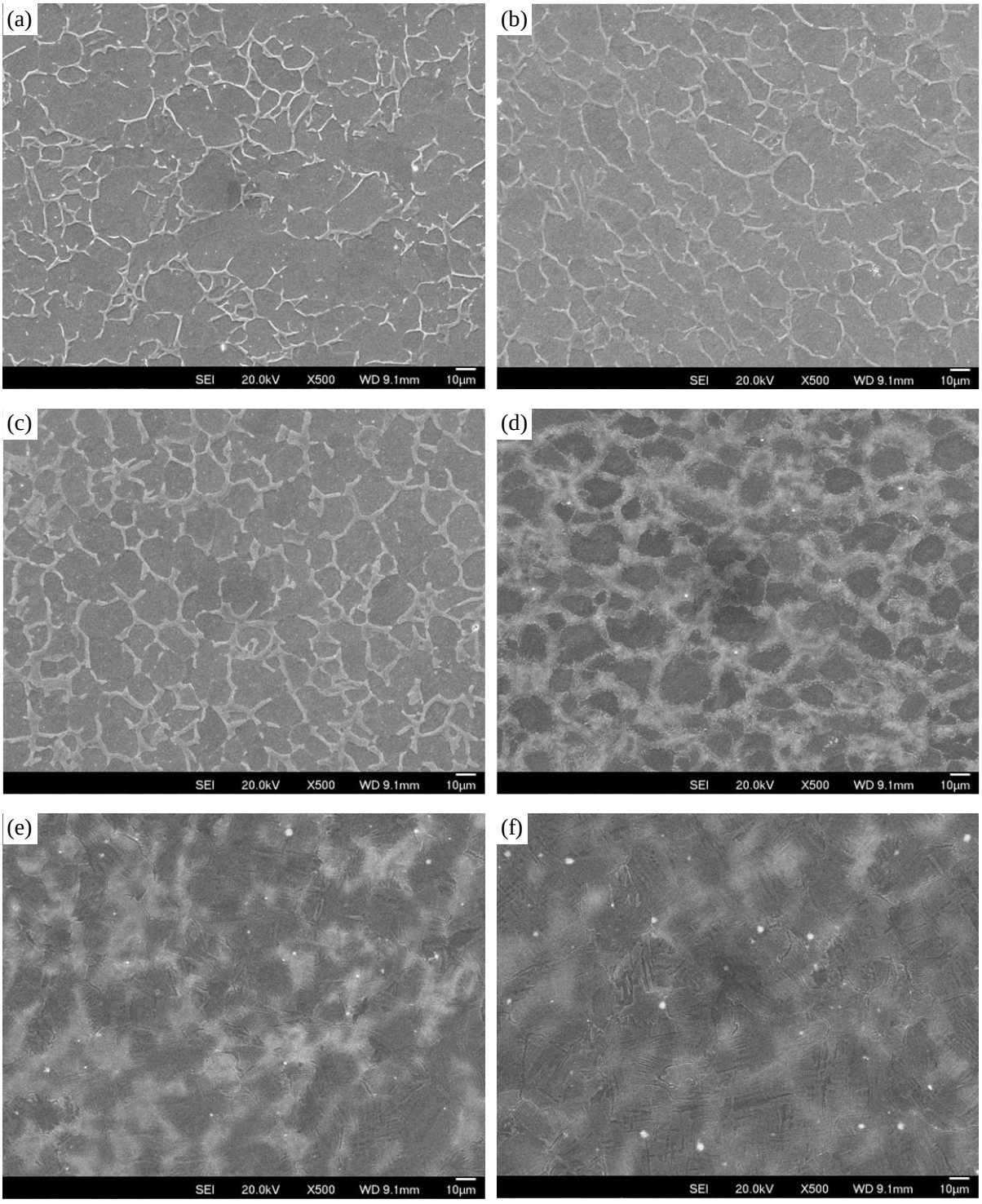

Figure 7.15 Secondary electron images of Ti-64 flow stress test pieces with heating rate at 50℃/s tested at (a) 800, (b) 900, (c) 950, (d) 1000, (e) 1100, and (f) 1200℃.

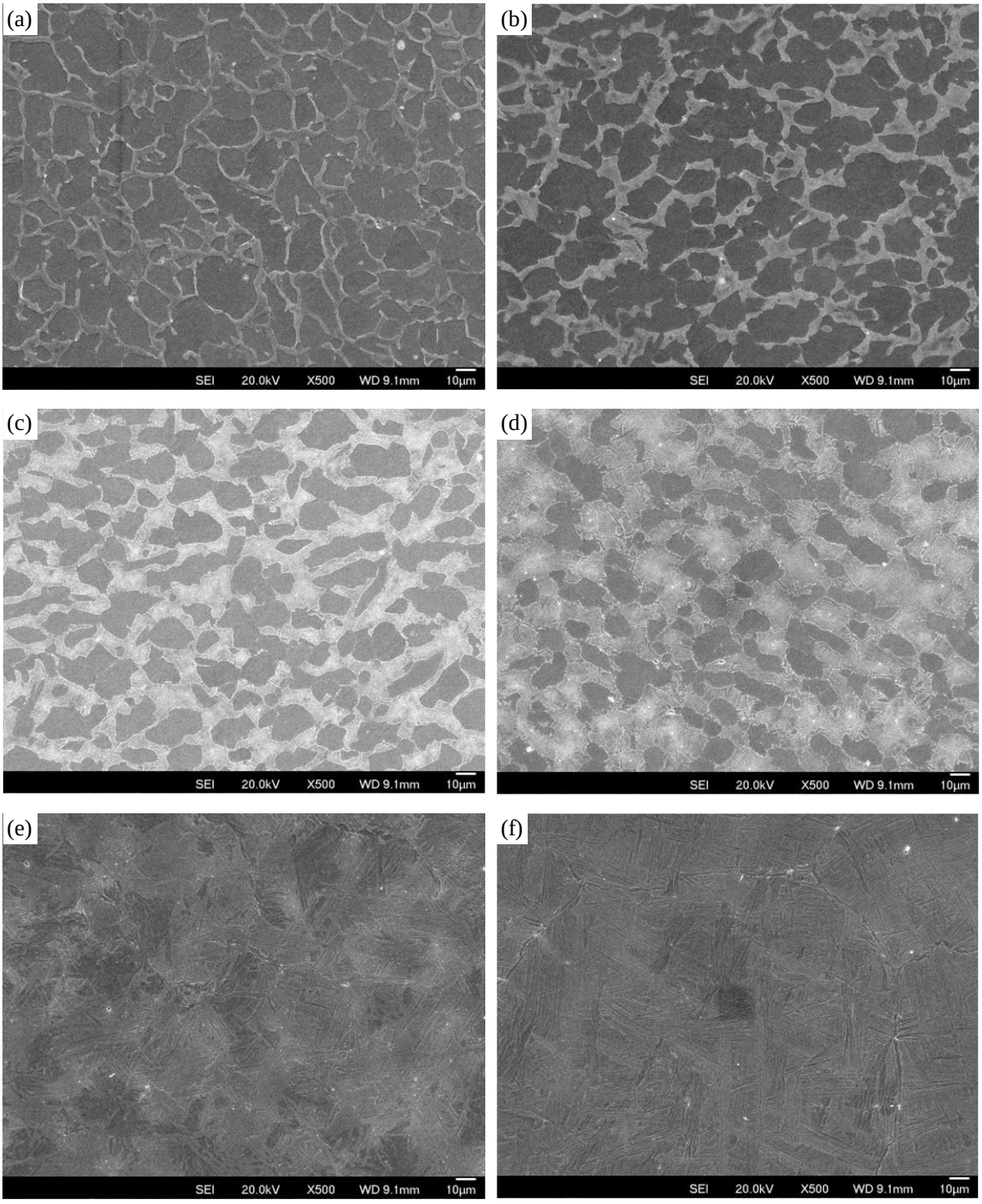

Figure 7.16 Secondary electron images of Ti-64 flow stress test pieces with heating rate at 2℃/s tested at (a) 800, (b) 900, (c) 950, (d) 1000, (e) 1100, and (f) 1200℃.

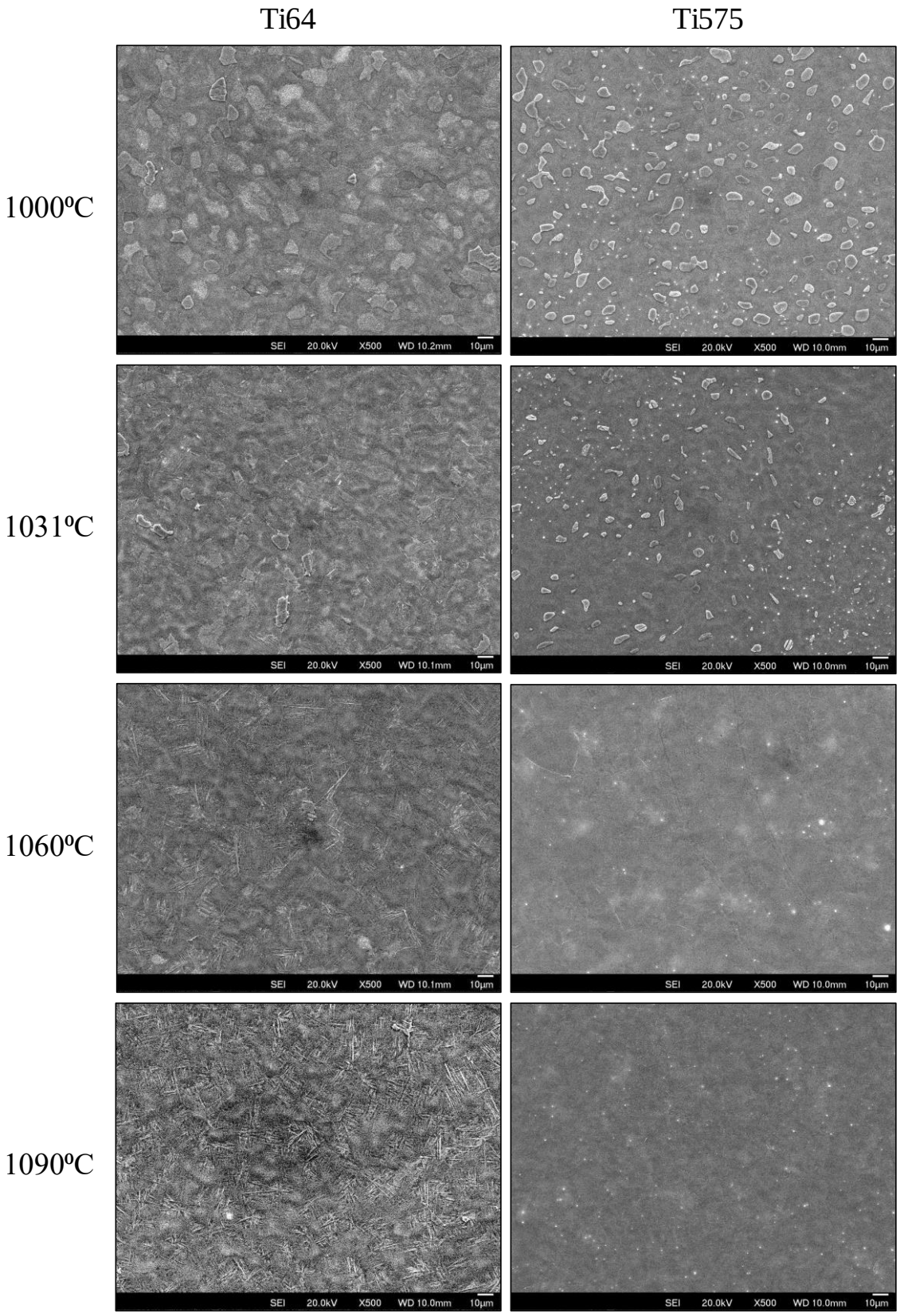

Figure 7.17 Secondary electron micrographs of Ti-64 and Ti-575 after heating at 25°C/s to elevated temperatures followed by water quenching.

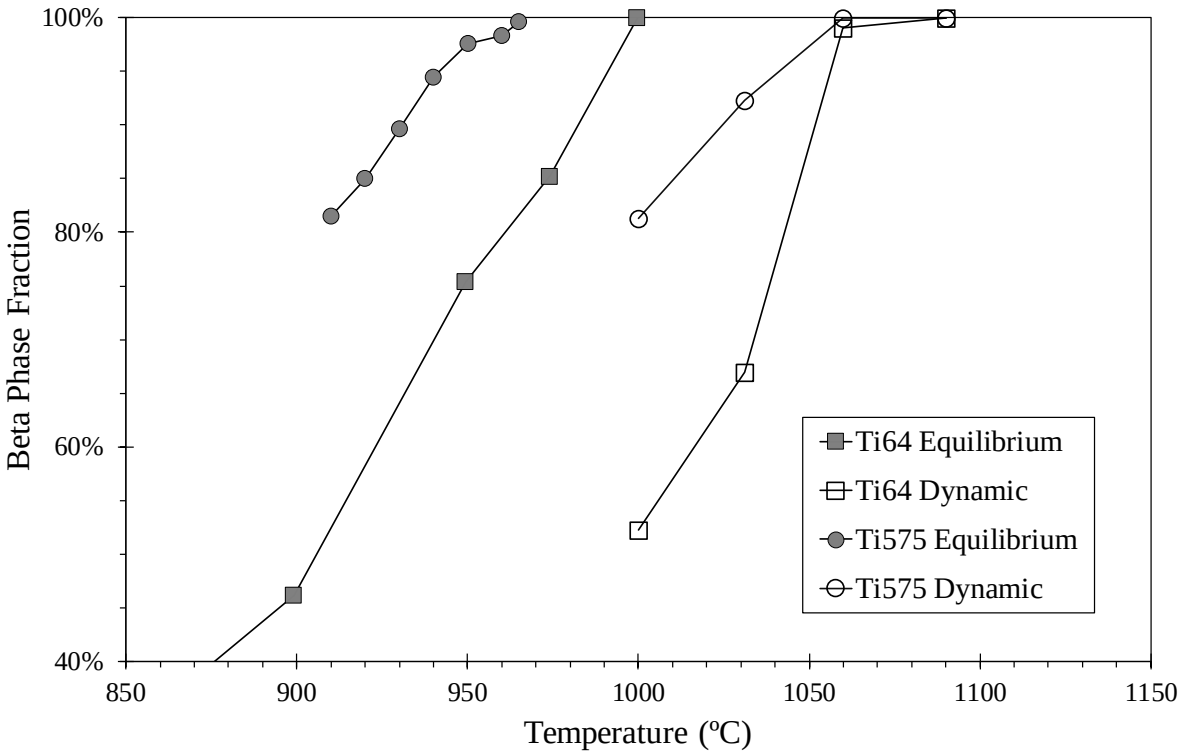

Figure 7.18 Equilibrium and dynamic beta approach curves for Ti-64 and Ti-575. The equilibrium beta approach curves were obtained from [13, 203].

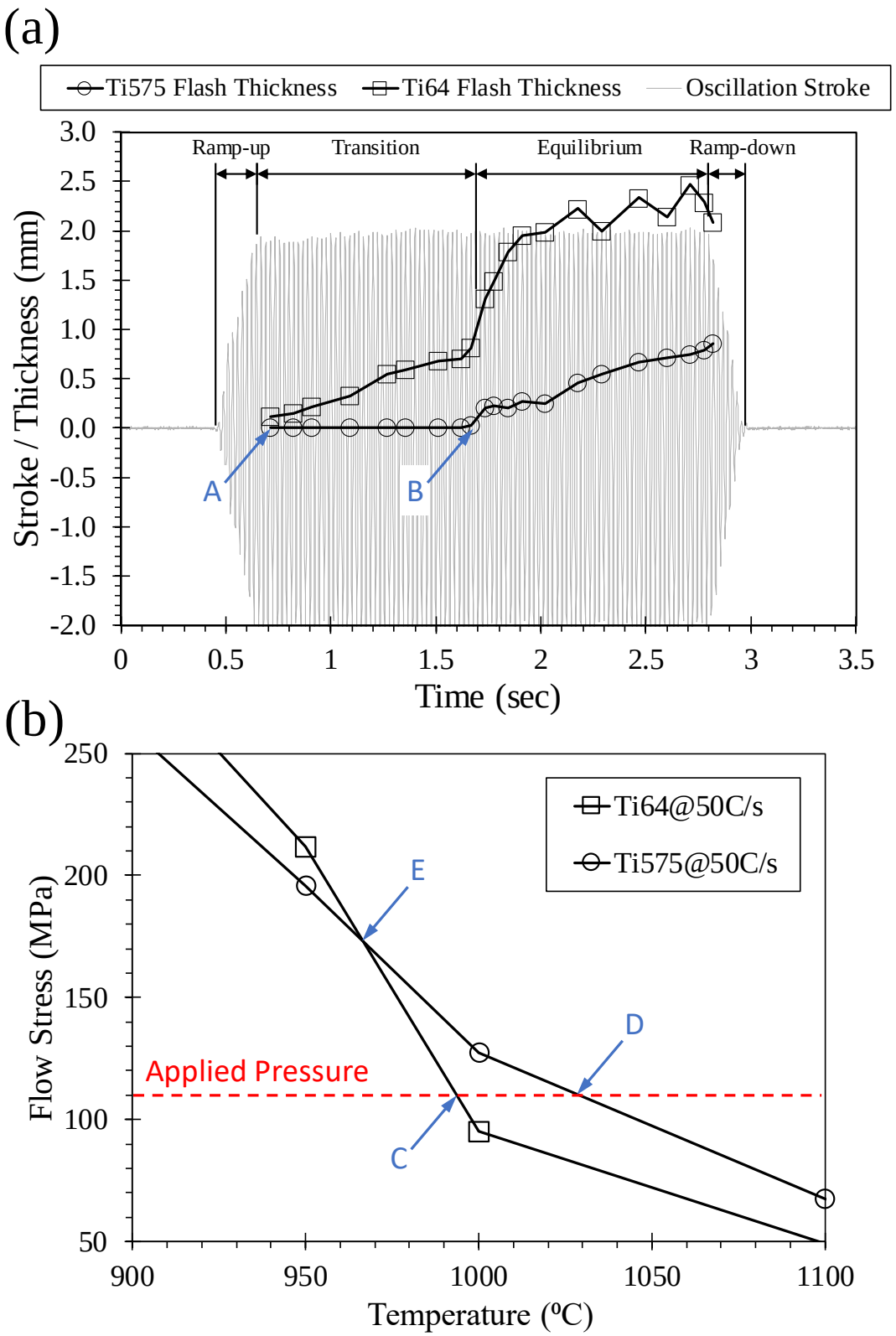

Figure 7.19 (a) Flash thickness curves of weld 473-03 with friction pressure of 110 MPa. (b) Flow stress curves measured at a heating rate of 50℃/s for Ti-64 and Ti-575. The friction pressure of weld 473-03 (110 MPa) is indicated by the red dashed line.

References

[1] Rolls-Royce, *The Jet Engine*, Fifth edit. The Technical Publications Department, Rolls-Royce plc, 1996.

[2] A. R. McAndrew and B. C. D. Flipo, "Linear Friction Welding for Near Net Shape Manufacturing of Titanium Alloy Ti-6Al-4V Aerospace Components," in *Proceedings of 2018 9th International Conference on Mechanical and Aerospace Engineering, ICMAE 2018*, 2018, no. July, pp. 126–130, doi: 10.1109/ICMAE.2018.8467692.

[3] S. Herranz *et al.*, "The milling of airframe components with low rigidity: A general approach to avoid static and dynamic problems," in *Proceedings of the Institution of Mechanical Engineers, Part B: Journal of Engineering Manufacture*, 2005, vol. 219, no. 11, pp. 789–801, doi: 10.1243/095440505X32742.

[4] P. Geng, G. Qin, H. Ma, J. Zhou, C. Zhang, and N. Ma, "Numerical modelling on the plastic flow and interfacial self-cleaning in linear friction welding of superalloys," *Journal of Materials Processing Technology*, vol. 296, no. April, p. 117198, 2021, doi: 10.1016/j.jmatprotec.2021.117198.

[5] C. Y. Zhang, C. Lu, C. W. Fei, L. J. Liu, Y. S. Choy, and X. G. Su, "Multiobject reliability analysis of turbine blisk with multidiscipline under multiphysical field interaction," *Advances in Materials Science and Engineering*, vol. 2015, 2015, doi: 10.1155/2015/649046.

[6] "Titanium Alloy Ti-6Al-4V Technical Datasheet." pp. 1–10, 2000, Accessed: Mar. 26, 2023. [Online]. Available: https://www.carpentertechnology.com/hubfs/7407324/Material Saftey Data Sheets/Ti 6Al-4V.pdf.

[7] B. Öztürk, L. Mengis, D. Dickes, U. Glatzel, and M. C. Galetz, "Influence of Water Vapor and Temperature on the Oxide Scale Growth and Alpha-Case Formation in Ti-6Al-4V Alloy," *Oxidation of Metals*, vol. 97, no. 3–4, pp. 241–260, 2022, doi: 10.1007/s11085-021-10088-x.

[8] P. A. Blenkinsop, "High Temperature Titanium Alloys.," *Defence Science Journal*, vol. 55, no. 2, pp. 149–173, 2005, doi: 10.1201/9781420037678-7.

[9] P. J. Bania, "An advanced alloy for elevated temperatures," *JOM*, vol. 40, no. 3, pp. 20–22, 1988.

[10] Y. Guo, "Microstructure and texture characterization of linear friction welding of Ti-6Al-4V and Ti-6Al-2Sn-4Zr-6Mo," University of Birmingham, 2012.

[11] T. Webster, "Process-Microstructure-Mechanical Property Relationships for Linear Friction Welded Ti-6Al-2Sn-4Zr-6Mo," University of Birmingham, 2019.

[12] J. Jiang, "Fatigue and Fracture of the Friction Welded Titanium Alloys," University of Birmingham, 2016.

[13] M. Thomas, J. Hewitt, M. Bache, R. Thomas, P. Garratt, and Y. Kosaka, "Timetal® 575: A Novel High Strength Forgeable α/β Titanium Alloy," in *Proceedings of the 13th World Conference on Titanium*, 2016, pp. 1537–1541, doi: 10.1002/9781119296126.ch257.

[14] M. Allan, M. Thomas, J. Brooks, P. Blackwell, T. Hub, and H. Road, "β recrystallisation characteristics of α +β titanium alloys for aerospace applications," in *Proceedings of the 13th World Conference on Titanium*, 2016, pp. 203–208.

[15] M. Thomas, J. Hewitt, M. Bache, R. Thomas, P. Garratt, and Y. Kosaka, "Determination and Analysis of the Cyclic and Dwell Fatigue Performance of Timetal® 575," in *Proceedings of the 13th World Conference on Titanium*, 2016, pp. 979–984, doi: 10.1002/9781119296126.ch167.

[16] M. Bodie, M. Thomas, and A. Ayub, "Effect of microstructure and cooling rate on the fatigue performance of TIMETAL® 575," in *The 14th World Conference on Titanium*, 2020, vol. 321, p. 12019, doi: 10.1051/matecconf/202032112019.

[17] J. S. Hewitt, P. D. Davies, M. J. Thomas, P. Garratt, and M. R. Bache, "Titanium alloy developments for aeroengine fan systems," *Materials Science and Technology (United Kingdom)*, vol. 30, no. 15, pp. 1919–1924, 2014, doi: 10.1179/1743284714Y.0000000669.

[18] Bureau d'Enquêtes et d'Analyses, "Investigation Report: Accident to the AIRBUS A380-861 equipped with Engine Alliance GP7270 engines registered F-HPJE operated by Air France on 30 September 2017 in cruise over Greenland (Denmark)," 2020. [Online]. Available: https://bea.aero/uploads/tx_elydbrapports/BEA2017-0568.en.pdf.

[19] A. Pilchak and M. Gram, "Cold Dwell Fatigue of Titanium Alloys," *The Journal of The Minerals, Metals & Materials Society*, vol. 74, no. 10, pp. 3691–3692, 2022, doi: 10.1007/s11837-022-05463-1.

[20] Y. Xu *et al.*, "Predicting dwell fatigue life in titanium alloys using modelling and experiment," *Nature Communications*, vol. 11, no. 1, pp. 1–13, 2020, doi: 10.1038/s41467-020-19470-w.

[21] S. Sheng, J. Flegler, B. J. Becs, and M. Dankert, "Component Fatigue Test Facilities for Full-Scale Low Pressure Steam Turbine End Stage Blades," in *Proceedings of the 1st Global Power and Propulsion Forum*, 2017, pp. 1–8.

[22] C. Leyens and M. Peters, *Titanium and Titanium Alloys - Fundamentals and Applications*. Wiley-VCH, 2003.

[23] G. Lutjering and J. C. Williams, *Titanium*, vol. 51, no. 1. Springer, 2018.

[24] S. Banerjee and P. Mukhopadhyay, *Phase transformations: examples from titanium and zirconium alloys*. Elsevier, 2010.

[25] I. Polmear, D. St. John, J.-F. Nie, and M. Qian, *Light Alloys: Metallurgy of the Light Metals: Fifth Ed.* 2017.

[26] W. B. Pearson, *A handbook of lattice spacings and structures of metals and alloys*. Elsevier, 1967.

[27] R. Boyer, G. Welsch, and E. W. Collings, *Materials Properties Handbook : Titanium alloys*. ASM International, 1994.

[28] Y. N. Wang and J. C. Huang, "Texture analysis in hexagonal materials," *Materials Chemistry and Physics*, vol. 81, no. 1, pp. 11–26, 2003, doi: 10.1016/S0254-0584(03)00168-8.

[29] N. E. Paton, J. C. Williams, and G. P. Rauscher, "Titanium science and Technology; eds., Jaffee RI and Burte HM," *Plenum Press, New York*, vol. 2, p. 1049, 1973.

[30] I. P. Jones and W. B. Hutchinson, "Stress-state dependence of slip in Titanium-6Al-4V and other HCP metals," *Acta Metallurgica*, vol. 29, no. 6, pp. 951–968, 1981.

[31] H. Fan and J. A. El-Awady, "Molecular Dynamics Simulations of Orientation Effects during Tension, Compression, and Bending Deformations of Magnesium Nanocrystals," *Journal of Applied Mechanics, Transactions ASME*, vol. 82, no. 10, 2015, doi: 10.1115/1.4030930.

[32] R. Abbaschian, L. Abbaschian, and R. E. Reed-Hill, *Physical Metallurgy Principles - Fourth Edition*. Cengate Learning, 2009.

[33] O. N. Senkov, B. C. Chakoumakos, J. J. Jonas, and F. H. Froes, "Effect of temperature and hydrogen concentration on the lattice parameter of beta titanium," *Materials Research Bulletin*, vol. 36, no. 7–8, pp. 1431–1440, 2001, doi: 10.1016/S0025-5408(01)00604-3.

[34] W. G. Burgers, "On the process of transition of the cubic-body-centered modification into the hexagonal-close-packed modification of zirconium," *Physica*, vol. 1, no. 7–12, pp. 561–586, 1934, doi: 10.1016/S0031-8914(34)80244-3.

[35] J. B. Newkirk and A. H. Geisler, "Crystallographic aspects of the beta to alpha transformation in titanium," *Acta Metallurgica*, vol. 1, no. 3, 1953, doi: 10.1016/0001-6160(53)90113-8.

[36] S. Nag, "Influence of beta instabilities on the early stages of nucleation and growth of alpha in beta titanium alloys," The Ohio State University, 2008.

[37] M. P. Ginebra, F. X. Gil, J. M. Manero, and J. Planell, "Effects of solution and cooliing rate on the Widmanstaetten morphologies in the Ti-6 Al-4 V alloy," in *Titanium' 95 Science and Technology, the eighth world conference on Titanium*, 1996, pp. 2563–2570.

[38] R. Davis, H. M. Flower, and D. R. F. West, "Martensitic transformations in Ti-Mo alloys," *Journal of Materials*

Science, vol. 14, no. 3, pp. 712–722, 1979, doi: 10.1007/BF00772735.

[39] D. A. Porter and K. E. Easterling, *Phase transformations in metals and alloys*. Chapman & Hall, London, 1992.

[40] Z. Babasafari *et al.*, "Effects of austenizing temperature, cooling rate and isothermal temperature on overall phase transformation characteristics in high carbon steel," *Journal of Materials Research and Technology*, vol. 9, no. 6, pp. 15286–15297, 2020, doi: 10.1016/j.jmrt.2020.10.071.

[41] M. Humbert, F. Wagner, H. Moustahfid, and C. Esling, "Determination of the orientation of a parent β grain from the orientations of the inherited α plates in the phase transformation from body-centred cubic to hexagonal close packed," *Journal of applied crystallography*, vol. 28, no. 5, pp. 571–576, 1995.

[42] J. C. Williams, *Critical Review--Kinetics and Phase Transformations*, vol. 3. 1973.

[43] H. Sasano, T. Suzuki, O. Nakano, and H. Kimura, "CRYSTAL STRUCTURES OF MARTENSITES IN Ti-Mo-Al ALLOYS," in *Titanium'80. Science and Technology*, 1980, no. 9, pp. 717–724.

[44] W. Mei, J. Sun, and Y. Wen, "Martensitic transformation from β to α′ and α″ phases in Ti-V alloys: A first-principles study," *Journal of Materials Research*, vol. 32, no. 16, pp. 3183–3190, 2017, doi: 10.1557/jmr.2017.276.

[45] D. Banerjee, K. Muraleedharan, and J. L. Strudel, "Substructure in titanium alloy martensite," *Philosophical Magazine A*, vol. 77, no. 2, pp. 299–323, 1998, doi: 10.1080/01418619808223754.

[46] A. L. Pilchak, "The effect of friction stir processing on the microstructure, mechanical properties and fracture behavior of investment cast Ti-6Al-4V," The Ohio State University, The Ohio State University, 2009.

[47] F. X. G. Mur, D. Rodríguez, and J. A. Planell, "Influence of tempering temperature and time on the α′-Ti-6Al-4V martensite," *Journal of alloys and compounds*, vol. 234, no. 2, pp. 287–289, 1996.

[48] S. C. Wang, M. Aindow, and M. J. Starink, "Effect of self-accommodation on α/α boundary populations in pure titanium," *Acta Materialia*, vol. 51, no. 9, pp. 2485–2503, 2003, doi: 10.1016/S1359-6454(03)00035-1.

[49] M. H. Muelier, R. L. Hitterman, and H. W. Knott, "The atomic position parameter in alpha uranium - room temperature and above," Illinois, 1961.

[50] S. Banumathy, R. K. Mandal, and A. K. Singh, "Structure of orthorhombic martensitic phase in binary Ti-Nb alloys," *Journal of Applied Physics*, vol. 106, no. 9, 2009, doi: 10.1063/1.3255966.

[51] A. R. G. Brown, D. Clark, J. Eastabrook, and K. S. Jepson, "The Titanium-Niobium System," *Nature*, vol. 201, no. 4922, pp. 914–915, 1964.

[52] K. Mukherjee and M. Kato, "Lattice Correspondence and Crystallography of Martensites in Titanium Alloys.," *Journal de Physique (Paris), Colloque*, vol. 43, no. 12, 1982, doi: 10.1051/jphyscol:1982441.

[53] A. V. Dobromyslov and V. A. Elkin, "The orthorhombic α″-phase in binary titanium-base alloys with d-metals of V-VIII groups," *Materials Science and Engineering A*, vol. 438–440, no. SPEC. ISS., pp. 324–326, 2006, doi: 10.1016/j.msea.2006.02.086.

[54] Y. Mantani and M. Tajima, "Phase transformation of quenched α″ martensite by aging in Ti-Nb alloys," *Materials Science and Engineering A*, vol. 438–440, no. SPEC. ISS., pp. 315–319, 2006, doi: 10.1016/j.msea.2006.02.180.

[55] D. Pionnier, M. Humbert, M. J. Philippe, and Y. Combres, "Study of the α″ phase texture obtained by martensitic β-α″ phase transformation induced by tensile test in a sheet of Ti5A12Sn4Zr4Mo2Cr1Fe," *Acta Materialia*, vol. 46, no. 16, pp. 5891–5898, 1998, doi: 10.1016/S1359-6454(98)00216-X.

[56] F. Zimmermann and M. Humbert, "Determination of the habit plane characteristics in the β–α′ phase transformation induced by stress in Ti–5Al–2Sn–4Zr–4Mo–2Cr–1Fe," *Acta Materialia*, vol. 50, no. 7, pp. 1735–1740, 2002, doi: 10.1016/S1359-6454(02)00022-8.

[57] M. Grujicic and C. P. Narayan, "A study of β → α″ martensitic transformation volume change in TiAlV alloys," *Materials Science and Engineering A*, vol. 151, no. 2, pp. 217–226, 1992, doi: 10.1016/0921-5093(92)90210-R.

[58] J. K. Mackenzie and J. S. Bowles, "The crystallography of martensite transformations—IV body-centred cubic

to orthorhombic transformations," *Acta Metallurgica*, vol. 5, no. 3, pp. 137–149, 1957.

[59] C. Hammond, "Orthorhombic martensites in titanium alloys," *Scripta Metallurgica*, vol. 6, no. 7, pp. 569–570, 1972.

[60] T. Sugimoto, K. Kamei, S. Komatsu, K. Sugimoto, and H. Matsumoto, "Aging behavior of alpha-double-prime-martensite formed in a quenched Ti-6 Al- 2 Sn-4 Zr-6 Mo alloy," *Titanium: Science and technology*, pp. 1583–1590, 1985.

[61] X. D. Wang, H. B. Lou, K. Ståhl, J. Bednarcik, H. Franz, and J. Z. Jiang, "Tensile behavior of orthorhombic α″-titanium alloy studied by in situ X-ray diffraction," *Materials Science and Engineering A*, vol. 527, no. 24–25, pp. 6596–6600, 2010, doi: 10.1016/j.msea.2010.06.065.

[62] Y. Guo, T. Jung, Y. L. Chiu, H. Li, S. Bray, and P. Bowen, "Microstructure and microhardness of Ti6246 linear friction weld," *Materials Science and Engineering A*, vol. 562, pp. 17–24, 2013, doi: 10.1016/j.msea.2012.10.089.

[63] Y. Guo, Y. Chiu, M. M. Attallah, H. Li, S. Bray, and P. Bowen, "Characterization of dissimilar linear friction welds of α-β Titanium alloys," *Journal of Materials Engineering and Performance*, vol. 21, no. 5, pp. 770–776, 2012, doi: 10.1007/s11665-012-0129-z.

[64] C. Hammond and J. Nutting, "The physical metallurgy of superalloys and titanium alloys," *Metal science*, vol. 11, no. 10, pp. 474–490, 1977.

[65] Y. Ohmori, T. Ogo, K. Nakai, and S. Kobayashi, "Effects of ω-phase precipitation on β→ α, α″ transformations in a metastable β titanium alloy," *Materials Science and Engineering: A*, vol. 312, no. 1–2, pp. 182–188, 2001.

[66] N. G. Jones, R. J. Dashwood, M. Jackson, and D. Dye, "β Phase decomposition in Ti–5Al–5Mo–5V–3Cr," *Acta Materialia*, vol. 57, no. 13, pp. 3830–3839, 2009.

[67] Q. Contrepois, C. Marc, and J. Lecomte-Beckers, "Characterization of the β phase decomposition in Ti-5Al-5Mo-5V-3Cr at slow heating rates," *Open Journal of Metal*, vol. 1, 2011.

[68] Z. Fan, "The [beta][yields][omega] transformation during room temperature aging in rapidly solidified Ti-6Al-4V alloy," *Scripta Metallurgica et Materialia;(United States)*, vol. 31, no. 11, 1994.

[69] E. Lee, "Microstructure Evolution and Microstructure/Mechanical Properties Relationships in α + β Titanium Alloys," Ohio State University, 2004.

[70] G. Lütjering, "Influence of processing on microstructure and mechanical properties of (α + β) titanium alloys," *Materials Science and Engineering A*, vol. 243, no. 1–2, pp. 32–45, 1998, doi: 10.1016/s0921-5093(97)00778-8.

[71] L. J. Hunter, "Effect of microstructure and oxygen content on the fracture behaviour of the alpha+ beta titanium alloy Ti-4Al-4Mo-2Sn-0.5Si wt.% (IMI 550)," University of Birmingham, 1997.

[72] S. Hosseini, "Fatigue of Ti-6Al-4V," in *Biomedical Engineering – Technical Applications in Medicine*, 2012, pp. 75–92.

[73] I. Bantounas, T. C. Lindley, D. Rugg, and D. Dye, "Effect of microtexture on fatigue cracking in Ti-6Al-4V," *Acta Materialia*, vol. 55, no. 16, pp. 5655–5665, 2007, doi: 10.1016/j.actamat.2007.06.034.

[74] S. L. Seminatin, S. L. KNISLEY, P. N. FAGIN, F. ZHANG, and D. R. BARKER, "Microstructure Evolution during Alpha-Beta Heat Treatment of Ti-6Al-4V," *Materials Science and Engineering A*, vol. 34A, pp. 2377–2386, 2003, [Online]. Available: www.smt.sandvik.com.

[75] R. Pederson, "Microstructure and phase transformation of Ti-6Al-4V," Lulea Univeristy of Technology, 2002.

[76] R. O. Ritchie, D. L. DAVIDSON, B. L.BOYCE, J. P.CAMPBELL, and O. RODER, "High-cycle fatigue of Ti – 6Al – 4V," *Fatigue & Fracture of Engineering Materials & Structures*, vol. 22, pp. 621–631, 1999.

[77] T. Sheppard and J. Norley, "Deformation characteristics of Ti–6Al–4V," *Materials science and technology*, vol. 4, no. 10, pp. 903–908, 1988.

[78] M. Peters, A. Gysler, and G. LÜtjering, "Influence of texture on fatigue properties of Ti-6Al-4V," *Metallurgical Transactions A*, vol. 15, no. 8, pp. 1597–1605, 1984, doi: 10.1007/BF02657799.

[79] R. K. Nalla, B. L. Boyce, J. P. Campbell, J. O. Peters, and R. O. Ritchie, "Influence of Microstructure on High-Cycle Fatigue of Ti-6Al-4V : Bimodal vs . Lamellar Structures," *Metallurgical and Materials Transactions A*, vol. 33A, no. March, pp. 899–918, 2002.

[80] A. N. & E.-S. M. E.-B. Reham Reda, "Optimizing the Mechanical Properties of Ti-6al-4v Castings," *International Journal of Mechanical and Production Engineering Research and Development (IJMPERD)*, vol. 5, no. 1, pp. 83–104, 2015, [Online]. Available: http://www.tjprc.org/view-archives.php?year=2015_26_2&id=32&jtype=2&page=2.

[81] M. Peters and G. Luetjering, "Control of microstructure and texture in Ti-6Al-4V," *Titanium*, vol. 80, pp. 925–935, 1980.

[82] F. Enrique, M. Ian, L. Peifeng, B. Iain, and T. Mathew, "Nano-scale characterisation of tri-modal microstructures in," in *The 14th World Conference on Titanium*, 2020, vol. 12025, pp. 1–10.

[83] R. Thomas, P. Garratt, M. Thomas, and Y. Kosaka, "HIGH-STRENGTH ALPHA-BETA TITANIUM ALLOY," US 2016/0108508 A1, 2016.

[84] P. J. Bania, "Beta titanium alloys and their role in the titanium industry," *Jom*, vol. 46, no. 7, pp. 16–19, 1994, doi: 10.1007/BF03220742.

[85] X. Pang *et al.*, "Comparative study of coatings with different molybdenum equivalent on titanium alloy forged plate for laser cladding: Microstructure and mechanical properties," *Surface and Coatings Technology*, vol. 446, no. July, p. 128760, 2022, doi: 10.1016/j.surfcoat.2022.128760.

[86] I. Weiss and S. L. Semiatin, "Thermomechanical processing of alpha titanium alloys - An overview," *Materials Science and Engineering: A*, vol. 263, no. 2, pp. 243–256, 1999, doi: 10.1016/s0921-5093(98)01155-1.

[87] I. V. Gorynin, "Titanium alloys for marine application," *Materials Science and Engineering: A*, vol. 263, no. 2, pp. 112–116, 1999, doi: 10.1016/s0921-5093(98)01180-0.

[88] H. J. Bunge, "Three-dimensional texture analysis," *International Materials Reviews*, vol. 32, no. 6, pp. 265–290, 1987.

[89] O. Engler and V. Randle, *Introduction to texture analysis : macrotexture, microtexture, and orientation mapping*, Second. 2010.

[90] H. J. Bunge, *Texture Analysis in Materials Science - Mathematical Methods*. Butterworth & Co, 1982.

[91] J. Voight, *Quaternion algebras*. Springer, 2021.

[92] L. Euler, "Formulae generales pro translatione quacunque corporum rigidorum (General formulas for the translation of arbitrary rigid bodies)," *Novi Commentarii academiae scientiarum Petropolitanae*, vol. 20, pp. 189–207, 1776.

[93] A. Nait-Ali, S. Hémery, and M. Gueguen, "How macrozone size and morphology influence yield in titanium alloys investigated using fast Fourier transform-based crystal plasticity simulations," *International Journal of Solids and Structures*, vol. 216, pp. 1–16, 2021, doi: 10.1016/j.ijsolstr.2021.01.008.

[94] P. O. Tympel, "Mechanics and micro-mechanisms of LCF and dwell fatigue in Ti-6Al-4V," Imperial College London, 2016.

[95] J. L. W. Warwick, "Texture, Microstructure and Deformation Mechanisms in Titanium Alloys," Imperial College London, 2011.

[96] L. G. Schulz, "A direct method of determining preferred orientation of a flat reflection sample using a geiger counter x-ray spectrometer," *Journal of Applied Physics*, vol. 20, no. 11, pp. 1030–1033, 1949, doi: 10.1063/1.1698268.

[97] H. J. Bunge, "Advantages of Neutron Diffraction in Texture Analysis," *Textures and Microstructures*, vol. 10, no. 4, pp. 265–307, 1989, doi: 10.1155/tsm.10.265.

[98] L. Lutterotti, R. Vasin, and H. R. Wenk, "Rietveld texture analysis from synchrotron diffraction images. I. Calibration and basic analysis," *Powder Diffraction*, vol. 29, no. 1, pp. 76–84, 2014, doi:

10.1017/S0885715613001346.

[99] D. J. Dingley and V. Randle, “Microtexture determination by electron back-scatter diffraction,” *Journal of Materials Science*, vol. 27, no. 17, pp. 4545–4566, 1992, doi: 10.1007/BF01165988.

[100] A. J. Schwartz, M. Kumar, B. L. Adams, and D. P. Field, *Electron Backscatter Diffraction in Materials Science*, Second. Springer, 2009.

[101] W. H. Bragg and W. L. Bragg, “The reflection of X-rays by crystals,” in *Proceedings of the Royal Society A*, 1913, vol. 88, pp. 428–438.

[102] S. I. Wright, “Fundamentals of Automated EBSD,” in *Electron Backscatter Diffraction in Materials Science*, A. J. Schwartz, M. Kumar, and B. L. Adams, Eds. Boston, MA: Springer US, 2000, pp. 51–64.

[103] J. Baczynski and J. J. Jonas, “Texture development during the torsion testing of α-iron and two if steels,” *Acta Materialia*, vol. 44, no. 11, pp. 4273–4288, 1996, doi: 10.1016/1359-6454(96)00114-0.

[104] R. W. Fonda and K. E. Knipling, “Texture development in near-α Ti friction stir welds,” *Acta Materialia*, vol. 58, no. 19, pp. 6452–6463, 2010, doi: 10.1016/j.actamat.2010.08.007.

[105] R. W. Fonda and K. E. Knipling, “Texture development in friction stir welds,” *Science and Technology of Welding and Joining*, vol. 16, no. 4, pp. 288–294, 2011, doi: 10.1179/1362171811Y.0000000010.

[106] S. Rahimi, B. P. Wynne, and T. N. Baker, “Development of Microstructure and Crystallographic Texture in a Double-Sided Friction Stir Welded Microalloyed Steel,” *Metallurgical and Materials Transactions A: Physical Metallurgy and Materials Science*, vol. 48, no. 1, pp. 362–378, 2017, doi: 10.1007/s11661-016-3833-8.

[107] S. Li, I. J. Beyerlein, and M. A. M. Bourke, “texture formation during equal channel angular extrusion of fcc and bcc materials: comparison with simple shear,” *Materials Science and Engineering A*, vol. 394, pp. 66–77, 2005.

[108] S. F. Frederick, “Manufacturing methods for production process for titanium sheet with controlled texture,” *McDonnell Douglas Astronautics Company, Huntington Beach, Calif. Air Force Materials Laboratory Contract Report No. AFML-TR-73-265*, pp. 80–90, 1973.

[109] S. F. Frederick and G. A. Lenning, “Producing basal textured Ti-6Al-4V sheet,” *Metallurgical Transactions B*, vol. 6, no. 4, pp. 601–605, 1975, doi: 10.1007/BF02913854.

[110] N. Stanford and P. S. Bate, “Crystallographic variant selection in Ti-6Al-4V,” *Acta Materialia*, vol. 52, no. 17, pp. 5215–5224, 2004, doi: 10.1016/j.actamat.2004.07.034.

[111] C. Jourdan, J. Gastaldi, P. Marzo, and G. Grange, “In situ statistical study of the nucleation, the variant selection and the orientation memory effect during the α⇌β titanium martensitic transformation,” *Journal of Materials Science*, vol. 26, no. 16, pp. 4355–4360, 1991, doi: 10.1007/BF00543651.

[112] M. Preuss, L. Pocock, and P. Bate, “Variant Selection and Texture Studies in Ti-6246,” in *Proceedings of the 11th World Conference on Titanium*, 2007, pp. 527–530.

[113] D. Pionnier, M. Humbert, M. J. Philippe, and Y. Combres, “Study of the α ″phase texture obtained by martensitic β–α ″phase transformation induced by tensile test in a sheet of Ti5Al2Sn4Zr4Mo2Cr1Fe,” *Acta materialia*, vol. 46, no. 16, pp. 5891–5898, 1998.

[114] M. G. Glavicic and S. L. Semiatin, “X-ray line-broadening investigation of deformation during hot rolling of Ti-6Al-4V with a colony-alpha microstructure,” *Acta Materialia*, vol. 54, no. 20, pp. 5337–5347, 2006, doi: 10.1016/j.actamat.2006.04.020.

[115] L. Zeng and T. R. Bieler, “Effects of working, heat treatment, and aging on microstructural evolution and crystallographic texture of α, α′, α″ and β phases in Ti-6Al-4V wire,” *Materials Science and Engineering: A*, vol. 392, no. 1–2, pp. 403–414, 2005, doi: 10.1016/j.msea.2004.09.072.

[116] L. Germain, N. Gey, and M. Humbert, “Reliability of reconstructed β-orientation maps in titanium alloys,” *Ultramicroscopy*, vol. 107, no. 12, pp. 1129–1135, 2007, doi: 10.1016/j.ultramic.2007.01.012.

[117] N. Gey and M. Humbert, “Specific analysis of EBSD data to study the texture inheritance due to the β → α phase transformation,” *Journal of Materials Science*, vol. 38, no. 6, pp. 1289–1294, 2003, doi:

10.1023/A:1022842712172.

[118] N. Gey, M. Humbert, M. J. Philippe, and Y. Combres, “Modeling the transformation texture of Ti-64 sheets after rolling in the β-field,” *Materials Science and Engineering: A*, vol. 230, no. 1–2, pp. 68–74, 1997, doi: 10.1016/s0921-5093(97)80111-6.

[119] N. Gey and M. Humbert, “Characterization of the variant selection occurring during the α→β→α phase transformations of a cold rolled titanium sheet,” *Acta Materialia*, vol. 50, no. 2, pp. 277–287, 2002, doi: 10.1016/S1359-6454(01)00351-2.

[120] M. Humbert, L. Germain, N. Gey, P. Bocher, and M. Jahazi, “Study of the variant selection in sharp textured regions of bimodal IMI 834 billet,” *Materials Science and Engineering: A*, vol. 430, no. 1–2, pp. 157–164, 2006, doi: 10.1016/j.msea.2006.05.047.

[121] J. H. Keeler and A. H. Geisler, “Preferred Orientations in Rolled and Annealed Titanium,” *Jom*, vol. 8, no. 2, pp. 80–90, 1956, doi: 10.1007/bf03377647.

[122] T. Webster, “Process-Microstructure-Mechanical Property Relationships for Linear Friction Welded Ti-6Al-2Sn-4Zr-6Mo,” University of Birmingham, 2019.

[123] A. Vairis and M. Frost, “High frequency linear friction welding of a titanium alloy,” *Wear*, vol. 648, 1998.

[124] A. Vairis and M. Frost, “On the extrusion stage of linear friction welding of Ti 6a1 4V,” *Materials Science and Engineering A*, vol. 271, no. 1–2, pp. 477–484, 1999, doi: 10.1016/s0921-5093(99)00449-9.

[125] A. Vairis and M. Frost, “Modelling the linear friction welding of titanium blocks,” *Materials Science and Engineering A*, vol. 292, no. 1, pp. 8–17, 2000, doi: 10.1016/S0921-5093(00)01036-4.

[126] I. Bhamji, M. Preuss, P. L. Threadgill, and A. C. Addison, “Solid state joining of metals by linear friction welding: A literature review,” *Materials Science and Technology*, vol. 27, no. 1, pp. 2–12, 2011, doi: 10.1179/026708310X520510.

[127] I. Bhamji, A. C. Addison, P. L. Threadgill, and M. Preuss, “Linear friction welding in aerospace engineering,” in *Welding and Joining of Aerospace Materials*, Woodhead Publishing Limited, 2012, pp. 384–415.

[128] A. R. McAndrew, P. A. Colegrove, C. Bühr, B. C. D. Flipo, and A. Vairis, “A literature review of Ti-6Al-4V linear friction welding,” *Progress in Materials Science*, vol. 92, pp. 225–257, 2018, doi: 10.1016/j.pmatsci.2017.10.003.

[129] U. U. Ofem, P. A. Colegrove, A. Addison, and M. J. Russell, “Energy and force analysis of linear friction welds in medium carbon steel,” *Science and Technology of Welding and Joining*, vol. 15, no. 6, pp. 479–485, 2010, doi: 10.1179/136217110X12731414739790.

[130] P. Threadgill, “Linear friction welding,” *The Welding Institute*, 2017. https://www.twi-global.com/technical-knowledge/job-knowledge/linear-friction-welding-146 (accessed Nov. 16, 2020).

[131] P. Wanjara and M. Jahazi, “Linear Friction Welding of Ti-6Al-4V: Processing, Microstructure, and Mechanical-Property Inter-Relationships,” *Metallurgical and Materials Transactions A*, vol. 36, no. August, 2005.

[132] W. Y. Li *et al.*, “Effect of friction time on flash shape and axial shortening of linear friction welded 45 steel,” *Materials Letters*, vol. 62, no. 2, pp. 293–296, 2008, doi: 10.1016/j.matlet.2007.05.037.

[133] R. Turner, J. C. Gebelin, R. M. Ward, and R. C. Reed, “Linear friction welding of Ti-6Al-4V: Modelling and validation,” *Acta Materialia*, vol. 59, no. 10, pp. 3792–3803, 2011, doi: 10.1016/j.actamat.2011.02.028.

[134] A. R. McAndrew, P. A. Colegrove, A. C. Addison, B. C. D. Flipo, and M. J. Russell, “Energy and Force Analysis of Ti-6Al-4V Linear Friction Welds for Computational Modeling Input and Validation Data,” *Metallurgical and Materials Transactions A: Physical Metallurgy and Materials Science*, vol. 45, no. 13, pp. 6118–6128, 2014, doi: 10.1007/s11661-014-2575-8.

[135] A. R. McAndrew, P. A. Colegrove, A. C. Addison, B. C. D. Flipo, M. J. Russell, and L. A. Lee, “Modelling of the workpiece geometry effects on Ti-6Al-4V linear friction welds,” *Materials and Design*, vol. 87, no. November, pp. 1087–1099, 2015, doi: 10.1016/j.matdes.2015.09.080.

[136] W. Y. Li, T. Ma, and J. Li, "Numerical simulation of linear friction welding of titanium alloy: Effects of processing parameters," *Materials and Design*, vol. 31, no. 3, pp. 1497–1507, 2010, doi: 10.1016/j.matdes.2009.08.023.

[137] J. Sorina-Müller, M. Rettenmayr, D. Schneefeld, O. Roder, and W. Fried, "FEM simulation of the linear friction welding of titanium alloys," *Computational Materials Science*, vol. 48, no. 4, pp. 749–758, 2010, doi: 10.1016/j.commatsci.2010.03.026.

[138] M. Grujicic, R. Yavari, J. S. Snipes, S. Ramaswami, C. F. Yen, and B. A. Cheeseman, "Linear friction welding process model for carpenter custom 465 precipitation-hardened martensitic stainless steel," *Journal of Materials Engineering and Performance*, vol. 23, no. 6, pp. 2182–2198, 2014, doi: 10.1007/s11665-014-0985-9.

[139] M. Karadge, M. Preuss, C. Lovell, P. J. Withers, and S. Bray, "Texture development in Ti-6Al-4V linear friction welds," *Materials Science and Engineering A*, vol. 459, no. 1–2, pp. 182–191, 2007, doi: 10.1016/j.msea.2006.12.095.

[140] A. Mateo *et al.*, "Welding repair by linear friction in titanium alloys," *Materials Science and Technology*, vol. 25, no. 7, pp. 905–913, 2009, doi: 10.1179/174328408X363380.

[141] A. Vairis and M. Frost, "High frequency linear friction welding of a titanium alloy," *Wear*, vol. 648, no. 1, pp. 117–131, 1998, doi: 10.1016/S0043-1648(98)00145-8.

[142] R. Turner, R. M. Ward, R. March, and R. C. Reed, "The magnitude and origin of residual stress in Ti-6Al-4V linear friction welds: An investigation by validated numerical modeling," *Metallurgical and Materials Transactions B: Process Metallurgy and Materials Processing Science*, vol. 43, no. 1, pp. 186–197, 2012, doi: 10.1007/s11663-011-9563-9.

[143] J. Romero, M. M. Attallah, M. Preuss, M. Karadge, and S. E. Bray, "Effect of the forging pressure on the microstructure and residual stress development in Ti-6Al-4V linear friction welds," *Acta Materialia*, vol. 57, no. 18, pp. 5582–5592, 2009, doi: 10.1016/j.actamat.2009.07.055.

[144] T. J. Ma, W. Y. Li, B. Zhong, Y. Zhang, and J. L. Li, "Effect of post-weld heat treatment on microstructure and property of linear friction welded Ti17 titanium alloy joint," *Science and Technology of Welding and Joining*, vol. 17, no. 3, pp. 180–185, 2012, doi: 10.1179/1362171811Y.0000000079.

[145] X. Boyat *et al.*, "Interfacial characteristics and cohesion mechanisms of linear friction welded dissimilar titanium alloys: Ti–5Al–2Sn–2Zr–4Mo–4Cr (Ti17) and Ti–6Al–2Sn–4Zr–2Mo (Ti6242)," *Materials Characterization*, vol. 158, no. September 2019, p. 109942, 2019, doi: 10.1016/j.matchar.2019.109942.

[146] R. R. Ye *et al.*, "Microstructure and microhardness of dissimilar weldment of Ni-based superalloys IN718-IN713LC," *Materials Science and Engineering A*, vol. 774, 2020, doi: 10.1016/j.msea.2019.138894.

[147] S. Tabaie, F. Rézaï-Aria, B. C. D. Flipo, and M. Jahazi, "Dissimilar linear friction welding of selective laser melted Inconel 718 to forged Ni-based superalloy AD730™: Evolution of strengthening phases," *Journal of Materials Science and Technology*, vol. 96, pp. 248–261, 2022, doi: 10.1016/j.jmst.2021.03.086.

[148] F. Khalfallah, Z. Boumerzoug, S. Rajakumar, and E. Raouache, "Optimization by RSM on rotary friction welding of AA1100 aluminum alloy and mild steel," *International Review of Applied Sciences and Engineering*, vol. 11, no. 1, pp. 34–42, 2020, doi: 10.1556/1848.2020.00005.

[149] S. Rajan, P. Wanjara, J. Gholipour, and A. S. Kabir, "Joining of dissimilar alloys Ti-6Al-4V and Ti-6Al-2Sn-4Zr-2Mo-0.1Si using linear friction welding," *Materials*, vol. 13, no. 17, pp. 1–25, 2020, doi: 10.3390/MA13173664.

[150] M. E. Nunn, "Aero engine improvements through linear friction welding," 2005, [Online]. Available: http://www.twi-global.com/technical-knowledge/published-papers/aero-engine-improvements-through-linear-friction-welding-august-2005/.

[151] P. Geng, G. Qin, H. Ma, J. Zhou, and N. Ma, "Linear friction welding of dissimilar Ni-based superalloys: Microstructure evolution and thermo-mechanical interaction," *Journal of Materials Research and Technology*, vol. 11, pp. 633–649, 2021, doi: 10.1016/j.jmrt.2021.01.036.

[152] E. Dalgaard, P. Wanjara, G. Trigo, M. Jahazi, G. Comeau, and J. J. Jonas, "Linear friction welding of Al-Cu part 2 - Interfacial characteristics," *Canadian Metallurgical Quarterly*, vol. 50, no. 4, pp. 360–370, 2011, doi:

10.1179/000844311X13112418194671.

[153] I. Bhamji, M. Preuss, R. J. Moat, P. L. Threadgill, and A. C. Addison, "Linear friction welding of aluminium to magnesium," *Science and Technology of Welding and Joining*, vol. 17, no. 5, pp. 368–374, 2012, doi: 10.1179/1362171812Y.0000000017.

[154] P. Wanjara, E. Dalgaard, G. Trigo, C. Mandache, G. Comeau, and J. J. Jonas, "Linear friction welding of Al-Cu: Part 1 - Process evaluation," *Canadian Metallurgical Quarterly*, vol. 50, no. 4, pp. 350–359, 2011, doi: 10.1179/000844311X13112418194644.

[155] P. Wanjara, J. Gholipour, K. Watanabe, K. Nezaki, Y. Tian, and M. Brochu, "Linear friction welding of IN718 to Ti6Al4V," *Materials Science Forum*, vol. 879, pp. 2072–2077, 2016, doi: 10.4028/www.scientific.net/MSF.879.2072.

[156] D. H. Zhang, Y. Zhang, and B. H. Wu, "Research on the adaptive machining technology of blisk," in *Advanced Materials Research*, 2009, vol. 69, pp. 446–450.

[157] T. Backhaus, S. Schrape, M. Harding, M. Voigt, and R. Mailach, "Validation Methods for 3D Digitizing Precision Concerning Jet Engine BLISKs," in *German Aerospace Congress*, 2017, no. September, pp. 1–9.

[158] J. B. Brownel, P. J. Gillbanks, J. P. Throssel, and J. R. Wilson, "METHOD FOR THE MANUFACTURE OR REPAIR OF A BLISK BY LINEAR FRICTION WELDING," 6,095,402, 2000.

[159] H. L. Ewalds and R. J. H. Wanhill, *Fracture mechanics*. 1984.

[160] A. Saxena, *Advanced Fracture Mechanics and Structural Integrity*. CRC Press, 2020.

[161] J. Schijve, *Fatigue of Structures and Materials*. Springer, 2004.

[162] N. Perez, *Fracture Mechanics*. Springer, 2004.

[163] S. Suresh, *Fatigue of materials*. Cambridge university press, 1998.

[164] T. L. Anderson, *Fracture Mechanics - Fundamentals and Applications*, vol. 110, no. 9. 2017.

[165] A. A. Griffith, "VI. The phenomena of rupture and flow in solids," *Philosophical transactions of the royal society of london. Series A, containing papers of a mathematical or physical character*, vol. 221, no. 582–593, pp. 163–198, 1921.

[166] G. R. Irwin, "Fracture Dynamics," in *Fracturing of Metals*, 1948, pp. 147–166.

[167] H. M. Westergaard, "Bearing pressures and cracks," *Trans AIME, J. Appl. Mech.*, vol. 6, pp. 49–53, 1939.

[168] P. C. Paris, "A rational analytic theory of fatigue," *The trend in engineering*, vol. 13, p. 9, 1961.

[169] P. Paris and F. Erdogan, "A critical analysis of crack propagation laws," *The American Society of Mechanical Engineering*, vol. 85, no. 4, pp. 528–533, 1963.

[170] X. Li and X. Jiang, "Effects of dislocation pile-up and nanocracks on the main crack propagation in crystalline metals under uniaxial tensile load," *Engineering Fracture Mechanics*, vol. 212, no. 111, pp. 258–268, 2019, doi: 10.1016/j.engfracmech.2019.03.038.

[171] P. Lukas, "Fatigue crack nucleation and microstructure," in *ASM Handbook: Fatigue and Fracture*, ASM International, 1996, pp. 96–109.

[172] K. J. Miller, "Materials science perspective of metal fatigue resistance," *Materials Science and Technology*, vol. 9, no. June, pp. 453–462, 1993.

[173] B. Taylor and E. Weidmann, "Metallographic preparation of titanium," *Struers Application Notes*, 2016. https://www.struers.com/en/Knowledge/Materials/Titanium#about (accessed Dec. 21, 2020).

[174] MathWorks, "2-D Gaussian filtering of images," *Matlab Documentation*, 2022. https://uk.mathworks.com/help/images/ref/imgaussfilt.html (accessed Apr. 16, 2022).

[175] MathWorks, "Adaptive image threshold using local first-order statistics," *Matlab Documentation*, 2022.

https://uk.mathworks.com/help/images/ref/adaptthresh.html (accessed Apr. 16, 2022).

[176] MathWorks, "Morphological Operations," *Matlab Documentation*, 2022. https://uk.mathworks.com/help/images/morphological-dilation-and-erosion.html (accessed Apr. 16, 2022).

[177] MathWorks, "Measure properties of image regions," *Matlab Documentation*, 2022. https://uk.mathworks.com/help/images/ref/regionprops.html (accessed Apr. 16, 2022).

[178] R. Castaing, "Electron probe microanalysis," *Advances in Electronics and Electron Physics*, vol. 13, pp. 317–386, 1960, doi: https://doi.org/10.1016/S0065-2539(08)60212-7.

[179] C. A. Anderson and M. F. Hasler, "Extension of electron microprobe techniques to biochemistry by the use of long wavelength X-rays," in *Proceedings of the Fourth International Conference on X-ray Optics and Microanalysis*, 1966, pp. 310–327.

[180] F. Bachmann, R. Hielscher, and H. Schaeben, "Texture analysis with MTEX- Free and open source software toolbox," *Solid State Phenomena*, vol. 160, pp. 63–68, 2010, doi: 10.4028/www.scientific.net/SSP.160.63.

[181] K.-L. Lin, "Phase Identification Using Series of Selected Area Diffraction Patterns and Energy Dispersive Spectrometry within TEM," *Microscopy Research*, vol. 02, no. 04, pp. 57–66, 2014, doi: 10.4236/mr.2014.24008.

[182] M. Klinger and A. Jäger, "Crystallographic Tool Box (CrysTBox): Automated tools for transmission electron microscopists and crystallographers," *Journal of Applied Crystallography*, vol. 48, no. 2015, pp. 2012–2018, 2015, doi: 10.1107/S1600576715017252.

[183] British Standards Institute, "Metallic materials – Vickers hardness test," BS-6507-1:2018.

[184] MathWorks, "Interpolate 2-D or 3-D scattered data," *Matlab Documentation*, 2024. https://uk.mathworks.com/help/matlab/ref/griddata.html (accessed May 03, 2024).

[185] W. Cheng, J. Outeiro, J.-P. Costes, R. M'Saoubi, H. Karaouni, and V. Astakhov, "A constitutive model for Ti6Al4V considering the state of stress and strain rate effects," *Mechanics of Materials*, vol. 137, p. 103103, 2019.

[186] British Standards Institute, "Metallic materials - Tensile testing," BS-6892-1:2019.

[187] British Standards Institute, "Aerospace series. Test methods for metallic materials. Constant amplitude force-controlled high cycle fatigue testing," BS-3987:2009.

[188] British Standards Institute, "Methods of Fatigue Testing - Part 1: Guide to general principles," BS-3518-1:1993. doi: 10.1016/b978-0-08-009729-9.50005-1.

[189] British Standards Institute, "Metallic materials — Fatigue testing — Axial force-controlled method," BS-1099:2017.

[190] British Standards Institute, "Metallic materials - Fatigue testing - Fatigue crack growth method," BS-12108:2018.

[191] British Standards Institute, "Fracture mechanics toughness tests —Part 1: Methods for determination of KIc, critical CTOD and critical J values of metallic materials."

[192] ASTM International, "Standard Test Method for Determining Residual Stresses by the Hole-Drilling Strain-Gage Method," ASTM-E837-20, 2020. doi: 10.1520/E0837-20.1.

[193] P. D. Panetta, R. B. Thompson, and F. J. Margetan, "Use of Electron Backscatter Diffraction in Understanding Texture and the Mechanisms of Backscattered Noise Generation in Titanium Alloys," in *Review of Progress in Quantitative Nondestructive Evaluation: Volume 17A*, D. O. Thompson and D. E. Chimenti, Eds. Boston, MA: Springer US, 1998, pp. 89–96.

[194] A. P. Woodfield, M. D. Gorman, J. A. Sutliff, and R. R. Corderman, "Effect of microstructure on dwell fatigue behavior of Ti-6242," 1999.

[195] E. Zhao, S. Sun, and Y. Zhang, "Recent advances in silicon containing high temperature titanium alloys," *Journal of Materials Research and Technology*, vol. 14, pp. 3029–3042, 2021, doi: 10.1016/j.jmrt.2021.08.117.

[196] G. G. E. Seward, S. Celotto, D. J. Prior, J. Wheeler, and R. C. Pond, "In situ SEM-EBSD observations of the hcp to bcc phase transformation in commercially pure titanium," *Acta Materialia*, vol. 52, no. 4, pp. 821–832, 2004, doi: 10.1016/j.actamat.2003.10.049.

[197] H. I. Aaronson, "Mechanisms of the massive transformation," *Metallurgical and Materials Transactions A: Physical Metallurgy and Materials Science*, vol. 33, no. 8, pp. 2285–2297, 2002, doi: 10.1007/s11661-002-0352-6.

[198] A. L. Pilchak and T. F. Broderick, "Evidence of a massive transformation in a Ti-6Al-4V solid-state weld?," *Jom*, vol. 65, no. 5, pp. 636–642, 2013, doi: 10.1007/s11837-013-0591-6.

[199] Y. Guo, Y. Chiu, H. Li, M. M. Attallah, S. Bray, and P. Bowen, "Microstructure and microtexture of linear friction welded Ti-6Al-4V," *Ti 2011 - Proceedings of the 12th World Conference on Titanium*, vol. 3, pp. 1995–1999, 2011.

[200] Y. Guo, M. M. Attallah, Y. Chiu, H. Li, S. Bray, and P. Bowen, "Spatial variation of microtexture in linear friction welded Ti-6Al-4V," *Materials Characterization*, vol. 127, pp. 342–347, 2017, doi: 10.1016/j.matchar.2017.03.019.

[201] F. Daus, H. Y. Li, G. Baxter, S. Bray, and P. Bowen, "Mechanical and microstructural assessments of RR1000 to IN718 inertia welds - effects of welding parameters," *Materials Science and Technology*, vol. 23, no. 12, pp. 1424–1432, 2007, doi: 10.1179/174328407X243997.

[202] M. Velu, "A Short Review on Fracture and Fatigue Crack Growth in Welded Joints," *Materials Today: Proceedings*, vol. 5, no. 5, pp. 11364–11370, 2018, doi: 10.1016/j.matpr.2018.02.103.

[203] S. Tamirisakandala *et al.*, "Effect of boron on the beta transus of Ti-6Al-4V alloy," *Scripta Materialia*, vol. 53, no. 2, pp. 217–222, 2005, doi: 10.1016/j.scriptamat.2005.03.038.

[204] M. H. Yoo, "Slip, twinning, and fracture in hexagonal close-packed metals," *Metallurgical Transactions A*, vol. 12, no. 3, pp. 409–418, 1981, doi: 10.1007/BF02648537.

[205] P. G. Partridge, "The crystallog raphy and defor- mation modes of hexagonal close-packed metals," *Metallurgical Reviews*, vol. 12, no. 1, pp. 169–194, 1967.

[206] M. J. Donachie and JR, *Titanium and titanium alloys*. Ohio: American society for metals, 1982.

[207] TIMETAL, "TIMETAL 6-4, 6-4 ELI & 6-4-.1Ru: Medium to high strength general-purpose alloys," 2000.

[208] S. Sheng, J. Flegler, B. J. Becs, and M. Dankert, "HCF component tests on full-scale low pressure steam turbine end stage blades," in *Proceedings of the ASME Turbo Expo*, 2016, vol. 8, pp. 1–9, doi: 10.1115/GT2016-56988.

[209] N. E. Paton, R. G. Baggerly, and J. C. Williams, "Report SC 526.7 FR.," 1976.

[210] A. ZARKADES and F. R. LARSON, *Elasticity of Titanium Sheet Alloys*. Pergamon Press Ltd, 1970.

[211] H. Shao, Y. Zhao, P. Ge, and W. Zeng, "In-situ SEM observations of tensile deformation of the lamellar microstructure in TC21 titanium alloy," *Materials Science and Engineering: A*, vol. 559, pp. 515–519, Jan. 2013, doi: 10.1016/j.msea.2012.08.134.

[212] G. Wang, Z. Chen, J. Li, J. Liu, Q. Wang, and R. Yang, "Microstructure and Mechanical Properties of Electron Beam Welded Titanium Alloy Ti-6246," *Journal of Materials Science & Technology*, vol. 34, no. 3, pp. 570–576, 2018, doi: https://doi.org/10.1016/j.jmst.2016.10.007.

[213] M. Kasemer, M. Echlin, J.-C. Stinville, T. Pollock, and P. Dawson, "On slip initiation in equiaxed α/β Ti-6Al-4V," *Acta Materialia*, vol. 136, pp. 288–302, Jul. 2017, doi: 10.1016/j.actamat.2017.06.059.

[214] "Introduction to EBSD," *University of California, Riverside*, 2023. https://cfamm.ucr.edu/document/ebsd-intro (accessed Jul. 13, 2023).

[215] G. Z. Voyiadjis, J. Jeong, and J. W. Kysar, "Grain size dependence of polycrystalline plasticity modeling in cylindrical indentation," *Computational Mechanics*, vol. 68, no. 3, pp. 499–543, 2021, doi: 10.1007/s00466-020-01940-z.

[216] "EBSD.com - How does EBSD work?," *Oxford Instrument*, 2023. https://www.ebsd.com/ebsd-for-beginners/how-does-ebsd-work (accessed Jul. 13, 2023).

[217] S. Tumanski, *Handbook of magnetic measurements*. CRC Press, 2011.

[218] S. Suwas, R. K. Ray, and R. K. R. Satyam Suwas, *Crystallographic Texture of Materials*. 2014.

[219] D. Liu and D. J. Pons, "Crack Propagation Mechanisms for Creep Fatigue : A Consolidated Explanation of Fundamental Behaviours from Initiation to Failure," *Metals*, vol. 8, no. 623, 2018, doi: 10.3390/met8080623.

[220] C. Laird, "The influence of metallurgical structure on the mechanisms of fatigue crack propagation," in *Fatigue crack propagation*, ASTM International, 1967.

[221] A. May, "Study of the cyclic behavior and the fatigue damage of an anisotropic 2017A aluminium alloy," Ecole Militaire Polytechnique, 2014.

[222] E. Nuttall, "Characterisation and Assessment of Linear Friction Welded Ti-6Al-4V Under Fatigue Loading," University of Birmingham, 2016.

Appendices

A Publication

Y. Chuang, H. Li, S. Bray, N. Martin, and P. Bowen, ‘‘Characterisation of Dissimilar Titanium Linear Friction Welds,’’ Proceedings of 15th World Conference on Titanium, 2023.

CRediT authorship contribution statement

Y. Chuang: Methodology, Software, Investigation, Formal analysis, Data curation, Visualisation, Writing - original draft.

H. Li: Supervision, Writing - review and editing.

S. Bray: Supervision.

N. Martin: Supervision.

P. Bowen: Supervision, Funding acquisition.

CHARACTERISATION OF DISSIMILAR TITANIUM LINEAR FRICTION WELDS

Yu-Chung Chuang[1], Hangyue Li[1], Simon Bray[2], Nigel Martin[2], Paul Bowen[1]

1 School of Metallurgy and Materials, University of Birmingham, Birmingham B15 2TT, UK
2 Rolls-Royce plc, PO Box 31, Derby DE24 8BJ, UK

Linear friction welding is an advantageous joining technique for manufacturing titanium components in low-pressure compressors for gas turbine engines where joining of dissimilar materials is needed. To fully optimise the joining parameters, thorough characterisation and assessment of the welds are essential. In this study, dissimilar linear friction welds in combination of Ti-6Al-4V and a newly developed high strength $\alpha+\beta$ titanium alloy were examined. Microhardness mapping was generated to evaluate the distribution of hardness across the entire joint in as-welded condition. Results showed that the weld exhibited superior hardness compared to both parent materials. The heat-affected zone in the new alloy exhibited inferior hardness relative to the parent material, while it is potentially recoverable after post-weld heat treatment. Scanning electron microscopy was used to characterise the microstructure in each weld zone and to establish correlations with the measured hardness values. Based on a combination of observed microstructures and hardness measurements, as well as chemical and crystallographic analysis, the microstructural evolution that occurred during linear friction welding in different zones of the joints is proposed. The texture of the weld was also investigated using electron backscattered diffraction. The texture in the central weld zone is found to be dependent on the oscillation direction. However, an oscillation-independent texture was measured particularly in the thermo-mechanically affected zone of the new alloy at the bifurcation point. This oscillation-independent texture is not obvious on the Ti-6Al-4V side. Texture simulation results suggest the existence of a strong β texture prior to phase transformation during cooling.

Keywords: Titanium alloy, Linear friction welding, Microstructure, Microhardness, Texture

1 Introduction

Titanium alloys are widely used in turbofan engines due to their high specific strength, excellent mechanical properties, and great weldability. As weight reduction is crucial in turbofan engine development, integrally bladed disks (Blisks) offer a significant weight reduction of 30% compared to the traditional mechanical assembly [1]. Linear friction welding (LFW) is an ideal method to join the blades and disc as it provides several advantages over traditional fusion welding techniques, including the self-cleaning effect [2], the ability to join dissimilar materials and produce narrower weld, as well as its solid-state joining nature. During the welding process, compressive pressure is applied to bring the two workpieces together, while one of the workpieces oscillates linearly whereas the other one remains stationary [3]. Frictional heat is generated by the oscillation, raising the temperature at the interface with a high heating rate. The workpiece material is extruded from the joint once it is softened enough by the heat experienced. When the oscillation terminates, the heat is no longer generated, and the temperature of the weld drops rapidly through thermal conduction to the workpieces. The compressive pressure is still applied at this stage to consolidate the joint.

The extremely high heating and cooling rates in linear friction welding result in dramatic changes in the microstructure. Generally, the microstructure in the titanium linear friction welds is classified into three distinct zones [4–7]. Firstly, the central weld zone (CWZ), a narrow region around the weld interface usually with martensitic-type of microstructure due to the high cooling rate. Secondly, the thermo-mechanically affected zone (TMAZ), located right next to the CWZ with significant plastic deformation on the grains. Thirdly, the heat-affected zone (HAZ) is located further away from TMAZ consisting of a similar appearance to the unaffected parent material (PM). The as-welded microstructure is generally considered metastable due to the lack of time for diffusion to occur.

There are numerous studies on the mechanical properties of titanium linear friction welds [3,4,8–10]. Wanjara *et al.* [4] and Romero *et al.* [9] both reported that Ti-6Al-4V (Ti-64) linear friction welds with appropriate process parameters have superior hardness and tensile strength to their parent material. In both studies, the hardness profile appears in a 'Λ' shape where the maximum value occurs at the weld interface for its fine martensitic microstructure. The exact shape of the profile varies with the applied process parameters and the employed alloys. Recently, Guo *et al.* [10] found an opposite 'V' shaped hardness profile in Ti-6Al-2Sn-4Zr-6Mo (Ti6246) linear friction welds due to the retained β phase and the formation of soft α'' martensite in the CWZ instead of hard α' martensite. The same phenomenon also appears in Ti-64:Ti6246 dissimilar linear friction welds, where the CWZ on the Ti-64 side is harder than Ti-64, whereas the CWZ on the Ti6246 side is softer than Ti6246 [11]. However, the hardness can be recovered by applying an appropriate post weld heat treatment, due to the formation of fine precipitates and the age hardening effect [10].

TIMETAL® 575 (Ti-5.3Al-7.7V-0.5Si, Ti-575) is a newly developed $\alpha+\beta$ titanium alloy with improved fatigue and tensile properties whilst maintaining similar ductility and density to Ti-64 [12,13]. The alloying elements in Ti-575 are intentionally chosen to be similar to Ti-64, thus allowing the usage of scrap Ti-64 as raw material in Ti-575 manufacture. Due to its novelty, research on Ti-575 is limited compared to the number of existing studies on Ti-64. Furthermore, to the best of author's knowledge, there is yet no study on linear friction welded Ti-575 at the time of writing. Therefore, characterisation and assessment

of Ti-575 after linear friction welding are of interest for its potential application in aerospace industry.

The aim of this study is to characterise the microstructure of Ti-64:Ti-575 dissimilar linear friction welds in several aspects, including microstructure characterisation, microhardness distribution, and texture development. Microhardness mappings and profiles were carried out to estimate the mechanical properties of the weld. The measured hardness of each weld region can be rationalised by the observed microstructure. The texture study helps understand the anisotropy of the welds, providing information for optimising the manufacturing process.

2 Materials and Experimental

Two types of commercial α+β alloys, Ti-64 and Ti-575, were studied in this research. The microstructures of the parent materials of Ti-575 and Ti-64 are shown in Figure 1. Ti-575 has a typical bi-modal microstructure with equiaxed primary α grains and transformed β region, whereas Ti-64 has a fully equiaxed microstructure with equiaxed α grains and intergranular β. Titanium silicides Ti_5Si_3 were found particularly in Ti-575, they were formed as a result of the addition of 0.5% silicon in the alloying elements. Tertiary α laths with 50 nm width can be seen in Ti-575, as shown in the inserted image in Figure 1 (a). The chemical composition of the α and β phases in the two alloys is listed in Table 1.

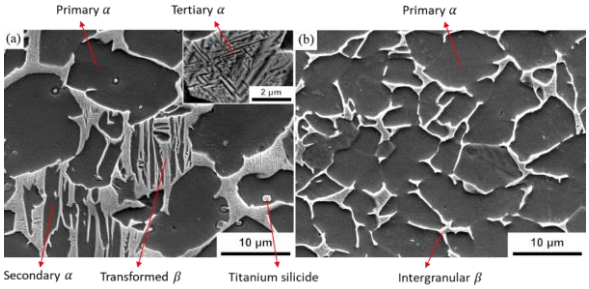

Figure 1 Secondary electron images of parent material in (a) Ti-575 and (b) Ti-64. α and β phase in SEI appears dark and bright, respectively.

Table 1 Chemical composition of α and β phase in Ti-575 and Ti-64 measured by EDS. (unit: wt.%)

Alloy	Phase	Ti	Al	V	Si
Ti-64	α	89.1	7.6	3.3	
	β	82.1	4.1	12.9	
Ti-575	α	88.5	6.6	4.3	0.7
	β	77.5	3.7	17.7	0.5

Ti-64 to Ti-575 dissimilar linear friction welds with dimensions 150 mm in length and 32 mm in width were supplied by Rolls-Royce plc in the as-welded condition. Samples for characterisation were extracted at the centre of the weld by electrical discharge machining along the X-Z plane, as shown in Figure 1 (a). They were mounted and mechanically polished down to 0.04 μm finishing using Struers oxide polishing suspension. Kroll's reagent with 2% HF, 10% HNO_3, and 88% H_2O was used to etch the surface for metallographic examination. Optical microscopy was carried out using a Keyence VHX-6000 digital optical microscope. Scanning electron microscopy was performed using Jeol-7000 FEG ESEM with 20 kV acceleration voltage to observe the microstructure of the etched samples. Energy-dispersive X-ray spectroscopy was performed using Oxford Ultim® Max EDS detector attached to Jeol-7000 for chemical composition analysis.

The microhardness variation across the entire weld was measured by a Struers DuraScan-5 microhardness tester with a step size of 0.1 mm, a load of 0.5 kg, and a 10-second holding time. Electron backscatter diffraction (EBSD) was carried out by the detector attached to Jeol-7000. The step size used in EBSD mapping was 0.1-0.3 μm, and the scanning area is 50x50-200x200 μm^2 depending on the size of the microstructural features. The obtained data were processed by MTEX and Oxford AZtec software for crystallography and texture analysis. The forge direction (FD) is parallel to the Z direction, while the oscillation direction (OD) lies on the X-Y plane with a 19° stagger to the X direction, as illustrated in Figure 2 (a). It is worth noting that the oscillation direction has a crucial influence on the texture of linear friction welds, and it does not parallel to the X direction on the sample surface. The pole figures displayed in this study are either aligned with the oscillation direction or with the X direction, depending on which direction the measured texture components align with.

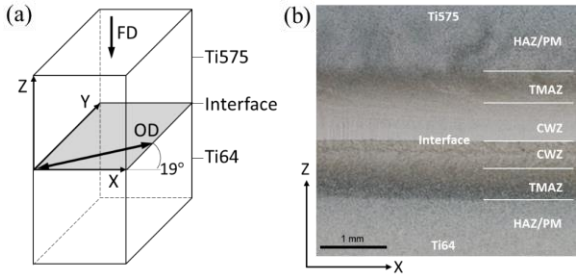

Figure 2 (a) Schematic diagram of weld geometry with forge direction (FD) and oscillation direction (OD). Samples were extracted along the X-Z plane. (b) An optical macrograph of the Ti-64:Ti-575 linear friction weld.

3 Results and Discussion

3.1 Microstructure Characterisation

Linear friction welding results in a narrow weld region which undergo a rapid heating and cooling treatment together with thermo-mechanical deformation. This process modified the microstructure significantly, as a result, TMAZ and CWZ can be easily distinguished from the optical micrographs, as shown in Figure 2 (b). The zone sizes of CWZ and TMAZ were measured and presented in Figure 3 (b).

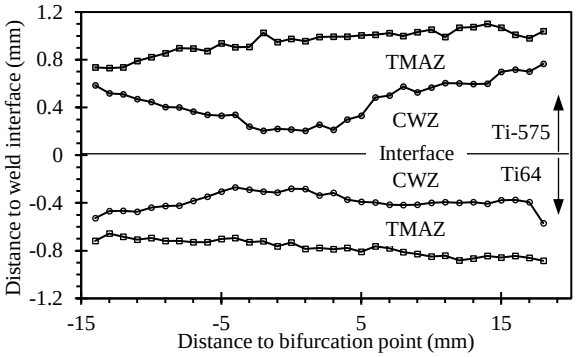

Figure 3 Zone size measurement of Ti-64:Ti-575 linear friction weld.

The microstructure of Ti-64 after linear friction welding has been studied extensively [4,7,11,14], therefore the current study focuses on characterising the weld microstructure on the Ti-575 side. The microstructure in the HAZ of Ti-575 in as-welded condition is shown in Figure 4 (a). In comparison with the microstructure of its parent material, most of the secondary and tertiary α laths within the transformed β were dissolved into β phase, due to the heat generated during the LFW process. The overall shape of the primary α grains remains equiaxed, which indicates that the heat was not able to soften the material enough for any deformation to occur.

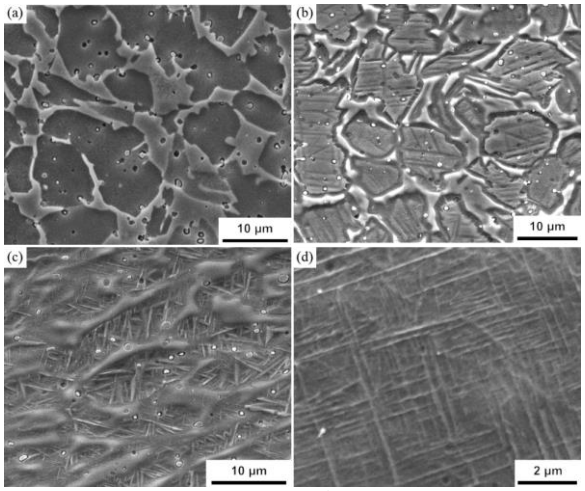

Figure 4 Secondary electron image of (a) HAZ, (b) outer TMAZ, (c) inner TMAZ, and (d) CWZ in Ti-575 in as-welded condition.

The TMAZ of Ti-575 can be divided into two regions: outer TMAZ and inner TMAZ. The microstructure of the outer TMAZ of Ti-575 in as-welded condition is shown in Figure 4 (b). Here, the majority of the primary α grains still remain equiaxed, which indicates that not much deformation occurs. Dark stripes appear within the primary α grains. The primary α grains segregate from the β phase, forming a groove about 1 μm wide.

Within inner TMAZ, as shown in Figure 4 (c), acicular laths with width of approximately 300 nm formed inside primary α grains, surrounded by the β phase. The shape of the α grains and β phase is severely deformed by the applied pressure and oscillation, due to local softening from the heat experienced. EBSD was used to confirm that those acicular laths consist of hexagonal close-packed (HCP) crystal structure, which is consistent with the α phase typically found in titanium alloys. Chemical analysis conducted by EDS demonstrated that the acicular laths possess a similar composition to the α phase measured in the Ti-575 parent material. The results from EBSD and EDS suggest that during the welding process, the primary α phase transformed into metastable β phase, which subsequently transformed back to α phase upon cooling, giving rise to the observed acicular α laths. In contrast, the pre-existing β phase remained relatively stable and was consequently retained within the microstructure.

Figure 4 (d) shows the microstructure of the as-welded CWZ in Ti-575. The intense heat generated near the weld interface significantly alters the microstructure locally. This region is dominated by fine acicular laths with width of approximately 40 nm, while no retained β phase was observed. EBSD analysis confirms that the laths in CWZ also possess HCP crystal structure. EDS analysis shows a uniform distribution of elements in CWZ, and the measured composition (86.0% Ti, 5.2% Al, 7.7% V, 0.8% Si, 0.3% Fe) is highly similar to the nominal alloy composition. All observations suggest that the temperature in CWZ exceeded β transus during welding, leading to a complete transformation into β phase. After the oscillation terminated, the high cooling rate resulted in a diffusionless martensitic phase transformation. The laths in CWZ are much thinner than those found in TMAZ, as they experienced a faster cooling rate. It is possible to form two types of martensite in the CWZ: α' with HCP structure and α'' with orthorhombic structure. Previous studies have confirmed the presence of α' martensite in Ti-64, which results in high hardness values in the CWZ [4,15]. However, research by Guo *et al.* [10] has shown that α'' martensite has lower hardness compared to the parent material. In the case of Ti-575, the superior hardness values observed in the CWZ suggest the presence of α' martensite, which will be discussed further in the subsequent section.

3.2 Hardness Characterisation

Figure 5 shows a microhardness map that covers the entire weld. As seen in comparison with Figure 3 (b), the hardness distribution is strongly correlated with the zone size measurement, as each weld zone possess distinctive hardness. Generally, the weld exhibits superior hardness compared to both parent materials, with the highest value observed at the CWZ of Ti-575 on the edges of the weld. At the bifurcation point, the CWZ is not only thinner but also softer than the edges. Although TMAZ is not as hard as CWZ, it is still harder than the parent materials. The HAZ in Ti-64 is hardly distinguishable from the parent material in terms of both microstructure and hardness, whereas the HAZ of Ti-575 is noticeably weaker than its parent.

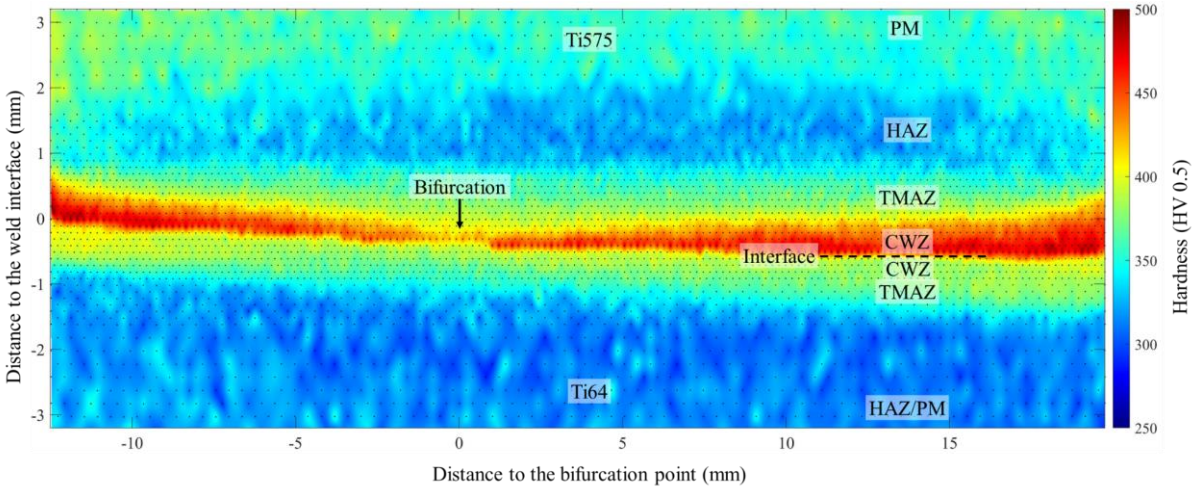

Figure 5 A microhardness mapping of a Ti-575:Ti64 linear friction weld. The little dots represent the actual locations of the indents. The values in between the indents were calculated by natural interpolation.

Figure 6 illustrates microhardness profiles at the bifurcation point and the right edge extracted from the microhardness map shown in Figure 5. The hardness values of parent materials are approximately 350 and 310 HV for Ti-575 and Ti-64, respectively. Moving toward the weld interface, a noticeable HAZ with an inferior hardness value of 320 HV was observed in Ti-575, whereas there is no significant reduction on the Ti-64 side. A previous study [16] on Ti-64:Ti6242 also reported similar hardness reduction in Ti6242 HAZ after LFW, this can be recovered by applying an appropriate post-weld heat treatment. The hardness values gradually increase in the TMAZ, reaching approximately 400 and 370 HV for Ti-575 and Ti-64, respectively, before entering CWZ. Within CWZ, the hardness continues to rise on both sides until reaching the weld interface, with a maximum value of 480 and 400 HV for Ti-575 and Ti-64, respectively. At the bifurcation point, the hardness of the weld is reduced compared to the edges. The reduction at the weld interface is significantly greater for Ti-575 (-50 HV) compared to Ti-64 (-10 HV). This reduction results in a narrower CWZ for both alloys and a hardness trough in HAZ of Ti-575, while the size of TMAZ remains approximately the same at about 1 mm for both alloys across the entire weld.

The microstructural features observed in each weld zone on the Ti-575 side can explain the corresponding hardness values. The superior hardness in CWZ is attributed to the ultra-fine martensitic α' laths formed due to rapid cooling above β transus. The width of α' laths on the Ti-575 side (~40 nm) is much thinner than the laths on the Ti-64 side (~300 nm), which leads to higher hardness in Ti-575 CWZ. Similarly, the acicular α laths in Ti-575 TMAZ also strengthen the material, nevertheless, their width (~300 nm) is similar to the α' laths in Ti-64 CWZ, resulting in comparable hardness values.

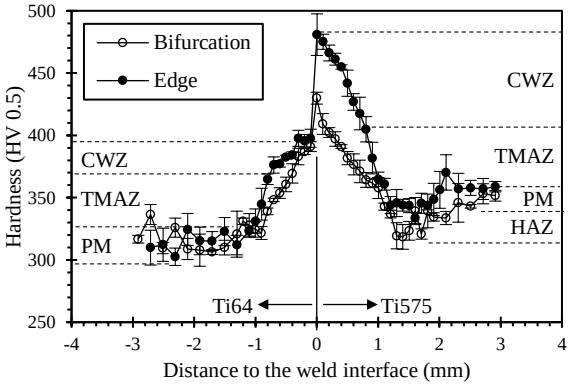

Figure 6 Microhardness profiles measured across the weld interface at the bifurcation point of the weld.

In Ti-575 parent material, as shown in Figure 1 (a), the width of the tertiary α laths is similar to the extremely fine α' laths found in Ti-575 CWZ. These tertiary α laths are thought to be the primary reason for Ti-575's higher hardness compared to Ti-64, as they are not present in Ti-64 parent material, as shown in Figure 1 (b). In Ti-575 HAZ, the heat experienced causes tertiary α laths to dissolve, resulting in a decrease in hardness to the same level as Ti-64.

3.3 *Texture Development*

The α texture measured from CWZ of Ti-575 and Ti-64 was shown in Figure 7. Both alloys exhibit similar texture which is dominated by transverse texture $\{10\bar{1}0\}\langle 11\bar{2}0\rangle_\alpha$ (T) with respect to the forge direction (FD) and oscillation direction (OD). There are several basal (B) and rolling (R/R') texture components with intermediate intensity, their misorientation angle from the transverse texture is either 60° or 90°, which is commonly seen in the misorientation profile of transformation textures. Similar textures were also found in the literature for Ti-64 CWZ [11,14,15,17].

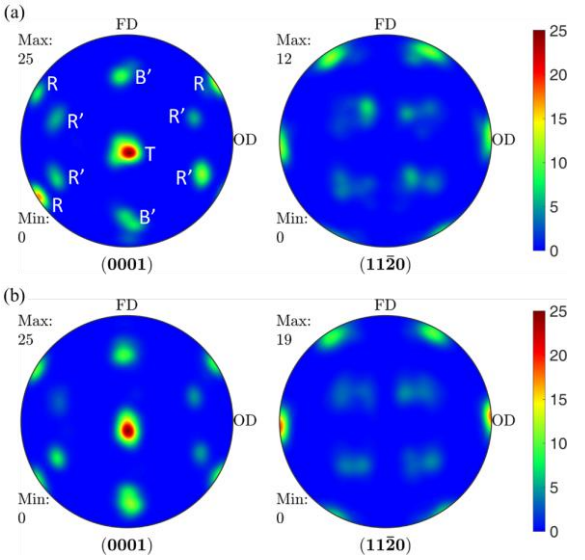

Figure 7 α texture measured in CWZ of (a) Ti-575 and (b) Ti-64. Pole figures are aligned with FD and OD.

Simulated texture by MTEX was used to demonstrate the development of observed texture, as shown in Figure 8. During welding, the deformation of β phase occurred with the bcc slip systems. Assuming $\{11\bar{2}\}\langle 111\rangle_\beta$ slip system was predominately active, this results in a β texture with a combination of $(11\bar{2})[111]_\beta$ and $(112)[\bar{1}\bar{1}1]_\beta$ texture, as shown in Figure 8 (b). Upon forging, β→α phase transformation occurred. The phase transformation follows the Burgers orientation relationship, resulting in the α texture inherited from the β texture, as shown in Figure 8 (c). The simulated α texture resembles the measured CWZ texture, despite the measured transverse component being exceptionally stronger. As the simulated texture does not take variant selection into account, therefore all 12 α variants can be equivalently formed during the phase transformation. However, upon forging only the transverse texture $\{10\bar{1}0\}\langle 11\bar{2}0\rangle_\alpha$ was preferentially selected. A possible explanation for such variant selection can be demonstrated as follow. It is known that strong transverse texture arises from unidirectional rolling at near or above β transus for α+β alloys [18]. When the temperature started decreasing for β→α phase transformation to occur in the ramp-down stage, the oscillation resembles the hot rolling action, therefore it is reasonable that LFW shares a similar variant selection mechanism with the hot-rolled titanium sheet. A similar texture development mechanism can also be found in the literature [17].

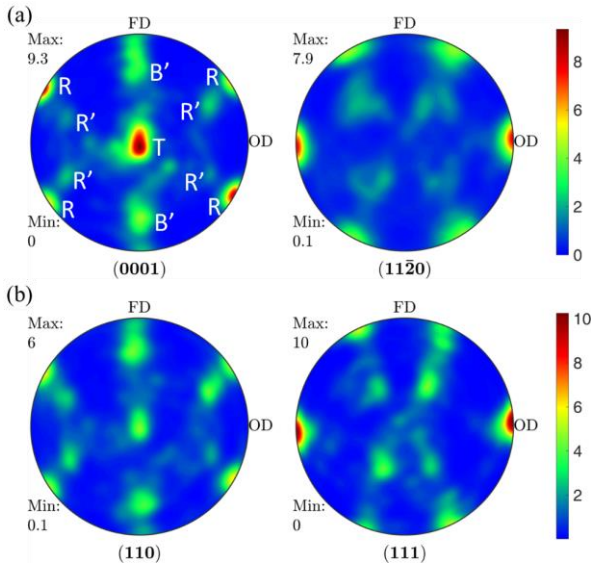

Figure 9 (a) α and (b) β texture measured in Ti-64 TMAZ at the bifurcation point. Pole figures are aligned with FD and OD.

The texture measured in CWZ is generally consistent throughout the entire weld. However, the texture in TMAZ is affected by the material flow direction. The following investigation in TMAZ is focused on the texture at the bifurcation point. Figure 9 illustrates the α and β texture measured from Ti-64 inner TMAZ at the bifurcation point. The texture here shares similar texture components with the CWZ texture, despite having lower intensity. The β texture resembles the simulated $(11\bar{2})[111]_\beta$ and $(112)[\bar{1}\bar{1}1]_\beta$ texture shown in Figure 8 (b), which indicates that the retained β in Ti-64 TMAZ was deformed and oriented to $(11\bar{2})[111]_\beta$ and $(112)[\bar{1}\bar{1}1]_\beta$ during welding. The α texture also resembles the inherited texture shown in Figure 8 (c), despite the fact that the transverse texture (T) and a pair of rolling textures (R) are notably stronger due to variant selection. It can be inferred from the inherited α texture that β→α phase transformation occurred in this region. However, since the β was only

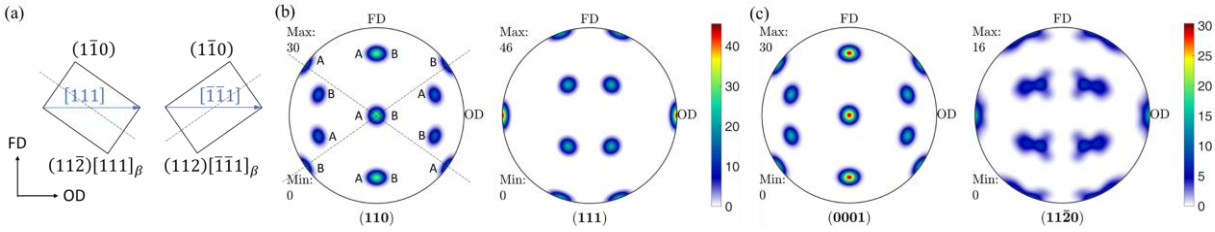

Figure 8 (a) Schematic visualisation of $(11\bar{2})[111]_\beta$ and $(112)[\bar{1}\bar{1}1]_\beta$ textures and their (b) simulated β texture. The texture components labelled as 'A' were inherited from $(11\bar{2})[111]_\beta$, while the components labelled as 'B' were inherited from $(112)[\bar{1}\bar{1}1]_\beta$. The dashed line associated with the longitudinal axis of $(1\bar{1}0)$ plane correlates to the texture components marked in Figure (b). (c) Simulated α texture inherited from the β textures following Burgers orientation relationship without variant selection.

partially transformed, plus the existence of retained primary α phase, the maximum texture intensity (9.3x) is considerably lower than the maximum texture intensity measured in CWZ (25x), where β phase was fully transformed into α phase.

On the other hand, Ti-575 inner TMAZ at the bifurcation point exhibits a completely different texture from the Ti-64 inner TMAZ, as shown in Figure 10. A basal texture (B) appears with a transverse texture (T) and rolling textures (R'), all with a similar level of intensity. Note that the coordinates of these pole figures are not aligned with forging and oscillation directions, but with X and Z directions, which are associated with the weld geometry. This indicates that the texture here is independent of the oscillation direction, but is dependent on the weld geometry. The misorientation angle from the transverse texture to the rolling and basal texture is respectively 60° and 90°, again is a sign of transformation texture. Similarly, simulated texture can be used to demonstrate texture development here. As shown in Figure 11, a $(110)[001]_{\beta}$ texture (with respect to the weld geometry) resembles the measured β texture, and the inherited α texture also resembles the measured α texture. Notice that there is no specific component with outstanding intensity in the measured texture, this implies that little or no variant selection occurred in Ti-575 TMAZ.

The dependency of the texture on the weld geometry can be attributed to the material extrusion. On both sides of the bifurcation point, the material was extruded along the ±X direction toward the edges, whereas at the bifurcation point, the material is restricted to flow along ±Z direction toward the weld interface. Furthermore, it is known that upon flowing the longitudinal axis of $(1\bar{1}0)$ plane as illustrated in Figure 11 (a) tends to align with the flowing direction [17]. Consequently, the longitudinal axis of $(1\bar{1}0)$ plane is aligned with the Z direction, resulting in strong basal texture. Such basal texture can also be found in Ti-64 inner TMAZ in Figure 9, although its intensity is weak but is still distinguishable, unlike the texture measured in CWZ (Figure 7), no basal texture is found at all. This suggests that the same texture development mechanism for Ti-575 inner TMAZ may also be applicable for Ti-64, despite the influence of the CWZ texture being much stronger in Ti-64 inner TMAZ.

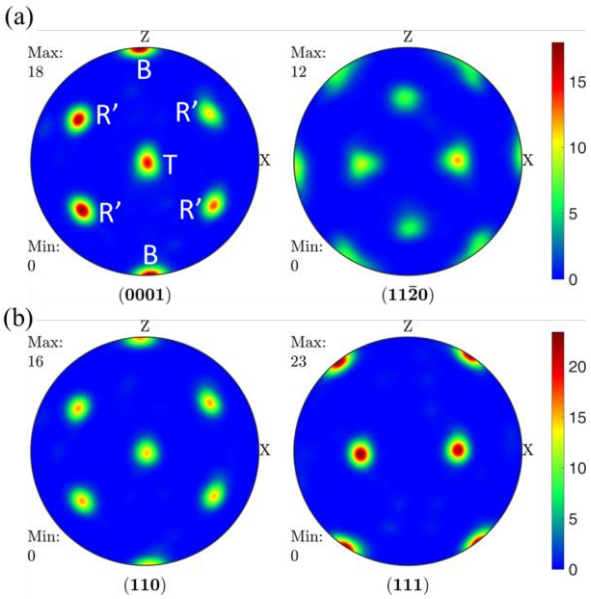

Figure 10 (a) α and (b) β texture measured in Ti-575 TMAZ at the bifurcation point. Pole figures are aligned with X and Z directions.

4 Conclusions

The microstructure, microhardness, and texture of a dissimilar Ti-64 and Ti-575 linear friction weld have been characterised. The major findings from the current study are listed as follows.

(1) The weld zone is found to have superior hardness to both parent materials. The maximum hardness is found at the weld interface on the Ti-575 side with a value of 500 HV due to the formation of exceptionally fine martensitic α' laths. However, a hardness trough was found at Ti-575 HAZ due to the dissolution of fine tertiary α laths. Potentially this can be recovered by applying appropriate post-weld heat treatment.

(2) The zone size and microhardness distribution were investigated. At the bifurcation point, the CWZ is thinner and the HAZ is larger compared to the edges. The overall hardness of the weld at the bifurcation point is lower than on the edges.

(3) The texture of the weld was investigated. In the CWZ of both Ti-64 and Ti-575, a strong transverse α texture was found. Such texture is dependent on the

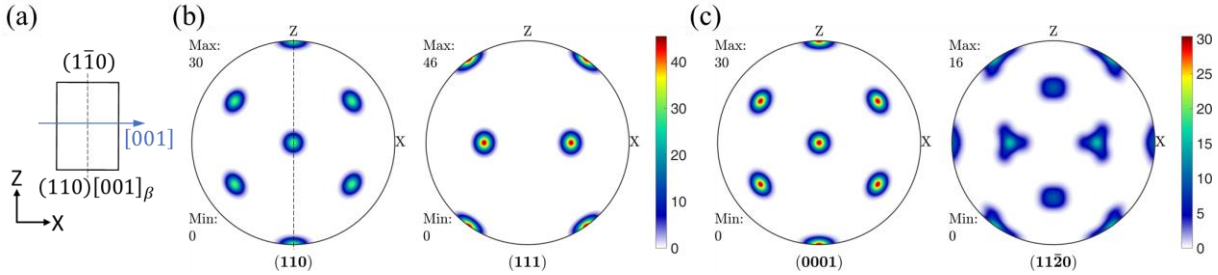

Figure 11 (a) Schematic visualisation of $(110)[001]_{\beta}$ texture and its (b) simulated β texture. The dashed line associated with the longitudinal axis of $(1\bar{1}0)$ plane correlates to the texture components marked in Figure (b). (c) Simulated α texture inherited from the β texture following the Burgers orientation relationship without variant selection.

oscillation direction. It is considered derived from the $\{112\}\langle 111\rangle_{\beta}$ texture with variant selection.

(4) In the inner TMAZ, Ti-64 exhibit a similar texture as the CWZ texture with weaker intensity, while Ti-575 exhibit a unique texture that is not dependent on the oscillation direction, but on the weld geometry. It is considered derived from the $\{110\}\langle 001\rangle_{\beta}$ texture with no variant selection occurring.

Acknowledgements

This work has been financially supported by a doctoral studentship from EPSRC, the University of Birmingham and Rolls-Royce plc.

References

[1] Rolls-Royce, The Jet Engine, Fifth edit, The Technical Publications Department, Rolls-Royce plc, 1996.

[2] P.Geng, G.Qin, H.Ma, J.Zhou, C.Zhang, N.Ma, J. Mater. Process. Technol. 296 (2021) 117198.

[3] A.Vairis, M.Frost, Wear 648 (1998) 117–131.

[4] P.Wanjara, M.Jahazi, Metall. Mater. Trans. A 36 (2005).

[5] W.Y.Li, T.Ma, Y.Zhang, Q.Xu, J.Li, S.Yang, H.Liao, Adv. Eng. Mater. 10 (2008) 89–92.

[6] W.Li, A.Vairis, M.Preuss, T.Ma, Int. Mater. Rev. 61 (2016) 71–100.

[7] A.R.McAndrew, P.A.Colegrove, C.Bühr, B.C.D.Flipo, A.Vairis, Prog. Mater. Sci. 92 (2018) 225–257.

[8] R.Turner, R.M.Ward, R.March, R.C.Reed, Metall. Mater. Trans. B Process Metall. Mater. Process. Sci. 43 (2012) 186–197.

[9] J.Romero, M.M.Attallah, M.Preuss, M.Karadge, S.E.Bray, Acta Mater. 57 (2009) 5582–5592.

[10] Y.Guo, T.Jung, Y.L.Chiu, H.Li, S.Bray, P.Bowen, Mater. Sci. Eng. A 562 (2013) 17–24.

[11] Y.Guo, Y.Chiu, M.M.Attallah, H.Li, S.Bray, P.Bowen, J. Mater. Eng. Perform. 21 (2012) 770–776.

[12] M.Bodie, M.Thomas, A.Ayub, in: 14th World Conf. Titan., 2020, p. 12019.

[13] M.Thomas, J.Hewitt, M.Bache, R.Thomas, P.Garratt, Y.Kosaka, in: Proc. 13th World Conf. Titan., 2016, pp. 1537–1541.

[14] Y.Guo, Y.Chiu, H.Li, M.M.Attallah, S.Bray, P.Bowen, Ti 2011 - Proc. 12th World Conf. Titan. 3 (2011) 1995–1999.

[15] Y.Guo, Microstructure and Texture Characterization of Linear Friction Welding of Ti-6Al-4V and Ti-6Al-2Sn-4Zr-6Mo, University of Birmingham, 2012.

[16] S.Rajan, P.Wanjara, J.Gholipour, A.S.Kabir, Materials (Basel). 13 (2020) 1–25.

[17] M.Karadge, M.Preuss, C.Lovell, P.J.Withers, S.Bray, Mater. Sci. Eng. A 459 (2007) 182–191.

[18] G.Lütjering, Mater. Sci. Eng. A 243 (1998) 32–45.

B Orientation Matrices

B.1 Miller Indices

Notice that in Miller indices, (hkl) and $[uvw]$ is always aligned with the specimen coordinate system but expressed with respect to the crystal coordinate system. One can find the crystallographic direction $[rst]$ which is parallel to the specimen transverse direction by

$$[rst] = (hkl) \times [uvw] \tag{B.1}$$

As $[uvw]//x$, $[rst]//y$, and $[hkl]//z$, the Miller indices can be treated as the position of the specimen coordinate system with respect to the crystal coordinate system. This is equivalent to the application of a passive rotation $\mathbf{R}_p$ on the specimen coordinates to crystal coordinates. According to Equation (2.6), we have

$$\begin{bmatrix} u' & r' & h' \\ v' & s' & k' \\ w' & t' & l' \end{bmatrix} = \mathbf{R}_p \begin{bmatrix} 1 & 0 & 0 \\ 0 & 1 & 0 \\ 0 & 0 & 1 \end{bmatrix} \tag{B.2}$$

where $[u'v'w']$, $[r's't']$, and $[h'k'l']$ are $[uvw]$, $[rst]$, and $[hkl]$ respectively normalised to unity. Moreover, since this passive rotation $\mathbf{R}_p$ is equivalent to the definition of orientation, g can be expressed in terms of Miller indices as

$$g = \begin{bmatrix} u' & r' & h' \\ v' & s' & k' \\ w' & t' & l' \end{bmatrix} \tag{B.3}$$

B.2 Euler Angles

Unlike extrinsic rotations, intrinsic rotations are slightly more difficult to analysis since they cannot be directly decomposed by elemental rotations about the specimen coordinate system using Equation (2.8). Nevertheless, it is proven that any given type of intrinsic rotation can

be translated into an equivalent extrinsic rotation. Take intrinsic z-y'-x'' rotation as an example, its general rotation matrix $\mathbf{R}$ can be expressed by

$$\mathbf{R} = \mathbf{R}_{z''}\ \mathbf{R}_{y'}\ \mathbf{R}_{z} \tag{B.4}$$

where $\mathbf{R}_{y'}$ is the intrinsic rotation matrix about the rotated y'-axis after $\mathbf{R}_z$, and $\mathbf{R}_{z''}$ is the intrinsic rotation matrix about the rotated z''-axis after $\mathbf{R}_{y'}$.

Notice that the intrinsic rotation $\mathbf{R}_{y'}$ about the y'-axis can be achieved solely by extrinsic rotations. Specifically, first rotate the y'-axis to align it with the y-axis by applying $\mathbf{R}_z^{-1}$ (as if to 'cancel' the effect of first rotation about the z-axis), then use the elemental rotation $\mathbf{R}_{\mathrm{y}}$ about the y-axis by the same angle to achieve the same effect as $\mathbf{R}_{y'}$ as if $\mathbf{R}_z$ was applied. Finally, reverse rotate the y-axis back to y'-axis by applying $\mathbf{R}_z$ to undo the application of $\mathbf{R}_z^{-1}$ in the first step. The whole process is equivalent to the intrinsic rotation $\mathbf{R}_{y'}$, except only using the elemental rotations. Mathematically, this process can be described as

$$\mathbf{R}_{y'} = \mathbf{R}_z\ \mathbf{R}_y\ \mathbf{R}_z^{-1} \tag{B.5}$$

Following the same logic, we can derive $\mathbf{R}_{x''}$ as

$$\mathbf{R}_{x''} = \mathbf{R}_{y'}\ \mathbf{R}_z\ \mathbf{R}_x\ \mathbf{R}_z^{-1}\ \mathbf{R}_{y'}^{-1} \tag{B.6}$$

Therefore we have

$$\begin{aligned}
\mathbf{R} &= \mathbf{R}_{x''}\ \mathbf{R}_{y'}\ \mathbf{R}_z \\
&= \mathbf{R}_{y'}\ \mathbf{R}_z\ \mathbf{R}_x\ \mathbf{R}_z^{-1}\ \mathbf{R}_{y'}^{-1}\ \mathbf{R}_y\ \mathbf{R}_z^{-1} \\
&= \mathbf{R}_{y'}\ \mathbf{R}_z\ \mathbf{R}_x \\
&= \mathbf{R}_z\ \mathbf{R}_y\ \mathbf{R}_z^{-1}\ \mathbf{R}_z\ \mathbf{R}_x \\
&= \mathbf{R}_z\ \mathbf{R}_y\ \mathbf{R}_x
\end{aligned} \tag{B.7}$$

which is equivalent to extrinsic X-Y-Z rotation and completes the proof.

As a result, the intrinsic z_1-x'-z_2'' rotation is equivalent to extrinsic Z_2-X-Z_1 rotation with respective angles φ_2, Φ, and φ_1. Its general rotation matrix can be expressed as

$$\mathbf{R} = \mathbf{R}_z(\varphi_1)\ \mathbf{R}_x(\Phi)\ \mathbf{R}_z(\varphi_2) \tag{B.8}$$

Together with Equation (2.10), (2.11), and (B.8), the orientation g can be expressed as

$$g = \mathbf{R}_z(\varphi_2)\ \mathbf{R}_x(\Phi)\ \mathbf{R}_z(\varphi_1) \tag{B.9}$$

B.3 Angle/Axis of Rotation

Since the application of rotation $\mathbf{R}$ does not alter the axis of rotation $\vec{\mathbf{v}}$, it can be seen as the invariant of rotation. Specifically, the axis of rotation is equivalent to the eigenvector of the rotation matrix. Mathematically, this property can be shown by

$$\begin{gathered} \mathbf{R}\ \vec{\mathbf{v}} = \vec{\mathbf{v}} \\ (\mathbf{R} - \mathbf{I})\ \vec{\mathbf{v}} = 0, \text{ where } \|\vec{\mathbf{v}}\| \neq 0 \end{gathered} \tag{B.10}$$

By solving the eigenvector, for rotation matrices described by Equation (B.3), the axis of rotation can be expressed as

$$\vec{\mathbf{v}} = \begin{bmatrix} t' - k' \\ h' - w' \\ v' - r' \end{bmatrix} \tag{B.11}$$

The angle of rotation θ is simply the angle between $\vec{\mathbf{v}}$ and $\mathbf{R}\ \vec{\mathbf{v}}$. It is also related to the magnitude of $\vec{\mathbf{v}}$, specifically,

$$\theta = \sin^{-1}\left(\frac{\|\vec{\mathbf{v}}\|}{2}\right) \tag{B.12}$$

C Programming Scripts

C.1 β Reconstruction Script

```
%% Specify Crystal and Specimen Symmetries

% crystal symmetry
CS = {'notIndexed',...
  crystalSymmetry('m-3m', [3.2 3.2 3.2], 'mineral', 'bcc', 'color', [0.53 0.81 0.98]),...
  crystalSymmetry('6/mmm', [3 3 4.7], 'X||a*', 'Y||b', 'Z||c*', 'mineral', 'hcp',
'color', [0.56 0.74 0.56])};

% plotting convention
setMTEXpref('xAxisDirection','east');
setMTEXpref('zAxisDirection','outOfPlane');

%% Specify File Names

% path to files
pname = 'path\to\file';

% which files to be imported
fname = [pname '\filename.cpr'];

%% Import the Data

% create an EBSD variable containing the data
ebsd = EBSD.load(fname,CS,'interface','crc');

%% beta reconstruction
beta2alpha = orientation.Burgers(ebsd('bcc').CS,ebsd('hcp').CS);
[grains,ebsd.grainId] = calcGrains(ebsd('indexed'),'threshold',1.5*degree);
job = parentGrainReconstructor(ebsd, grains);
job.p2c = beta2alpha;
job.calcGraph('threshold',1.5*degree)
job.calcVariants('threshold',1.5*degree)
job.clusterGraph('numIter',3)
job.plotGraph
job.calcParentFromGraph

ipfKey = ipfColorKey(ebsd('bcc'));
ipfKey.inversePoleFigureDirection = vector3d.Z;
job.mergeSimilar('threshold',5*degree)
job.mergeInclusions('maxSize',100)
color = ipfKey.orientation2color(job.parentGrains.meanOrientation);
plot(job.parentGrains,color)

hold on
isBig = job.parentGrains.grainSize > 1000;
shape = crystalShape.cube(ebsd('bcc').CS);
plot(job.parentGrains(isBig),0.5*shape)
```

C.2 TEM Diffraction Pattern Analysis Script

```
%% Index TEM diffraction patterns while performing tilt experiment.
analyser = Analyser;

analyser.angle_tol = 0.05; % angular tolerance (5%)
analyser.d_tol = 0.05; % d-spacing tolarance (5%)
analyser.tilt_tol = 0.1; % tilt tolerance (10%)

% tilt angles (degree)
analyser.tilts = [
% X     Y
  -3.45 19.41  % pattern 1
  11.62 -12.92 % pattern 2
  12.43 14.13  % pattern 3
  ];

% measured d-spacings (1/nm)
analyser.inv_ds = [
% spot: A     B     C     D
        5.671 7.331 4.381 6.997 % pattern 1
        3.864 4.407 2.093 4.382 % pattern 2
        7.309 7.324 3.837 9.092 % pattern 3
        ];

% measured angles between each pair of spots (degree)
analyser.angles = [
% AB    BC    CD    DA
  36.65 50.60 54.05 38.71 % pattern 1
  28.36 61.26 61.85 28.53 % pattern 2
  30.40 74.59 50.95 24.06 % pattern 3
  ];

% consider all possible crystal structures
analyser.candidates = [HcpTi BccTi];

results = analyser.Analyse();
results = Analyser.PostProcessing(results);
disp('==========analysis completed==========');
```

C.2.1. Class: Analyser

```
classdef Analyser
  properties
    d_tol
    angle_tol
    tilt_tol
    tilts
    inv_ds
    angles
    candidates
  end

  methods
    function obj = Analyser()

    end

    function obj = set.candidates(obj, candidates)
      assert(isa(candidates, 'CrystalStructure'))
      obj.candidates = candidates;
    end

    function results = Analyse(this)
      results = [];
      for i = 1:length(this.candidates)
        crystal = this.candidates(i);
        crystalName = string(class(crystal));
        disp("!!!!!!!!!!!! Analysing" + crystalName + " !!!!!!!!!!!!")
        result = this.AnalyseCrystal(crystal);
        if ~isempty(result)
          result{:,'crystal'} = repmat(crystalName,height(result),1);
          results = [results; result];
        end
      end

      if isempty(results)
        disp('==============No solution for all cyrstal structures==================')
        return
      end
    end
  end

  methods (Access = private)
    function result = AnalyseCrystal(this, crystal)
      tilts = this.tilts;
      inv_ds = this.inv_ds;
      angles = this.angles;

      for i = 1:size(tilts,1)
        fprintf('==========analysing a%.1f b%.1f==========\n',tilts(i,:));
        za{i} = this.getZoneAxisAll(crystal, inv_ds(i,:), angles(i,:));
      end

      %%
      solutions = [];
```

```
      recur(1,[]);

      if isempty(solutions)
        result = [];
        fprintf('==========No solution found==========\n');
        return
      end

      %% calculate error
      fprintf('Calculating error...\n');
      for i = 1:size(solutions,2)
        for j = 1:length(solutions(:,i))
          error_d = 0;
          for k = 1:length(inv_ds(i,:))
            error_d = max([error_d, abs(1/crystal.getD(solutions(j,i).("plane" +
char(k+64))) - inv_ds(i,k)) / inv_ds(i,k)]);
          end
          solutions(j,i).error_d = error_d;

          error_ang = 0;
          for k = 1:length(angles(i,:))-1
            error_ang = max([error_ang, abs(crystal.getPlaneAngle(solutions(j,i).("plane"
+ char(k+64)), solutions(j,i).("plane" + char(k+1+64))) - angles(i,k)) / angles(i,k)]);
          end
          solutions(j,i).error_ang = error_ang;
        end
      end

      %% remove duplicates
      fprintf('Removing duplicates...\n');
      for i = 1:size(solutions,1)
        for j = size(solutions,1):-1:i+1
          if isDuplicate(solutions(i,:), solutions(j,:))
            solutions(j,:) = [];
          end
        end
      end

      %% prepare result table
      fprintf('Preparing result table...\n');
      result = [];
      for i = 1:size(solutions,2)
        t = struct2table(solutions(:,i));
        t{:,'error_ang'} = round(t{:,'error_ang'},4);
        t{:,'error_d'} = round(t{:,'error_d'},4);
        t.Properties.VariableNames = cellfun(@(c) "fig" + i + "_" +
string(c),t.Properties.VariableNames);
        result = [result t];
      end
      result = unique(result);
      result(:,contains(result.Properties.VariableNames,'planeC') |...
        contains(result.Properties.VariableNames,'planeD')) = [];

      %% calculate tilt error
      fprintf('Calculating tilt error...\n');
      for i = 1:size(tilts,1)
```

```
        for j = i+1:size(tilts,1)
          tiltError = [];
          tiltAngle = Analyser.TotalTiltAngle(tilts(i,:),tilts(j,:));
          for k = 1:height(result)
            tiltError(k,:) =
abs(crystal.getVectorAngle(result{k,"fig"+i+"_ZoneAxis"},result{k,"fig"+j+"_ZoneAxis"}) -
tiltAngle) / tiltAngle;
          end
          result{:,"error_tilt"+i+j} = tiltError;
        end
      end

      %% get forbidden reflections
      fprintf('Getting forbidden reflections...\n');
      forbiddenPlanes = cell(height(result), 1);
      for i = 1:height(result)
        columns = result.Properties.VariableNames(~cellfun(@isempty,
strfind(result.Properties.VariableNames,'plane')));
        k = 1;
        for j = 1:length(columns)
          column = columns{j};
          if abs(crystal.getStructureFactor(result{i, column})) < 1e-5
            forbiddenPlanes{i} = [forbiddenPlanes{i} result{i, column}];
            k = k + 1;
          end
        end
      end
      if ~isempty(forbiddenPlanes)
        result{:,'forbidden'} = forbiddenPlanes;
      end

      fprintf('==========analysis completed==========\n');

      %% inner functions
      function recur(depth, ZAs)
        d = depth - 1;
        if d >= 2
          for idx = 1:d-1
            if ~this.checkAngle(Analyser.TotalTiltAngle(tilts(idx,:), tilts(d,:)),
crystal.getVectorAngle(ZAs(idx).ZoneAxis,ZAs(d).ZoneAxis), this.tilt_tol)
              return
            end
          end
        end
        if d == length(za)
          solutions = [solutions; ZAs];
        else
          for idx = 1:length(za{depth})
            recur(depth + 1, [ZAs za{depth}(idx)]);
          end
        end
      end

      function bool = isDuplicate(solution1, solution2)
        bool = false;
        for idx = size(solution1,2)
```

```
      if solution1(idx).error_d ~= solution2(idx).error_d || ...
          solution1(idx).error_ang ~= solution2(idx).error_ang || ...
          ~isSameFamily(solution1(idx).ZoneAxis, solution2(idx).ZoneAxis)
        return
      end
    end
    bool = true;
  end

  function bool = isSameFamily(za1, za2)
    family = crystal.getVectorFamily(za1);
    bool = ismember(za2, family, 'rows');
  end
end

function zaAll = getZoneAxisAll(this, crystal, inv_ds, angles)
  hkld = crystal.getAllFamilies();

  zaAll = [];
  headers = {};
  getZoneAxisAll_inner();

  function getZoneAxisAll_inner()
    for i = 1:2
      error = abs(1./hkld(:,4) - inv_ds(i)) / inv_ds(i);
      [error, order] = sort(error,'ascend');
      hkl = hkld(order,1:3);
      hkl(error > this.d_tol,:) = [];
      headers{i} = hkl;
    end

    for i = 1:size(headers{1},1)
      for j = 1:size(headers{2},1)
        planesA = crystal.getFamily(headers{1}(i,:));
        planesB = crystal.getFamily(headers{2}(j,:));
        za = getZoneAxis(planesA,planesB);
        if isempty(za)
          continue
        end

        zaAll = [zaAll za];
      end
    end
  end

  function results = getZoneAxis(planesA,planesB)
    results = [];
    id = 1;
    for i = 1:size(planesA,1)
      for j = 1:size(planesB,1)
        planes(1,:) = planesA(i,:);
        planes(2,:) = planesB(j,:);
        planes(3,:) = planes(2,:) - planes(1,:);
        planes(4,:) = planes(3,:) - planes(1,:);
        ZA = cross(planes(1,:), planes(2,:));
```

```
            if ~checkPlanes(planes, ZA)
              continue
            end

            for k = 1:size(planes,1)
              results(id).("plane" + char(k+64)) = planes(k,:);
            end
            ZA = ZA / gcd(ZA(1),gcd(ZA(2),ZA(3)));
            results(id).ZoneAxis = ZA;
            id = id + 1;
            fprintf('zone axis added: [%d%d%d]\n', ZA);
          end
        end
      end

      function bool = checkPlanes(planes, ZA)
        bool = false;
        if all(ZA == 0)
          return
        end

        for i = 1:length(angles)
          if ~this.checkD(inv_ds(i), 1/crystal.getD(planes(i,:)))
            return
          end

          if dot(ZA,planes(i,:)) ~= 0
            return
          end

          for j = i+1:length(angles)
            if ~this.checkAngle(sum(angles(i:j-1)), crystal.getPlaneAngle(planes(i,:),
planes(j,:)))
              return
            end
          end
        end
        bool = true;
      end
    end

    function bool = checkD(this, actual, expected)
      d_tol = this.d_tol;
      bool = abs(actual - expected) / actual < d_tol;
    end

    function bool = checkAngle(this, actual, expected, tol)
      if nargin < 4
        tol = this.angle_tol;
      end
      if actual < 1e-2
        bool = abs(actual - expected) < tol;
      else
        bool = abs(actual - expected) / actual < tol;
      end
    end
```

```
  end

  methods (Static)
    function angle = TotalTiltAngle(tilt1, tilt2)
      Rx = @(theta) [1 0 0;...
        0 cosd(theta) -sind(theta);...
        0 sind(theta) cosd(theta)];
      Ry = @(theta) [cosd(theta) 0 sind(theta);...
        0 1 0;...
        -sind(theta) 0 cosd(theta)];

      vA = [0 0 1]';
      vB = Rx(tilt1(1))*Ry(tilt1(2))*vA;
      vC = Rx(tilt2(1))*Ry(tilt2(2))*vA;
      angle = acos(dot(vB,vC)/norm(vB)/norm(vC))*360/2/pi;
    end

    function planes = getPlanePermutations(n)
      planes = [];
      for h = n:-1:-n
        for k = n:-1:-n
          for l = n:-1:-n
            if ~any([h k l])
              continue
            end
            planes(end+1,:) = [h k l];
          end
        end
      end
    end

    function results = PostProcessing(results)
      if isempty(results)
        return
      end
      %% sort result
      error_columns = results.Properties.VariableNames(~cellfun(@isempty,
strfind(results.Properties.VariableNames,'error')));
      helper = sum(results{:,error_columns},2);
      [~,order] = sort(helper, 'ascend');
      results = results(order,:);

      %% swap colums
      crystalCol = find(~cellfun(@isempty,
strfind(results.Properties.VariableNames,'crystal')));
      forbiddenCol = find(~cellfun(@isempty,
strfind(results.Properties.VariableNames,'forbidden')));
      results = movevars(results, forbiddenCol, 'After', crystalCol);

      %% excel output
      if exist('output.xlsx','file')
        delete('output.xlsx')
      end
      writetable(results, 'output.xlsx');
      disp('All results have been saved to output.xlsx');
    end
```

```
  end
end
```

C.2.2. Class: HcpTi

```
classdef HcpTi < CrystalStructure

  properties
    a = 0.295;
    c = 0.4686;
  end

  methods
    function obj = HcpTi(a,c)
      if nargin >= 1
        obj.a = a;
      end
      if nargin >= 2
        obj.c = c;
      end
    end

    function sf = getStructureFactor(this, planes)
      for planeID = 1:size(planes,1)
        plane = planes(planeID, 1:3);
        sf(planeID,:) = exp(2*pi*1i*dot(plane,[0 0 0])) + ...
          exp(2*pi*1i*dot(plane,[1/3 2/3 1/2]));
      end
    end

    function d = getD(this, hkl)
      a = this.a;
      c = this.c;
      h = hkl(:,1);
      k = hkl(:,2);
      l = hkl(:,3);
      d = sqrt(1./(4./3.*(h.^2+h.*k+k.^2)./a.^2+(l./c).^2));
    end

    function family = getFamily(~, hkl)
      h = hkl(1);
      k = hkl(2);
      l = hkl(3);
      i = -(h+k);
      family = [];
      for l = [-l l]
        putSet(h,k,l);
        putSet(i,k,l);
        putSet(i,h,l);
      end
      family = unique(family,'rows');

      function putSet(h,k,l)
        family(end+1,:) = [h k l];
        family(end+1,:) = [k h l];
```

```
    family(end+1,:) = [-h -k l];
    family(end+1,:) = [-k -h l];
  end
end

function UVTW = getMillerBravaisVector(~, uvw)
  for i = 1:size(uvw)
    u = uvw(i,1);
    v = uvw(i,2);
    w = uvw(i,3);
    U = (2*u-v);
    V = (2*v-u);
    T = -(U+V);
    W = 3*w;
    gcdNum = gcd(U,gcd(V,gcd(T,W)));
    UVTW(i,:) = [U V T W] / gcdNum;
  end
end

function uvw = getMillerVector(~, UVTW)
  for i = 1:size(UVTW)
    U = UVTW(i,1);
    V = UVTW(i,2);
    W = UVTW(i,4);
    u = 2*U + V;
    v = 2*V + U;
    w = W;
    gcdNum = gcd(u,gcd(v,w));
    uvw(i,:) = [u v w] / gcdNum;
  end
end

function angle = getPlaneAngle(this, planeA, planeB)
  a = this.a;
  c = this.c;
  h1 = planeA(1);
  k1 = planeA(2);
  l1 = planeA(3);
  h2 = planeB(1);
  k2 = planeB(2);
  l2 = planeB(3);
  rad = acos((h1*h2+k1*k2+1/2*(h1*k2+h2*k1)+3*a^2/4/c^2*l1*l2) ...
    / sqrt((h1^2+k1^2+h1*k1+3*a^2/4/c^2*l1^2)*(h2^2+k2^2+h2*k2+3*a^2/4/c^2*l2^2)) );
  angle = rad*360/2/pi;
end

function angle = getVectorAngle(this, VectorA, VectorB)
  a = this.a;
  c = this.c;
  u1 = VectorA(1);
  v1 = VectorA(2);
  w1 = VectorA(3);
  u2 = VectorB(1);
  v2 = VectorB(2);
  w2 = VectorB(3);
  rad = acos( (a^2*(u1*u2 + v1*v2 - 1/2*(u1*v2+v1*u2)) + c^2*w1*w2) ...
```

```
        / (sqrt(a^2*(u1^2 - u1*v1 + v1^2) + c^2*w1^2) * sqrt(a^2*(u2^2 - u2*v2 + v2^2) +
c^2*w2^2)) );
      angle = rad * 360/2/pi;
    end

    function family = getVectorFamily(this, uvw)
      UVTW = this.getMillerBravaisVector(uvw);
      hkl = UVTW([1 2 4]);
      planes = this.getFamily(hkl);
      planes = [planes(:,1:2) -sum(planes(:,1:2),2) planes(:,3)];
      family = this.getMillerVector(planes);
    end

  end
end
```

C.2.3. Class: BccTi

```
classdef BccTi < CrystalStructure

  properties
    a = 0.331;
  end

  methods
    function obj = BccTi(a)
      if nargin >= 1
        obj.a = a;
      end
    end

    function sf = getStructureFactor(this,planes)
      sf = 1 + (-1).^(planes(:,1) + planes(:,2) + planes(:,3));
    end

    function d = getD(this,hkl)
      a = this.a;
      h = hkl(:,1);
      k = hkl(:,2);
      l = hkl(:,3);
      d = sqrt(a.^2./(h.^2+k.^2+l.^2));
    end

    function family = getFamily(~,hkl)
      family = [];
      permutation([], hkl)
      family = unique(family,'rows');

      function permutation(array, topick)
        if isempty(topick)
          negative_permutation(array);
        end
        for i = 1:length(topick)
          permutation([array topick(i)], topick([1:i-1 i+1:end]));
        end
```

```
      end

      function negative_permutation(array)
        for i = [-1 1]
          for j = [-1 1]
            for k = [-1 1]
              family(end+1,:) = array .* [i j k];
            end
          end
        end
      end
    end

    function angle = getPlaneAngle(~,planeA,planeB)
      h1 = planeA(:,1);
      k1 = planeA(:,2);
      l1 = planeA(:,3);
      h2 = planeB(:,1);
      k2 = planeB(:,2);
      l2 = planeB(:,3);
      rad = acos((h1.*h2+k1.*k2+l1.*l2) ...
        ./ sqrt((h1.^2+k1.^2+l1.^2).*(h2.^2+k2.^2+l2.^2)) );
      angle = rad*360/2/pi;
    end

    function angle = getVectorAngle(~,VectorA,VectorB)
      u1 = VectorA(1);
      v1 = VectorA(2);
      w1 = VectorA(3);
      u2 = VectorB(1);
      v2 = VectorB(2);
      w2 = VectorB(3);
      rad = acos((u1*u2+v1*v2+w1*w2) ...
        / sqrt((u1^2+v1^2+w1^2)*(u2^2+v2^2+w2^2)) );
      angle = rad * 360/2/pi;
    end

    function family = getVectorFamily(this,uvw)
      family = this.getFamily(uvw);
    end

  end
end
```

C.2.4. Class: CrystalStructure

```
classdef (Abstract) CrystalStructure < matlab.mixin.Heterogeneous
  methods (Abstract)
    d = getD(this, hkl);
    family = getFamily(this, hkl);
    angle = getPlaneAngle(this, planeA,planeB);
    sf = getStructureFactor(this, planes);
    angle = getVectorAngle(this, VectorA,VectorB);
    family = getVectorFamily(this, uvw);
  end
```

```
  methods
    function hkld = getAllFamilies(this)
      planes = Analyser.getPlanePermutations(6);

      planes = this.reduceByFamily(planes);

      d = this.getD(planes);

      idx = d < 0.07; %0.7A = 0.07nm
      d(idx) = [];
      planes(idx,:) = [];

      [d,order] = sort(d, 'descend');
      hkld = [planes(order,:) d];
    end

    function hkld = getSelectedFamilies(this)
      hkld = this.getAllFamilies();

      sf = this.getStructureFactor(hkld(:,1:3));
      hkld(abs(sf) < 1e-5,:) = [];
    end

    function planes = reduceByFamily(this,planes)
      i = 1;
      while i <= size(planes,1)
        plane = planes(i,:);
        family = this.getFamily(plane);
        family(ismember(family,plane,'rows'),:) = [];
        planes(ismember(planes,family,'rows'),:) = [];
        i = i + 1;
      end
    end
  end
end
```

C.3 Hardness Indent Measurement Script

```
%% Determine the locations and sizes of the indents from an optical image.

%% INPUT
force = 0.5; % the force (kg) used in indentation
angle = 136; % the angle (degree) of indenter
pixel2um = 100/239; % the ratio of image pixel to the actual length in micron (um), e.g.
100 um = 239 pixels
threshold = 130; % the color threshold to identify the indents
areaMin = 4500; % the minimum indent size in pixel^2
correction = 5; % fitting with corrected data
origin_y = 3.2; % the Y location of the reference indent
origin_x = 0; % the X location of the reference indent

filepath = '\path\to\your\image.png';

%% image preprocessing
image = imread(filepath);

image_gray = rgb2gray(image);
image_binary = image_gray < threshold;
image_binary = imclearborder(image_binary); % remove border
image_binary = bwareaopen(image_binary, areaMin); % remove small noises
image_binary = imclose(image_binary,strel('diamond',5)); % close gaps inside indents
image_binary = imfill(image_binary, 'holes'); % fill holes inside indents
image_binary = imopen(image_binary,strel('diamond',15)); % remove large noises (dusts,
black dots)
figure
imshow(image_binary);

indents = regionprops(image_binary);

%% get locations and hardness
locations = vertcat(indents.Centroid);
boxes = vertcat(indents.BoundingBox);
diagonals = boxes(:,3:4);

locations_um = locations * pixel2um;
diagonals_um = (diagonals + correction) * pixel2um;

[locations_um, order] = sortrows(locations_um,[2 1],'descend'); % must be sorted for
mapping locations and aligning peaks
diagonals_um = diagonals_um(order,:);

d = locations_um(:,1).^2 + locations_um(:,2).^2; % distance to origin (top left corner)
[~,index] = min(d);
origin_um = locations_um(index,:); % get the top left indent

y = origin_y - (locations_um(:,2) - origin_um(2)) / 1000;
x = origin_x + (locations_um(:,1) - origin_um(1)) / 1000;
hardness = 2 * force * sind(angle/2) ./ ((mean(diagonals_um,2)/1000).^2); %HV

save('output.mat', 'x','y','hardness');
```

C.4 Hardness Mapping Script

```
%% Plot hardness distribution as a contour map.

%% INPUT
load('output.mat'); % load the output from indent measurement

%% Gridify data
xmin = min(x);
xmax = max(x);
ymin = min(y);
ymax = max(y);
[grid.x,grid.y] = meshgrid(xmin:0.02:xmax,ymin:0.02:ymax);
grid.hardness = griddata(x, y, hardness, grid.x, grid.y, 'natural');

%% Plot contour
[~,h] = contourf(gird.x, grid.y, grid.hardness, 100,'LineColor','none');
axis image
hold on
scatter(x, y, 1.5,'o','b','filled')
ax = gca;
axis normal
set(ax,'CLim',[250,500]);
set(ax,'YLim',[-3.2, 3.2]);
ax.FontName = 'Times New Roman';
ax.FontSize = 16;

colorbarhandle = colorbar('peer',ax);
set(get(colorbarhandle, 'label'), 'String', 'Hardness (HV 0.5)','FontSize',20,
'FontName', 'Times New Roman');
xlabel('Distance to the bifurcation point (mm)','FontSize',20, 'FontName', 'Times New
Roman');
ylabel('DIstance to the weld interface (mm)','FontSize',20, 'FontName', 'Times New
Roman');
colormap jet
set(gca,'TickDir',"in")
```

D Fractography

D.1 Tensile Test Pieces

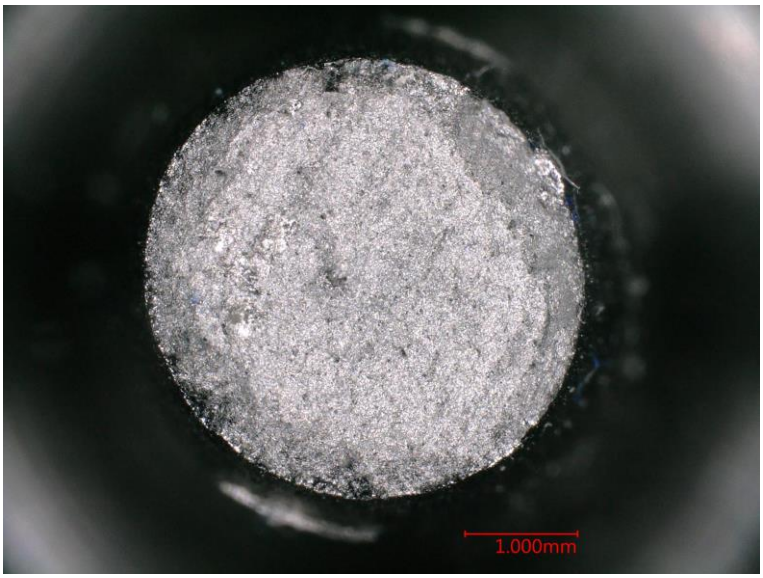

Figure D.1 Optical macrograph of the fracture surface of specimen HT001.

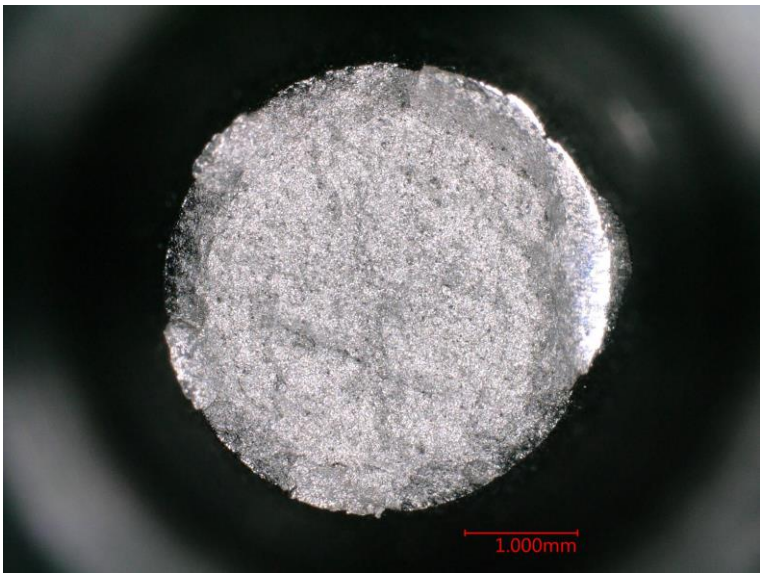

Figure D.2 Optical macrograph of the fracture surface of specimen HT002.

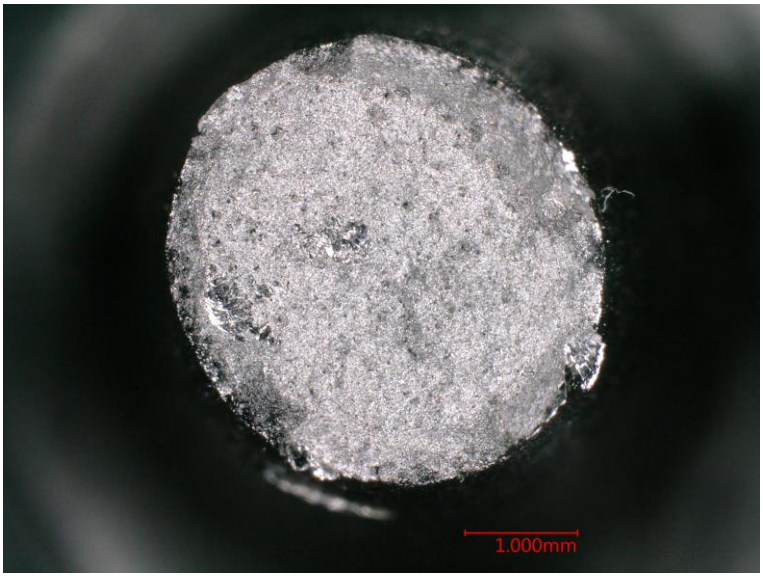

Figure D.3 Optical macrograph of the fracture surface of specimen HT003.

Figure D.4 Optical macrograph of the fracture surface of specimen HT004.

D.2 High Cycle Fatigue Test Pieces

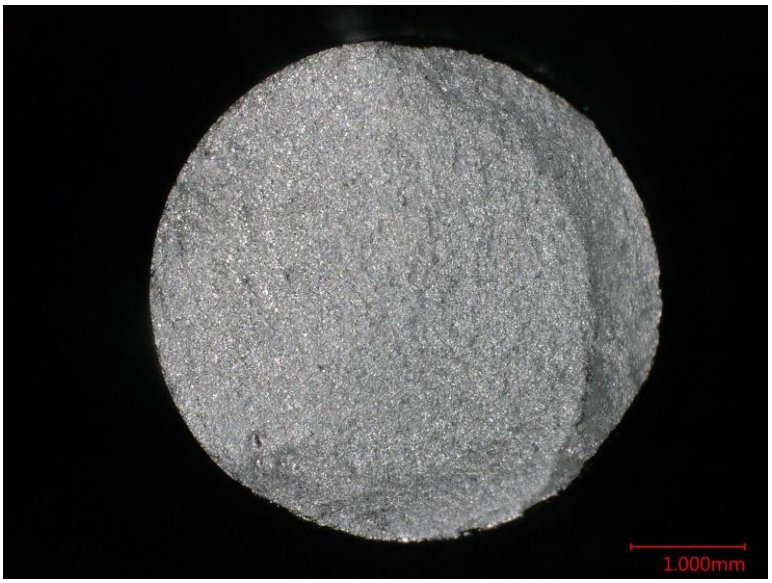

Figure D.5 Optical macrograph of the fracture surface of specimen HF001.

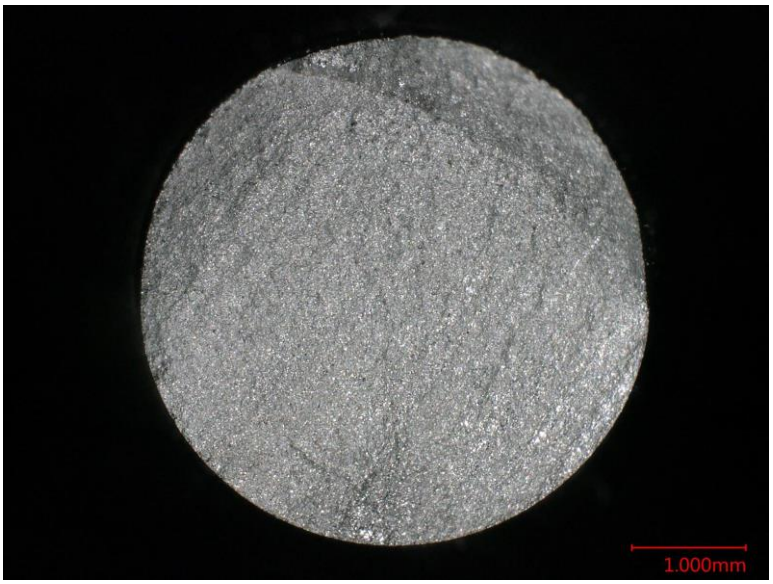

Figure D.6 Optical macrograph of the fracture surface of specimen HF002.

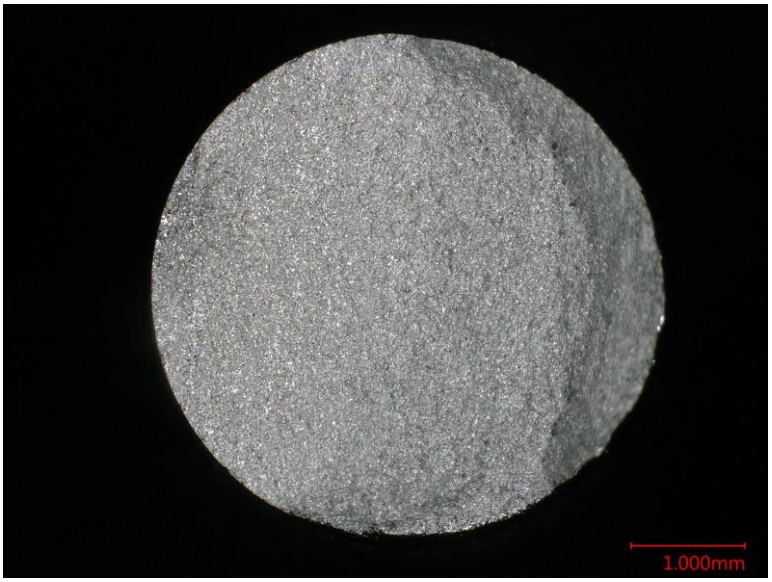

Figure D.7 Optical macrograph of the fracture surface of specimen HF003.

Figure D.8 Optical macrograph of the fracture surface of specimen HF004.

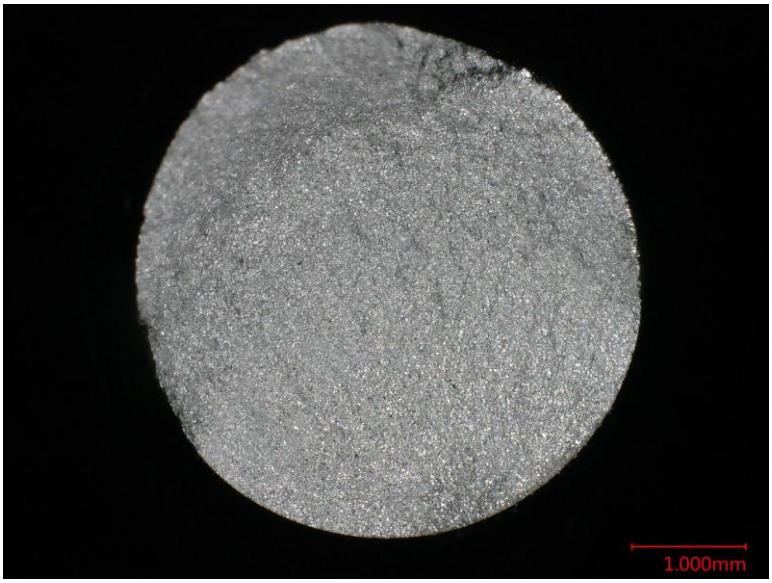

Figure D.9 Optical macrograph of the fracture surface of specimen HF005.

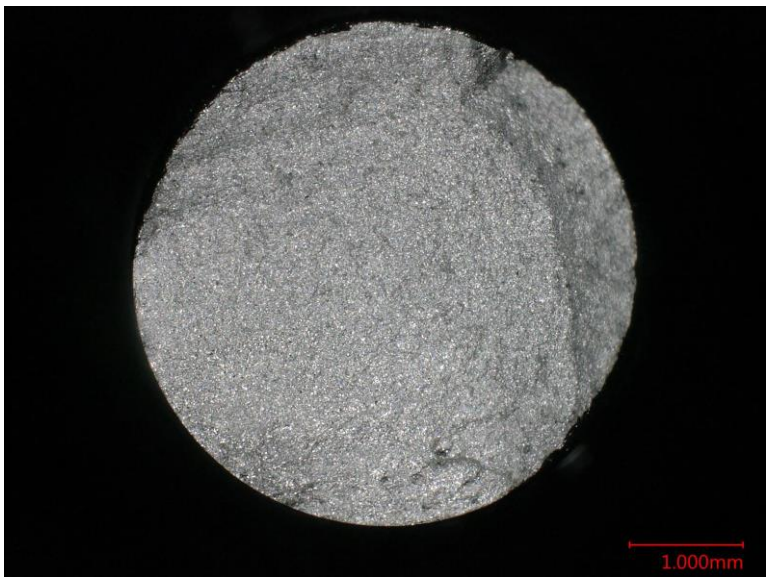

Figure D.10 Optical macrograph of the fracture surface of specimen HF006.

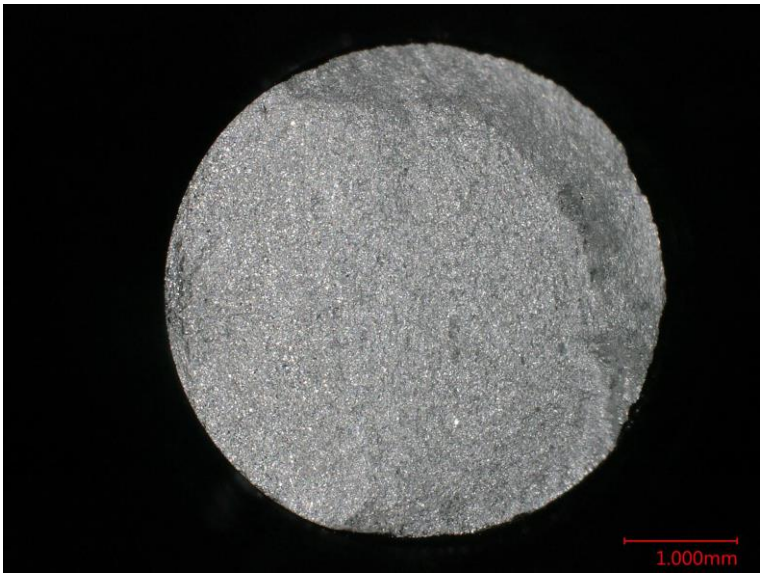

Figure D.11 Optical macrograph of the fracture surface of specimen HF007.

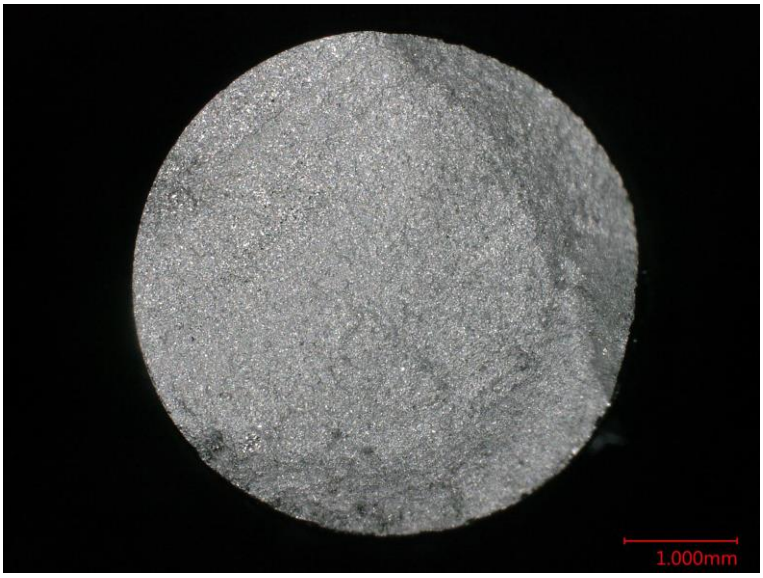

Figure D.12 Optical macrograph of the fracture surface of specimen HF008.

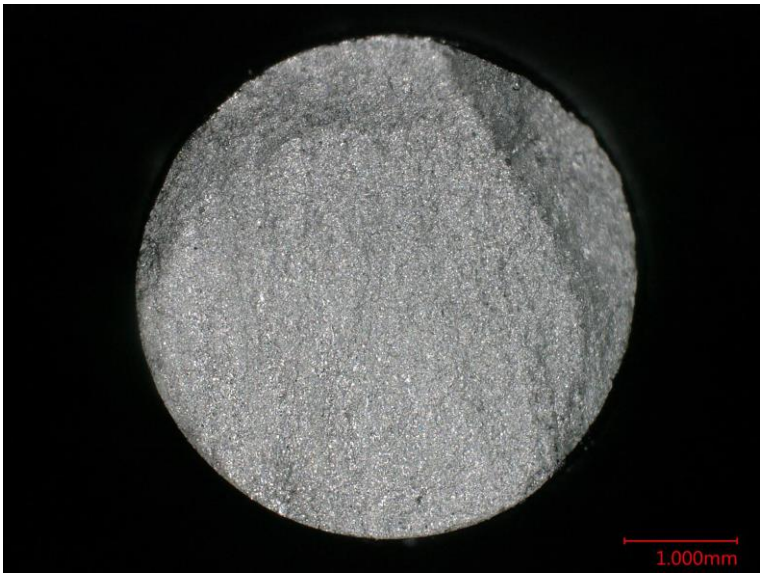

Figure D.13 Optical macrograph of the fracture surface of specimen HF009.

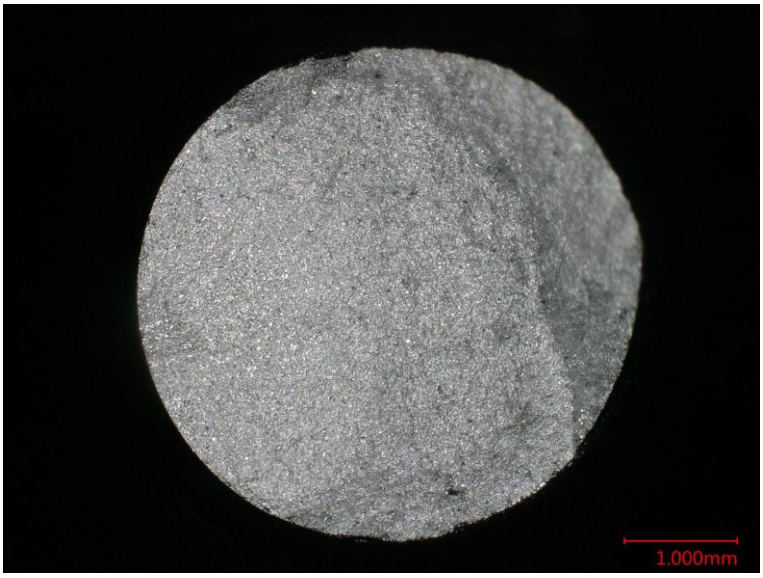

Figure D.14 Optical macrograph of the fracture surface of specimen HF010.

Figure D.15 Optical macrograph of the fracture surface of specimen HF011.

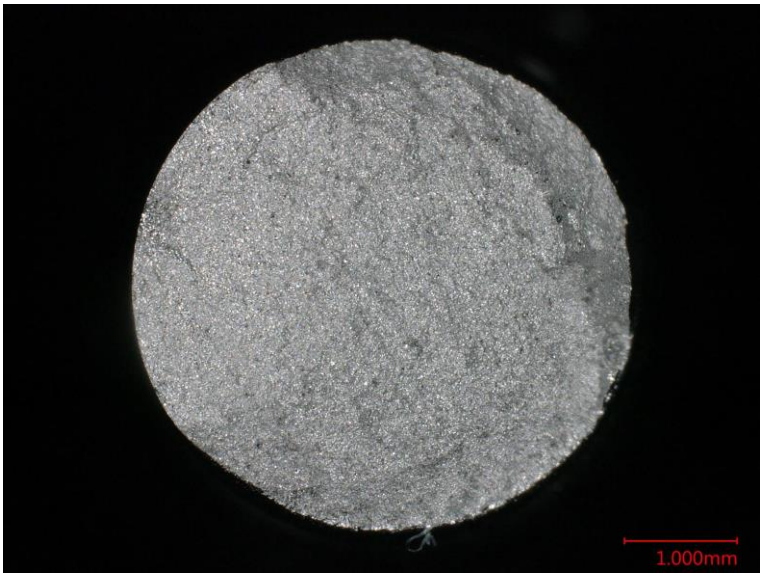

Figure D.16 Optical macrograph of the fracture surface of specimen HF012.

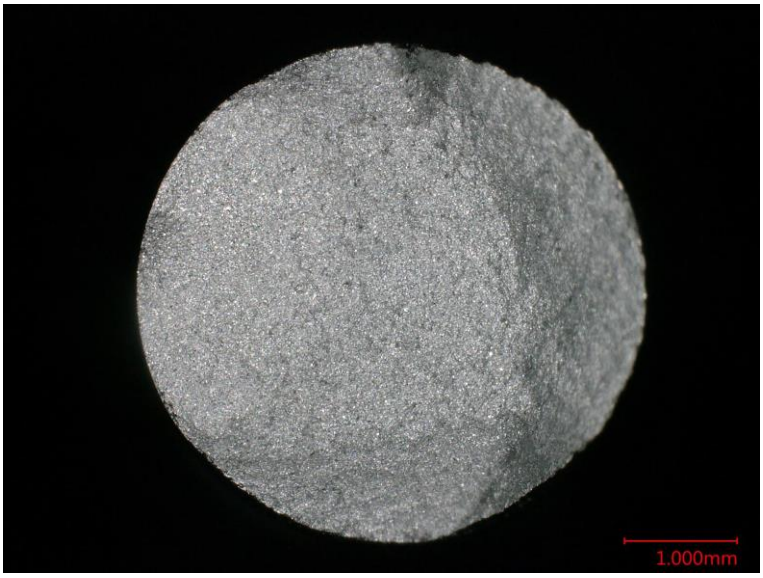

Figure D.17 Optical macrograph of the fracture surface of specimen HF013.

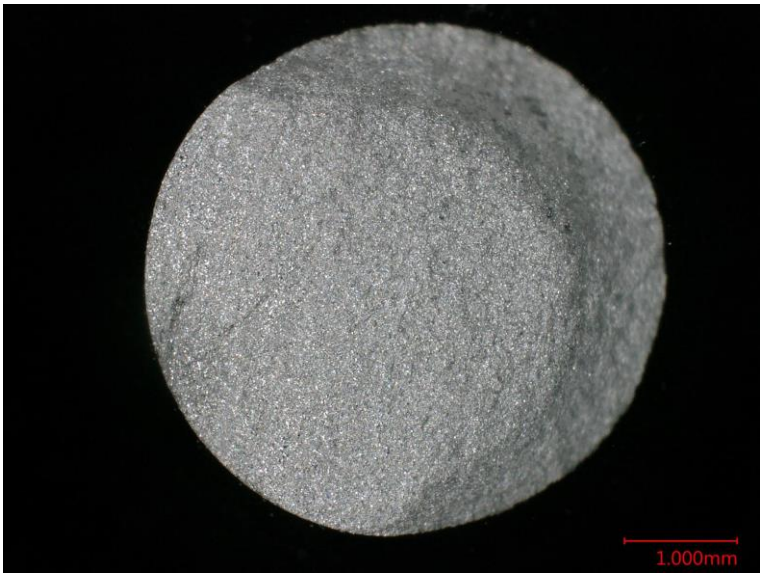

Figure D.18 Optical macrograph of the fracture surface of specimen HF014.

Figure D.19 Optical macrograph of the fracture surface of specimen HF015.

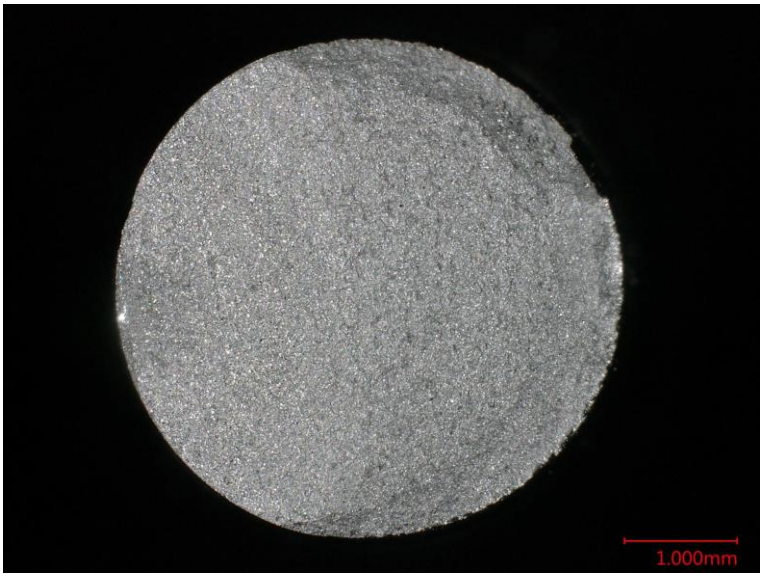

Figure D.20 Optical macrograph of the fracture surface of specimen HF016.

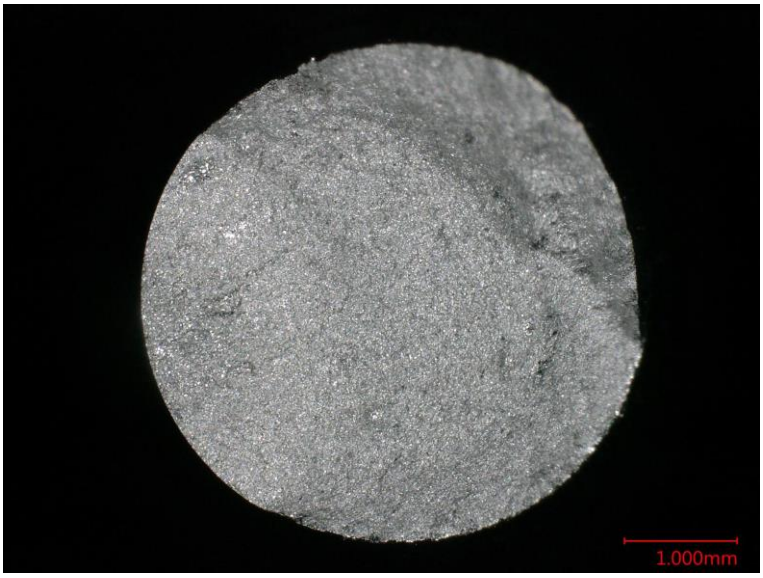

Figure D.21 Optical macrograph of the fracture surface of specimen HF017.

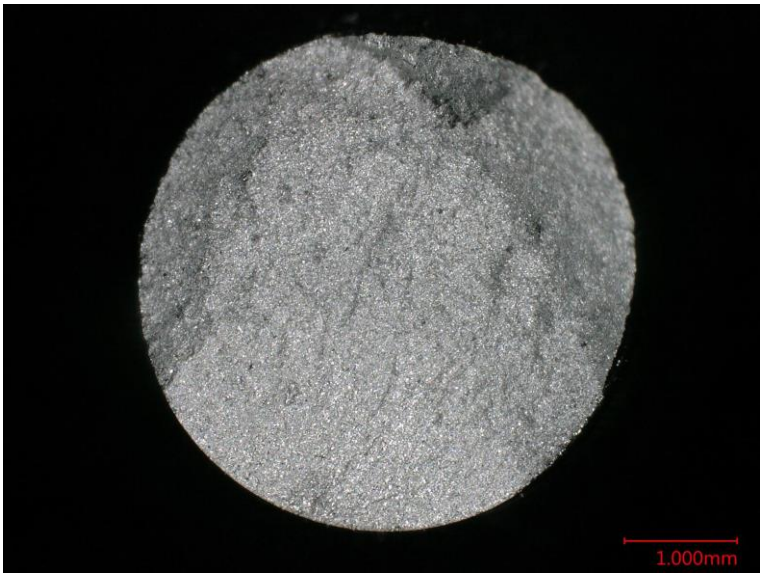

Figure D.22 Optical macrograph of the fracture surface of specimen HF018.

D.3 Fatigue Crack Growth Threshold Test Pieces

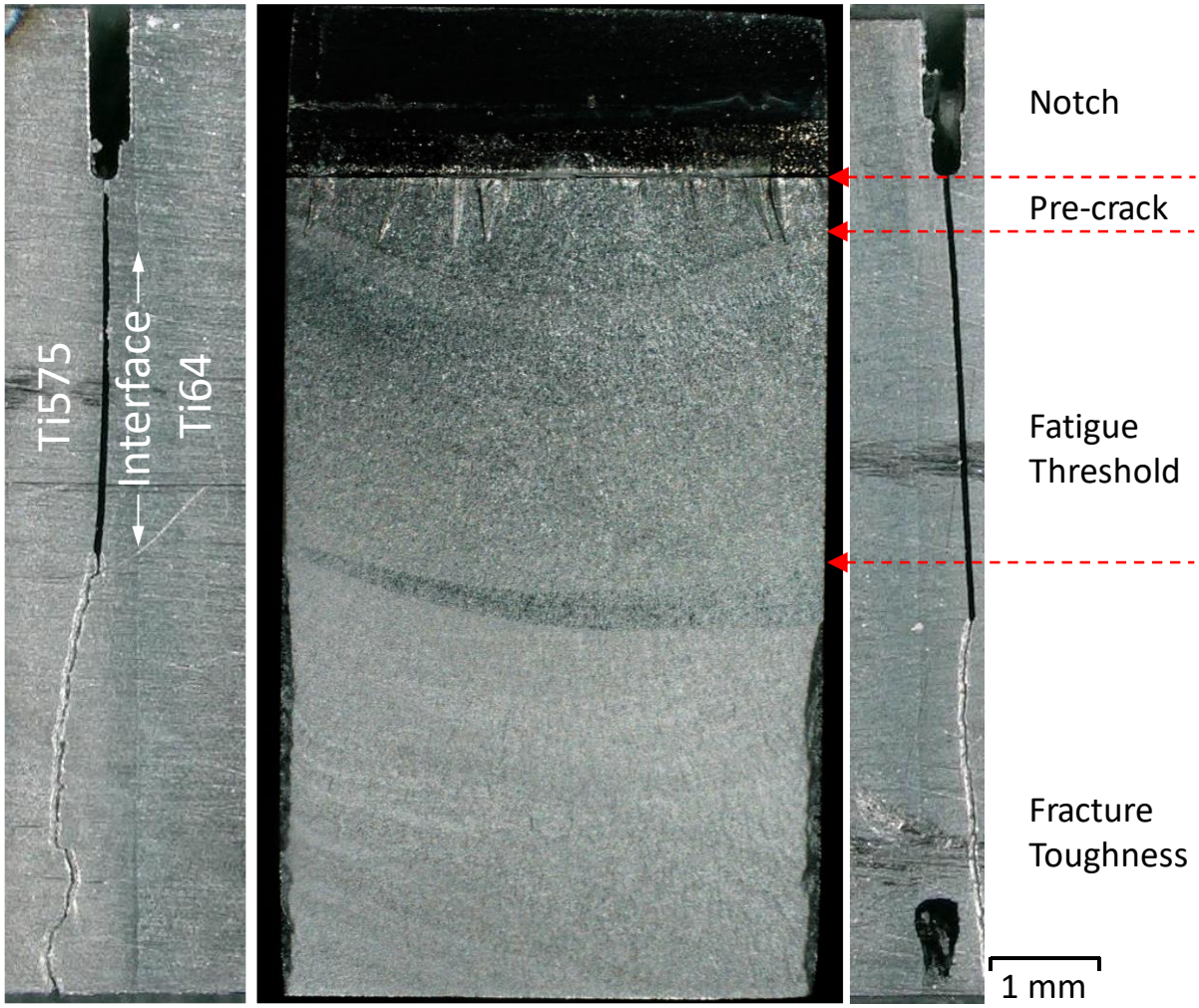

Figure D.23 Optical macrographs of the front and side views of the fracture surface of specimen CP001L after fatigue crack growth threshold testing and fracture toughness testing. Each stage of the testing is indicated by the red dashed arrows.

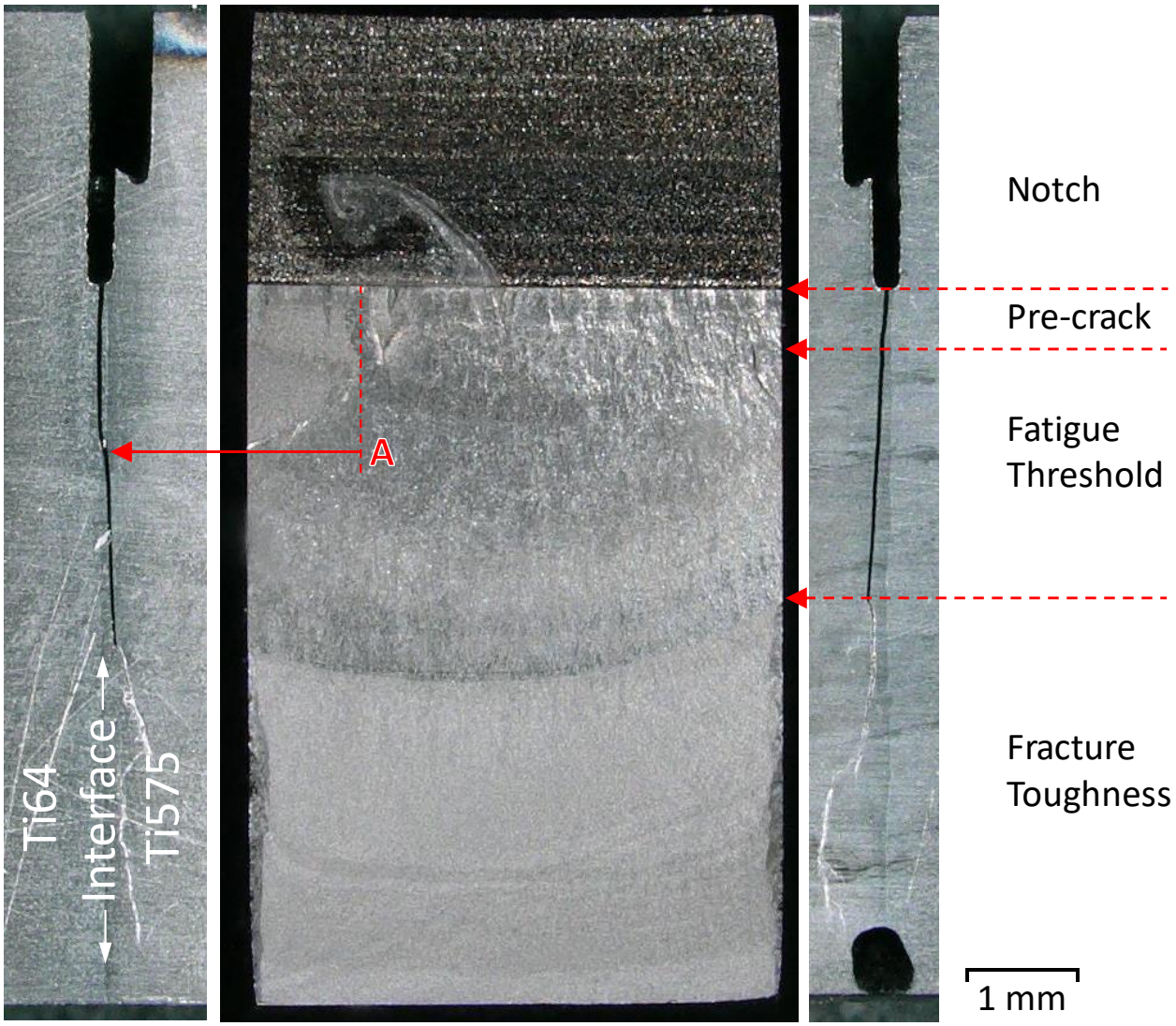

Figure D.24 Optical macrographs of the front and side views of the fracture surface of specimen CP001R after fatigue crack growth threshold testing and fracture toughness testing. Each stage of the testing is indicated by the red dashed arrows. Annotation 'A' indicates the location where crack went across the weld interface.

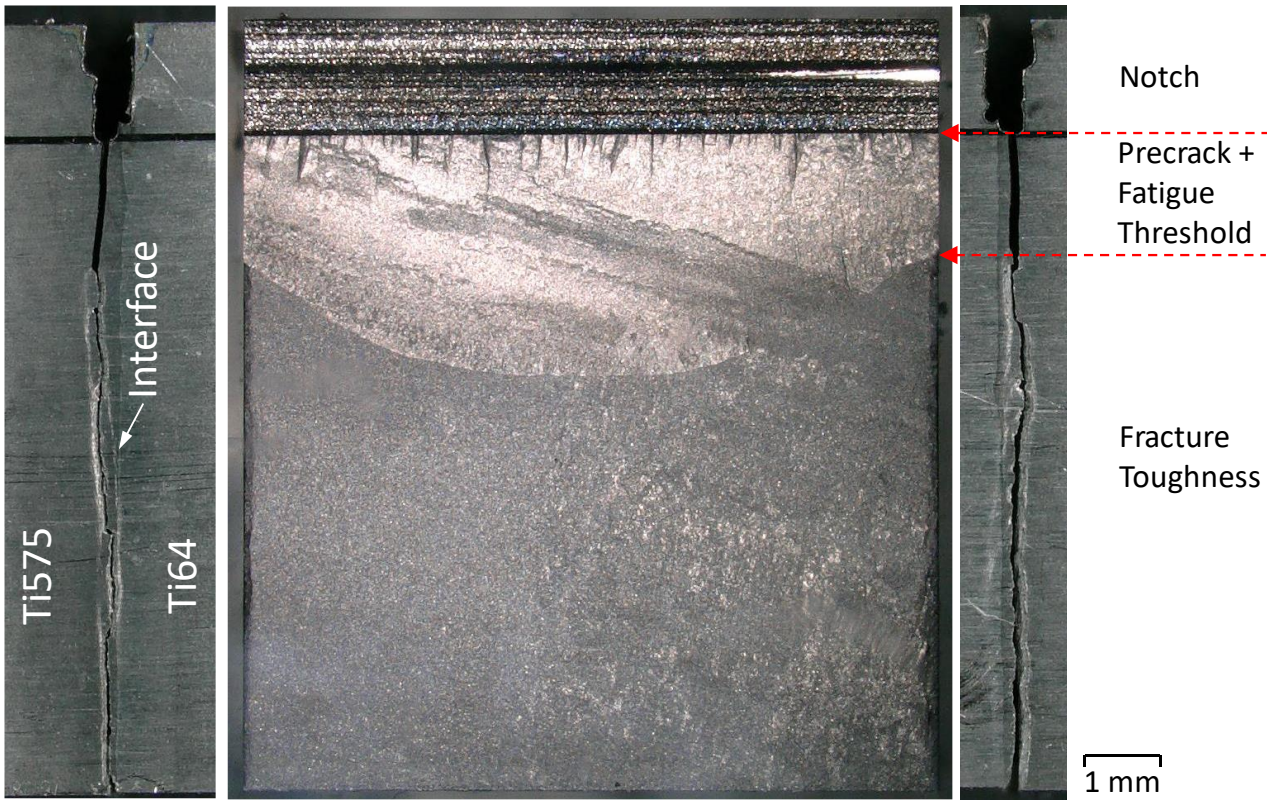

Figure D.25 Optical macrographs of the front and side views of the fracture surface of specimen CP002 after fatigue crack growth threshold testing and fracture toughness testing. Each stage of the testing is indicated by the red dashed arrows.

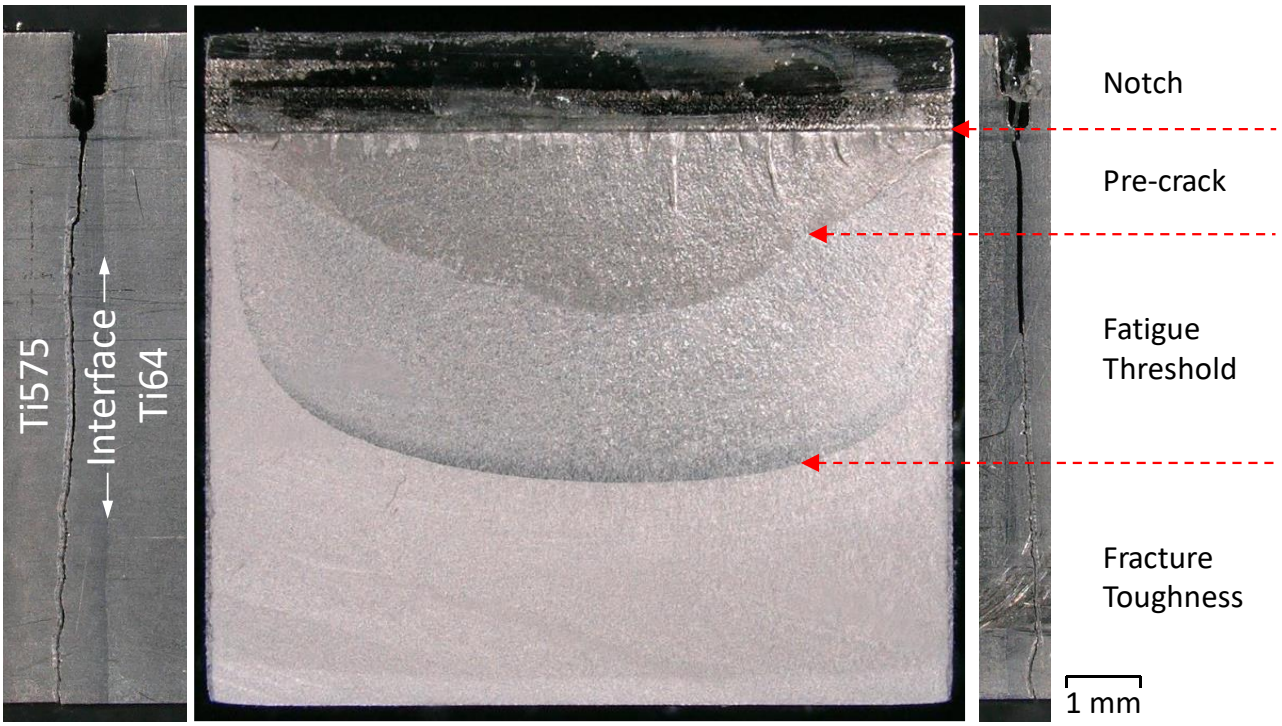

Figure D.26 Optical macrographs of the front and side views of the fracture surface of specimen CP003 after fatigue crack growth threshold testing and fracture toughness testing. Each stage of the testing is indicated by the red dashed arrows.

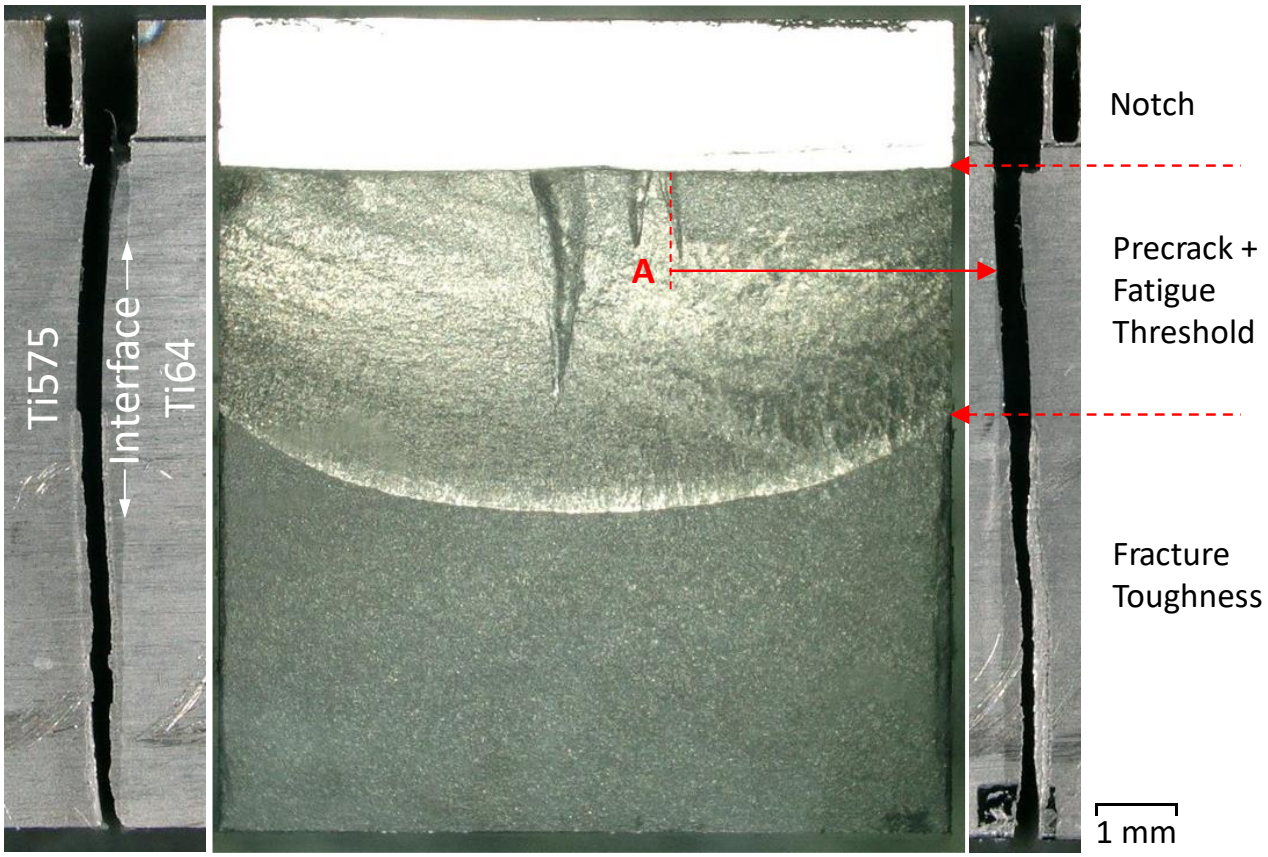

Figure D.27 Optical macrographs of the front and side views of the fracture surface of specimen CP004 after fatigue crack growth threshold testing and fracture toughness testing. Each stage of the testing is indicated by the red dashed arrows. Annotation 'A' indicates the location where crack went across the weld interface.

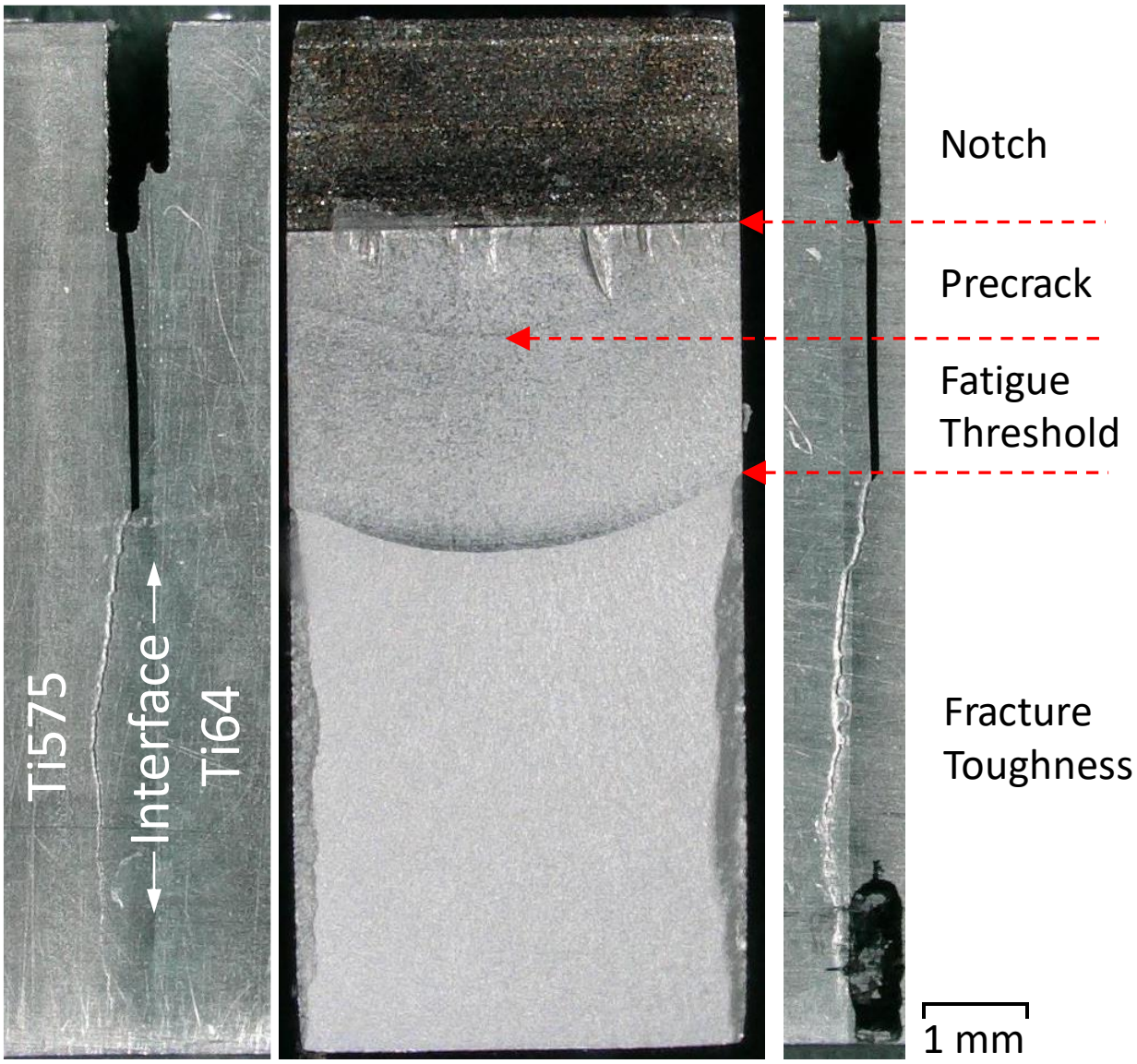

Figure D.28 Optical macrographs of the front and side views of the fracture surface of specimen CP005L after fatigue crack growth threshold testing and fracture toughness testing. Each stage of the testing is indicated by the red dashed arrows.

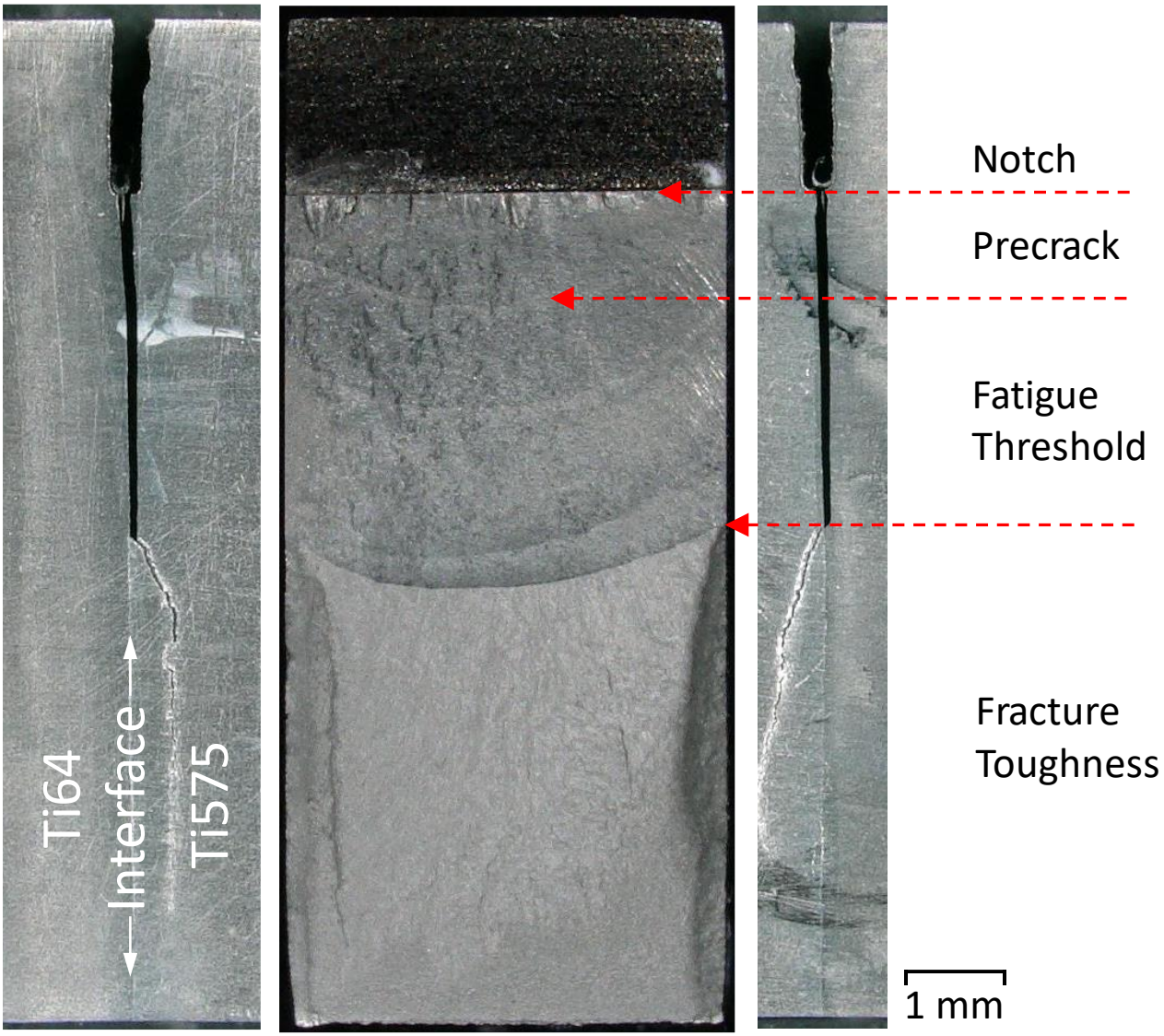

Figure D.29 Optical macrographs of the front and side views of the fracture surface of specimen CP005R after fatigue crack growth threshold testing and fracture toughness testing. Each stage of the testing is indicated by the red dashed arrows.

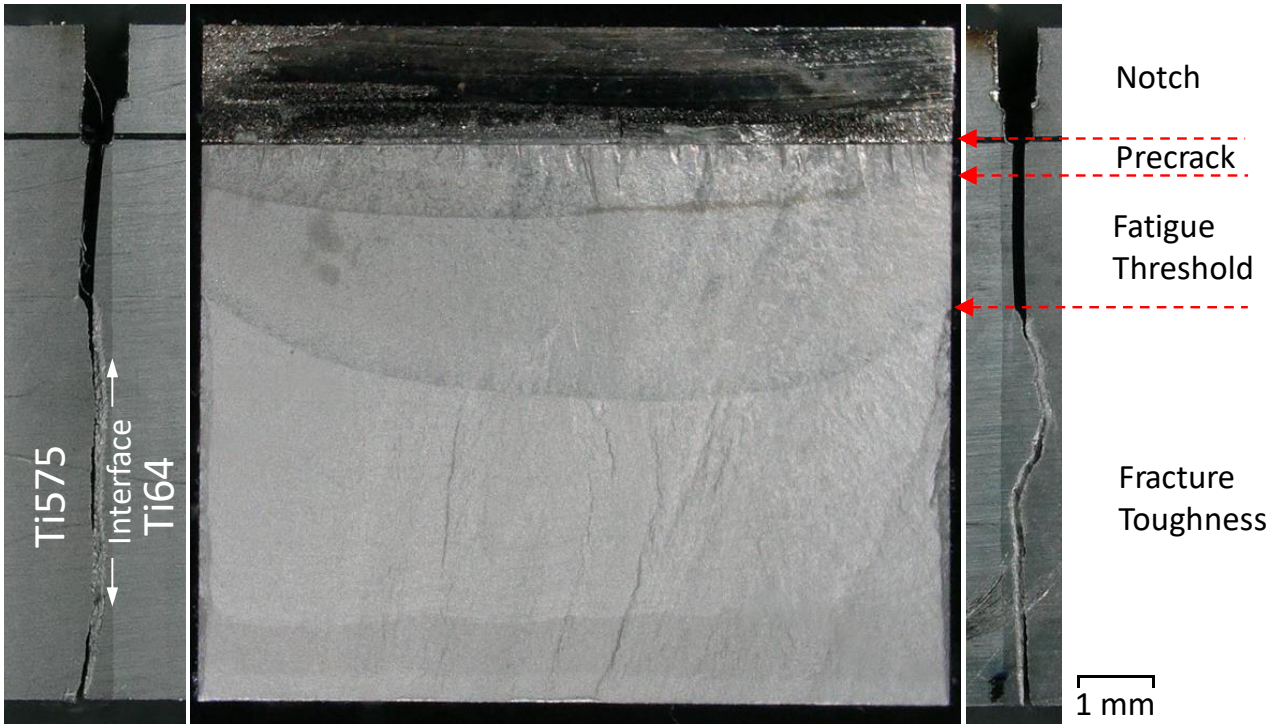

Figure D.30 Optical macrographs of the front and side views of the fracture surface of specimen CP006 after fatigue crack growth threshold testing and fracture toughness testing. Each stage of the testing is indicated by the red dashed arrows.

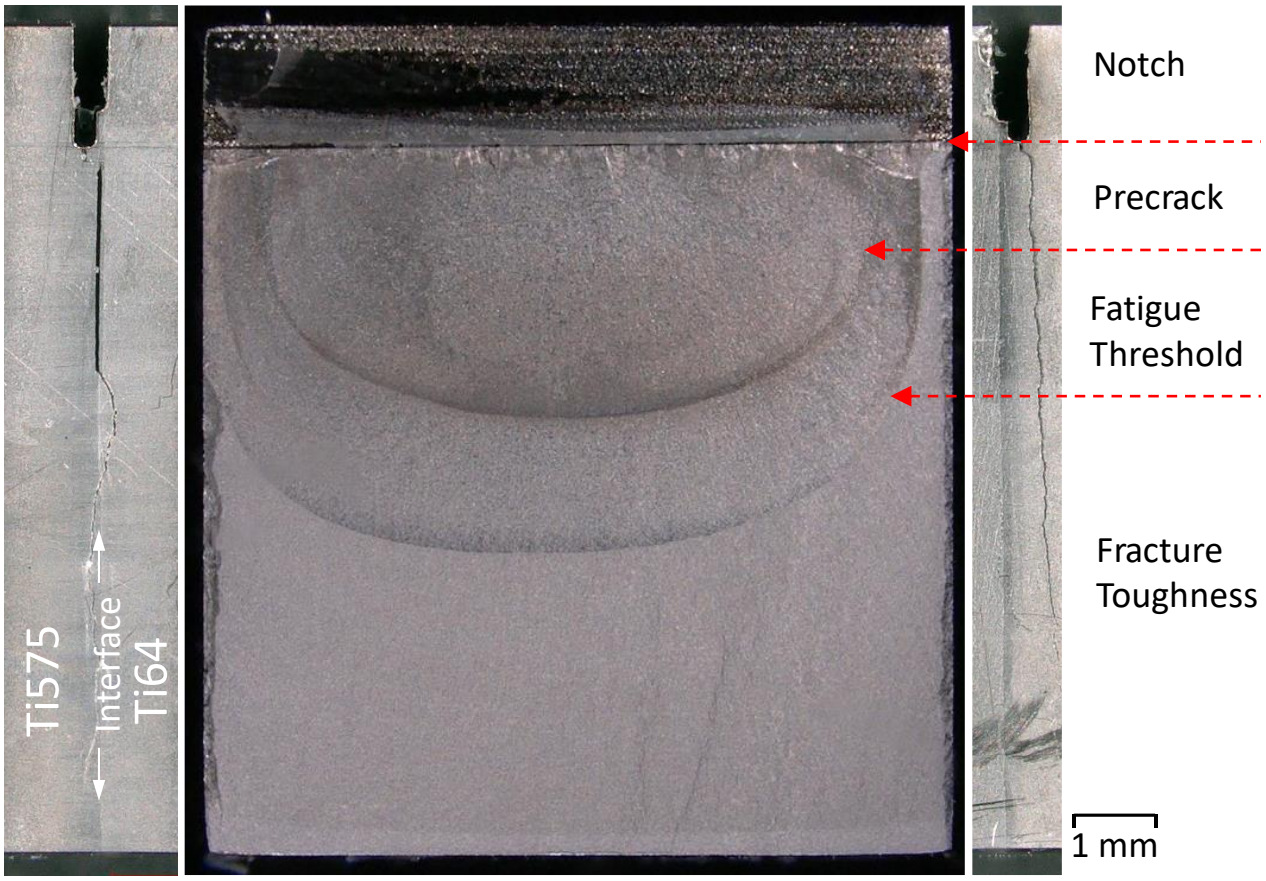

Figure D.31 Optical macrographs of the front and side views of the fracture surface of specimen CP007 after fatigue crack growth threshold testing and fracture toughness testing. Each stage of the testing is indicated by the red dashed arrows.

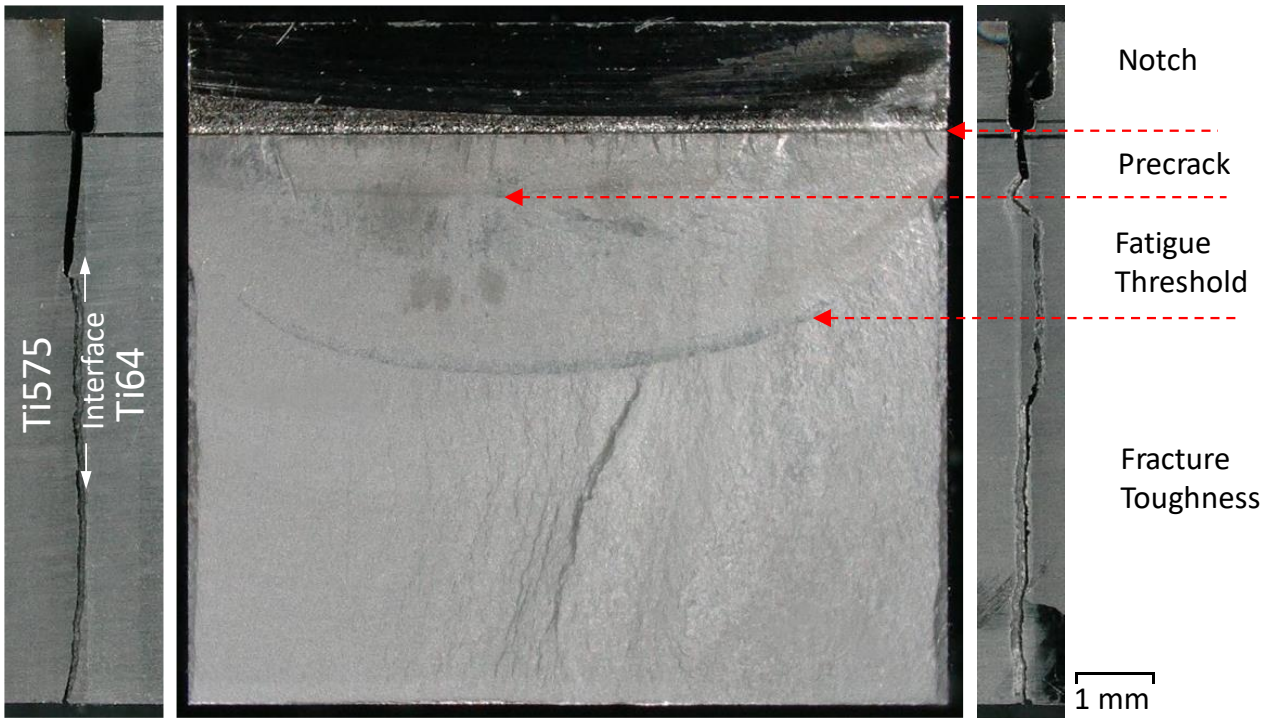

Figure D.32 Optical macrographs of the front and side views of the fracture surface of specimen CP008 after fatigue crack growth threshold testing and fracture toughness testing. Each stage of the testing is indicated by the red dashed arrows.

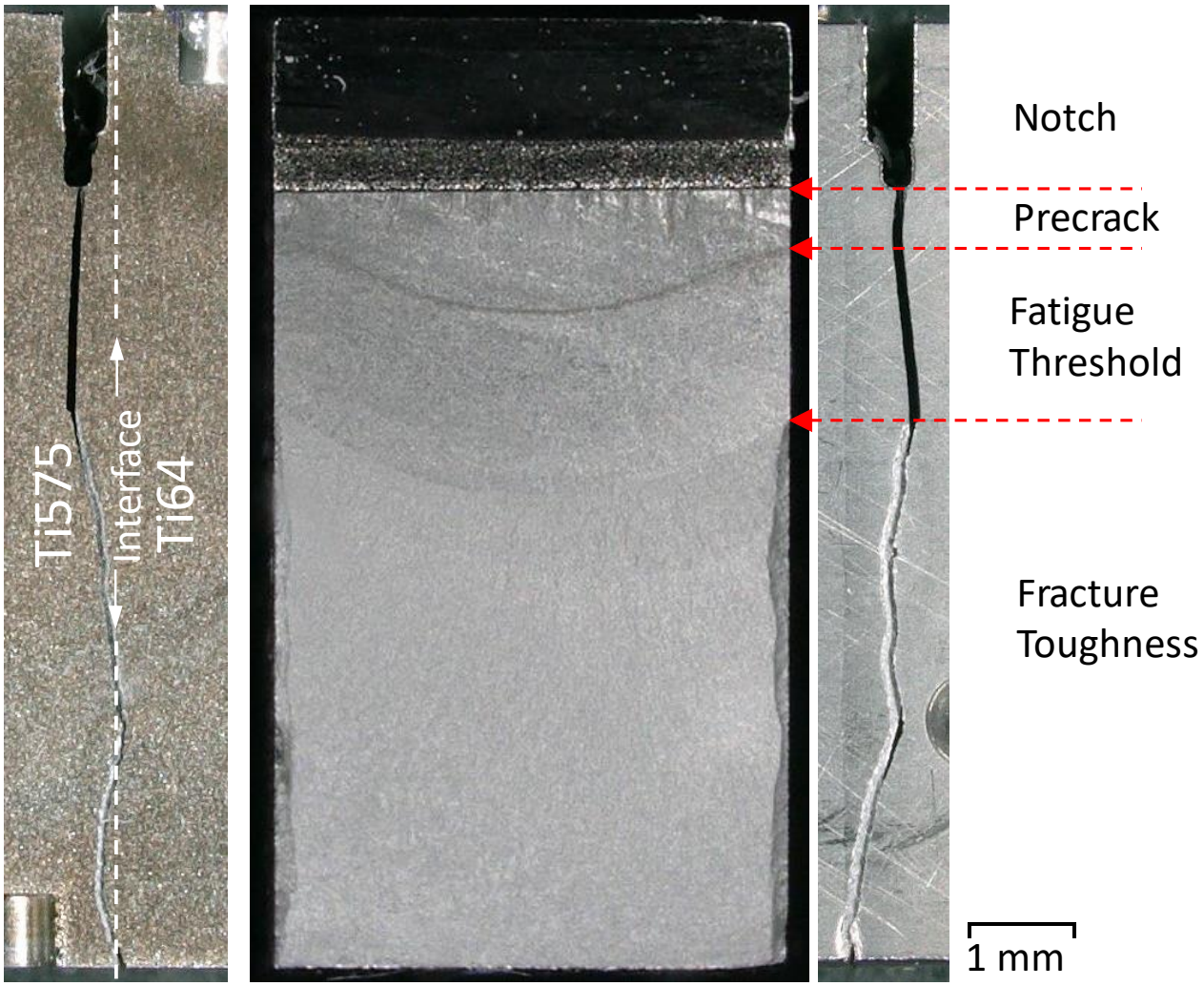

Figure D.33 Optical macrographs of the front and side views of the fracture surface of specimen CP009L after fatigue crack growth threshold testing and fracture toughness testing. Each stage of the testing is indicated by the red dashed arrows.

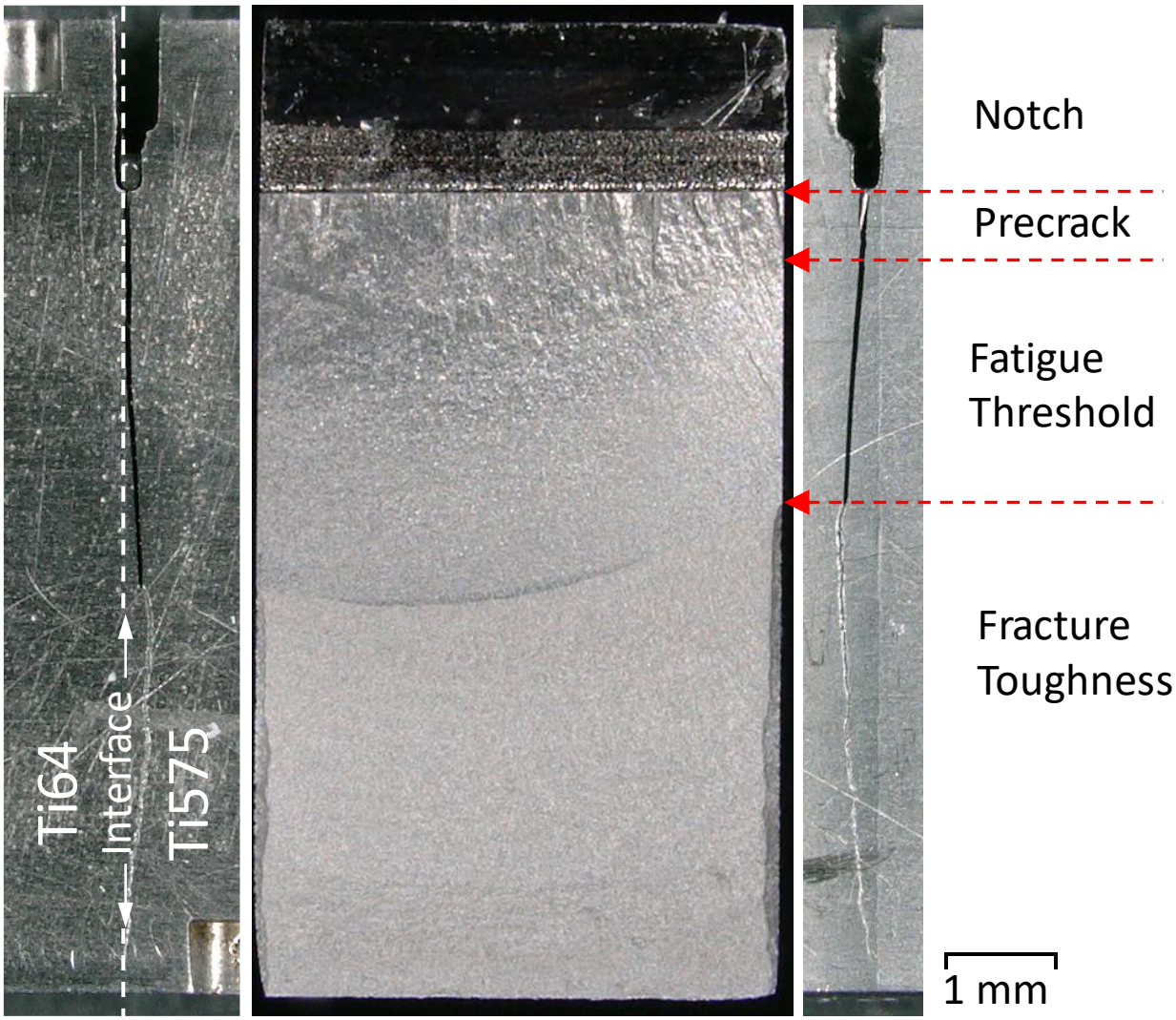

Figure D.34 Optical macrographs of the front and side views of the fracture surface of specimen CP009R after fatigue crack growth threshold testing and fracture toughness testing. Each stage of the testing is indicated by the red dashed arrows.

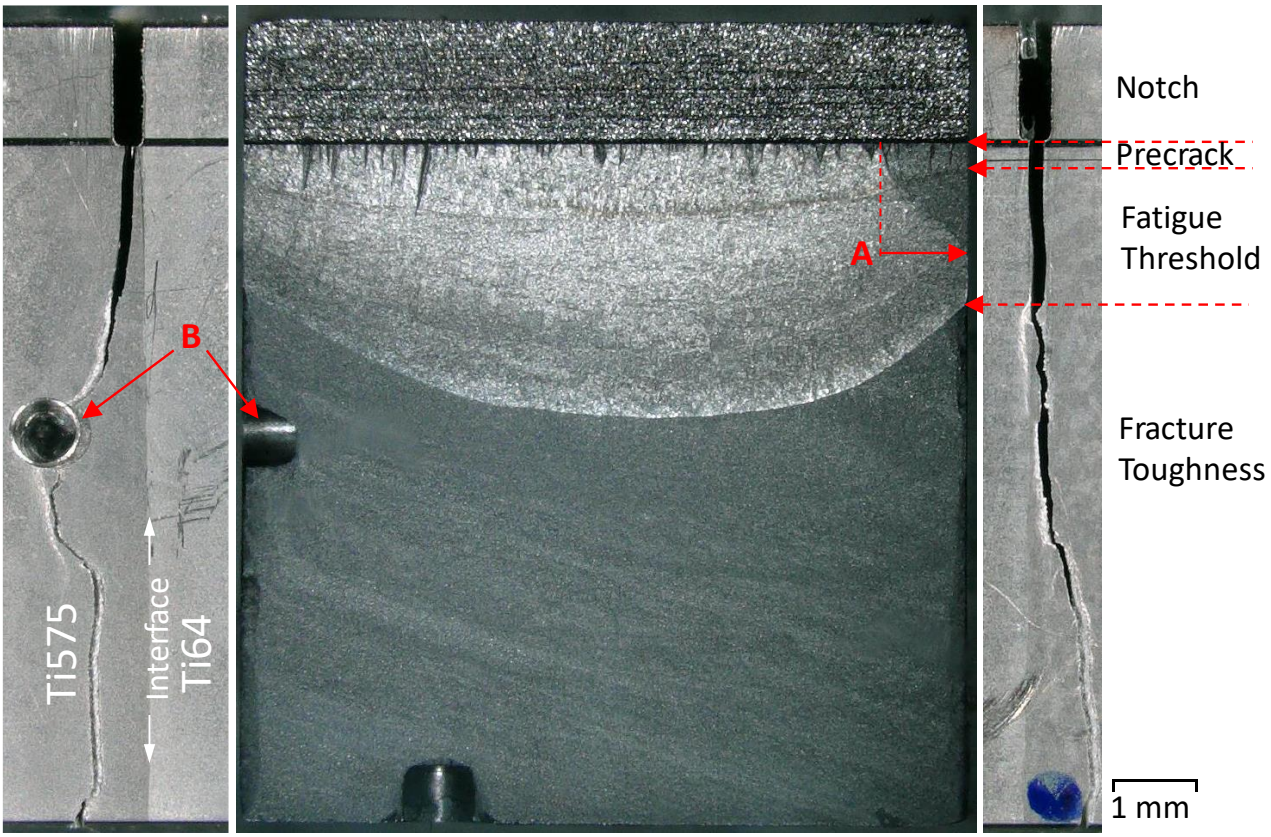

Figure D.35 Optical macrographs of the front and side views of the fracture surface of specimen CP010 after fatigue crack growth threshold testing and fracture toughness testing. Each stage of the testing is indicated by the red dashed arrows. Annotation 'A' indicates the location where crack went across the weld interface. Annotation 'B' indicates the hole drilled for residual stress measurement.

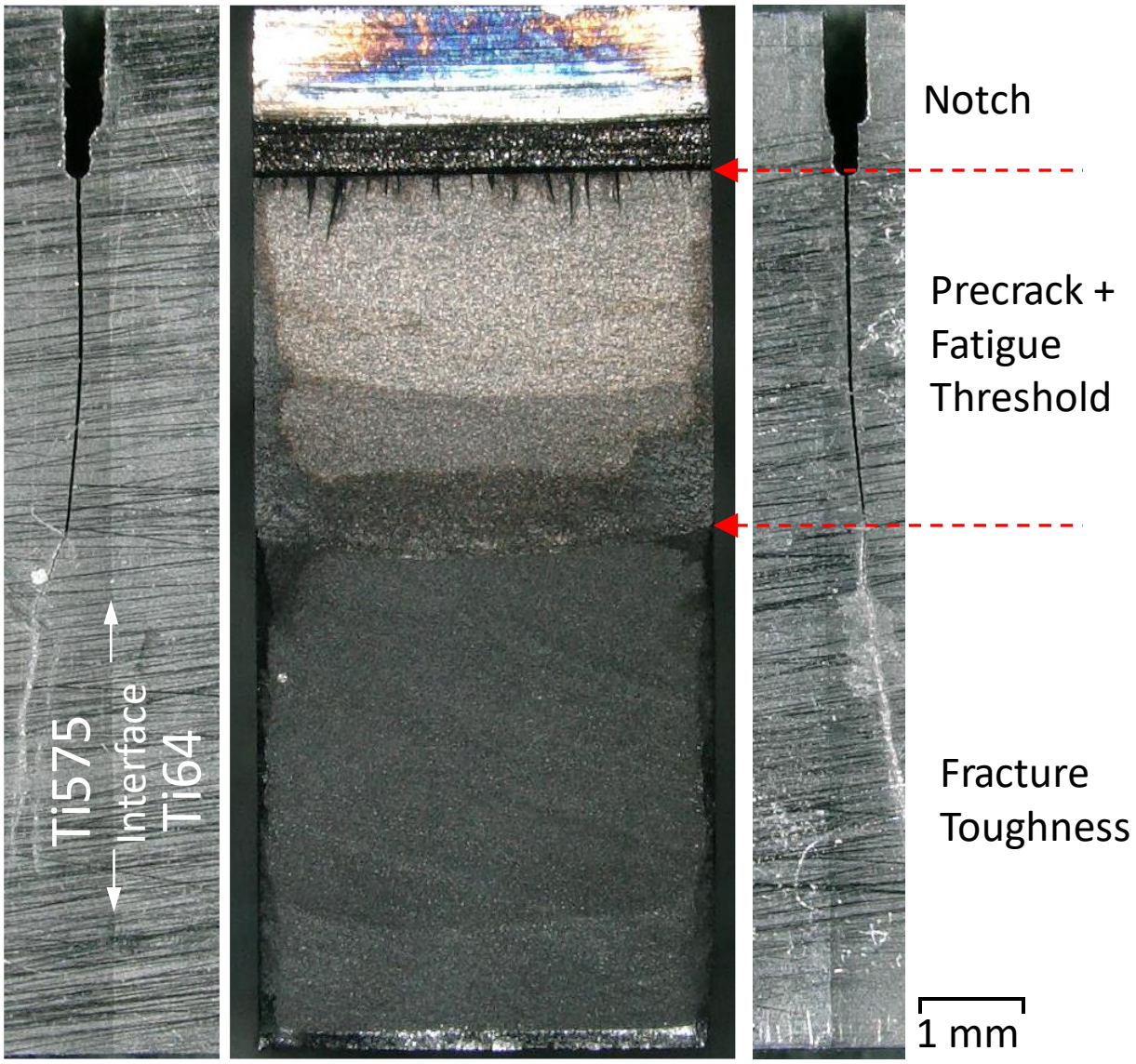

Figure D.36 Optical macrographs of the front and side views of the fracture surface of specimen CP011L after fatigue crack growth threshold testing and fracture toughness testing. Each stage of the testing is indicated by the red dashed arrows.

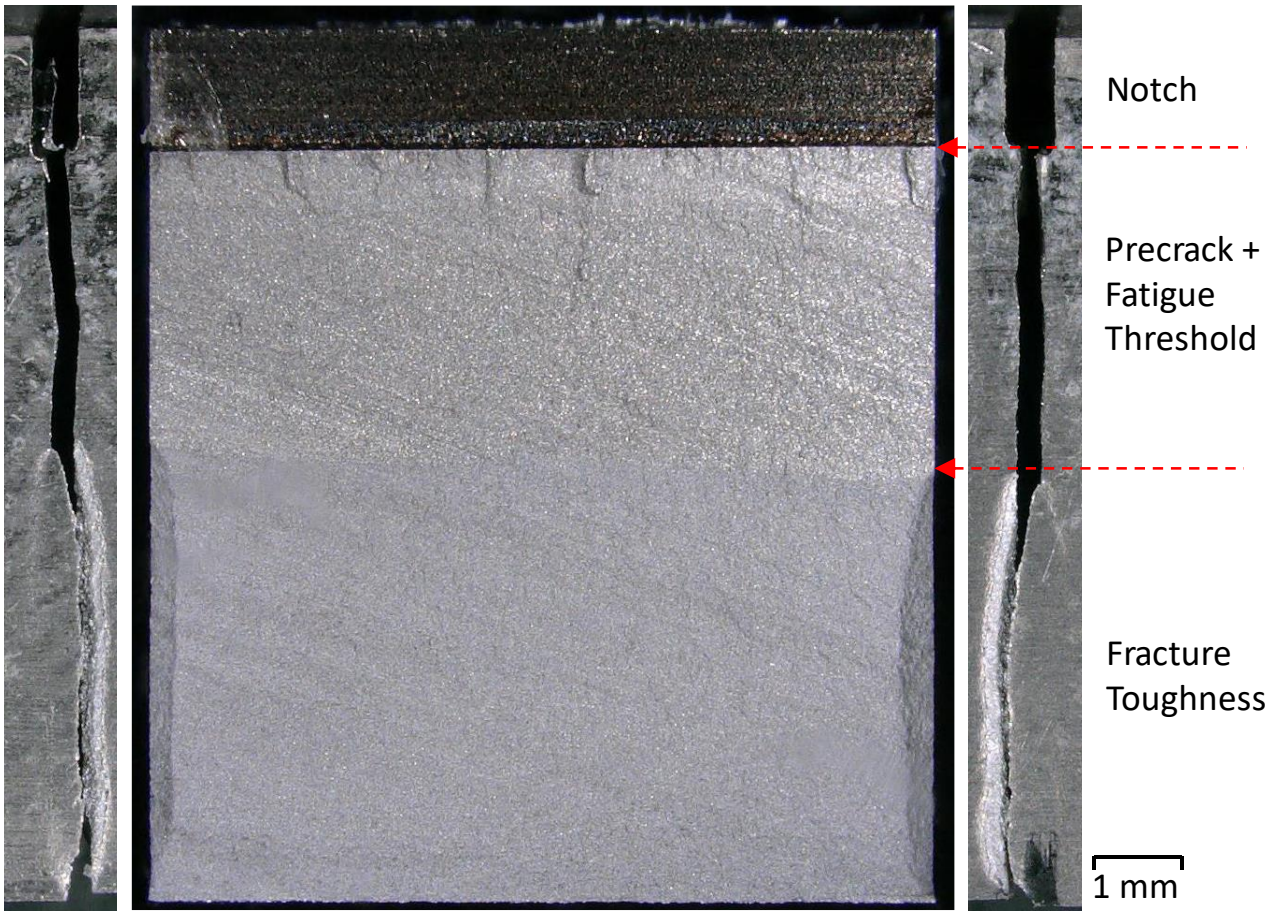

Figure D.37 Optical macrographs of the front and side views of the fracture surface of specimen CP012 after fatigue crack growth threshold testing and fracture toughness testing. Each stage of the testing is indicated by the red dashed arrows.

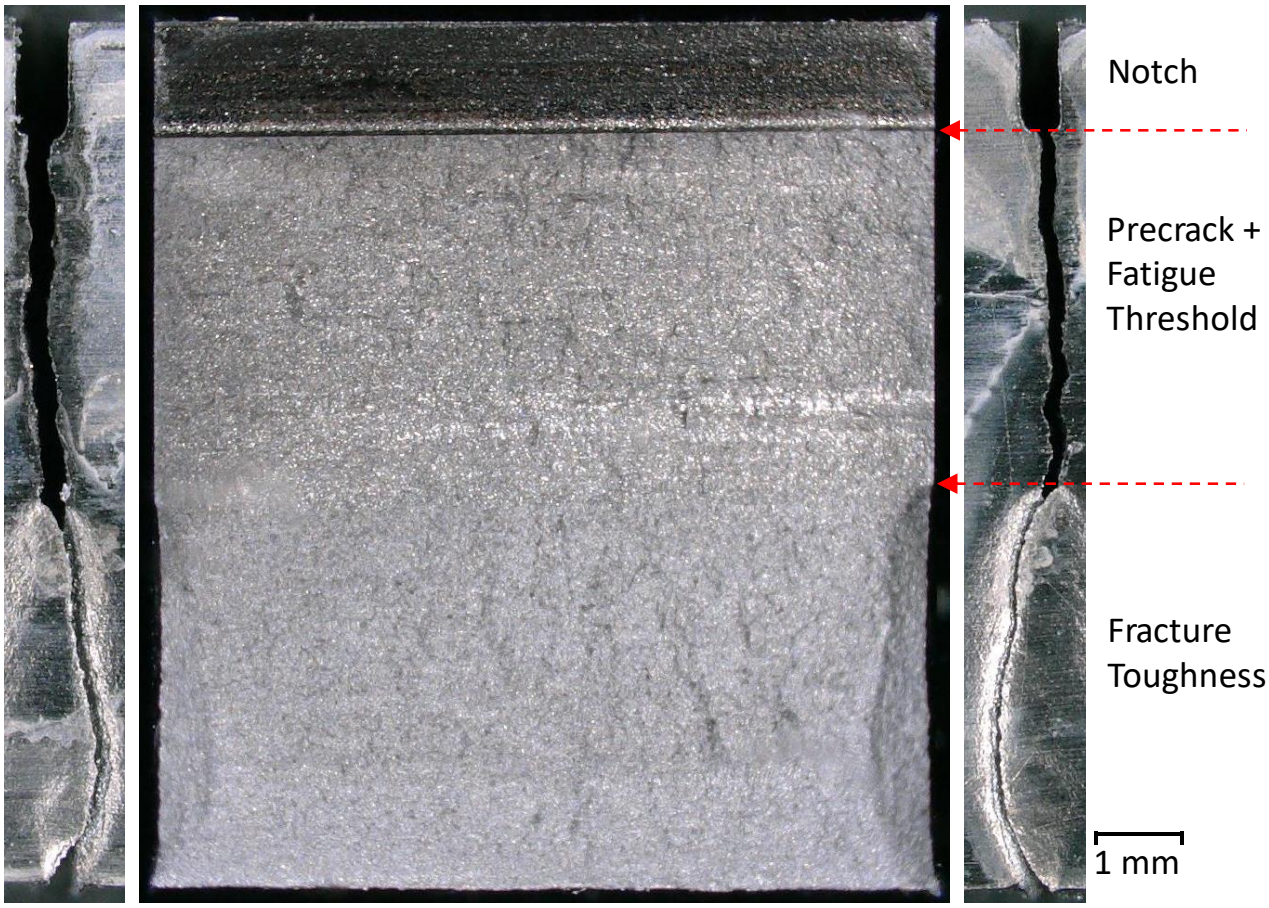

Figure D.38 Optical macrographs of the front and side views of the fracture surface of specimen CP014 after fatigue crack growth threshold testing and fracture toughness testing. Each stage of the testing is indicated by the red dashed arrows.

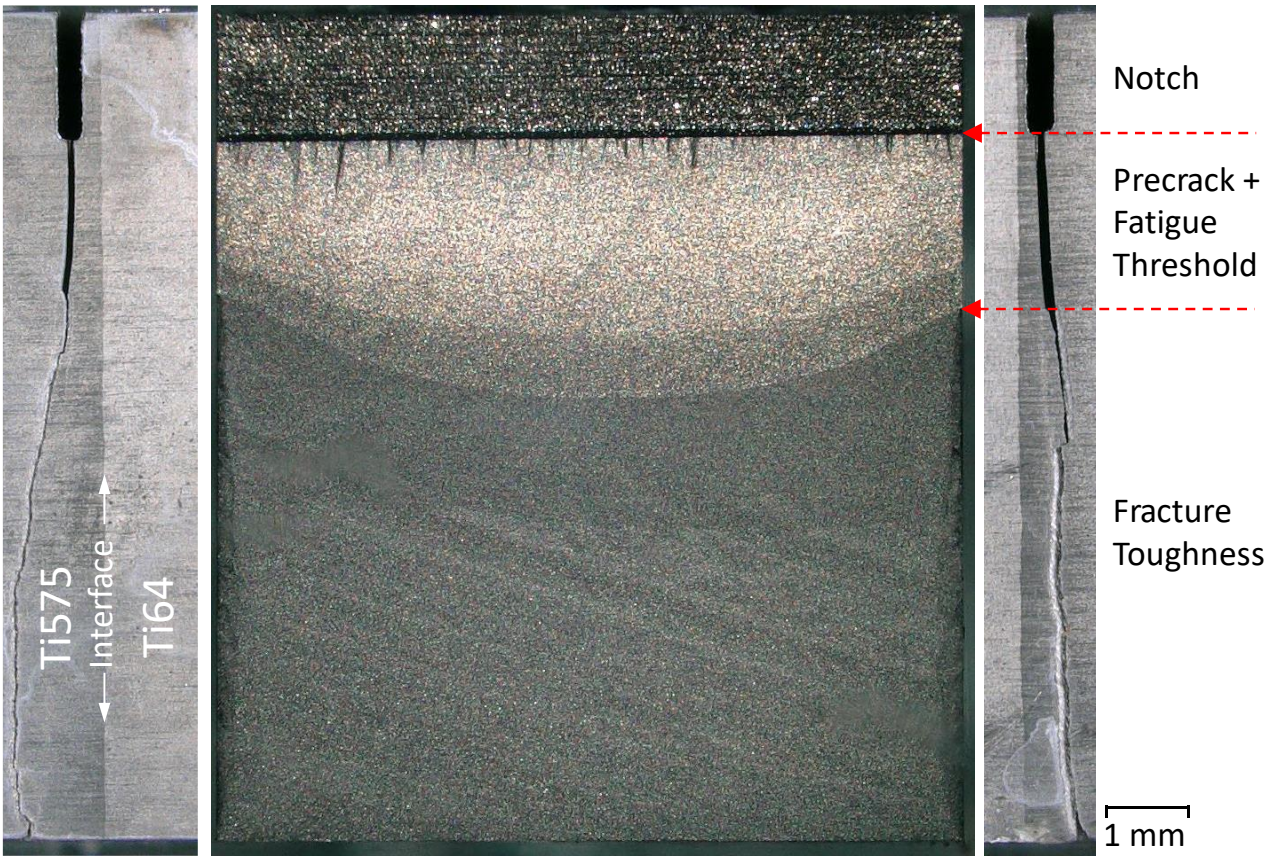

Figure D.39 Optical macrographs of the front and side views of the fracture surface of specimen CP017 after fatigue crack growth threshold testing and fracture toughness testing. Each stage of the testing is indicated by the red dashed arrows.

D.4 Fatigue Crack Propagation Test Pieces

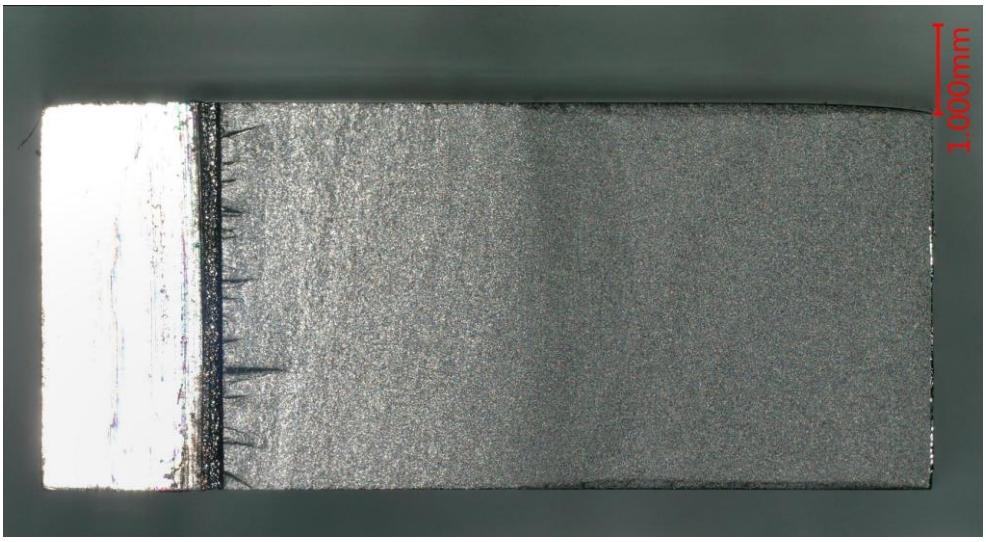

Figure D.40 Optical macrograph of the fracture surface of specimen CP011L.

Figure D.41 Optical macrograph of the fracture surface of specimen CP013L.

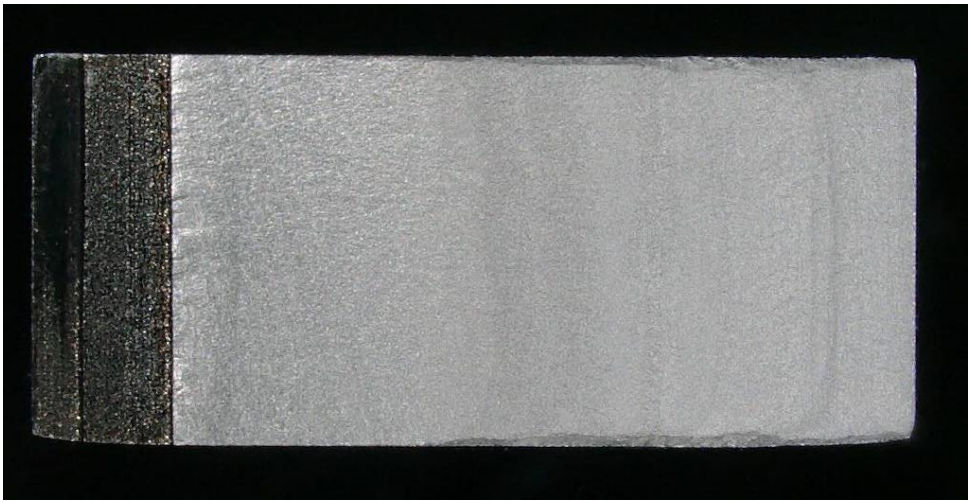

Figure D.42 Optical macrograph of the fracture surface of specimen CP013R.

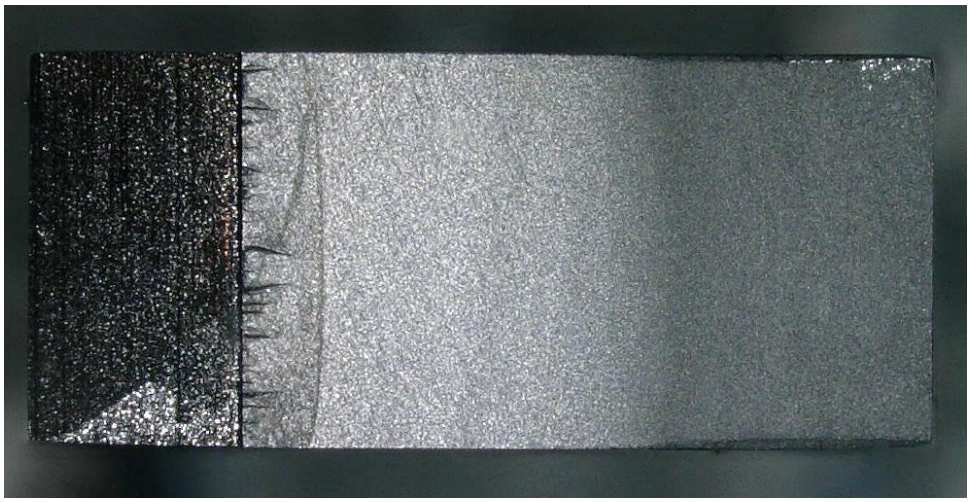

Figure D.43 Optical macrograph of the fracture surface of specimen CP015L.

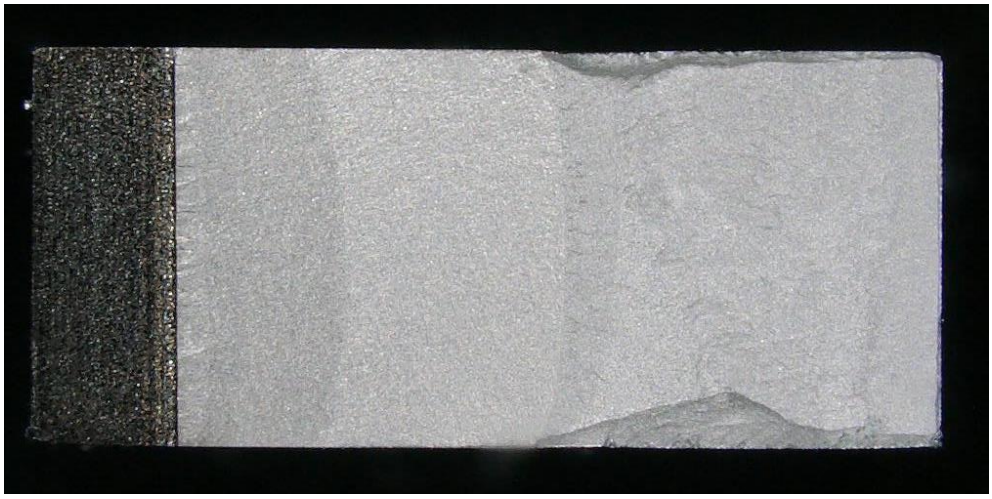

Figure D.44 Optical macrograph of the fracture surface of specimen CP015R.

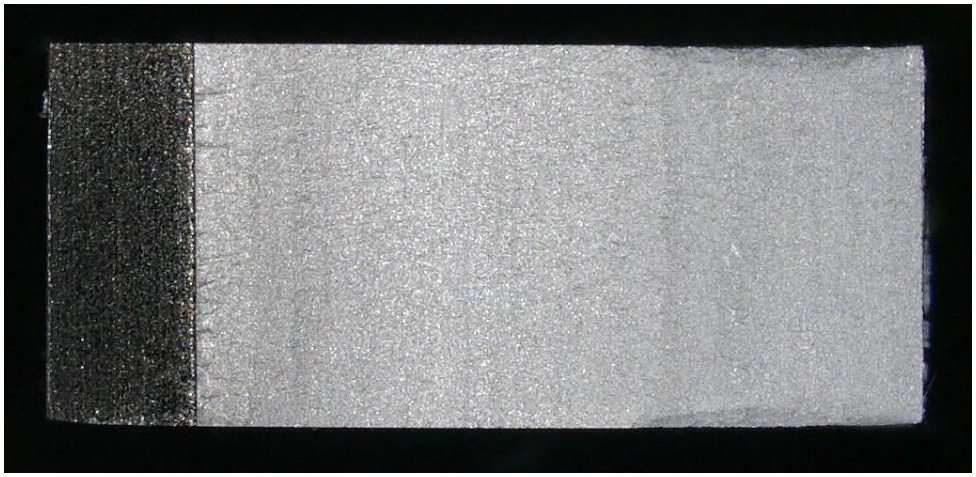

Figure D.45 Optical macrograph of the fracture surface of specimen CP016L.

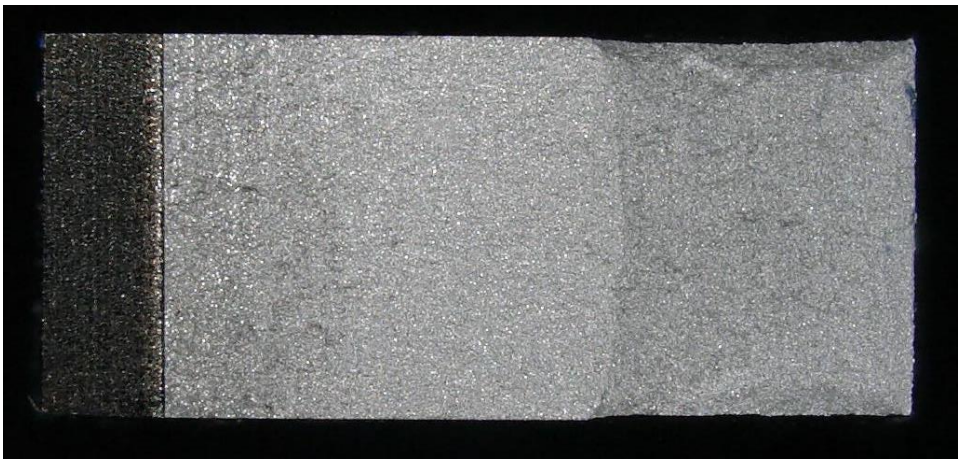

Figure D.46 Optical macrograph of the fracture surface of specimen CP016R.

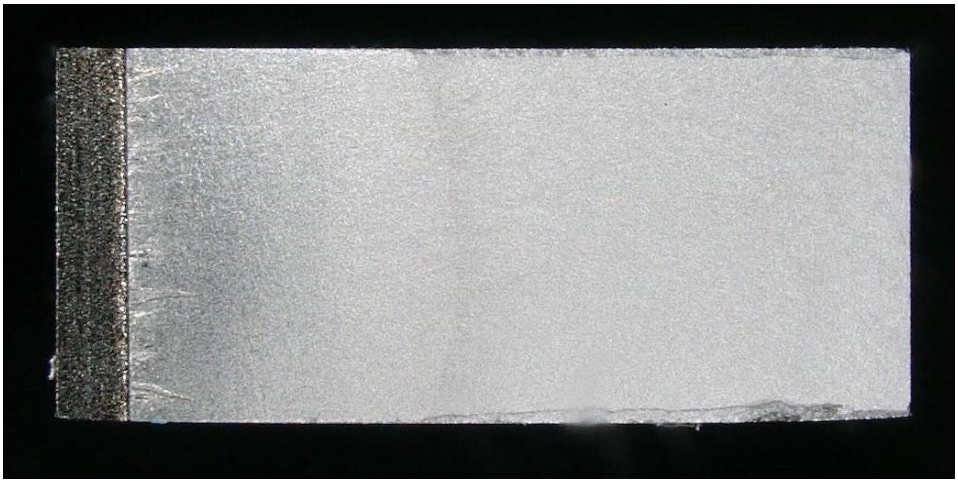

Figure D.47 Optical macrograph of the fracture surface of specimen CP021L.

Figure D.48 Optical macrograph of the fracture surface of specimen CP021R.

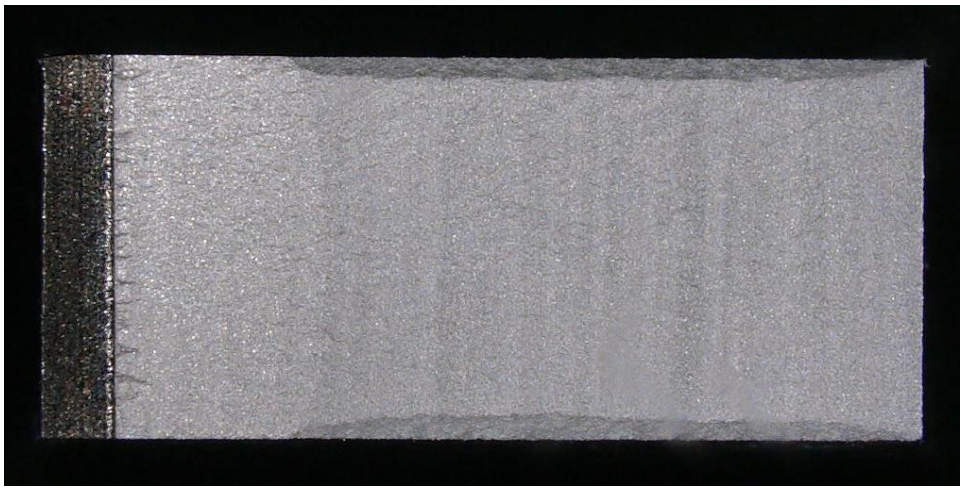

Figure D.49 Optical macrograph of the fracture surface of specimen CP022L.

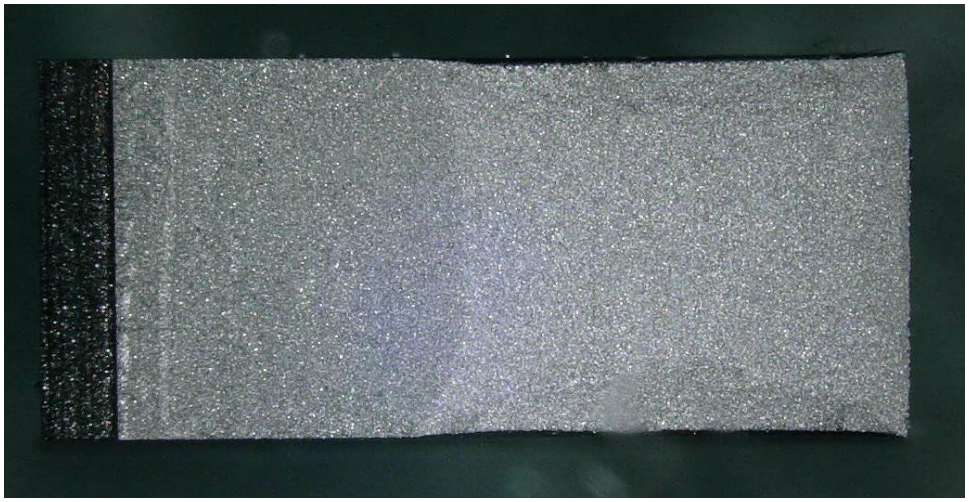

Figure D.50 Optical macrograph of the fracture surface of specimen CP022R.

D.5 Fractographs in the Fracture Region

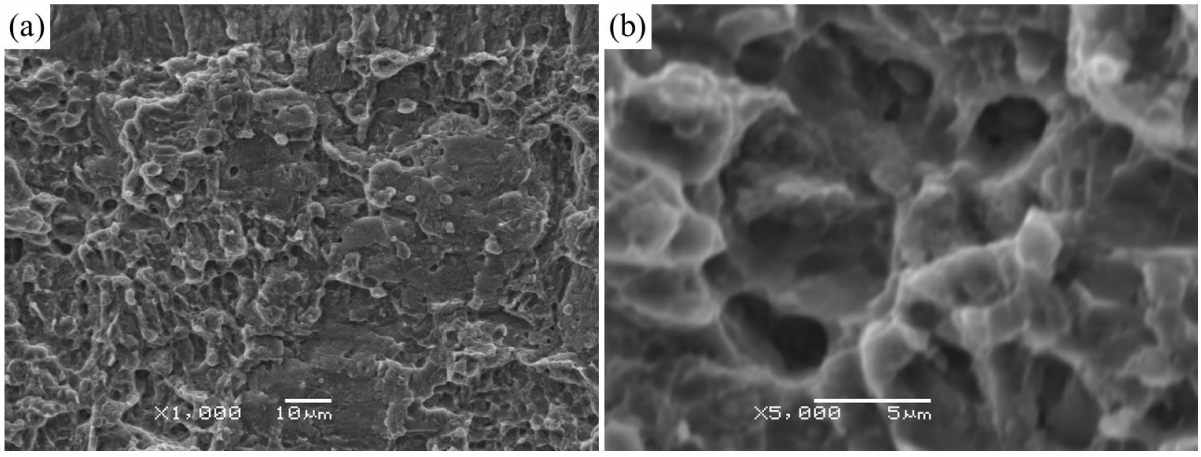

Figure D.51 (a) Low and (b) high magnification secondary electron images of the fracture surface of CP002 in fracture region. ($K_Q = 29.8$ MPa$\sqrt{\text{m}}$)

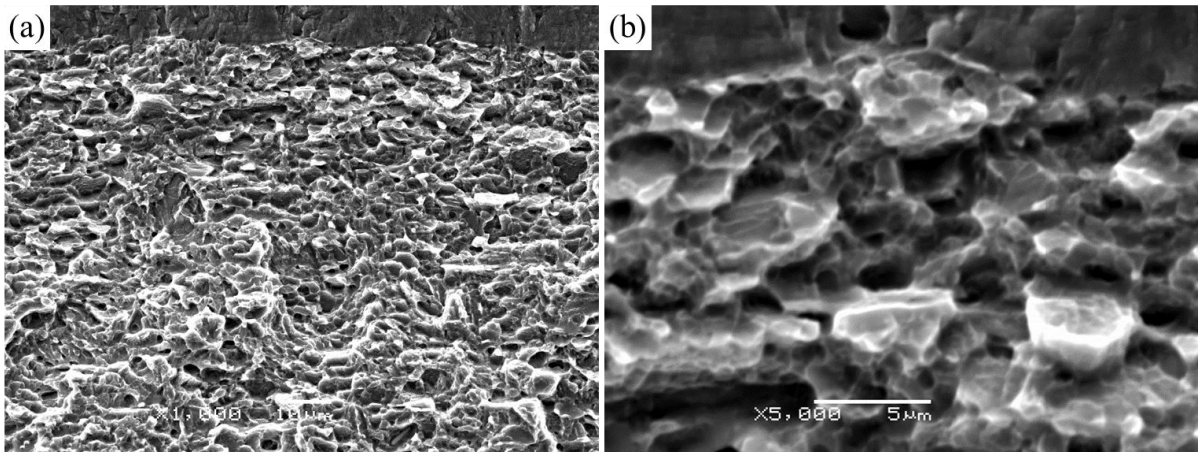

Figure D.52 (a) Low and (b) high magnification secondary electron images of the fracture surface of CP003 in fracture region. ($K_Q = 25.0$ MPa$\sqrt{\text{m}}$)

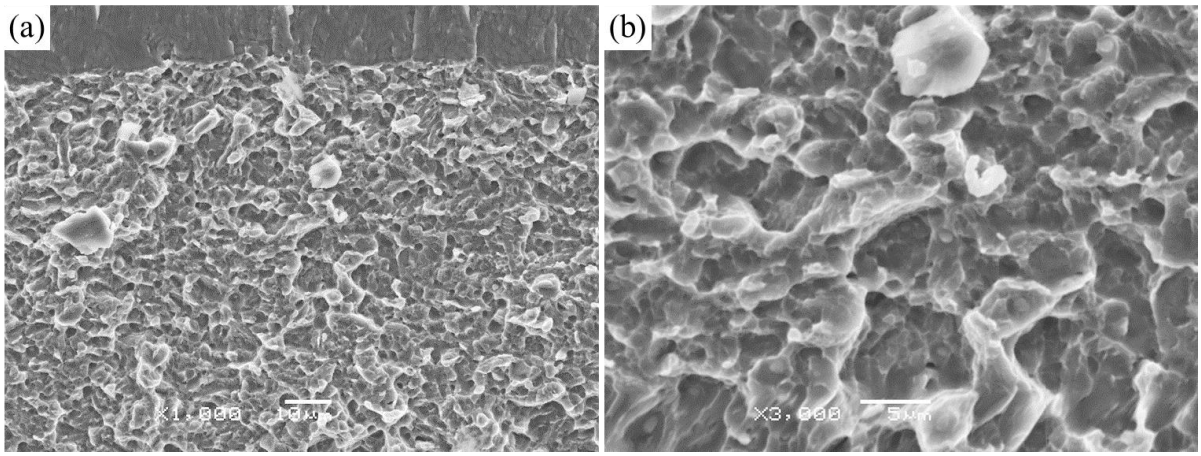

Figure D.53 (a) Low and (b) high magnification secondary electron images of the fracture surface of CP005L in fracture region. ($K_Q = 33.7$ MPa$\sqrt{\text{m}}$)

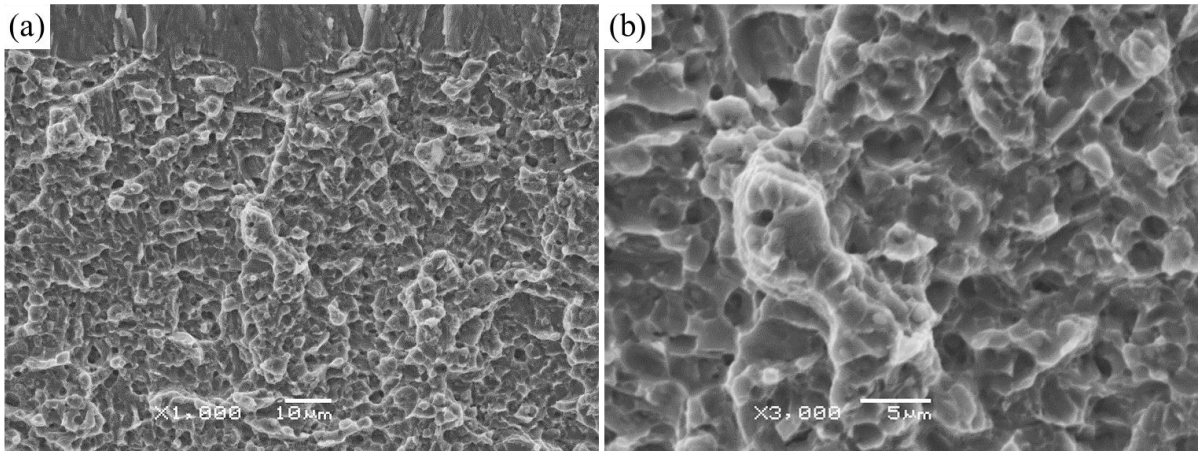

Figure D.54 (a) Low and (b) high magnification secondary electron images of the fracture surface of CP009L in fracture region. ($K_Q = 30.5$ MPa$\sqrt{\text{m}}$)

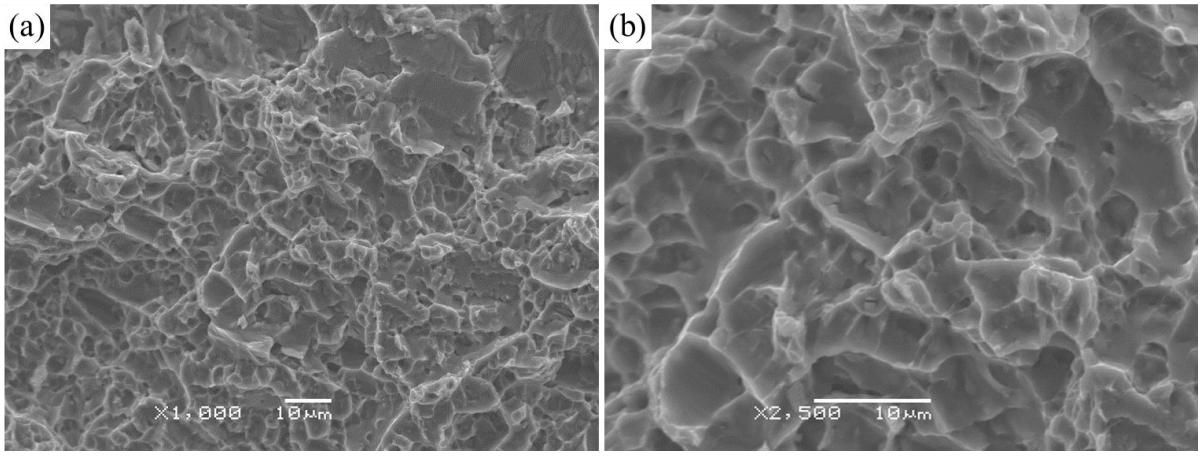

Figure D.55 (a) Low and (b) high magnification secondary electron images of the fracture surface of CP012 in fracture region. ($K_Q = 44.8$ MPa$\sqrt{\text{m}}$)

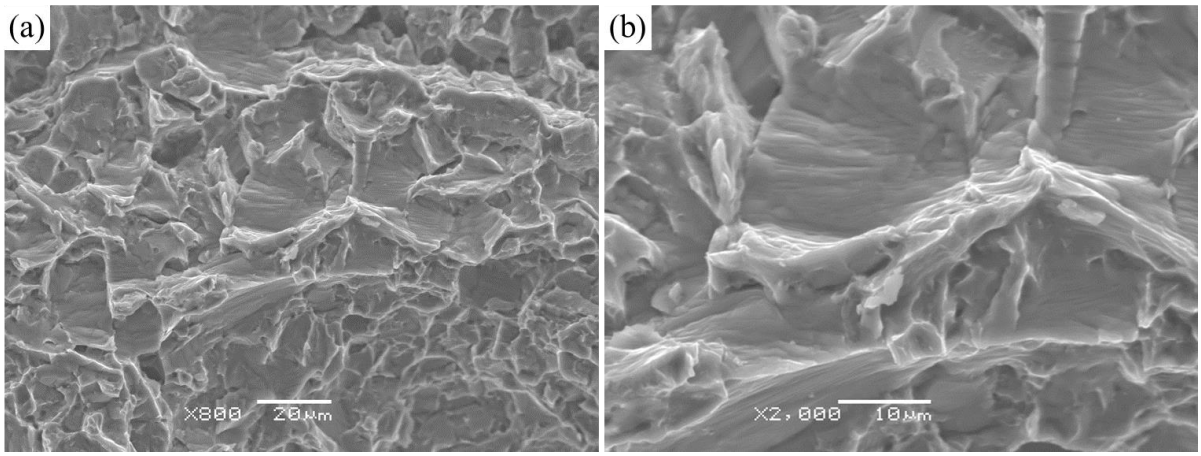

Figure D.56 (a) Low and (b) high magnification secondary electron images of the fracture surface of CP014 in fracture region. ($K_Q = 66.8$ MPa$\sqrt{\text{m}}$)

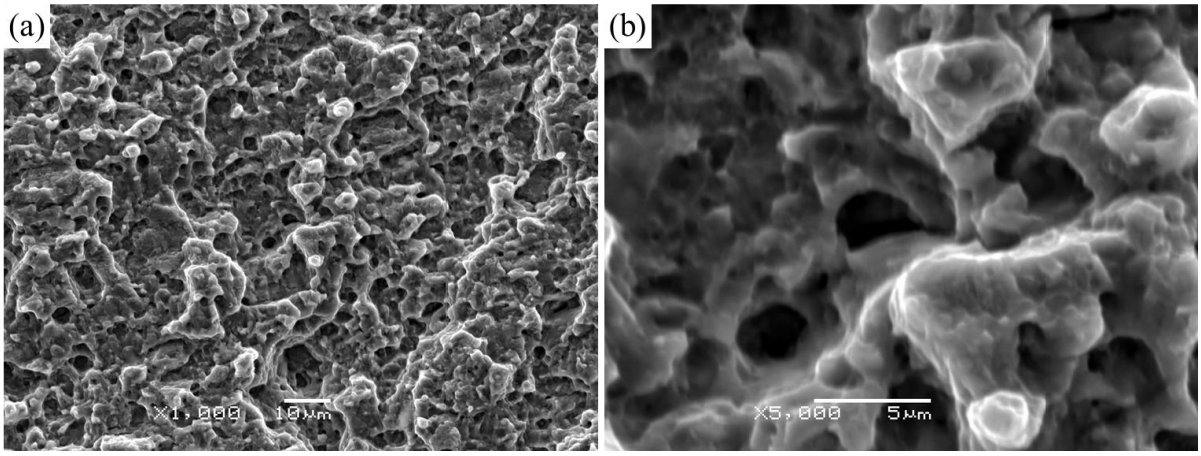

Figure D.57 (a) Low and (b) high magnification secondary electron images of the fracture surface of CP015L in fracture region. ($K_{max} = 31.0$ MPa$\sqrt{\text{m}}$)

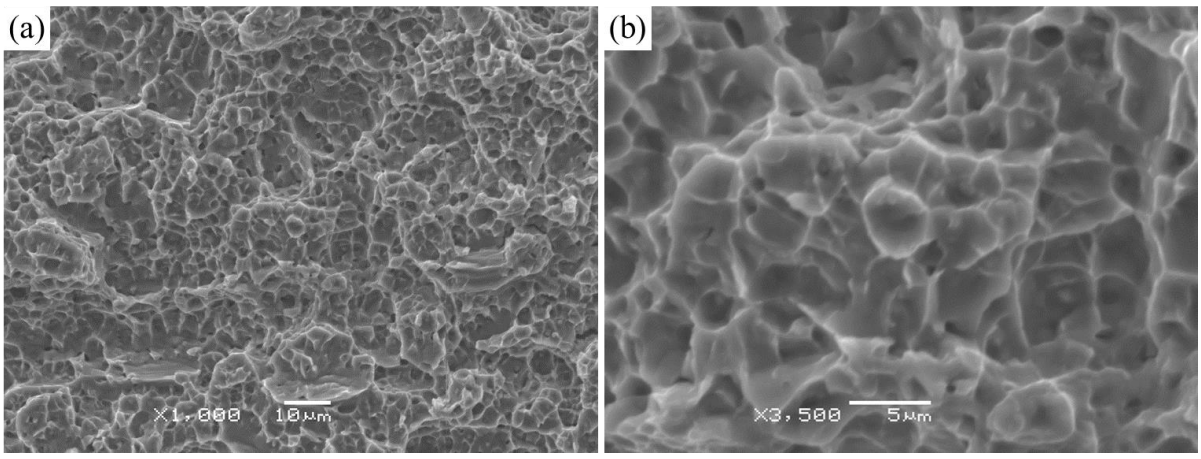

Figure D.58 (a) Low and (b) high magnification secondary electron images of the fracture surface of CP016L in fracture region. ($K_{max} = 50.3$ MPa$\sqrt{\text{m}}$)

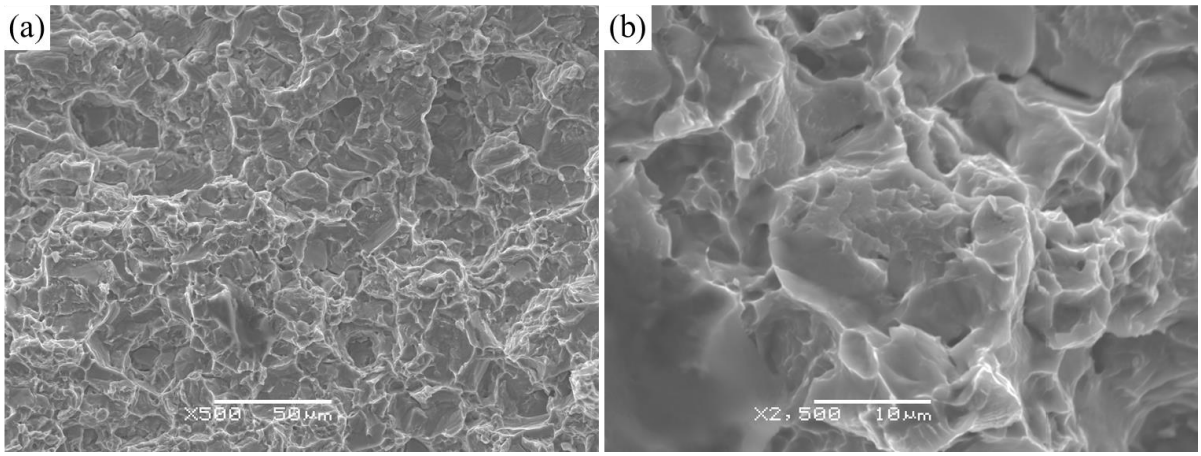

Figure D.59 (a) Low and (b) high magnification secondary electron images of the fracture surface of CP022R in fracture region. ($K_Q = 80.4$ MPa$\sqrt{\text{m}}$)

E Hard Alpha Particles in Linear Friction Welds

E.1 Introduction

In the realm of engineering, the performance of service components is subject to intricate loading conditions, which often include high-frequency vibrations leading to high cycle fatigue. The presence of a defect of appropriate size within a component can trigger the initiation of a fatigue crack. Subsequently, this crack progresses under the influence of high cycle fatigue, and once it reaches a critical length, it can result in catastrophic failure.

A notable incident that exemplifies the severity of such situations occurred on July 19, 1989, when United Airlines Flight 232, a McDonnell Douglas DC-10-10, tragically crash-landed in Sioux City, Iowa, claiming 112 lives. The root cause of this crash was identified as a fatigue crack that originated from a hard alpha metallurgical defect in the compressor disc, leading to the uncontained failure of the fan rotor disk assembly [1]. While literature exists on hard alpha defects originating from melt-related processes, there remains limited research characterising hard alpha defects arising from the welding process.

Consequently, as a direct response to this incident, manufacturing methods that may produce hard alpha defects have been refined, with particular emphasis on melting techniques. While there is substantial literature available on friction welding and titanium alloys, little attention has been directed towards defects produced during linear friction welding and their subsequent impact on mechanical properties.

The aim of this study is to extend our comprehension of hard alpha particles (HAPs) and fatigue behaviour in Ti-6Al-4V (Ti-64) self-similar linear friction welds in succession of previous works carried out by Dungey [2] and Nuttall [3].

E.2 Methods

E.2.1. Materials

Self-similar Ti-64 linear friction welds were studied in this research. All welds utilised in this study were supplied by Rolls-Royce plc. The desired weld upset, ranging from 0.2 to 0.8 mm, was targeted and closely monitored during the process, with the actual upset falling within a small range around the target value. It is worth noting that typical production welds in the industry often exhibit an upset exceeding 4 mm. In contrast, the low level of upset is deliberately employed in this research to promote higher amount of HAPs within the weld.

Throughout the study, all welds were produced under consistent process parameters, including a forging pressure of 80 MPa, a frequency of 45 Hz, and an amplitude of 2 mm. Following the welding process, a post-weld heat treatment at 600℃ for 1 hours was applied to the welds in vacuum, followed by gas fan quench. The post-weld heat treatment was employed to relieve residual stresses and recover toughness at the weld joint.

E.2.2. HAPs Distribution Analysis

Macro-slices and cylindrical test pieces were then machined from the weld blocks so that the weld was located in the middle of the gauge length, as illustrated in Figure E.1. Macro-slices were extracted using Electron Discharge Machining (EDM) for metallographic examination. The detailed metallographic sample preparation procedure can be found in Section 3.2.2.

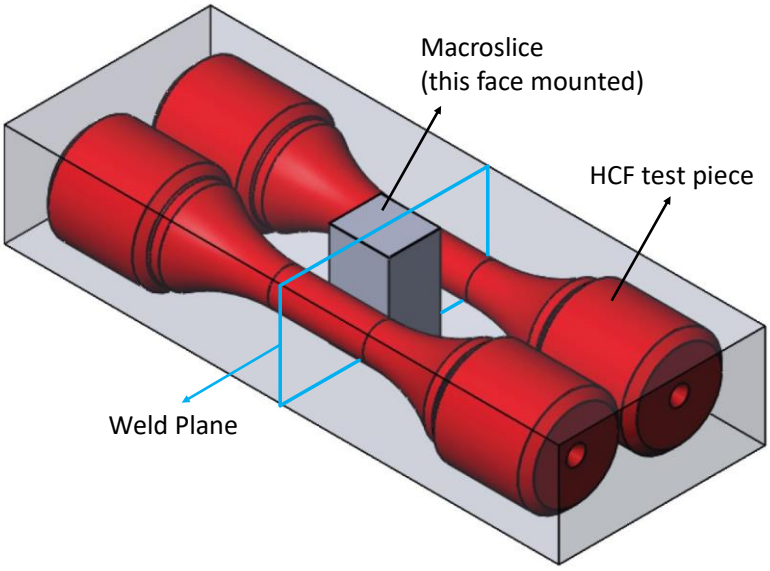

Figure E.1 Schematic diagram of sample extraction arrangement.

The amount and size of HAPs in the welds were assessed by inspecting the cross-section of the welds using optical microscope after etching. HAPs appear to have knots and trails appearance. Typical appearance of HAPs trails and HAPs knots are illustrated in Figure E.2 and Figure E.3, respectively. The HAPs distribution was quantified from two aspects: HAPs trail fraction and maximum HAPs knot size. The HAPs trail fraction is the proportion of the HAPs trails within the thickness of the weld, it can be expressed as

$$\text{HAPs trail fraction} = \frac{\sum l}{L} \tag{E.1}$$

where l is the length of a HAPs trail and L is the length of the weld cross-section. It should be noted that the HAPs trail fraction is estimated on an optical micrograph at low magnification (30x), this may overestimate the actual volume fraction of HAPs distributed at the weld interface.

The maximum HAPs knot size measured from the largest HAPs found under high magnification optical micrographs (1000x). HAPs located within 100 μm are considered as a continuous single HAPs, however, small HAPs with length lower than 10 μm are neglected

in this analysis. The welds with significantly high HAPs trail fraction and/or large HAPs knot size were selected for specific high cycle fatigue testing conditions.

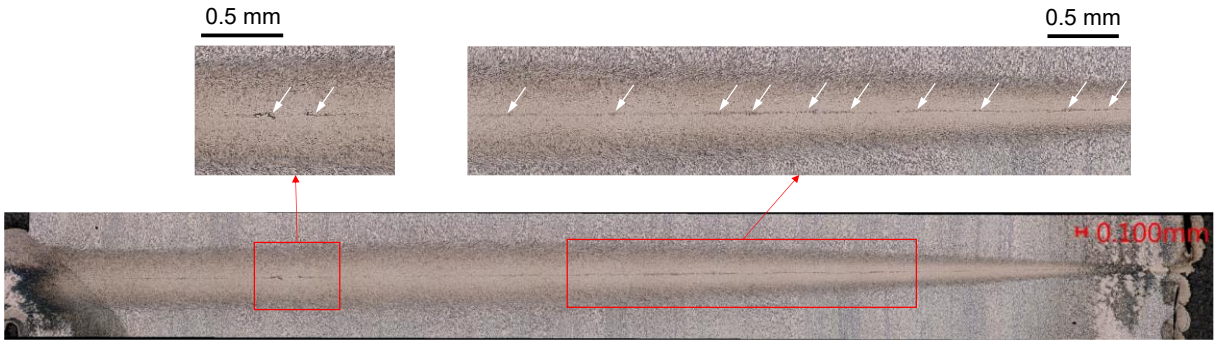

Figure E.2 Optical micrograph of the cross-section of sample 477-02. The HAPs at the weld interface are indicated by the white arrows.

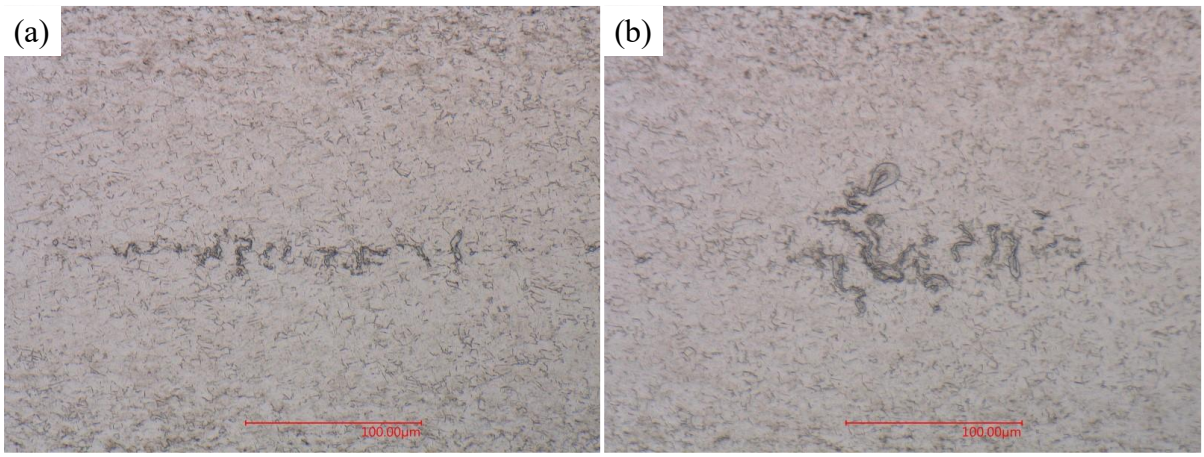

Figure E.3 Optical micrographs showing examples of HAPs in the form of (a) trail and (b) knot taken from sample 477-20.

E.2.3. High Cycle Fatigue Testing

Cylindrical test-pieces were used for high cycle fatigue testing. The experimental procedure of high cycle fatigue testing can be found in Section 3.3.5. The stress ratio R is either 0.2 or 0.3 for comparison with the previous results. The maximum stress σ_{max} used in the HCF tests are chosen depending on the theoretical minimum stress for HAPs failure, which is calculated as follows.

According to the failure mechanism proposed by Nuttall [3], a HAPs region can be divided into two zones: inner zone and intermediate zone. The inner zone is assumed to undergo a

cleavage fracture immediately after applying the load, as it appears like a flat facet on the fracture surface, hence it is considered that the fracture stress required to break the inner zone is far lower than the maximum applied stress σ_{max}. Consequently, the inner zone can be regarded as the initiation site of HAPs failures, and the size of the inner zone is recognised as the initial crack size. For the crack to break through the intermediate zone, the crack must meet the K_{max} criterion, which can be expressed as

$$K_{max} \geq K_{Ic}^{HAP} \tag{E.2}$$

where K_{Ic}^{HAP} is the fracture toughness of HAPs. The exact value of K_{Ic}^{HAP} has not been determined experimentally yet. Nuttall proposed that $K_{Ic}^{HAP} \approx 3.0\ \mathrm{MPa}\sqrt{\mathrm{m}}$ based on the fracture toughness calculated for the exposed HAPs after high cycle fatigue testing.

The intermediate region usually exhibits an elliptic shape on the fracture surface, hence it was modelled as an elliptical crack in an infinite body, as shown in Figure E.4. The stress intensity factor K of an elliptical crack can be expressed as [4]

$$K = \frac{\sigma(\pi a)^{1/2}}{\Phi}\left(\sin^2\beta + \frac{a^2}{c^2}\cos^2\beta\right)^{1/4} \tag{E.3}$$

where σ is the applied stresses, a and c are the minor and major radius of the ellipse, β is the angle describing the location on the crack border, as illustrated in Figure E.4. The maximum stress intensity factor K_{max} occurs when maximum stress σ_{max} is applied at the minor axis of the ellipse (i.e. $\beta = \pi/2$). Φ is the elliptic integral, it can be expressed as

$$\Phi = \int_0^{\pi/2}\left[1 - \frac{c^2 - a^2}{c^2}\sin^2\theta\right]^{1/2} d\theta \tag{E.4}$$

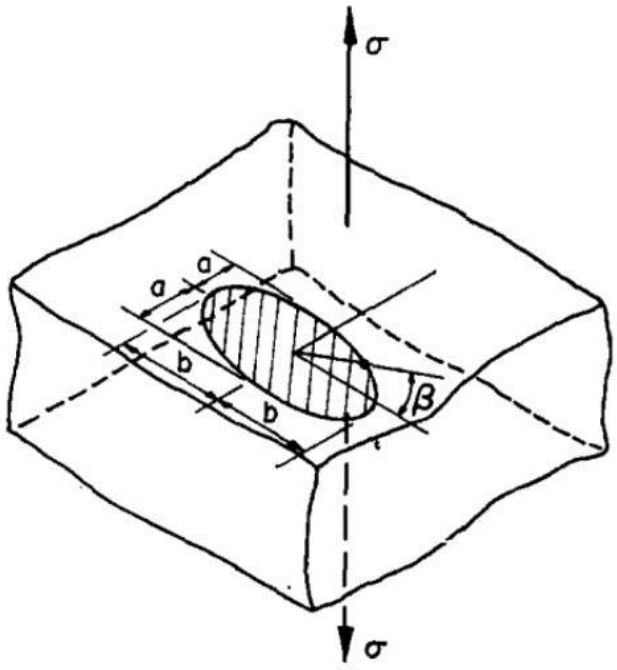

Figure E.4 An illustration of an elliptical crack in an infinite body subjected to uniform tension [4].

If the subjected stress intensity factor satisfies the K_{max} criterion, the crack can break through the intermediate zone. After the crack propagate through the entire HAPs, for it to keep propagate through the material, the subjected stress intensity factor range ΔK must meet the ΔK criterion, which is expressed as

$$\Delta K \geq \Delta K_{th} \tag{E.5}$$

where ΔK_{th} is the fatigue crack growth threshold.

The K_{max} and ΔK criteria with respect to the crack size and the applied stress are illustrated in Figure E.5 and Figure E.6. The largest HAPs found in Nuttall's study have an inner zone size of 95 μm. Following Figure E.5, the minimum σ_{max} to satisfy K_{max} criterion is

$$\sigma_{max} \geq 390 \text{ MPa} \tag{E.6}$$

The largest intermediate zone size found in Nuttall's study is 550 μm, following Figure E.6, e.g. at stress ratio $R = 0.2$, the required stress range $\Delta\sigma$ to satisfy ΔK criterion is approximately 230 MPa, which is equivalent to

$$\sigma_{max} \geq 287.5 \text{ MPa} \tag{E.7}$$

Since the K_{max} criterion is more restrictive than the ΔK criterion, the theoretical minimum stress required for HAPs failure is therefore determined as 390 MPa.

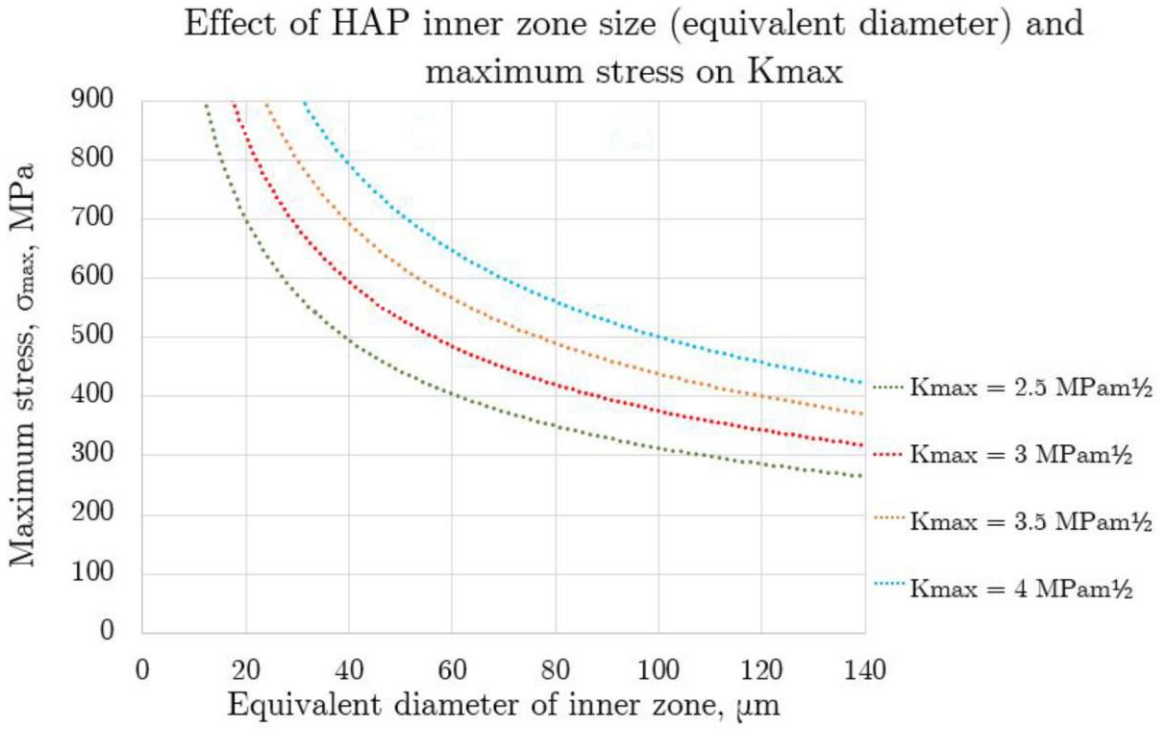

Figure E.5 A schematic showing the effect of inner zone size and maximum stress on K_{max} by plotting equivalent diameter of inner zone against maximum stress. A $K_{max} = 3.0$ MPa$\sqrt{\text{m}}$ is suggested for fracture to occur in the HAPs inner zone, shown by the red line. [3]

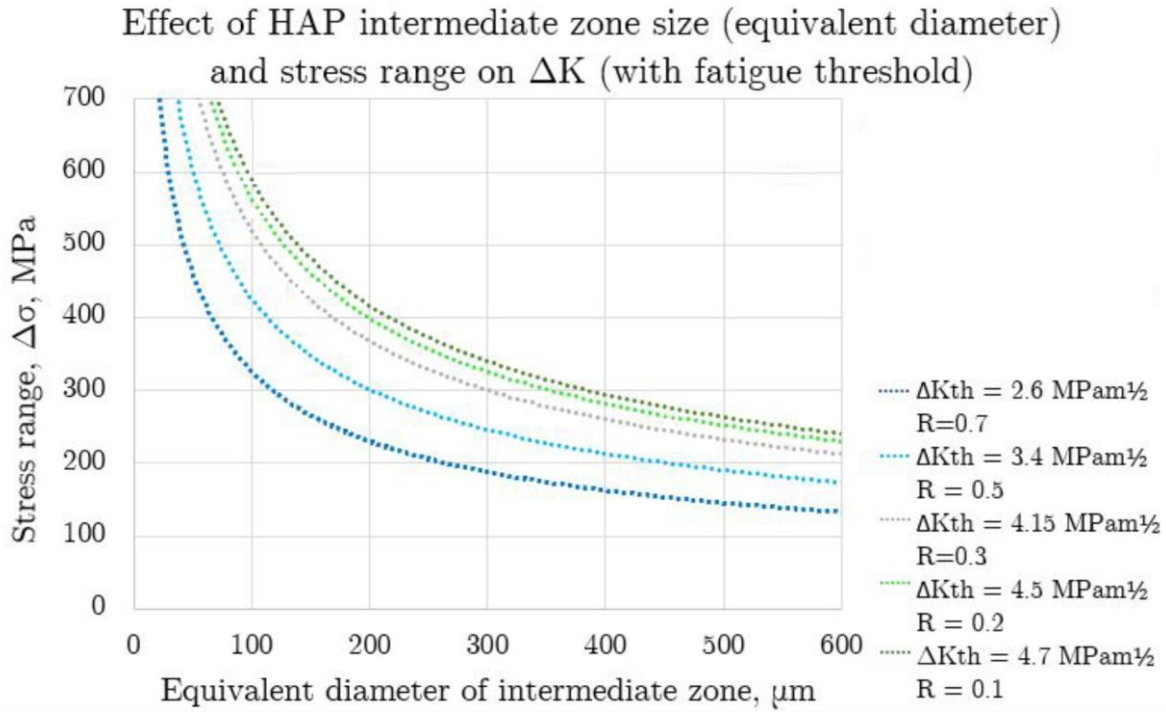

Figure E.6 A schematic showing the effect of intermediate zone size and stress range on ΔK_{th} by plotting equivalent diameter of inner zone against stress range. Lines of equal ΔK_{th} were plotted for penny shaped cracks at each of the threshold values for R = 0.1, 0.2, 0.3, 0.5 and 0.7. [3]

With the theoretical minimum σ_{max} and the HAPs distribution analysis results, the test pieces with significantly high HAPs trail fraction and/or large HAPs knot size were tested at lower range of stresses, specifically

$$350 \text{ MPa} \leq \sigma_{max} \leq 600 \text{ MPa} \tag{E.8}$$

in order to capture the minimum stress for HAPs failure experimentally. The test pieces with low volume fraction of HAPs and/or smaller HAPs were tested at higher range of stresses, specifically

$$800 \text{ MPa} \leq \sigma_{max} \leq 1000 \text{ MPa} \tag{E.9}$$

to establish the S-N curve of the test pieces. Higher stress also yields higher chance for HAPs failures as the two criteria proposed by Nuttall are easily satisfied and the HAPs crack is more likely to fracture before the parent material fails.

HAPs failures usually exhibit a debit in life compared to parent failures. The debit in life was calculated as a percentage of expected parent life, as

$$\text{Debit in life } (\%) = \frac{\text{parent life} - \text{weld life}}{\text{parent life}} \times 100\% \tag{E.10}$$

where parent life is the lowest number of cycles completed at the tested stress by a parent failure, weld life is the number of cycles completed by the weld failure.

According to the established S-N curve in this study, it was found that testing at lower range of stresses tend to run out after 1.5x10^7 cycles. It was assumed that the damage accumulated in the test pieces at such low stress was not sufficient to cause a premature parent failure in the succeeding tests. Therefore, the test pieces were firstly tested at $\sigma_{max} = 350$ MPa, if the test pieces ran out, then they would undergo another HCF testing at a 50 MPa higher stress. If the test piece keeps running out, it will be repeatedly tested each time with higher stress until it fails or 500 MPa is reached. The assumption was proven true since all test pieces run out after the series of HCF testing from 350 MPa to 500 MPa.

After the test pieces run out at 500 MPa, a notch with 0.2 mm depth was put into the weld by electrical discharge machining, and then it was pre-cracked at $\sigma_{max} = 850$ MPa with $R = 0.3$ for 1000 cycles, finally a monotonic tensile loading was applied to break open the test piece. This procedure promotes crack propagating along the HAPs in the welds, therefore the HAPs have higher chance to be exposed on the fracture surfaces.

E.2.4. Combination Criteria

On the fracture surfaces of the high cycle fatigue test pieces, it is often observed that multiple HAPs regions are located in proximity. As the inner zone of a HAPs region is considered as an embedded elliptic crack, multiple co-planar cracks in close proximity can lead to an interaction and to more severe effects than single cracks alone. The combination criteria and interaction rules for co-planar embedded cracks are given by British Standard BS-7910 [5]. A selection of relevant combination criteria and interaction rules are listed in Table E.1. If

multiple flaws exist, each flaw should be checked for interaction with each of its neighbouring flaws using the original flaw dimensions.

Table E.1 Interaction rules for embedded co-planar flaws.

Schematic flaws	Criteria for interaction	Effective dimensions after interaction
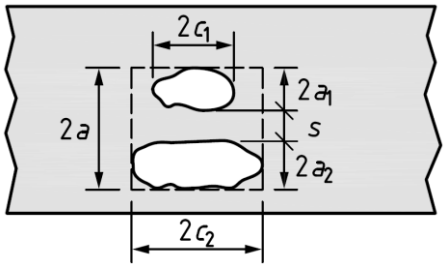	$s \leq a_1 + a_2$	$2a = 2a_1 + 2a_2 + s$ $2c = \max(2c_1, 2c_2)$
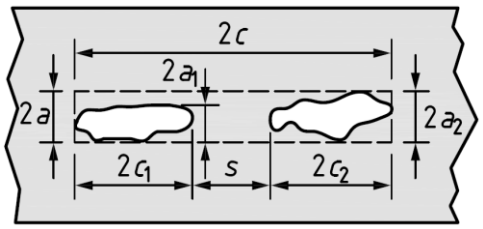	$s \leq \max(a_1, a_2)$ for all flaws	$2a = \max(2a_1, 2a_2)$ $2c = 2c_1 + 2c_2 + s$
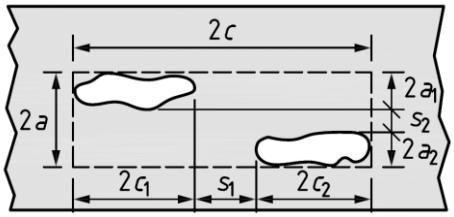	$s_1 \leq \max(a_1, a_2)$ for all flaws $s_2 \leq a_1 + a_2$	$2a = 2a_1 + 2a_2 + s_2$ $2c = 2c_1 + 2c_2 + s_1$

E.2.5. Fractography

After the fracture surfaces of the welds were exposed, the fracture surfaces were examined by optical and electron microscopes. The examination specifically focused on searching for the HAPs within the initiation site. Low-magnification optical macrographs and high-magnification secondary electron images were used to identify the initiation site on a fracture surface, by tracing the river pattern resulting from a brittle fracture back to the initiation facet. If HAPs were found, the size of the HAPs was measured for theoretical calculations.

The methods of optical microscopy and scanning electron microscopy is mentioned in Section 3.2.3 and 3.2.4.

E.3 Results

E.3.1. HAPs Distribution

The HAPs distribution analysis in all 30 macro-slices in terms of HAPs trail fraction and maximum HAPs knot size is listed in Table E.2. Figure E.7 illustrates the relationship between upset and HAPs distribution.

The HAPs distribution suggests that an upset value less than 0.5 mm tend to yield higher HAPs volume fraction and larger HAPs size in the weld. Test pieces with both large HAPs and high HAPs volume fractions are selected for high cycle fatigue testing at low stresses (350-600 MPa), others are used for testing at high stresses (800-1000 MPa).

Table E.2 HAPs distribution analysis results.

Sample ID (PDR477-)	Upset (mm)	HAPs trail fraction	Max HAPs knot size (μm)
001	0.39	48%	94
002	0.20	78%	130
003	0.27	47%	0
004	0.20	69%	84
005	0.29	56%	405
006	0.19	14%	32
007	0.19	58%	269
008	0.23	37%	125
009	0.25	46%	86
010	0.26	32%	0
011	0.56	0%	30
012	0.21	41%	206
013	0.36	71%	257
014	0.61	17%	0
015	0.44	77%	197
016	0.42	33%	0
017	0.23	67%	261
018	0.28	64%	590
019	0.30	45%	179
020	0.28	48%	171
021	0.70	0%	0
022	0.45	50%	121
023	0.49	71%	302
024	0.28	16%	0
025	0.31	79%	0
026	0.27	44%	0
027	0.22	13%	0
028	0.20	67%	256
029	0.85	13%	60
030	0.28	38%	269

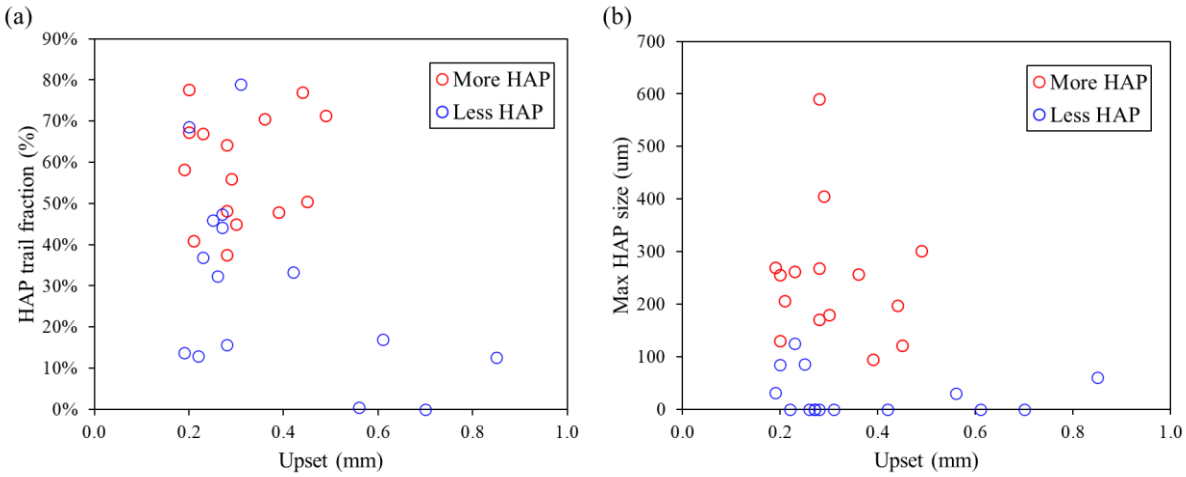

Figure E.7 HAPs statistic results showing (a) HAPs trail fraction and (b) maximum HAPs knot size with respect to upset. Samples with both large HAPs trail fraction and large maximum HAPs knot size are shown in red.

E.3.2. High Cycle Fatigue

The results of high cycle fatigue testing in the current study are listed in Table E.3 and presented in Figure E.8. Test pieces with low HAPs content are tested at high stresses (800-1000 MPa), one test piece (HF010) failed at the weld interface, all other test pieces failed in the parent material. The S-N curve is established from the best fit of the parent failures data. Test pieces with high HAPs content are tested at low stresses (350-600 MPa), to investigate the lowest σ_{max} for the occurrence of HAPs failures. Test pieces ran out after completing 1.5×10^7 cycles and was tested multiple times at higher stress levels. However, no HAPs failure has been observed in a total of 16 test pieces.

Table E.3 High cycle fatigue testing results.

Test piece ID (HF-)	Upset (mm)	R	σ_{max} (MPa)	Cycles completed	Failure location
001	0.39	0.2	500	1.50×10^7	Run out
002	0.20	0.2	500	1.50×10^7	Run out
003	0.27	0.2	500	1.46×10^7	Run out
004	0.20	0.3	800	4.50×10^5	Parent
005	0.29	0.2	450	1.50×10^7	Run out
005	0.29	0.2	500	1.50×10^7	Run out
007	0.19	0.2	350	1.45×10^7	Run out
007	0.19	0.2	400	1.50×10^7	Run out
007	0.19	0.2	450	1.50×10^7	Run out
007	0.19	0.2	500	1.50×10^7	Run out
009	0.25	0.3	900	2.71×10^5	Parent
010	0.26	0.3	1000	1.24×10^4	Weld
011	0.56	0.3	1000	3.32×10^4	Parent
012	0.21	0.2	500	1.50×10^7	Run out
013	0.36	0.2	350	1.44×10^7	Run out
013	0.36	0.2	400	1.50×10^7	Run out
013	0.36	0.2	450	1.50×10^7	Run out
013	0.36	0.2	500	1.50×10^7	Run out
014	0.61	0.3	950	8.83×10^4	Parent
015	0.44	0.2	500	1.50×10^7	Run out
016	0.42	0.3	1000	3.13×10^4	Parent
017	0.23	0.2	350	1.50×10^7	Run out
017	0.23	0.2	400	1.50×10^7	Run out
017	0.23	0.2	450	1.50×10^7	Run out
017	0.23	0.2	500	1.50×10^7	Run out
017	0.23	0.3	850	8.42×10^5	Parent
018	0.28	0.2	600	1.10×10^7	Parent
019	0.30	0.2	500	1.50×10^7	Run out
020	0.28	0.2	500	1.50×10^7	Run out
021	0.70	0.3	850	6.80×10^5	Parent
022	0.45	0.2	500	1.50×10^7	Run out
023	0.49	0.2	450	1.50×10^7	Run out
023	0.49	0.2	500	1.50×10^7	Run out
024	0.28	0.3	950	6.29×10^4	Parent
025	0.31	0.2	500	1.42×10^7	Run out
026	0.27	0.2	500	1.50×10^7	Run out
027	0.22	0.3	900	4.04×10^5	Parent
028	0.20	0.2	500	1.50×10^7	Run out
030	0.28	0.2	500	1.50×10^7	Run out

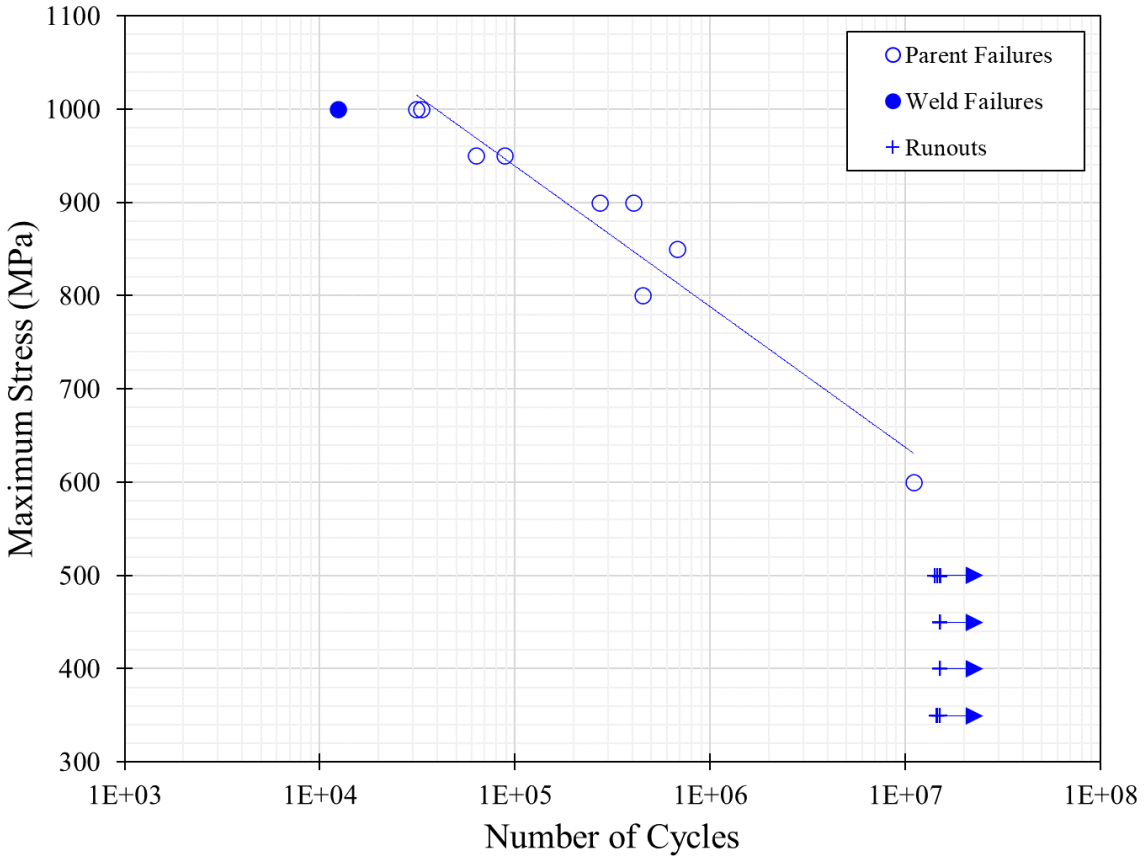

Figure E.8 High cycle fatigue testing results of HAPs test pieces. The lines indicate the best fit of the parent failures data.

E.3.3. Fractography

The fracture surfaces of the high cycle fatigue test pieces with a weld failure or were successfully broke open at the weld interface are examined by an optical microscope and a scanning electron microscope, all the images are shown in Figure E.9 to Figure E.17. HAPs regions can be identified as the bright spots under an optical microscope, since they are relatively flat compared to the fracture surface of the weld interface, hence they reflect the co-axial light directly into the camera. The discovered HAPs regions are embedded in the test pieces in an elliptic shape, therefore the stress intensity factor K of the HAPs regions can be calculated from Equation (E.3). Combination criteria was used for HAPs regions in Figure E.16 and Figure E.17 as they are located in close proximity. The results are listed in Table E.4. All other fracture surfaces can be found in Section E.7.

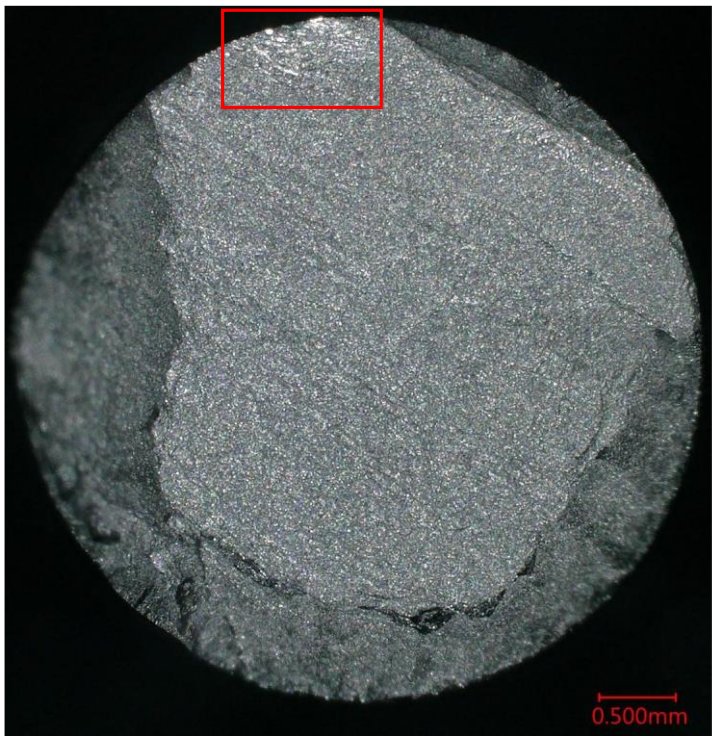

Figure E.9 Optical micrograph of the fracture surface of HF010. The initiation site is marked in the red box.

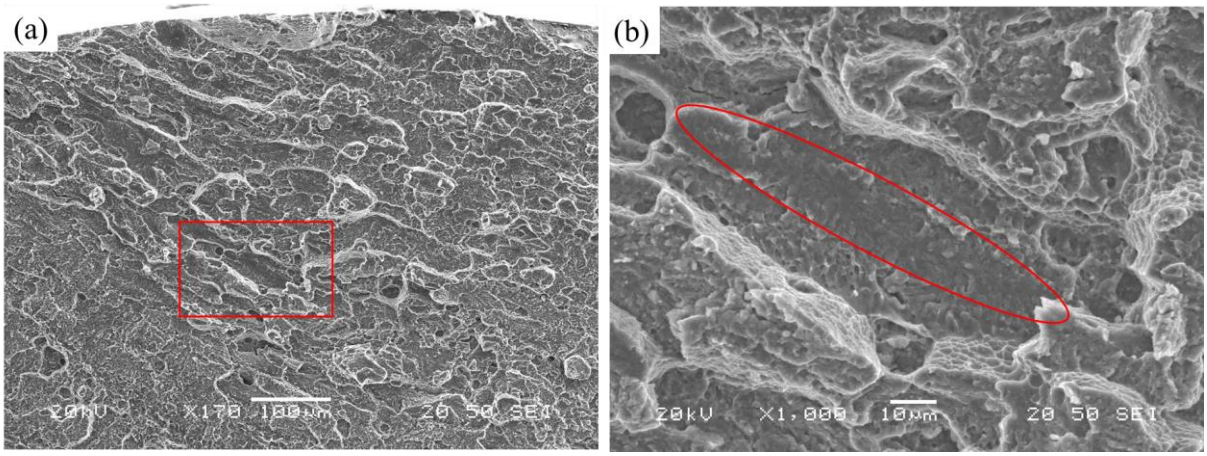

Figure E.10 Secondary electron images of (a) the initiation site in HF010 and (b) a close-up view of a HAPs found in this region. The inner zone is marked by the red ellipse.

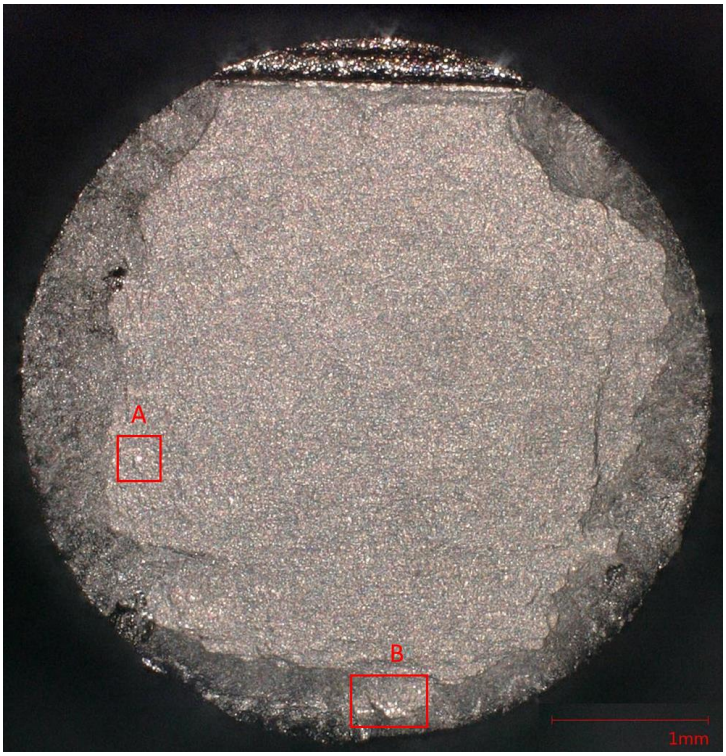

Figure E.11 Optical macrograph of the break-open fracture surface of HF003. The location of discovered HAPs is marked in the red box.

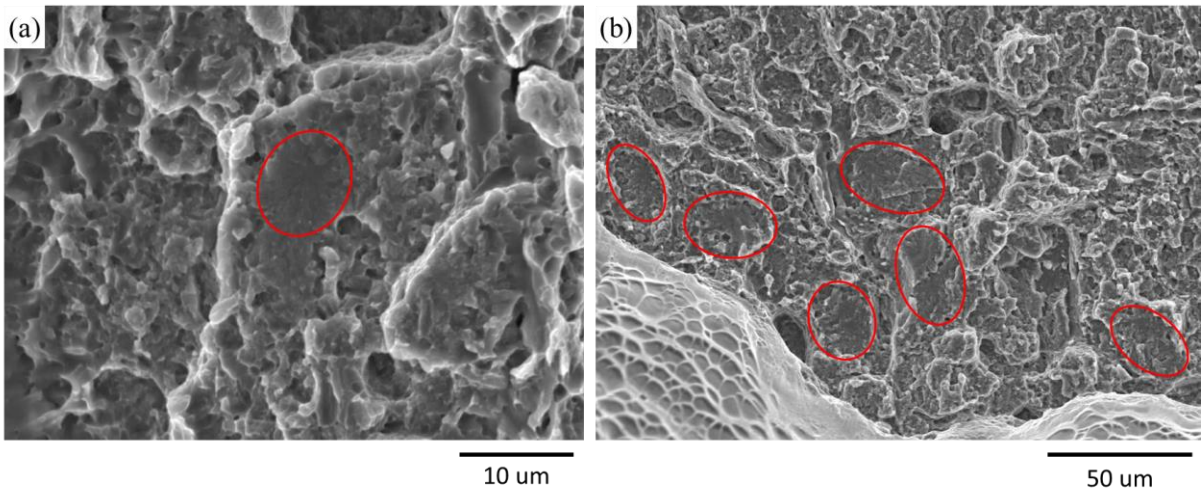

Figure E.12 Secondary electron images of HAPs found in (a) region A and (b) region B in HF003. The inner zone is marked by the red ellipse.

Figure E.13 Optical macrograph of the break-open fracture surface of HF022. The location of discovered HAPs is marked in the red box.

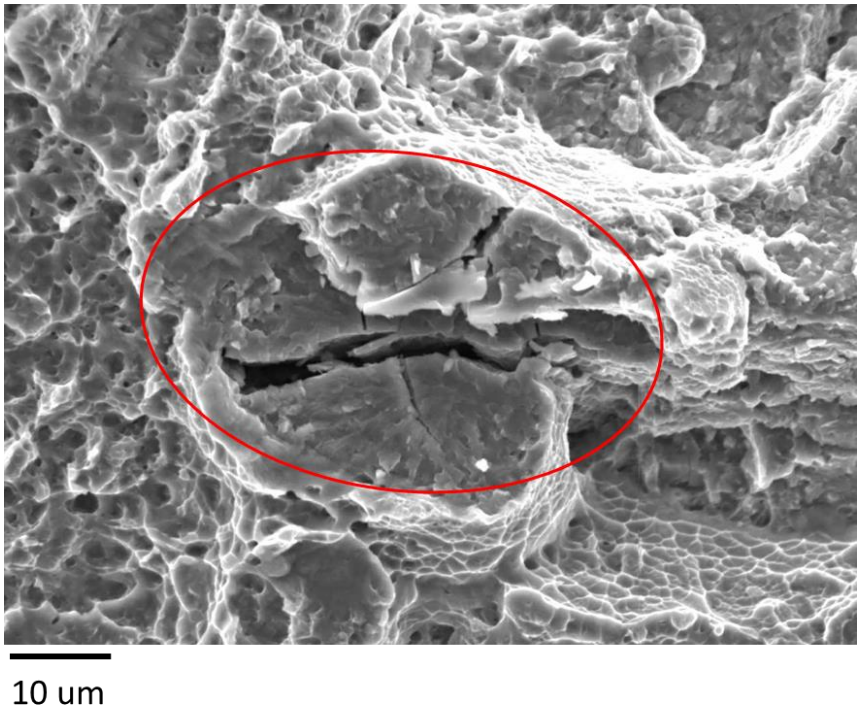

Figure E.14 Secondary electron images of HAPs found in HF022. The inner zone is marked by the red ellipse.

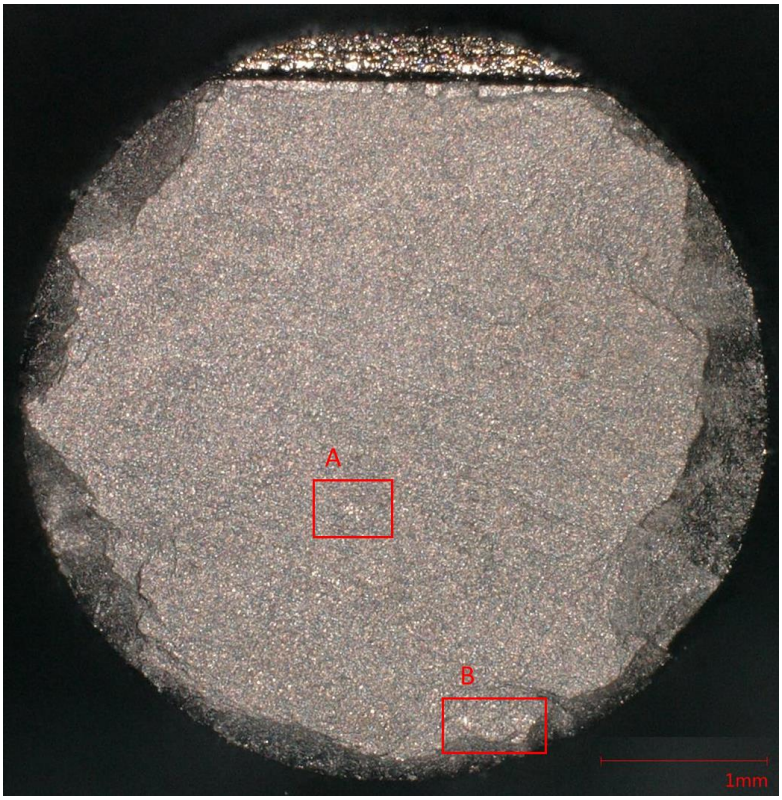

Figure E.15 Optical macrograph of the break-open fracture surface of HF026. The location of discovered HAPs is marked in the red box.

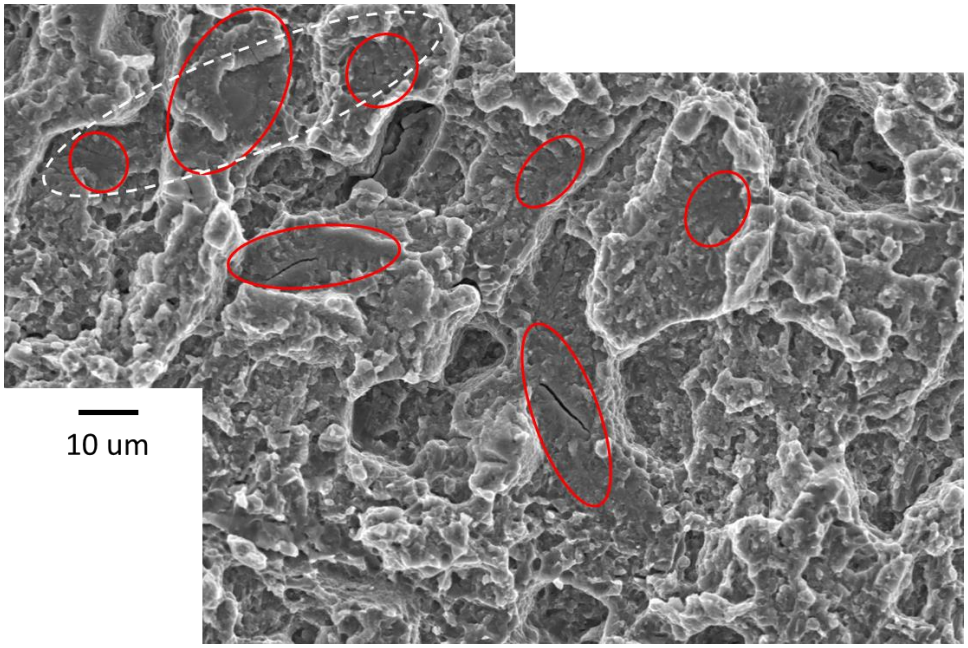

Figure E.16 Secondary electron images of HAPs found in region A in HF026. The inner zone is marked by the red ellipse. The HAPs regions inside white dash ellipse satisfies the combination criteria.

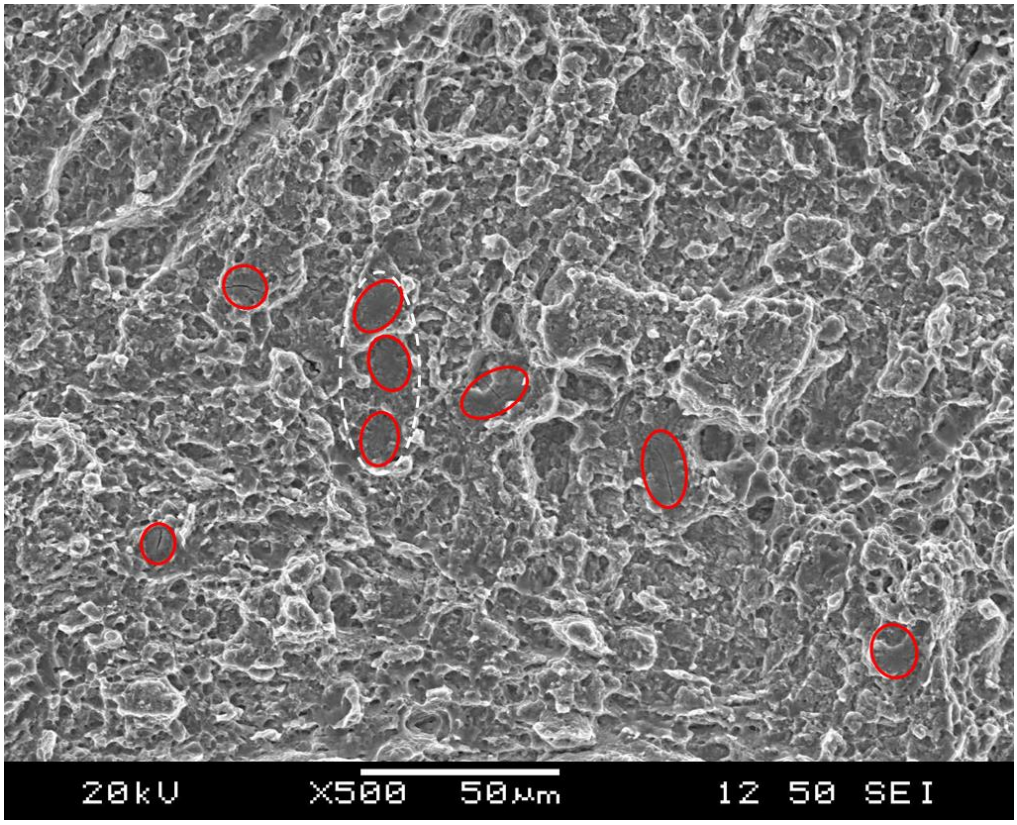

Figure E.17 Secondary electron images of HAPs found in region B in HF026. The inner zone is marked by the red ellipse. The HAPs regions inside white dash ellipse satisfies the combination criteria.

Table E.4 List of stress intensity factor and stress intensity factor range for the largest HAPs inner zone size found on the fracture surfaces.

Test-piece ID (HF-)	σ_{max} (MPa)	R	N_f	Failure location	Debit	2c x 2a (µm)	K_{max} (MPa$\sqrt{m}$)	ΔK (MPa$\sqrt{m}$)
010	1000	0.3	1.24×10^{-4}	Weld	60%	139x15	4.7	3.3
003	500	0.2	1.46×10^{-7}	Run out	N/A	27x14	1.9	1.5
022	500	0.2	1.50×10^{-7}	Run out	N/A	54x36	2.8	2.3
026	500	0.2	1.50×10^{-7}	Run out	N/A	47x42	2.7	2.2

E.4 Discussion

Including the previous studies from Dungey [2] and Nuttall [3], a total of 16 HAPs failures have been documented to date, as listed in Table E.5. The high cycle fatigue testing results plotted using maximum stress σ_{max} are presented in Figure E.18. The lowest observed σ_{max} resulting in a HAPs failure is 550 MPa, which are corresponding to at least one relatively large HAPs inner zone within the test pieces, e.g. 80x60 in HF010 in Dungey's study. With

a common HAPs size and distribution, a σ_{max} of at least 775 MPa is required. Since HAPs failures exhibit a strong correlation with the size of HAPs regions, it is more effective to use the stress intensity factor K to characterise them. As Equation (E.2) suggests that the applied K_{max} must exceed K_{Ic}^{HAP} to trigger HAPs failure, the upper limit of K_{Ic}^{HAP} can be estimated by identifying the lowest observed K_{max} which resulted in a HAPs failure. The lowest observed K_{max} for all HAPs failures is 3.0 MPa$\sqrt{\text{m}}$, e.g. HF011 in Nuttall's study.

Table E.5 List of the stress intensity factor and stress intensity factor range of the largest HAPs inner zone size found on the fracture surfaces for all HAPs failures. Results from previous studies [2], [3] are also included.

Test-piece ID	Upset (mm)	σ_{max} (MPa)	R	Life (N_f)	Failure location	Debit	2c x 2a (μm)	K_{max} (MPa$\sqrt{\text{m}}$)	ΔK (MPa$\sqrt{\text{m}}$)
Dungey [2]									
LF013	1.52	780	0	7.97×10^{-3}	Weld	90%	25x25	3.1	3.1
LF009	0.47	800	0	1	Weld	100%	300x200	11.3	11.3
HF010	1.04	550	0.2	7.25×10^{-4}	Weld	90%	80x60	4.0	3.2
MM021	1.21	550	0.2	5.24×10^{-5}	Weld	50%	60x40	3.5	2.8
MM033	1.33	900	0.22	8.23×10^{-3}	Weld	60%	20x20	3.2	2.6
Nuttall [3]									
HF074	0.50	550	0.2	2.46×10^{-5}	Weld	63%	88x25	3.2	2.5
HF007	0.25	775	0.3	1.30×10^{-5}	Weld	9%	70x15	3.6	2.5
HF011	0.18	775	0.3	1.03×10^{-5}	Weld	28%	70x10	3.0	2.1
HF004	0.20	850	0.3	6.40×10^{-4}	Weld	0%	30x14	3.3	2.3
HF008	0.25	850	0.3	7.50×10^{-3}	Weld	88%	60x50	5.2	3.7
HF009	0.20	850	0.3	1.10×10^{-5}	Weld	0%	30x10	3.0	2.1
HF012	0.18	850	0.3	2.26×10^{-4}	Weld	65%	40x10	3.1	2.2
HF020	0.45	850	0.3	7.42×10^{-4}	Weld	0%	50x10	3.2	2.2
HF086	0.36	850	0.3	3.40×10^{-3}	Weld	95%	100x90	6.8	4.7
HF014	0.17	850	0.7	1.52×10^{-5}	Weld	92%	110x13	3.8	1.1
Current study									
HF010	0.26	1000	0.3	1.24×10^{-4}	Weld	60%	139x15	4.7	3.3

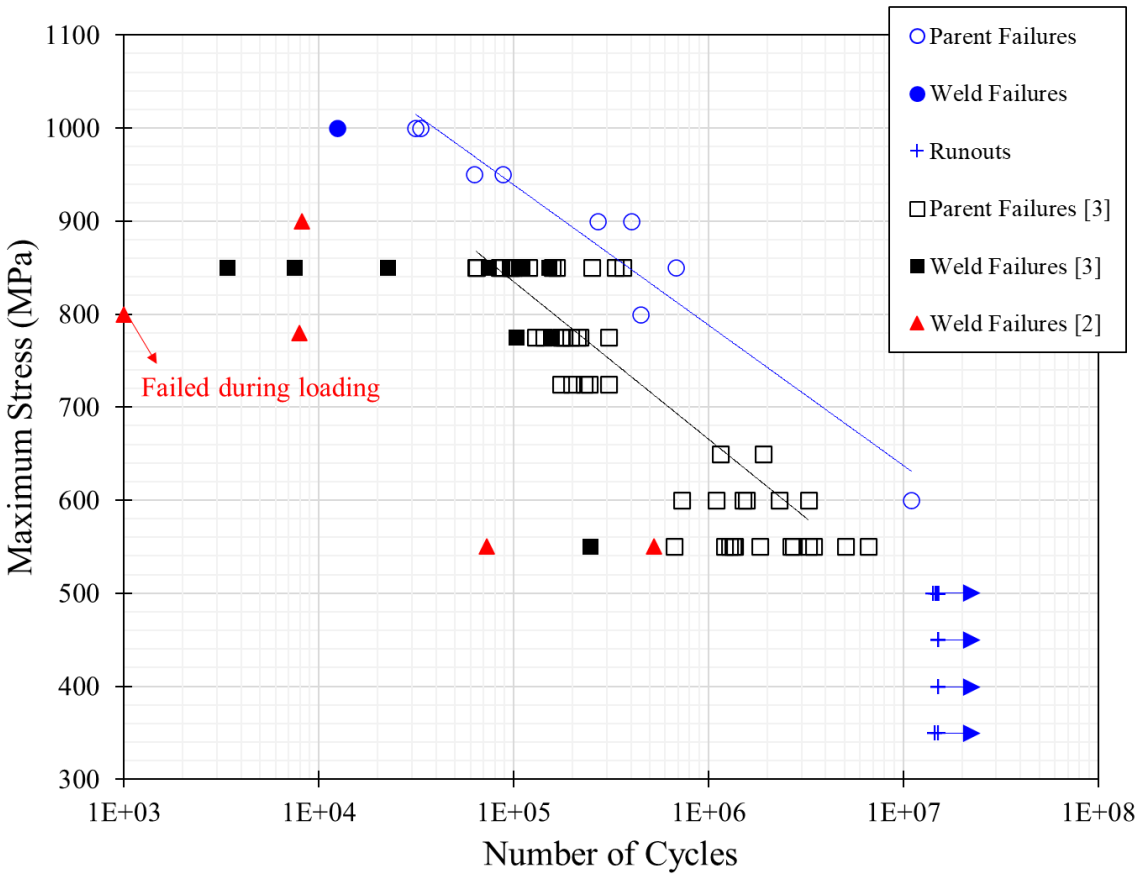

Figure E.18 High cycle fatigue testing results of HAP test pieces. Results from previous studies [2], [3] are also included. The lines indicate the best fit of the parent failures data.

In the current and Nuttall's studies, efforts have been made to expose the HAPs regions in the parent failures and runout test pieces, the results are listed in Table E.6. As Equation (E.2) suggests that the applied K_{max} must exceed K_{Ic}^{HAP} to trigger HAPs failure, it implies that in break-open test pieces, the applied K_{max} should be kept below K_{Ic}^{HAP} to prevent HAPs failures from occurring. Therefore, the lower limit of K_{Ic}^{HAP} can be estimated by identifying the largest observed K_{max} which did not result in a HAPs failure. In Nuttall's study of HF077, this K_{max} value is 3.2 MPa$\sqrt{\text{m}}$. Note that the estimated lower limit of K_{Ic}^{HAP} is slightly greater than the estimated upper limit (3.0 MPa$\sqrt{\text{m}}$). This suggests that there may be other factors preventing HAPs failure in HF077. It is reasonable to assume that when the applied K_{max} exceeds 3.0 MPa$\sqrt{\text{m}}$, the probability of HAPs failure increases,

but it may not necessarily result in HAPs failure, at least when the applied K_{max} is lower than 3.2 MPa$\sqrt{\text{m}}$. As the estimated upper limit of K_{Ic}^{HAP} is 3.0 MPa$\sqrt{\text{m}}$ and there are five observations with K_{max} approximately 3.0 MPa$\sqrt{\text{m}}$ that did not lead to HAPs failures, it is reasonable to assume that the value of K_{Ic}^{HAP} is likely in close proximity to 3.0 MPa$\sqrt{\text{m}}$.

Table E.6 List of stress intensity factor and stress intensity factor range for the largest HAPs inner zone size found in the break-open test pieces. Results from previous studies [3] are included.

Test-piece ID (HF-)	σ_{max} (MPa)	R	N_f	Failure location	Debit	2c x 2a (μm)	K_{max} (MPa$\sqrt{\text{m}}$)	ΔK (MPa$\sqrt{\text{m}}$)
Current study								
003	500	0.2	1.46×10^{-7}	Run out	N/A	27x14	1.9	1.5
022	500	0.2	1.50×10^{-7}	Run out	N/A	54x36	2.8	2.3
026	500	0.2	1.50×10^{-7}	Run out	N/A	47x42	2.7	2.2
Nuttall [3]								
066	550	0.2	1.80×10^{-6}	Parent	N/A	70x25	3.1	2.5
072	550	0.2	2.74×10^{-6}	Parent	N/A	58x20	2.8	2.2
077	550	0.2	1.21×10^{-6}	Parent	N/A	80x28	3.2	2.6

It is of interest to investigate the critical HAPs size for HAPs failures when σ_{max} is 350 MPa, which is close to the in-service stress condition. Figure E.19 illustrates the effect of σ_{max} and HAPs inner zone size on K_{max} for both circular and elliptic HAPs regions. An aspect ratio of four was selected for the elliptic HAPs regions as it is representative for the typical observed HAPs regions. In the case of circular HAPs regions, at $\sigma_{max} =$ 350 MPa, the critical HAPs inner zone size required to achieve $K_{max} = 3.0$ MPa$\sqrt{\text{m}}$ is 115x115 μm. For elliptic HAPs regions with an aspect ratio of four, a size of 215x54 μm is required. Among all the observed HAPs failures, only the HAPs region with dimensions of 300x200 μm in LF009, as documented in Dungey's study, is vulnerable to failure when subjected to a maximum stress of 350 MPa.

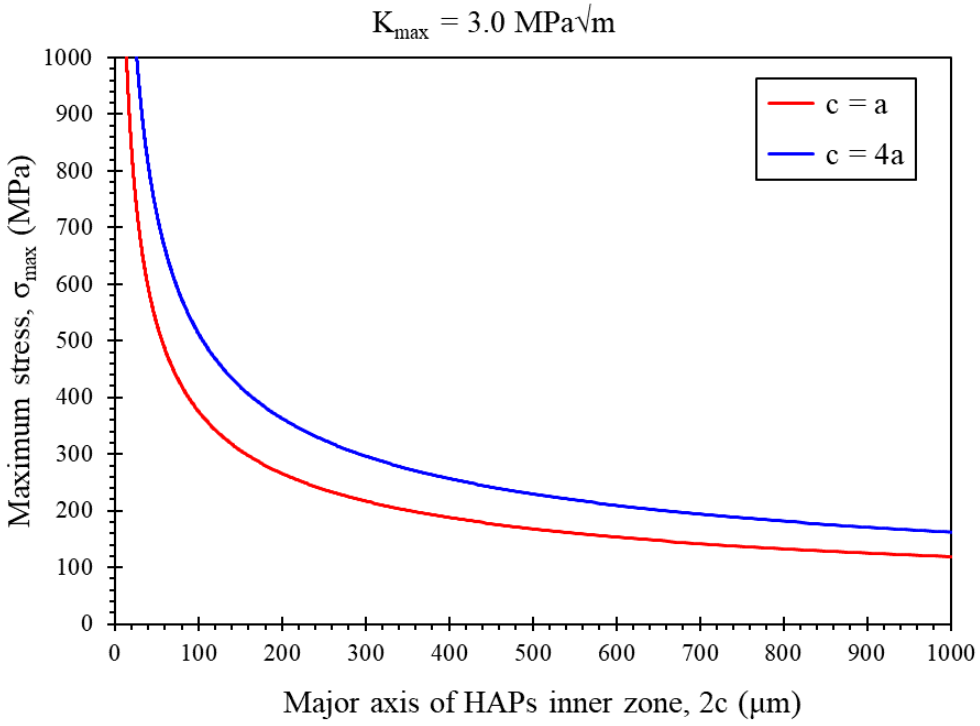

Figure E.19 A chart illustrating the effect of HAPs inner zone size and σ_{max} on K_{max}, with the $K_{max} = 3.0$ MPa$\sqrt{\text{m}}$ contour highlighted. Circular HAPs regions are represented by the red line, while elliptical HAPs regions with an aspect ratio of 4 are indicated by the blue line.

E.5 Conclusions

1. The relationship between upset and HAPs distribution was studied by examination of macro-slices cross-sections. The results indicates that lower upset values (less than 0.5 mm) tend to yield higher volume fraction and larger HAPs regions.

2. High cycle fatigue testing was focused on σ_{max} values between 350 to 600 MPa at stress ratio $R = 0.2$. No HAPs failure has been observed in a total of 16 test pieces. Fractography of the break-open test pieces suggests that the size of the exposed HAPs regions is smaller than the ones found in the previous studies from Dungey and Nuttall. The lowest observed σ_{max} resulting in a HAPs failure still remains at 550 MPa.

3. HAPs failures are considered highly associated with both the applied σ_{max} and the inner zone size and can be characterised by K_{Ic}^{HAP}. The value of K_{Ic}^{HAP} is estimated at approximately 3.0 MPa$\sqrt{\text{m}}$ by high cycle fatigue testing results.

4. According to the estimated K_{Ic}^{HAP} value, the critical HAPs size at $\sigma_{max} = 350$ MPa is 115x115 μm for circular HAPs regions, or 215x54 μm for elliptic HAPs regions. Based on the extensive high cycle fatigue testing conducted in both previous and current studies, it is uncommon to encounter such large HAPs regions within linear friction welded joints.

E.6 References

[1] National Transportation Safety Board, "Aircraft Accident Report - United Airlines Flight 232, McDonnell Douglas DC-10-10, Sioux Gateway Airport, Sioux City, Iowa, July 19, 1989.," Washington, D.C., NTSB/AAR-90/06, 1990.

[2] C. Dungey, "The Influence of Process History & Defect Type on the Fatigue Behaviour of Ti-6Al-4V under Complex Aeroengine Load Regimes," University of Birmingham, 2006.

[3] E. Nuttall, "Characterisation and Assessment of Linear Friction Welded Ti-6Al-4V Under Fatigue Loading," University of Birmingham, 2016.

[4] American Society for Testing and Materials and National Aeronautics and Space Administration, *Fracture Toughness Testing and Its Applications*. American Society for Testing and Materials, 1965.

[5] British Standards Institute, "Guide to methods for assessing the acceptability of flaws in metallic structures," BS-7910:2019, 2019.

E.7 Fracture Surfaces

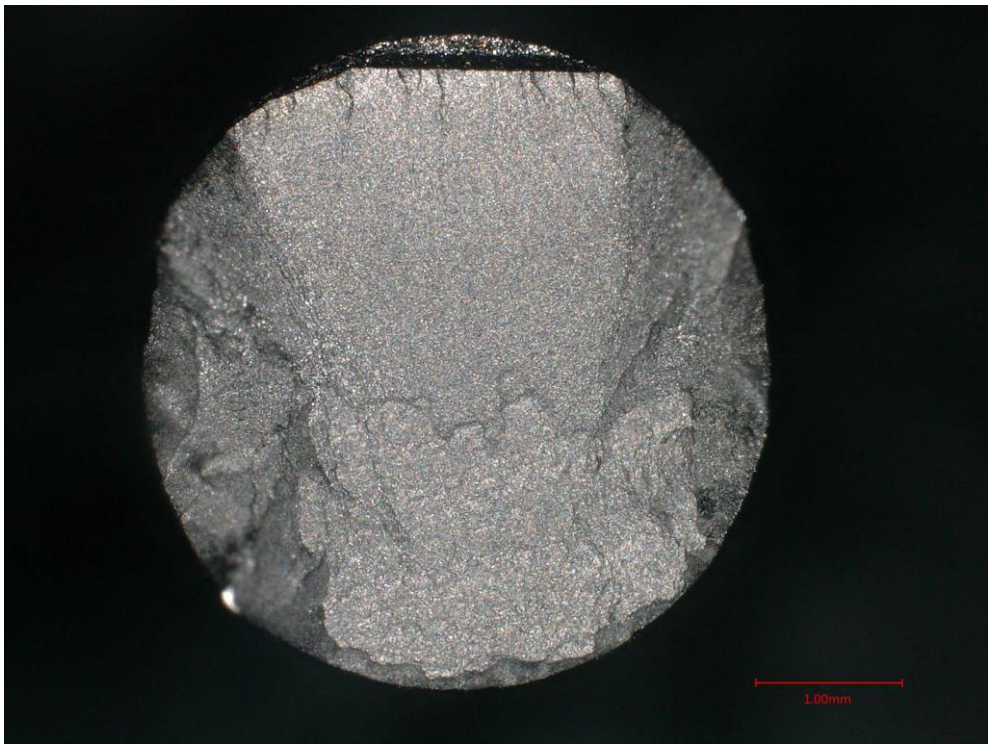

Figure E.20 Optical macrograph of the fracture surface of HF002.

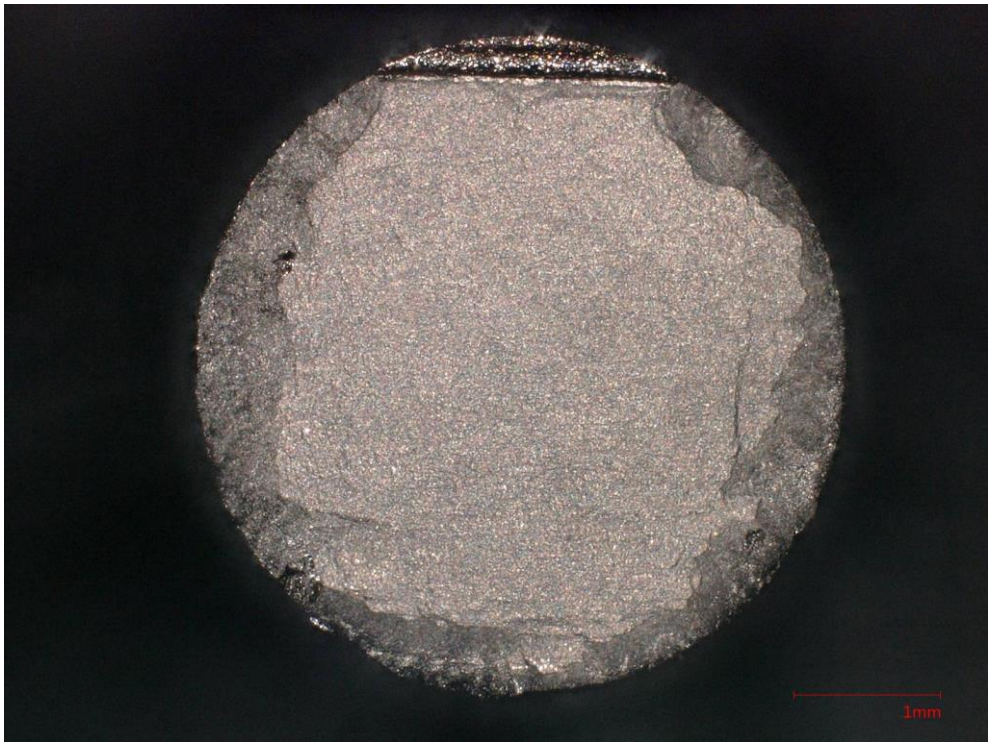

Figure E.21 Optical macrograph of the fracture surface of HF003.

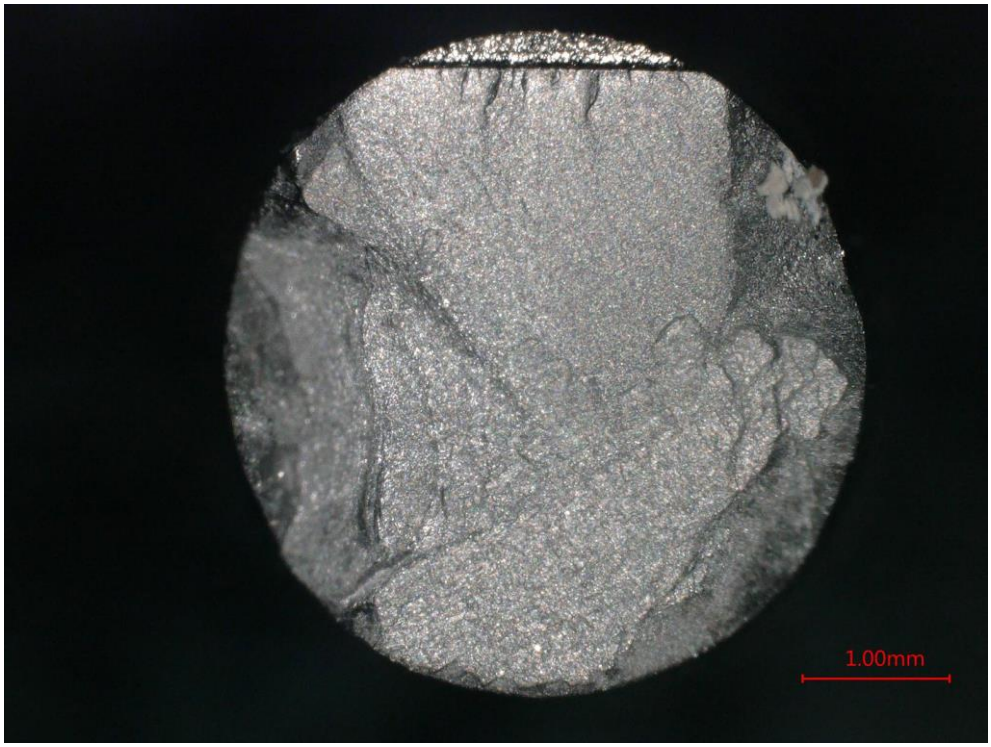

Figure E.22 Optical macrograph of the fracture surface of HF005.

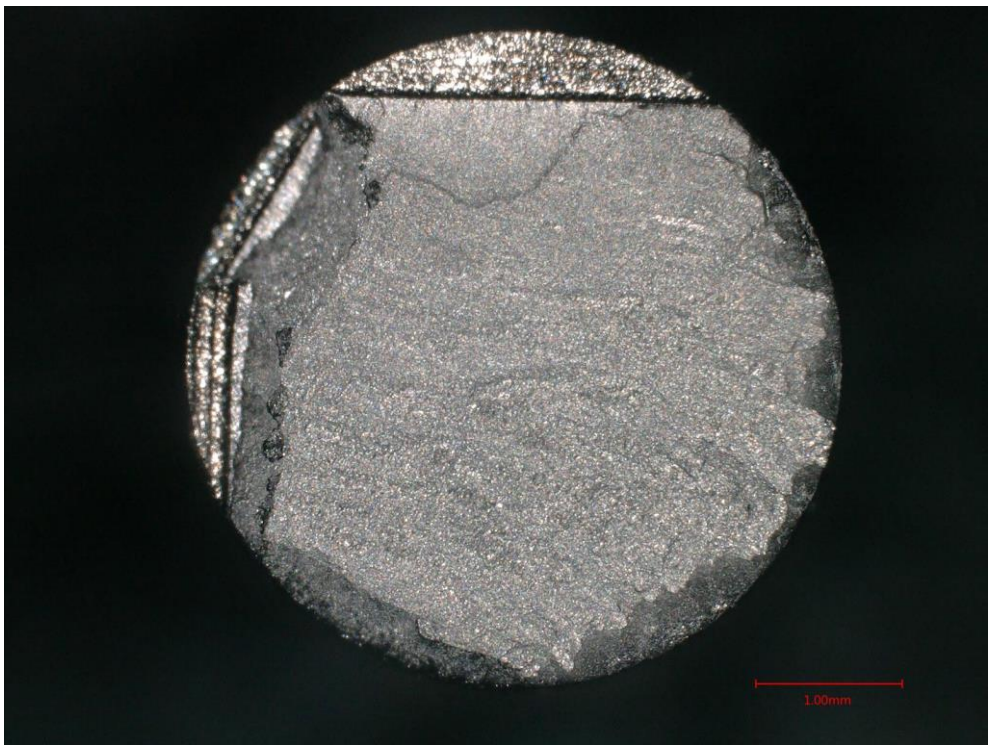

Figure E.23 Optical macrograph of the fracture surface of HF007.

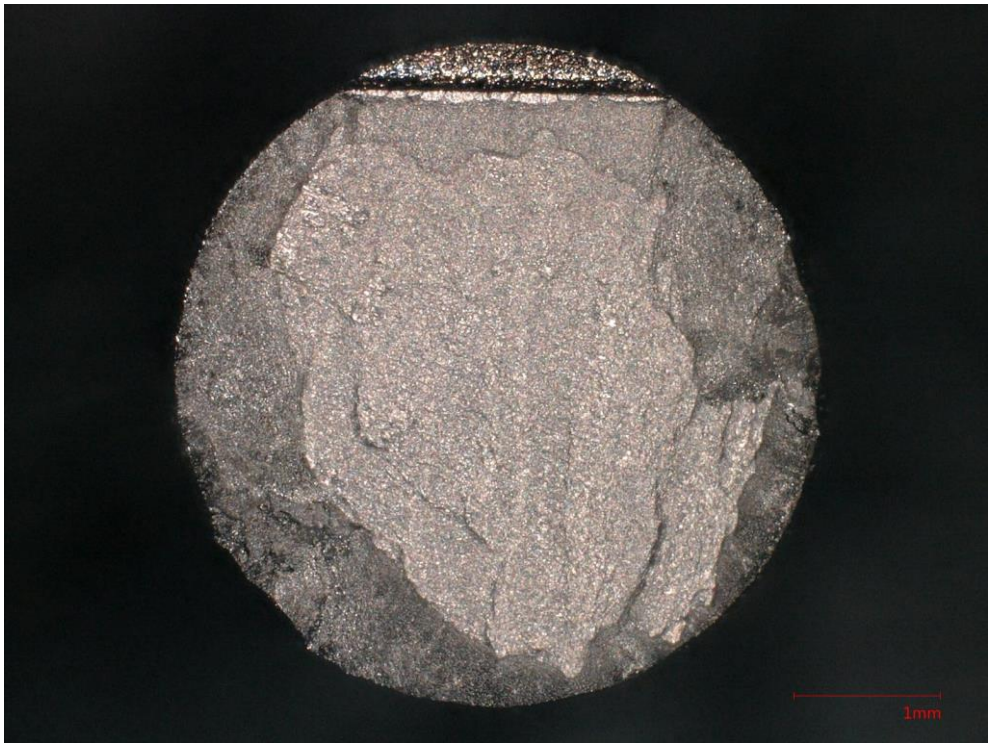

Figure E.24 Optical macrograph of the fracture surface of HF012.

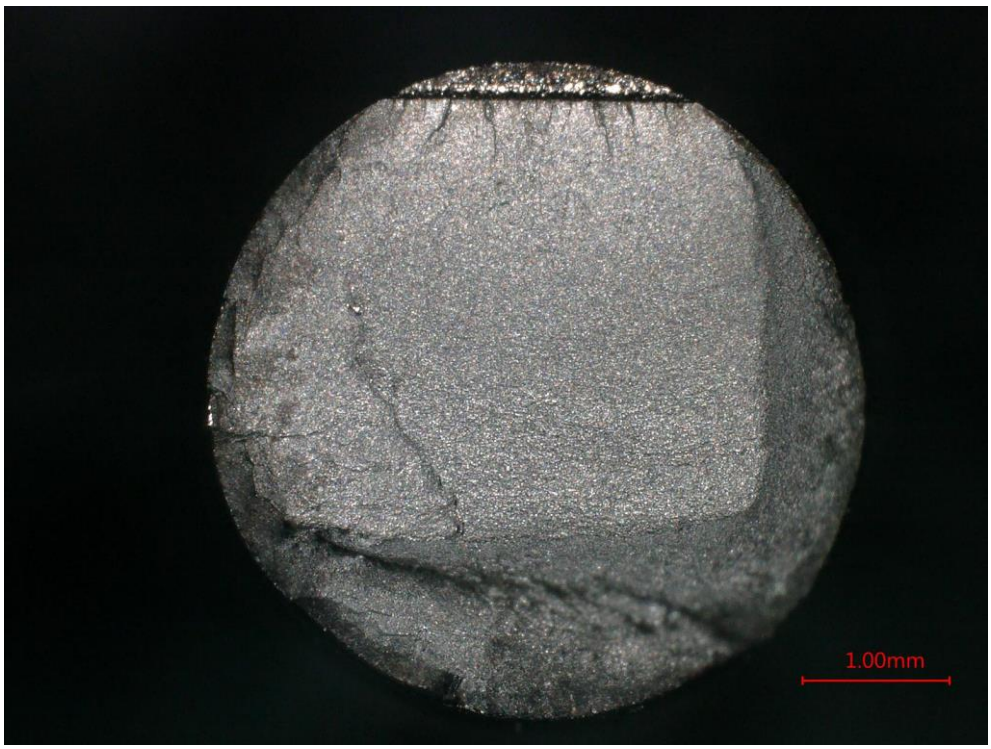

Figure E.25 Optical macrograph of the fracture surface of HF013.

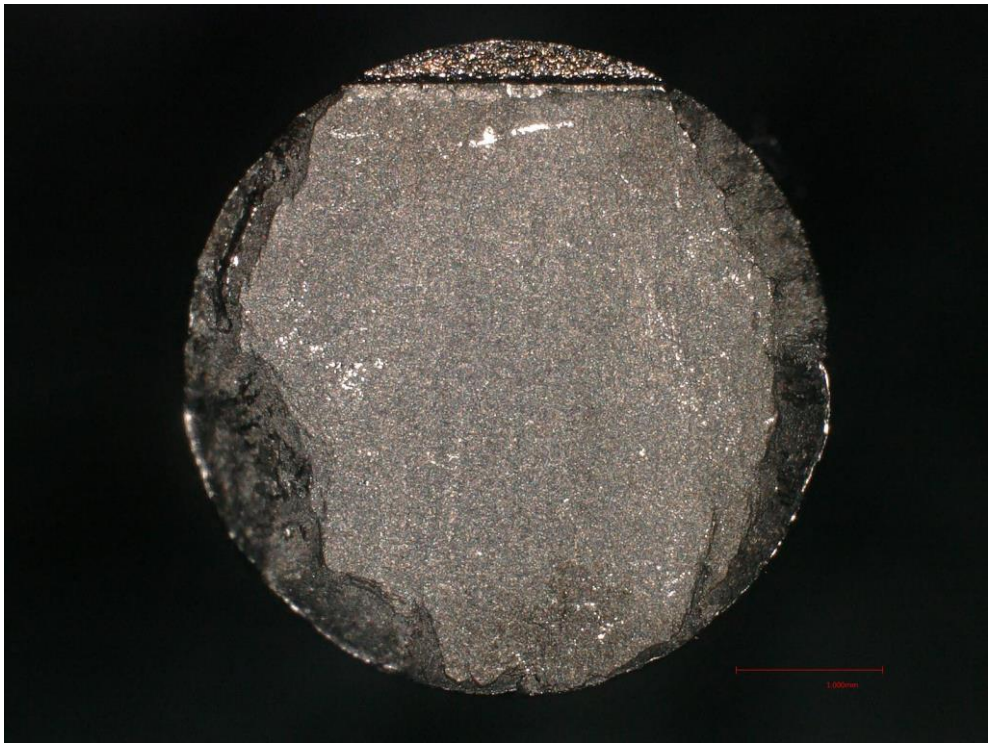

Figure E.26 Optical macrograph of the fracture surface of HF015.

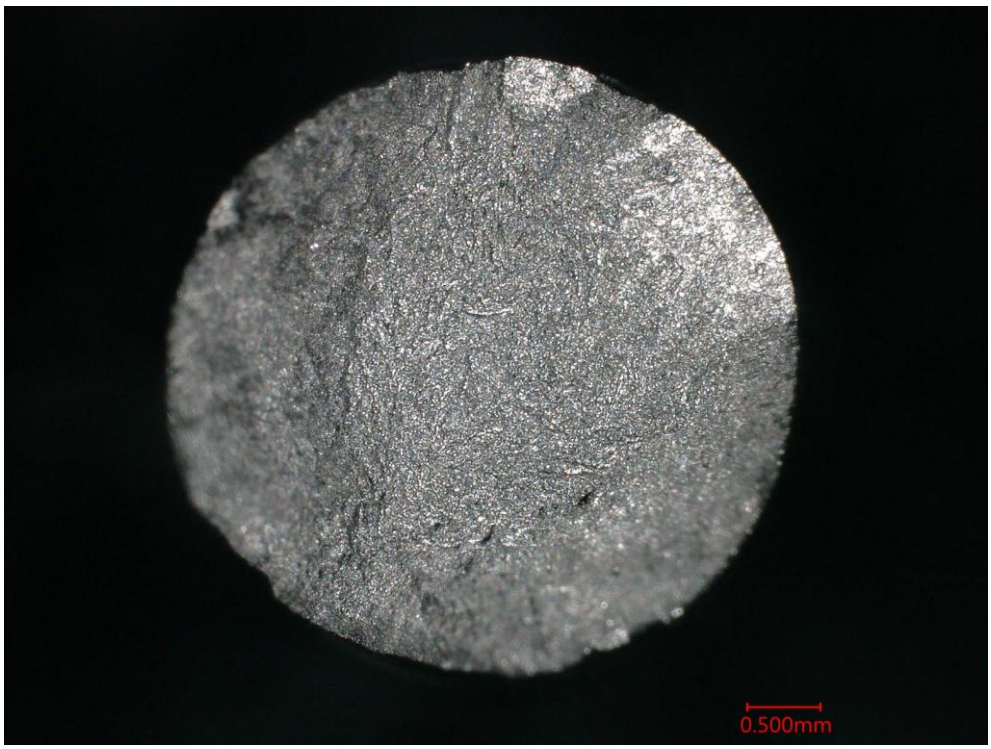

Figure E.27 Optical macrograph of the fracture surface of HF016.

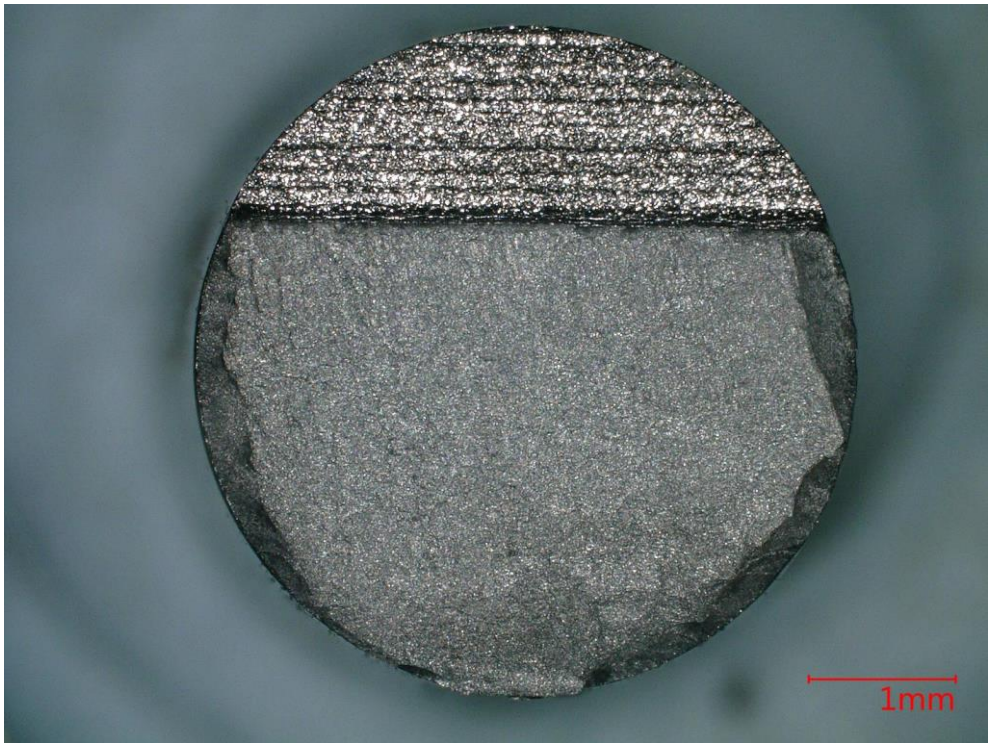

Figure E.28 Optical macrograph of the fracture surface of HF018.

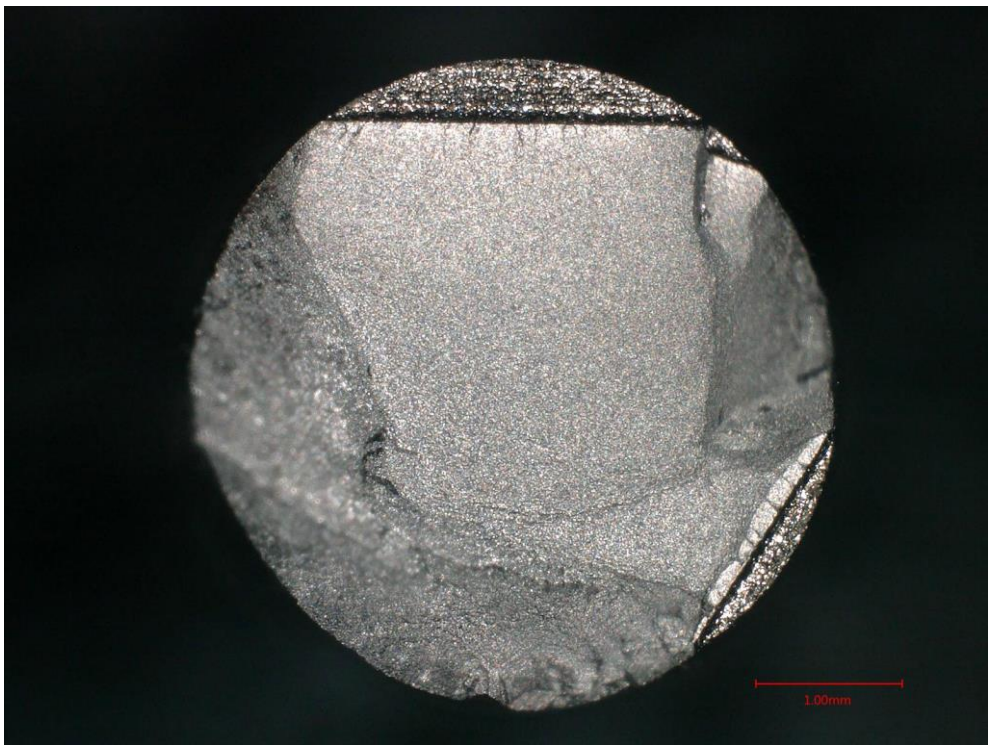

Figure E.29 Optical macrograph of the fracture surface of HF020.

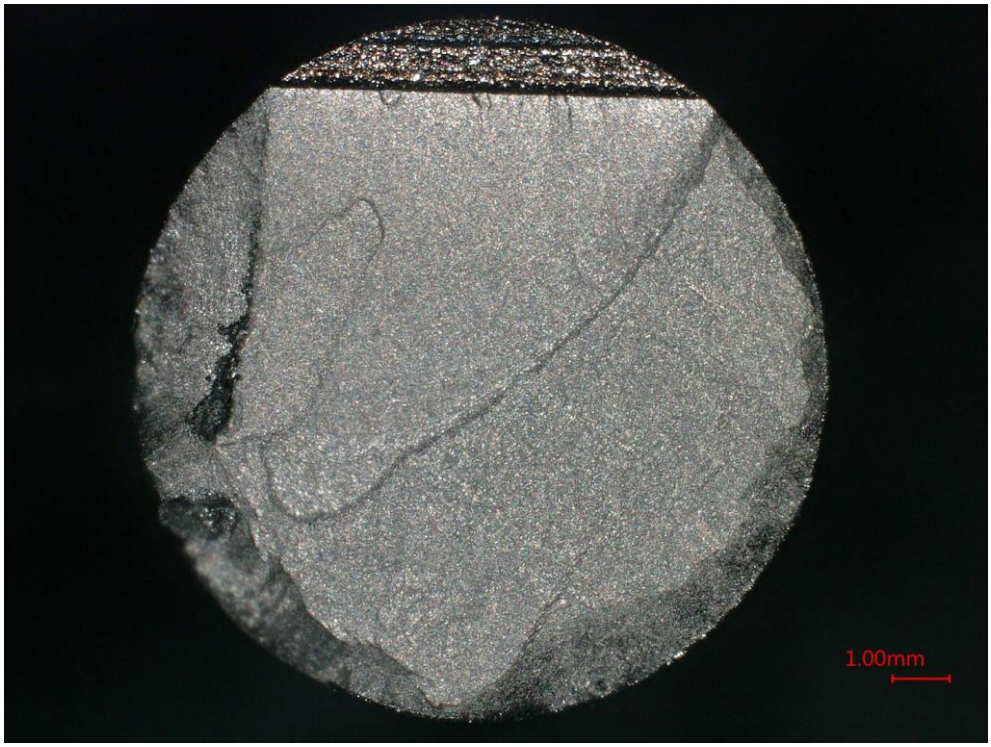

Figure E.30 Optical macrograph of the fracture surface of HF023.

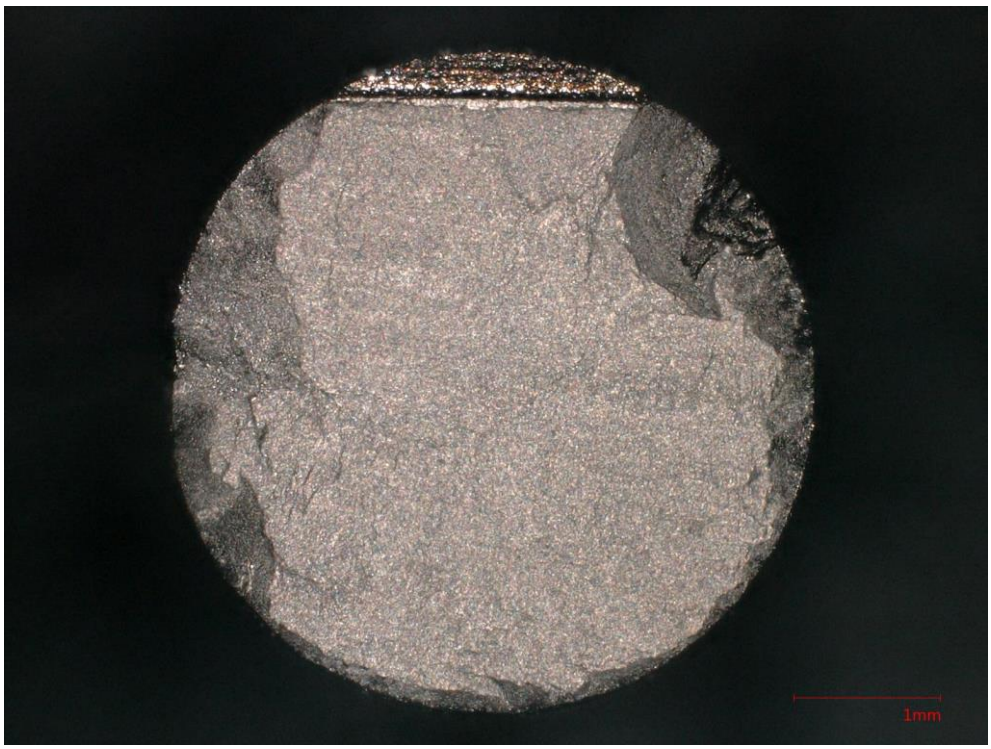

Figure E.31 Optical macrograph of the fracture surface of HF025.

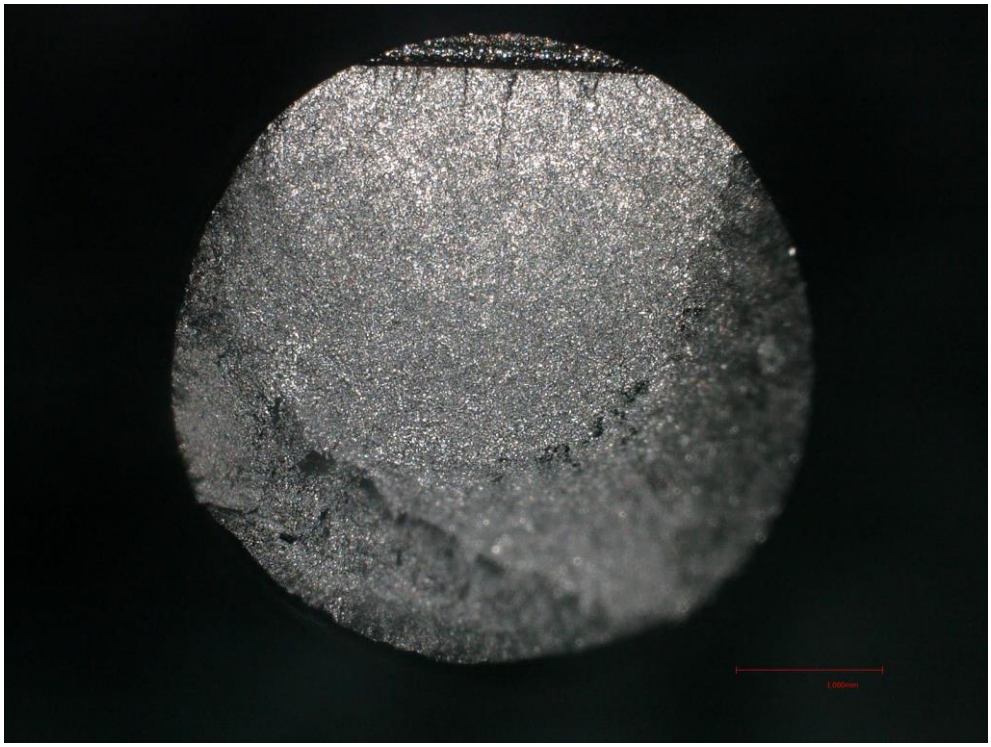

Figure E.32 Optical macrograph of the fracture surface of HF028.

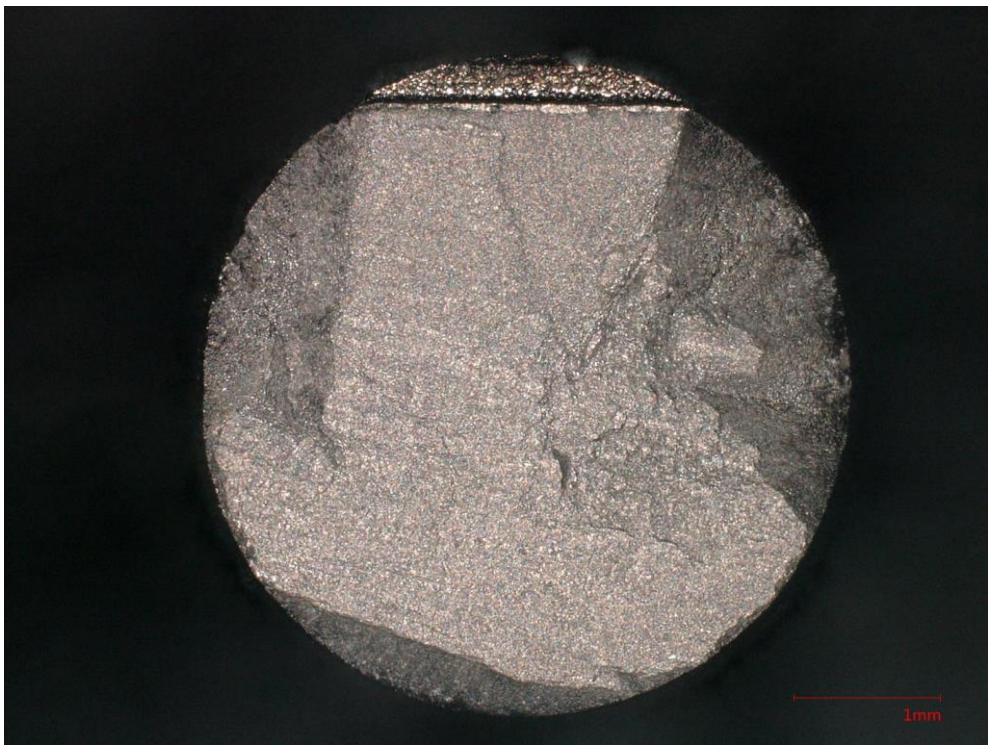

Figure E.33 Optical macrograph of the fracture surface of HF030.